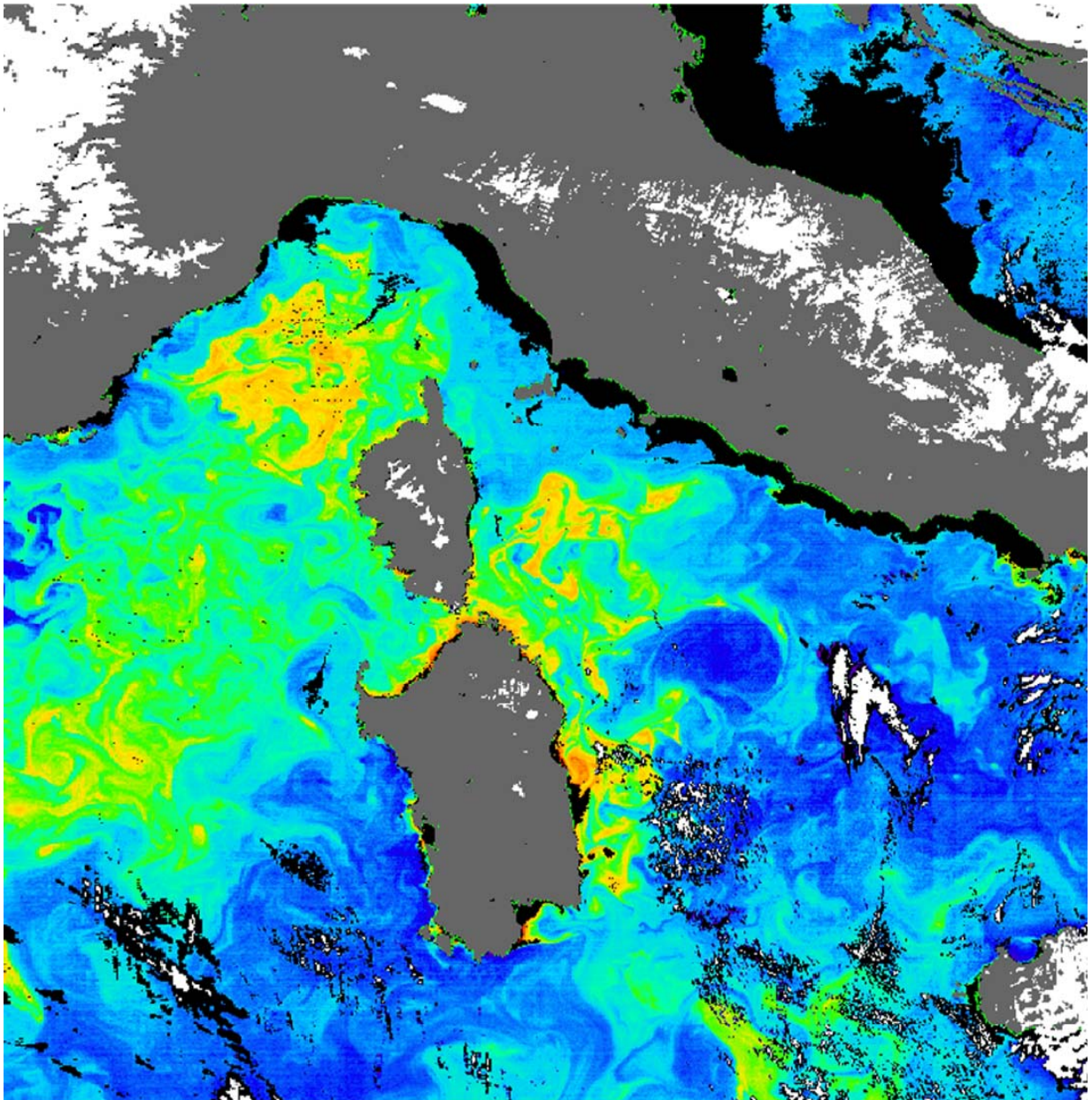


— MERIS ATBD 2.7 —
Atmospheric Correction of the MERIS observations Over
Ocean Case 1 waters

D. Antoine & A. Morel

LABORATOIRE D'OCÉANOGRAPHIE DE VILLEFRANCHE

*Issue 5, revision 1
July 2011*



Pigment distribution derived from MERIS over the Mediterranean Sea.

Table of contents

1	INTRODUCTION	1
2	OVERVIEW	1
2.1	WHAT IS THE OBJECTIVE OF THE ATMOSPHERIC CORRECTION ALGORITHM?	1
2.2	THE PRINCIPLE OF “ATMOSPHERIC CORRECTIONS”	2
2.3	ACCURACY NEEDED FOR ATMOSPHERIC CORRECTIONS.	2
3	ALGORITHM DESCRIPTION	8
3.1	THEORETICAL DESCRIPTION	8
3.1.1	<i>Physics of the problem</i>	8
3.1.1.1	Simulating the radiative transfer	8
3.1.1.2	Signal decomposition	10
3.1.1.3	Accounting for multiple aerosol scattering.	11
3.1.1.4	The algorithm	12
3.1.1.4.1	Computation of the ratio $[\rho_{\text{path}} / \rho_{\text{r},\tau_{\text{a}}=0}]$ and identification of the actual aerosol.....	12
3.1.1.4.2	The test at 510 nm.....	20
3.1.1.4.3	Computation of the diffuse transmittance, and getting the water-leaving radiance	23
3.1.1.4.4	Retrieval of the aerosol optical thickness, τ_{a}	25
3.1.1.4.5	Additional steps	25
3.1.1.5	Implementation / test of the algorithm.	25
3.1.1.5.1	Aerosols over the ocean.	25
3.1.1.5.2	Conditions selected for simulating radiative transfer in the atmosphere.....	26
3.1.1.5.2.1	The “standard” atmospheric vertical structure.....	26
3.1.1.5.2.2	Peculiar aerosol vertical repartitions.....	27
3.1.1.5.2.3	Aerosol models and their optical properties.	27
3.1.1.5.2.4	Generating the lookup tables (LUTs)	33
3.1.1.5.3	Test in “standard” conditions (the “standard” set of aerosol assemblages).....	33
3.1.1.5.3.1	Estimation of the path reflectance	33
3.1.1.5.3.2	Retrieval of the aerosol optical thickness	34
3.1.1.5.3.3	Impact on the pigment index retrieval	35
3.1.1.5.4	Test with absorbing aerosols	37
3.1.1.6	Sensitivity studies.....	38
3.1.1.6.1	Vertical distribution of aerosols / “special” aerosols	38
3.1.1.6.2	Atmospheric pressure.....	41
3.1.1.6.3	Inland waters.....	43
3.1.1.6.4	Wind speed	45
3.1.1.6.5	High aerosol optical thickness	47
3.1.1.6.6	Stratospheric aerosols, thin cirrus clouds.....	48
3.1.1.7	Ancillary data and aerosol climatology.....	52
3.1.1.7.1	Ancillary data: identification and accuracy requirements	52
3.1.1.7.1.1	Extraterrestrial irradiance	52
3.1.1.7.1.2	Wind speed at the sea level.....	52
3.1.1.7.1.3	Atmospheric pressure at the sea level.....	52
3.1.1.7.1.4	Total ozone amount	52
3.1.1.7.1.5	Relative humidity	53
3.1.1.8	Remaining issues.....	53
3.1.1.8.1	Bidirectionality of the oceanic reflectance and the diffuse transmittance.....	53
3.1.1.8.2	The “mixing ratio”	53
3.1.2	<i>Mathematical description of the algorithm</i>	54
3.1.3	<i>Error budget estimates</i>	58
3.1.3.1	Are the aerosol models representative of reality?	58
3.1.3.2	Other possible error sources	59
3.1.3.2.1	Aerosol model identification / Correctness of the test at 510 nm.....	59
3.1.3.2.2	Interpolation within LUTs	59
3.1.3.2.3	Estimation of the diffuse transmittance, $t_{\text{d}}(\theta_{\text{v}},\lambda)$	59
3.1.3.2.4	Uncertainties in the ozone concentration	61
3.1.3.2.5	The effect of whitecaps	61

	ii
3.1.3.2.6 Instrumental errors. 1.: stray light.....	64
3.1.3.2.7 Instrumental errors. 2.: calibration errors.....	65
3.1.3.2.8 Residual sun glint.....	68
3.1.3.2.9 Gaseous absorption.....	69
3.1.3.2.10 Non-identified Case 2 waters.....	69
3.1.3.2.11 Polarisation.....	73
3.1.3.3 Expected global accuracy.....	73
3.2 PRACTICAL CONSIDERATIONS.....	74
3.2.1 <i>Lookup tables</i>	74
3.2.2 <i>Exception handling</i>	74
3.2.3 <i>Outputs of the atmospheric correction</i>	74
4 ASSUMPTIONS, CONSTRAINTS, AND LIMITATIONS.....	75
4.1 ASSUMPTIONS.....	75
4.2 CONSTRAINTS, LIMITATIONS.....	75
5 REFERENCES.....	77
6 SYMBOLS.....	81
7 APPENDIX: PUBLICATIONS.....	84

Foreword

This Algorithm Theoretical Basis Document (MERIS ATBD 2.7) describes the present advancement and implementation of the algorithm for atmospheric correction of MERIS observations over oceanic Case 1 waters.

The present document must be considered as a snapshot of the algorithm state; it does not mean that the algorithm cannot be further improved as compared to what is presented here.

This ATBD version 5.1 is a minor update of version 5.0 (December 2005), which was itself a major update of version 4.1 (18 February 2000). The latter was peer-reviewed before being made available on the ENVISAT web pages.

In parallel to the generation of this ATBD, several papers have been published in the open literature. These publications describe in details

- (1) The theoretical work upon which the proposed algorithm is based:
Antoine and Morel, 1998, Relative importance of multiple scattering by air molecules and aerosols in forming the atmospheric path radiance in the visible and near infrared parts of the spectrum, *Applied Optics* 37, 2245-2259.
- (2) The algorithm itself and its initial implementation:
Antoine and Morel, 1999, A multiple scattering algorithm for atmospheric correction of remotely-sensed ocean colour (MERIS instrument): principle and implementation for atmospheres carrying various aerosols including absorbing ones, *International Journal of Remote Sensing*, 20, 1875-1916.
- (3) The test of the technique for detecting desert dust over the ocean:
Nobileau, D. and D. Antoine, 2005, Detection of blue-absorbing aerosols using near infrared and visible (ocean colour) remote sensing observations. *Remote Sensing of Environment*, 95, 368-387.
- (4) The application of the above technique to the Mediterranean Sea:
Antoine D. and D. Nobileau, (2006). Recent increase of Saharan dust transport over the Mediterranean Sea, as revealed from ocean color satellite (SeaWiFS) observations. *Journal of Geophysical Research, Atmosphere*, 111, D12214, doi:10.1029/2005JD006795
- (5) Validation of MERIS atmospheric correction over the BOUSSOLE site:
Antoine, D., F. D'Ortenzio, S. B. Hooker, G Bécu, B. Gentili, D. Tailliez, and A. J. Scott (2008), Assessment of uncertainty in the ocean reflectance determined by three satellite ocean color sensors (MERIS, SeaWiFS and MODIS-A) at an offshore site in the Mediterranean Sea (BOUSSOLE project), *Journal of Geophysical Research*, 113, C07013, doi:10.1029/2007JC004472

These five publications are provided in Appendix.

Villefranche sur Mer, Monday, 18 July 2011

!!!! Warning !!!!

The performance tests that are presented in sections

- 3.1.1.5.3 “Tests in standard conditions”
- 3.1.1.6 “Sensitivity studies”
- 3.1.3.2 “Other possible error sources”

are all based on the initial implementation of the MERIS atmospheric correction algorithm (*i.e.*, ATBD 4.1, 18 February 2000). These tests remain valid as far as the main difference between ATBD 4.1 and the present ATBD 5.1 lies in the selected set of aerosol models. The behaviour of the new implementation is essentially the same since the structure of the algorithm has not changed.

In particular, the sensitivity studies (3.1.1.6) refer to “standard aerosols” models that do no longer exist in the MERIS lookup tables (the urban model and the dust model of Schütz, 1980).



1 Introduction

The feasibility of deriving the chlorophyll concentration from its influence on the spectral composition of the light backscattered by the upper oceanic layers (the "ocean colour") was demonstrated by Clarke *et al.* (1970). Following this pioneer investigation, the Coastal Zone Colour Scanner (CZCS) was developed and launched by NASA in November 1978, onboard the Nimbus-7 platform (Hovis *et al.*, 1980; Gordon *et al.*, 1980). This instrument has repeatedly observed the world ocean during 8 years (1979-1986), generating the first picture of the algal biomass distribution over the world ocean (Feldman *et al.*, 1989). Thanks to this experimental sensor, the capability of such a remote-sensing technique is now definitely proven. The success as well as the limitations and deficiencies of the CZCS, and the fact that it stopped its activity in 1986, led to the definition of a new generation of ocean colour sensors, supported by the JGOFS (Joint Global Ocean Flux Study) community and designed to fill the need for a global, repetitive and operational coverage of the oceanic algal biomass.

The procedures used to extract the marine signal from the signals measured by the remote sensor in various spectral bands are collectively called the "atmospheric correction". The purposes of this document are (1) to propose a structure for the MERIS atmospheric correction algorithm over the open ocean (case 1 waters) and (2) to identify the studies that could be carried out in view of refining the algorithms. The theoretical work upon which the proposed algorithm is based is summarised in the present ATBD (section 3.1.1), and it is treated in details elsewhere (Antoine and Morel, 1998, *Applied Optics* 37, 2245-2259, given in Appendix 1). The algorithm itself and its implementation are fully devised in another paper (Antoine and Morel, 1999, *International Journal of Remote Sensing*, 20, 1875-1916). A third paper deals with some tests of the algorithm for detecting absorbing aerosols over the ocean (Nobileau, D. and D. Antoine, 2005, Detection of blue-absorbing aerosols using near infrared and visible (ocean colour) remote sensing observations. *RemoteSensing of Environment*, 95, 368-387).

2 Overview

2.1 What is the objective of the atmospheric correction algorithm?

The atmospheric correction (its principles are recalled below) should allow the "water-leaving radiances" to be retrieved at each pixel of a MERIS scene, from the total radiance received by the instrument. At the top of atmosphere level, the "marine radiances" are those radiances originating from photons that have crossed the atmosphere down to the ocean and then have twice crossed the air-sea interface before reaching the sensor after a second atmospheric travel. These radiances carry information about the optical properties of the oceanic upper layers, and are related to the water-leaving radiances at the zero level, through a diffuse transmittance term.

The water-leaving radiances are combined into the "bio-optical algorithms", which allow the near-surface pigment (chlorophyll) concentration ($\text{Chl}_{\langle\text{sat}\rangle}$) to be computed. $\text{Chl}_{\langle\text{sat}\rangle}$ is, for instance, the parameter of interest for the biogeochemical study of the carbon fluxes within the ocean interior (quantification and description of $\text{Chl}_{\langle\text{sat}\rangle}$ distributions, primary production estimation, ecosystem modelling...), and is needed for other purposes (heating rate of the mixed layer, description of upper ocean dynamics, fisheries optimization...).



2.2 The principle of “atmospheric corrections”

When an ocean-colour sensor measures the radiance backscattered by the ocean-atmosphere system, it receives in the visible part of the spectrum a signal that is largely dominated by the “atmospheric path radiance”. This radiance originates from photons scattered by air molecules and/or aerosols, which can also have been reflected at the sea surface, but have never penetrated the ocean. In the most favorable conditions of observation (clear atmosphere, small sun-zenith angle and favorable viewing angle), the water-leaving radiance represents only about 10% of the total radiance, and have then to be properly extracted (from the accuracy of this extraction depends the quality of the end-product of ocean-colour data processing, *i.e.*, the near-surface chlorophyllous pigment concentration).

Under the assumption of separability of radiances, the determination of the radiances originating from molecular scattering (Rayleigh scattering) is easily handled, as only the illumination and observation conditions have to be known, even if a precise knowledge of atmospheric pressure (and wind speed) at the sea surface is also needed for accurate calculations. The central problem of atmospheric correction lies in the estimation of the radiances due to aerosol scattering. Indeed, the aerosol distribution (along the vertical as well as through the field of view), and the aerosol optical properties are not known when processing an ocean colour scene.

Experience has been acquired in this domain since the launch of the CZCS, and even if the new ocean-colour sensors have different, improved, characteristics, the work achieved with the CZCS provides guidelines to prepare the new atmospheric correction algorithm. Both the limited number of channels and the relatively poor radiometric sensitivity of the CZCS led to the development of specific correction schemes designed partly to remedy to these weaknesses. These schemes are obsolete for processing data from MERIS, to the extent that increased radiometric sensitivity and additional channels in the near-IR spectral region considerably reduce the limitations encountered with the CZCS. The basic principle of the atmospheric corrections is to gain information about aerosol thanks to the radiances measured in near-IR bands (> 700 nm, where the water-leaving radiances are zero over case 1 waters), and to extrapolate this knowledge toward the visible domain.

2.3 Accuracy needed for atmospheric corrections.

Radiometric characteristics and calibration of MERIS are defined in terms of reflectances; radiances at the TOA level are accordingly converted into reflectances through (see Table of symbols and definitions)

$$\rho(\lambda, \theta_s, \theta_v, \Delta\phi) = \pi L(\lambda, \theta_s, \theta_v, \Delta\phi) / E_s(\lambda) \mu_s \quad (1)$$

where $E_s(\lambda)$ is the extraterrestrial irradiance for the wavelength in question, μ_s is the cosine of the solar zenith angle θ_s , θ_v is the satellite viewing angle, and $\Delta\phi$ is the azimuth difference between the sun-pixel and pixel-sensor half vertical planes. Angular dependencies will be thereafter omitted for the sake of clarity.



Table 2.1 shows the radiometric characteristics of MERIS, compared with those of the CZCS and three future instruments, SeaWiFS, POLDER and MODIS (for these last 3 instruments, the central wavelength for some bands is slightly different from that of MERIS, at ± 5 nm). These values, given in terms of reflectance, clearly show the increase in radiometric performance, from the CZCS to the new generation instruments.

Band (λ), nm	NEΔρ					[ρ _w] _N
	CZCS [‡]	SeaWiFS [‡]	POLDER [•]	MERIS	MODIS [‡]	
412		0.00068		0.000427	0.00018	0.055
443	0.0011	0.00043	0.00036	0.000241	0.00016	0.035
560	0.00064	0.00027	0.00014	0.000201	0.00010	0.004
670	0.00051	0.00023	0.00020	0.000104	0.00004	0.0004
709				0.000143		0
778				0.000143	0.000085	0
865		0.00015	0.00016	0.000201	0.000076	0

[‡]: taken from Gordon (1997)

[•]: taken from Deschamps *et al.* (1994)

Table 2.1: comparison of the radiometric characteristics of MERIS and other instruments. Approximate values of ρ_w are given for a chlorophyll concentration of 0.03 mg Chl m⁻³ (see also Fig. 2.1 (a)).

Water-leaving reflectances, ρ_w, are obtained after the measured total reflectances have been corrected for atmospheric effects. These water-leaving reflectances are related to the bio-optical state of the water body, through the ratio of the backscattering coefficient to the absorption coefficient, [b_b/a] (see Morel and Gentili, 1991, 1993, 1996)

$$\rho_w(\lambda, \theta_s, \theta', \Delta\phi) = \pi t_{\theta_s}(\lambda) \Re(\theta') \frac{f(\lambda, \theta_s)}{Q(\lambda, \theta_s, \theta', \Delta\phi)} \left[\frac{b_b(\lambda)}{a(\lambda)} \right] \quad (2)$$

The ratio [b_b/a] can be similarly related to the normalised water-leaving reflectance, [ρ_w]_N. This reflectance [ρ_w]_N is defined (Gordon and Clark, 1981) as the reflectance at nadir (θ_v = 0), for a sun at zenith (θ_s = 0), and without atmosphere (t_{θ_s} = 1). The relationships writes (see Morel and Gentili, 1996)

$$[\rho_w]_N(\lambda) = \pi \Re_0 \frac{f_0(\lambda)}{Q_0(\lambda)} \left[\frac{b_b(\lambda)}{a(\lambda)} \right] \quad (3)$$

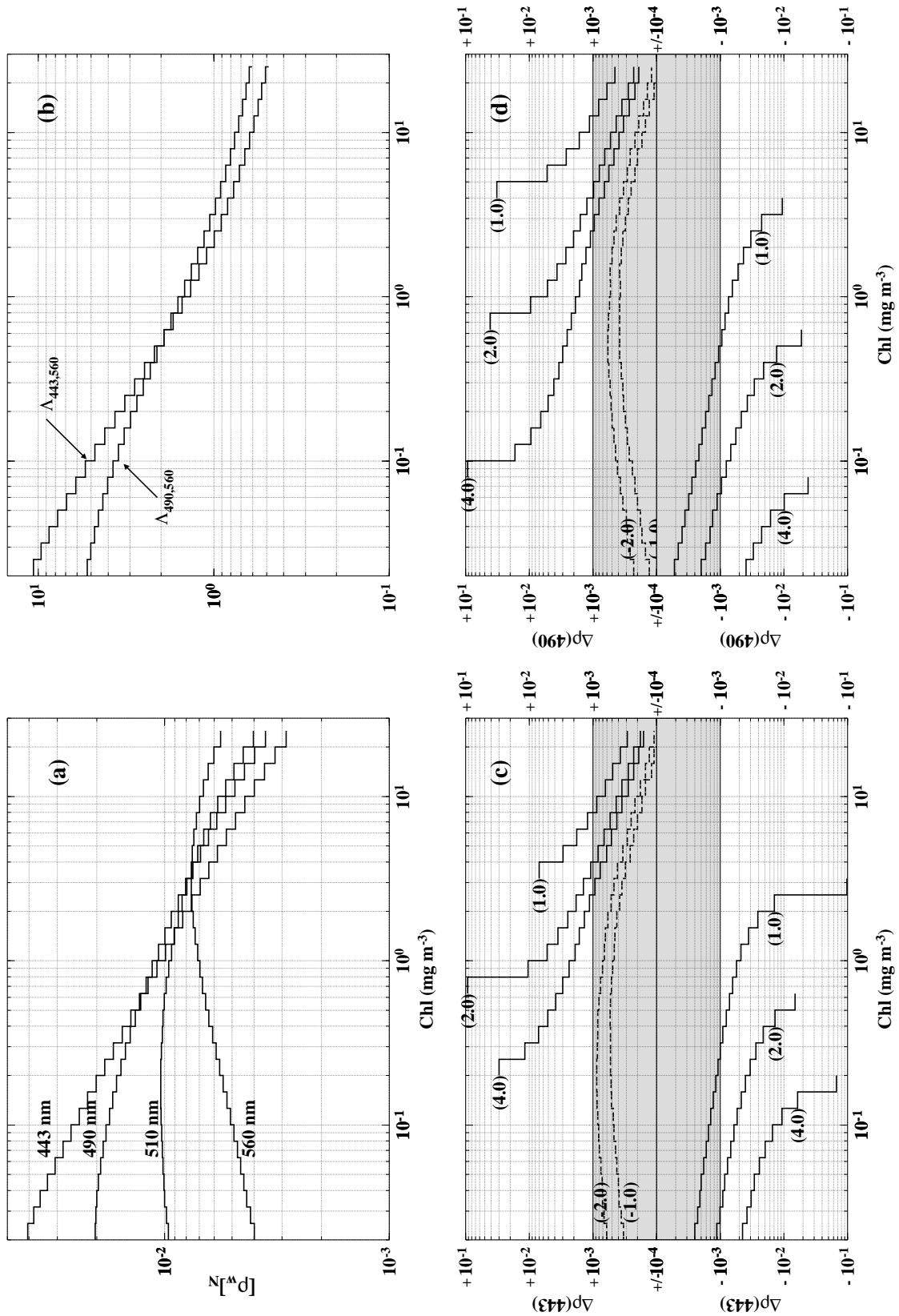


Figure 2.1: (a) Normalised water-leaving reflectances (Eq. (3)), plotted as a function of chlorophyll concentration (Chl), and for the wavelengths indicated. The steps in the curves correspond to increments of 0.1 in $\log(\text{Chl})$. (b) ratio of (b_p/a) at 443 or 490 nm to (b_p/a) at 560 nm ($\Lambda_{443,560}$ and $\Lambda_{490,560}$). (c) Allowable error in atmospheric correction at 443 nm, $\Delta\rho(443)$ (i.e., the maximum error above which a wrong chlorophyll concentration is retrieved, corresponding



to the previous class). The error $\Delta\rho(443)$ is calculated by assuming several ratios for $[\Delta\rho(443) / \Delta\rho(560)]$, as indicated (see text). The long-dashed curves are for errors of opposite signs at 443 and 560 nm. The shaded area is for errors within $\pm 1 \cdot 10^{-3}$. (d) as in (b), but for the wavelength couple 490-560.

where the subscripts 0 indicate that the corresponding quantities are for $\theta_s = \theta_v = 0$. In Eq. (3), the product $(\pi \mathfrak{R}_0 (f_0/Q_0))$ is a constant (if the dependence of \mathfrak{R}_0 upon wind speed is ignored), so that $[\rho_w]_N$ can be considered as an inherent optical property of the medium.

The MERIS instrument has been designed to allow, in principle, the detection of 10 classes of chlorophyll concentration, (Chl), within each of the 3 orders of magnitude between 0.03, 0.3, 3, and 30 mg Chl m^{-3} (*i.e.*, a total of 30 classes). These classes are regularly distributed according to a constant logarithmic increment of 0.1. Shifting from one class to the next (previous) one corresponds to a change in (Chl) by a factor $10^{\pm 0.1}$ (*i.e.*, +25% or -20%).

A first requirement for atmospheric correction is to allow 30 values of $[\rho_w]_N$ to be discriminated at any wavelength where the pigment concentration influences the reflectance. The corresponding changes in $[\rho_w]_N$, as computed through Eq. (3), are displayed in Fig. 2.1(a) for several wavelengths, which are possibly used for retrieving (Chl). At 443 nm, the changes in $[\rho_w]_N$ are of about $2.5 \cdot 10^{-3}$ when (Chl) < 0.1 mg m^{-3} , of about $1 \cdot 10^{-3}$ when (Chl) ~ 1 mg m^{-3} , and about $5 \cdot 10^{-4}$ for higher concentrations. At 490 nm, the changes are steadily of about $5-7 \cdot 10^{-4}$, except when (Chl) < 0.1 ; they are of about $2 \cdot 10^{-4}$ for these low concentrations. At 560 nm, the changes in $[\rho_w]_N$ are of about $2 \cdot 10^{-4}$ whatever (Chl). These values remain about the same when the constraints on θ_s , θ_v , and t_{θ_s} are relaxed, that is when ρ_w is examined for other geometries, instead of $[\rho_w]_N$, and they represent the desired discriminative skill of the atmospheric correction at these wavelengths. The change in $[\rho_w]_N$ to be detected is smaller at 560 nm than it is at 443 nm or at 490 nm, and this more stringent condition was used to specify the noise equivalent reflectances for all wavelengths of the MERIS instrument ($Ne\Delta\rho, < 2 \cdot 10^{-4}$; see Table 2.1). It should be reminded that this skill in discrimination, expressed in terms of reflectance changes, does not prejudice of the absolute accuracy of the instrument, and therefore of the correct retrieval of the true values of the reflectance.

It is now assumed that (Chl) is calculated, as usual, with a function Φ of the ratio of $[b_b/a]$ at two wavelengths, denoted A_{λ_1, λ_2} , which is used as an index of the bio-optical state.

$$\text{Chl} = \Phi \left(\left[\frac{b_b}{a}(\lambda_1) \right] / \left[\frac{b_b}{a}(\lambda_2) \right] \right) = \Phi(A_{\lambda_1, \lambda_2}) \quad (4)$$

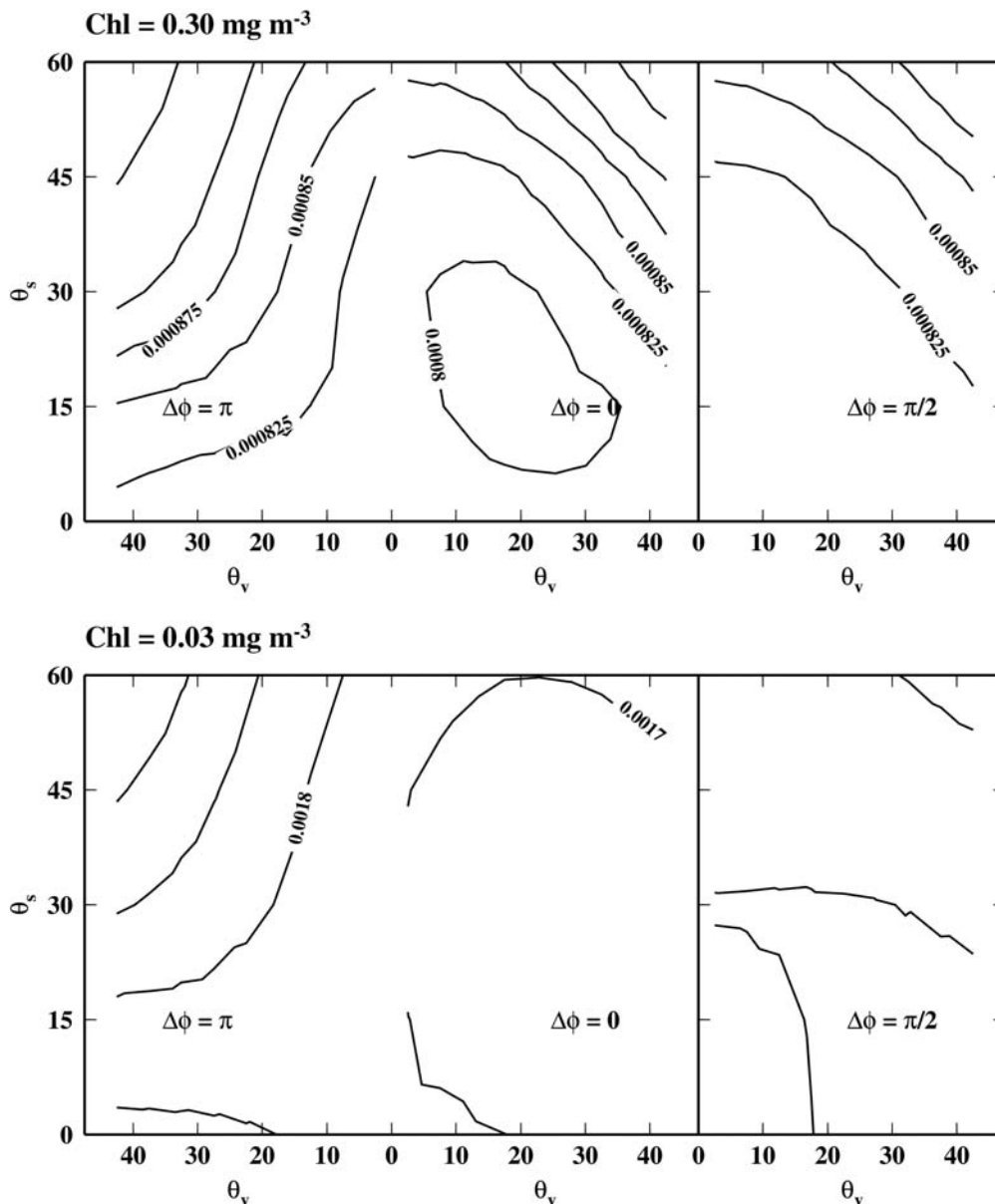


Figure 2.2. The numbers which are contoured here represent 5 percent of the water-leaving reflectance at 443 nm, shown as a function of the solar zenith angle and viewing angle. Left part: antisun and sun half-vertical planes. Right part: perpendicular plane. Upper and lower panels: chlorophyll concentration is 0.3 and 0.03 mg Chl m^{-3} , respectively. The influence of the solar elevation on the diffuse reflectance of the ocean is taken into account (Morel *and* Gentili, 1991), as well as the anisotropy of the radiance field emerging from the ocean (Morel and Gentili, 1993).

A second requirement for atmospheric correction is that it must be accurate enough to allow 30 (Chl) values to be discriminated. In other words, 30 values of A_{λ_1, λ_2} must be discriminated between 0.03 and 30 mg (Chl) m^{-3} . The A ratio is displayed in Fig. 2.1(b) as a function of (Chl), and for several couples of wavelengths. For a given geometry, it is related to $([\rho_w]_N(\lambda_1) / [\rho_w]_N(\lambda_2))$ through the values of the (f_0/Q_0) ratio at the two wavelengths. The change in $A_{443,560}$ between adjacent classes of chlorophyll, (ΔA), varies continuously from about 0.9 when (Chl) is 0.03 mg m^{-3} , to 0.1 when (Chl) is 0.3 mg m^{-3} , and to 0.03 when (Chl) is 30 mg m^{-3} .



For the wavelength couple 490-560 nm, and for the same values of (Chl), the changes in $A_{490,560}$ are 0.2, 0.1, and 0.05.

After atmospheric correction, the allowable errors in $[\rho_w]_N(\lambda_1)$ and $[\rho_w]_N(\lambda_2)$ are those that would lead to an error in their ratio A_{λ_1, λ_2} equal, at the most, to ΔA . These errors, denoted $\Delta\rho(\lambda_1)$ and $\Delta\rho(\lambda_2)$, are accordingly computed as

$$\frac{([\rho_w]_N(\lambda_1) + \Delta\rho(\lambda_1))}{([\rho_w]_N(\lambda_2) + \Delta\rho(\lambda_2))} = \frac{[\rho_w]_N(\lambda_1)}{[\rho_w]_N(\lambda_2)} + \Delta A \quad (5)$$

For a given (Chl) class, Eq. (5) can be solved by fixing the relevant ΔA value, by calculating the reflectances $[\rho_w]_N(\lambda_1)$ and $[\rho_w]_N(\lambda_2)$, and by making an assumption about the error ratio $(\Delta\rho(\lambda_1) / \Delta\rho(\lambda_2))$ (in such a way that the number of unknowns is reduced to 1). In the following, λ_1 will be either 443 nm or 490 nm, and λ_2 is 560 nm (*i.e.*, wavelengths possibly used for retrieving (Chl)). Errors at 443 nm and 490 nm are expected to be greater than those at 560 nm, because the accuracy of atmospheric correction may deteriorate when going away from the near infrared (*i.e.*, during the extrapolation toward the visible). The ratios $(\Delta\rho(443) / \Delta\rho(560))$ and $(\Delta\rho(490) / \Delta\rho(560))$ are thus fixed, somewhat arbitrarily, to 4, 2 or 1. It is as well conceivable that errors are of opposite signs at the two wavelengths, so that error ratios of -4 , -2 , and -1 have been also tested.

The acceptable errors $\Delta\rho(443)$ resulting from these computations are displayed in Fig. 2.1(c) as a function of (Chl). They have been computed for each (Chl) class, and for the ΔA values corresponding to an underestimation by one class of concentration. They are at first negative, and then positive after the $A_{443,560}$ ratio becomes lower than the ratio $(\Delta\rho(443) / \Delta\rho(560))$. A symmetrical pattern (*i.e.*, $\Delta\rho$ at first positive and then negative) would have been obtained for errors corresponding to an overestimation by one class of concentration. The acceptable error $\Delta\rho(443)$ is increasing as its ratio to $\Delta\rho(560)$ increases. It is also increasing as the reflectances become closer at 443 and 560 nm (the error is undetermined when both reflectances are equal). The accuracy requirement for atmospheric correction is accordingly not too severe when $\sim 0.3 < (\text{Chl}) < \sim 3 \text{ mg m}^{-3}$; it is always greater than $\pm 1 \cdot 10^{-3}$, and most of the time greater than $\pm 2 \cdot 10^{-3}$ when $\Delta\rho(443)$ and $\Delta\rho(560)$ have the same sign (*i.e.*, about 10% of $[\rho_w]_N(443)$ when $(\text{Chl}) = \sim 0.3 \text{ mg m}^{-3}$). On the contrary, the accuracy requirement is increasingly demanding either for low or for high chlorophyll concentrations, and is between about $\pm 1 \cdot 10^{-3}$ and $\pm 5 \cdot 10^{-4}$, depending on the ratio of errors at 443 and 560 nm. When the signs of the allowable errors $\Delta\rho(443)$ and $\Delta\rho(560)$ are opposite, they always must be below $\pm 1 \cdot 10^{-3}$, and often lower than $\pm 5 \cdot 10^{-4}$ (see the two long-dashed curves in Fig. 2.1(c)). Therefore, an additional constraint on atmospheric correction would be identical signs for $\Delta\rho(443)$ and $\Delta\rho(560)$. Fulfillment of this condition depends upon a correct retrieval of the spectral dependence of aerosol scattering.

When the wavelength couple 490-560 nm is used instead of the couple 443-560 nm (Fig. 2.1(d)), the conclusions about the allowable errors at 490 nm are roughly the same than those for $\lambda = 443$ nm, except for concentrations below about $0.1 \text{ mg (Chl) m}^{-3}$, where the $A_{490,560}$ ratio is less



sensitive to changes in (Chl) than is the ratio $A_{443,560}$ (see Fig. 2.1(b)). The couple 490-560 could prove to be useful, however, for concentrations above about $3 \text{ mg (Chl) m}^{-3}$, where the allowable errors are slightly greater at 490 nm than they are at 443 nm. In addition, when (Chl) is high, the water-leaving reflectance is a little larger at 490 nm than it is at 443 nm.

To sum up, the first requirement (retrieval of 30 reflectance values) requires that atmospheric correction errors be maintained within $\pm 1-2 \cdot 10^{-3}$ at 443 nm, within $\pm 5 \cdot 10^{-4}$ at 490 nm, and within $\pm 2 \cdot 10^{-4}$ at 560 nm. If it is assumed that atmospheric correction errors in the 440-500 nm domain are about twice the errors at 560 nm, the second requirement (discrimination of 30 (Chl) values) requires errors within $\pm 1 \cdot 10^{-3}$ at 443 nm (then $\pm 5 \cdot 10^{-4}$ at 560 nm), or within $\pm 5 \cdot 10^{-4}$ at 490 nm (then $\pm 2 \cdot 10^{-4}$ at 560 nm). When expressed as relative errors, all the above requirements are greater than 1% of the normalised oceanic reflectances at 443 nm (and often 2-5%), except when $(\text{Chl}) > 3 \text{ mg m}^{-3}$. The situation is about the same for the wavelength couple 490-560 nm, except when $\text{Chl} < 0.1 \text{ mg m}^{-3}$ and the $A_{490,560}$ ratio is equal to 1.

Note, finally, that the accuracy requirement for the new generation ocean colour sensors has been also defined as being a 5% accuracy on the reflectance in the 400 nm domain (*e.g.*, Gordon, 1997). The numerical values shown in Fig. 2.2, in the space defined by the solar zenith angle and the viewing geometry, represent five percents of water-leaving reflectances at 443 nm, computed for chlorophyll concentrations of 0.3 and 0.03 mg m^{-3} . The requirement obtained by this way is consistent with the one derived here on the basis of the 30 (Chl) classes to be detected.

3 Algorithm description

3.1 Theoretical description

3.1.1 Physics of the problem

3.1.1.1 Simulating the radiative transfer

The radiant field within the ocean-atmosphere system is described by the radiative transfer equation (RTE), which expresses the propagation of radiance within a medium of known inherent optical properties (Preisendorfer, 1961). For a passive medium (*i.e.*, with no internal source of radiation), this equation accounts for the loss of radiance due to scattering and absorption in the direction of propagation, and for the gain of radiance due to scattering from other directions. The two parameters of this integro-differential equation are the attenuation coefficient and the phase function. Even in the case of a homogeneous medium, there is no analytical solution for this equation (except for very peculiar, simplified, cases). A fortiori, there is no analytical solution for a complex system such as the atmosphere-ocean medium. Only numerical solutions are then possible.

The Monte Carlo technique has been used in the present study. With this method, any composition and vertical structure is possible for the various media, and no simplifying hypothesis is needed. Furthermore, within the Monte Carlo code developed at LOV, photons can be sorted out



with respect to their history (number and type of scattering events), allowing any term to be studied (*i.e.*, radiances due to single or multiple scattering, radiances due to aerosol and/or molecules scattering, direct and diffuse part of the total radiances...).

With the purpose of defining an atmospheric correction scheme, some working conditions are necessary, and the ocean-atmosphere system is to be represented in a simplified manner. Indeed, even if realistic atmospheres can be simulated via the Monte Carlo technique, a simplified, more or less generic, vertical structure has to be defined in view of generalised calculations. Sensitivity studies will be accordingly needed in order to infer the differences caused when the actual conditions differ from those in the standard atmosphere adopted when defining the algorithm (see 3.1.1.6.1).

To generate TOA total radiances for molecular or compound (molecules plus aerosols) atmospheres, Monte Carlo simulations of the radiative transfer were carried out by using a code already described (Morel and Gentili, 1991, 1993), and validated against other radiative transfer codes (Mobley *et al.*, 1993). This code does not account for polarisation, and the simplified geometry of a plane-parallel atmosphere is adopted. Photons are collected at the TOA level within 432 solid angles (“photon counters”), defined by a 5 degrees increment in zenith angle and a 7.5 degrees increment in azimuth; there is no counter aiming directly at nadir. The apparent diameter of the sun disk is set to 0.5° .

For Rayleigh scattering, a 50-layer profile is taken from Elterman (1968), in correspondence with $\tau_r = 0.0904$ at 550 nm, *i.e.*, a standard atmosphere with an atmospheric pressure of 1013.25 hPa. The anisotropy of the air molecules is ignored, the depolarization factor is zero, and the spectral dependency is expressed as $\lambda^{-4.09}$. Gas absorption is reduced to that of ozone, with a 50-layer vertical distribution also taken from Elterman (1968), and resulting in a total ozone content of 350 DU (1 DU = $2.69 \cdot 10^{16}$ molecules cm^{-2}). The selection of various aerosol types and of their vertical distribution is dealt with later on (section 3.1.1.5).

This atmosphere is bounded by a flat, Fresnel-reflecting, interface with a perfectly absorbing ocean, so that multiple crossings of the interface by photons are not considered. This uncoupling of atmosphere and ocean is fully verified for Case 1 waters in the near infrared, and is an acceptable approximation for the visible wavelengths. The expression “TOA total reflectance” hereafter used means therefore the sum of the path reflectance simulated above a black ocean plus the water-leaving reflectance independently calculated through Eq. (2) and transmitted through the atmosphere. The algorithm uses at first the total radiance measured in near infrared bands, which is equal to the path radiance because there is no oceanic signal for Case 1 waters. The principle and implementation of the algorithm would remain the same over Case 2 waters, provided that the non-zero signal in the near infrared has been previously assessed or assumed in an independent way, and subtracted from the total reflectance.

Simulations were carried out to generate the ρ_{path} values for 6 wavelengths, several geometries (θ_s , θ_v , $\Delta\phi$), and 4 aerosol optical thicknesses. The same geometries and wavelengths were considered to calculate $\rho_{r,\tau_a=0}$, which the reflectance for a pure Rayleigh atmosphere. For each aerosol model and each ensemble made up of (λ , θ_s , θ_v , $\Delta\phi$), five couples ($[\rho_{\text{path}} / \rho_{r,\tau_a=0}]$, τ_a), including the couple (1, 0) for an aerosol-free atmosphere, were fitted to a third order polynomial, to express the $[\rho_{\text{path}} / \rho_{r,\tau_a=0}]$ versus τ_a relationship, and the corresponding coefficients stored.



3.1.1.2 Signal decomposition

There are several ways to decompose the total signal received at the sensor level. The validity of any decomposition depends on a correct definition of the various terms involved. Coherence is also needed between the terms accounted for in the decomposition, the terms used in the correction algorithm, and the terms that we are able to calculate. A rapid insight is given below into the problem of signal decomposition; additional details can be found in Antoine and Morel, 1998, published in *Applied Optics* (given as Appendix 1 to this ATBD).

From this section and for the remaining of this document, the signals will be defined in terms of reflectance instead of radiance, according to the following transformation:

$$\rho(\lambda, \theta_s, \theta_v, \Delta\phi) = \pi L(\lambda, \theta_s, \theta_v, \Delta\phi) / E_s(\lambda) \mu_s \quad (6)$$

where $E_s(\lambda)$ is the extraterrestrial irradiance for the wavelength in question, μ_s is the cosine of the solar zenith angle θ_s , θ_v is the satellite viewing angle, and $\Delta\phi$ is the azimuth difference between the sun-pixel and pixel-sensor half vertical planes. Angular dependencies will be thereafter omitted for the sake of clarity.

The total reflectance at the sensor level, $\rho_t(\lambda)$, can be split into the following components: $\rho_{\text{path}}(\lambda)$, the "path reflectance" generated by single and multiple scattering within the atmosphere and by reflection of diffuse radiation at the air-sea interface, $T(\lambda)\rho_g(\lambda)$, the reflectance due to direct specular reflection in the viewing direction (sun glint), $t_d(\lambda)\rho_{\text{wc}}(\lambda)$, the reflectance of whitecaps (if any), and $t_d(\lambda)\rho_w(\lambda)$, the water-leaving reflectance. $T(\lambda)$ and $t_d(\lambda)$ are the direct and diffuse atmospheric transmittances, respectively. The purpose of the atmospheric correction algorithm is thus to provide accurate estimates of $\rho_{\text{path}}(\lambda)$, $T(\lambda)\rho_g(\lambda)$, $t_d(\lambda)\rho_{\text{wc}}(\lambda)$ and $t_d(\lambda)$.

$$\rho_t(\lambda) = \rho_{\text{path}}(\lambda) + T(\lambda)\rho_g(\lambda) + t(\lambda)\rho_{\text{wc}}(\lambda) + t_d(\lambda)\rho_w(\lambda) \quad (7)$$

For what follows $T(\lambda)\rho_g(\lambda)$ and $t_d(\lambda)\rho_{\text{wc}}(\lambda)$ are left out and the main term under examination is the path radiance. For that purpose $\rho_{\text{path}}(\lambda)$ is decomposed into the following components, assuming that radiances due to aerosol or molecular scattering are separable: $\rho_{\text{r}, \tau_a=0}(\lambda)$, the reflectance due to multiple scattering by air molecules (Rayleigh reflectance), $\rho_a(\lambda)$, the reflectance due to multiple scattering by aerosols, and $\rho_{\text{ra}}(\lambda)$, the reflectance due to combined, successive, scattering by air molecules and aerosols (coupling term)

$$\rho_{\text{path}}(\lambda) = \rho_{\text{r}}(\lambda) + \rho_a(\lambda) + \rho_{\text{ra}}(\lambda) \quad (8)$$

As said above, attention has to be paid to the definition of these various terms. Indeed, in the above expression, $\rho_{\text{r}}(\lambda)$ and $\rho_a(\lambda)$ are defined as the reflectances for a pure molecular atmosphere (*i.e.*, aerosol-free) and a hypothetical atmosphere with only aerosols (and no molecules) (*e.g.*, Deschamps *et al.*, 1983). The $\rho_{\text{ra}}(\lambda)$ term thus appears as a correction term, usually negative.

The reflectances $\rho_{\text{r}}(\lambda)$ and $\rho_a(\lambda)$ can also and more realistically be defined as the reflectances for a two component atmosphere (molecules and aerosols), and by abandoning the



assumption that radiances are separable. In this situation, the $\rho_{ra}(\lambda)$ term exactly represents the coupling of aerosol and Rayleigh scattering. These last terms are those that we can extract from a Monte Carlo simulation for a two component atmosphere, provided that the histories of the photons are kept. However, and from a practical viewpoint, it is necessary to compute the $\rho_r(\lambda)$ term for aerosol-free atmospheres: this is the only term that we are able to calculate when processing ocean colour observations, as aerosols are never *a priori* known (they are the term that we try to calculate).

In summary: from simulations, we shall retain the two following terms: the total reflectance at the sensor level, for a given ocean-atmosphere system and the Rayleigh reflectance for the same system when aerosols are removed. Such preliminary computations were carried out for several aerosol models, or aerosol model assemblages (see 3.1.1.5.2 for their definition), for optical thicknesses encompassing most of the plausible values over the ocean, and for which remote sensing is possible (from 0.03 to 0.5 at 550 nm), for six wavelengths among the 16 MERIS bands (3 in the visible: 443, 510 and 560 nm, 3 in the near IR: 709, 778 and 865 nm), 13 solar zenith angles (from 20 to 60°, each 4°), and a flat air-sea interface (see 3.1.1.6 for sensitivity studies about the conditions at the air-sea interface). From the simulations, the radiances or reflectances can be expressed as a function of the above parameters and for any viewing geometry (for the Monte Carlo outputs, the sole limitation comes from the spatial discretisation).

No absorbing gases are considered, as it is assumed that their effect on the total radiances has been estimated before entering into the present atmospheric correction scheme.

The first step in the atmospheric correction for ocean colour is to estimate $\rho_{r, \tau_a=0}(\lambda)$. For that, the atmospheric pressure and the wind speed should be known. If they are unknown, standard, mean, values are adopted (the impact on the correction is treated as a sensitivity study, see 3.1.1.6.2). The path reflectance is now investigated in the realistic case of multiple scattering in a compound (molecules + aerosols) atmosphere.

3.1.1.3 Accounting for multiple aerosol scattering.

Gordon (1997) has shown that for non-absorbing aerosols, and for moderate optical thicknesses (< 0.1), an algorithm based on the single scattering approximation could work well in most cases, with errors within ± 0.002 in reflectance at 443 nm. For higher optical thicknesses, or as soon as the actual aerosol absorbs radiation, multiple scattering has to be accounted for (but see 3.1.1.5.6).

It is known that multiple aerosol scattering enhances the signal with respect to that corresponding to single scattering (Deschamps *et al.*, 1983; Gordon *et al.*, 1988). This effect, which increases with increasing aerosol optical depth (in terms of signal magnitude), has to be accounted for in the present atmospheric correction for MERIS to meet the required accuracy (see Gordon and Wang, 1994; Gordon, 1997). In the same manner as for the single scattering, an indirect method is inevitable to cope with multiple aerosol scattering, which cannot be directly computed because the aerosols are unknown.

In our study about multiple scattering (see Appendix), we showed that the path reflectance is linearly (or nearly linearly) increasing with increasing aerosol load. For practical purposes, it has



been decided to use the ratio of this path reflectance to the reflectance due to multiple Rayleigh scattering (for an aerosol-free atmosphere, $\rho_{r, \tau_a=0}(\lambda)$); this ratio also linearly increases when aerosol are progressively introduced in the atmosphere, and has a precise physical meaning.

Some examples of such relationships are displayed in Fig. 3.1, and for given geometric conditions and wavelengths. This figure shows that the relationship between both terms (the ratio and τ_a) is nearly linear. After some trials, we decided to fit the experimental points (obtained for 5 values of the aerosol optical thickness, including 0) by a quadratic function. The first step of the atmospheric correction lies on these relationships, so they have to closely match the data obtained from the simulated reflectances.

It is worth noting that the term used here ($\rho_{r, \tau_a=0}(\lambda)$) is not a realistic quantity, as far as it is compared with the "true" Rayleigh multiple scattering reflectance, resulting from a Monte Carlo simulation for a two-component atmosphere (aerosols + molecules). If this difference is of importance from the point of view of a systematic study of atmospheric reflectances, it is of no concern for our purpose. Indeed, our goal is to retrieve the global contribution of aerosol and Rayleigh reflectances in the MERIS channels, in view of retrieving the water-leaving reflectances. The above definition for $\rho_{r, \tau_a=0}(\lambda)$ is "operational", in that sense that it allows the correction to be done. The way this term is related to the "true" term is out of the scope of this ATBD (but see Appendix).

The principle for the algorithm and its implementation will be therefore to store in lookup tables the coefficients of relationships like those in Fig. 3.1, obtained for various aerosols. In parallel, a technique is necessary to navigate within this table, to identify the couple of aerosol that is the closest to the actual one.

3.1.1.4 The algorithm

3.1.1.4.1 Computation of the ratio $[\rho_{\text{path}} / \rho_{r, \tau_a=0}]$ and identification of the actual aerosol

A preliminary step consists in tabulating the $[\rho_{\text{path}} / \rho_{r, \tau_a=0}]$ versus τ_a relationships. Specific relationships are established for every aerosol model and wavelength, and for all illumination and observation conditions. One relationship is then necessary for each ensemble comprising aerosol (or fixed aerosol assemblage), wavelength, sun zenith angle, viewing angle, and azimuth difference. In parallel, the $\rho_{r, \tau_a=0}(\lambda)$ values have also to be stored for the various illumination and observation conditions, to get the $[\rho_{\text{path}}(\lambda) / \rho_{r, \tau_a=0}(\lambda)]$ ratio.

When starting the atmospheric correction, we dispose on one hand of $\rho_{\text{path}}(\lambda)$ (measured) and $\rho_{r, \tau_a=0}(\lambda)$ (tabulated) for each wavelengths, and on the other hand of tabulated relationships linking the ratio of these 2 terms to $\tau_a(\lambda)$, for N aerosol models. The central problem to be addressed is therefore the selection, among the aerosol models used to generate the look-up tables, of the two models that most closely bracket the actual aerosol. The principle is to rely on the look-up tables, which should allow (numbering as in Fig. 3.1).

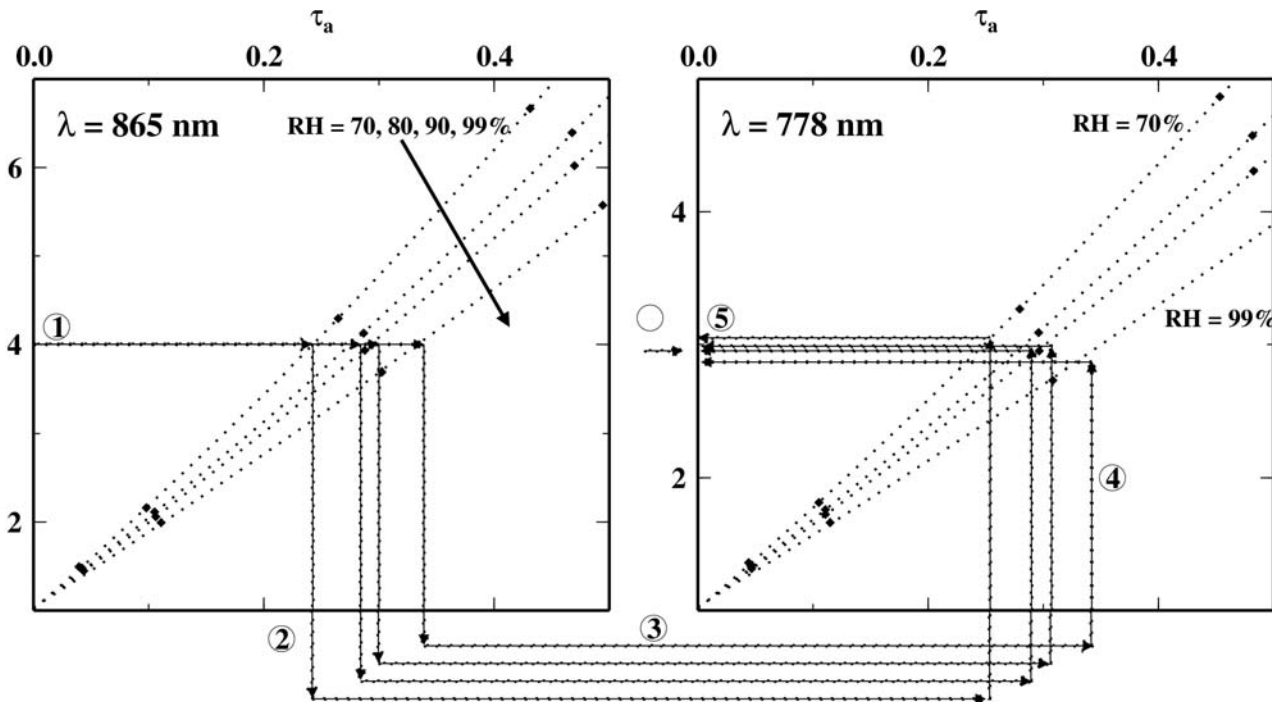


Figure 3.1: Variation of the path reflectance at 865 and 778 nm as a function of τ_a , and expressed as the ratio $[\rho_{\text{path}} / \rho_r]$, when $\theta_s = 40^\circ$, $\theta_v = 30^\circ$, and $\Delta\phi = \pi/2$. The maritime aerosol model is used, for 4 values of the relative humidity, as indicated. Arrows symbolise a possible way for identifying a couple of aerosol models enclosing the actual aerosol. The circled numbers identify the successive steps of this scheme, as discussed in the text (section 3.1.1.4.1).

(1-2) the values of $\tau_a(865)$ to be calculated from the $[\rho_{\text{path}}(865) / \rho_{r, \tau_a=0}(865)]$ ratio, for several aerosol models,

(3) to extrapolate τ_a from 865 to 778 nm, for each aerosol model,

(4-5) to obtain the $[\rho_{\text{path}}(778) / \rho_{r, \tau_a=0}(778)]$ ratios from $\tau_a(778)$, and therefore to select a couple of aerosol models, by comparing the actual $[\rho_{\text{path}}(778) / \rho_{r, \tau_a=0}(778)]$ ratio, and these various ratios. Finally, to estimate the $[\rho_{\text{path}}(\lambda) / \rho_{r, \tau_a=0}(\lambda)]$ ratio in the visible bands from the knowledge of the spectral behaviour of this couple of aerosol models.

The principle is to firstly rely on a very simple set of candidate aerosol models, supposedly representing typical clear oceanic atmospheres (and described below). A "first-step" atmospheric correction is then carried out by using this first set of candidate aerosol models, and then the error that is made at 510 nm is examined. At 510 nm, the water-leaving reflectance for case 1 waters is weakly variable for chlorophyll concentrations up to 1 mg Chl m^{-3} , and thereafter smoothly decreases with increasing pigment concentration. The use of a mean value for this water-leaving reflectance with its associated statistical error, is then possible (see later on; section 3.1.1.4.2). It is then feasible to obtain the error in the atmospheric correction at 510 nm, by subtracting from the total, measured, reflectance, the sum [path reflectance, estimated by the correction + supposed mean value of the water-leaving reflectance].

If this error is above a predefined threshold, we have an indication that the actual aerosols do not correspond to the simple cases first envisaged. We can then move to another (others) set(s) of aerosol models (see section 3.1.1.5, implementation).



The successive steps of such a correction scheme are as follows (see Fig. 3.2(a), (b), (c), and (d), and also section 3.1.2). For a given pixel, and thus for a given geometry (θ_v , θ_s , $\Delta\phi$):

- (1) The ratio $[\rho_{\text{path}}(\lambda) / \rho_{r, \tau_a=0}(\lambda)]$ is computed at 865 and 778 nm, $\rho_{r, \tau_a=0}(\lambda)$ being taken in tabulated values (at these wavelengths, and for oceanic Case 1 waters, $\rho_{\text{path}} = \rho_t$).
- (2) A first set of N aerosol models is selected, which, in principle, is representative of clear oceanic atmospheres (see 3.1.1.5 for details about the implementation). For these N aerosol models, N $\tau_a(865)$ values are calculated from the $[\rho_{\text{path}}(865) / \rho_{r, \tau_a=0}(865)]$ ratio.
- (3) N values of $\tau_a(778)$ are computed for the N aerosol models, from the knowledge of their spectral optical thicknesses (normalised by their values at 865 nm; tabulated values).
- (4) N values of $[\rho_{\text{path}}(778) / \rho_{r, \tau_a=0}(778)]$ are computed from the N values of $\tau_a(778)$ for the N aerosol models, from the tabulated relationships between both quantities.
- (5) The actual $[\rho_{\text{path}}(778) / \rho_{r, \tau_a=0}(778)]$ is then compared to the N individual values obtained at step (4), and the 2 that most closely bracket the actual one indicate the two aerosol models that most likely are similar to the actual one.
- (6) 2 values of $\tau_a(510)$ are calculated from the normalised spectral optical thicknesses of the 2 “bracketing” aerosol models. Step (2) is now inverted, to calculate two $[\rho_{\text{path}}(510) / \rho_{r, \tau_a=0}(510)]$ ratios from the two $\tau_a(510)$.
- (7) The following step lies on the assumption that, for a given wavelength λ , the actual $[\rho_{\text{path}}(\lambda) / \rho_{r, \tau_a=0}(\lambda)]$ ratio falls between the two $[\rho_{\text{path}}(\lambda) / \rho_{r, \tau_a=0}(\lambda)]$ ratios calculated at step (6), proportionately in the same manner as it does at 778 nm; $\rho_{\text{path}}(510)$ is now known.
- (8) By making an assumption on the water-leaving reflectance at 510 nm (see below), the error in the atmospheric correction, $\Delta\rho_{510}$, can be assessed:

$$\Delta\rho(510) = [(\rho_t(510)_{\text{measured}} - \rho_{\text{path}}(510)_{\text{estimated}}) / t_d(510)] - \rho_w(510)_{\text{supposed}} \quad (9)$$

- (9) A test is then made on this $\Delta\rho(510)$ value. Following the answer, either the correction is continued at step (10), or it is carried out once more from step (2), by selecting however a different set of N' aerosol models. In the latter situation, the correction is actually carried out for several aerosol databases, so that steps 2-8 are carried out several times; several couples of aerosol models are then selected (one at each time steps 2-8 are done), and the couple kept at the end is the one leading to the lower $\Delta\rho(510)$. The practical way of navigating within the tables will be exposed later on (section 3.1.1.5.4).
- (10) For every wavelength λ of the visible domain, 2 values of τ_a are calculated from the knowledge of the spectral scattering coefficients of the 2 “bracketing” aerosol models.



- (11) Step (2) is now inverted, to calculate two $[\rho_{\text{path}}(\lambda) / \rho_{r, \tau_a=0}(\lambda)]$ ratios from the two $\tau_a(\lambda)$ for the visible bands, and then to obtain $\rho_{\text{path}}(\lambda)$ (see step 7).
- (12) The water-leaving reflectance at the instrument level is then obtained as the difference between the total, measured, reflectance, ρ_t , and the estimated path reflectance, ρ_{path} .
- (13) the last step consists in calculating the diffuse transmittance, to derive the water-leaving reflectance.

General sketch

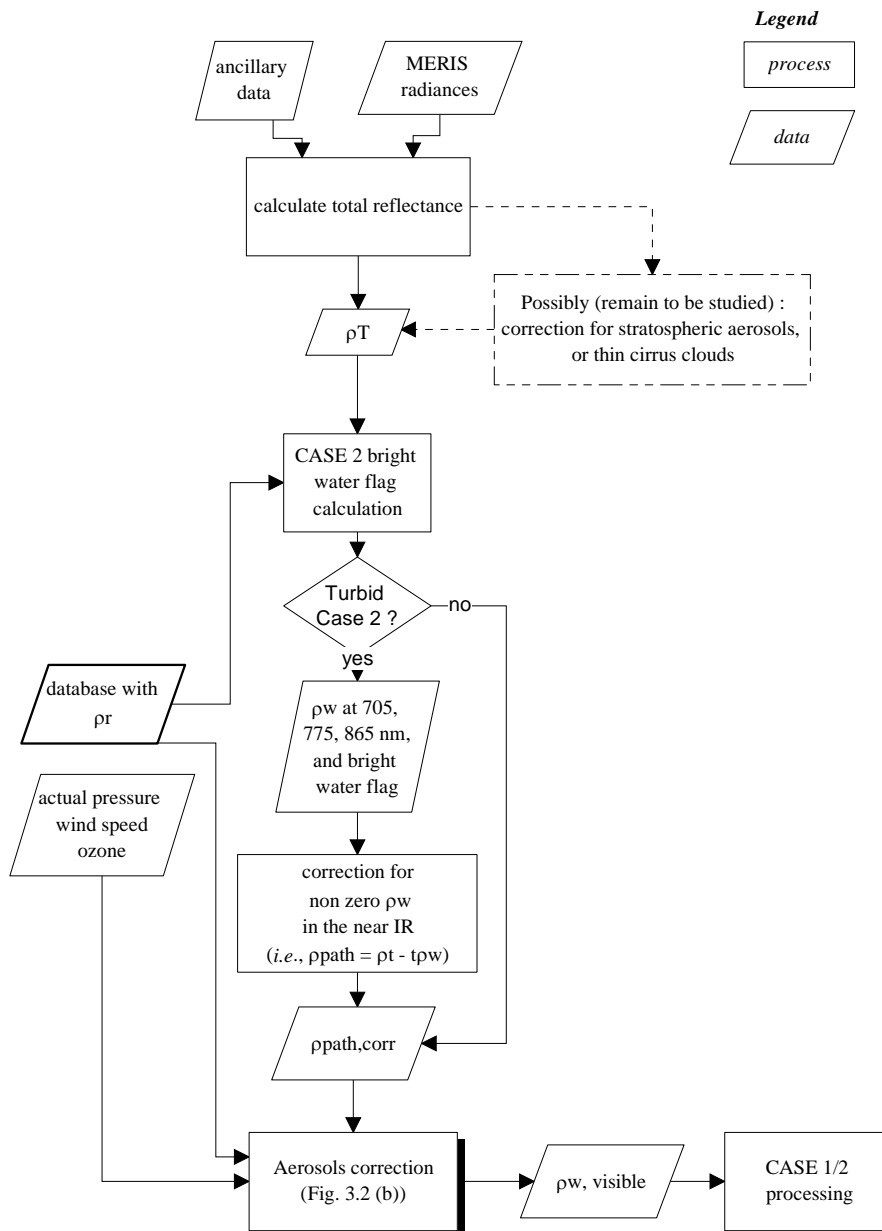


Figure 3.2a: general sketch of the algorithm

Aerosols correction

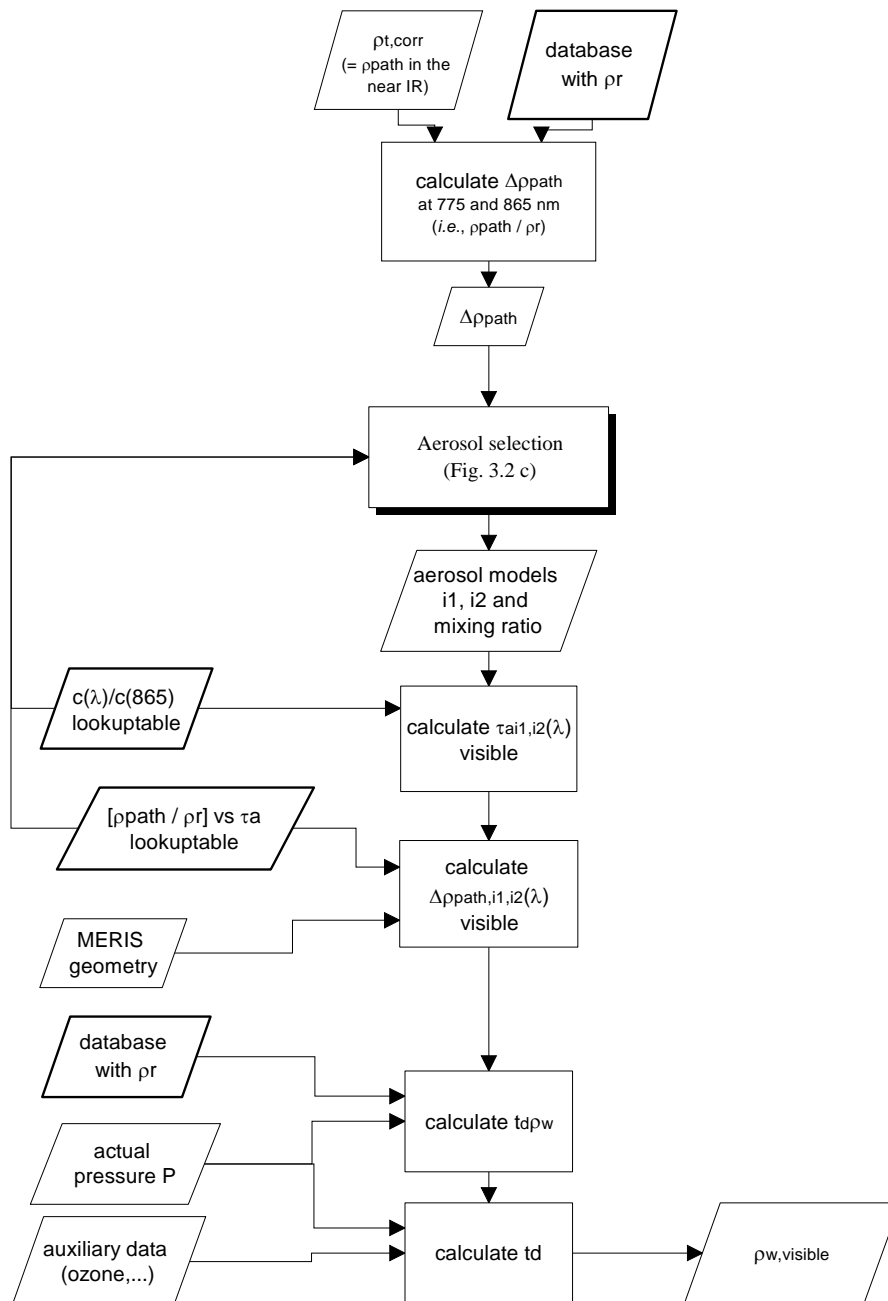


Figure 3.2b: detail of the aerosol correction (see also section 3.1.2.)

Aerosols selection

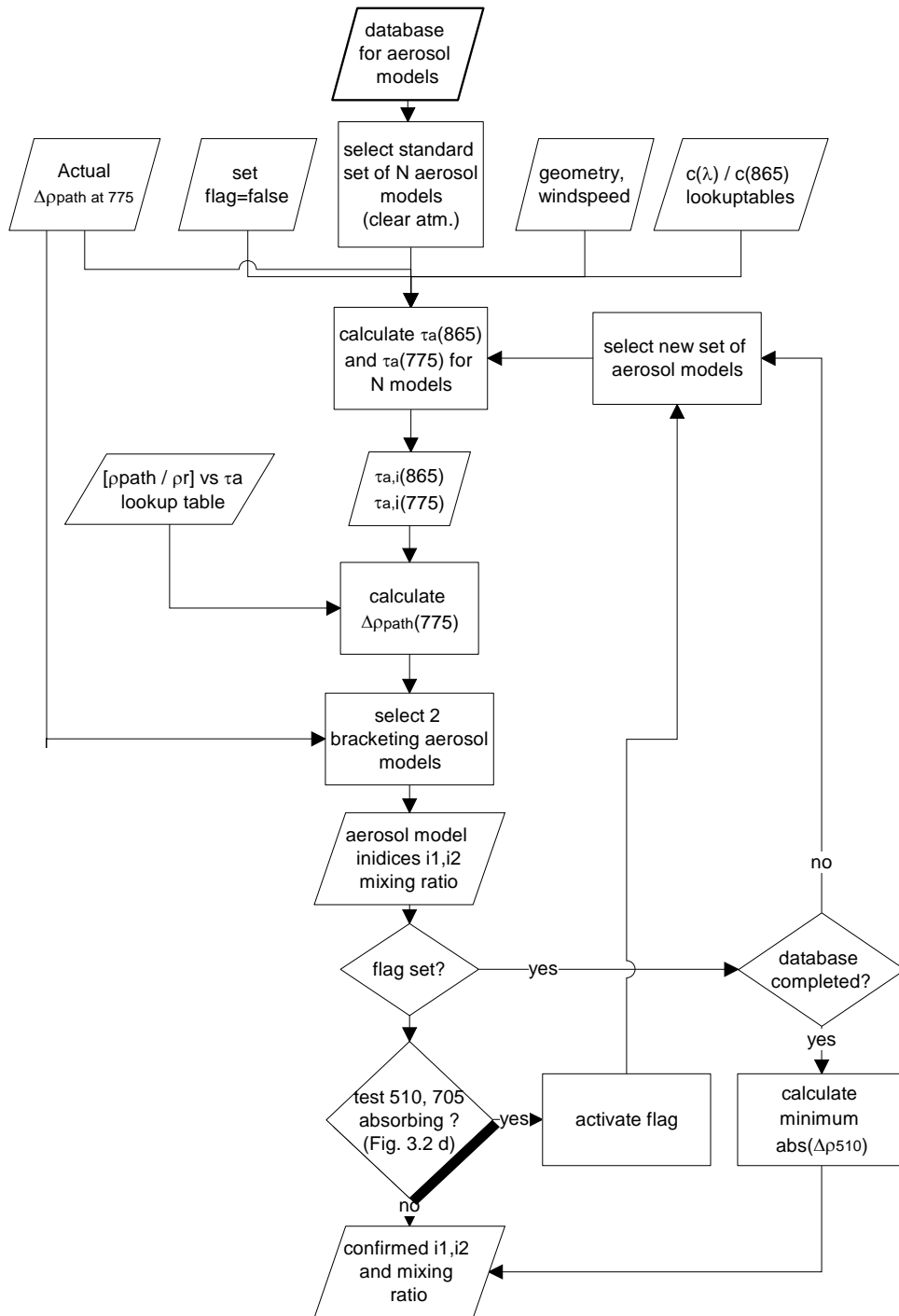


Figure 3.2c: detail of the aerosol selection (see also section 3.1.2.)



Detection of blue-absorbing aerosols

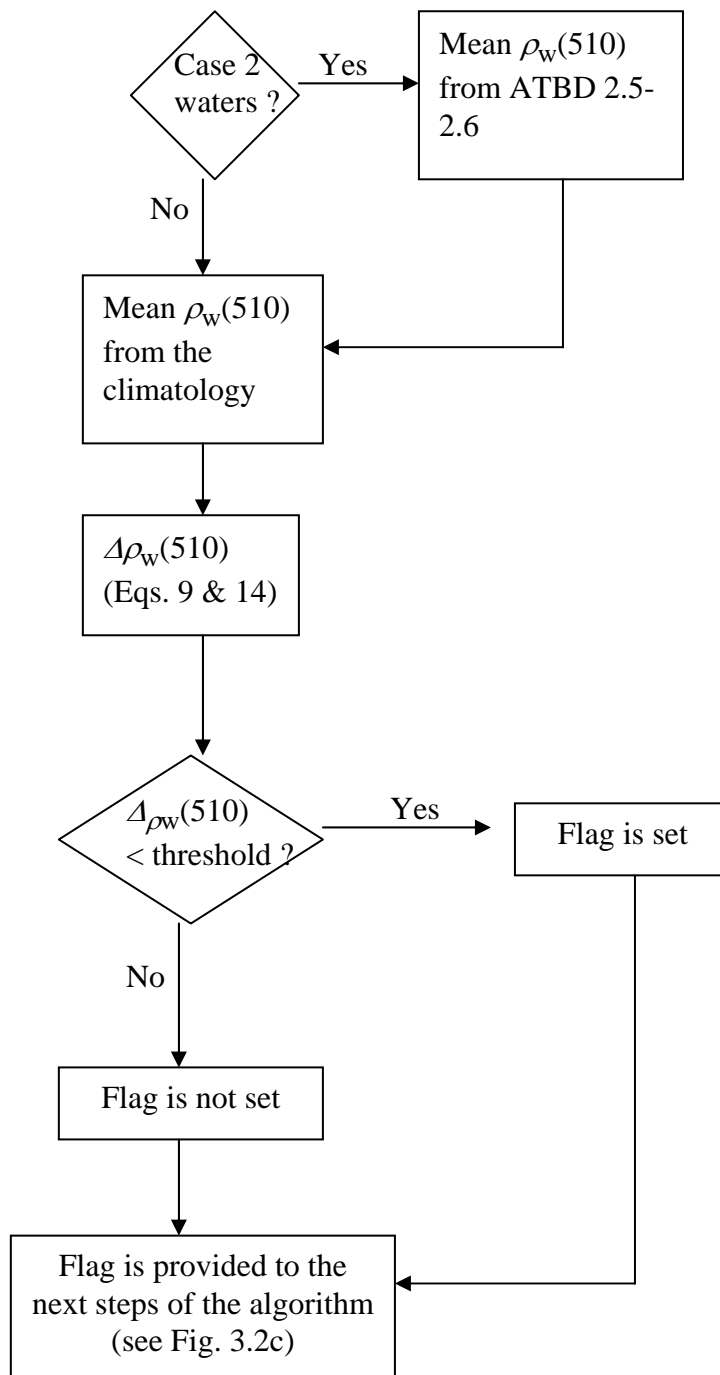


Figure 3.2d: detail of the tests at 510 and 709 nm (see also section 3.1.2.)

3.1.1.4.2 The test at 510 nm

Experimental data suggest a weakly variable reflectance at 510 nm for oceanic Case 1 waters, whatever (Chl) (the “hinge point”, Duntley *et al.*, 1974; Gordon and Clark, 1981). Bio-optical models (*e.g.*, Gordon *et al.*, 1988; Morel, 1988), mainly based on the interpretation of experimental data, accordingly predict a narrow range of values for $R(0^-)(510)$, over the whole domain of (Chl) (0.03 to 30 mg m^{-3}). The curves displayed in Fig. 3.3 indeed show limited variations of $R(0^-)(510)$. The data points in Fig. 3.3, extracted from measured reflectance spectra, as well confirm this constancy: however noisy may be these $R(0^-)(510)$ data, they at least do not show any significant trend. Therefore, it seems wise to assume a constant value for the diffuse reflectance at 510 nm, with a mean of $\sim 2\%$ if the data shown in Fig. 3.3 are considered. The corresponding mean value for the normalised water-leaving reflectance, hereafter noted $[\overline{\rho_w(510)}]_N$, is of about $1 \cdot 10^{-2}$ (with $(\pi R_0 / Q_0) \sim 0.47$) at least for the concentration range 0.03 to 3 mg(Chl) m^{-3} (see Fig. 2.1(a)). This value for $[\overline{\rho_w(510)}]_N$ is slightly larger than the value derivable at 520 nm from a normalised water-leaving radiance of $5 \text{ mW m}^{-2} \text{ nm}^{-1} \text{ sr}^{-1}$ (Gordon and Clark, 1981), and from an extraterrestrial irradiance of about $1900 \text{ mW m}^{-2} \text{ nm}^{-1}$ (Neckel and Labs, 1984). The natural noise in the reflectance at 510 nm, for a given chlorophyll concentration, is accounted for by attaching an uncertainty $\sigma_{\rho_w(510)}$ of $\pm 3 \cdot 10^{-3}$ (at $\pm 1 \sigma$) to $[\overline{\rho_w(510)}]_N$.

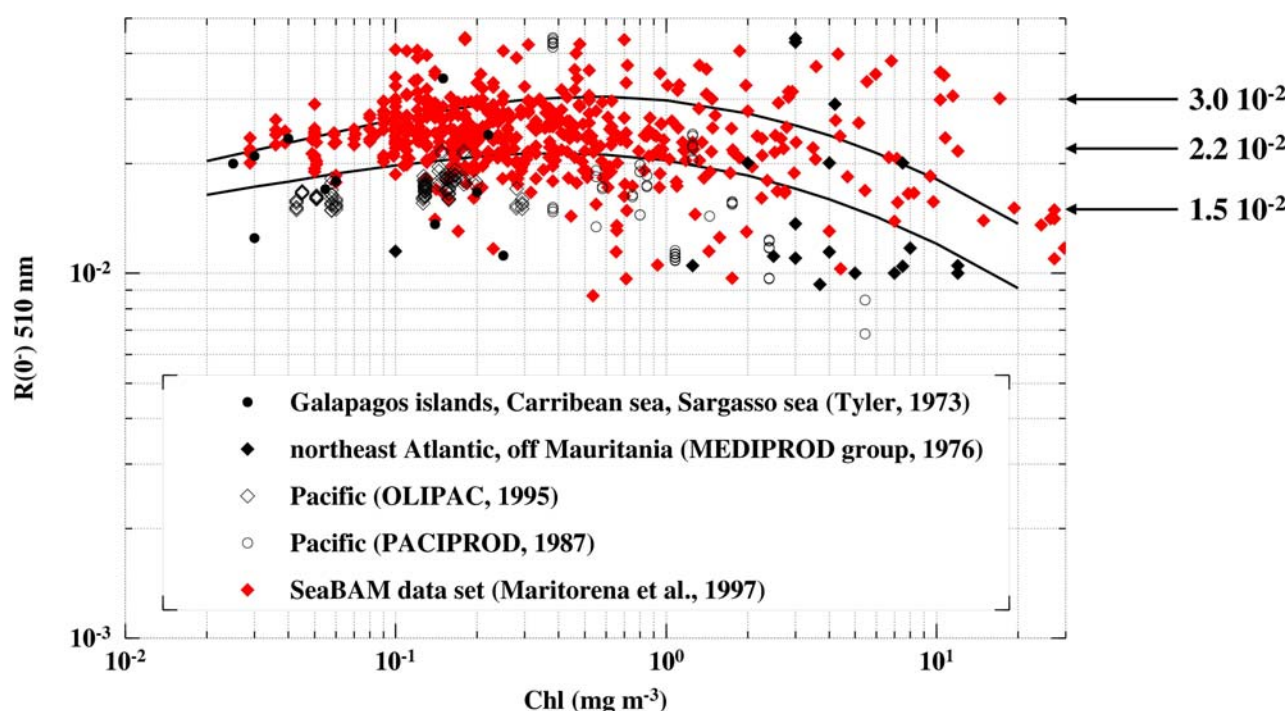


Figure 3.3: Oceanic diffuse reflectance at 510 nm, for Case 1 waters with variable chlorophyll concentration. The two curves have been obtained from the model of Morel (1988) (see also Morel and Gentili (1991) for the dependence of the reflectance on the sun zenith angle), either for a sun at zenith (bottom), or with a sun zenith angle of 60° (top). The various symbols correspond to values extracted from reflectance spectra measured at sea, as indicated.

To obtain the error in atmospheric correction at 510 nm, the $[\overline{\rho_w(510)}]_N$ value is “de-normalised”, in view of being compared with the apparent water-leaving reflectance (*i.e.*, the actual



water-leaving reflectance plus the error in atmospheric correction). The transformation of $[\rho_w(510)]_N$ into $\rho_w(510)$ is performed through (see Morel and Gentili, 1996)

$$\rho_w(510) = \overline{[\rho_w(510)]_N} (\varepsilon_c \ t_{\theta_s}) \frac{\Re(\theta')}{\Re_0} \frac{f_1(\theta_s)}{Q(\theta_s, \theta_v, \Delta\phi)} \left[\frac{f_{1,0}(\lambda)}{Q_0(\lambda)} \right]^{-1} \quad (10)$$

$$\text{with } \Re(\theta') = \left[\frac{(1 - \bar{\rho})}{(1 - \bar{r}R)} \frac{(1 - \rho_F(\theta'))}{n^2} \right] \quad (10')$$

The chlorophyll concentration has to be known to use the (f_1 / Q) , while actually it is not the case when the error in atmospheric correction is computed. The ratio of (f_1 / Q) for the actual geometry to $(f_{1,0} / Q_0)$ (*i.e.*, f/Q for $\theta_s = \theta_v = 0$) is, however, nearly insensitive to changes in the chlorophyll concentration (changes with Chl are within $\pm 10\%$), at least in the concentration range $0.03\text{-}3 \text{ mg m}^{-3}$ and for geometries typical of ocean colour remote sensing. Therefore, the knowledge of the chlorophyll concentration is not required to use the above equation, and the error in the atmospheric correction at 510 nm, $\Delta\rho(510)$, is obtained as

$$\Delta\rho(510) = \left[(\rho_t(510)_{\text{measured}} - \rho_{\text{path}}(510)_{\text{estimated}}) / t_d(510) \right] - \rho_w(510) \quad (11)$$

If $\Delta\rho(510)$ is lower than a given threshold (*cf.* publication in Remote sensing of environ., appendix), then the presence of absorbing aerosols is indicated (positive answer). If the answer of the test is negative (clear maritime atmosphere), the atmospheric correction is extended to the whole spectrum (412 to 680 nm). If the answer is positive (*i.e.*, presence of absorbing aerosols), then a confirmation is asked. Indeed, when $\Delta\rho$ is below the selected threshold, it could be due to an overestimation of $\rho_w(510)$, rather than to an incorrect atmospheric correction. The verification is carried out through a second test, using however the lower limit of $[\rho_w(510)]_N$, that is its value minus the standard deviation $\sigma_{\rho_w(510)}$.

The present algorithm must be applicable globally. Therefore, using unique values for $[\rho_w(510)]_N$ and $\sigma_{\rho_w(510)}$ might be inappropriate. This option has been actually abandoned in the operational implementation of the MERIS algorithms. Indeed, the changes of the marine reflectance at 510 nm are minimal yet significant enough so that ignoring them, in particular their seasonal changes, could lead to bias the dust detection.

A climatology of the monthly average of these two quantities has been therefore derived from 7 years of the standard SeaWiFS level-3 data (1998 to 2004; data from the NASA reprocessing #4), at a spatial resolution of $1/6^\circ$, *i.e.*, about half the resolution of the SeaWiFS level-3 "Standard Mapped Images" data. For a given month, the climatological monthly averages have been computed from the 7 individual monthly composites, by dividing the sum of individual values by the total number of pixels (these two values are available in the Level-3 SeaWiFS binned products). The standard deviation was similarly derived from 7 monthly values of the sum of squares of the data and over the 7 years, so that it includes both a spatial dimension (changes within the $1/6^\circ$ bin) and a temporal dimension (variability within a month and among the 7 years).

Because the standard NASA atmospheric correction scheme for the SeaWiFS sensor cannot cope with absorbing aerosols, however, an overcorrection of the visible observations occurs when they are present in the atmosphere, leading to underestimated marine reflectances at 510 nm [e.g., Schollaert *et al.*, 2003]. The lowest $\rho_w(510)$ values were therefore reset to a minimum value of 0.008, as empirically determined from *in situ* observations [see, e.g., Fig. 3 in Nobileau and Antoine, 2005]. Similarly, large values have been put to an upper limit of 0.016, assuming that larger values cannot be found in Case 1 waters. A similar bounding has been applied to $\sigma(\rho_w)$, with extrema of $1.5 \cdot 10^{-3}$ and $5 \cdot 10^{-3}$.

Examples of the climatology for the months of January and July are shown in Fig. 3.3bis. As expected, the changes between these two seasons are low, yet significant enough as regards the error budget at 510 nm to justify the need for using this climatology instead of a unique value.

When processing a pixel, $\bar{\rho}_w(510)$ and $\sigma(\rho_w)$ are spatially interpolated from the surrounding grid points of the monthly climatology. There is no time interpolation, *i.e.*, the monthly averaged value for a given month is used for all days in this month.

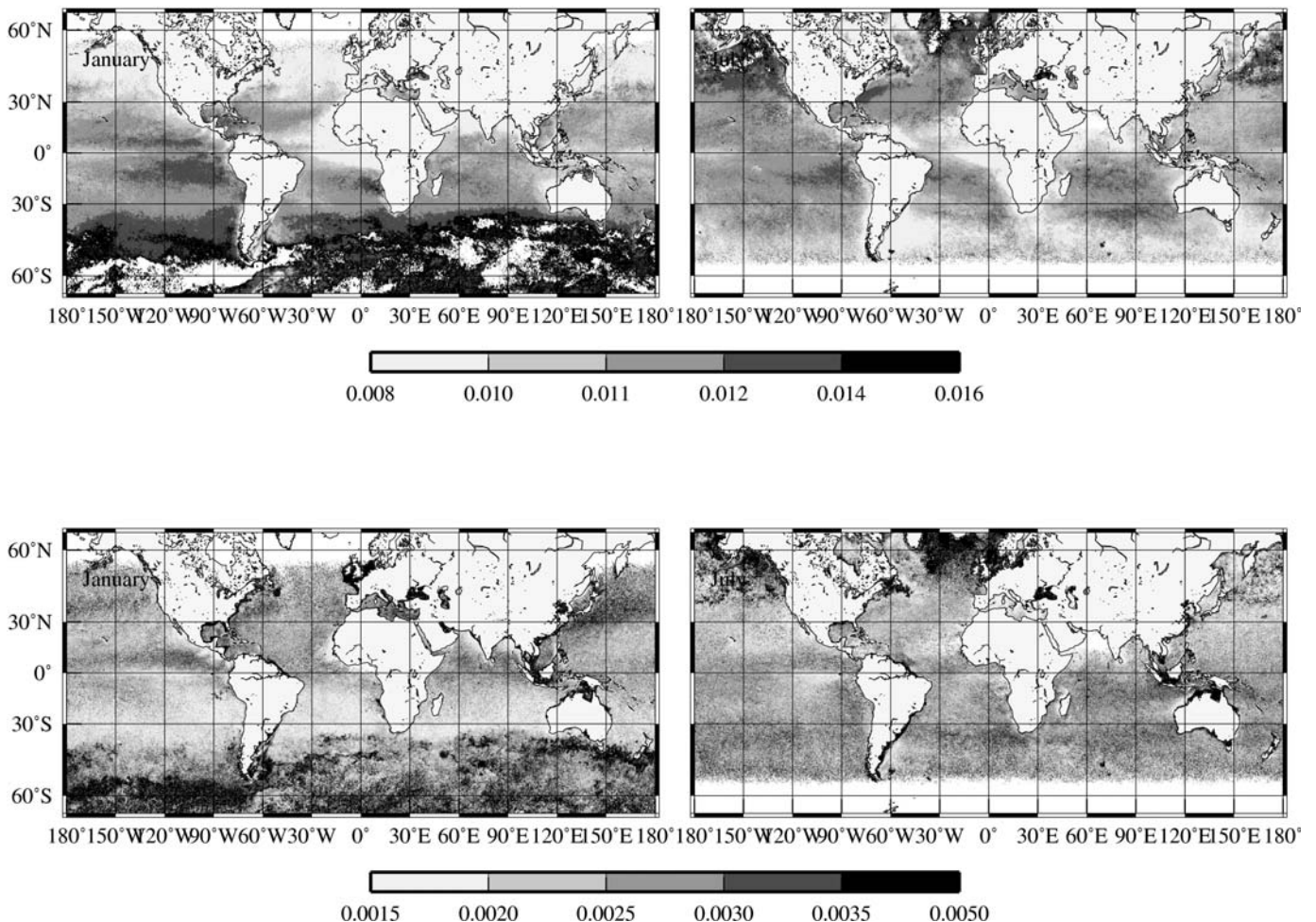


Figure 3.3 bis: 7-year (1998-2004) monthly climatology of the average marine reflectance at 510 nm, $\bar{\rho}_w(510)$ (top), and of its standard deviation, $\sigma(\rho_w)$ (bottom), for the months of January (left column) and July (right), and as derived from 7 years of standard SeaWiFS level-3 composite data (see text).



3.1.1.4.3 Computation of the diffuse transmittance, and getting the water-leaving radiance

NOTE: This section describes how diffuse transmittances were determined in initial implementations of the MERIS atmospheric corrections. It is valid for all data processed until 2010. Starting from the MERIS 3rd reprocessing (January-March 2011), the formulation detailed below was replaced by full radiative transfer computations, as described at the end of this section.

This step of the atmospheric correction is of great importance, even if it has been usually considered as a routine operation. The diffuse transmittance term actually conceals several processes, each one either removing radiation from, or adding radiation to, the water-leaving radiance travelling along the pixel-to-sensor path. In addition, any error in $t_d(\lambda, \theta)$ is directly transferred to as the same error in the water-leaving reflectance. The expression used to calculate the diffuse transmittance should account (1) for the loss of radiance due to absorption along the path from the pixel to the sensor, (2) for the loss of radiance due to scattering of water-leaving radiances out of the viewing direction, and (3) for the gain of radiance due to the scattering of water-leaving radiance from the neighboring pixels into the viewing direction (this third contribution implies that $t_d(\lambda, \theta)$ can be theoretically > 1 , *e.g.*, the environment effect).

In the following, it is supposed that the target is homogeneous, and $t_d(\lambda, \theta)$, where θ is the viewing angle, is then

$$t_d(\lambda, \theta) = t_{oz}(\lambda, \theta) t_w(\lambda, \theta) t_{ag}(\lambda, \theta) t_{aa}(\lambda, \theta) t_{rs}(\lambda, \theta) t_{as}(\lambda, \theta) \quad (12)$$

where $t_{oz}(\lambda, \theta)$ is the transmission factor related to absorption by ozone

$t_w(\lambda, \theta)$ is the transmission factor related to absorption by water vapor

$t_{ag}(\lambda, \theta)$ is the transmission factor related to absorption by other absorbing gases

$t_{aa}(\lambda, \theta)$ is the transmission factor related to absorption by aerosols

$t_{rs}(\lambda, \theta)$ is the transmission factor related to scattering by molecules

$t_{as}(\lambda, \theta)$ is the transmission factor related to scattering by aerosols

In principle, the choice of the wavelengths for the MERIS channels ensures that $t_w(\lambda, \theta)$ and $t_{ag}(\lambda, \theta)$ are unity. The contributions of absorption by ozone and aerosols are simply expressed as:

$$t_{oz}(\lambda, \theta) = \exp\left(-\frac{\tau_{oz}}{\mu}\right) \quad \text{and} \quad t_{aa}(\lambda, \theta) = \exp\left(-\frac{(1 - \omega_a) \tau_a}{\mu}\right) \quad (13)$$

The individual contributions of scattering by aerosols and molecules are expressed as:

$$t_{as}(\lambda, \theta) = \exp\left(-\frac{\omega_a F_a \tau_a}{\mu}\right) \quad (14)$$

$$t_{rs}(\lambda, \theta) = \exp\left(-\frac{\omega_r F_r \tau_r}{\mu}\right) \quad (15)$$



where μ is the cosine of θ , τ_x is the optical thickness of the component x , $\overline{\omega}_a$ and $\overline{\omega}_r$ are the single scattering albedos of aerosols and molecules. the ratio $\overline{\omega}_a$ can take different values depending on the aerosol model and $\overline{\omega}_r$ is unity for the channels here considered. F_a and F_r are the backward scattering probabilities of aerosols and molecules, respectively (*i.e.*, the ratio of the backward scattering coefficient to the total scattering coefficient). F_a can take various values depending on the aerosol model, and F_r is 0.5. By assembling the expressions for $t_{aa}(\lambda, \theta)$ and $t_{as}(\lambda, \theta)$, it follows that the contribution of aerosols to the diffuse transmittance is

$$t_a(\lambda, \theta) = \exp\left(-\frac{(1 - \overline{\omega}_a(1 - F_a)) \tau_a}{\mu}\right) \quad (16)$$

By reassembling the above expression with those for ozone and Rayleigh scattering, and by using the numerical values of $\overline{\omega}_r$ and F_r , it follows that the diffuse transmittance is

$$t_d(\lambda, \theta) = \exp\left(-\frac{\tau_{oz} + (1 - \overline{\omega}_a F_a) \tau_a + 0.5 \tau_r}{\mu}\right) \quad (17)$$

Note that F_a stands now for the forward scattering probability of aerosols.

$\tau_r(\lambda)$ is set to a fixed value for standard atmospheric pressure (P_0), and has to be multiplied by P/P_0 if P is the actual atmospheric pressure. $\tau_{oz}(\lambda)$ is computed from the knowledge of the ozone integrated content (mAtm cm), combined with the ozone absorption coefficients for the wavelength in question. $\tau_a(\lambda)$ is obtained at the end of the atmospheric correction (see below). The ratios $\overline{\omega}_a$ and F_a are obtained in the same way, *i.e.*, by averaging the values for the 2 aerosols selected by the atmospheric correction following the mixing ratio.

Note that the aerosol contribution to $t_d(\lambda, \theta)$ was ignored in the CZCS algorithms, because it is usually small, except for large optical thicknesses, *i.e.*, when the CZCS atmospheric correction was anyway unable to work properly. The aerosol term is included here in the calculation of the diffuse transmittance, to avoid introducing inaccuracies at the end of an *a priori* accurate atmospheric correction.

What is now done for the MERIS 3rd reprocessing:

The formulation described above has been considered not accurate enough (see, e.g., section 3.1.3.2.3 of this ATBD). It has been replaced by full radiative transfer computations. The practical implementation of these RT computation is described in two documents:

Specification of the Scientific Contents of the MERIS Level-1b & 2 Auxiliary Data Products (doc number PO-RS-PAR-GS-0002).

Specification of the Contents of the MERIS Radiative Transfer Tools used to Generate the Level-2 Auxiliary Data Products (doc number PO-RS-PAR-GS-0003)

The two documents are publicly available from the ENVISAT web page, at the following link:

<http://www.envisat.esa.int>



3.1.1.4.4 Retrieval of the aerosol optical thickness, τ_a

Once a couple of aerosol models (the two “bracketing” aerosols) has been selected by the atmospheric correction algorithm, the two values of $\tau_a(865)$ associated with these two aerosol models are averaged following the “mixing” ratio. From the tabulated spectral variations of the selected aerosol models (or aerosol model assemblages), the optical thickness can also be estimated at any wavelength in the visible, with however a lesser accuracy.

3.1.1.4.5 Additional steps

The links with the other segments of the ground processing, as they are described in the ATBD(s) 2.5, 2.6, 2.8 and 2.9, are shown in Fig. 3.2a. The first link is with the “Case 2 bright waters flag”, which should indicate if sediment-dominated waters are actually observed. Water-leaving reflectances in the near-IR are then passed on to the atmospheric correction algorithm. These reflectances are subtracted from the total reflectances, before entering the atmospheric correction. The other links are at the end of the atmospheric correction, which pass the water-leaving reflectances either at the Case 1 (ATBD 2.9) or Case 2 (ATBD 2.8) processing, depending on the value of the “Case 2 waters flag”.

Another entry in the atmospheric correction (not discussed in this ATBD, and not implemented at present time) concerns the effect of stratospheric aerosols (in case of perturbed conditions; for instance after significant volcanic eruptions) or of thin cirrus clouds (see section 3.1.1.6.6). If such a correction is operated for MERIS, it should be at the top level of the algorithm, that is after radiances have been transformed into reflectances, and before entering the atmospheric correction. It can be anticipated that such a correction would be carried out *a priori*, by subtracting from the total reflectance known (precomputed) values of the reflectance due to the stratospheric aerosols. Preliminary studies (Gordon *et al.*, 1997) indicate that this kind of correction is not so straightforwardly carried out.

3.1.1.5 Implementation / test of the algorithm.

3.1.1.5.1 Aerosols over the ocean.

In principle, all kinds of aerosols are possibly encountered over the oceans. The presence of a peculiar aerosol type, and its relative proportion in the total aerosol load, are depending on the history of the air mass in question. When the region of interest is free from any continental influence, however, the situation can be described following a more or less general vertical structure and composition (WCRP, 1986): The oceanic boundary layer (from the sea surface to an altitude of about 2 km) contains a “maritime” aerosol, mainly composed of the “sea-salt component” (liquid water and sea-salt particles), always containing however a small background of “water-soluble” particles (small particles, below about 0.05 μm , *e.g.*, ammonium, calcium sulfate, organic compounds...). This boundary layer aerosol is non-absorbing (ω_0 about 0.97-0.98). Above the boundary layer, within the “free troposphere” (about 2-12 km), aerosols from continental origin are always present, even if their optical thickness is usually very low (*e.g.*, WCRP, 1986). This aerosol of continental origin is usually moderately absorbing (ω_0 about 0.9-0.95). Finally, the stratosphere and the upper atmosphere (12-30-100 km) contain a background of non-absorbing aerosol, which can be represented by particles consisting of a 75% solution of



sulfuric acid in water (H_2SO_4). The optical thickness of this aerosol is extremely low (about 0.005 at 550 nm), except during the months (years) following large volcanic eruptions.

Within this ensemble of three aerosol types, the boundary layer aerosol usually contributes to about 75% of the total aerosol optical thickness at 550 nm.

Even in absence of volcanic eruptions, deviations from this “generic” vertical structure and composition are observed, and are usually due to air masses of continental origin. In this case, the layer that is frequently affected is the free troposphere, which can then contain significant concentrations of particles of continental origin (either desert dust or insoluble particles of other terrestrial origins, usually referred to as the “rural aerosol”). This kind of aerosols are moderately (“rural aerosol”), or strongly (desert dust), absorbing. In the case of desert dust outbreaks, the optical thickness can be very high. The other perturbation of continental origin is due to human activities. It is more confined to the coastal regions (and usually east of continents), and is characterised by the presence of “soot-like” absorbing particles, incorporated into the “rural” aerosol. This kind of perturbation usually concerns the boundary layer.

With such a sketch of aerosol climatology, it is obviously not intended to encompass all possible situations, either intermediate or clearly different from those exposed here. For example, the maritime aerosol can be slightly different from an ocean to another one (*e.g.*, between Pacific and Atlantic oceans, Villevalde *et al.*, 1994), desert dusts have different optical properties as a function of their origin (Sahara or Asian deserts); they are not only present in the free troposphere, as they ultimately sink into the ocean, etc...

3.1.1.5.2 Conditions selected for simulating radiative transfer in the atmosphere.

3.1.1.5.2.1 The “standard” atmospheric vertical structure.

The standard atmosphere vertical structure adopted here is based on the profile recommended by WCRP (1986) for open oceanic areas. It is typical of clear oceanic atmospheres, and is as follows (the definition of the aerosol models is provided in the next section):

- Boundary layer (0-2 km):
 - Maritime or coastal or rural aerosol model (Shettle and Fenn, 1979; Gordon and Wang, 1994), for RH = 50 or 70 or 90 or 99%.
 - (non-absorbing aerosols, ω about 0.98-0.99)
 - Optical thickness is made varying from 0.03 to 2 at 550 nm.
- Free troposphere (2-12 km):
 - Continental aerosol (WCRP, 1986)
 - (slightly absorbing aerosol: $0.95 < \omega < 0.98$)
 - Optical thickness is constant, and equal to 0.025 at 550 nm.
- Stratosphere (12-50 km):
 - A 75% solution of sulfuric acid in water (WCRP, 1986)
 - (non-absorbing aerosol, ω about 0.99)
 - Optical thickness is constant, and equal to 0.005 at 550 nm.

The constant contribution of the continental + H_2SO_4 aerosols is not so important if we consider the aerosol optical thickness of the atmosphere; its influence on the spectral variation of this optical thickness, however, is significant and results in a spectral change close to that observed over remote ocean areas. The total optical thickness resulting from this aerosol

assemblage is spectrally varying according to Ångström exponents between about 0 and 0.5, when the wavelengths 443 and 865 nm are considered.

In order to incorporate a spectrally flatter aerosol, one peculiar assemblage has been also defined, where the free troposphere and the stratosphere are free of any aerosols, and the boundary layer contains the maritime model with a relative humidity of 99%.

3.1.1.5.2.2 Peculiar aerosol vertical repartitions.

Absorbing aerosols

The use of other sets of aerosol models is dictated by the test at 510 nm. This additional set includes the 6 dust aerosol models proposed by Moulin *et al.* (2001) ("BDS" and "BDW" models). When introduced, they are distributed homogeneously from the surface to either 2 or 5 or 7 km. At the end, they represent 18 aerosol assemblages.

The backgrounds of continental aerosol (2-12 km) and of stratospheric aerosol (12-30 km) are still present, and a maritime aerosol model is also present in the boundary layer, with a minimal optical thickness of 0.05.

When dust is present in the free troposphere, the 5 optical thicknesses are 0.05, 0.2, 0.5, 0.8 and 2 at 550 nm.

"Blue aerosols"

Three so-called "blue" aerosol models (see later for their optical properties) have been also introduced, with a vertical profile that follows an exponential decrease of the optical thickness with a scale height of 2 km.

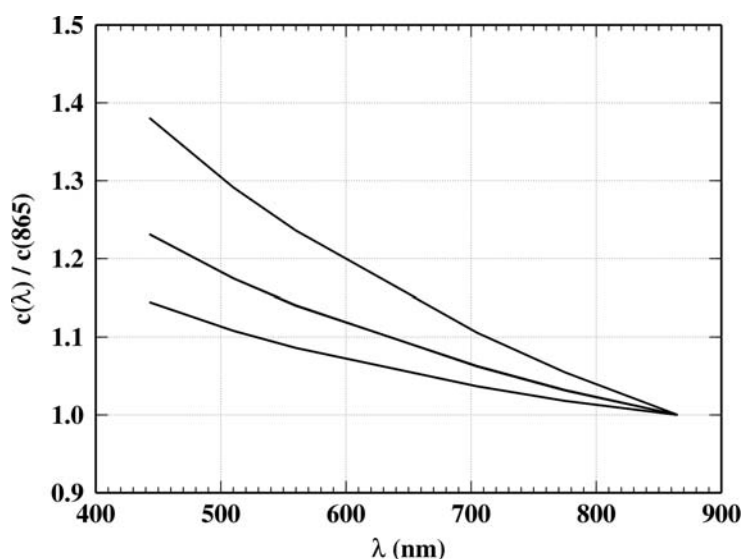


Figure 3.6. Aerosol extinction normalised at 865 nm, as a function of wavelength. From top to bottom: "standard assemblage" with the maritime model for RH = 70, 80, and 99%.

3.1.1.5.2.3 Aerosol models and their optical properties.

The aerosol models used in the present work are constructed from the basic aerosol components defined in Shettle and Fenn (1979) (thereafter referred to as S&F79), WCRP (1986), and Moulin *et al.* (2001). These components consist of spherical particles (allowing the Mie theory to be applied), characterised by a peculiar particle mixing ratio, and size frequency distributions following log-normal laws or the modified gamma function (see Tables 3.1, 3.2 and 3.3). For some



of these aerosols, the index of refraction of the particles depends on the relative humidity (RH); the real part of this index tends to that of water as RH increases, and its imaginary part (which determines absorption) decreases (Table 3.4). The aerosol models are the following:

- “Maritime model” (Shettle and Fenn, 1979; see also Gordon and Wang, 1994): this is a mixture of sea salt solution in water, plus a contribution of tiny continental particles. The index of refraction and the mean radius of particles is RH-dependent.

- “Rural model” (Shettle and Fenn, 1979; see also Gordon and Wang, 1994): this is an aerosol made only of tiny continental particles. The index of refraction and the mean radius of particles is RH-dependent.

- “Coastal model” (Shettle and Fenn, 1979; see also Gordon and Wang, 1994): this is a mixture of sea salt solution in water, plus a contribution of tiny continental particles. The index of refraction and the mean radius of particles is RH-dependent.

- “Blue aerosols”: these non-absorbing models are called “blue” because of the high spectral dependence of their scattering (they are similar to models used by the POLDER mission). They are made of a single component of spherical particles for the whole size spectrum, with a Junge power-law size distribution (see below). Those models have a complex refractive indices of (1.44,0) - wavelength invariant - and Ångström exponent alpha of 2, 2.5 and 3.

- “Continental model” (WCRP, 1986): this model is a mixture of water soluble (29%), dust-like (70%), and soot particles (1%). These 3 basic components are not necessarily the same than in Shettle and Fenn (1979).

- “Stratospheric model” (WCRP, 1986): this model is represented by a 75% solution of sulfuric acid in water. It is non-absorbing, and the size distribution follows a modified gamma function (see below).

- “Desert Dust models” (Moulin *et al.*, 2001): these models are made of three log-normal distributions and two refractive indices.

The size distributions of the models defined by Shettle and fenn (1979), Moulin *et al.* (2001) and by WCRP (1986) are represented by lognormal distributions (Eq. 18), except for the H₂SO₄ model, which is represented by a modified gamma function (Eq. 18'). The blue aerosols follow a Junge power-law size distribution (Eq. 19):

$$n(r) = \frac{dN(r)}{dr} = \sum_{i=1}^2 \left[\left(\frac{N_i}{\ln(10) r \sigma_i \sqrt{2\pi}} \right) \exp \left(-\frac{(\log(r) - \log(r_i))^2}{2 \sigma_i^2} \right) \right] \quad (18)$$

$$n(r) = \frac{dN(r)}{dr} = A \left(\frac{r}{r_0} \right)^\alpha \exp \left[-b \left(\frac{r}{r_0} \right)^\gamma \right], \quad \text{with } r_0 = 1 \mu\text{m} \quad (18')$$

$$n(r) = r^{\alpha-3} \quad (19)$$

Aerosol model	Particles (components)	Volume percentage	Particle percentage
Maritime (S&F79)	Rural aerosol mixtures‡ Sea-salt solution in water (“oceanic”)		99 % 1 %

	Laboratoire d'Océanographie de Villefranche	Doc: MERIS_ATBD_2.7_v5.1-July2011
		Name: MERIS Atmospheric Correction Over Case 1 Waters
		Issue: 5
		Draft Rev: 1
		Date: July 18, 2011
		Page: 29

Coastal (S&F79)	Rural aerosol mixtures‡ Sea-salt solution in water (“oceanic”)		99 % 1 %
Rural	Rural aerosol mixtures‡		100 %
Dust (Moulin et al., 2001)	Large particles Medium particles Small particles		3.9 10 ⁻⁵ % 45.79 54.21 %
Continental (WCRP, 1986)	Water soluble Dust-like Soot	29 70 1	93.876 % 2.27 10 ⁻⁶ % 0.06123 %
H ₂ SO ₄ (WCRP, 1986)	75% solution of sulfuric acid in water	100	100

Table 3.1. proportion of the aerosol components (‡ 70% of water-soluble particles, 30% of dust-like particles).

Aerosol component (S&F 79)		Parameters of the size distribution		
		r_0	$\sigma/\ln(10)$	$\exp(\sigma)$
Rural aerosol mixtures	RH 50%	0.02748	0.35	2.238724
	RH 70%	0.02846		
	RH 80%	0.03274		
	RH 90%	0.03884		
	RH 99%	0.05215		
Sea-salt solution in water	RH 50%	0.1711	0.40	2.51188
	RH 70%	0.2041		
	RH 80%	0.3180		
	RH 90%	0.3803		
	RH 99%	0.7505		

Table 3.2. parameters of the aerosol size distributions: models from Shettle and Fenn (1979)

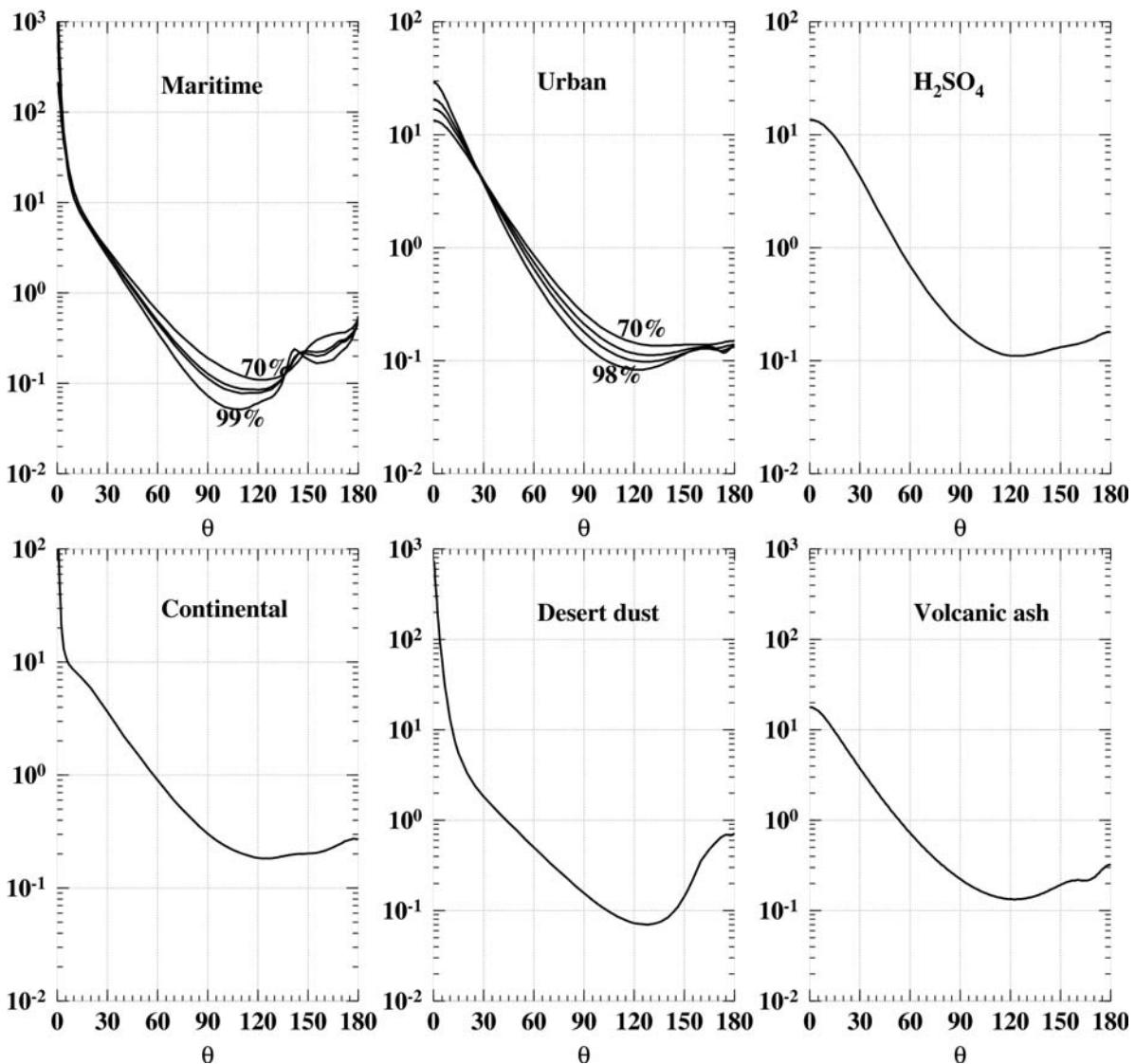


Figure 3.4: Examples of aerosol phase functions, for the aerosols as indicated. Wavelength is 550 nm.

(WCRP, 1986)	r_0	$\sigma/\ln(10)$	$\exp(\sigma)$	
Water soluble	0.005	0.475	2.99	
Dust-like	0.5	0.475	2.99	
Soot	0.0118	0.30	2.00	
	A	α	γ	b
75% H ₂ SO ₄	324	1	1	18
Volcanic ash	5461.33	1	0.5	16

Table 3.3. parameters of the aerosol size distributions: models from WCRP (1986)

	Parameters of the size distribution		
	r_0	$\sigma/\ln(10)$	$\exp(\sigma)$
Large dust particles	6.24		1.89
Medium dust particles	0.022		3.2
Small dust particles	0.001		2.13



Table 3.3 bis. parameters of the aerosol size distributions: models from Moulin *et al.* (2001)

	443 nm		510 nm		560 nm	
	n	n'	n	n'	n	n'
Sea salt (S&F79)‡	1.500	.251 10 ⁻⁷	1.500	.117 10 ⁻⁷	1.499	.112 10 ⁻⁷
Water-soluble (S&F79) ‡	1.530	.500 10 ⁻²	1.530	.500 10 ⁻²	1.530	.600 10 ⁻²
Dust-like (S&F79) ‡	1.530	.800 10 ⁻²	1.530	.800 10 ⁻²	1.530	.800 10 ⁻²
Oceanic, RH = 70%	1.416	.128 10 ⁻⁷	1.414	.622 10 ⁻⁸	1.412	.720 10 ⁻⁸
Oceanic, RH = 80%	1.358	.444 10 ⁻⁸	1.355	.249 10 ⁻⁸	1.354	.452 10 ⁻⁸
Oceanic, RH = 90%	1.349	.319 10 ⁻⁸	1.348	.193 10 ⁻⁸	1.345	.406 10 ⁻⁸
Oceanic, RH = 99%	1.339	.165 10 ⁻⁸	1.336	.124 10 ⁻⁸	1.335	.357 10 ⁻⁸
Water soluble (WCRP86)	1.530	.500 10 ⁻²	1.530	.500 10 ⁻²	1.530	.600 10 ⁻²
Dust-like (WCRP86)†	1.530	.800 10 ⁻²	1.530	.800 10 ⁻²	1.530	.800 10 ⁻²
Soot (WCRP86) †	1.750	.455	1.750	.450	1.750	.439
Volcanic ash (WCRP86)	1.500	.800 10 ⁻²	1.500	.800 10 ⁻²	1.500	.800 10 ⁻²
75 % H ₂ SO ₄ solution	1.436	.100 10 ⁻⁷	1.431	.100 10 ⁻⁷	1.430	.106 10 ⁻⁷
Moulin, BDS models	1.53	0.0091	1.53	0.0073	1.53	0.0054
Moulin, BDW models	1.53	0.0045	1.53	0.0030	1.53	0.0020

Table 3.4. complex refractive indices, n – i n', for wavelengths 443, 510, and 560 nm.

‡ S&F79 stands for Shettle and Fenn (1979). These aerosol components are combined to generate the aerosol models listed in Tables 3.1 and 3.2.

† WCRP86 stands for WCRP (1986). These aerosol components are combined to generate the aerosol models listed in Tables 3.1 and 3.3.

Table 3.4 continued, complex refractive indices, n – i n', for wavelengths 709, 778, and 865 nm.

	709 nm		778 nm		865 nm	
	n	n'	n	n'	n	n'
Sea salt (S&F79)‡	1.489	.287 10 ⁻⁶	1.485	.151 10 ⁻⁵	1.480	.793 10 ⁻⁵
Watersoluble (S&F79) ‡	1.529	.732 10 ⁻²	1.525	.944 10 ⁻²	1.520	.121 10 ⁻¹
Dustlike (S&F79) ‡	1.529	.800 10 ⁻²	1.525	.800 10 ⁻²	1.520	.800 10 ⁻²
Soot (S&F79) ‡	1.750	.430	1.750	.430	1.750	.430
Oceanic, RH = 70%	1.408	.164 10 ⁻⁶	1.405	.822 10 ⁻⁶	1.402	.404 10 ⁻⁵
Oceanic, RH = 80%	1.351	.801 10 ⁻⁷	1.350	.346 10 ⁻⁶	1.348	.138 10 ⁻⁵
Oceanic, RH = 90%	1.343	.675 10 ⁻⁷	1.342	.275 10 ⁻⁶	1.340	.985 10 ⁻⁶
Oceanic, RH = 99%	1.333	.521 10 ⁻⁷	1.332	.189 10 ⁻⁶	1.330	.498 10 ⁻⁶
Water soluble (WCRP86)	1.529	.733 10 ⁻²	1.525	.944 10 ⁻²	1.520	.121 10 ⁻¹
Dustlike (WCRP86)†	1.529	.800 10 ⁻²	1.525	.800 10 ⁻²	1.520	.800 10 ⁻²
Soot (WCRP86) †	1.750	.430	1.750	.430	1.750	.430
Volcanic ash (WCRP86)	1.500	.800 10 ⁻²	1.500	.800 10 ⁻²	1.500	.800 10 ⁻²
75 % H ₂ SO ₄ solution	1.428	.304 10 ⁻⁷	1.427	.975 10 ⁻⁷	1.425	.212 10 ⁻⁶
Moulin, BDS models	1.53	0.00385	1.53	0.00292	1.53	0.00120
Moulin, BDW models	1.53	0.0007	1.53	0.0005	1.53	0.0005

‡ S&F79 stands for Shettle and Fenn (1979). These aerosol components are combined to generate the aerosol models listed in Tables 3.1 and 3.2.

† WCRP86 stands for WCRP (1986). These aerosol components are combined to generate the aerosol models listed in Tables 3.1 and 3.3.

The aerosol phase functions have been computed by using Mie theory, and for the six MERIS bands selected for the present study (443, 510, 560, 709, 778, and 865 nm). Examples are shown in Fig. 3.4. It has been previously checked that the use of the central wavelength (rather than averaging over the bandwidth) does not produce significant differences in the resulting phase function (*cf* JRC contract, 1995).

The extinction coefficients computed from these phase functions are shown on Fig. 3.5, for given conditions, as the ratio of $c(\lambda)$ to $c(865)$. This ratio characterises the spectral dependency of the aerosol extinction

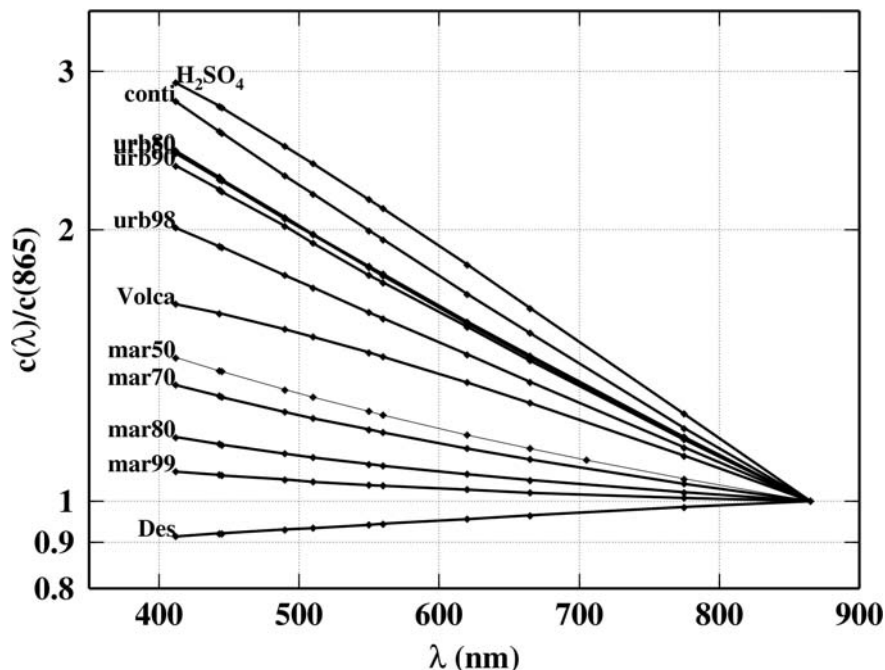


Figure 3.5: the ratio $c(\lambda)/c(865)$ as a function of wavelength (linearlog scale), and for several aerosol models selected for the present study (“mar” is the maritime model for various relative humidities, “urb” is the urban model, etc..).

The complete set of aerosol assemblages therefore contains 34 aerosol assemblages:

- Maritime model (part of the initial set)
RH = 99% for the maritime model (Shettle and Fenn, 1979), the free troposphere and the stratosphere are free of any aerosols ==> 1 assemblage
- Maritime model (part of the initial set)
4 RH (50, 70, 90, and 99%) for the maritime model (Shettle and Fenn, 1979), plus constant backgrounds in the free troposphere and the stratosphere ==> 4 assemblages
- Coastal model (part of the initial set)
4 RH (50, 70, 90, and 99%) for the maritime model (Shettle and Fenn, 1979), plus constant backgrounds in the free troposphere and the stratosphere ==> 4 assemblages
- Rural model (part of the initial set)
4 RH (50, 70, 90, and 99%) for the maritime model (Shettle and Fenn, 1979), plus constant backgrounds in the free troposphere and the stratosphere ==> 4 assemblages
- “Blue aerosols”
==> 3 assemblages

These first sixteen models form the initial set of aerosol models that is used in any case.



- Dust aerosol (only examined if the test at 510 nm is positive)

The 18 models defined in Moulin et al. (2001), plus constant backgrounds in the boundary layer (maritime, RH=99%, optical thickness is 0.05), the free troposphere and the stratosphere
==> 18 assemblages

The use of these 18 models is dictated by the test at 510 nm.

3.1.1.5.2.4 Generating the lookup tables (LUTs)

Lookup tables have been generated, containing (1) the 3 coefficients of the quadratic relationship between $[\rho_{\text{path}} / \rho_{r, \tau_a=0}]$ and τ_a , (2) the Rayleigh reflectances for an aerosol free atmosphere $\rho_{r, \tau_a=0}$, and (3) the aerosol extinction coefficients for all aerosol assemblages, normalised by their value at 865 nm. The “data” needed to make up these tables have been generated by Mie computations (phase functions and extinction coefficients), and by radiative transfer computations, with the following conditions:

Aerosols : all aerosol assemblages, as described above.
 $\tau_a(550)$: 0.03, 0.1, 0.3, 0.5 (and 2, see section 3.1.1.6.5) for the “standard cases”
0.05, 0.2, 0.5, 0.8 (and 2, see section 3.1.1.6.5) for the “non standard cases”
 λ : 443, 510, 560, 709, 778, 865 nm
 θ_s : From 20 to 68°, each 4° (13 values)

Atmospheric pressure is 1013.25 hPa.

The sea surface is flat, and the ocean is totally absorbing (no water-leaving radiances)

The values obtained for the ratio $[\rho_{\text{path}} / \rho_{r, \tau_a=0}]$ at 5 different aerosol optical thicknesses, and the ratio 1 for an aerosol-free atmosphere (so: 6 points) are fitted to a second order polynomial and the 3 coefficients are stored in the LUT. To test the algorithm, additional simulations are carried out, while their results are not incorporated in the lookup tables.

3.1.1.5.3 Test in “standard” conditions (the “standard” set of aerosol assemblages)

3.1.1.5.3.1 Estimation of the path reflectance

cf. Warning page iv

The lookup tables described in the previous section have been used to test the proposed algorithm, by introducing into the algorithm total reflectances at the TOA level, as simulated with the maritime aerosol for RH = 85%. Results are presented either for specific geometries (Fig. 3.7; configurations typical of a MERIS scan), or in a more general form in Fig. 3.8; these results show that, for the clear maritime atmospheres, the required accuracy (± 0.002 in reflectance at 443 nm) is reached by the algorithm. The error at 560 nm is usually $\frac{1}{2}$ or $\frac{1}{4}$ of the error at 443 nm, even if larger errors at 560 nm are sometimes encountered. Errors above the ± 0.002 limit are actually obtained either for geometrical configurations where sun glint should actually avoid any correction, or for high optical thicknesses. It is noticeable that better results are obtained when the Monte Carlo technique (with its unavoidable stochastic noise) is abandoned for the generation of the pseudo data and the lookup tables, and replaced by an exact technique. This has been tested for instance with the Matrix Operator Method.

3.1.1.5.3.2 Retrieval of the aerosol optical thickness

Fig. 3.9 shows the relative error in the aerosol optical thickness, as retrieved for 865 nm. Most of these errors are within $\pm 15\%$, and often considerably less.

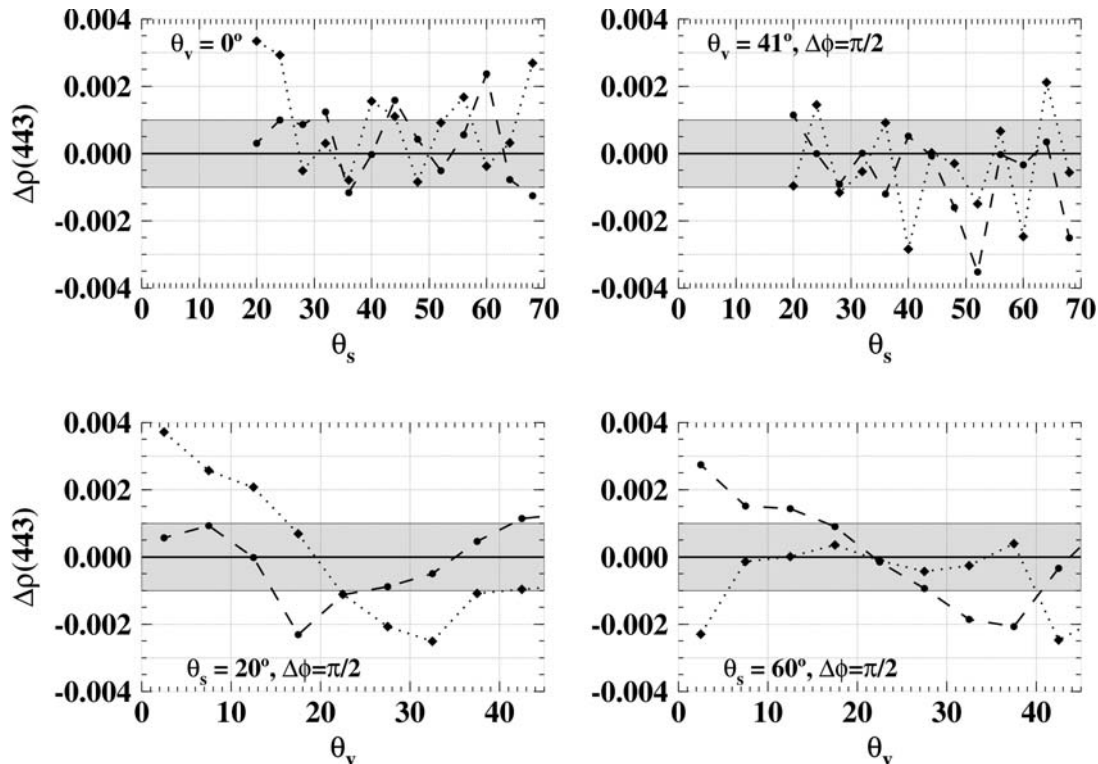


Figure 3.7. Error in the retrieved top of atmosphere water leaving reflectance at 443 nm, for the maritime aerosol with $RH = 85\%$, and for the geometrical conditions indicated. Dotted line is for $\tau_a(550)$ about 0.3, dashed line for $\tau_a(550)$ about 0.1 (*i.e.*, about the mean over remote oceanic areas).

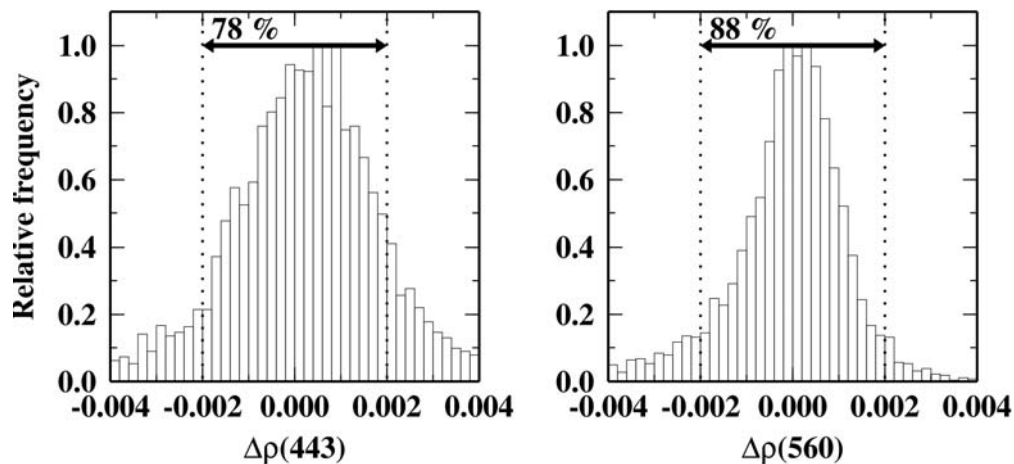


Figure 3.8. Histogram of the error in the retrieved top of atmosphere water leaving reflectance at 443 and 560 nm (expressed as the frequency of each class relative to the most represented class), for the maritime aerosol with $RH = 85\%$. The results for the 4 aerosol optical thicknesses and various geometries are here pooled together (4004 cases). The percentage of errors within ± 0.002 is indicated.

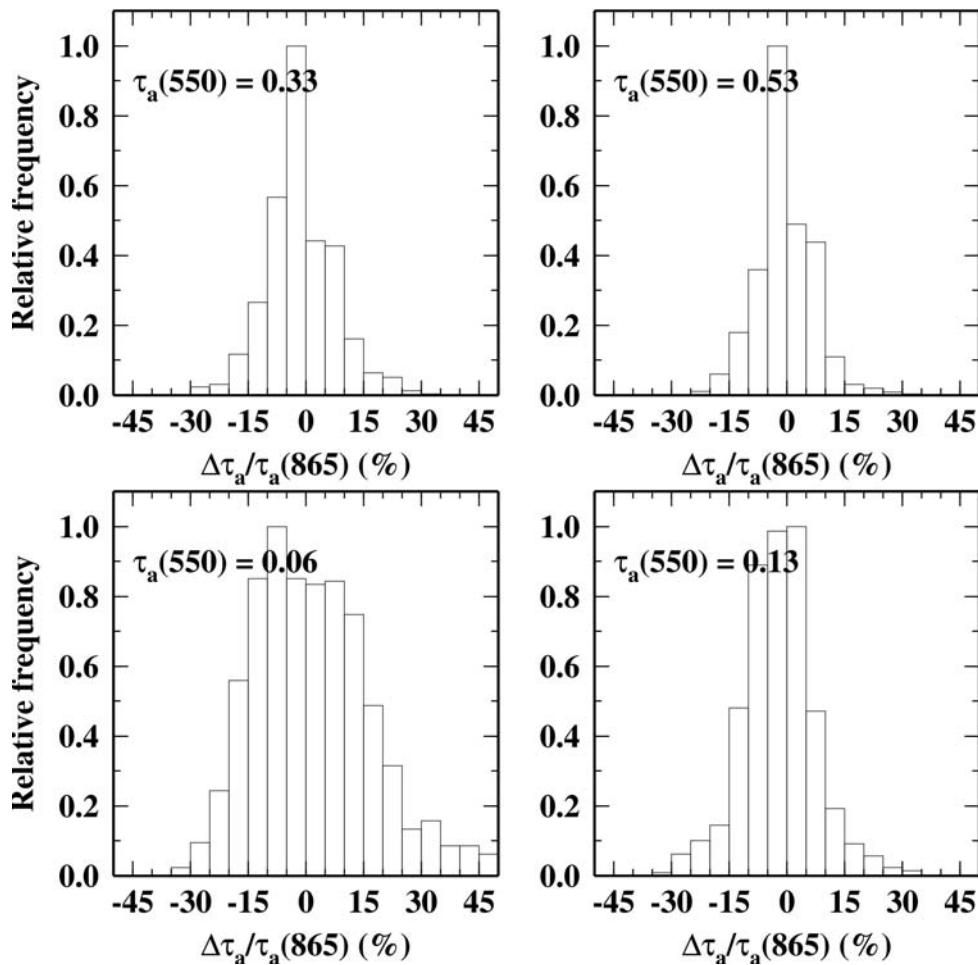


Figure 3.9. Histogram of the relative error in the aerosol optical thickness retrieved at 865 nm (same 4004 cases as in Fig. 3.8).

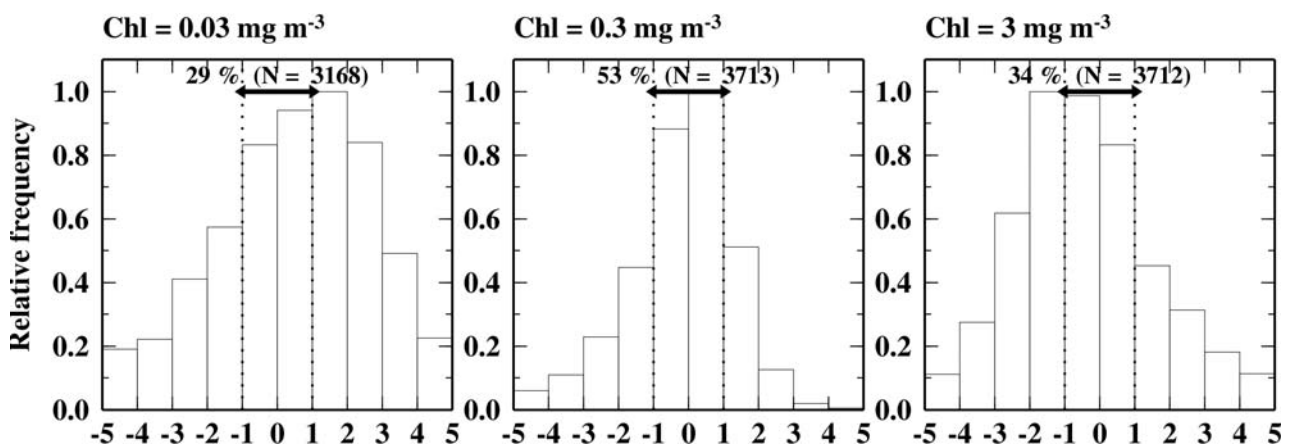


Figure 3.10. Histograms of the error in the pigment index due to the error $\Delta\rho$ in the atmospheric correction, for 3 nominal values of Chl, as indicated (the same 4004 cases as in Fig. 3.8, for each panel). The percentage of “exact retrievals” is indicated, as well as the total number of cases for which a chlorophyll concentration has been computed.

3.1.1.5.3.3 Impact on the pigment index retrieval



The impact of the errors in the atmospheric correction on the pigment index (Chl) retrieval can now be assessed. The bio-optical algorithms defined for MERIS (see ATBD 2.9 and Morel and Gentili, 1996) have been used here, under the form of a polynomial expression

$$\text{Log}_{10}(\text{Chl}) = 0.4389 - 3.3626 \text{Ir}_{13} + 3.9348 \text{Ir}_{13}^2 - 3.0787 \text{Ir}_{13}^3 + 0.6298 \text{Ir}_{13}^4 \quad (20)$$

where Ir_{13} is the decimal logarithm of the largest among the three following ratios of the fully normalised water-leaving reflectances: (443/560) (490/560) and (510/560).

The error $\Delta\rho(\lambda)$ obtained at the end of the atmospheric correction is equal to $t_d(\theta_v, \lambda) \Delta\rho_w(\lambda)$. To infer the impact of the error in atmospheric correction on the pigment concentration retrieval, fully normalised water-leaving reflectances were derived from the marine reflectances through (see list of symbols)

$$[t_d \cdot \rho_w(\lambda, \theta_s, \theta', \Delta\phi)] = \pi t_d(\lambda, \theta_v) t_{\theta_s}(\lambda) \mathfrak{R}(\theta') \frac{f_1(\lambda, \theta_s)}{Q(\lambda, \theta_s, \theta', \Delta\phi)} \frac{b_b(\lambda)}{a(\lambda)} \quad (21)$$

$$\mathfrak{R}(\theta') = \left[\frac{(1 - \bar{\rho})}{(1 - \bar{r}R)} \frac{(1 - \rho_F(\theta'))}{n^2} \right] \quad (22)$$

A new pigment concentration, Chl' , is then computed and compared to the initial concentration, Chl . An iterative procedure is necessary, because the value of the f/Q ratio is dependent upon the chlorophyll concentration, which is the unknown of the problem (see Morel and Gentili, 1996; MERIS ATBD 2.9). The comparison has been made for pigment concentrations of 0.03, 0.3 and 3 mg m^{-3} . The histograms of the errors in Chl are shown in Fig. 3.10.

Each of the three histograms in Fig. 3.10 merges the errors in the retrieved chlorophyll concentration for $\tau_a = 0.03, 0.1, 0.3$ and 0.5 at 550 nm, and for several geometries. These errors are expressed in terms of a number of (Chl) classes: values between x and $x+1$ (x being an integer between 0 and 4) mean that the retrieved (Chl) concentration is overestimated by x (Chl) class. Along the same line, values between $x-1$ and x mean that the retrieved (Chl) concentration is underestimated by x (Chl) class. Therefore, all values between -1 and $+1$ correspond to an “exact retrieval” in terms of (Chl) classes. Less than 40% of the retrieval fulfill this condition when $\text{Chl} = 0.03 \text{ mg m}^{-3}$ (Fig. 3.10), and a slight positive bias affect the retrieved concentrations. The results for $\text{Chl} = 0.3 \text{ mg m}^{-3}$ are in better shape, with no bias and 65% of exact retrievals. A bias of about minus one class (*i.e.*, -20%) occurs for $\text{Chl} = 3 \text{ mg m}^{-3}$, and 46% of the errors are within the limit of ± 1 class.

When $\text{Chl} = 0.03 \text{ mg m}^{-3}$, the low percentage of exact retrievals is actually consistent with the severe accuracy requirement for the domain of low (Chl) (see Fig. 3.1(c); remind that a shift of only one class of concentration represents a -20% or $+25\%$ change in (Chl)). The discrimination of 10 (Chl) classes between 0.03 and 0.3 mg m^{-3} , as initially aimed at, seems limited by the accuracy of the atmospheric correction. Lowering the number of (Chl) classes to be detected to 5 between 0.03 and 0.3 mg m^{-3} , for instance, would increase the acceptable errors in $\rho_w(443)$.



The bias observed when $\text{Chl} = 3 \text{ mg m}^{-3}$ was not expected to the extent that the errors in atmospheric correction are the same for the three panels of Fig. 3.10. Errors that do not bias the pigment retrieval for low and moderate chlorophyll concentrations (*i.e.*, high $\rho_w(443)$), have an impact for higher concentrations because the actual blue-to-green ratio is close to 1. This bias is a consequence of the nature of the algorithm, which performs extrapolation of the atmospheric contribution from the near infrared toward the visible, with, in general, increasing errors with decreasing wavelength. As far as we know, this problem, occurring for chlorophyll concentrations around 3 mg m^{-3} , seems not to have been acknowledged.

3.1.1.5.4 Test with absorbing aerosols

Here the reader is referred to the two following publications, provided in Appendix:

Antoine and Morel, 1999, "A multiple scattering algorithm for atmospheric correction of remotely-sensed ocean colour (MERIS instrument): principle and implementation for atmospheres carrying various aerosols including absorbing ones", *International Journal of Remote Sensing*, 20, 1875-1916.

Nobileau, D. and D. Antoine, 2005, Detection of blue-absorbing aerosols using near infrared and visible (ocean colour) remote sensing observations. *Remote Sensing of Environment*, 95, 368-387.



3.1.1.6 Sensitivity studies

cf. Warning page iv

In this section, the impact of various parameters on the atmospheric correction is examined through sensitivity studies. The principle is to operate the correction by using the database generated for the prescribed standard conditions (*i.e.*, a flat sea surface, and specified constant values for atmospheric pressure and ozone content), to process data issued from simulations where the conditions are different, regarding one parameter of interest. The amplitude of the error in the retrieved water leaving reflectances should then provide information to decide if the natural variability in the parameter in question has to be accounted for (by increasing the dimension of the lookup tables) or, on the contrary, if this parameter can be kept to a constant and mean value.

3.1.1.6.1 Vertical distribution of aerosols / “special” aerosols

Even if the standard vertical structure of aerosols adopted to implement the algorithm has been derived from observations and from the recommendations of aerosol specialists, it is clear that different vertical structures are possible over the ocean. Different aerosol types (*i.e.*, composed of other components than the standard aerosols used before) are also possibly encountered. The following have been tested here:

- (1) In the free troposphere, the desert dust model of Schütz (1980) is replaced by the dust-like aerosol component described in WCRP (1986). The dust and the boundary-layer aerosol (the maritime model, with RH = 80%) are each responsible for 50% of the optical thickness, τ_a , which is set to 0.05 and 0.50 at 550 nm. This profile illustrates a situation where the aerosol in the lookup tables and the actual aerosol have a similar spectral behaviour in the near infrared, whereas their absorption characteristics diverge in the visible.
- (2) The continental aerosol within the free troposphere is replaced by an aerosol whose particle size distribution follows a Junge law, with $\nu = 3$, with refractive indices of 1.33 (water) and 1.50 (continental particles), and with $\tau_a = 0.1$ at 550 nm. The boundary layer is as above, with an optical thickness of 0.03 or 0.3. This situation corresponds to blowing over the ocean of continental, non-absorbing, particles.
- (3) The urban model with small particles is replaced by a model with a larger mode (Shettle and Fenn, 1979). The constant background in the free troposphere remains as in the standard cases (clear atmospheres). This situation could be encountered above near coastal waters, overlaid by air masses close to their source of soot particles.
- (4) A moderately absorbing mixture of oceanic particles and desert dust (dust particles being either 10 or 50% of the total particle number) replaces the pure maritime aerosol in the boundary layer. The constant background in the free troposphere remains as in the standard cases (clear atmospheres). This profile corresponds to the sinking of desert dust into the sea.
- (5) A convective atmosphere is simulated by annihilating the vertical structure in the boundary layer and the free troposphere, and by replacing the standard maritime and continental aerosols by the same mixtures as above, with a scale height of 3 kilometers within the whole troposphere. The total aerosol optical thickness is set to 0.05 and 0.3.
- (6) Idem as (5) but for the urban aerosol (with RH = 80 or 99%).
- (7) The extension of the desert dust layer is reduced to 4 km (between the altitudes 2 and 6 km), instead of 10 km (2 to 12 km) in the previous profiles, with an optical thickness of 0.1. The



boundary layer aerosol is the maritime model with $RH = 80\%$. This structure aims at representing a dust layer after a long transport over the ocean (it is likely that this kind of layer tends to narrow during its transport; Powell, 1995).

The 7 aerosol distributions were used to simulate TOA total radiances for $\theta_s = 20, 40,$ and 60° . The error of atmospheric correction at 443 nm obtained for these aerosols are pooled together for several geometries, and they are presented in Fig. 3.19 and discussed below in reference to the numbering used above. The corresponding errors in the retrieved pigment index are presented in Fig. 3.20.

- (1) Absorption is systematically detected for $\tau_a = 0.5$, and less frequently for $\tau_a = 0.05$. The increasing departure of the $[c(\lambda) / c(865)]$ ratios with decreasing wavelength, between the two desert dust models (WCRP (1986), used for the test, and Schütz (1980), in the lookup tables) leads however to an over-correction of about 0.004 at 443 nm. These rather bad results emphasise the need for a correct representation of the absorption properties of the aerosols in the visible domain.
- (2) The situation is approximately converse of that in (1), *i.e.*, an under-correction, with however a greater percentage of errors within ± 0.002 . Introducing aerosols with a strong scattering selectivity within the lookup tables (they are not represented now) would probably brought the bias observed here close to 0.
- (3) The reasonably good results for the correction of the large urban aerosols indicate that some uncertainty in the representation of the coarse mode of the aerosol size distribution is probably acceptable.
- (4) Atmospheric correction is accurate when only a few absorbing particles are present in the boundary layer. The correction is here effected with the standard aerosol assemblages (no detection of absorption).
- (5) The high percentage of errors within ± 0.002 confirms that an exact representation of the vertical distribution of aerosols is not crucial when this aerosol is not too much absorbing.
- (6) The same comment as above could be made, except that now the aerosol is strongly absorbing. The rather good results in fact show that some uncertainty in the vertical extension of the absorbing aerosol layer do not lead to large errors if the aerosol in the lookup tables is close enough to the actual one.
- (7) Same comment as for (6)

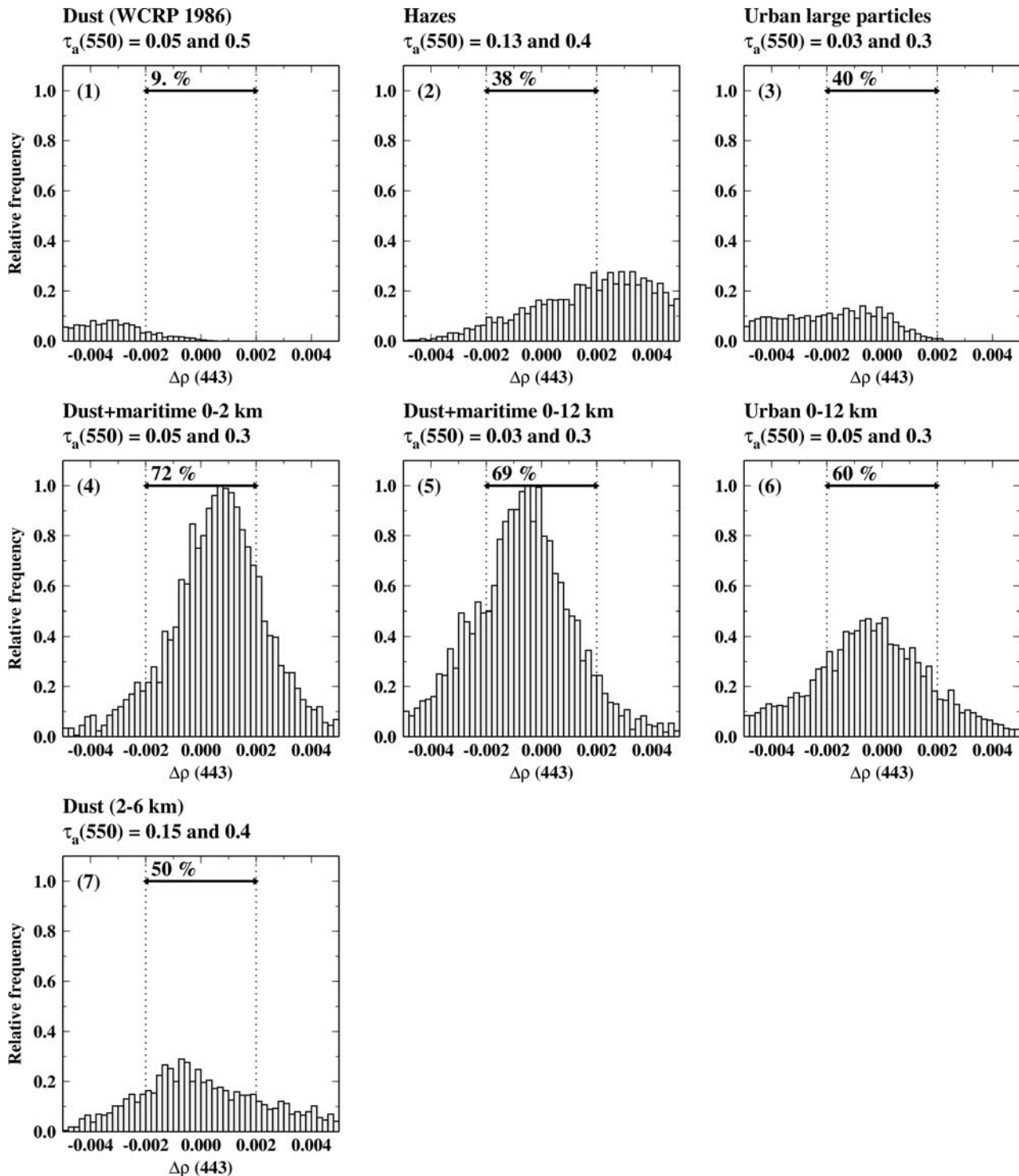


Figure 3.19. Histograms of the error in the atmospheric correction at 443 nm, for the peculiar situations described in the text (section 3.1.1.6.1). Results for various geometries and aerosol optical thicknesses are pooled together. The percentages indicate how many errors are within ± 0.002 .

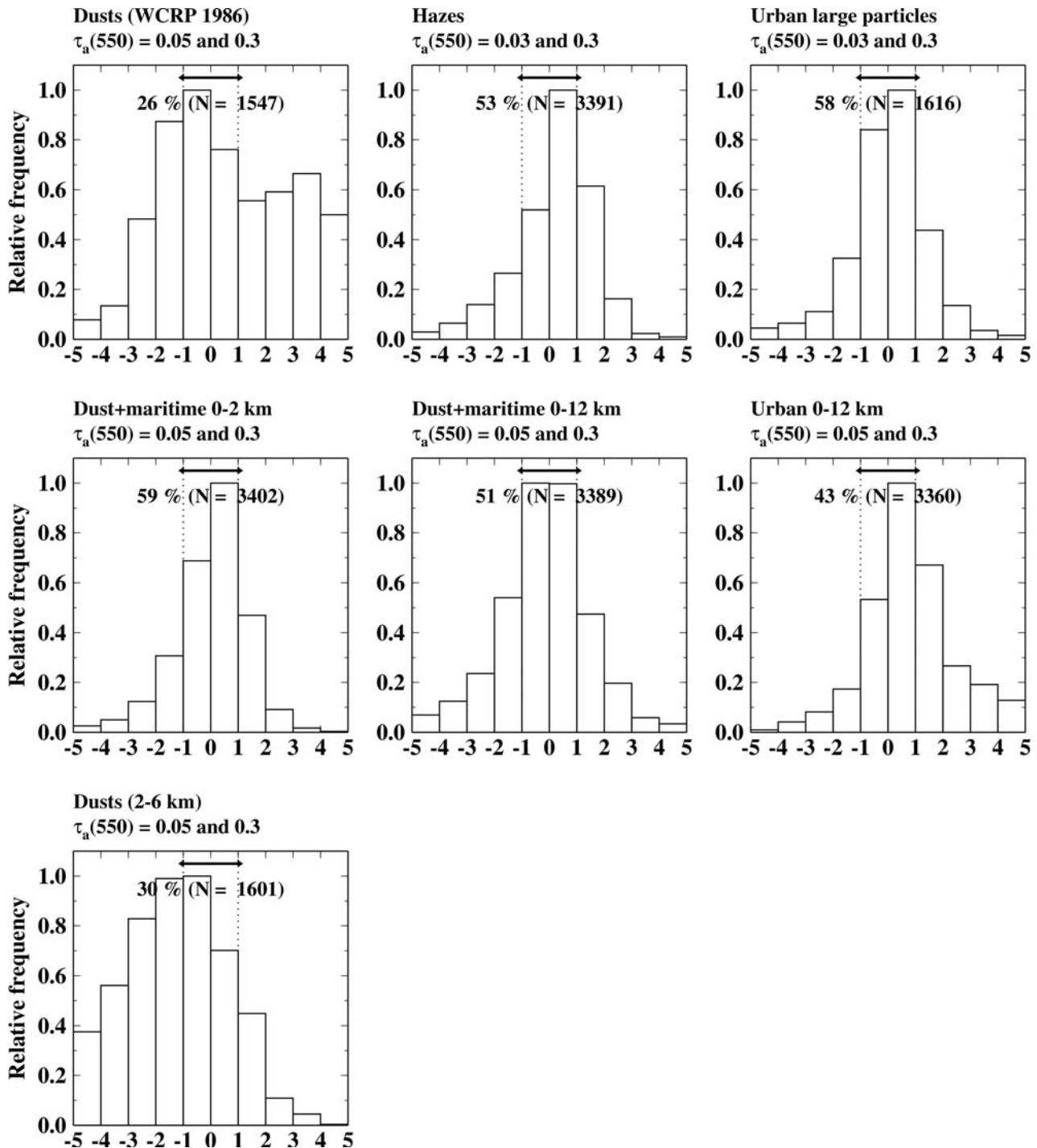


Figure 3.20. Histograms of the errors in the retrieved pigment index, corresponding to the errors of the atmospheric correction shown in Fig. 3.19. The nominal value of the pigment index is $0.3 \text{ mg Chl m}^{-3}$.

3.1.1.6.2 Atmospheric pressure

The importance of atmospheric pressure in sizing the Rayleigh reflectances has been already emphasised for the CZCS algorithms (André and Morel, 1989). The lookup tables that are used in the present work (and containing for instance the relationships between $[\rho_{\text{path}} / \rho_r, \tau_{\text{a}}=0]$ and

τ_a) have been generated from simulations where the atmospheric pressure is kept to a constant value, namely 1013.25 hPa. If the actual atmospheric pressure is not 1013.25 hPa, then the actual and the tabulated $[\rho_{\text{path}}(\lambda) / \rho_{r, \tau_a=0}(\lambda)]$ ratios could not coincide.

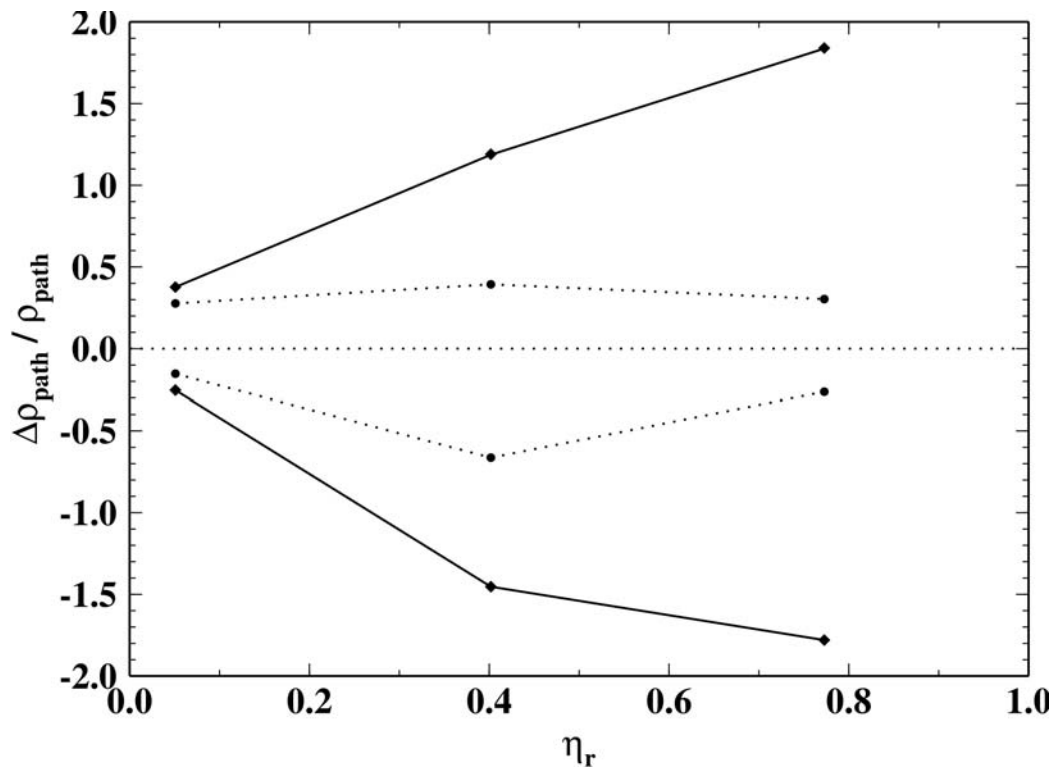


Figure 3.21. Relative changes (percents) of the TOA path reflectance, in response to relative changes in atmospheric pressure, $\Delta P/P$, of $\pm 2\%$, and displayed as a function of η_r (solid curves). The conditions are: $\theta_s = 40^\circ$, maritime aerosol (RH = 85%). The three points correspond to the mean error for several geometries (θ_v from 0 to 60° each 4° , and $\Delta\phi = 0, \pi/2$ and π), and the three increasing values of η_r correspond to (1) $\lambda = 865$ nm and $\tau_a(550) = 0.3$, (2) $\lambda = 443$ nm and $\tau_a(550) = 0.3$, and (3), $\lambda = 443$ nm and $\tau_a(550) = 0.05$. The dotted curves show the relative errors in the path reflectance, after Eq. (27) has been used to calculate its value for a standard pressure $P = 1013.25$ hPa, from its value at $P' = P(1 + \Delta P/P)$.

The relative change $\Delta\rho_{r, \tau_a=0}/\rho_{r, \tau_a=0}$ resulting from a relative change $\Delta P/P$ is close to $\Delta P/P$, even if not strictly equal because of multiple scattering effects (Gordon *et al.*, 1988). The situation is different for ρ_{path} , that is within a compound atmosphere containing molecules (optical thickness τ_r) and aerosols (τ_a). When τ_r is increased, the reflectance due to pure Rayleigh scattering, as well as the reflectance corresponding to heterogeneous scattering obviously tend to increase. In the meantime, however, the reflectance due to aerosol scattering only is decreasing: the increase in molecule concentration tends to “mask” the aerosol signal, at least if τ_r is large compared to τ_a . As a consequence, the repercussion of $\Delta P/P$ on $\Delta\rho_{\text{path}}/\rho_{\text{path}}$ is progressively decreasing when the contribution of molecules (τ_r) to the total optical thickness decreases, *i.e.*, when $\eta_r (= \tau_r / (\tau_a + \tau_r))$ is decreasing. For instance, when $\Delta P/P = +2\%$, $\Delta\rho_{\text{path}}/\rho_{\text{path}}$ at 443 nm is of about +1.5% when τ_a is 0.05 ($\eta_r \sim 0.8$), less than +1% when τ_a is 0.3 ($\eta_r \sim 0.4$), and nearly zero at 865 nm when τ_a is 0.3



($\eta_r \sim 0.05$). The following simple and empirical correction is then proposed to account for the changes in atmospheric pressure

$$\rho'_{\text{path}} = \rho_{\text{path}} \left(1 + (\Delta P/P)\eta_r \right) \quad (27)$$

where ρ_{path} and ρ'_{path} are the path reflectances for the standard pressure P and the pressure $P' = P (1 + \Delta P/P)$. Using Eq. (27) allows to recover the exact value of ρ_{path} within $\pm 0.5\%$ (Fig. 3.21). Therefore, if atmospheric pressure significantly differs from the mean value (± 5 hPa for instance), Eq. (27) can be used to correct the measured value of ρ_{path} in the near infrared, from P' to P , before introducing it into the algorithm. At this stage, τ_a is still unknown, and can be taken from the surrounding pixels (a $\pm 20\%$ error on τ_a does not appreciably degrade the accuracy of Eq. (27)). The whole scheme is then operated by using the lookup tables generated for the standard pressure, and the values of ρ_{path} obtained at the end in the visible domain are again corrected by using Eq. (27), but now from P to P' . This technique has been applied to the same situations as shown in Fig. 3.7, with $P = 993$ and 1033 hPa (*i.e.*, changing the standard pressure by plus or minus 2%), and the results are shown in Fig. 3.22.

3.1.1.6.3 Inland waters

A peculiar problem is addressed here, and concern the possibility of using the present atmospheric correction algorithm for inland waters (at least if they cover significant areas and are Case 1 waters), and especially if the altitude of these waters is significantly above the 0 level. This problem is connected to the sensitivity to atmospheric pressure, P .

The variations in P due to weather changes above the ocean are of the order of $\pm 2\%$ (see above), while they are much more important when “moving” a target from the sea level to an altitude of one or several kilometers. In addition, in the case of ocean areas, the small variations in P affect nearly all layers, while in the case of an increasingly elevated target, the layers with the greatest molecule concentration are progressively removed, the aerosol content remaining about the same (the boundary layer and the stratosphere remain unchanged; only the “free troposphere” grow smaller). One can therefore expect that the ratio $[\rho_{\text{path}} / \rho_{r,\tau_a=0}]$ will increase more rapidly with τ_a as the number of molecules decreases. It is likely that the coupling between scattering due to aerosol and scattering due to molecules is also affected.

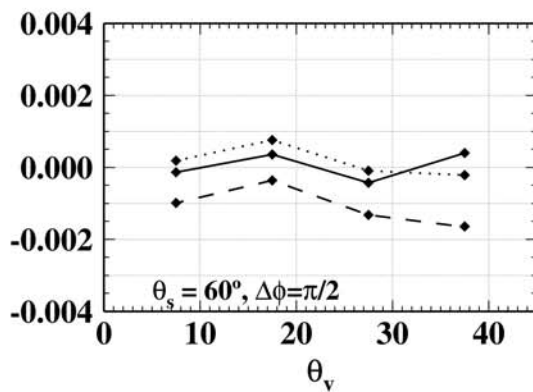
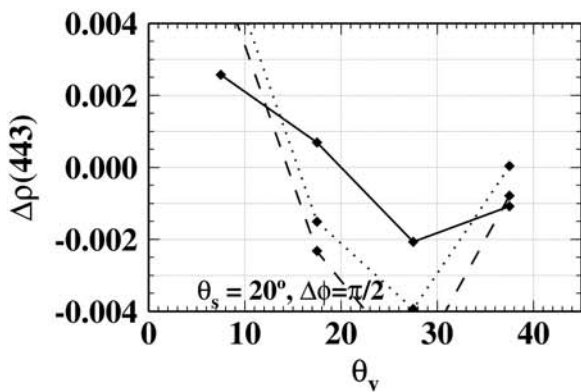
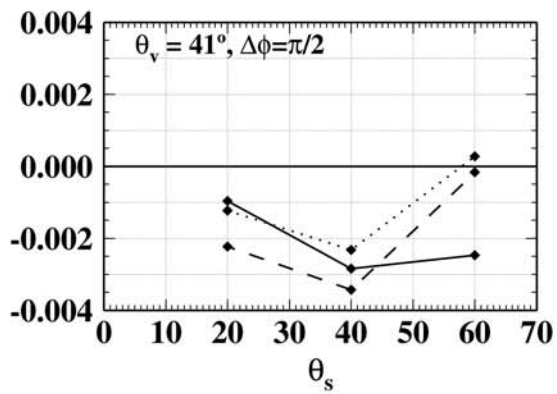
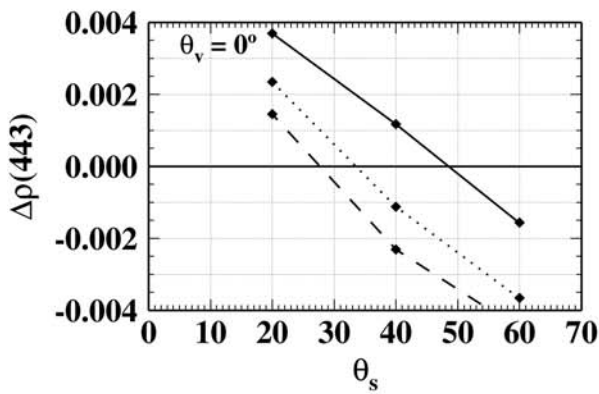
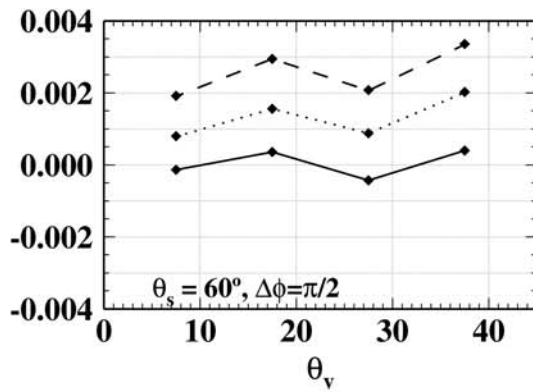
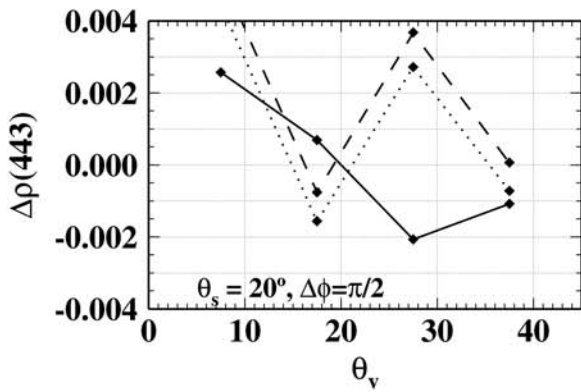
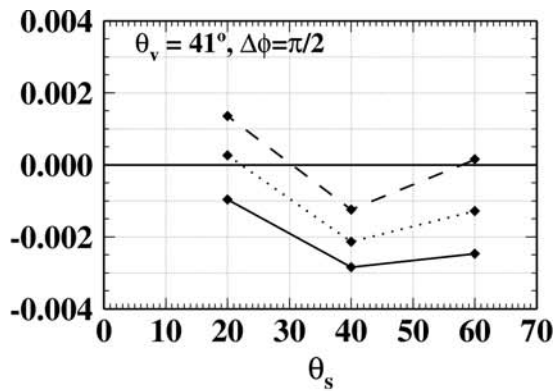
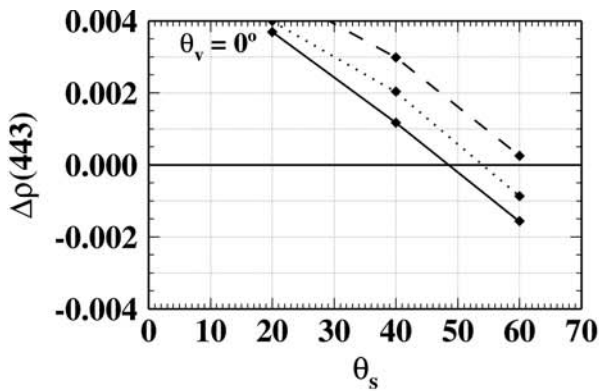


Figure 3.22. Error in the retrieved top of atmosphere water leaving reflectance at 443 nm, for the maritime aerosol with RH = 85%, for $\tau_a(550)$ about 0.03 and 0.30, and for the geometrical conditions indicated. Solid lines are the results obtained when the actual pressure is the standard pressure. Dashed and dotted lines are for the standard pressure less 20 hPa (*i.e.*, 993 hPa, upper 4 panels), or plus 20 hPa (*i.e.*, 1033 hPa, lower 4 panels), and respectively without or with the correction for the change in pressure (Eq. 27).

Simulations have been carried out to assess these effects, by modifying as follows the vertical atmospheric profiles:

- The boundary layer is still the layer between the altitude of the target and this altitude plus 2 kilometers. It contains the continental aerosol, with an optical of 0.3 at 550 nm.
- The stratosphere is obviously still the layer between altitudes 12 and 50 km, with the H₂SO₄ aerosol (optical thickness of 0.005 at 550 nm).
- The “free troposphere” is the remaining (for instance from 4 to 12 km if the target is at an altitude of 2 kilometers), and contains the continental aerosol. The aerosol optical thickness for this layer results from the integration of the extinction coefficients over less than 10 one-kilometer layers, each with an extinction coefficient of 0.0025 km⁻¹ (this led to an optical thickness of 0.025 when elevation was 0).
- The vertical profile for molecular scattering (Elterman, 1968) is integrated over the altitudes corresponding to the 3 levels

The ratios $[\rho_{\text{path}} / \rho_{r,\tau_a=0}]$ at 443 and 865 nm are shown in Fig. 3.23, as a function of τ_a , and for several altitudes (including the sea level), with an increment of 1 km. Drastic changes appear in the slope of this relationships, clearly preventing from using the present atmospheric correction algorithm as soon as the target is not at the sea level.

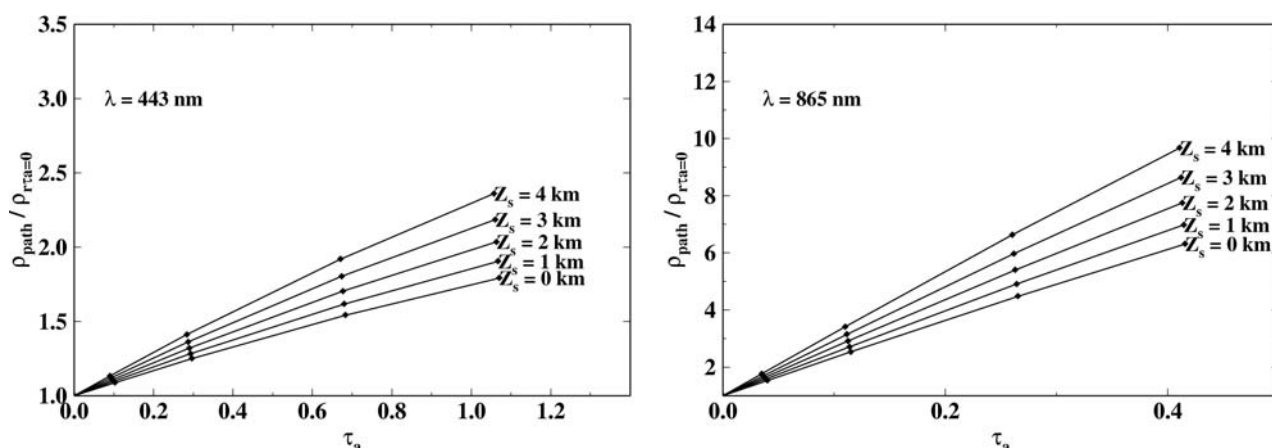


Figure 3.23. The relationship $[\rho_{\text{path}} / \rho_{r,\tau_a=0}]$ as a function of τ_a , at 443 and 865 nm, and for compound atmospheres (aerosols plus molecules) bounded by a Fresnel reflecting interface located at various altitudes, as indicated.

3.1.1.6.4 Wind speed

The relationship $[\rho_{\text{path}} / \rho_{r,\tau_a=0}]$ versus τ_a is probably modified when the sea surface is no longer flat. When wind blows at the sea surface, whitecaps are one cause of changes in the TOA reflectances; their effect on atmospheric correction will be assessed in section 3.1.3.2.5. Sea



surface roughness also modifies the sun glint pattern as well as the fate of any diffuse photon interacting with the surface. The latter effect is examined here (see also Gordon and Wang, 1992a, 1992b), by assuming that the sun glint reflectance has been previously calculated and subtracted from the total reflectance (see section 3.1.3.2.8 for a discussion of this assumption).

Monte Carlo simulations have been carried out for atmospheres bounded by a wind-roughened ocean, with facet slopes normally distributed, independently of the wind direction. The probability density of surface slopes for the direction $(\theta_s, \theta_v, \Delta\phi)$ is given by (Cox and Munk, 1954)

$$p(\theta_s, \theta_v, \Delta\phi) = \frac{1}{\pi \sigma^2} \exp\left(\frac{-\tan^2(\beta)}{\sigma^2}\right) \quad (28)$$

where β is the angle between the local normal and the normal to the facet, and σ is the root mean square of slopes, and is a function of wind speed, W , through (Cox and Munk, 1954)

$$\sigma^2 = 0.003 + 5.12 \cdot 10^{-3} W \quad (29)$$

The sun glint reflectance at the TOA level is:

$$\rho_G = \pi \rho_F p(\theta_s, \theta_v, \Delta\phi) / (4 \cos(\theta_v) \cos(\theta_s) \cos^4(\beta) T(\theta_v) T(\theta_s)) \quad (29')$$

where β is the angle between the local normal and the normal to the facet ($\cos(\beta) = (\cos(\theta_v) + \cos(\theta_s)) / 2 \cos(\omega)$), with $\cos(2\omega) = \cos(\theta_v) \cos(\theta_s) - \sin(\theta_v) \sin(\theta_s) \cos(\Delta\phi)$, and where $T(\theta)$ is the direct transmittance of the atmosphere for angle θ , and is equal to $e^{-\tau/\cos(\theta)}$, with τ the total optical thickness (Rayleigh + aerosols + ozone + etc...).

Shadowing effects are not accounted for in the Monte Carlo simulations. The resulting $[\rho_{\text{path}} / \rho_{r, \tau_a=0}]$ versus τ_a curves, obtained at 443 and 865 nm with the maritime aerosol and $\sigma = 0$ and 0.2, are displayed in Fig. 3.23, for $\theta_s = 36^\circ$, $\Delta\phi = \pi/2$, and $\theta_v = 12^\circ$ (panel (a)) or $\theta_v = 57^\circ$ (panel (b)). The light field is more and more diffuse as the wavelength decreases, or, for a given wavelength, when θ_v increases. The impact of the rough surface on the reflectances is accordingly reduced in the visible, as compared to the near infrared, and also when aiming at the ocean at large viewing angles for $\lambda = 865$ nm. The curves obtained at $\lambda = 443$ nm are nearly superimposed when obtained either for $\sigma = 0$ or for $\sigma = 0.2$, because the spatial redistribution of reflected photons cannot further increase the diffuse character of the light field. On the contrary, the redistribution of radiances at 865 nm leads to some changes in the slope of the $[\rho_{\text{path}} / \rho_{r, \tau_a=0}]$ versus τ_a relationship when $\theta_v = 12^\circ$.

Two, perhaps three, sets of lookup tables should thus be generated (for the relationship $[\rho_{\text{path}} / \rho_{r, \tau_a=0}]$ versus τ_a), in correspondence with $W = 0$ and with moderate wind speeds, probably around 5 and 10 m s⁻¹. This is actually what has been done in the present operational implementation of the algorithm (with wind speeds of X and Y m s⁻¹).

Higher wind speeds are not to be considered, because the importance of the changes here examined would become much lower than that due to the reflectance of whitecaps. Switching from

one set of lookup tables to another one, or interpolating between them, must rely on the knowledge of wind speed, available either from other sensors, or from meteorological centers.

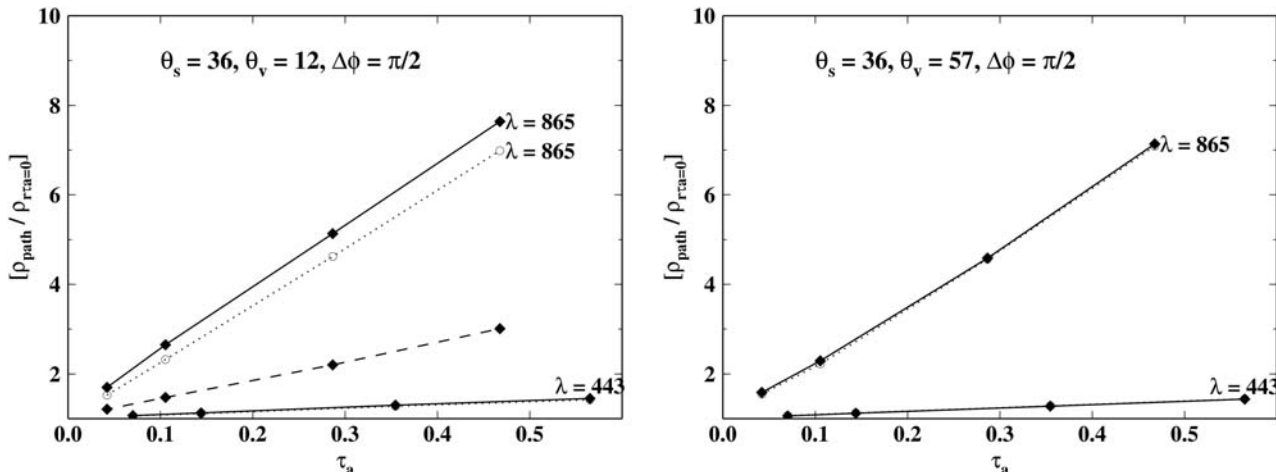


Figure 3.24. The $[\rho_{\text{path}} / \rho_{r, \tau_a=0}]$ ratio at 443 and 865 nm is drawn as a function of τ_a , and for $\theta_s = 36^\circ$, $\Delta\phi = \pi/2$, and $\theta_v = 12^\circ$ (left) or 57° (right). The aerosol is the maritime model (RH = 85%). Dotted curves are for a perfectly flat sea surface, and solid curves are for a windroughened interface, characterised by $\sigma = 0.2$. Dashed line is as the dotted line, but for the $[\rho_t / \rho_{r, \tau_a=0}]$ ratio (*i.e.*, the sun glint has not been corrected).

3.1.1.6.5 High aerosol optical thickness

Atmospheric correction primarily aims at retrieving the optical properties of the surface ocean, when seen through a scattering and absorbing atmosphere. When using the technique proposed here, however, atmospheric properties are also recovered, as by-products of the algorithm. One of these properties is the aerosol optical thickness, τ_a , which is of considerable interest for studies of the earth radiation budget and climate (*e.g.*, Charlson *et al.*, 1992), as well as for ocean biogeochemistry (*e.g.*, Donaghay *et al.*, 1991). When τ_a becomes high, say above 0.6-0.8 at 550 nm, it is probably illusory to try an assessment of the oceanic surface properties (at least with the accuracy required here), because the error on τ_a would cause prohibitively large errors on ρ_w . It is however conceivable to recover the value of τ_a . Therefore, it is examined in this section whether τ_a is still retrievable when it is high. A value of 2 at 550 nm has been chosen; it is probably a maximum, and could correspond for instance to a massive blowing of dust over the ocean. The Lookup tables have been accordingly modified, *i.e.*, the quadratic fits of $([\rho_{\text{path}} / \rho_{r, \tau_a=0}] \text{ versus } \tau_a)$ have been performed over 6 couples, instead of 5, and including now the couple corresponding to $\tau_a = 2$. The error in atmospheric correction at 443 nm, as well as the relative error on the aerosol optical thickness at 865 nm, are displayed in Fig. 3.25 for the four aerosol types. In most cases (*i.e.*, 70 to 90%), atmospheric correction fails, meaning that ρ_w is not recovered with the required accuracy (*i.e.*, ± 0.002 in reflectance). The retrieval of τ_a , however, remains acceptable, with most of the relative errors within $\pm 30\%$ (*i.e.*, τ_a retrieved with an error of about ± 0.3). Therefore, with the MERIS instrument, the retrieval, and thus the global mapping, of the aerosol optical thickness at 865 nm seems possible even for highly turbid atmospheres.

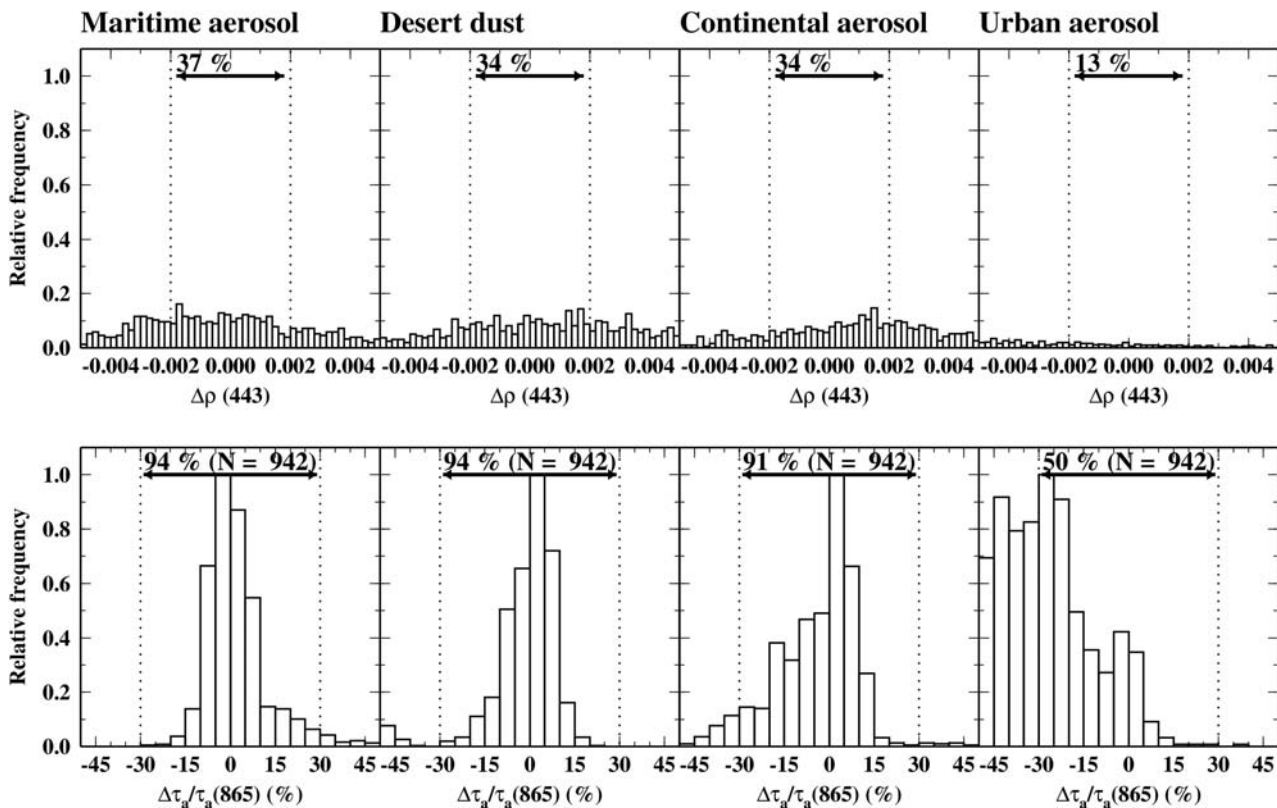


Figure 3.25. Upper 4 panels: histograms of the error in atmospheric correction at 443 nm, when $\tau_a(550) = 2$, and for several geometries (as in Fig. 3.8). Lower 4 panels: histograms of the relative errors in the aerosol optical thickness at 865 nm, corresponding to the situations shown in the 4 upper panels.

3.1.1.6.6 Stratospheric aerosols, thin cirrus clouds

The representation adopted in the present work for the stratosphere corresponds to the “background stratospheric aerosol (BSA)” described in WCRP (1986), which is aimed at representing unperturbed conditions (*i.e.*, no recent volcanic eruption). Perturbed stratospheric aerosol profiles may correspond either to the presence of particles of volcanic origin in the lower half of the stratosphere, or to the presence of a thin layer of cirrus clouds at the base of the stratosphere. Based on a few simple and preliminary tests, the impact of such structures on the atmospheric correction has been assessed. As for the volcanic aerosols, 3 profiles have been used, corresponding to the “VSA” profiles described in WCRP (1986), where the stratosphere is divided into 3 levels

- (1) from 30 to 50 km, the aerosol remains unperturbed in any case (H_2SO_4), with $\tau_a = 0.003$ at 550 nm
- (2) from 20 to 30 km, the aerosol type is either H_2SO_4 or volcanic ash. For the H_2SO_4 aerosol, $\tau_a(550)$ is 0.05 or 0.1, and define respectively the “ancient” and “recent” profiles. For the volcanic ash (absorbing; see Table 3.4, Figs. 3.4 and 3.5), the optical thickness at 550 nm is 0.3, and define the “fresh” profile.
- (3) from 12 to 20 km, τ_a remains 0.0306 at 550 nm, whatever the aerosol type (either H_2SO_4 or volcanic ash).

Atmospheric correction has been applied to TOA path reflectances simulated with the 3 peculiar stratospheres and for $\theta_s = 20, 40, \text{ and } 60^\circ$. The results are presented in Fig. 3.26, except for the “fresh” aerosol profile, which lead, as expected, to so large errors (negative errors < -0.01) that it is useless to display them. The errors shown in Fig. 3.26 clearly indicate that the atmospheric correction algorithm proposed here, and implemented as described in this ATBD, cannot successfully apply to TOA reflectances as soon as a significant increase of the concentration of the H_2SO_4 aerosol occurred (say, $\tau_a > 0.1$ in the stratosphere; see also Gordon *et al.*, 1997). The situation is even more dramatic when volcanic ash is present. This high sensitivity of the algorithm to products of volcanic origin advocates for a correction of their effect on the TOA reflectances, before atmospheric correction is applied (or, at least, for raising a flag to indicate their possible presence).

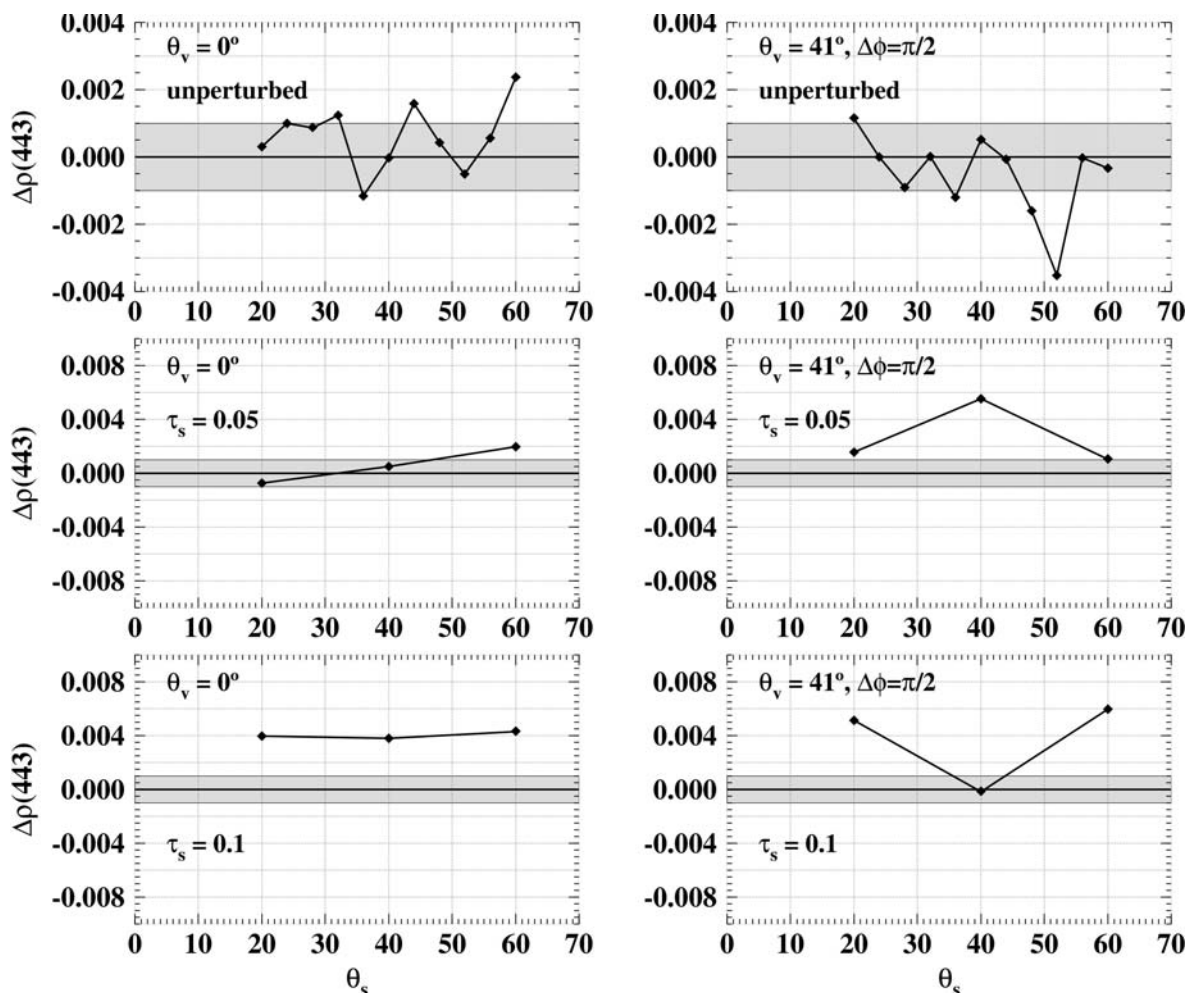


Figure 3.26. Error in atmospheric correction at 443 nm, as a function of θ_s , and for the viewing geometries indicated. Upper 2 panels: standard case, *i.e.*, no perturbation of the stratosphere. Middle panels: the “ancient” profile has been used (see text). Lower 2 panels: the “recent” profile has been used (see text).

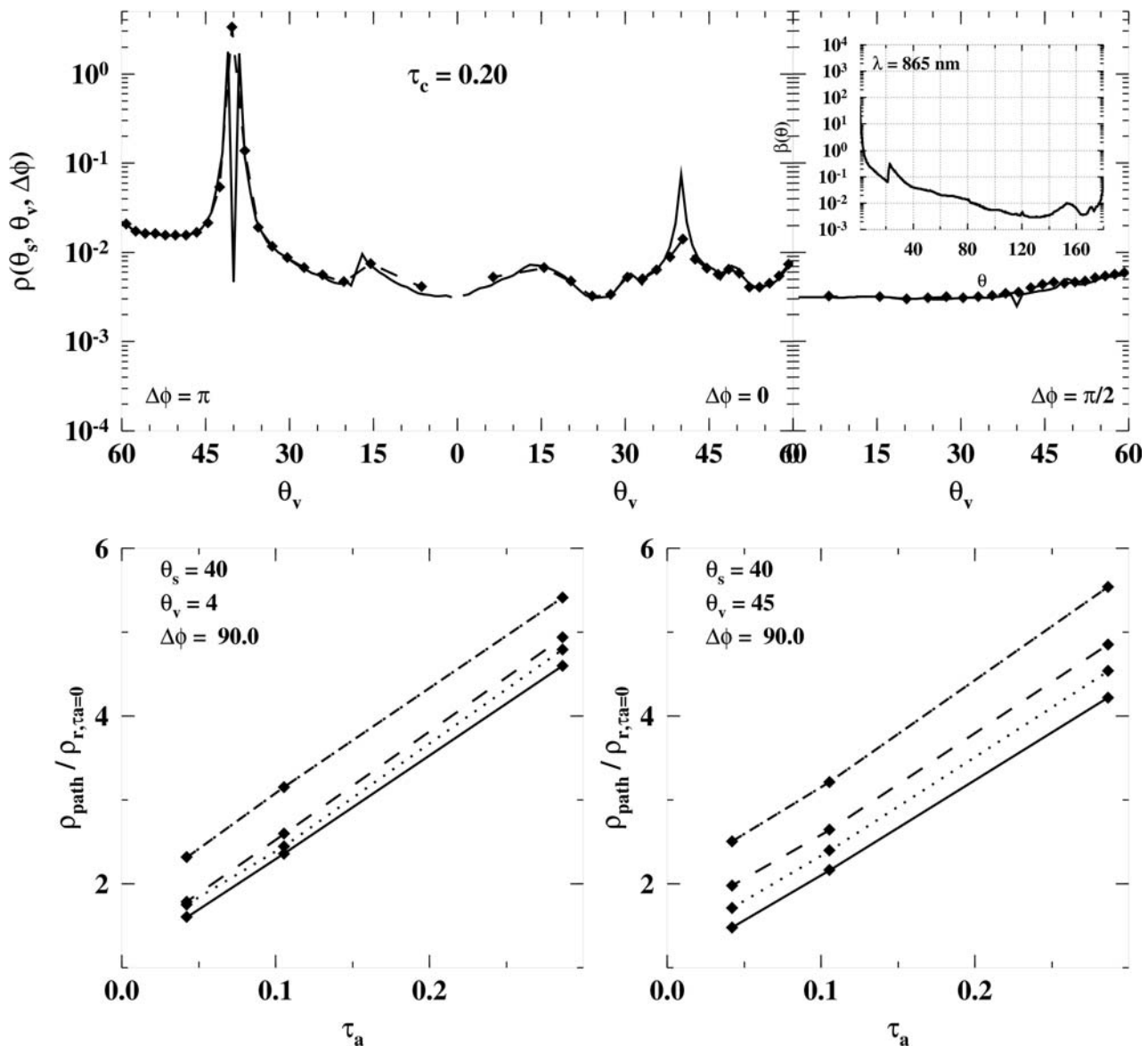


Figure 3.27. Upper panel: single scattering reflectance of a hypothetical pure cirrus layer, as a function of the viewing angle θ_v , and within the principal (antisolar, $\Delta\phi = \pi$, and solar, $\Delta\phi = 0$), and perpendicular ($\Delta\phi = \pi/2$) planes (the phase function is shown in insert). The optical thickness of the cirrus layer is 0.2 at 550 nm. The solar zenith angle is 40° . Solid line is the analytical, exact, calculation; Black diamonds linked by a dashed line are the output of a Monte Carlo simulation. Lower 2 panels: The relationship ($[\rho_{\text{path}} / \rho_{r, \tau_a=0}]$ versus τ_a) at 865 nm, and for the geometries indicated. Results are for the standard atmosphere (no cirrus, solid line), and for atmospheres containing a cirrus layer with an optical thickness of 0.05 (dotted lines), 0.1 (dashed lines), and 0.2 (dotted-dashed lines) at 550 nm.

The situation is different for cirrus clouds, which are located a little further down in the atmosphere (say, at the top of the troposphere), are not absorbing, and whose phase function is markedly different from that of stratospheric aerosols (see insert in Fig. 3.27). A prerequisite to any sensitivity study was to examine the possibility of simulating TOA radiances with the Monte Carlo code in a realistic way, when one of the atmospheric scatterers (*i.e.*, the cirrus) has a strongly peaked, and especially irregular, phase function. The angular discretisation has been accordingly doubled (*i.e.*, $\Delta\theta = 2.5^\circ$), and simulations have been performed with a phase function corresponding to hexagonal plates (Brogniez *et al.*, 1995). The single scattering reflectance has been simulated for a pure cirrus layer (the Monte Carlo code is provided with the capability of

keeping track of the photon histories, *i.e.*, the number and kind of scattering events they have undergone), and compared to the single scattering reflectance calculated analytically for the same medium with the following equation (τ_c is the cirrus optical thickness; see also list of symbols)

$$\rho_{c,s} = \left[\frac{\pi \omega}{\mu_v + \mu_s} p(\gamma^-) \left(1 - e^{-\tau_c (1/\mu_v + 1/\mu_s)} \right) \right] + \left[\frac{\pi \omega}{\mu_s - \mu_v} p(\gamma^+) \rho_F(\theta_v) e^{-\tau_c / \mu_v} \left(e^{-\tau_c / \mu_s} - e^{-\tau_c / \mu_v} \right) \right] + \left[\frac{\pi \omega}{\mu_s - \mu_v} p(\gamma^+) \rho_F(\theta_s) e^{-\tau_c / \mu_s} \left(e^{-\tau_c / \mu_s} - e^{-\tau_c / \mu_v} \right) \right]$$

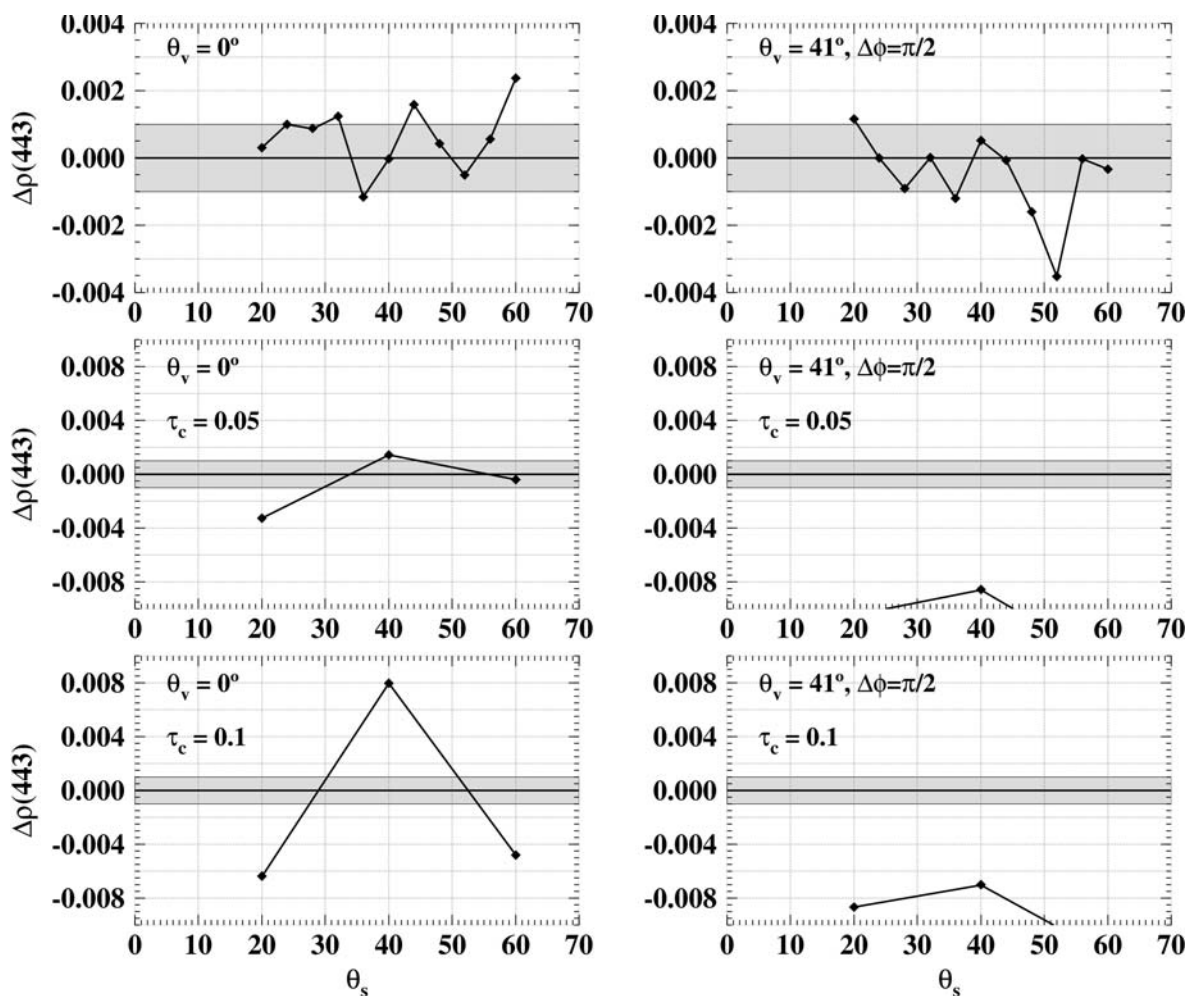


Figure 3.28. Error in atmospheric correction at 443 nm, as a function of θ_s , and for the viewing geometries indicated. Upper 2 panels: standard case, *i.e.*, no perturbation of the stratosphere. Middle panels: a layer of thin cirrus clouds is introduced between altitudes 10 and 12 km, with $\tau_c = 0.05$. Lower two panels: τ_c is now 0.1.

The results are displayed in Fig. 3.27 (upper panel), and show that the Monte Carlo technique, despite the inevitable averaging over photon counters, can reproduce most of the features of the primary scattering by cirrus. The peak in the backward direction (rainbow) is a little smoothed, and the double peak in the forward direction (halo) is reduced to a unique peak in the Monte Carlo results. This last result, however, is of no importance, precisely because these peaks scatter in a small angular domain around the forward direction; the involved radiation correspond



to the region of maximum sun glint which is anyway discarded when performing the atmospheric correction. A few simulations have been therefore carried out, with a cirrus layer introduced in the standard atmospheric profile between altitudes 10 and 12 km, and for several cirrus optical thicknesses. The impact on the $[\rho_{\text{path}} / \rho_{r, \tau_a=0}]$ versus τ_a relationship is displayed on Fig. 3.27. It seems that the algorithm will be perturbed by the presence of cirrus clouds, as soon as their optical thickness is greater than about 0.05. This is confirmed on Fig. 3.28, where errors of the atmospheric correction at 443 nm are displayed for $\tau_c = 0.05$ and 0.1. Therefore, a test should be developed, in view of indicating the presence of cirrus clouds, and a correction possibly performed before entering the atmospheric correction. This kind of procedure could be problematic to implement (*e.g.*, see Gordon *et al.*, 1997).

3.1.1.7 Ancillary data and aerosol climatology

3.1.1.7.1 Ancillary data: identification and accuracy requirements

The ancillary data needed to perform the atmospheric correction are listed in Table 3.5, along with the reflectance or transmission term(s) that they influence.

3.1.1.7.1.1 Extraterrestrial irradiance

The extraterrestrial mean irradiance is taken from the level 1b output.

3.1.1.7.1.2 Wind speed at the sea level

This parameter could be accessed through the meteorological and weather forecast centers (*e.g.*, the European Center for Meteorological and Weather Forecast in Readings, ECMWF), or from wind scatterometer measurements. The typical accuracy attached to wind speed is of about 2 m s⁻¹. Wind speed is expected to be attached with the input level 1B product (note that wind direction is also needed if it is considered in the definition of the sun glint flag).

3.1.1.7.1.3 Atmospheric pressure at the sea level

From the results in 3.1.1.6.2, it seems that about 5-10 mbars could be a reasonable accuracy for the atmospheric pressure. This parameter could be accessed through the meteorological and weather forecast centers (*e.g.*, ECMWF). Atmospheric pressure is expected to be attached with the input level 1B product.

3.1.1.7.1.4 Total ozone amount

An accuracy of about 10-20 mAtm-cm (Dobson Units, DU) is a reasonable goal for the total ozone amount of the atmosphere. This parameter could be accessed from the measurements of a Total Ozone Mapping Spectrometer (TOMS). By default, climatological values have to be used. No information is needed about other absorbing gases (H₂O, O₂...), because the channels used in the atmospheric correction do not overlap the absorption bands of these gases (if corrections would be needed, however, they would be carried out before entering into the atmospheric correction). Ozone is expected to be attached with the input level 1B product.



3.1.1.7.1.5 Relative humidity

The relative humidity is not required to operate the algorithm, yet it could provide a useful constraint (or verification) on the aerosol model identification. This parameter could be accessed through the meteorological and weather forecast centers (*e.g.*, ECMWF).

Ancillary data	Affected term(s)
Extraterrestrial irradiance $E_s(\lambda)$	$L_{\text{path}}(\lambda) \rightarrow \rho_{\text{path}}(\lambda)$
Wind speed at the sea level	$\rho_{r, \tau_a=0}(\lambda)$ (also $\rho_G(\lambda)$ and $\rho_{\text{wc}}(\lambda)$) not studied here
Atmospheric pressure at the sea level	$\rho_{r, \tau_a=0}(\lambda), t_d(\lambda)$
Total ozone amount	$\rho_{r, \tau_a=0}(\lambda), t_d(\lambda)$
Relative humidity	Aerosol identification

Table 3.5: Ancillary data

3.1.1.8 Remaining issues

3.1.1.8.1 Bidirectionality of the oceanic reflectance and the diffuse transmittance

Yang and Gordon (1997) state that the diffuse transmittance from the pixel to the TOA level is different (by up to 5%) if computed either for a uniform water-leaving radiance distribution, or for a distribution that account for the anisotropic character of the radiance field emerging from the ocean (even for a uniform scene, where all pixels have the same chlorophyll concentration).

3.1.1.8.2 The “mixing ratio”

One of the assumptions on which the proposed algorithm relies is: for an aerosol A, bracketed by aerosols A1 and A2 in the near-IR following a “mixing ratio” (called here X) defined by the multiple aerosol scattering terms $[\rho_{\text{path}} / \rho_{r, \tau_a=0}]$, X remains valid for the visible wavelengths. X actually slightly changes from the near-IR to the visible domain, and this is the main origin of the error in atmospheric correction (when the aerosol type is correctly identified). The possibility of estimating the change in X with wavelength remains to be examined.



3.1.2 Mathematical description of the algorithm

The following options are assumed here:

- Atmospheric pressure : known
A standard value of 1013.25 hPa has been used when generating the lookup tables $[\rho_{\text{path}}(\lambda) / \rho_{\text{r}, \tau_{\text{a}}=0}(\lambda)]$ versus τ_{a}
- Wind speed : known. Two values were considered when generating the lookup tables $[\rho_{\text{path}}(\lambda) / \rho_{\text{r}, \tau_{\text{a}}=0}(\lambda)]$ versus τ_{a} .

The following algorithm description concerns clear sky pixels located out of the sun glint area, without whitecaps, and for Case 1 waters. The signals (total radiances) are assumed to be corrected for gaseous absorption, if any (including water vapor, ozone, and oxygen).

The 11 wavelengths are: 412, 443, 490, 510, 560, 620, 665, 681.25, 709, 778, 865 nm.

When operating the atmospheric correction for a given pixel (*i.e.*, for a geometry, θ_s , θ_v , $\Delta\phi$), the successive steps are as follows (angular dependencies are omitted for the sake of clarity, except when needed in peculiar cases):

- 0 Input data are taken from the level 1b:
 - Total radiance at the instrument entrance for all wavelengths ($L_t(\lambda)$)
 - Ancillary data (Wind speed, Atmospheric Pressure, Ozone)
 - Geometry (θ_s , θ_v , $\Delta\phi$)
- 1 Transform total radiance at the sensor level into total reflectance (Eq. (1)).

For $\lambda = 412, 443, 490, 510, 560, 620, 665, 681.25, 709, 778, 865$ nm.

External data: μ_s , $E_s(\lambda)$

- 2 Correct the Rayleigh reflectances for possible pressure variations (only for passing them on to the “Case 2 Bright waters flag”):

The Rayleigh reflectance, $\rho_{\text{r}, \tau_{\text{a}}=0}(\lambda, \theta_s, \theta_v, \Delta\phi, W)_{\text{TAB}}$, is interpolated within a lookup table for the geometry in question, and then corrected to account for the actual value of the atmospheric pressure, P (only for wavelengths 709, 778, and 865 nm)

$$\rho_{\text{r}, \tau_{\text{a}}=0}(\lambda) = \rho_{\text{r}, \tau_{\text{a}}=0}(\lambda)_{\text{TAB}} \frac{[1 - \exp(-\tau_{\text{r}}(P / P_0) / \mu)]}{[1 - \exp(-\tau_{\text{r}} / \mu)]} \quad (30)$$

where τ_{r} is the Rayleigh optical thickness at P_0 , and P_0 is 1013.25 hPa, and μ is $\cos(\theta_v)$.



•3 At 709, 778 and 865 nm, $\rho_{r, \tau_a=0}$ is subtracted from the total reflectance, and the results are passed on to the “Case 2 bright waters flag” and “Case 2 bright waters atmospheric correction” algorithms (ATBDs 2.5 and 2.6). If these schemes return values for the water-leaving reflectances that are not zero, then they are subtracted from the total (path) reflectances (in the 3 channels here considered) before entering the Case 1 waters atmospheric correction.

External data: look-up table of $\rho_{r, \tau_a=0}(\lambda, \theta_s, \theta_v, \Delta\phi, W)$, W , and P

•4 The ratio $[\rho_{\text{path}}(\lambda) / \rho_{r, \tau_a=0}(\lambda)]$ (thereafter referred to as $\Delta\rho_{\text{path}}$) is formed at 778 and 865 nm. The values of ρ_{path} at 778 and 865 nm have been previously corrected for atmospheric pressure changes, if their actual values are different by at least 5 hPa from the standard value (1013.25 hPa). The correction is done following

$$\rho_{\text{path}} = \rho_{\text{path}} (1 + (\Delta P / P) \eta_r) \quad (31)$$

with $\Delta P = (P_{\text{standard}} - P_{\text{actual}})$, and $\eta_r = \tau_r / (\tau_r + \tau_a)$. The Rayleigh optical thickness, τ_r , is taken from tabulated values, and the aerosol optical thickness, τ_a , is taken from the pixels previously processed.

$$\Delta\rho_{\text{path}}(865) = \rho_{\text{path}}(865) / \rho_{r, \tau_a=0}(865) \quad (32)$$

$$\Delta\rho_{\text{path}}(778) = \rho_{\text{path}}(775) / \rho_{r, \tau_a=0}(775) \quad (32')$$

where $\rho_{r, \tau_a=0}(775)$ and $\rho_{r, \tau_a=0}(865)$ are for the standard pressure.

•5 For the N aerosol models of the “standard” database (index i), carry out the calculation of $\tau_a(865)_i$:

$$\tau_a(865)_i = \text{func}_i(\Delta\rho_{\text{path}}(865)_i), i = 1, N \quad (33)$$

where func_i is the relationship between $\Delta\rho_{\text{path}}$ and τ_a , for aerosol model i, for wavelength 865 nm, and interpolated for the geometry in question. This function is a polynomial expression of degree 2, so that 3 coefficients have to be interpolated.

External data: look-up table of $\text{func}_i(A, \lambda, \theta_s, \theta_v, \Delta\phi, W)$

•6 calculate the N values of $\tau_a(778)_i$, from the N values of $\tau_a(865)_i$, by using the tabulated ratios $c(778)_i / c(865)_i$ (thereafter referred to as Δc)

$$\tau_a(778)_i = \tau_a(865)_i \times \Delta c(778)_i, i = 1, N \quad (34)$$

External data: look-up table of $\Delta c(A, \lambda)$

•7 For the N aerosol models, carry out the calculation of $\Delta\rho_{\text{path}}(778)$



$$\Delta\rho_{\text{path}}(778)_i = \text{func}^{-1}_i(\tau_a(778)_i), i = 1, N \quad (35)$$

External data: look-up table of $\text{func}_i(A, \lambda, \theta_s, \theta_v, \Delta\phi)$

- 8 Select the 2 aerosol models (indices $i1$ and $i2$ within the N models) that most closely bracket the actual one, so that:

$$\Delta\rho_{\text{path}}(778)_{i1} < \Delta\rho_{\text{path}}(778)_{\text{actual}} < \Delta\rho_{\text{path}}(778)_{i2} \quad (36)$$

where $\Delta\rho_{\text{path}}(778)_{i1}$ is the maximum of the $\Delta\rho_{\text{path}}$ values that are lower than $\Delta\rho_{\text{path}}(778)_{\text{actual}}$, and where $\Delta\rho_{\text{path}}(778)_{i2}$ is the minimum of the $\Delta\rho_{\text{path}}$ values that are greater than $\Delta\rho_{\text{path}}(778)_{\text{actual}}$.

- 9 Calculate X , the “mixing ratio”, needed to interpolate between the two candidate aerosols

$$X = (\Delta\rho_{\text{path}}(778)_{\text{actual}} - \Delta\rho_{\text{path}}(778)_{i1}) / (\Delta\rho_{\text{path}}(778)_{i2} - \Delta\rho_{\text{path}}(778)_{i1}) \quad (37)$$

The aerosol optical thickness at 865 nm is now computed as:

$$\tau_a(865) = (1 - X) \tau_a(865)_{i1} + X \tau_a(865)_{i2} \quad (38)$$

- 10 Carry out the test at 510 and 709 nm:

$$\tau_a(510)_{i1} = \tau_a(865)_{i1} \times \Delta c(510)_{i1} \quad (39)$$

$$\tau_a(510)_{i2} = \tau_a(865)_{i2} \times \Delta c(510)_{i2} \quad (39')$$

$$\Delta\rho_{\text{path}}(510)_{i1} = \text{func}^{-1}_{i1}(\tau_a(510)_{i1}) \quad (40)$$

$$\Delta\rho_{\text{path}}(510)_{i2} = \text{func}^{-1}_{i2}(\tau_a(510)_{i2}) \quad (40')$$

$$\Delta\rho_{\text{path}}(510)_{\text{estimated}} = (1 - X) \Delta\rho_{\text{path}}(510)_{i1} + X \Delta\rho_{\text{path}}(510)_{i2} \quad (41)$$

$$\text{Then: } \rho_{\text{path}}(510)_{\text{estimated}} = \Delta\rho_{\text{path}}(510)_{\text{estimated}} \times \rho_{r, \tau_a=0}(510) \quad (42)$$

The mean normalised water-leaving reflectance at 510 nm, $[\overline{\rho_w(510)}]_N$, is “de-normalised”:

$$\rho_w(510) = [\overline{\rho_w(510)}]_N (\varepsilon_c t_{\theta_s}) \frac{\Re(\theta')}{\Re_0} \frac{f_1(\theta_s)}{Q(\theta_s, \theta_v, \Delta\phi)} \left[\frac{f_{1,0}(\lambda)}{Q_0(\lambda)} \right]^{-1} \quad (43)$$

The error in atmospheric correction at 510 nm is therefore obtained as:

$$\Delta\rho_w(510) = \left[(\rho_t(510)_{\text{measured}} - \rho_{\text{path}}(510)_{\text{estimated}}) / t_d(510) \right] - (\rho_w(510) - \sigma_{\rho_w}(510)) \quad (44)$$



where $\rho_w(510)$ is interpolated from the monthly climatology, and $\sigma_{\rho_w}(510)$ is the standard deviation of $\rho_w(510)$, and is also interpolated from the monthly climatology.

The flag at 510 nm is set to 1 if we have $\Delta\rho_w(510)$ is $< -2 \cdot 10^{-3}$.

If the flag has not been raised, then the correction is continued at step •11, by using the couple of aerosol models selected at step •8, and the “mixing ratio” calculated at step •9.

If the flag has been raised, then the correction is carried out 3 times more, from step 5 to step 9, by selecting 3 sets of dust models (i.e., the 6 Moulin et al. dust models for the three vertical repartitions indicated in 3.1.1.5.2.2). When these 3 groups of aerosol models have been examined, each one providing a couple of possible models, the couple that is kept at the end is the one that leads to the lower $\Delta\rho_w(510)$. Notice however that, if this final $\Delta\rho_w(510)$ is too large (this is possible if the tests are erroneous), the situation is reset to that of non-absorbing aerosols.

•11 For any wavelength λ in the visible, calculate the 2 values $\tau_a(\lambda)_{i1}$ and $\tau_a(\lambda)_{i2}$, from $\tau_a(865)_{i1}$ and $\tau_a(865)_{i2}$, by using the tabulated ratios $\Delta c(\lambda)_{i1}$ and $\Delta c(\lambda)_{i2}$

$$\tau_a(\lambda)_{i1} = \tau_a(865)_{i1} \times \Delta c(\lambda)_{i1} \quad (46)$$

$$\tau_a(\lambda)_{i2} = \tau_a(865)_{i2} \times \Delta c(\lambda)_{i2} \quad (46')$$

External data: look-up table of $\Delta c(A, \lambda)$

•12 For the aerosols i1 and i2, carry out the calculation of $\Delta\rho_{\text{path}}(\lambda)$ for the visible wavelengths:

$$\Delta\rho_{\text{path}}(\lambda)_{i1} = \text{func}^{-1}_{i1}(\tau_a(\lambda)_{i1}) \quad (47)$$

$$\Delta\rho_{\text{path}}(\lambda)_{i2} = \text{func}^{-1}_{i2}(\tau_a(\lambda)_{i2}) \quad (47')$$

External data: look-up table of $\text{func}_i(A, \lambda, \theta_s, \theta_v, \Delta\phi)$

•13 For any wavelength of the visible domain, calculate:

$$\Delta\rho_{\text{path}}(\lambda)_{\text{estimated}} = (1 - X) \Delta\rho_{\text{path}}(\lambda)_{i1} + X \Delta\rho_{\text{path}}(\lambda)_{i2} \quad (48)$$

$$\rho_{\text{path}}(\lambda)_{\text{estimated}} = \Delta\rho_{\text{path}}(\lambda) \times \rho_{t, \tau_a=0}(\lambda) \quad (49)$$

$$\text{If necessary (i.e., } \Delta P > 5 \text{ hPa): } \rho_{\text{path}}(\lambda)_{\text{estimated}} = \rho_{\text{path}}(\lambda)_{\text{estimated}} (1 + (\Delta P/P)\eta_t) \quad (49')$$

Where ΔP is now $(P_{\text{actual}} - P_{\text{standard}})$

$$t_d(\lambda, \theta_v) \rho_w(\lambda) = \rho_t(\lambda)_{\text{measured}} - \rho_{\text{path}}(\lambda)_{\text{estimated}} \quad (50)$$

•14 $t_d(\lambda, \theta_v)$ is computed as:

$$t_d(\lambda, \theta_v) = \exp\left(-\frac{\tau_{\text{oz}} + (1 - \omega_A F_A) \tau_A + 0.5 \tau_R}{\mu}\right) \quad (\text{see 3.1.1.4.4 for details}) \quad (51)$$



$$\omega_a(\lambda) = (1 - X) \omega_a(\lambda)_{i1} + X \omega_a(\lambda)_{i2} \quad (52)$$

$$F_a = (1 - X) F_a(865)_{i1} + X F_a(865)_{i2} \quad (F_a \text{ is nearly wavelength independent}) \quad (53)$$

•15 Finally, the reflectance is obtained as:

$$\rho_w(\lambda) = [t_d(\lambda, \theta_v) \rho_w(\lambda)] / t_d(\lambda, \theta_v) \quad (54)$$

External data: $E_s(\lambda), \theta_s, \theta_v, \tau_r(\lambda), \tau_{oz}(\lambda), \tau_a(\lambda), \omega_a(\lambda), F_a$

3.1.3 Error budget estimates

3.1.3.1 Are the aerosol models representative of reality?

The main assumption upon which the present atmospheric correction scheme relies is that the aerosol models used here are good approximations of the actual aerosols over the oceans; therefore they can be used as inputs of simulations of the radiative transfer in the atmosphere, the results of which being used to generate lookup tables. In principle, this assumption should be valid; the aerosol models used here have been generated after many measurements of aerosol chemical and optical properties, with the aim of defining models as representative as possible of reality. Recent measurements (Schwindling, 1995) of the aerosol optical properties (phase function and spectral optical thickness) have shown for instance that the Shettle and Fenn (1979) aerosol models fairly represent actual aerosols over the Western American coasts. The natural environment is however so variable that a question immediately arises: what kind of improvement the use of an inevitably restricted set of aerosol models brings (restricted as compared to reality)? In other words: does it help to dispose of a database generated for, say, 30 aerosol models, while hundreds of different aerosol types or aerosol assemblages are possibly encountered over the ocean (even if admittedly they should be similar to those of the database)?

From the various tests of the algorithm, and also from the results of the sensitivity studies concerning the vertical distribution of aerosols, the answer seems to be positive. In a way, the lookup tables “capture” the essential features of possible aerosol spectral dependencies; as a consequence, when the actual aerosol type or the actual aerosol vertical distribution are not “present” within the database, the correction remains possible, and a reasonable accuracy is preserved. The selected couple of aerosol models is sometimes however unrealistic (this is one of the justifications for using an aerosol climatology).

As a conclusion, the present atmospheric correction should works well, to the extent that we have now some indications that the aerosol models used here are close to reality. It is nevertheless impossible to be fully assertive on this point before the operational use of the algorithm. This observation led us to incorporate the single scattering algorithm into the whole scheme, as a basic and secure “bottom level” algorithm.



3.1.3.2 Other possible error sources

cf. Warning page iv

3.1.3.2.1 Aerosol model identification / Correctness of the test at 510 nm

In principle, the test at 510 nm ensures that the selected aerosol model is not too different from the actual aerosol: during one step of the correction, if the selected model is totally unrealistic, the error of the atmospheric correction at 510 nm will be large enough to prevent its definitive selection. Ambiguities may subsist, however: for instance a couple of aerosol models can be selected because it is the one which leads to the minimal error at 510 nm, while the similar spectral behaviour of this couple of models and of the actual one is fortuitous. This kind of confusion is possible, for instance between a dry maritime aerosol and the mixture of particles of continental origin with a wet maritime aerosol.

3.1.3.2.2 Interpolation within LUTs

The tests of the algorithm presented in this document, as well as the sensitivity analyses, have been carried out with the exact geometry (*i.e.*, the angles θ_s , θ_v , and $\Delta\phi$ selected to test the algorithm correspond to entries of the lookup tables). The linear interpolations that will be necessary during the operational use of the algorithm (because the actual values of θ_s , θ_v , and $\Delta\phi$ will be always intermediate between the entries of the lookup tables) should not introduce significant inaccuracies, provided that each entry of the lookup tables has been adequately sampled. Multiple linear interpolations should recover the exact values at $\pm 0.5\%$ at the maximum, and even much less in many cases.

To meet this requirement, the sampling of the lookup tables indices should be of $\sim 5^\circ$ for θ_s and θ_v , and of $\sim 7.5^\circ$ for $\Delta\phi$ (see MERIS "Table Generation Requirement Document", TGRD, sections 3.6 and 5.6).

3.1.3.2.3 Estimation of the diffuse transmittance, $t_d(\theta_v, \lambda)$

In section 3.1.1.4.4 (computation of $t_d(\theta_v, \lambda)$), it was precised that neighbouring effects (adjacent pixels with marked chlorophyll steps), or even the effect of the bidirectionality of the oceanic diffuse reflectance (for a homogeneous scene) were not accounted for. More importantly, it should be reminded that Eq. (17) is valid under the assumption of single scattering, that is when Rayleigh scattering and aerosol scattering are uncoupled (Gordon and Morel, 1983).

Recently, Yang and Gordon (1997) stated that $t_d(\theta_v, \lambda)$ is not identical if computed either for a uniform water-leaving radiance distribution, or for a distribution that account for the anisotropic character of the radiance field emerging from the ocean (the difference reaching 5%, even for a uniform scene, where all pixels have the same chlorophyll concentration).

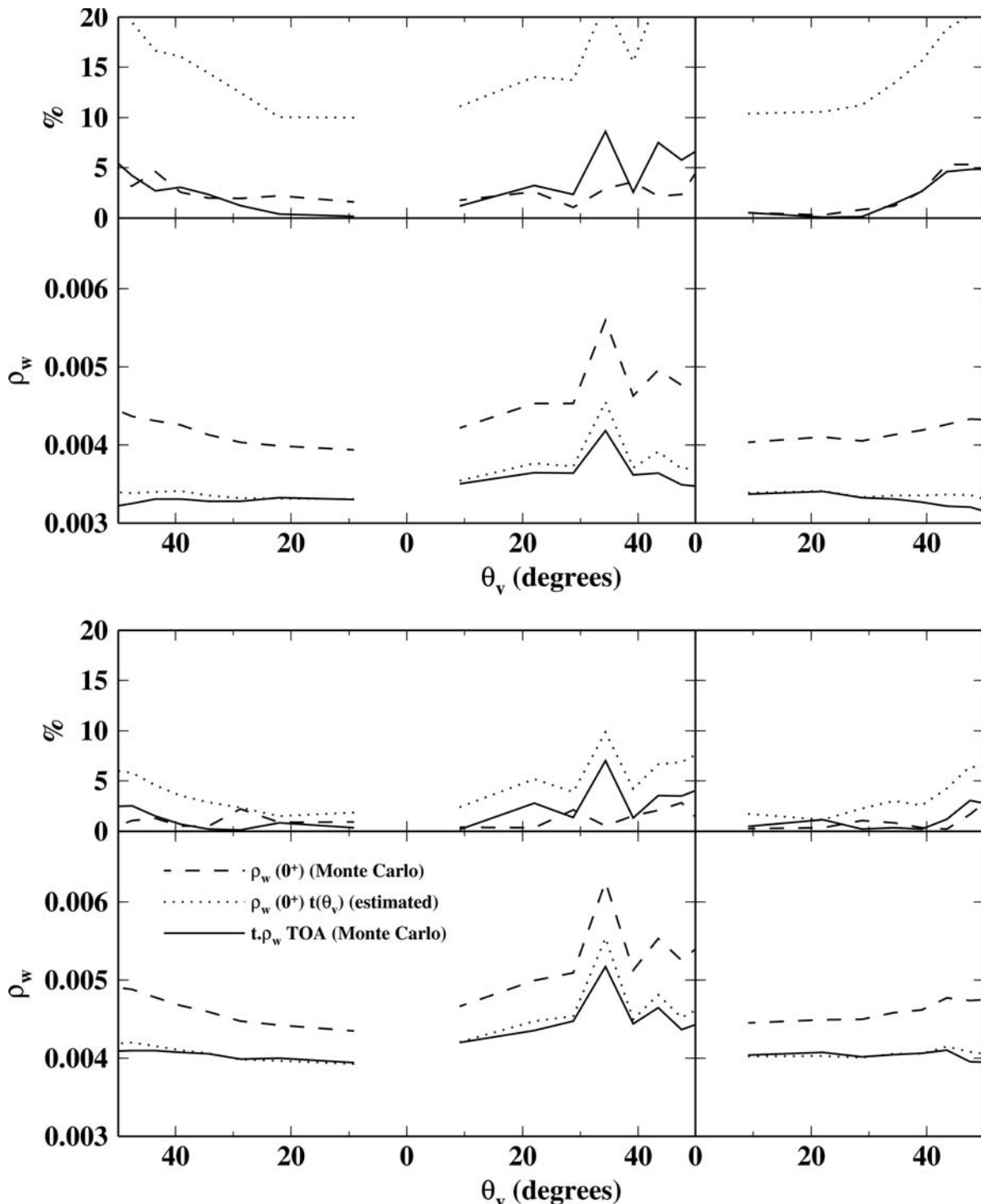


Figure 3.29. Values of the water-leaving reflectance, $\rho_w(0^+)$, and of the “marine reflectance”, $t_d(\theta_v)$. ρ_w (TOA), at 560 nm, as a function of the satellite viewing angle, and within the principal plane and perpendicular half plane (left and right panels, respectively). The sun zenith angle is 35° . Upper and lower panels are respectively for the urban aerosol with RH=80% (absorbing), and for the maritime aerosol with RH=80% (non-absorbing). The dashed and solid lines are, respectively, the values of $\rho_w(0^+)$ and of $t_d(\theta_v)$. ρ_w (TOA) as obtained via Monte Carlo simulations. The dotted line is the value of $\rho_w(0^+)$ multiplied by an estimated value of $t_d(\theta_v)$. The relative difference between the 2 curves is shown as percents (solid curve on the upper plots of each panel). The dotted lines correspond to a calculation of $t_d(\theta_v)$ ignoring the effect of aerosols. The conditions are: $\tau_a = 0.3$ at 550 nm, (Chl) = 0.3 mg m^{-3} .



From the above remarks, the ability of Eq. (17) to provide accurate estimates of $t_d(\theta_v, \lambda)$ is challenged, at least when the turbidity of the atmosphere becomes moderately high. No attempt has been made here to examine possible improvements of Eq. (17). A few calculations have been however carried out, to assess the accuracy to which $t_d(\theta_v, \lambda)$ can be derived. Monte Carlo simulations have been done, providing simultaneously the values of the water-leaving reflectance, $\rho_w(0^+)$, and of the “marine reflectance”, which represents the product $[t_d(\theta_v, \lambda) \cdot \rho_w(0^+)]$ at the TOA level.

This estimate of the marine reflectance is then compared to the product $\rho_w(0^+) \cdot t_d(\theta_v, \lambda)$, where the transmittance is computed from Eq. (17), and by using the exact values for optical thicknesses (τ_T , τ_{O_3} , τ_a), single scattering albedo (ω_a) and aerosol forward scattering probability (F_a). Results are given in Fig. 3.29, for two aerosols (the absorbing urban aerosol, and the non-absorbing maritime aerosol, both with RH = 80%), for $\lambda = 560$ nm, for $\tau_a = 0.3$ at 550 nm, and for (Chl) = 0.3 mg m⁻³. This figure shows that for a non-absorbing aerosol, $t_d(\theta_v, \lambda)$ is given within 5% by Eq. (17), and is given within 10% for an absorbing aerosol. The dotted lines in each upper plots, and for each aerosol, correspond to the same relative difference as above, when aerosols, however, are not considered in Eq. (17). Inaccuracies in the parameters of Eq. (17) would even lead to greater errors. Note also that the results presented here are not independent of the adopted angular discretisation. Indeed, as the elementary field of view tends to an infinitesimal point, the diffuse transmittance t_d tends toward the direct transmittance, $T = e^{-\tau/\mu}$ (e.g., Gordon and Morel, 1983).

Clearly, Eq. (17) is not sufficiently precise to preserve the required accuracy for the water-leaving radiances. The development of a more accurate parameterisation of $t_d(\theta_v, \lambda)$ seems inevitable. It is out of the scope of the present ATBD, and is therefore part of the studies that remain to be carried out.

3.1.3.2.4 *Uncertainties in the ozone concentration*

This section has been deleted, and just kept here for keeping numbering of the document.

3.1.3.2.5 *The effect of whitecaps*

Whitecaps mainly tend to uniformly increase reflectance in the whole visible-to-near-IR spectrum (e.g., Koepke, 1984), and this effect could alter the atmospheric correction. The Monte Carlo code presently used does not allow the whitecap reflectance to be separately and specifically studied. Therefore, simple tests are carried out here, by adding to total TOA reflectance, as obtained through our simulations, an additional contribution due to whitecaps, as extracted from the outputs of the 6S model (Vermotte *et al.*, 1994). Two parallel simulations are then carried out for the same conditions, except that only the 6S model accounts for the possible occurrence of whitecaps for high wind speeds and of their contribution to the total radiance at the sensor level.

The additional whitecap reflectance is added to the total reflectance, and the atmospheric correction is carried out following three approaches

- (1) the classical algorithm is operated to examine the error in the retrieved water-leaving radiances when the whitecaps contribution is ignored,
- (2) a correction for whitecaps reflectance is introduced (see below), and operated with the exact wind speed, and

- (3) the same correction is made with an incorrect value for the wind speed. These two last tests aim at examining the possibility of correcting the whitecaps contribution, and, if proven to be possible, to get an idea about the accuracy needed for wind speed.

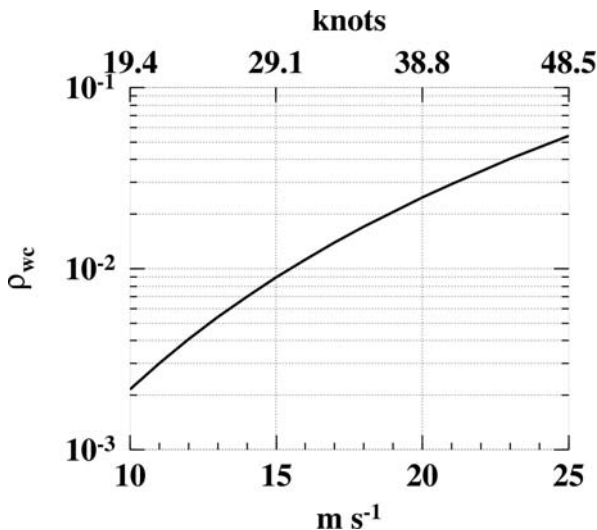


Figure 3.30. Reflectance of whitecaps as a function of wind speed (Koepke, 1984).

The 6S model has been run for a wind speed of 15 m s⁻¹ (about 30 knots), which ensures that whitecaps actually occur and also that visible remote sensing remains possible. The maritime and continental aerosol models

used in the 6S model have been selected to run the simulations with optical thicknesses of 0.1 and 0.3 at 560 nm. The correction for whitecaps used in tests (2) and (3) defined above is based on the definitions of Koepke (1984). The whitecaps reflectance, $\rho_{wc}(\lambda)$, is (the following expression is used in the 6S model):

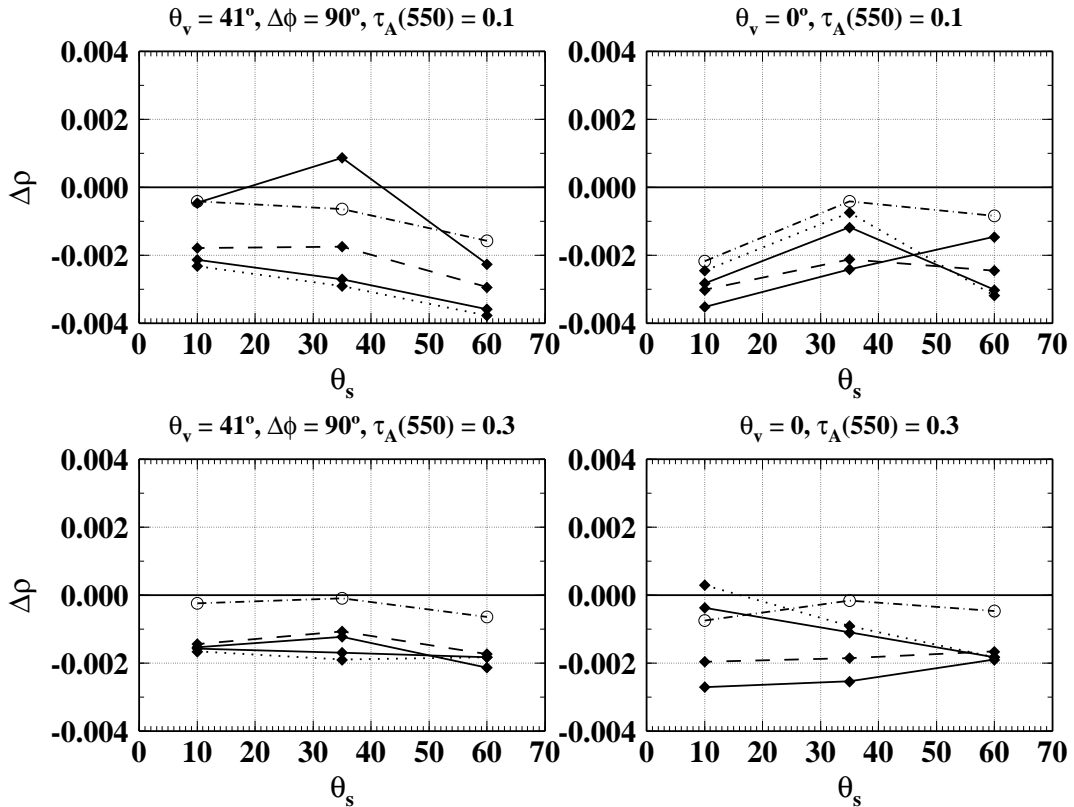
$$\rho_{wc}(\lambda) = [2.95 \cdot 10^{-6} \cdot ws^{3.52}] \rho_{ef}(\lambda) \quad (56)$$

where ws is wind speed, and the bracketed expression is the relative area covered by whitecaps. $\rho_{ef}(\lambda)$ is the effective ocean foam reflectance (accounting for variations in the area and reflectance of individual whitecaps), which is constant (0.22 ± 0.11). The change in $\rho_{wc}(\lambda)$ with wind speed is shown in Fig. 3.30.

The whitecaps reflectance is then multiplied by the diffuse transmittance (without accounting for the transmittance due to scattering and absorption by aerosols), and added to the total reflectance at the TOA level obtained without whitecaps (but with the same wind speed).

So, if the correction for whitecaps is needed, their reflectance, as computed from the above expression, is multiplied by the diffuse transmittance and subtracted from the total radiances before entering the algorithm. The results of the three tests are displayed in Fig. 3.31. When the aerosol scattering is almost independent of wavelength (6S maritime aerosol), ignoring or incorrectly correcting for whitecaps does not lead to serious errors in the retrieved marine reflectances (whitecaps are “seen” as an additional aerosol load). Most of the curves in each of the 4 upper plots of Fig. 3.31 remain between ± 0.002 . The correction made when the exact wind speed is known is obviously the more accurate (and its accuracy is about the same than that of the classical algorithm operated over an ocean without foam); it is however out of reach to exactly know the wind speed when operating the routine algorithms.

443 nm (6S maritime aerosol)



443 nm (6S continental aerosol)

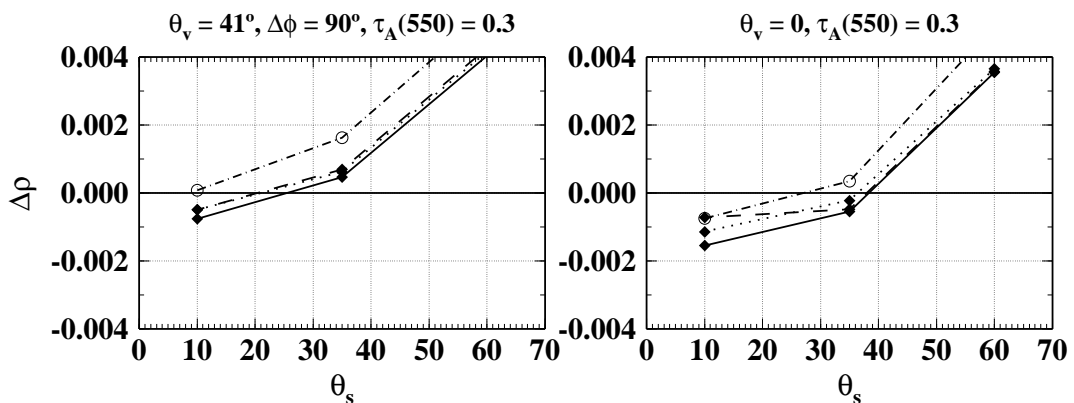


Figure 3.31. Error in the top of atmosphere water-leaving reflectance as a function of the solar zenith angle θ_s . Four upper plots: simulations have been carried out for the 6S maritime model, with $\tau_a(560) = 0.1$ or 0.3 , as indicated. Two lower plots: simulations have been carried out for the 6S continental model, with $\tau_a(560) = 0.3$. On each plot, the open circles linked by a dashed line are the results of the correction without whitecaps; the dotted line shows the error $\Delta\rho$ when the whitecaps contribution is ignored; the dashed line shows the error when the correction for whitecaps is applied with the exact wind speed (15 m s^{-1}); the two solid lines show the error when this correction is applied for an inexact wind speed (*i.e.*, 10 or 17 m s^{-1}). Plots on the left (right) column are for viewing at the scan edge (scan center).

In summary, correction for whitecaps should not be attempted for aerosols with small Ångström exponents (< 0.1) (see Gordon and Wang, 1994a; Gordon, 1997). The situation is worse when the aerosol scattering is strongly changing with wavelength (6S continental aerosol): whitecaps cannot be only “seen” as an additional aerosol load, and produce an apparent, erroneous,



spectral behaviour for aerosols (the selection of the 2 candidate aerosols can be affected). If whitecaps are ignored, the error in marine radiances becomes too high. The tentative whitecaps correction, as described above, as well is not satisfactory (except for the unrealistic situation of an exact knowledge of wind speed), and can even lead to greater errors than those obtained in absence of whitecaps correction if wind speed is overestimated by only 2 m s^{-1} . A more precise algorithm for whitecaps correction is clearly needed (but see Gordon and Wang, 1994b; Gordon, 1997). For the present time, a flag could be introduced, only to indicate that wind actually was blowing during image acquisition, and that whitecaps probably were present.

The present tests have been carried out for a wind speed of 15 m s^{-1} , *i.e.*, for ρ_{wc} about $8\text{-}9 \cdot 10^{-3}$. The correction could be much more problematic for higher wind speed, when ρ_{wc} can reach $2\text{-}3 \cdot 10^{-2}$. The extent to which atmospheric correction remains possible in such conditions is unknown at present time.

The above tests and comments are based on the assumption that the whitecaps reflectance is wavelength-independent. Recent measurements (Frouin *et al.*, 1996) on the contrary show a significant decrease of this reflectance in the near-IR, say beyond 800 nm (and so could concern the channel at 865 nm). The impact on the atmospheric correction of this decrease has not been addressed here (but see Gordon and Wang, 1994a; Gordon, 1997).

3.1.3.2.6 Instrumental errors. 1.: stray light

Instrumental errors (*i.e.*, errors in the instrument calibration) are not *a priori* predictable. It is therefore impossible to carry out an exhaustive sensitivity analysis about their effect on the accuracy of the atmospheric correction. The sensitivity analyses carried out in the previous sections partly cover the topic here addressed: the spectrally dependent “errors” induced by changes in various environmental factors, as previously examined, could be assimilated to calibration errors, providing then a first quantitative insight into the response of the atmospheric correction to inappropriate calibration of the instrument. The problem actually is more complex, because the sign of calibration errors can change between channels. The loss of accuracy in the atmospheric correction can be anticipated as being more important in this case than when all errors are either positive or negative. A more complete quantification of this problem is provided in section 3.1.3.2.7 below).

A peculiar “instrumental error” originates from straylight in the instrument optics (due to first order scattering events and also to “ghost images”). A first attempt to assess the impact of the additional irradiance due to straylight on the atmospheric correction process is made here, by increasing by a few percents the simulated radiances that would be recorded in absence of instrumental errors (the straylight is proportional to the measured radiance). The increase is not neutral, and is greater in the near-IR channels than in the visible ones. Percentages of increase, taken from a study of straylight in the MERIS instrument, are 2.3, 2.7 and 3.2% for the wavelengths 410, 620 and 865 nm, respectively. They have been obtained for a homogeneous ocean scene. These values are linearly interpolated for the other wavelengths. The radiances simulated here for the maritime aerosol model with humidity ratios of 70, 80, and 99% are increased following these percentages, and they are introduced in the atmospheric correction

procedure. The errors obtained at the end of the correction are shown on Fig. 3.32 (to be compared with Fig. 3.7 for instance).

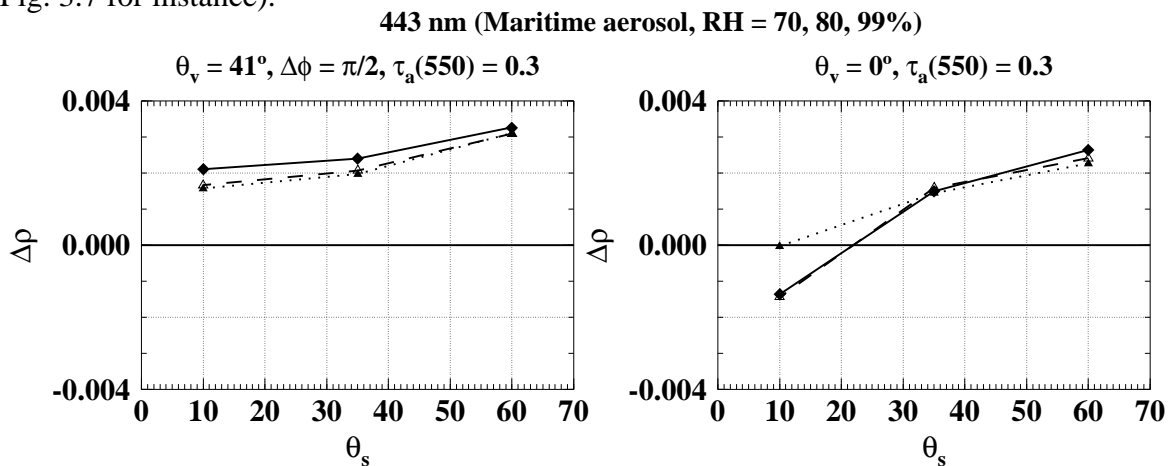


Figure 3.32. Error in the retrieved top of atmosphere water leaving reflectance at 443 nm, when straylight is added to the “infield” radiance (*i.e.*, the radiance that would be measured in absence of straylight). The solid, dotted, and dashed lines are for the maritime aerosol model, with RH = 70, 80, and 99%, respectively, and with $\tau_a(550) = 0.3$. Results are displayed as a function of the solar zenith angle, either for viewing at the scan edge (left) or at the scan center (right).

The results in Fig. 3.32 show that, over a homogeneous ocean scene, the impact of straylight is not so critical (the $\Delta\rho$ are due to an apparent spectral variation in the near-IR that is not the actual one). Furthermore, as the gain adjustment would implicitly incorporate the effect of straylight, the spectral variations of the measured radiances could be unchanged, with no impact on the atmospheric correction. The problem is by far more critical over cloudy areas (*e.g.*, small clouds scattered within an ocean scene). The ratio of straylight to in-field radiance can reach 0.5 in such conditions, at a distance of 20 pixels from the cloud edge. Clearly, the atmospheric correction will fail in that case. If straylight cannot be corrected before entering the pixel processing, a distance ζ will have to be defined, in terms of a number of pixels from the cloud edge, to discard those pixels which are closer than ζ from a cloud edge (note that a correction for straylight is included in the MERIS processing).

3.1.3.2.7 Instrumental errors. 2.: calibration errors

Calibration errors are a second possible source of error in the atmospheric correction and retrieval of the pigment index and atmospheric properties. The comprehensive calibration procedure that is planned for MERIS should provide TOA reflectances with a radiometric accuracy of 2-4%, relative to the sun (Rast and Bézy, 1995). It is as well conceivable that larger errors may occur in some instances. The impact of such errors cannot be fully assessed, precisely because the “pattern” of these calibration errors can vary (it is not predictable), for instance with positive and negative errors randomly distributed among bands, or errors systematically positive or negative for all bands, or for only a subset of bands, etc... Therefore, only a few situations, presumably representative of possible error combinations, have been examined here. They are similar to those examined by Gordon (1997), while the absolute values of the errors are set to little larger values when they are of opposite signs. The atmospheric correction algorithm is therefore applied to TOA reflectances that are calculated as:



$$\rho_t' = \rho_t (1 + \alpha(\lambda)) \quad (57)$$

where ρ_t is the “true” TOA reflectance (*i.e.*, the reflectance obtained through the Monte Carlo simulations), $\alpha(\lambda)$ is the wavelength-dependent calibration error, and ρ_t' would be accordingly the erroneously registered TOA reflectance. The atmospheric correction errors at 443 nm are displayed in Fig. 3.33, for the maritime aerosol (RH = 85%) when $\tau_a(550) = 0.1$, and for the 5 following error combinations:

$\alpha(\lambda) = 0$ in all bands (reference case)

$\alpha(443) = 0, \alpha(778) = 0.05, \alpha(865) = 0.05$ $\alpha(443) = 0.05, \alpha(778) = 0.05, \alpha(865) = 0.05$

$\alpha(443) = 0, \alpha(778) = -0.05, \alpha(865) = 0.05$ $\alpha(443) = 0, \alpha(778) = 0.05, \alpha(865) = -0.05$

A degradation of the atmospheric correction accuracy obviously occurs when the $\alpha(\lambda)$ errors are not all zeros, and especially when all errors are +5% at all wavelengths. In all other situations examined, this degradation remains however reasonable (only a few points are outside the ± 0.002 limit). It is also less than that obtained by Gordon (1997), who showed errors around ± 0.004 - 0.005 (*i.e.*, at least twice the errors for $\alpha(\lambda) = 0$ in all bands).

With the present algorithm, which uses the ratio $[\rho_{\text{path}} / \rho_{r, \tau_a=0}]$, a relative error α on ρ_{path} directly results in a relative error α in $[\rho_{\text{path}} / \rho_{r, \tau_a=0}]$. With an algorithm based on the $[\rho_{\text{path}} - \rho_{r, \tau_a=0}]$ difference, the relative error α on ρ_{path} becomes $\alpha (\rho_{\text{path}} / [\rho_{\text{path}} - \rho_{r, \tau_a=0}])$. The ratio $(\rho_{\text{path}} / [\rho_{\text{path}} - \rho_{r, \tau_a=0}])$ decreases as the aerosol optical thickness increases. For the wavelength 865 nm, and for $\theta_s = 60^\circ$, $\theta_v = 37^\circ$, and $\Delta\phi = \pi/2$, this ratio is 2.56 when $\tau_a = 0.03$, 1.76 when $\tau_a = 0.1$, 1.28 when $\tau_a = 0.3$, and 1.17 when $\tau_a = 0.5$. Therefore, in the case of clear maritime atmospheres (*i.e.*, τ_a about 0.1), the present algorithm would be twice less sensitive to calibration errors than is an algorithm based on the $[\rho_{\text{path}} - \rho_{r, \tau_a=0}]$ difference.

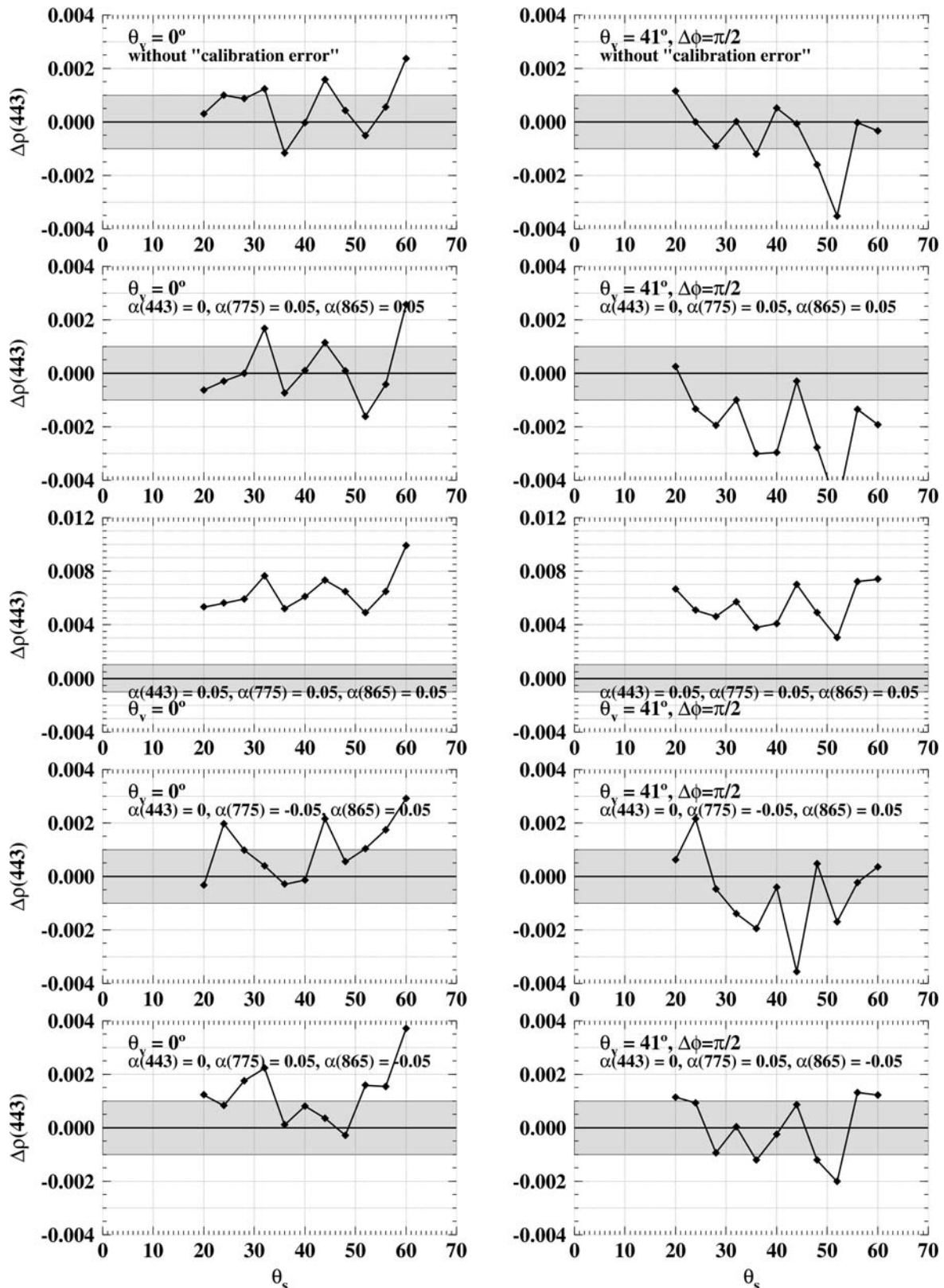


Figure 3.33. Error in the retrieved top of atmosphere water leaving reflectance at 443 nm, for the reference case (no calibration errors; upper 2 panels), and for several combinations of calibration errors, as indicated (see text). Results are displayed as a function of the solar zenith angle, either for viewing at the scan edge (right) or at the scan center (left).

3.1.3.2.8 Residual sun glint

A test, and the associated flag, is planned to identify the sun glint pattern over the ocean. This test is based on the Cox and Munk's model (1954) for the distribution of wave slopes, and makes use of a threshold reflectance, above which the pixel is considered as contaminated by sun glint (to be confirmed); this pixel is not further processed. For some pixels that are not identified by this test, the TOA reflectance may still contain a residual sun glint effect (*i.e.*, some photons directly transmitted through the atmosphere, before and after their reflexion on a wave facet).

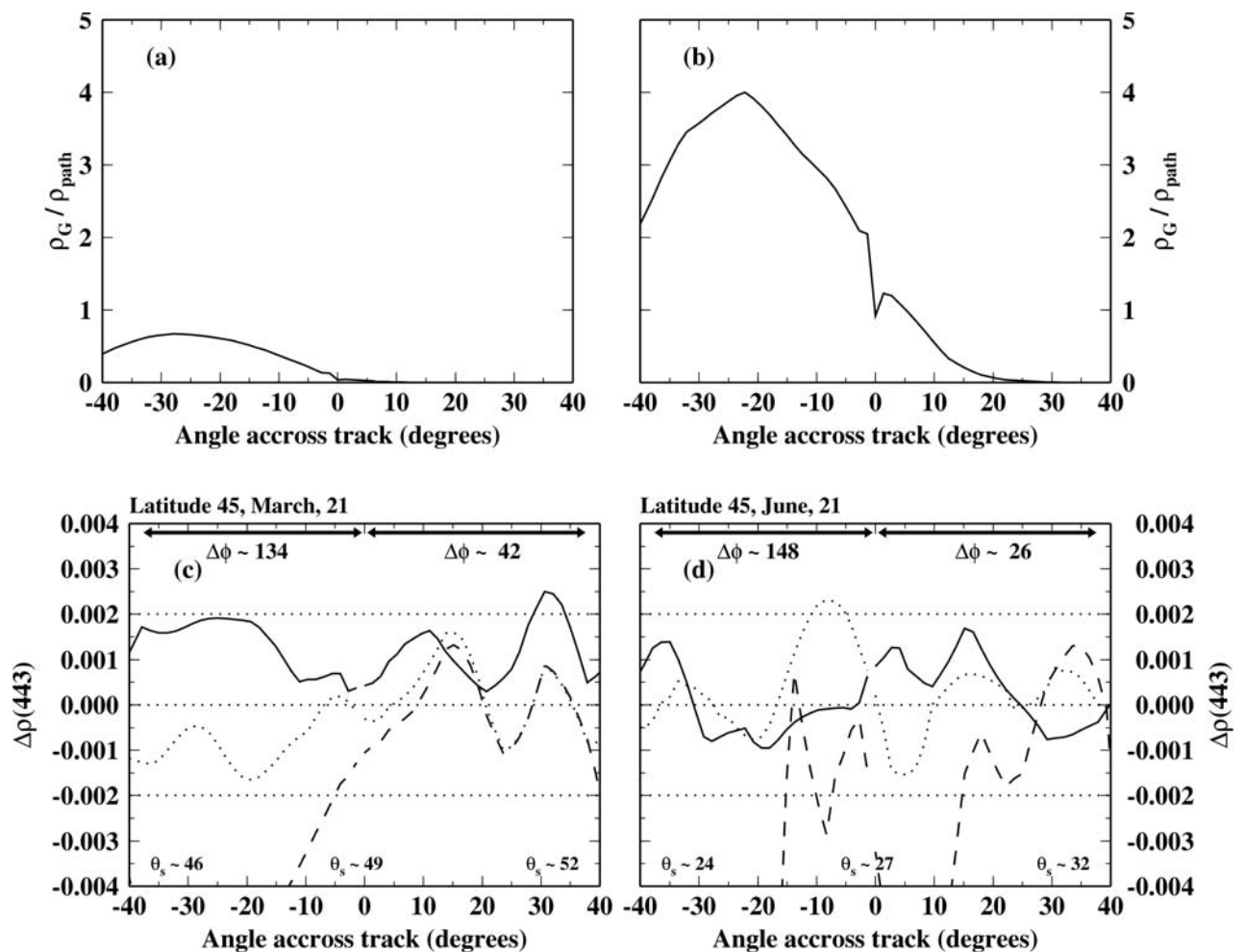


Figure 3.34. Panel (a) and panel (b): ratio of the glint reflectance, ρ_G (Eq. 29'), to the path reflectance, ρ_{path} , at 865 nm, and as a function of the viewing angle. The geometry corresponds to a MERIS scan at 45° north, for an acquisition at the vernal equinox (a), or at the summer solstice (b). Panel (c) and panel (d): for the geometries in (a) and (b), error in the atmospheric correction at 443 nm, when (1) the actual interface is flat ($\sigma = 0$, reference case; solid lines), (2) the interface is roughened, with a wind speed of 7.5 m s^{-1} ($\sigma = 0.2$), and the glint reflectance as been calculated exactly, and removed from ρ_t before entering into the algorithm (dotted lines), and (3) as in (2), whereas the glint reflectance has not been calculated and is therefore not removed from ρ_t (dashed lines). Note that the lookup tables for ρ_t and $[\rho_{path} / \rho_t]$ are for $\sigma = 0$ in any case.

The sensitivity study to wind speed (surface roughness; section 3.1.1.6.4) assumed that the sun glint reflectance, ρ_G , was correctly estimated, and subtracted from the total reflectance before



applying the atmospheric correction. This step is mandatory to the extent that the relationships $[\rho_{\text{path}} / \rho_{r, \tau_a=0}]$ versus τ_a are deeply modified if they are actually estimated with ρ_t (*i.e.*, ρ_{path} plus a non identified contribution of ρ_G) instead of ρ_{path} (dashed line in Fig. 3.23). Even with an exact knowledge of wind speed, existing models cannot actually provide an accurate value of ρ_G in the area of maximum sun glint ($\Delta\phi \sim \pi$, $\theta_v \sim \theta_s$). The reflectance ρ_G is there much greater than the path reflectance (see Fig. 3.34, panels (a) and (b)), so that no attempt to perform the correction will be made within this area. For some other geometries, around the maximum sun glint, the TOA total reflectance may still contain some photons directly transmitted through the atmosphere before and after reflection on a wave facet (“residual sun glint”; ρ_G is then less than an half of ρ_{path}). If the value of ρ_G for these geometries is not calculable accurately, it should be nevertheless computed, at least in view of identifying those pixels possibly affected by specular reflection. The identification could rely on a threshold, either on ρ_G (*e.g.*, Gordon 1997), or on the ratio $\rho_G / \rho_{\text{path}}$ (to be defined). For these pixels, atmospheric correction either would not be performed, or would be carried out and a flag raised. Note finally that ignoring the effect of shadowing on the sun glint pattern, as done in the present work, can only lead to significant errors for grazing viewing direction and sun illumination (simultaneous large θ_s and large θ_v values), and $\Delta\phi$ around π , this geometrical configuration, where ρ_G anyway becomes small, actually does not occur along a MERIS track.

When atmospheric correction is applied to TOA reflectances simulated over a rough ocean ($\sigma = 0.2$, corresponding to a wind speed of 7.5 m s^{-1}), and if these reflectances have been corrected for the exact value of ρ_G , the results remain correct (*i.e.*, $\Delta\rho(443)$ within ± 0.002) even when lookup tables generated for $\sigma = 0$ are used (dotted lines in Fig. 3.34, panels (c) and (d)). If ρ_G is not corrected, then atmospheric correction totally fails actually as soon as $\rho_G >$ about 0.0002 (dashed lines in Fig. 3.34; panels (c) and (d)). The conclusions are (1) at least 2 set of lookup tables ($[\rho_{\text{path}} / \rho_{r, \tau_a=0}]$ versus τ_a) have to be generated, for 2 values of the wind speed, (2) the glint reflectance has to be calculated as exactly as possible, and removed from the TOA reflectance before entering the algorithm.

3.1.3.2.9 Gaseous absorption

When presenting the “detailed mathematical model” (section 3.1.2), the signals (total radiances) were assumed to be corrected for gaseous absorption, if any. Indeed, these absorption are not accounted for when generating lookup tables. In principle, the MERIS channels used for atmospheric correction over Case 1 waters and the pigment index retrieval are exempt from significant gaseous absorptions. The only source of error could originate from neglecting the possible, yet uncertain, effect of the H_2O continuum.

3.1.3.2.10 Non-identified Case 2 waters

The architecture of the MERIS ground segment includes tests dedicated to the identification of Case 2 waters. It is conceivable, however, that in some instances these tests fail in discriminating between Case 1 and Case 2 waters; in such situations, pixels erroneously flagged as

Case 1 waters may go through the present algorithm, with expected drawbacks in the processing. This possible cause of failure of the algorithm is examined below.

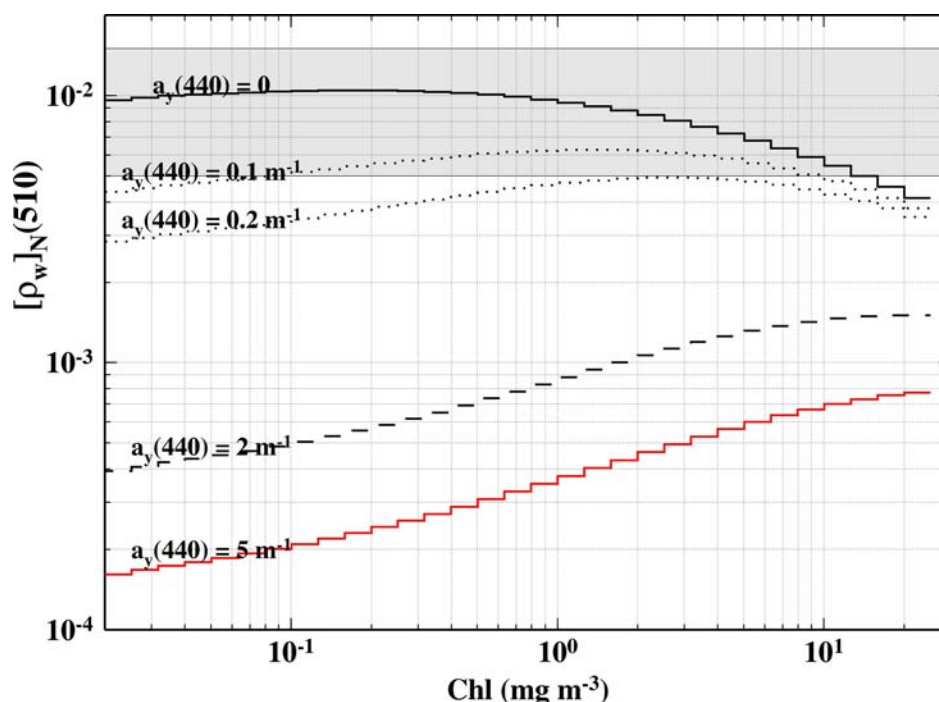


Figure 3.35. normalised water-leaving reflectances at 510 nm, for oceanic Case 1 waters ($a_y(440)=0$), and for yellow substance dominated Case 2 waters (curves for $a_y(440) \neq 0$). The shaded area correspond to $\pm 1 \sigma$ of $[\rho_w]_N(510)$ when $a_y(440) = 0$ (see section 3.1.1.4.2 and Fig. 3.3).

Case 2 waters dominated by yellow substance

In principle, yellow-substance-dominated Case 2 waters should not lead to any error in atmospheric correction, because the assumption of a black ocean remains valid when an additional absorption (with respect to that of water and phytoplankton) occurs within the water body. The problem lies in the test that is carried out at 510 nm (identification of aerosol absorption), and which is based on a constant value of the normalised water-leaving reflectance at 510 nm; this value of $[\rho_w]_N(510)$ ($1 \cdot 10^{-2}$) is only valid for Case 1 waters. When yellow substance actually absorbs, the value of $[\rho_w]_N(510)$ obviously decreases from its value for Case 1 waters (see Fig. 3.35). The consequence is that yellow substance absorption will be erroneously identified as aerosol absorption. Tests have been performed, where absorption by yellow substance is calculated as (Sathyendranath *et al.*, 1989):

$$a_y(\lambda) = a_y(440) e^{-0.14(\lambda - 440)} \quad (58)$$

where a_y is the absorption coefficient of yellow substance, whose value at 440 nm is, somewhat arbitrarily, fixed to values of 0.1, 0.2, 0.5, 2, and 5 m^{-1} . The results of atmospheric correction over yellow substance dominated Case 2 waters are presented in Fig. 3.36, for the maritime aerosol model (RH = 85%), and $\tau_a = 0.1$ at 550 nm. The threshold in $a_y(440)$, above which atmospheric

correction fails because of an erroneous aerosol selection, seems to be around 0.5 m^{-1} (*i.e.*, a reasonably high value)

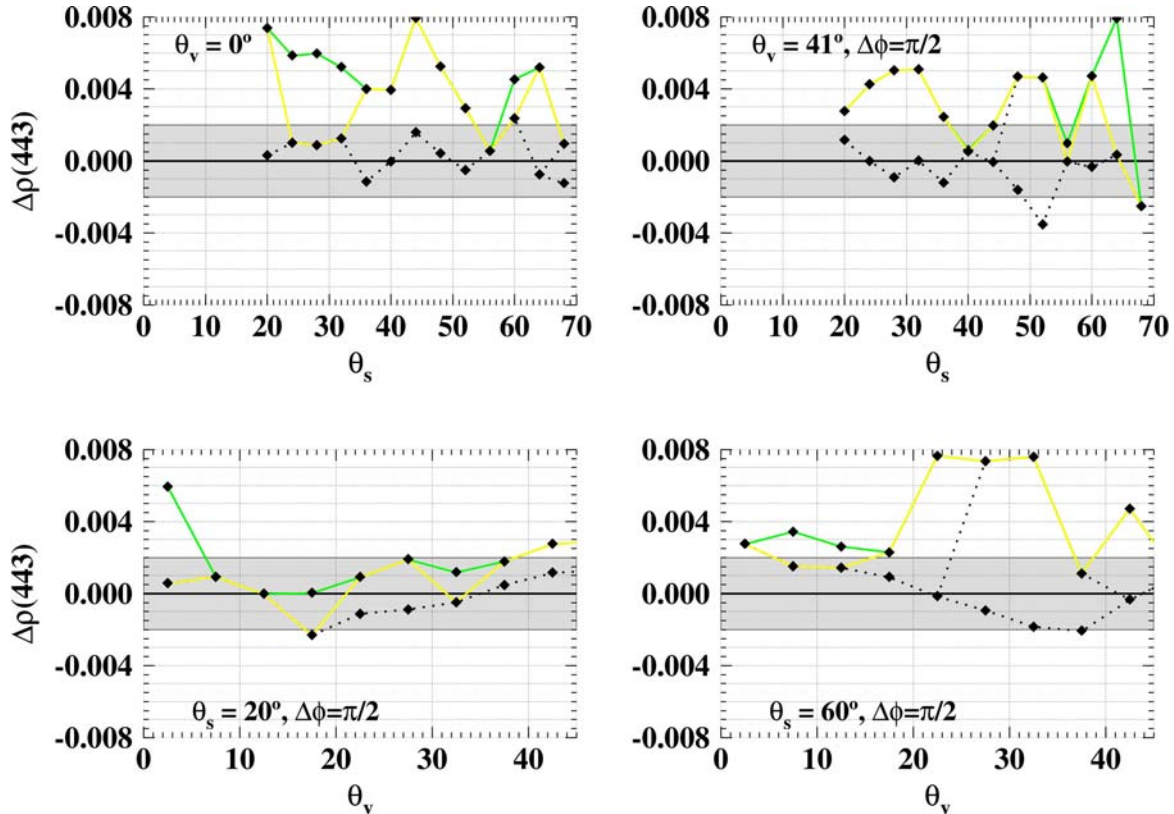


Figure 3.36. Error in the retrieved top of atmosphere water leaving reflectance at 443 nm, for the reference case (no yellow substance; dotted lines), and for several values of $a_y(440)$ (0.1 and 0.2 m^{-1} , dotted lines; 0.5 m^{-1} , yellow line; 1 m^{-1} , green line). Results are displayed either as a function of the solar zenith angle (upper 2 panels), or as a function of the viewing angle (lower 2 panels).

Case 2 waters dominated by suspended matter (sediment) scattering

A test is planned for identifying sediment-dominated Case 2 waters (MERIS ATBD 2.5: Case 2 turbid water flag, and MERIS ATBD 2.6: Case 2 (sediment) bright water atmospheric correction). The behaviour of the atmospheric correction is examined now, in the case where sediment-dominated Case 2 waters are non-identified and actually observed. The idea is the same as for yellow-substance-dominated Case 2 waters: what is the threshold, here in terms of additional scattering, above which the “Case 1 atmospheric correction” fails. Tests have been performed, where sediment scattering is calculated as (sediments are supposed to be non absorbing particles):

$$b_x(\lambda) = b_x(550) (\lambda / 550)^{-n} \quad (59)$$

where $b_x(550)$ is the scattering coefficient at 550 nm, and n characterises the spectral dependency of sediment scattering. $b_x(550)$ is computed as the product $[b_x^*(550) \text{ SPM}]$, where $b_x^*(550)$ is the specific scattering coefficient of sediments (set to $0.008 \text{ m}^2 \text{ mg}^{-1}$), and SPM is the sediment concentration in mg m^{-3} . The concentration SPM has been fixed to values of 0, 0.003, 0.03, 0.1, 0.3, 1, 3, and 10 g m^{-3} . The exponent n is set to 0.812, in correspondence with a particle size

distribution following a Junge distribution with $m = 4$, a size range of 0.45 to 20 μm , and a refractive index of 1.15. The backscattering ratio, as derived from the particle phase function calculated (MIE theory) with the parameters above, is equal to 1.4%.

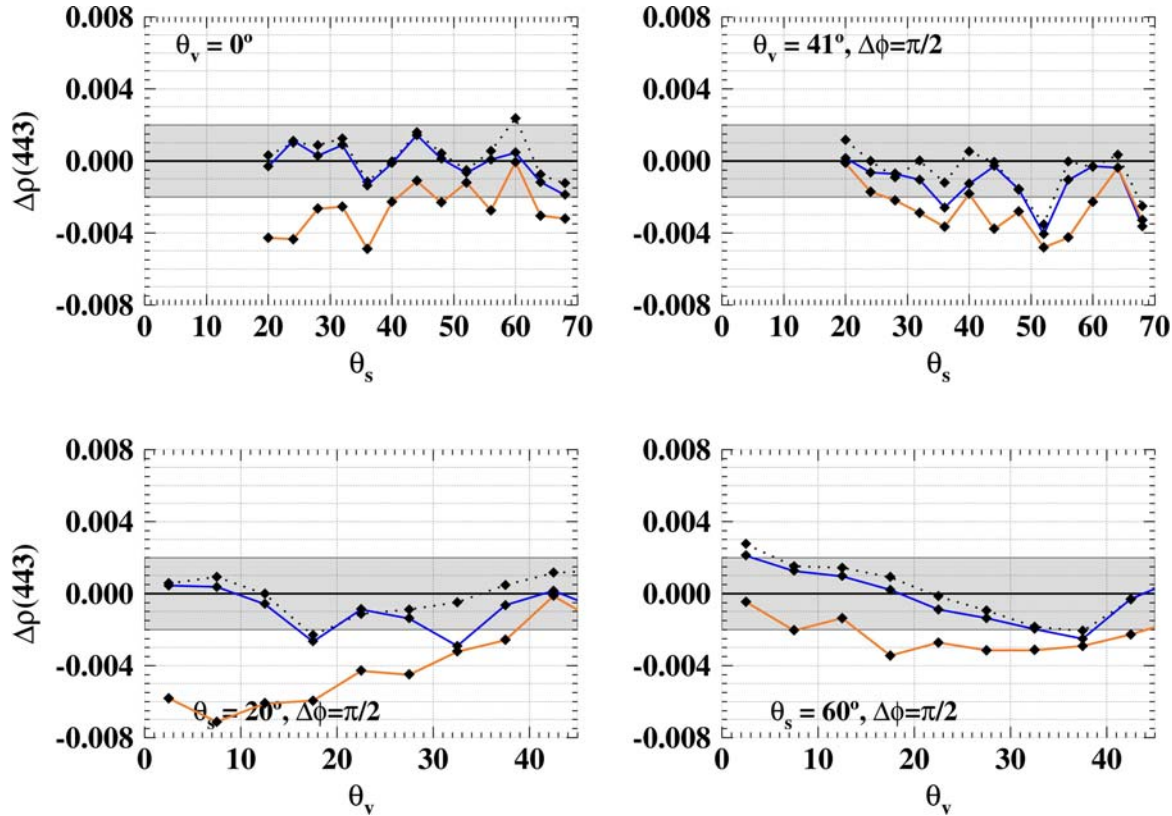


Figure 3.37. Error in the retrieved top of atmosphere water leaving reflectance at 443 nm, for the reference case (no additional scattering; dotted lines), and for several values of SPM (see text), namely $\text{SPM} = 0.003 \text{ g m}^{-3}$ (depp blue curve), 0.03, 0.1, and 0.3 g m^{-3} (yellow curve), and 1 and 3 g m^{-3} (light blue curve). Results are displayed either as a function of the solar zenith angle (upper 2 panels), or as a function of the viewing angle (lower 2 panels)..

In the near infrared, where the effect of phytoplankton on the water-leaving radiance is null, this radiance is calculated as:

$$\rho_w(\lambda, \theta, \phi) = E_d(0^+)(\lambda) \mathfrak{R}(\theta) \frac{f_1}{Q}(\lambda, \theta, \phi) \frac{b_b(\lambda)}{a(\lambda)} \quad (60)$$

where $b_b(\lambda)$ is the sum of the backscattering coefficients of water itself plus the sediments, $a(\lambda)$ is absorption by water only, and the (f_1/Q) ratio, calculated for Case 1 waters, is nevertheless used (for want of anything else). This last point is not really important when our only aim is to get an idea of the threshold in water-leaving reflectance (in the near infrared) above which atmospheric correction fails (whatever the relevance of the relationship between this water-leaving reflectance and the sediment load).

In the visible, the bio-optical model that we used is the model for Case 1 waters, and the additional backscattering due to sediments is simply added to the backscattering of phytoplankton and water.



Atmospheric correction has been applied to TOA reflectances simulated for these sediment-dominated Case 2 waters, and the results are shown in Fig. 3.37. The same errors in the retrieved marine reflectances are obtained for SPM concentrations of 0.03, 0.1, and 0.3 g m⁻³, and also for concentrations of 1 and 3 g m⁻³. The error in the aerosol selection are indeed identical for several SPM concentrations, because the impact of the additional marine signal in the near infrared evolves in steps. It was not expected that, in some instances, the accuracy of the correction remains acceptable with SPM = 1 g m⁻³. This result indicates, however, that the Case 2 turbid water flag (ATBD 2.5) will be useful if it triggers off for SPM concentrations around 0.3-0.5 g m⁻³ (*i.e.*, about $5 \cdot 10^{-4}$ to $2 \cdot 10^{-3}$ in terms of reflectance at 865 nm, and about $1.5 \cdot 10^{-3}$ to $5 \cdot 10^{-3}$ in terms of reflectance at 778 nm).

3.1.3.2.11 Polarisation

The issue of polarisation does not interfere with the present development of the atmospheric correction for MERIS. The total and Rayleigh radiances will be changed if polarisation is included in the systematic radiative transfer simulations, so that the lookup tables will not contain the same numerical values. The principle of the algorithm and its operation remain however unchanged either with or without including polarisation in the simulations. The question of including or not polarisation actually is close to that concerning the choice of a method (code) to carry out the systematic simulations (final implementation of the algorithm). A comparison has been made between Rayleigh radiances computed by taking into account polarisation (Gordon *et al.*, 1988): the “Exact Radiative Transfer Equation” is used, where the radiance is replaced by a column vector containing the Stokes parameters describing the state of polarisation of the light), and the Rayleigh radiances computed with the Monte Carlo code presently used (without polarisation). Differences are observed between the radiances generated by these 2 codes, of a few percent (2-5%), sometimes up to 10%. This preliminary test indicates that polarisation should be taken into account (even if MERIS is not sensitive to polarisation, the measured radiances can change with polarisation). Following Gordon (1997), however, the slight gain in accuracy resulting from the use of the vector theory in computing the lookup tables ($[\rho_{\text{path}} / \rho_{\tau_a=0}]$ versus τ_a) would be really small, as regards the considerable computational cost when accounting for polarisation.

3.1.3.3 Expected global accuracy

Considering the tests and sensitivity studies carried out and presented in this ATBD, the expected global accuracy of the algorithm should be within ± 0.002 in reflectance; this is slightly greater than the required accuracy (see section 2.3). Errors exceeding this threshold will occur in some cases, corresponding to extreme situations examined here.



3.2 Practical considerations

3.2.1 Lookup tables

A full description of the Lookup tables used in the operational implementation of the present algorithm, as well as the way they are derived, is to be found in two documents:

Specification of the Scientific Contents of the MERIS Level-1b & 2 Auxiliary Data Products (doc number PO-RS-PAR-GS-0002).

Specification of the Contents of the MERIS Radiative Transfer Tools used to Generate the Level-2 Auxiliary Data Products (doc number PO-RS-PAR-GS-0003)

The two documents are publicly available from the ENVISAT web page, at the following link:
<http://www.envisat.esa.int>

3.2.2 Exception handling

Criteria are to be defined, with the corresponding flags, to identify the pixels for which the atmospheric correction has failed, or has been carried out in non-optimal conditions. The following “science flags” are individually provided in the Level-2 products:

- (1) The test at 510 nm has revealed the presence of absorbing aerosols and absorbing aerosol models have been used in the atmospheric correction. Flag name in the MERIS level-2 products is ABSOA_DUST.
- (2) Case 2 turbid waters have been identified from a test in the near infrared (ATBD 2.5). Flag name is CASE2_S
- (3) Yellow substance dominated Case 2 waters have been identified (ATBD 2.8). Flag name is CASE2_Y. It is actually not set.
- (4) Case 2 turbid waters have been identified from a test at 560 nm (no ATBD). Flag name is CASE2_ANOM.
- (5) Ice or haze have been detected (test performed at 412 nm; cf. publication in Remote Sensing of Environment provided in appendix). Flag name is ICE_HAZE.
- (6) High glint contamination has been identified. Flag name is HIGH_GLINT.
- (7) Medium glint contamination has been identified. Flag name is MEDIUM_GLINT.
- (8) The sun zenith angle is $> 70^\circ$. Flag name is LOW_SUN..
- (9) White scatterers (typically coccolithophorids) have been identified. Flag name is WHITE_SCATTERER.

In addition to these individual flags, “Product Confidence Data” (PCD) are also provided. They are formed by the logic combination of several individual flags. PCDs concerning atmospheric corrections are:

3.2.3 Outputs of the atmospheric correction

The outputs of the atmospheric correction will be

- (1) The water-leaving reflectances in the MERIS bands 1 to 8, for cloud-free pixels. Their definition is:

$$\rho'_w = \frac{\pi L_w}{E_d(0^+)}$$

The aerosol optical thickness at 865 nm.



(2) The aerosol angstrom coefficient, α , computed as:

$$\alpha = -\log\left(\frac{\tau_a(778)}{\tau_a(865)}\right) / \log\left(\frac{778}{865}\right)$$

(3) flag(s) indicating the level of confidence of the atmospheric correction (see section 3.2.4)

4 Assumptions, constraints, and limitations

4.1 Assumptions

- The aerosol models used in the simulations (to generate the lookup tables) are assumed to be good approximations of the actual aerosols over the oceans. This point has been discussed in 3.1.3 (Error budget estimates).
- The “mixing ratio” is wavelength-independent. This point has been discussed in section 3.1.1.8 (remaining issues).
- The oceanic diffuse reflectance at 510 nm is weakly varying with the chlorophyll concentration, and it can be derived from a monthly climatology (section 3.1.1.4.2).
- The TOA total reflectance in the visible is adequately represented by summing the atmospheric path reflectance, obtained through radiative transfer simulations over a black, Fresnel-reflecting, ocean, and the product $t \cdot \rho_w$, calculated independently (section 3.1.1.1).
- The plane-parallel atmosphere is a good approximation of the real atmosphere for radiative transfer simulations, at least when the remote sensing configuration is concerned (see Ding and Gordon, 1994).
- It has been assumed here that the algorithm is applied to TOA reflectances that have been previously corrected for gaseous absorption, if any (including water vapour, oxygen and ozone).

4.2 Constraints, limitations

- The algorithm is designed to be operated over Case 1 waters. Its application over coastal turbid Case 2 waters (in a situation where pixel classification would have failed) cannot produce correct results.
- Problems could also be encountered over open ocean, when highly reflecting detached coccoliths are present (*e.g.*, Balch et al., 1989, 1991; Gordon and Balch, 1997), and more generally for any departure of the optical properties from those typical of Case 1 waters (if not identified).
- The algorithm obviously works over cloud free pixels, off the sun glint area (section 3.1.3.2.8).



Laboratoire
d'Océanographie
de Villefranche

Doc: MERIS_ATBD_2.7_v5.1-July2011
Name: MERIS Atmospheric Correction Over Case 1 Waters
Issue: 5
Draft Rev: 1
Date: July 18, 2011
Page: 76

- The algorithm development heavily relied upon aerosol models, radiative transfer models, as well as bio-optical models. The algorithm reliability is therefore connected to the quality of these models (*cf.* The “Reference model for MERIS level-2 processing”, ESA document PO-TN-MEL-GS-0026, issue 4r1, 13 July 2001).



5 References

- André J.M. and A. Morel, 1989. Simulated effects of barometric pressure and ozone content upon the estimate of marine phytoplankton from space. *J. Geophys. Res.* **94**, 1029-1037.
- Antoine D. and A. Morel, Relative importance of multiple scattering by air molecules and aerosols in forming the atmospheric path radiance in the visible and near infrared parts of the spectrum, accepted in *Appl. Opt.*
- Antoine D. and A. Morel, A multiple scattering algorithm for atmospheric correction of remotely sensed ocean color (MERIS instrument): principle and implementation for atmospheres carrying absorbing aerosols, Submitted to *Int. J. Remote Sensing*.
- Balch, W.M., R.W. Eppley, M.R. Abbott, and F.M. Reid, 1989, Bias in satellite-derived pigment measurements due to coccolithophorids and dinoflagellates, *J. Plankton Res.*, **11**, 575-581.
- Balch, W.M., P.M. Holligan, S.G. Ackleson, and K.J. Voss, 1991, Biological and optical properties of mesoscale coccolithophore blooms in the gulf of Maine, *Limnol. Oceanogr.*, **34**, 629-643.
- Brognez, G., J. C. Buriez, V. Giraud, F. Parol, and C. Vanbauce, 1995, *Mon. Weath. Rev.*
- Charlson, R. J., Schwartz, S. E., Hales, J. M., Cess, R. D., Coakley, J. A., Hansen, J. E, and Hofmann, D. J., 1992, Climate forcing by Anthropogenic aerosols, *Science* **255**, 423-430.
- Clark, D.K., H.R. Gordon, K.J. Voss, Y. Ge, W. Broenkow, and C. Trees, 1997, Validation of atmospheric correction over the oceans, *J. Geophys. Res.* **102D**, 17209-17217.
- Clarke G.L., G.C. Ewing et C.J. Lorenzen, 1970. Spectra of backscattered light from the sea obtained from aircraft as a measure of chlorophyll concentration. *Science* **167**, 1119-1121.
- Cox C. et W. Munk, 1954. Statistics of the sea surface derived from sun glitter. *J. Mar. Res.* **13**, 198-227.
- D'Almeida, G. A., P. Koepke, and E. P. Shettle, 1991, Atmospheric aerosols: global climatology and radiative characteristics, A. Deepak Ed., Hampton, Virginia USA, 561 pp.
- Deschamps P.Y., F.M. Bréon, M. Leroy, A. Podaire, A. Bricaud, J.C. Buriez and G. Sèze, 1994. The POLDER mission: instrument characteristics and scientific objectives, *IEEE Trans. on Geosci. and Rem. Sens.* **32**, 598-615.
- Deschamps P.Y., M. Herman et D. Tanre, 1983. Modeling of the atmospheric effects and its application to the remote sensing of ocean color. *Appl. Opt.* **22**, 3751-3758.
- Ding, K., and Gordon, H. R., 1994, Atmospheric correction of ocean-color sensors: effects of the Earth's curvature, *Appl. Opt.* **33**, 7096-7106.
- Donaghay, P. L., Liss, P. S., Duce, R. A., Kester, D. R., Hanson, A. K., Villareal, T., Tindale, N. W., and Gifford, D. J., 1991, The role of episodic atmospheric nutrient inputs in the chemical and biological dynamics of oceanic ecosystems, *Oceanogr.* **4**, 62-70.
- Duntley, S.Q., Wilson, W.H., and Edgerton, C.F., 1974, Detection of ocean chlorophyll from Earth orbit, in "ocean color analysis", S.Q. Duntley, R.W. Austin, W.W. Wilson, C.F. Edgerton, and S.E. Moran, Eds., (Scripps Institution of Oceanography, U. California at San Diego), SIO Ref. 74-10.
- Elterman L., 1968, UV, visible, and IR attenuation for altitudes to 50 km, Air Force Cambridge Research Laboratories, Environmental Research papers, N° 285, AFCRL-68-153, 49pp.
- Feldman G.C., N. Kuring, C. Ng, W. Esaias, C. McClain, J. Elrod, N. Maynard, D. Endres, R. Evans, J. Brown, S. Walsh, M. Carle et G. Podesta, 1989. Ocean color: availability of the global data set. *EOS* **70**, 634.



- Frouin R., M. Schwindling and P.Y. Deschamps, 1996, Spectral reflectance of sea foam in the visible and near-infrared: in-situ measurements and remote sensing implications, *J. Geophys. Res.* **101**, 14361-14371.
- Gordon H.R., 1997. Atmospheric correction of ocean color imagery in the Earth observing system era, *J. Geophys. Res.* **102D**, 17081-17106.
- Gordon, H.R. and W.M. Balch, 1997, MODIS detached coccolith concentration ATBD, version 3, available at <http://eosps0.gsfc.nasa.gov/atbd/modistables.html>.
- Gordon H.R., J.W. Brown et R.H. Evans, 1988. Exact Rayleigh scattering calculations for use with the Nimbus-7 Coastal Zone Color Scanner. *Appl. Opt.* **27**, 862-871.
- Gordon, H. R., and Clark, D. K., 1981, Clear water radiances for atmospheric correction of Coastal Zone Color Scanner imagery, *Appl. Opt.* **20**, 4175-4180.
- Gordon, H.R., Brown, O.B., Evans, R.H., Brown, J.W., Smith, R.C., Baker, K.S., and Clark, D.K., 1988, A semianalytic radiance model of ocean color. *J. Geophys. Res.* **93**, 10909-10924.
- Gordon H. R., D. K. Clark, J. L. Mueller and W. A. Hovis, 1980, Phytoplankton pigments from the Nimbus-7 Coastal Zone Color Scanner: comparisons with surface measurements, *Science* **210**, 63-66.
- Gordon H.R. and A. Morel, 1983, Remote assessment of ocean color for interpretation of satellite visible imagery, A review. In *Lecture notes on Coastal and Estuarine Studies*, 4, Springer Verlag, New York.
- Gordon H.R. and M. Wang, 1992a. Surface-roughness considerations for atmospheric correction of ocean color sensors. I: the rayleigh-scattering component. *Appl. Opt.* **31**, 4247-4260.
- Gordon H.R. and M. Wang, 1992b. Surface-roughness considerations for atmospheric correction of ocean color sensors. II: error in the retrieved water-leaving radiance. *Appl. Opt.* **31**, 4261-4267.
- Gordon H.R. and M. Wang, 1994a. Retrieval of water-leaving radiance and aerosol optical thickness over the oceans with SeaWiFS: a preliminary algorithm. *Appl. Opt.* **33**, 443-452.
- Gordon H.R. and M. Wang, 1994b. Influence of oceanic whitecaps on atmospheric correction of ocean-color sensors. *Appl. Opt.* **33**, 7754-7763.
- Gordon H.R., T. Zhang, F. He, and K. Ding, 1997, Effects of stratospheric aerosols and thin cirrus clouds on the atmospheric correction of ocean color imagery: simulations, *Appl. Opt.* **36**, 682-697.
- Herman, J. R., Bhartia, P. K., Torres, O., Hsu, C., Setfor, C., and Celarier, E., 1997, Global distribution of UV-absorbing aerosols from Nimbus 7/TOMS data, *J. Geophys. Res.* **102**, 16911-16922.
- Hovis W. A., D. K. Clark, F. Anderson, R. W. Austin, W. H. Wilson, E. T. Baker, D. Ball, H. R. Gordon, J. L. Mueller, S. Z. ElSayed, B. Sturm, R. C. Wrigley and C. S. Yentsch, 1980, Nimbus-7 Coastal Zone Color Scanner: system description and initial imagery, *Science* **210**, 60-63.
- Husar, R. B., Prospero, J. M., and Stowe, L. L., 1991, Characterization of tropospheric aerosols over the oceans with the NOAA advanced very high resolution radiometer optical thickness operational product, *J. Geophys. Res.* **102**, 16889-16909.
- JRC contract, 1995, Ocean color remote sensing simulator, Aerosol scattering phase functions, April 1995, ACRI-FUB-LOV-PML, 24 pp.
- Kishino, M., Ishizaka, J., Saitoh, S., Senga, Y., and Utashima, M., 1997, Verification plan of ocean color and temperature scanner atmospheric correction and phytoplankton pigment by moored optical buoy system, *J. Geophys. Res.* **102**, 17197-17207.
- Koepke P., 1984. Effective reflectance of whitecaps. *Appl. Opt.* **23**, 1816-1824.



- Maritorena S., J. E. O'Reilly, and B. Schieber, 1997, The SeaBAM evaluation data set, available at http://seabass.gsfc.nasa.gov/~seabam/Public/maritorena_oreilly_schieber/.
- MEDIPROD group, 1976, "Résultats de la campagne CINECA 5 - J. Charcot - Capricorne 7403 (1^{er} Mars au 20 Avril 1974)," Publications du CNEXO, N°10.
- Mobley C.D., B. Gentili, H.R. Gordon, Z. Jin, G.W. Kattawar, A. Morel, P. Reinersman, K. Stamnes and R.H. Stavn, 1993. Comparison of numerical models for computing underwater light fields. *Appl. Opt.* **32**, 7484-7504.
- Morel A., 1988. Optical modeling of the upper ocean in relation to its biogenous matter content (case 1 waters). *J. Geophys. Res.* **93**, 10749-10768.
- Morel A. and B. Gentili, 1991. Diffuse reflectance of oceanic waters: its dependence on sun angle as influenced by the molecular scattering contribution. *Appl. Opt.* **30**, 4427-4438.
- Morel A. and B. Gentili, 1993. Diffuse reflectance of oceanic waters. II. Bidirectional aspects. *Appl. Opt.* **32**, 6864-6879.
- Morel, A., and Gentili, B., 1996, Diffuse reflectance of oceanic waters. III. implication of the bidirectionality for the remote sensing problem, *Appl. Opt.* **35**, 4850-4862.
- Moulin, C., Guillard, F., Dulac, F., and Lambert, C. E., 1997, Long-term daily monitoring of Saharan dust load over ocean using Meteosat ISCCP-B2 data. 1. Methodology and preliminary results for 1983-1994 in the Mediterranean, *J. Geophys. Res.* **102**, 16947-16958.
- Moulin, C., Gordon, H. R., Banzon, V. F. and Evans, R. H. (2001), Assessment of Saharan dust absorption in the visible from SeaWiFS imagerie. *J. Geophys. Res.*, 106, 18239-18249.
- Neckel H. and D. Labs, 1984. The solar radiation between 300 and 12500 Å. *Sol. Phys.* **90**, 205-258.
- Nobileau, D. and D. Antoine, (2005), Detection of blue-absorbing aerosols using near infrared and visible (ocean color) remote sensing observations. *Remote Sens. Environ.*, **95**, 368-387.
- OLIPAC (JGOFS) campaign, data unpublished.
- PACIPROD campaign, data unpublished.
- Powell, K. A, 1995, Observations of Saharan dust by LITE, *EOS Trans.*, AGU fall meeting suppl. **76**, S73.
- Preisendorfer R.W., 1961. Application of radiative transfer theory to light measurements in the sea. *Monogr. Int. Union Geod. Geophys. Paris* **10**, 11-30.
- M. Rast and J. L. Bézy, 1995, The ESA medium resolution imaging spectrometer (MERIS): requirements to its mission and performance of its system, in RSS95, Remote Sensing in Action, Proc. 21st Annual Conf. Remote Sensing Soc., 11-14 September, 1995, University of Southampton, Eds. P.J. Curran and Y.C. Robertson, Taylor and Francis Pub. 1995, 125-132.
- Sathyendranath, S., Prieur, L., and Morel, A., 1989, A three-component model of ocean colour and its application to remote sensing of phytoplankton pigments in coastal waters. *Int. J. Remote Sensing* **10**, 1373-1394.
- Schollaert, S.E., Yoder, J.A., Westphal, D.L and O'Reilly, J.E. (2003). Influence of dust and sulfate aerosols on ocean color spectra and chlorophyll-a concentrations derived from SeaWiFS off the U.S. East Coast. *J. Geophys. Res.*, 108 (C6): 3191, doi: 10.1029/2000JC000555
- Schütz, L., 1980, Long-range transport of desert dust with special emphasis on the Sahara, *Ann. N. Y. Acad. Sci.* **338**, 515-532.
- Schwindling, M., 1995, Modèles et mesures pour l'observation spatiale de la couleur de l'océan: diffusion atmosphérique par les aérosols et réflexion de surface par l'écume, Thèse de Doctorat de l'Université des Sciences et Techniques de Lille, France, 1995, 245 pp.



Laboratoire
d'Océanographie
de Villefranche

Doc: MERIS_ATBD_2.7_v5.1-July2011
Name: MERIS Atmospheric Correction Over Case 1 Waters
Issue: 5
Draft Rev: 1
Date: July 18, 2011
Page: 80

- Shettle E.P. and Fenn R.W., 1979. Models for the aerosols of the lower atmosphere and the effects of humidity variations on their optical properties. Environmental Research Papers, AFGL-TR-79-214, Air Force Geophysics Laboratory, 20 September 1979.
- Stowe, L. L., Ignatov, A. M., and Singh, R. R., 1997, Development, validation, and potential enhancements to the second-generation operational aerosol product at the national environmental satellite, data, and information service of the national oceanic and atmospheric administration, *J. Geophys. Res.* **102**, 16923-16934.
- Tyler, J.E., 1973, "Measurements of photosynthesis, available radiant flux, and supporting oceanographic data, Data report, SOCR Discoverer expedition, May 1970," S.I.O. Ref. 73-16, Univ. California.
- Vermote E., D. Tanré, J.L. Deuzé, M. Herman and J.J. Morcrette, 1994. Second simulation of the satellite signal in the solar spectrum (6S). Laboratoire d'optique atmosphérique, 183 pp.
- Vilvalde, Y. V., Smirnov, A. V., O'Neill, N. T., Smyshlyaev, S. P., and Yakovlev, V. V., 1994, Measurement of aerosol optical depth in the Pacific ocean and the North Atlantic, *J. Geophys. Res.* **99**, 20983-20988.
- World Climate Research Program, 1986, A preliminary cloudless standard atmosphere for radiation computation, Int. Ass. Meteorol. Atm. Phys., Radiation Commission, March 1986, WCP-112, WMO/TD-N° 24, 60 pp (1986)
- Yang H., and H.R. Gordon, 1997, Remote sensing of ocean color: assessment of the water-leaving radiance bidirectional effects on the atmospheric diffuse transmittance, Submitted to *Appl. Opt.*



6 Symbols

Symbol	definition	Dimension / units
Geometry, wavelengths		
λ	Wavelength	nm
θ_s	Sun zenith angle ($\mu_s = \cos(\theta_s)$)	degrees
θ_v	Satellite viewing angle ($\mu_v = \cos(\theta_v)$)	degrees
$\Delta\phi$	Azimuth difference between the sun-pixel and pixel-sensor half vertical planes	degrees
Atmosphere and aerosol properties		
$F_0(\lambda)$	Mean extraterrestrial spectral irradiance	$\text{W m}^{-2} \text{nm}^{-1}$
ε_c	Eccentricity of the Earth orbit	dimensionless
$F_a(\lambda)$	Aerosol forward scattering probability	dimensionless
$F_r(\lambda)$	Rayleigh forward scattering probability	dimensionless
$\tau_a(\lambda)$	Optical thickness due to aerosol scattering	dimensionless
$\tau_r(\lambda)$	Optical thickness due to Rayleigh scattering	dimensionless
η_r	Contribution of molecules to the total optical thickness ($=\tau_r / (\tau_r + \tau_a)$)	dimensionless
$\tau_{ag}(\lambda)$	Optical thickness due to gaseous absorption	dimensionless
$\varpi_a(\lambda)$	Aerosol single scattering albedo	dimensionless
$\varpi_r(\lambda)$	Rayleigh single scattering albedo	dimensionless
$P_r(\lambda, \gamma)$	Rayleigh phase function $p_r(\gamma^\pm) = P_r(\lambda, \gamma^\pm) + [\rho_F(\theta_s) + \rho_F(\theta_v)] P_r(\lambda, \gamma^\pm)$ where γ^\pm is the scattering angle $\cos(\gamma^\pm) = \pm \cos(\theta_0) \cos(\theta_v) - \sin(\theta_0) \sin(\theta_v) \cos(\Delta\phi)$	sr^{-1}
$P_a(\lambda, \gamma)$	Aerosol phase function $p_a(\gamma^\pm) = P_a(\lambda, \gamma^\pm) + [\rho_F(\theta_s) + \rho_F(\theta_v)] P_a(\lambda, \gamma^\pm)$	sr^{-1}
ν	Exponent of the Junge law for the distribution of aerosol particles (sensitivity studies)	dimensionless
$c(\lambda)$	Attenuation coefficient for wavelength λ	m^{-1}
$t_{\theta_s}(\lambda, \theta_s)$	Irradiance transmittance for a sun zenith angle θ_s $t_{\theta_s}(\lambda, \theta_s) = E_d(0^+) / (\mu_s \varepsilon_c F_0)$, where $E_d(0^+)$ is the downwelling irradiance just above the sea surface	dimensionless



$t_d(\lambda, \theta)$	Diffuse transmittance for angle θ	dimensionless
	$t_d(\lambda, \theta) = L_{\text{TOA}}(\lambda, \theta_s, \theta_v, \Delta\phi) / L_{0^+}(\lambda, \theta_s, \theta_v, \Delta\phi)$	
$L(\lambda, \theta_s, \theta_v, \Delta\phi)$	Radiance	$\text{W m}^{-2} \text{ nm}^{-1} \text{ sr}^{-1}$
	Subscripts : TOA \rightarrow top of atmosphere 0^+ \rightarrow just above the sea surface w for water-leaving radiance, just above the sea surface u for upwelling radiance, just below the sea surface	
P	Atmospheric pressure at sea level	hPa
RH	Relative humidity	percents
$\rho(\lambda, \theta_s, \theta_v, \Delta\phi)$	Reflectance ($\pi L / F_0 \mu_s$)	dimensionless
	where the product πL is the TOA upwelling irradiance if upwelling radiances are equal to $L(\lambda, \theta_s, \theta_v, \Delta\phi)$ for any values of θ_v within $0 - \pi/2$ and any $\Delta\phi$ within $0 - 2\pi$.	
	Subscripts t: total reflectance w: water-leaving reflectance path: path reflectance r: Rayleigh reflectance rs: Rayleigh reflectance (single scattering only) a: aerosol reflectance as: aerosol reflectance (single scattering only) ra: heterogeneous aerosol-molecule scattering G: sun glint reflectance wc: whitecaps reflectance	
$\rho^*(\lambda, \theta_s, \theta_v, \Delta\phi)$	Reflectance within a compound atmosphere, containing molecules and aerosols (subscripts as for ρ)	dimensionless
$\varepsilon(\lambda_1, \lambda_2)$	Ratio $\rho_{\text{as}}(\lambda_1) / \rho_{\text{as}}(\lambda_2)$	dimensionless
$\varepsilon'(\lambda_1, \lambda_2)$	Ratio $[\rho_{\text{path}}(\lambda_1) - \rho_r(\lambda_1)] / [\rho_{\text{path}}(\lambda_2) - \rho_r(\lambda_2)]$	dimensionless
$f(\tau_a)$	Relationship between the ratio $[\rho_{\text{path}} / \rho_r]$ and τ_a	dimensionless
Water properties		
Chl	Chlorophyll concentration	mg m^{-3}
$a(\lambda)$	Total absorption coefficient (due to water and algae)	m^{-1}
$b_b(\lambda)$	Total backscattering coefficient (due to water and algae)	m^{-1}
A_{λ_1, λ_2}	Ratio of (b_b/a) at λ_1 to (b_b/a) at λ_2	dimensionless
$R(\lambda, 0^-)$	Diffuse reflectance of oceanic Case 1 waters, at null depth	dimensionless



f	Ratio of $R(0^-)$ to (b_p/a) ; subscript 0 when $\theta_s = 0$	dimensionless
$Q(\lambda, \theta_s, \theta_v, \Delta\phi)$	Factor describing the bidirectional character of the diffuse reflectance of oceanic Case 1 waters; subscript 0 when $\theta_s = \theta_v = 0$	sr
$[\rho_w]_N(\lambda)$	Normalised water-leaving reflectance (<i>i.e.</i> , the reflectance if there were no atmosphere, and for $\theta_s = \theta_v = 0$)	dimensionless

Air-water interface

$\mathfrak{R}(\theta)$	Geometrical factor, accounting for all refraction and reflection effects at the air-sea interface (Morel and Gentili, 1996)	dimensionless
------------------------	---	---------------

$$\mathfrak{R}(\theta') = \left[\frac{(1 - \bar{\rho})}{(1 - \bar{r}R)} \frac{(1 - \rho_F(\theta'))}{n^2} \right] \text{ (subscript 0 when } \theta' = 0)$$

where

n	is the refractive index of water	dimensionless
$\rho_F(\theta)$	is the Fresnel reflection coefficient for incident angle θ	dimensionless
$\bar{\rho}$	is the mean reflection coefficient for the downwelling irradiance at the sea surface	dimensionless
\bar{r}	is the average reflection for upwelling irradiance at the water-air interface	dimensionless
θ'	is the refracted viewing angle ($\theta' = \sin^{-1}(n \cdot \sin(\theta_v))$)	degrees

σ	Root-mean square of wave facet slopes	dimensionless
β	Angle between the local normal and the normal to a facet	
p	Probability density of surface slopes for the direction $(\theta_s, \theta_v, \Delta\phi)$	dimensionless

Miscellaneous

W	Wind speed	dimensionless
X	Aerosol mixing ratio defined on the basis of the $[\rho_{\text{path}} / \rho_T]$ ratio At 778 nm.	dimensionless



7 Appendix: publications

The full text of the following three publications is provided hereafter:

- (1) Antoine D. and A. Morel, 1998, Relative importance of multiple scattering by air molecules and aerosols in forming the atmospheric path radiance in the visible and near infrared parts of the spectrum, *Applied Optics* 37, 2245-2259.
- (2) Antoine D. and A. Morel, 1999, A multiple scattering algorithm for atmospheric correction of remotely-sensed ocean color (MERIS instrument): principle and implementation for atmospheres carrying various aerosols including absorbing ones, *International Journal of Remote Sensing*, 20, 1875-1916.
- (3) Nobileau, D. and D. Antoine, 2005, Detection of blue-absorbing aerosols using near infrared and visible (ocean color) remote sensing observations. *Remote Sensing of Environment*, 95, 368-387.
- (4) Antoine D. and D. Nobileau, (2006). Recent increase of Saharan dust transport over the Mediterranean Sea, as revealed from ocean color satellite (SeaWiFS) observations. *Journal of Geophysical Research, Atmosphere*, 111, D12214, doi:10.1029/2005JD006795
- (5) Antoine, D., F. D'Ortenzio, S. B. Hooker, G Bécu, B. Gentili, D. Tailliez, and A. J. Scott (2008), Assessment of uncertainty in the ocean reflectance determined by three satellite ocean color sensors (MERIS, SeaWiFS and MODIS-A) at an offshore site in the Mediterranean Sea (BOUSSOLE project), *Journal of Geophysical Research*, 113, C07013, doi:10.1029/2007JC004472

Relative importance of multiple scattering by air molecules and aerosols in forming the atmospheric path radiance in the visible and near-infrared parts of the spectrum

David Antoine and André Morel

Single and multiple scattering by molecules or by atmospheric aerosols only (homogeneous scattering), and heterogeneous scattering by aerosols and molecules, are recorded in Monte Carlo simulations. It is shown that heterogeneous scattering (1) always contributes significantly to the path reflectance (ρ_{path}), (2) is realized at the expense of homogeneous scattering, (3) decreases when aerosols are absorbing, and (4) introduces deviations in the spectral dependencies of reflectances compared with the Rayleigh exponent and the aerosol angstrom exponent. The ratio of ρ_{path} to the Rayleigh reflectance for an aerosol-free atmosphere is linearly related to the aerosol optical thickness. This result provides a basis for a new scheme for atmospheric correction of remotely sensed ocean color observations. © 1998 Optical Society of America

OCIS codes: 010.0010, 010.1100, 010.1310, 010.4450, 290.1090, 290.4210, 290.5850, 290.5870.

1. Introduction

When correcting for atmospheric-effect Earth observations taken from satellite sensors, or when inverting ground-based measurements of sky radiances, one must estimate the path radiance or the path reflectance if the following transformation is used (symbols and definitions are listed in Table 1):

$$\rho(\lambda, \theta_v, \theta_s, \Delta\phi) = \pi L(\lambda, \theta_v, \theta_s, \Delta\phi) / E_s(\lambda) \cos(\theta_s).$$

Except if they are expressly needed, wavelength and angular dependencies will hereafter be omitted for clarity. In the case of a satellite sensor aiming at the ocean, the path reflectance at the top of the atmosphere (TOA) originates from single and multiple scattering by molecules and aerosols, which affect photons traveling downward through the atmosphere and also photons traveling upward after they have been reflected at the air-water interface. Therefore,

estimating the path reflectance requires that the combined effects of aerosols and molecules on the radiative field be understood and assessed.

According to previously adopted assumptions, reflectances that are due to Rayleigh and aerosol scattering are separable,¹ so they can be calculable for single-component atmospheres and then summed to simulate the path reflectance. In this case the determination of that part of the path reflectance that originates from molecular scattering (Rayleigh scattering) is easily dealt with, for only the illumination and observation conditions have to be known. In contrast, the numerical density of aerosol particles, their chemical nature, and their vertical distribution vary greatly, so they are *a priori* unknown in most situations. When it is assumed, however, that the reflectance that is due to aerosol scattering is calculable (under some assumptions), the approach then consists in adding this reflectance to the Rayleigh reflectance (both having been obtained for single-component atmospheres) and finally in introducing a corrective term that accounts for the nonadditive character of the reflectances (which are apparent optical properties). This term is usually referred to as the coupling term between aerosol and molecule scattering and involves heterogeneous multiple scattering. The attribute "heterogeneous" is used here to identify molecule-particle scattering, as opposed to

The authors are with the Laboratoire de Physique et Chimie Marines, Université Pierre et Marie Curie et Centre National de la Recherche Scientifique, B.P. 08, F-06238 Villefranche sur Mer Cedex, France.

Received 11 July 1997; revised manuscript received 17 November 1997.

0003-6935/98/122245-15\$15.00/0

© 1998 Optical Society of America

Table 1. Symbols and Definitions

Symbol	Definition	Dimension/Units
θ_s	Sun zenith angle	Degrees
θ_v	Viewing angle	Degrees
$\Delta\phi$	Azimuth difference between the Sun-pixel and pixel-sensor half-vertical planes	Degrees
$E_s(\lambda)$	Extraterrestrial irradiance	$W\ m^{-2}\ nm^{-1}$
η_a	Contribution of aerosols to the total optical thickness	Dimensionless
η_r	$1 - \eta_a$	Dimensionless
λ	Wavelength	nm
$L(\lambda, \theta_s, \theta_v, \Delta\phi)$	Radiance	$W\ m^{-2}\ nm^{-1}\ sr^{-1}$
n	Operational exponent	Dimensionless
$P_a(\gamma)$	Aerosol phase function	sr^{-1}
$P_r(\gamma)$	Rayleigh phase function	sr^{-1}
γ^\pm	Scattering angle	Degrees
$\rho(\lambda, \theta_s, \theta_v, \Delta\phi)$	Reflectance, defined as $\pi L/E_s \cos(\theta_s)$, where the product πL is the TOA upwelling irradiance if upwelling radiances are equal to $L(\lambda, \theta_s, \theta_v, \Delta\phi)$ for any values of θ_v . Subscripts: path, path reflectance; r , Rayleigh reflectance; rs , Rayleigh reflectance (single scattering only); a , aerosol reflectance; as , aerosol reflectance (single scattering only); ra , heterogeneous aerosol-molecule scattering. Superscript: *, a reflectance for a compound atmosphere	Dimensionless
$\bar{\rho}_x$	Bulk reflectance integrated over a solid angle Ω of 4.4 sr, where x is one of the subscripts defined for ρ	Dimensionless
$\langle \bar{\rho}_x \rangle$	Relative contribution of $\bar{\rho}_x$ to $\bar{\rho}_{path}$, where x is one of the subscripts defined for ρ	%
$\rho_F(\theta)$	Fresnel reflection coefficient for angle θ	Dimensionless
RH	Relative humidity	%
τ_a	Aerosol optical thickness	Dimensionless
τ_r	Rayleigh optical thickness	Dimensionless
ω	Single scattering albedo	Dimensionless
c	Attenuation coefficient	m^{-1}

homogeneous molecule-molecule or aerosol-aerosol multiple scattering. In fact, the validity of the above approximations is not firmly established, mainly because heterogeneous scattering, which necessarily occurs in the atmosphere, has not been clearly studied. As far as we know, the creation of a flux resulting from multiple molecule-aerosol scattering events, the spatial rearrangement of the scattered flux, and the relative importance of multiple scattering when the aerosol load increases have not yet been thoroughly examined or quantified. The study presented in this paper aims at filling this gap.

In the present study Monte Carlo simulations were carried out in compound (molecules plus aerosols), multilayered atmospheres, so all kinds and orders of scattering are considered. In addition, the code is provided with the capacity of keeping track of the photons, allowing the total reflectance to be decomposed into three partial reflectances, corresponding to the contributions of (1) single and multiple scattering by molecules only (in the presence of aerosols, however), (2) single and multiple scattering by aerosols only (in the presence of molecules), and finally (3) heterogeneous scattering by both aerosols and molecules. The addition of these three partial reflectances is strictly valid, unlike for the sum of reflectances separately computed for single-component atmospheres.

A detailed study of the three terms was undertaken, permitting a better understanding of their changes in response to changes in the vertical struc-

ture of the atmosphere, the aerosol optical thickness, and the ratio of aerosol to total optical thicknesses. The partial reflectances were first examined for specific geometries, and then their contribution to the global flux were assessed. The spectral dependencies of the three terms were also analyzed and compared with the Rayleigh exponent and the aerosol angstrom exponent. The effect of aerosol absorption on results obtained for nonabsorbing aerosols was assessed. We show that, for a given aerosol, the relative change of the path reflectance in response to increasing aerosol optical thickness is monotonically and unambiguously related to the aerosol optical thickness. The result was applied to the problem of atmospheric correction of ocean color observations from space, and a new scheme is presented that implicitly accounts for the three terms described above.

2. Decomposition of the Top-of-the-Atmosphere Signal

The TOA signal includes three terms, as follows:

(1) The photons specularly reflected at the air-water interface, after a direct path from the Sun, and then traveling back to the TOA without scattering; they form the sun-glint term and are not considered here.

(2) The contribution of whitecaps and foam, which return toward the TOA a fraction of the direct sunlight and of diffuse sky light; this term is not examined either.

(3) The path reflectance, which is the term specifically studied here; it is generated along the two-way path through the atmosphere, mainly by backscattering along the downward path, and mainly by forward scattering along the upward path, after reflection of the skylight at the interface.

A first approximation has consisted in simply expressing the path reflectance for a given compound atmosphere, ρ_{path} , as the sum^{1,2}

$$\rho_{\text{path}} = \rho_{\text{rs}} + \rho_{\text{as}}, \quad (1)$$

where ρ_{rs} is the Rayleigh reflectance of the same atmosphere in absence of aerosol, ρ_{as} is the aerosol reflectance in absence of air molecules, and both reflectances result from single scattering (as indicated by the subscript *s*). Equation (1), which is strictly valid only under the assumption of single scattering, implies that the optical thicknesses τ_r and τ_a , for Rayleigh and aerosols, respectively, are small enough (i.e., below 0.1). In this approximation, and with a flat sea surface, ρ_{rs} and ρ_{as} can be expressed from the corresponding phase functions as

$$\rho_{\text{as(rs)}}(\lambda, \theta_s, \theta_v, \Delta\phi) = \tau_{\text{a(r)}}(\lambda) \omega_{\text{a(r)}}(\lambda) p_{\text{a(r)}}(\lambda, \theta_s, \theta_v, \Delta\phi) / 4\mu_s\mu_v, \quad (2)$$

where

$$p_{\text{a(r)}}(\lambda, \theta_s, \theta_v, \Delta\phi) = P_{\text{a(r)}}(\lambda, \gamma_-) + [\rho_{\text{F}}(\theta_s) + \rho_{\text{F}}(\theta_v)] P_{\text{a(r)}}(\lambda, \gamma_+), \quad (2')$$

with

$$\cos(\gamma_{\pm}) = \pm \cos(\theta_s)\cos(\theta_v) - \sin(\theta_s)\sin(\theta_v)\cos(\Delta\phi),$$

where ω_a and ω_r are the aerosol and the Rayleigh single-scattering albedos (ratio of scattering to attenuation, close to 1 for most oceanic aerosols and to unity for air molecules, at least at the wavelengths considered here), and p_a and p_r are related [through Eq. (2')] to the aerosol and Rayleigh phase functions, P_a and P_r , respectively, through $\rho_{\text{F}}(\theta)$, the Fresnel reflection coefficient at the interface.

Even for a clear atmosphere (i.e., small τ_a), τ_r is never small in the short-wavelength domain, so a first improvement, introduced by Gordon *et al.*,³ has consisted in computing the reflectance that is due to Rayleigh scattering as a result of multiple-scattering events between molecules. Another improvement has consisted in considering all kinds of multiple scattering, and Deschamps *et al.*⁴ proposed splitting ρ_{path} into three terms, as follows:

$$\rho_{\text{path}} = \rho_r + \rho_a + C_{\text{ra}}, \quad (3)$$

where ρ_r is the reflectance that is due to multiple scattering by air molecules (Rayleigh reflectance) in an aerosol-free atmosphere, ρ_a is the reflectance that is due to multiple scattering by aerosols in a hypothetical atmosphere containing exclusively aerosols (no molecules) and C_{ra} is defined as a coupling term describing the interactions between molecular and

aerosol scattering; in most cases it is found to be negative.^{4,5} The term C_{ra} is denoted $C^{\text{R,P}}$ in Ref. 4 and ρ_{ra} by Gordon and Wang.⁶

Another type of decomposition has also been proposed,⁷ in which both heterogeneous and homogeneous multiple scattering (by aerosols or molecules) is accounted for as a whole in a correction term, CT, according to

$$\rho_{\text{path}} = \rho_s + \text{CT}. \quad (4)$$

Here ρ_s represents the single-scattering reflectance computed from Eq. (2), with, however, a single compound phase function for the mixture of aerosols and molecules. The correction term CT can then be expanded as the sum of a Rayleigh correction term and of a correction for aerosol scattering, which is proportional to τ_a . This decomposition scheme will not be examined here, and the two phase functions, for molecules and aerosols, will always be considered separately and introduced in the following computations with their appropriate weights.

When aerosol particles are added to a given amount of molecules such that a compound atmosphere is built, the radiative regime changes. It can thus be expected that ρ_r will not remain unchanged. Similarly, the hypothetical ρ_a is likely affected by the additional presence of molecules. The additivity that is suggested by Eq. (3) is formal to the extent that the coupling term C_{ra} includes several phenomena. In addition to the effect of heterogeneous scattering, it reflects the changes in the radiative regime, namely, the changes in the previously defined reflectances ρ_r and ρ_a , when molecules and aerosols are simultaneously present. These changes and therefore the magnitude of C_{ra} (hereafter called the corrective term) are not simply predictable.

A strict additivity can be restored, provided that the definitions of the three terms are accordingly modified. Let ρ_r^* be the reflectance that originates from scattering (single and multiple) by molecules only but in the presence of aerosols and ρ_a^* be the equivalent term for aerosols, also in the presence of molecules; then

$$\rho_{\text{path}} = \rho_r^* + \rho_a^* + \rho_{\text{ra}}^*, \quad (5)$$

where now ρ_{ra}^* stands for that part of ρ_{path} that strictly results from heterogeneous scattering (from double to multiple collisions). From Eqs. (3) and (5) it follows that

$$C_{\text{ra}} = \rho_{\text{ra}}^* + [\rho_r^* - \rho_r] + [\rho_a^* - \rho_a], \quad (6)$$

which expresses that the corrective term C_{ra} includes a necessarily positive term ρ_{ra}^* , to which are added two terms corresponding to the changes in the radiative regime, from single-component atmospheres to the two-component atmosphere. If these changes, represented by the differences enclosed by brackets in Eq. (6), are revealed to be negative and are not compensated for by the magnitude of ρ_{ra}^* , C_{ra} may become negative⁴ (see Appendix A of Ref. 8).

The practical way to estimate each of the terms in

Eq. (5), as well as C_{ra} in Eq. (6), is to keep track of the photons in a Monte Carlo simulation and to sort them according to their histories, i.e., according to the nature and number of scattering events that they have undergone. We do this here by using a Monte Carlo code described elsewhere^{9,10} and validated against other radiative transfer codes.¹¹ The practical way to operate this code is detailed in Appendix A, along with a description of the parameters selected to simulate the path reflectance.

3. Results

A. Two-Layer and Multilayer Atmospheres

Before we enter into an analysis of the terms that appear in Eq. (6), a prerequisite is to assess the effect of the vertical stratification of aerosols on the total reflectance. In previous studies,^{4,6,12} and with a view to sparing time in extensive computations, simplified atmospheres were considered; aerosols were confined within the lower boundary layer, and only molecules were present above this layer. According to previous tests,⁴ such a simplification would be reliable when $\theta_v < 30^\circ$, and the reflectances computed for a two-layer atmosphere remained in agreement (to better than 10^{-3}) with those obtained when a more realistic aerosol vertical distribution¹³ was used. With regard to Eq. (5), this agreement means that the ρ_{path} values coincide for the simplified and for the more-realistic vertical distributions, notwithstanding the possible variations in the three constitutive terms. This last point, and more generally the validity of the two-layer approximation, deserves examination when θ_v exceeds 30° .

With this aim, fifty 1-km-thick atmospheric layers (from 0 to 50 km) were considered with specific values for Rayleigh scattering coefficient, aerosol content (without aerosol absorption), and ozone absorption.¹⁴ For comparison with the associated two-layer atmosphere, we distributed the same aerosol along the vertical, with the result that the optical thickness was unchanged (Fig. 1). Such modeled, stratified atmospheres admittedly differ from natural ones, as different aerosols actually are present in the boundary layer, the troposphere, and the stratosphere. This choice of a unique aerosol type along the vertical was mandatory for the sake of comparison with the corresponding two-layer atmosphere, which obviously contains only one aerosol type.

Examples of ρ_{path} computed for 50 and 2 layers are displayed in Fig. 2(a), with four increasing aerosol loads (maritime type¹⁵). The differences between the two kinds of curve are minute and are below 0.5% on the average, that is, within the weak stochastic noise inherent in Monte Carlo simulations. The absence of significant differences was systematically verified for other aerosol types and illumination-viewing geometries (Table 2). It can therefore be concluded that, for a given aerosol optical thickness, the TOA total reflectances are safely computed by use of a two-layer system, even for viewing angles exceed-

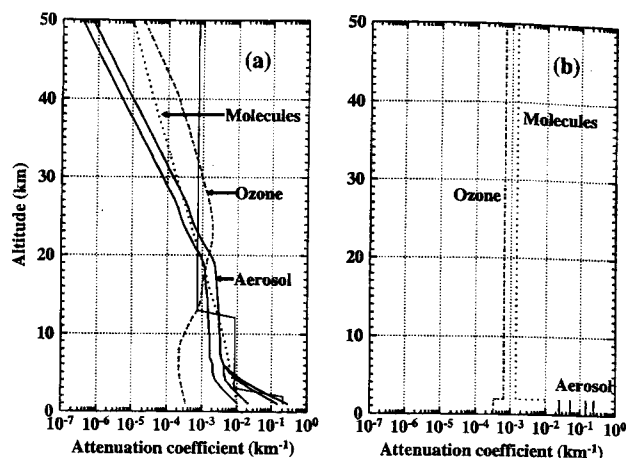


Fig. 1. Vertical profiles that we used for molecules, ozone, and aerosol. (a) Vertical repartition of the attenuation coefficients at 550 nm, taken from Elterman.¹⁴ The four solid curves correspond to $\tau_a = 0.05, 0.1, 0.3, 0.5$. For the last three values, only the bottom layer aerosol contents (<5 km) are changed while the whole profile is shifted to yield an optical thickness of 0.05. The profile with steps at 2 and 12 km is used for sensitivity studies (see text). (b) For molecules and ozone the optical thicknesses over the 0–2- and 2–50-km layers, computed from the vertical profiles shown in (a), are homogeneously distributed in the same layers to construct an equivalent simplified atmosphere. For aerosols, their whole content [0–50 km in (a)] has been confined within the 0–2-km boundary layer.

ing 30° and actually as great as 70° , and provided that aerosols are not absorbing.

This result is nonetheless surprising to the extent that the reflectances ρ_a^* , ρ_r^* , and ρ_{ra}^* all change when the aerosol vertical distribution is changed [Figs. 2(b)–2(d)], whereas their sum remains unchanged. By comparing the results for the two distributions (subscripts 2 and 50, respectively), one can see that, for the (dominant) Rayleigh component, $\rho_{r,50}^*$ is always inferior to $\rho_{r,2}^*$, whereas the contrary holds true with respect to the two other terms, $\rho_{a,50}^*$ and particularly $\rho_{ra,50}^*$, always above $\rho_{a,2}^*$ and $\rho_{ra,2}^*$. The more noticeable change affects the heterogeneous scattering, which is enhanced by 40–60% when aerosols are spread over the 50 layers instead of being confined within the 2-km-thick lower layer.

As a consequence, it must be stressed for what follows that a vertically resolved atmosphere is needed if an analysis of the partial reflectances is to be undertaken, even if aerosol absorption is not considered. Consequently, it was necessary to verify that realistic changes in the aerosol vertical distribution do not significantly modify the partial reflectances shown in Fig. 2. With this purpose we performed simulations by using another vertical distribution, namely, that proposed in the World Climate Research Program,¹⁶ keeping the Rayleigh scatterers and ozone absorption distribution as in Fig. 1(a). The total aerosol optical thickness was the same as in previous simulations, but only three layers were considered, the boundary layer (0–2 km), the free troposphere (2–12 km), and the stratosphere

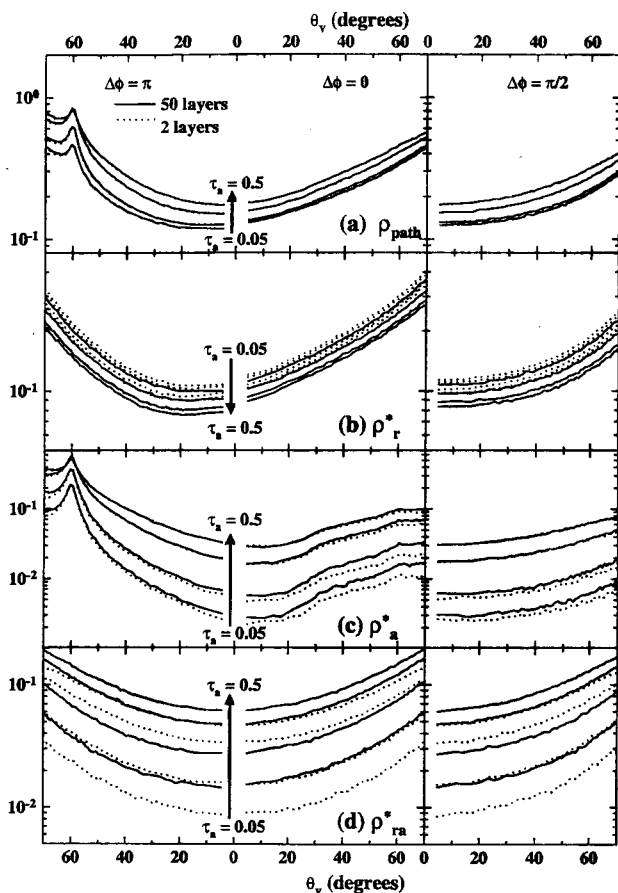


Fig. 2. TOA reflectances for $\lambda = 445$ nm, $\theta_s = 60^\circ$, and four values of $\tau_a(550)$ (0.05, 0.1, 0.3, and 0.5). The aerosol is the maritime model with a relative humidity of 70%. Reflectances are displayed as a function of viewing angle θ_v throughout the Sun and anti-Sun half-vertical planes ($\Delta\phi = 0$ and $\Delta\phi = \pi$, respectively) and in the perpendicular half-plane ($\Delta\phi = \pi/2$). Viewing angle θ_v is limited to 70° . Solid curves, results for the 50-layer structured atmosphere; dotted curves, results for the simplified two-layer atmosphere. (a) Global path reflectances, ρ_{path} ; (b) reflectances that are due only to multiple Rayleigh scattering, ρ_r^* ; (c) reflectances that are due to multiple scattering by aerosols only, ρ_a^* ; (d) reflectances that are due to heterogeneous scattering, ρ_{ra}^* .

(12–50 km), each with its specific mean extinction coefficient. The mean differences in ρ_a^* , ρ_r^* , and ρ_{ra}^* resulting from the use of these two different profiles and computed for all azimuth angles and for viewing angles less than 70° (see Appendix A) were, respectively, +2.7, -3.8, and +5%, with standard deviations of 2.5, 3.2, and 2.8%. We therefore be-

lieve that the partial reflectances are simulated in a realistic way when the aerosol is vertically distributed as shown in Fig. 1(a) and that for real atmospheres, which necessarily differ in vertical structure from the 50-layer atmosphere in Fig. 1(a), the reflectances remain close enough to those simulated here to permit a generalization of the results discussed below.

B. Analyzing the Terms of the Total Signal Decomposition

1. Scattering in Single-Component versus Two-Component Atmospheres

The aerosol-free and the molecule-free atmospheres were considered with a view to computing the reflectances ρ_a and ρ_r [Eq. (3)]. Then we distributed the same global amount of molecules and aerosols vertically among the 50 layers as described above, to build the related compound atmosphere and compute the three terms that appear in Eq. (5). The comparison among the three atmospheres allowed C_{ra} [in Eq. (6)] to be derived. To the extent that the molecular phase function is unique, such a triplet of atmospheres is determined by three modifiable parameters, namely, the aerosol phase function and the optical thicknesses τ_a and τ_r . One can make modifications as a purely numerical experiment or equally well by changing the wavelength, as long as the aerosol nature is kept unchanged. The Sun's zenith angle θ_s is an additional (external) parameter. All the results have to be analyzed in terms of their dependence on the viewing zenith angle θ_v and the azimuth difference $\Delta\phi$.

The seven terms that appear in Eqs. (3) and (5) are plotted as a function of wavelength for a particular aerosol load and nature and a specific geometry (Fig. 3). The trends shown by this figure remain valid in all circumstances, whereas they vary quantitatively according to the geometrical and aerosol conditions (discussed below). From this example some general trends and behaviors are already obvious and are summarized as follows:

(1) In the compound atmosphere ρ_r^* and ρ_a^* are systematically below their germane terms, ρ_r and ρ_a , specific to the single-component atmospheres, so the differences in parentheses in Eq. (6) are systematically negative.

Table 2. Parameters Defining the 64 cases Used for Comparison of Atmospheres Made of 2 or 50 Layers

Parameter	Sampling
Rayleigh optical thickness (τ_r)	0.23 and 0.015, corresponding to $\lambda = 445, 865$ nm
Aerosol models	Maritime model, with relative humidity 70%; angstrom exponent, -0.4^a Rural model, with relative humidity 98%; angstrom exponent, -1.2^a
Aerosol optical thickness (τ_a)	0.05, 0.1, 0.3, 0.5 at 550 nm; τ_a values range from 0.03 to 0.6, according to λ
Sun zenith angle	$0^\circ, 20^\circ, 40^\circ, \text{ and } 60^\circ$

^aThe exponent was computed for the λ couple 865–445 nm.

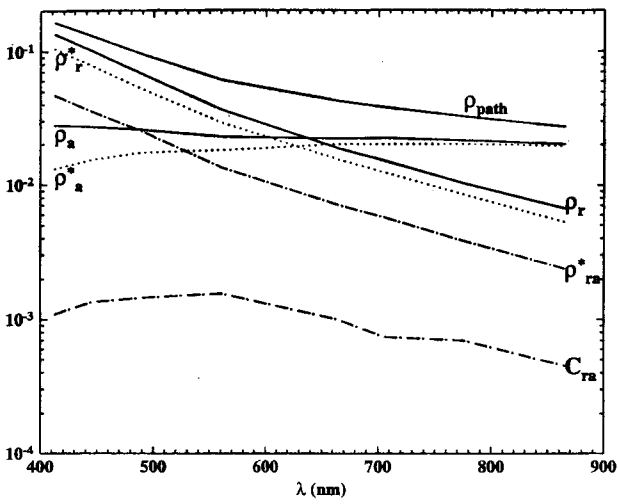


Fig. 3. TOA reflectances for a vertically structured (50-layer) atmosphere as a function of wavelength when $\theta_s = 40^\circ$, $\theta_v = 30^\circ$, and $\Delta\phi = \pi/2$. The aerosol is the maritime model with a relative humidity of 70% and an optical thickness of 0.3 at 550 nm. The various reflectances as indicated are described in the text.

(2) The heterogeneous reflectance ρ_{ra}^* is apparently created at the expense of homogeneous multiple scattering of both kinds.

(3) The spectral dependencies of ρ_r and ρ_a approximately follow the $\lambda^{-4.09}$ and $\lambda^{-0.4}$ laws, as do the corresponding scattering coefficients (see below). For ρ_a the approximate maintenance of the angstrom exponent is possible because the shape of the phase function for this particular aerosol is practically insensitive to wavelength.

(4) The spectral variations in ρ_a^* depart from those in ρ_a , and, in this instance, the exponent becomes clearly positive. The spectral selectivity of ρ_r^* remains close but not equal to that of ρ_r .

(5) The heterogeneous scattering reflectance ρ_{ra}^* is rather important in magnitude, occasionally exceeding ρ_a^* and amounting to approximately half of the Rayleigh term in this example. Its spectral dependence seems, somewhat surprisingly, to be governed mainly by that of molecular scattering.

(6) Finally, the correction term C_{ra} is much smaller than ρ_{ra}^* , as expected from the negative terms, as already identified in the first item in this list. Here C_{ra} is positive, yet this result is not general. When various figures such as Fig. 3 are examined, C_{ra} actually appears to be the most changeable term and does not always have values as small as those shown in Fig. 3.

The respective magnitudes of all the terms, as described above, are not modified when various θ_v directions are considered at a single wavelength (Fig. 4). The inequalities $\rho_r^* < \rho_r$ and $\rho_a^* < \rho_a$ are maintained everywhere [Fig. 4(a)]. The forward lobe of the aerosol phase function results in formation of a peak centered on the direction corresponding to the reflected Sun rays ($\Delta\phi = \pi$). Despite the asymmetrical disposition of ρ_r^* and ρ_a^* , the heterogeneous

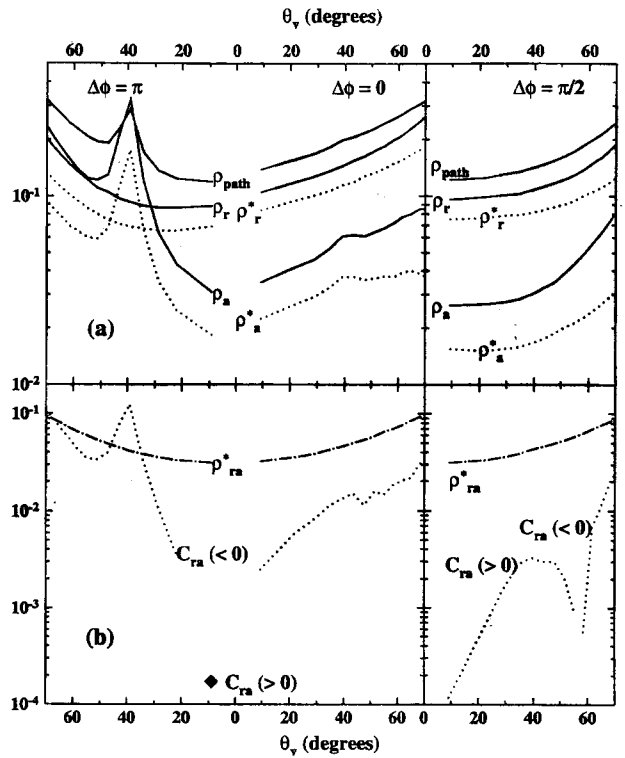


Fig. 4. TOA reflectances as a function of θ_v , and in the vertical planes as in Fig. 2, when $\lambda = 445$ nm and $\theta_s = 40^\circ$, for a vertically structured (50-layer) atmosphere containing either both aerosols and molecules (dotted and dashed curves) or only one of these two scatterers (solid curves). The aerosol is the maritime model with a relative humidity of 70% and $\tau_a(550) = 0.3$. (a) The path reflectance and the reflectances that are due to multiple scattering by aerosols (ρ_a^* and ρ_a) or molecules (ρ_r^* and ρ_r). (b) The reflectances that are due to heterogeneous scattering, ρ_{ra}^* , and the correction term, C_{ra} .

scattering reflectance ρ_{ra}^* is practically symmetrical with respect to the nadir [Fig. 4(b)], and this symmetry is not significantly altered when θ_s is changed (up to 60° ; not shown). With such an angular distribution the ρ_{ra}^* values are higher than those for the pure aerosol term (ρ_a^*) in almost all azimuthal directions, except around the anti-Sun direction ($\Delta\phi$ near π). The behavior of C_{ra} [Fig. 4(b)], either positive or negative, is rather complex, although it is numerically understandable from Eq. (6).

2. Evolution of the Three Partial Reflectances for Increasing Aerosol Optical Thickness

When the aerosol load is progressively increased, the directly related term ρ_a^* [Fig. 5(a)] increases almost linearly with τ_a , with different slopes according to the wavelength and also to the geometry (θ_v and θ_s ; not shown). The slopes of the $\rho_a^*(\tau_a)$ curves are always less than that of the unique $\rho_a(\tau_a)$ curve, and the differences ($\rho_a^* - \rho_a$) are accordingly always negative. As expected from Fig. 3, the lower ρ_a^* slopes occur at the shortest wavelength [445 nm in Fig. 5(a)]. The molecular reflectance ρ_r^* [Fig. 5(b)] decreases abruptly from its initial value ρ_r as soon as

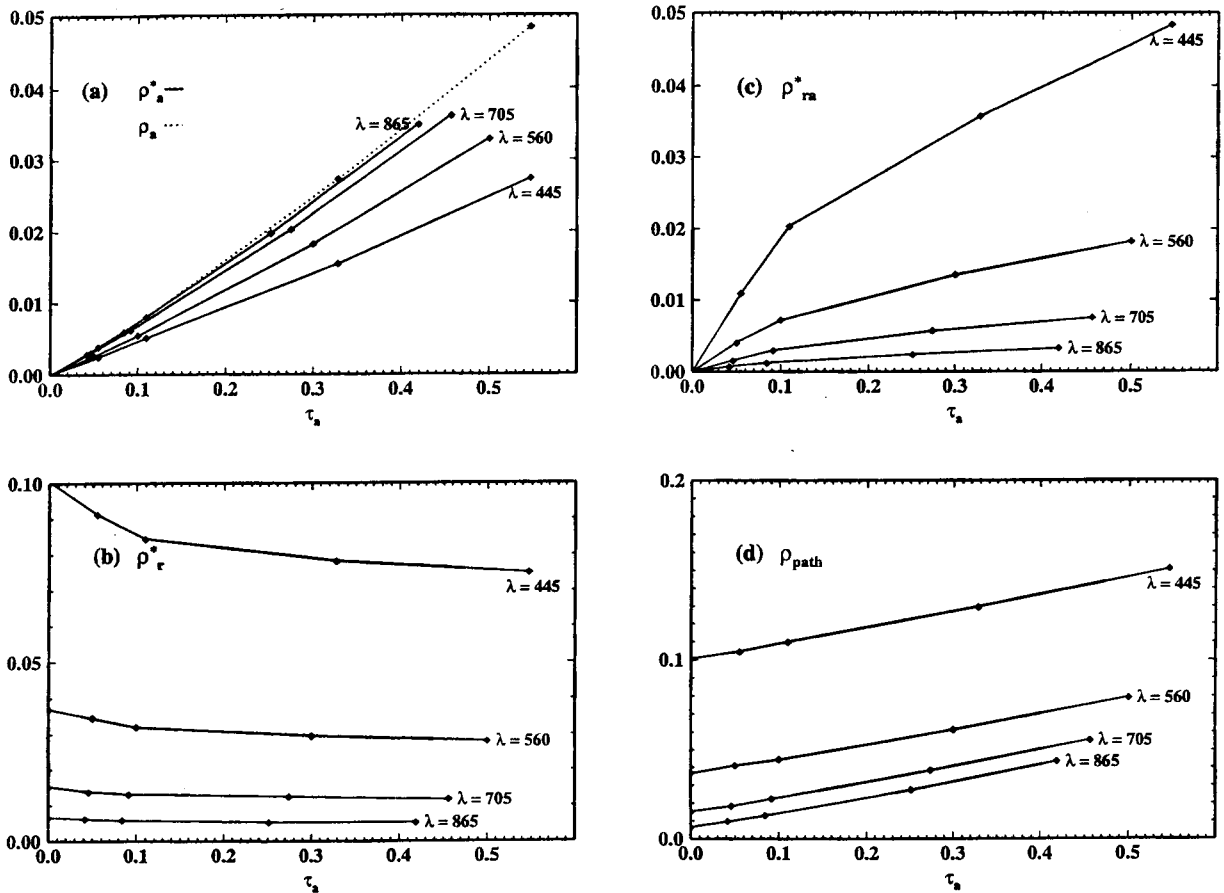


Fig. 5. Reflectances as a function of τ_a for the wavelengths indicated and when $\theta_s = 40^\circ$, $\theta_v = 30^\circ$, and $\Delta\phi = \pi/2$ (the aerosol is the maritime model with a relative humidity of 70%). (a) Reflectances that are due to multiple scattering by aerosols only: The dotted curve is for ρ_a and is therefore unique and the solid curves are for ρ_a^* . (b) Reflectances that are due only to multiple Rayleigh scattering, ρ_r^* . (c) Reflectance that is due to heterogeneous scattering, ρ_{ra}^* . (d) Path reflectance, ρ_{path} . Filled diamonds, simulations carried out for $\tau_a(550) = 0.05, 0.1, 0.3, 0.5$.

aerosols are present and then more slowly when $\tau_a > 0.1$. The strong depression that affects the initial part of the ρ_r^* curve is related to the steep rise of the heterogeneous scattering, ρ_{ra}^* [Fig. 5(c)]. The introduction of a small amount of aerosol is more efficient in creating ρ_{ra}^* than are further additions (i.e., when $\tau_a > 0.1$). For the geometry selected in Fig. 5 and $\lambda = 445$ nm, ρ_{ra}^* is always greater than ρ_a^* . The addition of the three partial reflectances leads to ρ_{path} [Fig. 5(d)], which varies with τ_a in a nearly linear way because of compensating effects, and has slopes that are only slightly different (for $\lambda = 445$ nm the slope is ~ 0.09 and for $\lambda = 865$ nm it is ~ 0.08). This simple result offers the possibility of developing an atmospheric correction scheme, as examined below.

The above results for a particular aerosol and a given illumination-viewing geometry remain essentially valid for other configurations. Because of the weak anisotropy of the Rayleigh scattering phase function, $\rho_r^*(\lambda, \tau_a)$ and to a lesser extent $\rho_{ra}^*(\lambda, \tau_a)$ change weakly when θ_s and θ_v are changed. With a much more asymmetrical pattern the phase function of aerosols induces significant variations in the $\rho_a^*(\lambda, \tau_a)$ values according to the geometrical configuration.

These rather complex, albeit understandable, variations (particularly those in C_{ra}) cannot be discussed in full detail.

3. Relative Proportions of the Three Partial Reflectances in the Global Upward Flux

In a first attempt to embrace the global phenomenon and to condense the results we integrated the upward reflectance field over all azimuth angles and over zenith angles from 0 to only 70° . This limitation was adopted because the Earth's sphericity is not represented in the modeling. The corresponding solid angle is 4.4 sr, and these integrated reflectances are denoted by overbars:

$$\bar{\rho} = \int_0^{2\pi} \int_0^{70} \rho(\theta_v, \Delta\phi) \cos(\theta_v) \sin(\theta_v) d\theta_v d\phi. \quad (7)$$

The flux within this solid angle actually represents at least 70% of the total flux integrated over 2π sr (in the unrealistic plane-parallel system). The spatially integrated values of the three partial reflectances [right-hand side of Eq. (5)] are then transformed into

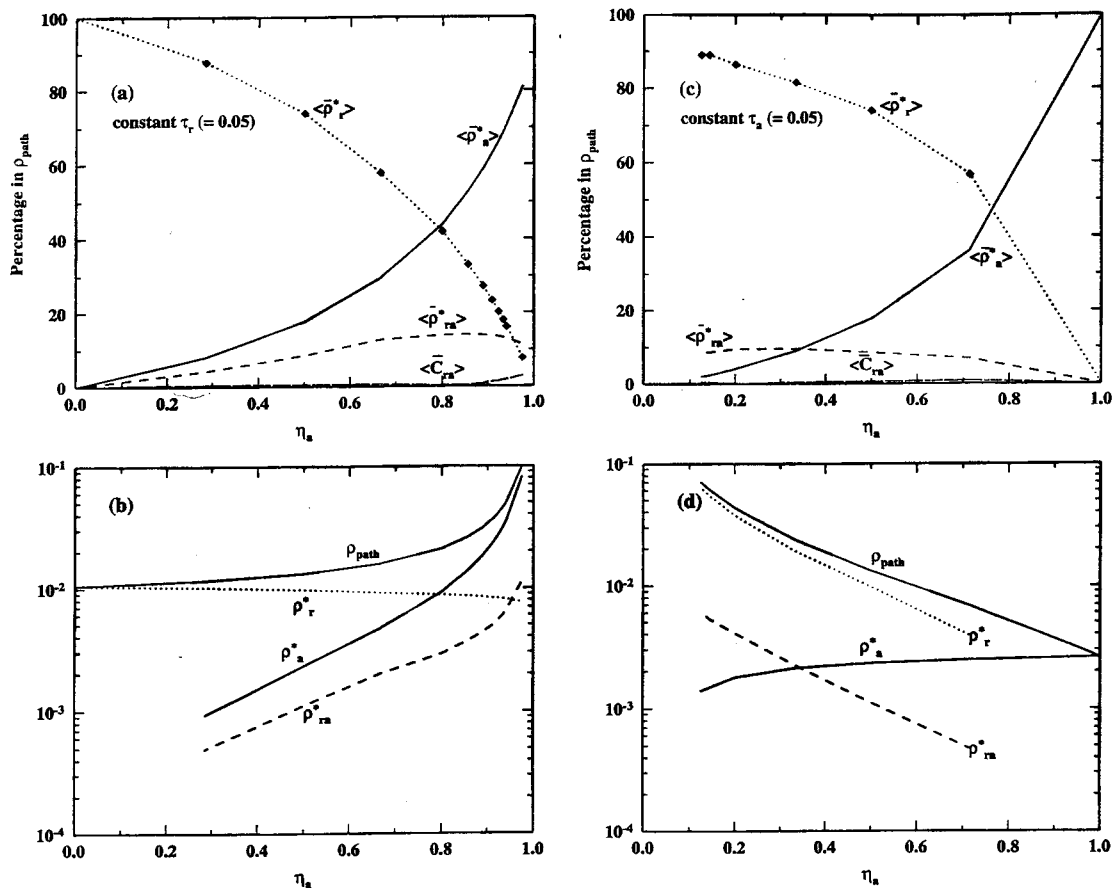


Fig. 6. Relative proportions $\langle \bar{\rho}_r^* \rangle$, $\langle \bar{\rho}_a^* \rangle$, $\langle \bar{\rho}_{ra}^* \rangle$, and $\langle \bar{C}_{ra} \rangle$ (in percent) displayed as a function of η_a (see text) (a) when τ_a is changed (from 0 to 2) and τ_r is kept fixed and (c) when τ_r is changed (from 0.02 to 0.35) and τ_a is kept fixed (the aerosol phase function is that of the maritime model, with a relative humidity of 70% and the Sun at its zenith). Filled diamonds, points of the computations, namely, $\tau_a = 0, 0.05, 0.1, 0.2, 0.3, 0.4, 0.5, 0.6, 0.7, 0.8, 2.0$ when $\tau_r = 0.05$; and $\tau_r = 0, 0.02, 0.05, 0.1, 0.2, 0.3, 0.35$ when τ_a is 0.05. The corresponding variations of $\bar{\rho}_{path}$, $\bar{\rho}_r^*$, $\bar{\rho}_a^*$, $\bar{\rho}_{ra}^*$ are displayed in (b) and (d).

relative contribution to $\bar{\rho}_{path}$, hereafter denoted $\langle \bar{\rho}_x^* \rangle$, and are computed as $\langle \bar{\rho}_x^* \rangle = \bar{\rho}_x^* / \bar{\rho}_{path}$, where x is r , a , or ra . These changes were examined as a function of the mixing ratio η_a , which is defined as

$$\eta_a = \tau_a / (\tau_a + \tau_r), \quad (8a)$$

and the opposite term, for molecular scattering, denoted η_r , is

$$\eta_r = 1 - \eta_a. \quad (8b)$$

In such a compound atmosphere the radiative regime is not unequivocally determined by the value of η_a . Simultaneous changes in τ_a and τ_r can lead to the same η_a value, while the radiative field is modified. In what follows, we vary the descriptor η_a by changing either τ_a (with τ_r constant) or τ_r (with τ_a constant). The relative proportions of the partial reflectances are displayed for particular cases in Figs. 6(a) and 6(c); the reflectances themselves, in Figs. 6(b) and 6(d). A generalization of these results is proposed in Fig. 7.

In Fig. 6(a), τ_r is set equal to 0.05, whereas τ_a varies from 0 to 2. In Fig. 6(c), τ_a is kept constant (0.05) and τ_r varies from 0.02 (corresponding to $\lambda \sim 850$ nm

when atmospheric pressure is 1013 hPa) to 0.35 ($\lambda \sim 400$ nm). In Figs. 6(a) and 6(c) the two relative contributions $\langle \bar{\rho}_a^* \rangle$ and $\langle \bar{\rho}_r^* \rangle$ exhibit inverse variations and behave roughly as quantities governed by a mixing rule. A slight departure from this rule occurs, however, and it originates from the presence of the third term, $\langle \bar{\rho}_{ra}^* \rangle$, which can reach $\sim 15\%$ of $\bar{\rho}_{path}$. The crossing point where $\langle \bar{\rho}_a^* \rangle = \langle \bar{\rho}_r^* \rangle$ ($\sim 45\%$) occurs at a η_a value that seems roughly independent of the way in which we varied η_a (by changing either τ_a or τ_r). In contrast, this crossing point moves with the value given to θ_s . It is near $\eta_a = 0.66$ when $\theta_s = 60^\circ$ (not shown), instead of 0.78 for $\theta_s = 0^\circ$. The relative contribution of heterogeneous scattering, identified as $\langle \bar{\rho}_{ra}^* \rangle$, is necessarily zero at both ends of the η_a scale and must exhibit a maximum somewhere inside the η_a (or the η_r) range. The maximum $\langle \bar{\rho}_{ra}^* \rangle$ value lies near $\eta_a = 0.8$ when the heterogeneous scattering is aerosol regulated as in Fig. 7(a) (τ_r constant), and in this case $\langle \bar{\rho}_{ra}^* \rangle$ may exceed $\langle \bar{\rho}_r^* \rangle$ at the extreme end of the η_a range. In a symmetrical manner, $\langle \bar{\rho}_{ra}^* \rangle$ experiences a maximum at $\eta_r = 0.8$ when it is molecule regulated [Fig. 7(c); τ_a constant], and it exceeds $\langle \bar{\rho}_a^* \rangle$ in the domain of low η_a values. The corrective

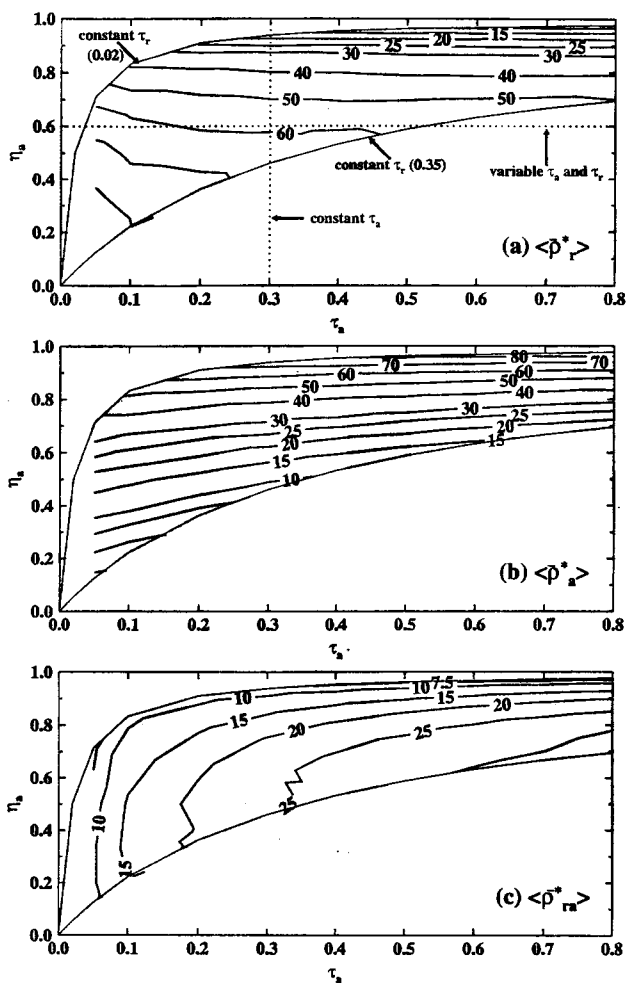


Fig. 7. Isolines of the relative proportions (a) $\langle \bar{\rho}_r^* \rangle$, (b) $\langle \bar{\rho}_a^* \rangle$, and (c) $\langle \bar{\rho}_{ra}^* \rangle$ (in percent of $\bar{\rho}_{\text{path}}$) within the η_a - τ_a plane. The hyperbolic envelopes correspond to the extrema of η_a for a given τ_a value and delimit the domain inside which τ_r varies from 0.02 to 0.35 (i.e., near infrared to ultraviolet). The aerosol is the maritime model, with a relative humidity of 70% and the sun at its zenith.

term $\langle \bar{C}_{ra} \rangle$, expressed relative to $\bar{\rho}_{\text{path}}$, is also shown in Figs. 6(a) and 6(c). It is small, except at both ends of the η_a range, is often negative, and may be zero; in this case the global flux for the compound atmosphere is simply the sum of the global fluxes for the two single-component atmospheres ($\bar{\rho}_{\text{path}} = \bar{\rho}_a + \bar{\rho}_r$).

As we have already said, the single parameter η_a is insufficient for use in exploring the whole domain of possible variations in the radiative regime, even if θ_s and the aerosol type are fixed. Curves such as those in Fig. 6, representing the $\langle \bar{\rho}_r^* \rangle$, $\langle \bar{\rho}_a^* \rangle$, and $\langle \bar{\rho}_{ra}^* \rangle$ terms, actually are not unique and depend on the selected τ_a - τ_r or τ_a - η_a couples. In Fig. 7, as an attempt to generalize the results of Fig. 6, we scale the problem by introducing τ_a . In the τ_a - η_a space the loci that correspond to constant τ_r are hyperbolas such as those drawn to delimit the domain considered (0.02 < τ_r < 0.35). The three curves shown in Fig. 6(a) actually explore the τ_a - η_a domain along the hyperbola that corresponds to $\tau_r = 0.05$. Similarly, the

three curves shown in Fig. 6(c) deal with situations found along a transect of the τ_a - η_a domain represented by the vertical dotted line in Fig. 7, with $\tau_a = 0.05$. The relative proportions of pure aerosol and pure molecule scattering [Figs. 7(a) and 7(b)] in forming $\bar{\rho}_{\text{path}}$ are controlled mainly by the mixing ratio, depicted by η_a . As an example, equal contributions (~40% each) are found when $\eta_a \sim 0.8$, whatever τ_a is (at least when $\tau_a > 0.1$). Whatever the aerosol load, the Rayleigh contribution ($\langle \bar{\rho}_r^* \rangle$) exceeds 50% of $\bar{\rho}_{\text{path}}$ as long as η_a is < 0.7 (approximately as long as $\tau_a < 2\tau_r$). The aerosol contribution, $\langle \bar{\rho}_a^* \rangle$, exceeds 40% above the same threshold in η_a ($\tau_a > 2\tau_r$). The roughly horizontal arrangement of the isolines of $\langle \bar{\rho}_r^* \rangle$ and $\langle \bar{\rho}_a^* \rangle$, and their inverse evolutions (i.e., increasing for $\langle \bar{\rho}_a^* \rangle$ and decreasing for $\langle \bar{\rho}_r^* \rangle$ with increasing η_a) reflect the mixing rule mentioned above. The approximately horizontal ordering is disturbed in the domain of small τ_a values (more precisely, when the $\langle \bar{\rho}_{ra}^* \rangle$ isolines undergo a drastic change in their orientation). In fact, $\langle \bar{\rho}_{ra}^* \rangle$ is determined by τ_r as long as $\tau_a > 2\tau_r$ and otherwise by τ_a . The maximum relative contribution of heterogeneous scattering (as much as 20–30%) lies in the middle of the η_a range, that is, when τ_a and τ_r are roughly similar and are both of sufficient magnitude (~0.2, with $\langle \bar{\rho}_{ra}^* \rangle$ greater than 20%). It has been also found that the relative change in the aerosol reflectance (i.e., $[\bar{\rho}_a^* - \bar{\rho}_a]/\bar{\rho}_a$) is determined mostly by the Rayleigh optical thickness τ_r , whatever τ_a is.

4. Spectral Aspects

The Rayleigh exponent for air molecules (-4.09) and any angstrom exponent for aerosols describe the spectral variations of the respective scattering coefficients. These exponents apply directly to reflectances only if these reflectances result from single scattering [namely, when the optical thickness is low enough that Eq. (2) is valid] and if the shape of the phase function is not wavelength dependent. If multiple scattering events occur, $\rho(\theta_v, \theta_s, \Delta\phi)$ is no longer a simple reproduction of a portion of the phase function [as implied by Eq. (2)]; thence the above exponents cannot be simply transferred to the spectral variations in reflectances. The spectral dependency of the path reflectance, or other partial reflectances, can be operationally expressed through an exponent defined as

$$n = \frac{\ln[\rho(\lambda_i)/\rho(\lambda_j)]}{\ln(\lambda_i/\lambda_j)}, \quad (9)$$

where ρ is any of the reflectances already discussed. The asterisks and subscripts used with ρ are transferred to the values of n with the same meaning. For what follows, we have used reflectances integrated over the solid angle previously used (i.e., 4.4 sr) to calculate the values of n for $\lambda_i = 445$ and $\lambda_j = 865$ nm.

In a conservative atmosphere (no absorption), multiple-scattering events result only in rearranging the radiance field that originates from singly scat-

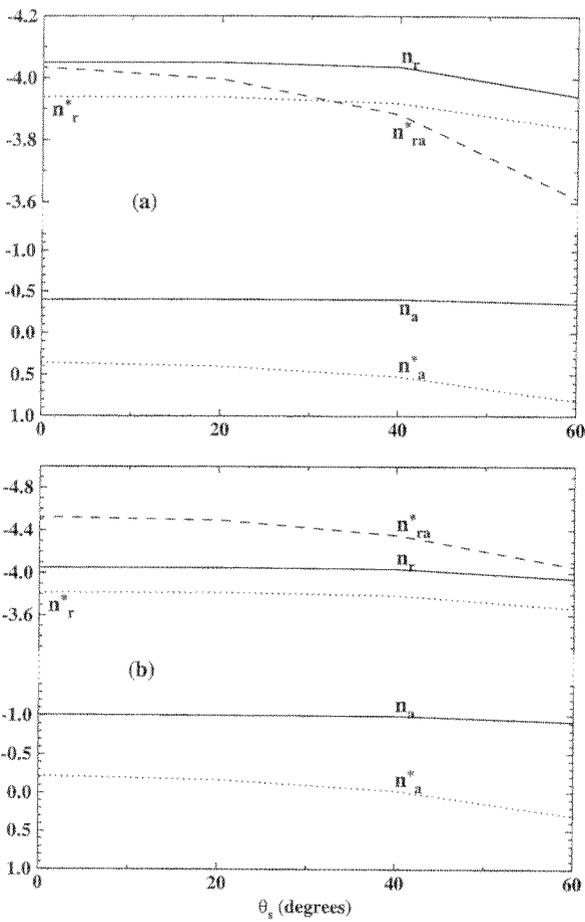


Fig. 8. Exponents that depict the variations of the various partial reflectances from $\lambda = 445$ to $\lambda = 865$ nm plotted as a function of θ_s and for two aerosol types [see text and Eq. (9)] and $\tau_a(550) = 0.3$. Note that the vertical axes are interrupted and the scales are different for the upper and lower parts of both (a) and (b).

tered radiation. Predominantly backscattered radiation is involved in the present problem. Radiance reflected at the interface, however, act as an additional source, located at the bottom of the atmosphere, and thus forward scattering is also involved. The exponent defined above will depend on the change in the global optical thickness ($\tau_a + \tau_r$) between the two wavelengths in question as well as on the respective weights of the phase functions with their specific asymmetry, which govern the radiance distribution.

The operational exponents were computed for single-component atmospheres (molecules, maritime aerosol, or rural aerosol) and then for the two corresponding compound atmospheres. The results for n as a function of the Sun's zenith angle are shown in Figs. 8(a) and 8(b). Their interpretation rests on the relative contributions to the total signal of the various types of scattering (single-multiple, homogeneous-heterogeneous) shown in Fig. 9 and generated as described in Appendix A. The behavior of the exponents can be summarized as follows:

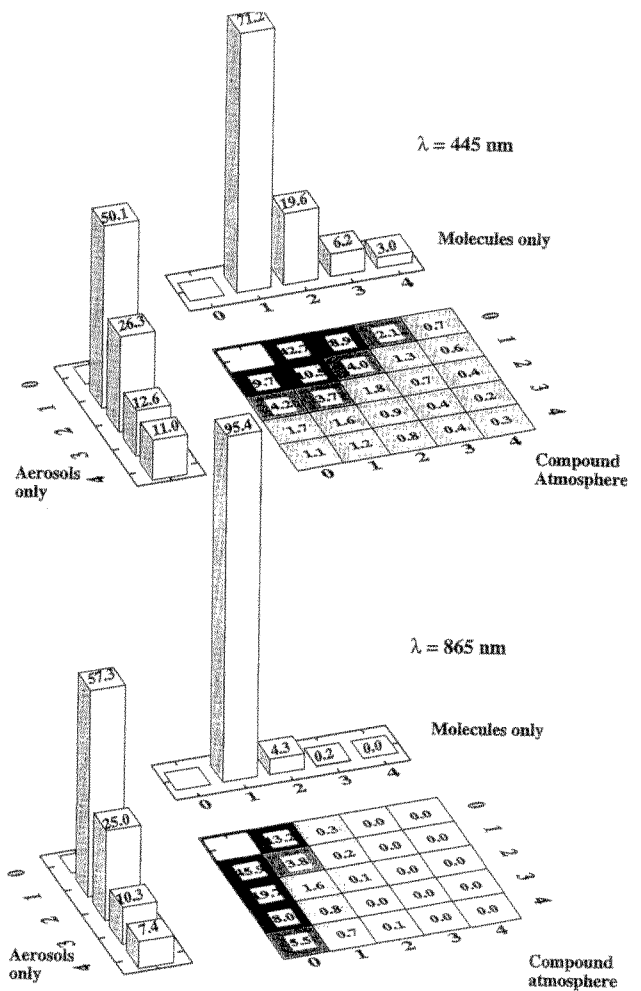


Fig. 9. Relative importances (in percent) in the total signal (integrated over all azimuths and over 0° – 70° for θ_s) of various scattering events, grouped as a function of their order and type of scattering. Computations are carried out for a 50-layer atmosphere and an aerosol of the maritime type with a relative humidity of 70%. The Sun's zenith angle is 40° . Top, $\lambda = 445$; bottom, $\lambda = 865$ nm. Results are shown for the single-component atmospheres and the corresponding compound atmospheres, with $\tau_a = 0.33$ and $\tau_r = 0.25$ at 445 and 865 nm, respectively, corresponding to $\tau_a(550) = 0.30$. Columns and rows are numbered according to the number of scattering events: 0, 1, 2, 3, and 4 or more scattering events, of either molecular or aerosol type. The parallelepipeds are proportional in height to the percentages of the scattering order and type in question. They are replaced by gray shades for the compound atmosphere.

(1) In the aerosol-free atmosphere [shown in Figs. 8(a) and 8(b)] the corresponding exponent n_r is close to that for Rayleigh scattering (-4.09). The departure from this value, which varies according to the Sun's position, results from the (weak) anisotropy of the Rayleigh phase function. The shape of the phase function is left practically unaltered in the quasi-single-scattering regime, which prevails at 865 nm, whereas it is smoothed by the effect of multiple scattering at 445 nm. Indeed (Fig. 9), the proportion of multiply scattered photons in the total signal in-

creases from less than 5% at 865 nm to 29% at 445 nm.

(2) The angstrom exponent for the maritime aerosol is -0.4 , well reproduced by n_a [Fig. 8(a)]. The radiative regime is almost the same at the two wavelengths, to the extent that the contribution of multiple scattering remains similar, 43% and 50% at 865 and 445 nm, respectively (Fig. 9); the θ_s dependence is weak in this rather diffuse regime.

(3) The angstrom exponent for the rural aerosol is -1.2 , whereas n_a is ~ -1.0 . With multiple-scattering events forming 30% (at 865 nm) or 50% (at 445 nm) of the global flux (not shown), the radiative regime is not the same at the two wavelengths and leads to a departure from the angstrom exponent value.

(4) For compound atmospheres [Figs. 8(a) and 8(b)] the situation is much more complex. The operational exponent related to the aerosol contribution, n_a^* , strongly departs from the preceding value, n_a (and thus from the angstrom exponent). Similarly, n_r^* differs from n_r (and from -4.09) in response to changes in the radiative regime. The exponent n_{ra}^* for the heterogeneous scattering contribution appears to be totally disconnected from the angstrom exponent and akin to the Rayleigh exponent, in spite of wide variations (-3.6 to -4.6). The spectral variations of ρ_{ra}^* are due not only to the specific spectral dependency of both scatterers but also to the variation of their proportions along the spectrum (as η_a and η_r are not constant). Illumination conditions are also involved through the shape of the phase functions, so n_{ra}^* and n_a^* are θ_s dependent. Therefore these exponents are apparent in the sense that they depend on the variable combinations of τ_a and τ_r and are not easily predictable for practical applications.

5. Influence of Aerosol Absorption

All the results presented above were obtained for nonabsorbing aerosols, whereas moderately or even strongly absorbing aerosols can be carried in the atmosphere. The effect of absorption on the three partial reflectances ρ_r^* , ρ_a^* , and ρ_{ra}^* , as well as on their integrated values (i.e., the $\bar{\rho}_x^*$ terms), has thus been examined through some additional simulations. In principle, making the aerosol absorbing (i.e., $\omega_a < 1$) implies concomitant changes in its phase function. Nonetheless, and for the sake of comparing the results of the present simulations with the previous ones for $\omega_a = 1$, the phase function (that of the maritime model with a relative humidity of 70%) was kept unchanged and used with $\omega_a = 0.8$ or 0.6 instead of 1. The aerosol vertical distribution was also as in Fig. 1(a). The partial reflectances ρ_r^* , ρ_a^* , and ρ_{ra}^* , and their sum ρ_{path} , are displayed in Fig. 10 as a function of τ_a and for $\omega_a = 1, 0.8, 0.6$. In this figure, τ_r is given the constant value 0.2 (corresponding to $\lambda \sim 460$ nm) instead of being set for fixed wavelengths, as was done in Fig. 5. As expected, all reflectances decrease as ω_a decreases, and all the partial reflectances apparently tend toward asymptotic values,

even if the τ_a domain considered is not wide enough always to reach a plateau. The levels of these plateaus are diminished by increasing absorption. The slopes of the $\rho_{path}(\tau_a)$ curves are lessened by absorption. Adding more and more absorbing particles does not increase the path reflectance as rapidly as do nonabsorbing aerosols and can even lead to a decrease in the path reflectance below its value for a purely molecular atmosphere, i.e., ρ_{path} becomes lower than ρ_r . This feature is observed, for instance, when $\tau_a = 0.1$ and for $\omega_a = 0.6$ [Fig. 10(d)].

The above results, however, seem contradictory to previous findings. Indeed, Gordon¹⁷ found that there is "an increase in the significance of the Rayleigh-aerosol interaction" as ω_a decreases. In fact, both conclusions are compatible when it is acknowledged that the true heterogeneous scattering, ρ_{ra}^* , is considered here, whereas in Gordon's study the Rayleigh-aerosol interaction is depicted by the corrective term C_{ra} . That corrective term increases strongly (in absolute value) as ω_a decreases because the differences in Eq. (6) result in negative values whose sum is greater than ρ_{ra}^* . The apparent contradiction between the two studies emphasizes the ambiguous meaning of the corrective term C_{ra} , which is usually and erroneously referred to as the coupling between aerosol and molecular scattering.

As regards the integrated reflectances and their respective contributions to $\bar{\rho}_{path}$ (i.e., $\bar{\rho}_r^*$ and $\langle \bar{\rho}_x^* \rangle$, respectively), had the results of the present simulations been used to redraw Figs. 6 and 7, the patterns in those figures (for instance, the arrangement of isolines in Fig. 7) would have been nearly identical to those already displayed for $\omega_a = 1$. The changes in the values of $\langle \bar{\rho}_x^* \rangle$, however, cannot be discussed because the $\bar{\rho}_{path}$ value varies when ω_a changes. On the contrary, the mean relative changes in $\bar{\rho}_r^*$, $\bar{\rho}_a^*$, and $\bar{\rho}_{ra}^*$ can be computed; for a range of 25 τ_a - τ_r couples (corresponding to $\tau_a = 0.05, 0.1, 0.3, 0.5, 0.7$ and $\tau_r = 0, 0.05, 0.1, 0.2, 0.35$) the mean changes are approximately $-5, -18,$ and -20% , respectively, when $\omega_a = 0.8$ instead of $\omega_a = 1$, and approximately $-11, -35,$ and -40% , respectively, when $\omega_a = 0.6$.

4. Application to Atmospheric Correction of Ocean Color Observations from Space

The process that consists of retrieving the ocean reflectance (the marine signal) from the TOA total signal recorded by a satelliteborne sensor is generally termed atmospheric correction. To achieve this correction one must estimate the path reflectance with high accuracy to preserve acceptable accuracy in the estimate of the marine signal, as the former represents at least 80%, and often more, of the total signal. For the new generation of ocean color sensors (POLDER,¹⁸ OCTS,¹⁹ SeaWiFS,²⁰ MERIS²¹) the general scheme for the atmospheric correction over Case 1 waters²² consists of identifying the nature, and quantifying the contribution, of the local aerosol by use of the signals recorded at two wavelengths in the near infrared (where oceanic Case 1 waters are black). This information is used to predict ρ_{path} in

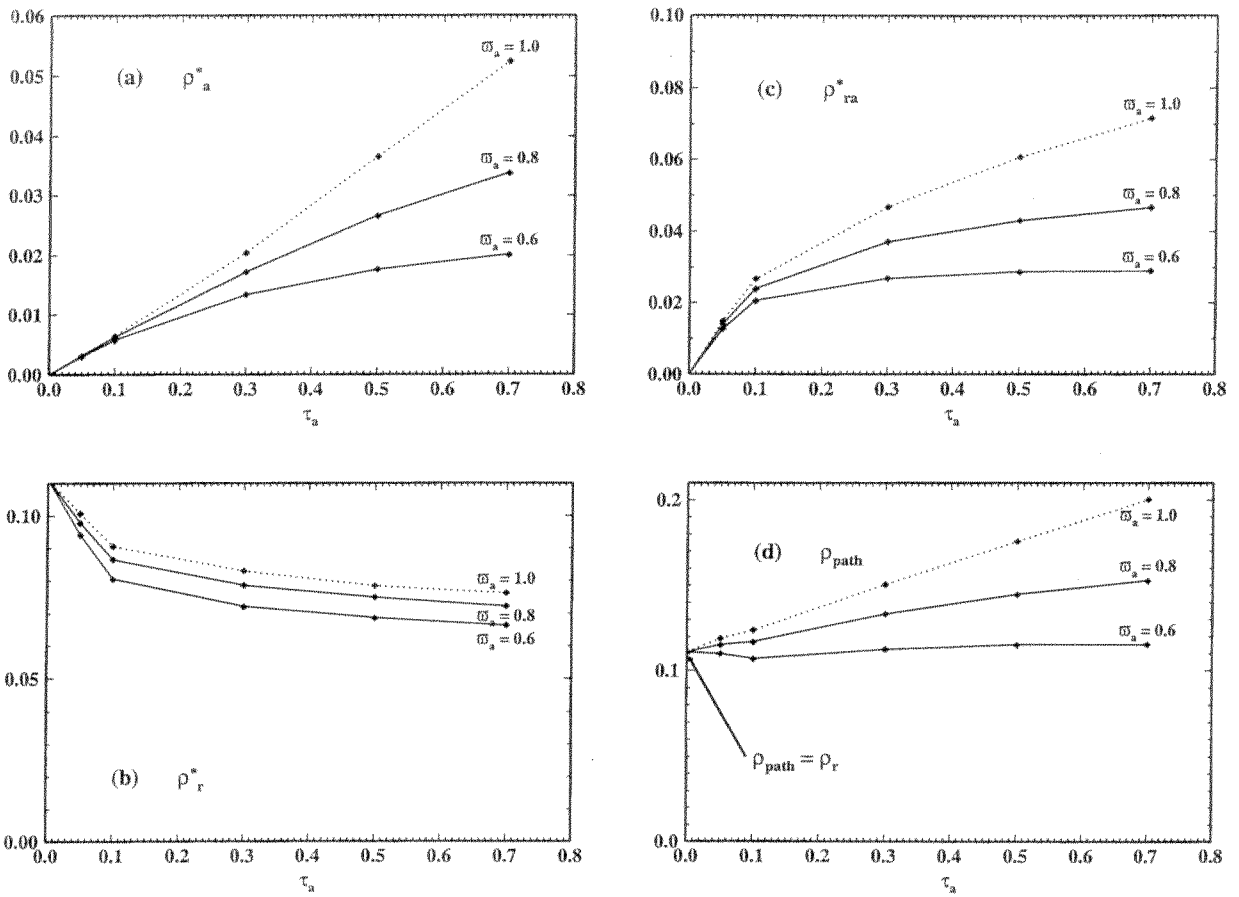


Fig. 10. Reflectances as a function of τ_a and when $\theta_s = 40^\circ$, $\theta_v = 30^\circ$, $\Delta\phi = \pi/2$, and $\tau_r = 0.2$ (i.e., $\lambda \sim 460$ nm); the phase function is that of the maritime model for a relative humidity of 70%. (a)–(d) As in Fig. 5; each curve is for one value of ω_a , as indicated.

the visible part of the spectrum; ρ_{path} is then subtracted from the total reflectance at the TOA level, and the marine contribution is assessed. The present scheme follows this mandatory pathway.

As shown above, the reflectance that is due to heterogeneous scattering, ρ_{ra}^* , is an important contribution to ρ_{path} , even for reduced aerosol loads (Figs. 5 and 6) and sometimes exceeds the homogeneous scattering by aerosols only, ρ_a^* . These reflectances, however, are not derivable in an independent way, as the aerosol type and concentration are unknown when the atmospheric correction process is started. To the extent that ρ_r^* also differs from ρ_r as a result of the presence of aerosols, this term is also unpredictable. In fact, the quantities available are the measured reflectance ρ_{path} and the computed reflectance ρ_r for molecules in absence of aerosols. In Gordon–Wang technique⁶ one uses these quantities by forming the difference $(\rho_{\text{path}} - \rho_r)$, which is related to ρ_{as} , the reflectance that is due to aerosols in the single-scattering approximation [Eqs. (3) and (6)]:

$$\rho_{\text{path}} - \rho_r = \rho_a^* + \rho_{\text{ra}}^* + [\rho_r^* - \rho_r] = f(\rho_{\text{as}}). \quad (10a)$$

In this scheme ρ_{as} , which has no physical reality, is used as a descriptor of the aerosol and as an index to identify its loading and type.

Taking advantage of the results shown in Fig. 5, we

can use the same quantities by forming the ratio $\rho_{\text{path}}/\rho_r$, with a view to reducing the effect of changes in barometric pressure, so that

$$\rho_{\text{path}}/\rho_r = (\rho_a^* + \rho_{\text{ra}}^* + \rho_r^*)/\rho_r = f(\tau_a). \quad (10b)$$

This ratio represents the relative increase in reflectance when aerosols are progressively added to molecules, and it can be related to τ_a . The monotonic relationship $f(\tau_a)$ again depends on aerosol type and loading and on geometry. Equations (10) have to be written for each wavelength, each geometrical configuration, and each aerosol type.

Examples of the variations in $\rho_{\text{path}}/\rho_r$ as a function of $\tau_a(\lambda)$ are displayed in Fig. 11 for the two wavelengths 865 and 775 nm. This figure also serves to describe the proposed scheme. With any measured value of $[\rho_{\text{path}}/\rho_r]$ at 865 nm it is possible to associate a set of values of $\tau_a(865)$; each one corresponds to a given aerosol model (steps 1 and 2 in Fig. 11), because multiple-scattering effects are different for different aerosols. A corresponding set of $\tau_a(775)$ values is obtained simply by use of the ratio of the aerosol extinction coefficients at the two wavelengths, (step 3), according to

$$\tau_a(775) = \tau_a(865)[c(775)/c(865)]. \quad (11)$$

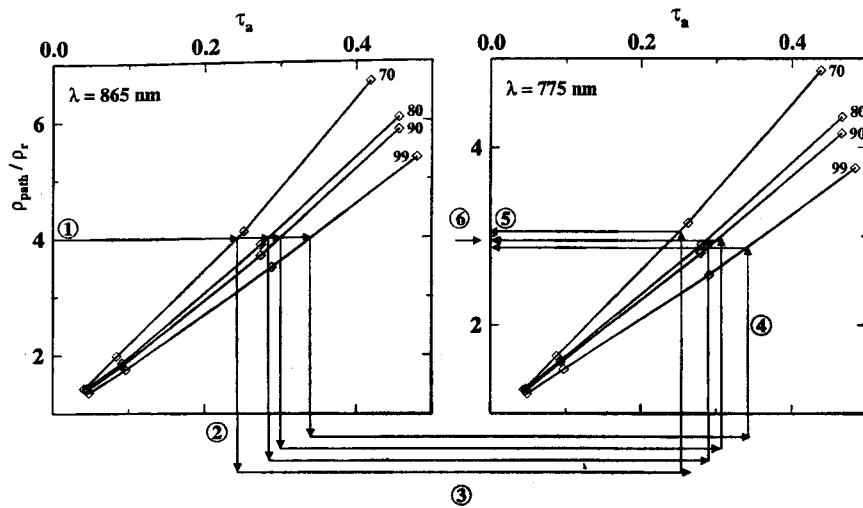


Fig. 11. Relative variation of the path reflectance at 865 and 775 nm for the maritime aerosol model displayed as a function of τ_a and expressed as the ratio $\rho_{\text{path}}/\rho_r$, when $\theta_s = 40^\circ$, $\theta_v = 30^\circ$, and $\Delta\phi = \pi/2$. The four curves are for four values of relative humidity, as indicated. Arrows symbolize a possible way to identify a couple of aerosol models enclosing the actual aerosol. The circled numbers identify the successive steps of this scheme, as discussed in the text.

A fixed value of the ratio $[\rho_{\text{path}}/\rho_r]$ at 775 nm [step 4, i.e., the converse of step 2 corresponds to each $\tau_a(775)$ value]. A set of plausible estimates for this ratio is produced and contains values that generally differ according to the aerosol type (step 5). The final step (6) consists in comparing these plausible values with the actual ratio $[\rho_{\text{path}}/\rho_r]$ at 775 nm with a view to selecting the two aerosol models that enclose the actual $[\rho_{\text{path}}/\rho_r]$ value. From these two bracketing values of $[\rho_{\text{path}}/\rho_r]$, and from the actual one, a mixing ratio is computed as in the Gordon-Wang method. By assuming that this ratio is wavelength independent one can then transfer the estimate of $[\rho_{\text{path}}/\rho_r]$ toward the visible spectrum, provided that the relationships with τ_a were previously established for all wavelengths. The path reflectance and hence the marine signal are then straightforwardly obtained in the visible.

5. Conclusion

A new and exact decomposition of the atmospheric path reflectance has been proposed, and the behavior of its three constitutive terms has been studied in response to changes in optical thicknesses (τ_a and τ_r). Between reflectances computed for single-component atmospheres and those computed for realistic compound atmospheres, notable differences exist that have been quantified. These changes are attributable to rearrangements of the radiative field, which occur when both molecules and aerosols scatter simultaneously (with extremely different phase functions) within all atmospheric layers. The coupling between scattering by aerosols and by molecules (ρ_{ra}^*) always contributes significantly to the path reflectance. Even for aerosol optical thickness as low as $\tau_a \sim 0.05$, ρ_{ra}^* represents $\sim 7\%$ of ρ_{path} in the near infrared and more than 10% in the visible (Fig. 7); this contribution becomes 10% (near infrared) and 25% (visible) when $\tau_a \sim 0.2$. The approximate character of splitting the aerosol and molecular contributions has been emphasized, even for small τ_a and τ_r . The use of such an approximation for future atmo-

spheric correction algorithms is questionable if full benefit is to be derived from the improved radiometric accuracy of the new-generation ocean color sensors.

The atmospheric correction scheme proposed here makes use of the ratio $[\rho_{\text{path}}/\rho_r]$. This ratio has a clear physical meaning, as it represents the relative increase in ρ_{path} when a given amount of aerosols is introduced within a molecular atmosphere. Based on the previous analysis, it is shown that this ratio can be simply related to the aerosol optical thickness, so its value is easily transferred from a wavelength to another one, in particular between the two wavelengths in the near infrared that are used to identify the aerosol type and loading.

The main differences between this scheme and others, in particular that of Gordon and Wang,⁶ are as follows. Here there is no need to rely on, and thus to produce, the single-scattering reflectance ρ_{as} [Eq. (2)] with a view to identifying the aerosol type. The transfer from one wavelength to another one is directly effected by means of the changes in aerosol optical thickness, $\tau_a(\lambda)$, which depends on the angstrom exponent only and not on the geometrical configuration [in contrast with the $\epsilon(\lambda_i, \lambda_j)$ coefficients in the Gordon-Wang method, which vary with geometry]. Relationships such as those shown in Fig. 11, however, have to be precomputed for all possible geometrical configurations, aerosol types, and wavelengths. As a result, the sizes of the lookup tables are similar for the present algorithm and for that of Gordon and Wang.⁶ Both methods have the advantage of providing (as a by-product of the atmospheric correction) an estimate of the aerosol content (through τ_a and provided that the aerosol type has been properly identified). Deriving a climatology of the aerosol distribution above the ocean is an important application of the ocean color sensors.

Appendix A

The Monte Carlo code used in the present study has been already described^{9,10} and validated against other radiative transfer codes.¹¹ The geometry is

that of a plane-parallel atmosphere; as a consequence, the results for slant directions ($\theta_s, \theta_v > 70^\circ$) cannot be reliably discussed because the sphericity of the Earth is not accounted for.²³ The photons are collected at different levels (and up to the TOA level) within 480 equal solid angles by division of the $0-\pi$ azimuth interval into 24 equal angles and of the $0-\pi/2$ zenith angle interval into 20 angular intervals, equally spaced with respect to $\sin(\theta_v)$. There is no counter directly aimed at nadir. In the simulations, the bottom of the atmosphere is bounded by a perfectly absorbing ocean, which is simply represented by a Fresnel-reflecting flat interface (no wind). Atmosphere and ocean are thus uncoupled, and multiple crossings of the air-sea interface by photons are discarded, as this phenomenon is of second-order importance. This uncoupling is totally justified for Case 1 waters in the near-infrared bands and is an acceptable approximation for the visible domain. The polarization is not accounted for. The apparent diameter of the Sun disk is set to 0.5° . For Rayleigh scattering, the anisotropy of the molecules is ignored and the depolarization factor is 0. The spectral dependency is expressed as $\lambda^{-4.09}$. The scattering coefficient is set, for each atmospheric 1-km layer, to the value corresponding to its average altitude.¹⁴ The resulting total optical thickness is that of a standard atmosphere with a barometric pressure of 1013.25 hPa.

The aerosol phase functions have been calculated from Mie theory, and the cumulative distribution functions were numerically derived from these phase functions. The humidity-dependent refractive indices and the log-normal particle size distributions are those of the oceanic and tropospheric aerosol components described by Shettle and Fenn.¹⁵ Two basic models are constructed, namely, the maritime (99% of tropospheric particles, 1% of oceanic) and the rural (100% of tropospheric particles) models; their optical properties are modified when the relative humidity is changed (see also Ref. 6). These aerosols are considered nonabsorbing ($\omega_a = 1$); their actual single-scattering albedos are greater than 0.98 (maritime model) or 0.96 (rural aerosol); except in the near infrared, where $\omega_a \sim 0.94$. The wavelengths considered are those generally selected for ocean color remote sensing. No attempt is made to account for the width and the shape of the actual spectral channels of a given sensor. In other words, the optical characteristics are those of the nominal wavelengths as indicated.

The directional counters are split into subcounters where the photons are sorted and accumulated as a function of the number and type of collisions that they have experienced before escaping the medium. Two examples of such photon sorting are provided in Fig. 9 for $\lambda = 445$ and $\lambda = 865$ nm. The two single-component atmospheres (molecules only or aerosols only) are represented with the relative proportions of photons escaping the atmosphere after one through more than four scattering events. The total number of photons constitutes the term ρ_a or ρ_r . The asso-

ciated compound atmosphere, with the same amount of molecules and particles, is represented by the chessboards in Fig. 9, which show percentages of collisions of various kinds. In these chessboards the reflectance ρ_a^* corresponds to all the terms that appear in the first column (no scattering by molecules), and ρ_r^* corresponds to the first row (no aerosol scattering). The reflectance ρ_{ra}^* corresponds to the 16 other boxes containing photons that have interacted several times with molecules and aerosols. Boxes 1-1, generally dominant in magnitude in heterogeneous scattering, correspond to two successive scattering events, once on aerosol, once on molecule (or the reverse).

This study was essentially supported by the European Space Agency (contract 11878/96/NL/GS from the European Space Research and Technology Center, which is duly acknowledged).

References

1. H. R. Gordon, "Removal of atmospheric effects from satellite imagery of the oceans," *Appl. Opt.* **17**, 1631-1636 (1978).
2. M. Viollier, D. Tanré, and P. Y. Deschamps, "An algorithm for remote sensing of water color from space," *Boundary-Layer Meteorol.* **18**, 247-267 (1980).
3. H. R. Gordon, J. W. Brown, and R. H. Evans, "Exact Rayleigh scattering calculations for use with the Nimbus-7 Coastal Zone Color Scanner," *Appl. Opt.* **27**, 862-871 (1988).
4. P. Y. Deschamps, M. Herman, and D. Tanré, "Modeling of the atmospheric effects and its application to the remote sensing of ocean color," *Appl. Opt.* **22**, 3751-3758 (1983).
5. H. R. Gordon and D. J. Castaño, "Aerosol analysis with the Coastal Zone Color Scanner: a simple method for including multiple scattering effects," *Appl. Opt.* **28**, 1320-1326 (1989).
6. H. R. Gordon and M. Wang, "Retrieval of water-leaving reflectance and aerosol optical thickness over the oceans with SeaWiFS: a preliminary algorithm," *Appl. Opt.* **33**, 443-452 (1994).
7. A. Jayaraman and P. Koepke, "Accounting for the multiple scattering effect in radiation intensities at the top of the atmosphere," *Appl. Opt.* **31**, 3473-3480 (1992).
8. H. R. Gordon, D. K. Clark, J. W. Brown, O. B. Brown, R. H. Evans, and W. W. Broenkow, "Phytoplankton pigment concentrations in the Middle Atlantic Bight: comparison of ship determinations and CZCS estimates," *Appl. Opt.* **22**, 20-36 (1983).
9. A. Morel and B. Gentili, "Diffuse reflectance of oceanic waters: its dependence on Sun angle as influenced by the molecular scattering contribution," *Appl. Opt.* **30**, 4427-4438 (1991).
10. A. Morel and B. Gentili, "Diffuse reflectance of oceanic waters. II. Bidirectional aspects," *Appl. Opt.* **32**, 6864-6879 (1993).
11. C. D. Mobley, B. Gentili, H. R. Gordon, Z. Jin, G. W. Kattawar, A. Morel, P. Reinersman, K. Stamnes, and R. H. Stavn, "Comparison of numerical models for computing underwater light fields," *Appl. Opt.* **32**, 7484-7504 (1993).
12. H. R. Gordon and D. J. Castaño, "Coastal Zone Color Scanner atmospheric correction algorithm: multiple scattering effects," *Appl. Opt.* **26**, 2111-2122 (1987).
13. R. A. McClatchey, R. W. Fenn, J. E. A. Selby, F. E. Voltz, and J. S. Garing, "Optical properties of the atmosphere," AFCRL 71-0279, environmental research paper 354 (U.S. Air Force Cambridge Research Laboratories, Bedford, Mass., 1971).
14. L. Elterman, "UV, visible, and IR attenuation for altitudes to 50 km," AFCRL-68-0153, environmental research paper 285

(U.S. Air Force Cambridge Research Laboratories, Bedford, Mass., 1968).

15. E. P. Shettle and R. W. Fenn, "Models for the aerosols of the lower atmosphere and the effects of humidity variations on their optical properties," AFGL-TR-79-0214, environmental research paper 676 (U.S. Air Force Geophysics Laboratory, Hanscom Air Force Base, Mass., 1979).
16. World Climate Research Program 112, "A preliminary cloudless standard atmosphere for radiation computation," WMO/TD-24 (World Meteorological Organization, Geneva, Switzerland, 1986).
17. H. R. Gordon, "Atmospheric correction of ocean color imagery in the Earth observing system era," *J. Geophys. Res.* **102**, 17,081-17,106 (1997).
18. P. Y. Deschamps, F. M. Bréon, M. Leroy, A. Podaire, A. Bricaud, J. C. Buriez, and G. Sèze, "The POLDER mission: instrument characteristics and scientific objectives," *IEEE Trans. Geosci. Remote Sens.* **32**, 598-615 (1994).
19. S. Saitoh, "OCTS on ADEOS," in *Oceanographic Application of Remote Sensing*, M. Ikeda and F. W. Dobson, eds. (CRC Press, Boca Raton, Fla., 1995), pp. 473-480.
20. S. B. Hooker, W. E. Esaias, G. C. Feldman, W. W. Gregg, and C. R. McClain, *An Overview of SeaWiFS and Ocean Color*, Vol. 1 of tech. rep. series NASA Tech. Memo. 104566 (NASA Greenbelt Space Flight Center, Greenbelt, Md., July 1992).
21. M. Rast and J. L. Bézy, "The ESA medium resolution imaging spectrometer (MERIS): requirements to its mission and performance of its system," in *RSS95, Remote Sensing in Action*, Proceedings of the 21st Annual Conference of the Remote Sensing Society, P. J. Curran and Y. C. Robertson, eds. (Taylor & Francis, London, 1995), pp. 125-132.
22. A. Morel and L. Prieur, "Analysis of variations in ocean color," *Limnol. Oceanogr.* **22**, 709-722 (1977).
23. K. Ding and H. R. Gordon, "Atmospheric correction of ocean-color sensors: effects of the Earth's curvature," *Appl. Opt.* **33**, 7096-7106 (1994).

A multiple scattering algorithm for atmospheric correction of remotely sensed ocean colour (MERIS instrument): principle and implementation for atmospheres carrying various aerosols including absorbing ones

DAVID ANTOINE† and ANDRÉ MOREL‡

Laboratoire de Physique et Chimie Marines (LPCM), Université Pierre et Marie Curie et CNRS, BP 08, F-06238 Villefranche sur Mer cedex, France

(Received 14 November 1997; in final form 6 February 1998)

Abstract. A multiple scattering algorithm for atmospheric correction of satellite ocean colour observations is described. This algorithm, precisely designed for the MERIS instrument, globally assesses the combined contributions of aerosols and molecules to the multiple scattering regime. The approach was introduced in a previous work, where it was shown that, for a given aerosol, multiple scattering effects can be assessed through the relationship between the aerosol optical thickness and the relative increase in the path radiance that results from the progressive introduction of this aerosol within an aerosol-free atmosphere. Based on considerations about the accuracy to which the water-leaving radiances should be retrieved, the need to account for multiple scattering is argued. The principle of the algorithm is then presented, and tests and sensitivity studies (especially as regards aerosol type and vertical distribution) are performed to assess its performance in terms of errors on the retrieved water-leaving reflectances and pigment concentrations. The algorithm is able to perform the correction for atmospheres carrying several aerosol types, including absorbing ones, through their identification in the near-infrared, and through the detection of their absorption by means of appropriate assumptions on the marine signals at 510 and 705 nm.

1. Introduction

The goal of the atmospheric correction applied to space-acquired ocean colour observations is to retrieve the water-leaving radiance at the sea level from the total radiance recorded at the top of the atmosphere (TOA). The water-leaving radiances transmitted through the atmosphere form at the TOA level what are called the 'marine radiances'. These radiances are thus made of photons that have crossed the atmosphere down to the ocean, then have twice crossed the air-sea interface before reaching the sensor after a second atmospheric travel. The spectrum of the water-leaving radiances carries information about the bio-optical state of the oceanic upper layers, which is of great importance for bio-geochemical studies of the ocean (e.g. Yoder *et al.* 1988, Lewis 1992). In addition, possible by-products of atmospheric

†e-mail: david@obs-vlfr.fr

‡e-mail: morel@obs-vlfr.fr

correction are the type and optical thickness of aerosols, which provide information of considerable interest for studies of the Earth radiation budget and climate (e.g. Charlson *et al.* 1992), as well as for ocean bio-geochemistry (e.g. Donaghay *et al.* 1991).

In the near-infrared (NIR) part of the spectrum ($700\text{ nm} < \lambda < 900\text{ nm}$), oceanic Case 1 waters (Morel and Prieur 1977) are totally absorbing ('black ocean'), so that the TOA signal is reduced to the 'atmospheric path radiance'. This radiance is made of photons scattered by air molecules and aerosols, also possibly reflected at the sea surface, but having never entered the ocean. In contrast, the radiance backscattered by the ocean-atmosphere system in the visible part of the spectrum is formed by the atmospheric path radiance plus the water-leaving radiance, even if the former largely dominates. Indeed, in the most favourable conditions of observation (clear atmosphere, small Sun zenith angle and favourable viewing angle), the water-leaving radiance in the visible domain represents at most about 10% of the total radiance. Extraction of such a small signal requires that the combined effects of molecules and aerosols in forming the path radiance be accurately quantified.

In the development of atmospheric correction algorithms, it is often assumed that the radiances due to Rayleigh and aerosol scattering are separable. They are then accordingly separately calculable for single component atmospheres and summed up to simulate the path radiance. Such an addition is strictly valid if only single scattering occurs, and is an approximation for a multiple scattering regime. Under this assumption of separable radiances, the determination of the Rayleigh part of the path is easily handled because only the illumination and observation angles have to be known, even if knowledge of atmospheric pressure and wind speed at the sea surface is also needed for accurate calculations (André and Morel 1989, Gordon and Wang 1992a, b). Over Case 1 waters, and still under the assumption of separability of radiances, the difference between the total and the Rayleigh radiances in the NIR represents the radiance due to aerosol scattering. If the latter is estimated at two wavelengths, the retrieval of the aerosol type and of the aerosol optical thickness, is, in principle, possible at these wavelengths. Next, the aerosol optical properties have to be extrapolated from the NIR toward the visible domain. Hypotheses are mandatory at this stage because the aerosol optical properties are not known when processing an ocean colour scene.

Until recently the only practical experience of atmospheric correction of ocean colour data was acquired with the Coastal Zone Color Scanner (CZCS), which functioned aboard the Nimbus 7 satellite from 1978 to 1986 (Gordon *et al.* 1980, Hovis *et al.* 1980). The algorithms developed for atmospheric correction of CZCS observations (e.g. Gordon 1978, Viollier *et al.* 1980, Bricaud and Morel 1987, André and Morel 1991) faced two main problems, originating from the limited radiometric sensitivity of the instrument and the absence of channels measuring backscattered radiation in the NIR part of the spectrum. As a consequence of the first limitation, it was useless to account for certain processes that had no detectable impact on the signal. Meanwhile, the absence of NIR channels made the estimate of the aerosol contribution a difficult task.

The European Medium Resolution Imaging Spectrometer (MERIS) (Rast and Bézy 1995) and other new-generation ocean colour sensors (e.g. POLDER (Deschamps *et al.* 1994); OCTS (Saitoh 1995); SeaWiFS (Hooker *et al.* 1992); MODIS (Salomonson *et al.* 1989)) lift the two limitations evoked above due to their improved radiometric characteristics and adequate channels in the NIR (three for

MERIS for atmospheric correction). One drawback in the improvement in radiometric performance is that the impact of some processes (below the digitization level for the CZCS and thus neglected) must be accounted for. Moreover, some working hypotheses used in the past now appear oversimplistic and have to be abandoned. In fact most of them have been progressively abandoned in the development of atmospheric correction algorithms for the new-generation sensors (e.g. Gordon and Wang (1994a), Wang and Gordon (1994) and Gordon (1997) for the SeaWiFS and MODIS instruments and Fukushima and Toratani (1997) for OCTS). These algorithms account for multiple scattering but still rely on the assumption of an operational separability of radiances. Therefore, in a first step, the Rayleigh radiance is calculated and subtracted from the total radiance in the NIR; the remaining signal then supposedly pertains to aerosol scattering.

In this work the assumption of separable aerosol and Rayleigh radiances is abandoned, and the combined contributions of aerosols and molecules to the multiple scattering regime are globally assessed. This approach was suggested previously in a study of the relative importance of various types (aerosol or molecule) and orders of scattering in forming the atmospheric path radiance (Antoine and Morel 1998). It was shown that, for a given aerosol, multiple scattering effects can be assessed through the relationship between the aerosol optical thickness and the relative increase in the path radiance that results from the progressive introduction of the aerosol into an aerosol-free atmosphere. An atmospheric correction algorithm is proposed here along these lines. It was designed for the MERIS instrument, yet is applicable to any other instrument with similar radiometric characteristics. The algorithm accounts for all multiple scattering effects. Its implementation allows observations in the visible to be corrected for atmospheres containing several kinds of aerosols, including absorbing ones, from their identification in the NIR. The algorithm implementation rests on the assumption of no oceanic signal in the NIR and therefore is only valid for Case 1 waters.

The accuracy to which the water-leaving radiances should be retrieved is first examined and the need to account for multiple scattering is discussed. The principle of the proposed multiple scattering algorithm is then presented. Tests and sensitivity studies were carried out to assess its performance in terms of errors on the retrieved water-leaving radiances and pigment concentrations. Possible improvements, as well as the limitations, of the present approach are also discussed.

2. The algorithm

2.1. Accuracy required for the atmospheric correction

Radiometric characteristics and the calibration of MERIS are defined in terms of reflectances; radiances at the TOA level are accordingly converted into reflectances (see table 1 for symbols and definitions) in the equation

$$\rho(\lambda, \theta_s, \theta_v, \Delta\phi) = \pi L(\lambda, \theta_s, \theta_v, \Delta\phi) / F_0(\lambda) \mu_s \quad (1)$$

Water-leaving reflectances, ρ_w , are obtained after the measured total reflectances have been corrected for atmospheric effects. These water-leaving reflectances are related to the bio-optical state of the water body through the ratio of the backscattering coefficient to the absorption coefficient (b_b/a) (see Morel and Gentili 1991, 1993, 1996)

$$\rho_w(\lambda, \theta_s, \theta', \Delta\phi) = \pi t_{\theta_s}(\lambda) \Re(\theta') \frac{f(\lambda, \theta_s)}{Q(\lambda, \theta_s, \theta', \Delta\phi)} \left(\frac{b_b(\lambda)}{a(\lambda)} \right) \quad (2)$$

Table 1. Glossary of symbols.

Symbol	Definition	Dimension/units
Geometry, wavelengths		
λ	Wavelength	nm
θ_s	Sun zenith angle ($\mu_s = \cos \theta_s$)	degrees
θ_v	Satellite viewing angle ($\mu_v = \cos \theta_v$)	degrees
$\Delta\phi$	Azimuth difference between the Sun-pixel and pixel-sensor half vertical planes	degrees
Atmosphere and aerosol properties		
$F_0(\lambda)$	Mean extraterrestrial spectral irradiance	$\text{W m}^{-2} \text{nm}^{-1}$
ε_c	Correction factor applied to $F_0(\lambda)$, and accounting for the changes in the Earth-Sun distance. It is computed from the eccentricity of the Earth orbit, $e=0.0167$, and from the day number D , as $\varepsilon_c = \left(1 + e \cos \left(\frac{2\pi(D-3)}{365} \right) \right)^2$	dimensionless
$F_a(\lambda)$	Aerosol forward scattering probability	dimensionless
$F_r(\lambda)$	Rayleigh forward scattering probability (= 1/2)	dimensionless
$\tau_a(\lambda)$	Optical thickness due to aerosol scattering	dimensionless
$\tau_r(\lambda)$	Optical thickness due to Rayleigh scattering	dimensionless
η_r	Contribution of molecules to the total optical thickness ($=\tau_r/(\tau_r + \tau_a)$)	dimensionless
$\tau_{ag}(\lambda)$	Optical thickness due to gaseous absorption	dimensionless
$\omega_a(\lambda)$	Aerosol single scattering albedo	dimensionless
$\omega_r(\lambda)$	Rayleigh single scattering albedo	dimensionless
$P_r(\lambda, \gamma)$	Rayleigh phase function $p_r(\gamma \pm) = P_r(\lambda, \gamma \pm) + [\rho_F(\theta_s) + \rho_F(\theta_v)] P_r(\lambda, \gamma \pm)$ where $\gamma \pm$ is the scattering angle $\cos(\gamma \pm) = \pm \cos \theta_0 \cos \theta_v - \sin \theta_0 \sin \theta_v \cos \Delta\phi$	sr^{-1}
$P_a(\lambda, \gamma)$	Aerosol phase function	sr^{-1}
ν	Exponent of the Junge law for the distribution of aerosol particles (sensitivity studies)	dimensionless
$c(\lambda)$	Attenuation coefficient for wavelength λ	m^{-1}
$t_{\theta_s}(\lambda, \theta_s)$	Irradiance transmittance for a Sun zenith angle θ_s $t_{\theta_s}(\lambda, \theta_s) = E_d(0^+) / (\mu_s \varepsilon_c F_0)$, where $E_d(0^+)$ is the downwelling irradiance just above the sea surface	dimensionless
$t_d(\lambda, \theta)$	Diffuse transmittance for angle θ $t_d(\lambda, \theta) = L_{\text{TOA}}(\lambda, \theta_s, \theta_v, \Delta\phi) / L_{0^+}(\lambda, \theta_s, \theta_v, \Delta\phi)$	dimensionless
$L(\lambda, \theta_s, \theta_v, \Delta\phi)$	Radiance	$\text{W m}^{-2} \text{nm}^{-1} \text{sr}^{-1}$
P	Atmospheric pressure at sea level	hPa
RH	Relative humidity	per cent
$\rho(\lambda, \theta_s, \theta_v, \Delta\phi)$	Reflectance ($\pi L / F_0 \mu_s$) where the product πL is the TOA upwelling irradiance if upwelling radiances are equal to $L(\lambda, \theta_s, \theta_v, \Delta\phi)$, for any values of θ_v within $0-\pi/2$ and any $\Delta\phi$ within $0-2\pi$ Subscripts t, total reflectance w, water-leaving reflectance path, path reflectance r, Rayleigh reflectance rs, Rayleigh reflectance (single scattering only) a, aerosol reflectance	dimensionless

Table 1. (Continued).

Symbol	Definition	Dimension/units
	as, aerosol reflectance (single scattering only) ra, heterogeneous aerosol-molecule scattering G, Sun glint reflectance	
$\rho^*(\lambda, \theta_s, \theta_v, \Delta\phi)$	Reflectance within a compound atmosphere, containing molecules and aerosols (subscripts as for ρ)	dimensionless
$\varepsilon(\lambda_1, \lambda_2)$	Ratio $\rho_{as}(\lambda_1)/\rho_{as}(\lambda_2)$	dimensionless
$\varepsilon'(\lambda_1, \lambda_2)$	Ratio $[\rho_{path}(\lambda_1) - \rho_r(\lambda_1)]/[\rho_{path}(\lambda_2) - \rho_r(\lambda_2)]$	dimensionless
$f(\tau_a)$	Relationship between the ratio $[\rho_{path}/\rho_r]$ and τ_a	dimensionless
Water properties		
<i>Chl</i>	Chlorophyll concentration	mg m^{-3}
$a(\lambda)$	Total absorption coefficient	m^{-1}
$b_b(\lambda)$	Total backscattering coefficient	m^{-1}
A_{λ_1, λ_2}	Ratio of (b_b/a) at λ_1 nm to (b_b/a) at λ_2 nm	dimensionless
$R(\lambda, 0^-)$	Diffuse reflectance at null depth, or irradiance ratio (E_u/E_d) (upward and downward irradiances respectively)	dimensionless
f	Ratio of $R(0^-)$ to (b_b/a) ; subscript 0 when $\theta_s = 0$	dimensionless
$Q(\lambda, \theta_s, \theta_v, \Delta\phi)$	Factor describing the bidirectional character of $R(\lambda, 0^-)$, subscript 0 when $\theta_s = \theta_v = 0$	sr
$[\rho_w]_N(\lambda)$	Normalized water-leaving reflectance (i.e. the reflectance if there were no atmosphere, and for $\theta_s = \theta_v = 0$)	dimensionless
Air-water interface		
$\Re(\theta')$	Geometrical factor, accounting for all refraction and reflection effects at the air-sea interface (Morel and Gentili 1996)	dimensionless
	$\Re(\theta') = \left[\frac{(1-\bar{\rho})(1-\rho_F(\theta'))}{(1-\bar{r}R)} \frac{1}{n^2} \right]$ (subscript 0 when $\theta' = 0$)	
	where	
	n is the refractive index of water	dimensionless
	$\rho_F(\theta)$ is the Fresnel reflection coefficient for incident angle θ	dimensionless
	$\bar{\rho}$ is the mean reflection coefficient for the downwelling irradiance at the sea surface	dimensionless
	\bar{r} is the average reflection for upwelling irradiance at the water-air interface	dimensionless
	θ' is the refracted viewing angle ($\theta' = \sin^{-1}(n \sin \theta_v)$)	degrees
σ	Root mean square of wave facet slopes	dimensionless
β	Angle between the local normal and the normal to a wave facet	
$p(\theta_s, \theta_v, \Delta\phi)$	Probability density of surface slopes for the direction ($\theta_s, \theta_v, \Delta\phi$)	dimensionless
Miscellaneous		
W	Wind speed	m s^{-1}
X	Aerosol mixing ratio defined on the basis of the (ρ_{path}/ρ_r) ratio at 775 nm	dimensionless

The ratio (b_b/a) can be similarly related to the normalized water-leaving reflectance $[\rho_w]_N$. This reflectance is defined (Gordon and Clark 1981) as the reflectance when aiming at nadir ($\theta_v = 0$), for the Sun at zenith ($\theta_s = 0$), and without atmosphere ($t_{\theta_s} = 1$). With this definition, $[\rho_w]_N$ is expressed as (see Morel and Gentili 1996)

$$[\rho_w]_N(\lambda) = \pi \mathcal{R}_0 \frac{f_0(\lambda)}{Q_0(\lambda)} \left(\frac{b_b(\lambda)}{a(\lambda)} \right) \quad (3)$$

where the subscripts 0 indicate that the corresponding quantities are for $\theta_s = \theta_v = 0$. In equation (3) the product $(\pi \mathcal{R}_0 (f_0/Q_0))$ is a constant (if the dependence of \mathcal{R}_0 upon wind speed is ignored), so that $[\rho_w]_N$ can be considered as an inherent optical property of the medium.

The MERIS instrument has been designed to allow, in principle, the detection of ten classes of chlorophyll concentration (*Chl*) within each of the three orders of magnitude between 0.03, 0.3, 3 and 30 mg*Chl* m⁻³ (i.e. a total of 30 classes). These classes are regularly distributed according to a constant logarithmic increment of 0.1. Shifting from one class to the next (previous) one corresponds to a change in *Chl* by a factor $10^{\pm 0.1}$ (i.e. +25% or -20%).

A first requirement for atmospheric correction is to allow 30 values of $[\rho_w]_N$ to be discriminated at any wavelength where the pigment concentration influences the reflectance. The corresponding changes in $[\rho_w]_N$, as computed through equation (3), are displayed in figure 1(a) for several wavelengths, which are possibly used for retrieving *Chl*. At 443 nm, the changes in $[\rho_w]_N$ are about 2.5×10^{-3} when *Chl* < 0.1 mg m⁻³, about 1×10^{-3} when *Chl* ~ 1 mg m⁻³, and about 5×10^{-4} for higher concentrations. At 490 nm, the changes are steadily about $5-7 \times 10^{-4}$, except when *Chl* < 0.1 they are of about 2×10^{-4} for these low concentrations. At 560 nm, the changes in $[\rho_w]_N$ are of about 2×10^{-4} , whatever *Chl*. These values remain about the same when the conditions on θ_s , θ_v and τ_{θ_s} are relaxed, that is when ρ_w is examined for any geometry different from that corresponding to the definition of $[\rho_w]_N$. These values represent the desired capacity of discrimination of the atmospheric correction at these wavelengths. The change in $[\rho_w]_N$ to be detected is smaller at 560 nm than it is at 443 nm or at 490 nm, and this more stringent condition was used to specify the noise equivalent reflectances for all wavelengths of the MERIS instrument ($Ne\Delta\rho < 2 \times 10^{-4}$). It should be noted that this capacity in discriminating small reflectance changes does not prejudice the absolute accuracy of the instrument, nor therefore the correct retrieval of the exact values of the reflectance.

It is now assumed that *Chl* is calculated through a certain function Φ of the ratio of (b_b/a) at two wavelengths (λ_1 and λ_2), denoted A_{λ_1, λ_2} , which is used as an index of the bio-optical state.

$$Chl = \Phi \left(\left[\frac{b_b}{a}(\lambda_1) \right] / \left[\frac{b_b}{a}(\lambda_2) \right] \right) = \Phi(A_{\lambda_1, \lambda_2}) \quad (4)$$

The requirement for atmospheric correction is that it must be accurate enough to allow 30 *Chl* values to be discriminated, given that the above $Ne\Delta\rho$ requirement is satisfied at each wavelength. In other words, 30 values of A_{λ_1, λ_2} must be discriminated between 0.03 and 30 mg*Chl* m⁻³. The $\Phi(A)$ function is displayed in figure 1(b) for several couples of wavelengths (for a given geometry the A ratio is related to $([\rho_w]_N(\lambda_1)/[\rho_w]_N(\lambda_2))$ through the values of the (f_0/Q_0) ratio at the two wavelengths).

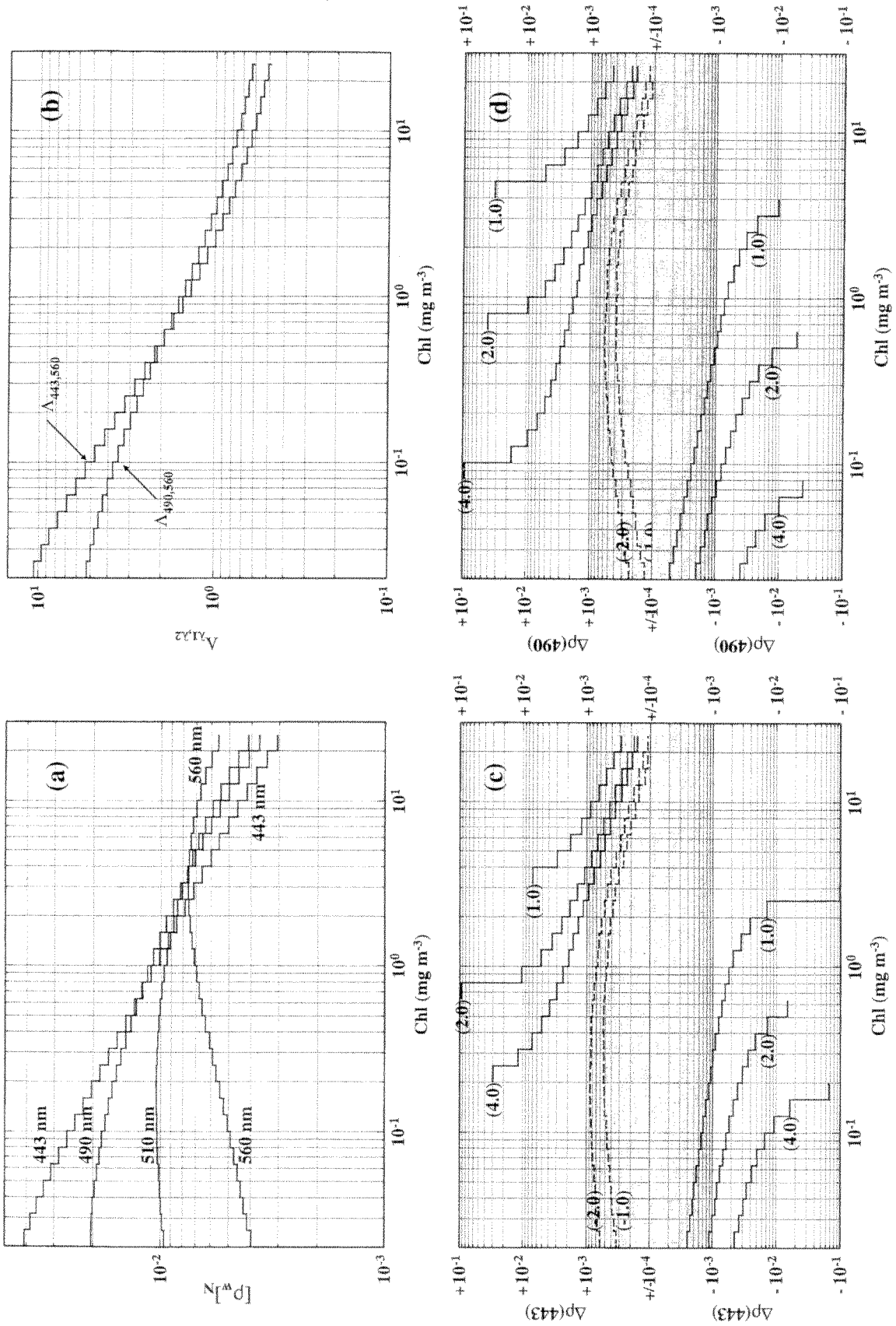


Figure 1. (a) Normalized water-leaving reflectances (equation (3)), plotted as a function of chlorophyll concentration (Chl) for the wavelengths indicated. The steps in the curves correspond to increments of 0.1 in $\log(Chl)$. (b) Ratio of (b_b/a) at 443 or 490 nm to (b_b/a) at 560 nm ($A_{443,560}$ and $A_{490,560}$). (c) Allowable error in atmospheric correction at 443 nm, $\Delta\rho(443)$ (i.e. the maximum error above which a wrong chlorophyll concentration is retrieved, corresponding to the previous class). The error $\Delta\rho(443)$ is calculated by assuming several ratios for $\Delta\rho(443)/\Delta\rho(560)$, as indicated (see text). The dashed curves are for errors of opposite signs at 443 and 560 nm. The shaded area is for errors within $\pm 1 \times 10^{-3}$. (d) As (b) but for the wavelength couple 490–560 nm.

The change in $A_{443,560}$ between adjacent classes of chlorophyll, denoted ΔA , varies continuously from about 0.9 when Chl is 0.03 mg m^{-3} , to 0.1 when Chl is 0.3 mg m^{-3} , and to 0.03 when Chl is 30 mg m^{-3} . For the wavelength couple 490–560 nm, the changes in $A_{490,560}$ are 0.2, 0.1 and 0.05 for the same values of Chl .

After atmospheric correction, the allowable errors in $[\rho_w]_N(\lambda_1)$ and $[\rho_w]_N(\lambda_2)$ are those that would lead to an error in their ratio A_{λ_1, λ_2} equal, at most, to ΔA . These errors, denoted $\Delta\rho(\lambda_1)$ and $\Delta\rho(\lambda_2)$, are accordingly computed as

$$\frac{([\rho_w]_N(\lambda_1) + \Delta\rho(\lambda_1))}{([\rho_w]_N(\lambda_2) + \Delta\rho(\lambda_2))} = \frac{[\rho_w]_N(\lambda_1)}{[\rho_w]_N(\lambda_2)} + \Delta A \quad (5)$$

For a given Chl class, solving equation (5) requires selection of the relevant ΔA value, calculation of the reflectances $[\rho_w]_N(\lambda_1)$ and $[\rho_w]_N(\lambda_2)$ and an assumption about the ratio of the errors $\Delta\rho(\lambda_1)$ and $\Delta\rho(\lambda_2)$ (in such a way that the number of unknowns is reduced to one). In the following, λ_1 will be either 443 nm or 490 nm, and λ_2 is 560 nm (i.e. wavelengths possibly used for retrieving Chl). Errors at 443 nm and 490 nm are expected to be greater than those at 560 nm, because the accuracy of atmospheric correction may deteriorate when going away from the NIR (i.e. during extrapolation toward the visible). The ratios $(\Delta\rho(443)/\Delta\rho(560))$ and $(\Delta\rho(490)/\Delta\rho(560))$ are thus fixed, somewhat arbitrarily, to 4, 2 or 1. It is not expected that errors be of opposite signs at the two wavelengths after in-orbit calibration adjustments; should that arise, error ratios of -4 , -2 , and -1 have also been considered and tested.

The acceptable errors $\Delta\rho(443)$ resulting from these computations are displayed in figure 1(c) as a function of Chl . They were computed for each Chl class and for the ΔA values corresponding to an underestimation by one class of concentration. They are negative at first, and then positive after the $A_{443,560}$ ratio becomes lower than the ratio $\Delta\rho(443)/\Delta\rho(560)$. A symmetrical pattern (i.e. $\Delta\rho$ at first positive and then negative) would have been obtained for errors corresponding to an overestimation by one class of concentration. The acceptable error $\Delta\rho(443)$ increases (regardless of the sign) as its ratio to $\Delta\rho(560)$ increases. It also increases as the reflectances become closer at 443 and 560 nm (the error becomes undetermined when both reflectances are equal). The accuracy requirement for atmospheric correction is accordingly not too severe when $\sim 0.3 < Chl < \sim 3 \text{ mg m}^{-3}$; it is only $\pm 1 \times 10^{-3}$, or even $\pm 2 \times 10^{-3}$, if $\Delta\rho(443)$ and $\Delta\rho(560)$ have the same sign (i.e. about 10% of $[\rho_w]_N(443)$ when $Chl = \sim 0.3 \text{ mg m}^{-3}$). On the contrary, the accuracy requirement is increasingly demanding for low and high chlorophyll concentrations, and is between about $\pm 1 \times 10^{-3}$ and $\pm 5 \times 10^{-4}$ depending on the ratio of errors at 443 and 560 nm. When $\Delta\rho(443)$ and $\Delta\rho(560)$ are of opposite sign, they always must be below $\pm 1 \times 10^{-3}$, and often lower than $\pm 5 \times 10^{-4}$ (see the two dashed curves in figure 1(c)). Therefore, an additional constraint on atmospheric correction would be identical signs for $\Delta\rho(443)$ and $\Delta\rho(560)$. Fulfilment of this condition depends upon correct retrieval of the spectral dependence of aerosol scattering, as well as on correct calibration of the instrument.

When the wavelength couple 490–560 nm is used instead of the couple 443–560 nm (figure 1(d)), the conclusions regarding allowable errors at 490 nm are roughly the same than those for $\lambda = 443$ nm, except for concentrations below about $0.1 \text{ mg Chl m}^{-3}$, where the $A_{490,560}$ ratio is less sensitive to changes in Chl than is the ratio $A_{443,560}$ (see figure 1(b)). The couple 490–560 nm could prove to be useful,

however, for concentrations above about 3 mgChl m^{-3} , where the allowable errors are slightly greater at 490 nm than they are at 443 nm. In addition, when *Chl* is high, the water-leaving reflectance is a little larger at 490 nm than it is at 443 nm.

In summary, the first requirement (retrieval of 30 reflectance values) requires that atmospheric correction errors be maintained within $\pm 1\text{--}2 \times 10^{-3}$ at 443 nm, within $\pm 5 \times 10^{-4}$ at 490 nm, and within $\pm 2 \times 10^{-4}$ at 560 nm. This value at 560 nm (see steps in figure 1(a)) is equal to the $Ne\Delta\rho$ specified for MERIS (see above). If it is assumed that atmospheric correction errors in the 440–500 nm domain are roughly twice the errors at 560 nm, the second requirement (discrimination of 30 *Chl* values) requires errors within $\pm 1 \times 10^{-3}$ at 443 nm ($\pm 5 \times 10^{-4}$ at 560 nm), or within $\pm 5 \times 10^{-4}$ at 490 nm ($\pm 2 \times 10^{-4}$ at 560 nm). When expressed as relative errors, all the above requirements represent about 1% of the normalized oceanic reflectances at 443 nm (and often 2–5%), except when $Chl > 3 \text{ mg m}^{-3}$. The situation is about the same for the wavelength couple 490–560 nm, except when $Chl < 0.1 \text{ mg m}^{-3}$, and when the $A_{490,560}$ ratio is equal to unity.

2.2. Formulation of the path reflectance for a compound (molecules plus aerosols) atmosphere

Reflectances at the TOA level are hereafter considered in the absence of oceanic whitecaps and foam, and for viewing directions out of specular reflection of direct Sun rays (Sun glint). The total reflectance at the top of atmosphere level, ρ_t , is therefore

$$\rho_t = \rho_{\text{path}} + t_d \rho_w \quad (6)$$

where ρ_{path} is the atmospheric path reflectance and t_d is the atmospheric diffuse transmittance (the product $t_d \rho_w$ is called here the ‘marine’ reflectance). The reflectance ρ_{path} is formed by all diffuse photons reaching the TOA apart from those that entered the ocean (note that the usual definition of the path reflectance does not include the reflection of diffuse photons at the air–sea interface). Atmospheric correction requires that the contributions to ρ_{path} of scattering by aerosols and molecules be quantified.

A possible approach consists of assuming that only single scattering occurs. Under this assumption, the Rayleigh reflectance, ρ_{rs} , and the aerosol reflectance, ρ_{as} , are separable, and ρ_{path} reduces to

$$\rho_{\text{path}} = \rho_{rs} + \rho_{as} \quad (7)$$

When $\tau_{a[r]} \lesssim 0.1$ and the sea surface is flat, the reflectances can be expressed from the corresponding phase functions as (see table 1)

$$\rho_{as[rs]}(\lambda, \theta_s, \theta_v, \Delta\phi) = \tau_{a[r]}(\lambda) \omega_{a[r]}(\lambda) p_{a[r]}(\lambda, \gamma \pm) / 4\mu_s \mu_v \quad (8)$$

The algorithms for the correction of CZCS observations were based on this decomposition of the total signal (e.g. Gordon 1978, Viollier *et al.* 1980, Bricaud and Morel 1987, André and Morel 1991). The same decomposition could also form the basis of a simple, moderately accurate, atmospheric correction algorithm for the new generation of ocean colour sensors, as proposed by Wang and Gordon (1994) and Gordon and Wang (1994 a). The principle would be to calculate ρ_{rs} in two NIR bands, obtaining two values of ρ_{as} by difference with ρ_{path} (equation (7)). The ratio

of the two ρ_{as} values, $\varepsilon(\lambda_1, \lambda_2)$, describes the spectral dependence of aerosol scattering

$$\varepsilon(\lambda_1, \lambda_2) = \frac{\tau_a(\lambda_1)\omega_a(\lambda_1)p_a(\lambda_1, \gamma \pm)}{\tau_a(\lambda_2)\omega_a(\lambda_2)p_a(\lambda_2, \gamma \pm)} \quad (9)$$

and, for a given aerosol, its variations with wavelength can be represented by simple laws (e.g. Ångström 1964). When, for instance, an exponential law is used (Wang and Gordon 1994), the value of ρ_{as} can be determined at any wavelength λ_{vis} in the visible from its values at two NIR bands $\lambda_{IR,1}$ and $\lambda_{IR,2}$, through (see figure 2)

$$\varepsilon(\lambda_{vis}, \lambda_{IR,2}) = \exp \left[\left(\frac{\lambda_{IR,2} - \lambda_{vis}}{\lambda_{IR,2} - \lambda_{IR,1}} \right) \log_e \left(\frac{\rho_{as}(\lambda_{IR,1})}{\rho_{as}(\lambda_{IR,2})} \right) \right] \quad (10)$$

It has been shown that equation (10) actually works reasonably well for low aerosol optical thicknesses ($\tau_a \lesssim 0.1$), and when the aerosol is not absorbing ($\omega_a = 1$); in such a case, the method would provide $t\rho_w$ within ± 0.002 (Gordon and Wang 1994a, Gordon 1997). The above technique, however, can no longer perform an accurate atmospheric correction as soon as τ_a is higher than about 0.1, or when $\omega_a < 1$ (Gordon 1997). Multiple scattering is actually responsible for this failure, even in conditions where it is usually neglected. For instance, Antoine and Morel (1998) showed, through Monte Carlo simulations, that multiple scattering still represents as much as 30% of the path reflectance at 865 nm when $\tau_a = 0.2$ (figure 9 in Antoine and Morel (1998)). The corresponding multiple photon collisions occur mainly with aerosol particles. Therefore multiple scattering is to be accounted for, except perhaps for the clearest atmospheres. When successive aerosol and molecule scattering occur, however, the assumption of separability of reflectances has to be abandoned. Equation (7) cannot hold true, and another formulation has to be used to express the path reflectance.

Antoine and Morel (1998) proposed a decomposition of the path reflectance as

$$\rho_{path} = \rho_r^* + \rho_a^* + \rho_{ra}^* \quad (11a)$$

In equation (11a), ρ_r^* is the reflectance due to single and multiple scattering by molecules only, but *in the presence of aerosols*, ρ_a^* is the equivalent term for aerosols, also *in presence of molecules*, and ρ_{ra}^* stands for that part of ρ_{path} which strictly results from successive aerosol and molecule scattering; this reflectance was referred to as the 'heterogeneous' scattering in the above reference. Equation (11a) is exact because it does not rely on the assumption of separable reflectances. The reflectances marked with asterisks differ from those usually considered for single component atmospheres, i.e. ρ_r , the reflectance due to multiple scattering by air molecules in an aerosol-free atmosphere; ρ_a , the reflectance due to multiple scattering by aerosols in a hypothetical atmosphere containing exclusively aerosols; and ρ_{ra} , a 'coupling term' (Deschamps *et al.* 1983, Gordon and Wang 1994 a). The word 'term' instead of 'reflectance' is used for ρ_{ra} because it is often negative. It has no physical meaning and actually represents the sum of ρ_{ra}^* and the corrective terms needed to account for the profound changes in the radiative regime between single component atmospheres and the corresponding compound atmosphere (i.e. the differences $(\rho_r^* - \rho_r)$ and $(\rho_a^* - \rho_a)$; see equation (6) in Antoine and Morel (1998))

$$\rho_{ra} = \rho_{ra}^* + (\rho_r^* - \rho_r) + (\rho_a^* - \rho_a) \quad (11b)$$

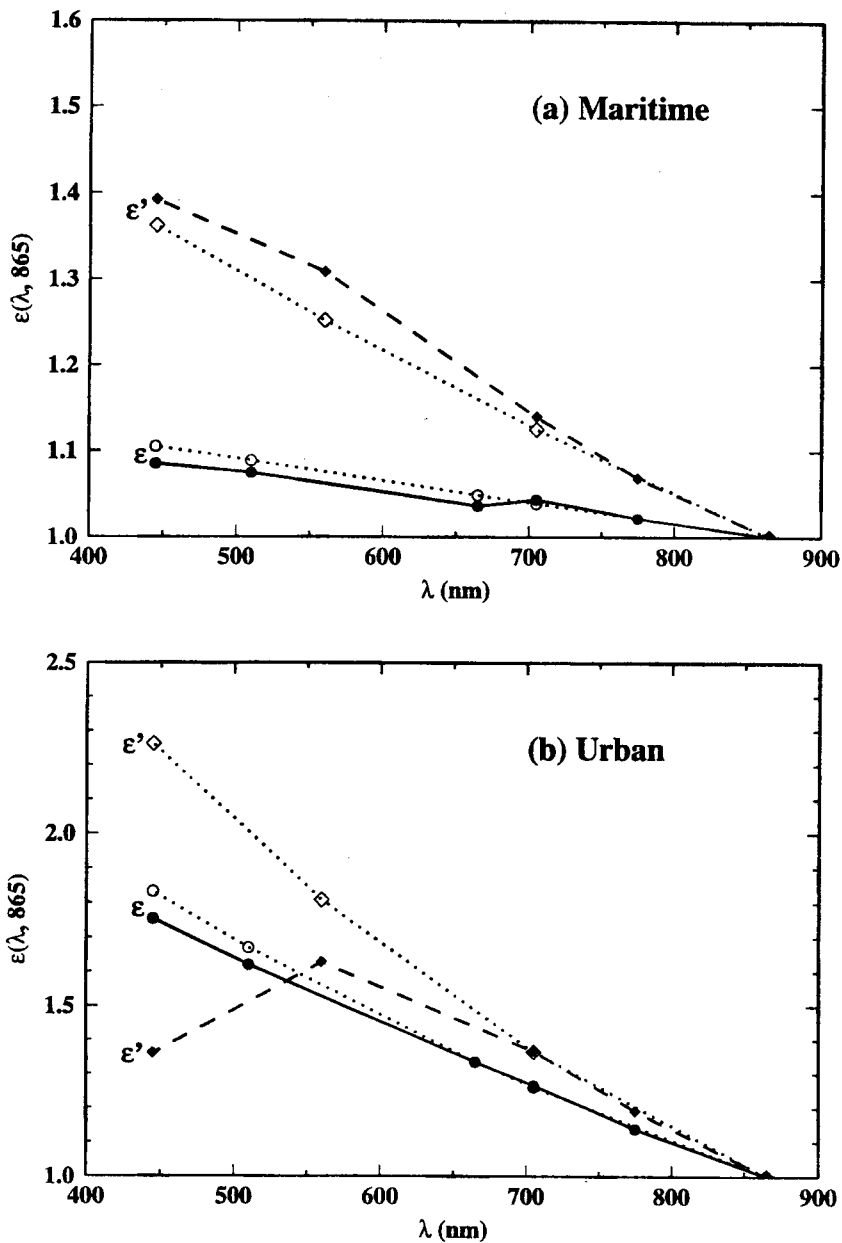


Figure 2. The ratios $\varepsilon(\lambda, 865)$ (solid curve, black circles; equation (9)), and the ratio $\varepsilon'(\lambda, 865)$ (dashed curve, black diamonds; equation (12)), plotted as a function of λ , and when $\tau_a(550) = 0.05$, $\theta_s = 60^\circ$, $\theta_v = 40^\circ$, and $\Delta\phi = \pi/2$. The dotted curves (open symbols) show the values of $\varepsilon(\lambda, 865)$ and $\varepsilon'(\lambda, 865)$ as extrapolated from $\varepsilon(775, 865)$ or $\varepsilon'(775, 865)$ through equation (10). (a) Maritime aerosol, (b) urban aerosol, both for $RH = 70\%$.

Equation (11a) is used below to provide some insight into the cause of failure in the single scattering algorithm, and will serve as a basis for the algorithm proposed in this paper.

When the single scattering algorithm is used, the difference $[\rho_{\text{path}}(\lambda_1) - \rho_r(\lambda_1)]$ has to be calculated at two wavelengths to form the following ε' ratio (see Gordon and Castaño 1987, Martin and Perry 1994; ε' is called $\varepsilon^{(e)}$ in Wang and Gordon (1994))

$$\varepsilon'(\lambda_1, \lambda_2) = \frac{\rho_{\text{path}}(\lambda_1) - \rho_r(\lambda_1)}{\rho_{\text{path}}(\lambda_2) - \rho_r(\lambda_2)} \quad (12a)$$

Writing equation (12a) implicitly assumes that the difference $[\rho_{\text{path}}(\lambda_1) - \rho_r(\lambda_1)]$ is equal to ρ_{as} . Considering equation (11a), ε' can be rewritten as

$$\varepsilon'(\lambda_1, \lambda_2) = \frac{\rho_a^*(\lambda_1) + \rho_{\text{ra}}^*(\lambda_1) + [\rho_r^*(\lambda_1) - \rho_r(\lambda_1)]}{\rho_a^*(\lambda_2) + \rho_{\text{ra}}^*(\lambda_2) + [\rho_r^*(\lambda_2) - \rho_r(\lambda_2)]} \quad (12b)$$

The difference $[\rho_r^*(\lambda_1) - \rho_r(\lambda_1)]$ in equation (12b) is systematically negative (Antoine and Morel 1998), thus the difference $[\rho_{\text{path}}(\lambda_1) - \rho_r(\lambda_1)]$ has no precise physical meaning, and *a fortiori* is not equal to the operational quantity ρ_{as} . The ratio ε' accounts for multiple scattering (even if not rigorously), whereas ε is only a theoretical value, to the extent that equation (8) is only valid under assumptions that are actually never met. The ε and ε' ratios are different in essence; there is no reason for them to behave similarly with wavelength. The discrepancy between ε and ε' is illustrated in figure 2, for two aerosol models and $\tau_a(550) = 0.05$. In the NIR, where multiple scattering should be of minor importance, $\varepsilon(775,865)$ markedly differs from $\varepsilon'(775,865)$. Moreover, the difference between the two ε is increasingly large toward the visible. The relative success of equation (10) in performing atmospheric correction at low τ_a is due to its ability to roughly reproduce the actual $(\rho_{\text{path}} - \rho_r)$ difference in the visible. The performance of equation (10) does not result from the fact that when $\varepsilon' \sim \varepsilon$, when $\tau_a \rightarrow 0$. Actually, when $\tau_a \rightarrow 0$, ε' and ε continue to differ conceptually and numerically (see figure 2), before being both undefined when aerosols are absent.

2.3. Principle of the multiple scattering algorithm

In as much as the molecular phase function is stable, the multiple scattering regime that results from mixing of aerosols and molecules is shaped by the phase function and the single scattering albedo of aerosols. The effect of multiple scattering on the path reflectance is therefore difficult to assess, precisely because the aerosol optical properties are the unknowns of the problem. A solution lies in establishing unambiguous relationships between a given aerosol type and the effect of multiple scattering on reflectances, when this aerosol is involved. To make use of such relationships, however, the aerosol type must be previously identified.

Antoine and Morel (1998) investigated the behaviour of the three terms in equation (11a). For a given aerosol, and whatever the geometry (θ_s , θ_v , $\Delta\phi$), the variations in ρ_r^* , ρ_a^* , and ρ_{ra}^* induced by increasing the aerosol load are as follows. The reflectance ρ_a^* increases nearly linearly when τ_a increases, and with slopes decreasing with wavelength and always lower than the slope of the unique $\rho_a(\tau_a)$ curve. The reflectance ρ_a^* is thus always smaller than the reflectance ρ_a . When aerosols are introduced, heterogeneous scattering appears and the reflectance ρ_r^* abruptly decreases from the ρ_r value. For additional aerosol loading, the reflectance ρ_r^* smoothly diminishes as ρ_{ra}^* continues to increase. In the end, the change in ρ_{path} resulting from the simultaneous changes of its three constitutive terms is nearly linear. These results are qualitatively valid either for absorbing or non-absorbing aerosols.

The change in ρ_{path} can be expressed in relative terms by forming the ratio $(\rho_{\text{path}}/\rho_r)$. This ratio depicts the relative increase in reflectance brought about by the progressive addition of aerosols within an atmosphere initially free from aerosols. For a given aerosol, a given wavelength and a given geometry, it is monotonically

related to τ_a through

$$(\rho_{\text{path}}/\rho_r) = (\rho_r^* + \rho_a^* + \rho_{ra}^*)/\rho_r = f(\tau_a) \quad (13)$$

where the function $f(\tau_a)$ is the unambiguous relationship used to assess multiple scattering effects. Using this function, however, cannot provide separate estimates of the aerosol and Rayleigh reflectances. Examples of this function are displayed in figure 3, for $\lambda = 865$ and 775 nm and for several aerosol models.

This figure also serves the purpose of describing the successive steps of the proposed algorithm. These steps consist of identifying in the NIR a couple of aerosol models as the closest to the actual aerosol and then using the spectral characteristics of these two models to correct the observations in the visible. More precisely, the successive steps are as follows, and the numbering below refers to the circled numbers in figure 3.

- (1) The ratio $(\rho_{\text{path}}/\rho_r)$ is formed at 775 and 865 nm, where ρ_{path} is the measured path reflectance ($\rho_{\text{path}} = \rho_t$ because $\rho_w = 0$ in the NIR), and ρ_r is the reflectance for an aerosol-free atmosphere, pre-computed and stored in look-up tables.
- (2) Because multiple scattering effects depend on the aerosol type, several values of $\tau_a(865)$ are compatible with the value of $(\rho_{\text{path}}/\rho_r)$ at 865 nm, and each one corresponds to a given aerosol model (equation (11a)).
- (3) This set of $\tau_a(865)$ values is then converted into the equivalent set at 775 nm, by making use of the spectral attenuation coefficients of each aerosol, according to

$$\tau_a(775) = \tau_a(865) [c(775)/c(865)] \quad (14)$$

- (4) To these $\tau_a(775)$ values correspond several values of the ratio $(\rho_{\text{path}}/\rho_r)$ at 775 nm, which differ according to the aerosol type.

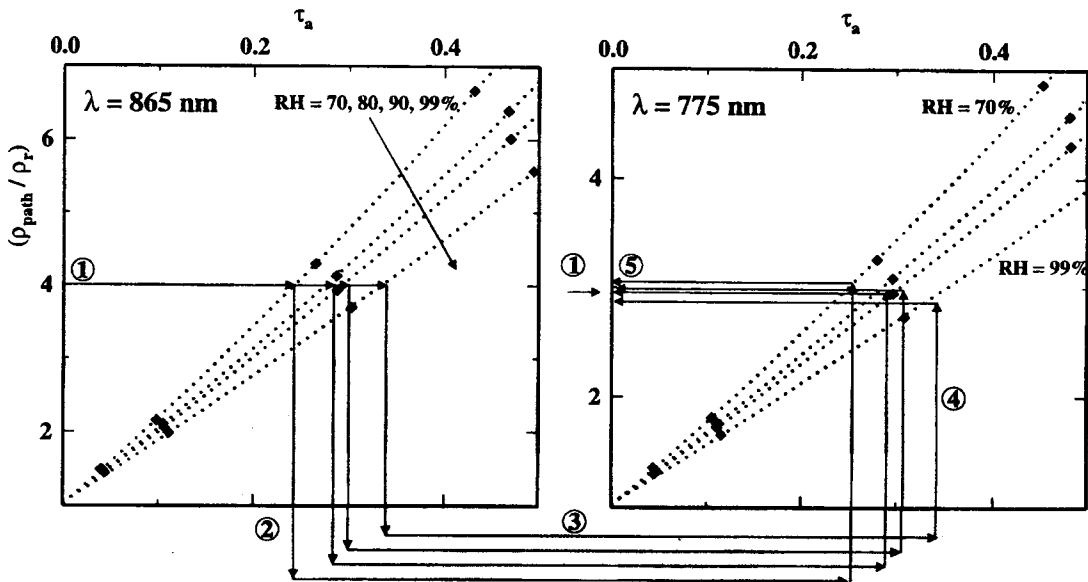


Figure 3. Variation of the path reflectance at 865 and 775 nm as a function of τ_a , and expressed as the ratio $(\rho_{\text{path}}/\rho_r)$, when $\theta_s = 40^\circ$, $\theta_v = 30^\circ$ and $\Delta\phi = \pi/2$. The maritime aerosol model is used, for four values of the relative humidity as indicated. Arrows symbolize a possible way to identify a couple of aerosol models enclosing the actual aerosol. The circled numbers identify the successive steps of this scheme, as discussed in the text (§2.3).

- (5) Comparing this set of values to the actual ratio $(\rho_{\text{path}}/\rho_r)$ at 775 nm (computed at step 1) allows the two aerosol models that most closely bracket the actual $(\rho_{\text{path}}/\rho_r)$ ratio to be selected. A 'mixing ratio', hereafter denoted X , can be computed from the actual and the two bracketing values of $(\rho_{\text{path}}/\rho_r)$ at 775 nm

$$X = \frac{(\rho_{\text{path}}/\rho_r)_{\text{actual}} - (\rho_{\text{path}}/\rho_r)_{\text{aerosol1}}}{(\rho_{\text{path}}/\rho_r)_{\text{aerosol2}} - (\rho_{\text{path}}/\rho_r)_{\text{aerosol1}}} \quad (15)$$

The remaining steps of the algorithm rest on the assumption that X is invariable with wavelength (Gordon and Wang 1994 a). It is then possible to estimate $(\rho_{\text{path}}/\rho_r)$ for the visible wavelengths from its values at 775 and 865 nm, provided that the relationships with τ_a (equation (13)) have been previously established for the appropriate wavelengths. Atmospheric correction of the visible observations is achieved by re-multiplying the ratio $(\rho_{\text{path}}/\rho_r)$ by the value of ρ_r , leading to ρ_{path} , and therefore to the marine reflectances:

$$(\rho_{\text{path}}/\rho_r)(\lambda_{\text{vis}})_{\text{actual}} = (\rho_{\text{path}}/\rho_r)(\lambda_{\text{vis}})_{\text{aerosol1}} X + (\rho_{\text{path}}/\rho_r)(\lambda_{\text{vis}})_{\text{aerosol2}} (1 - X) \quad (16)$$

$$\rho_w = \{ \rho_t - [(\rho_{\text{path}}/\rho_r)_{\text{actual}} \rho_r] \} / t_d \quad (17)$$

where the diffuse transmittance, t_d , is approximated as (e.g. Gordon *et al.* 1983)

$$t_d(\lambda, \theta_v) = \exp[\{ \tau_{\text{ag}}(\lambda) + [1 - \omega_r(\lambda) F_r(\lambda)] \tau_r(\lambda) + [1 - \omega_a(\lambda) F_a(\lambda)] \tau_a(\lambda) \} / \mu_v] \quad (18)$$

If the selection of the two bracketing aerosol models is realistic, and if the independence of X on wavelength is verified, the accuracy when retrieving $(\rho_{\text{path}}/\rho_r)$ in the visible is, in principle, independent of τ_a . Therefore, provided that the aerosol has been correctly identified, the errors in atmospheric correction are mainly due to the slight, yet inevitable, differences between X as calculated at 775 nm and the actual value of X in the visible.

Aerosol optical thickness at 865 nm is retrieved as a by-product of the atmospheric correction, and as the mean of the two values associated with the two bracketing aerosol models (see Gordon 1997). The aerosol optical thickness can be estimated at any wavelength in the visible from its value at 865 nm, by using the spectral characteristics of the two selected aerosol models.

3. Selection of aerosol models and test of the algorithm

3.1. Principle of, and conditions selected for, the algorithm implementation

Implementing the proposed algorithm consists in establishing the $f(\tau_a)$ function from radiative transfer simulations for a set of aerosol models, and for several wavelengths (λ) and geometries ($\theta_s, \theta_v, \Delta\phi$). In these simulations the choice of aerosol models is critical, particularly regarding their spectral optical thicknesses. Assumptions about the composition and vertical distribution of these aerosols are mandatory because they are highly variable in the real world. Generic cases are thus defined and used in simulations of the radiative transfer, in view of generating look-up tables for the function $f(\tau_a)$.

A two-layer representation has often been adopted for the vertical structure of the atmosphere, with aerosols confined within the boundary layer and all molecules above (e.g. Deschamps *et al.* 1983, Gordon and Wang 1994 a). Such a model was motivated by the observation that the bottom layers of the atmosphere are the main contributors to the aerosol optical thickness, whereas most molecules occupy higher

levels. Uncoupling the two scattering media is indeed a valid simplification when aerosols are non-absorbing; minute differences are observed when TOA total reflectances are computed either for a simplified two-layer atmosphere or for 50-layer atmospheres with a mixing of aerosols and molecules (Antoine and Morel 1998). When the aerosol does absorb, however, its vertical repartition and extension can no longer be neglected, so that atmospheres with layers of finite thickness must be considered (Gordon 1997). In addition, the two-layer representation inevitably accounts for only one aerosol type, whereas it is recognized that several kinds of aerosols occupy different atmospheric levels (e.g. World Climate Research Program (WCRP) 1986). According to this observation, the boundary layer (0–2 km), the free troposphere (2–12 km), and the stratosphere (12–50 km) are separately considered in the present work. Aerosols are assumed to be uniformly mixed within each of these three layers (figure 4).

To generate TOA total radiances for molecular or compound (molecules plus aerosols) atmospheres, Monte Carlo simulations of the radiative transfer were carried out by using a code already described (Morel and Gentili 1991, 1993), and validated against other radiative transfer codes (Mobley *et al.* 1993). This code does not account for polarization and the simplified geometry of a plane-parallel atmosphere is adopted. Photons are collected at the TOA level within 432 solid angles ('photon counters') defined by 5° increments in zenith angle and 7.5° increments in azimuth; there is no counter aiming directly at nadir. The apparent diameter of the Sun disc is set to 0.5° .

For Rayleigh scattering, a 50-layer profile is taken from Elterman (1968), in correspondence with $\tau_r = 0.0904$ at 550 nm, i.e. a standard atmosphere with an atmospheric pressure of 1013.25 hPa (figure 4). The anisotropy of the air molecules is ignored, the depolarization factor is zero, and the spectral dependency is expressed as $\lambda^{-4.09}$. Gas absorption is reduced to that of ozone, with a 50-layer vertical

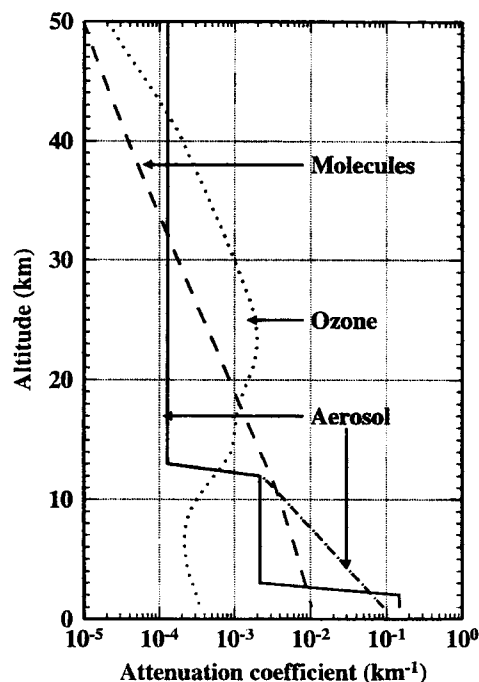


Figure 4. Vertical profiles of the attenuation coefficients used in the present work, for $\lambda = 560$ nm. The profiles for molecules and ozone are from Elterman (1968). The vertical profiles for aerosol attenuation are described in the text.

distribution also taken from Elterman (1968) (figure 4), and resulting in a total ozone content of 350 DU ($1 \text{ DU} = 2.69 \times 10^{16} \text{ molecules cm}^{-2}$). The selection of various aerosol types and of their vertical distribution is dealt with later on.

This atmosphere is bounded by a flat, Fresnel-reflecting, interface (i.e. no wind) with a perfectly absorbing ocean, so that multiple crossings of the interface by photons are not considered. This uncoupling of atmosphere and ocean is fully verified for Case 1 waters in the NIR, and is an acceptable approximation for the visible wavelengths. The expression 'TOA total reflectance' hereafter used means therefore the sum of the path reflectance simulated above a black ocean plus the water-leaving reflectance independently calculated through equation (2) and transmitted through the atmosphere (equation (18)). The algorithm first uses the total radiance measured in NIR bands, which is equal to the path radiance because there is no oceanic signal for Case 1 waters. The principle and implementation of the algorithm would remain the same over Case 2 waters, provided that the non-zero signal in the NIR has been previously assessed or assumed in an independent way, and subtracted from the total reflectance. It has been verified that the accuracy of the Monte Carlo outputs, when a reasonable number of photons is used, is typically 2% (when results are compared to those obtained, for instance, with a code based on the 'matrix operator method'). Lowering this noise to 1% would necessitate about four times more photons (and computation time). In addition, such a 2% noise is deliberately accepted in the pseudo data, in view of simulating in a more realistic way the outputs of a real instrument, the radiometric accuracy of which is not expected to be better than 2%.

Simulations were carried out to generate the ρ_{path} values for six wavelengths, several geometries (θ_s , θ_v , $\Delta\phi$) and four aerosol optical thicknesses (see table 2). The same geometries and wavelengths were considered to calculate ρ_r . For each aerosol model and each ensemble made up of (λ , θ_s , θ_v , $\Delta\phi$), five couples ($(\rho_{\text{path}}/\rho_r)$, τ_a), including the couple (1, 0) for an aerosol-free atmosphere, were fitted to a third-order polynomial, to express the $f(\tau_a)$ function (equation (13)), and the corresponding coefficients stored.

3.2. Clear maritime atmospheres

3.2.1. Defining the structure of the atmosphere and the aerosol types

The presence within the atmosphere of a peculiar aerosol type, the vertical location and extension of this aerosol and its relative proportion in the total aerosol load depend on the past trajectory of the air mass in question and also on local processes (e.g. generation of sea spray by wind, pumping of aerosols by clouds). When the air mass is free from any significant continental influence, the aerosols in the marine boundary layer are usually produced locally (e.g. Hoppel *et al.* 1990) and

Table 2. Relevant information for the radiative transfer simulations performed in the present work.

Parameter	Sampling
Wavelengths, λ (nm)	443, 510, 560, 705, 775, 865
θ_s	From 20 to 68 degrees, every 4 degrees
θ_v , $\Delta\phi$	The upper hemisphere is divided into 432 counters, according to $\Delta\phi_v = 5$ degrees and $\Delta(\Delta\phi) = 7.5$ degrees
τ_a	0.03, 0.1, 0.3, 0.5 at 550 nm for clear maritime atmospheres 0.05, 0.2, 0.5, 0.8 at 550 nm for absorbing aerosols

are therefore of the maritime type. This situation can be described by the vertical structure proposed by WCRP (1986), which is adopted here to represent clear maritime atmospheres (figure 4).

The non-absorbing maritime aerosol of the oceanic boundary layer is mainly composed of liquid water and sea-salt particles (the 'sea-salt component'), with a residual background of small continental particles, with sizes below about $0.05\ \mu\text{m}$ ('water-soluble' particles, e.g. ammonium, calcium sulphate, organic compounds). Within the free troposphere, a background of aerosols from continental origin is always present, with a slight absorption ($\omega \sim 0.9\text{--}0.95$) and an Ångström exponent of about 1.5 (small particles). The optical thickness of this aerosol is fixed to 0.025 at 550 nm. Finally, the stratosphere contains a background of non-absorbing particles, consisting of a 75% solution of sulphuric acid in water (H_2SO_4), with extremely low optical thickness (~ 0.005 at 550 nm). The boundary layer aerosol typically contributes 75% of the total aerosol optical thickness at 550 nm. The influence of the constant contribution of the continental and H_2SO_4 aerosols on the spectral variation of optical thickness is nevertheless significant. It results in spectral changes close to those observed over remote ocean areas (e.g. Reddy *et al.* 1990, Villevalde *et al.* 1994), with Ångström exponents between about 0 and 0.5, when the wavelengths 443 and 865 nm are considered (see figure 5).

The aerosol models for each layer are constructed from the basic aerosol components defined in Shettle and Fenn (1979) and in WCRP (1986) (details in tables 3a and 3b). The aerosol phase functions here computed using Mie theory for the six MERIS bands selected for the present study (443, 510, 560, 705, 775 and 865 nm). The word 'assemblage' is used to describe the ensemble composing the

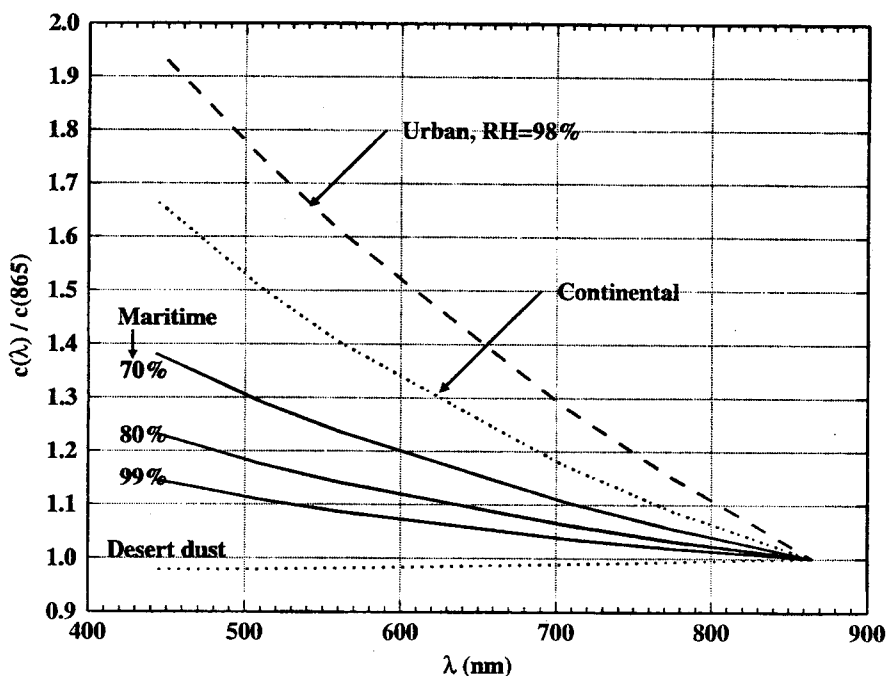


Figure 5. Aerosol extinction normalized at 865 nm, as a function of wavelength. Solid curves from top to bottom: 'standard assemblage' with the maritime model for $RH=70$, 80 and 99%. Dashed curve: assemblage containing the urban model, with $RH=98\%$. Lower dotted curve: assemblage containing desert dust (75% of the optical thickness of the whole troposphere). Upper dotted curve: assemblage containing the continental aerosol (50% of the optical thickness of the whole troposphere).

Table 3a. Aerosol components and their respective contributions (as per cent of the volume or as per cent of the number of particles) in the composition of the aerosol models. The principle of 'external mixing' was applied when calculating the optical properties of the aerosol models.

Aerosol model	Components	Volume %	Particle %
Maritime (Shettle and Fenn 1979)	Rural aerosol mixtures ^a		99
	Sea-salt solution in water		1
Urban (Shettle and Fenn 1979)	Rural aerosol mixtures ^a		80
	Soot		20
Continental (WCRP 1986)	Water soluble	29	93.876
	Dust-like	70	2.27×10^{-6}
	Soot	1	0.06123
Dust (Schütz 1980)	Desert dusts	100	100
H ₂ SO ₄ (WCRP 1986)	75% solution of sulphuric acid in water	100	100

^a 70% of water soluble particles and 30% of dust-like particles.

Table 3b. Parameters defining the size distribution of the various aerosol components of the aerosol models used in the present work.

Aerosol component	Parameters of the size distribution				
		r_0	$\sigma/\ln(10)$	$\exp\sigma$	
Rural aerosol mixtures (Shettle and Fenn 1979)	RH 70%	0.02846	-0.35	2.238724	
	RH 80%	0.03274			
	RH 85%	0.03679			
	RH 90%	0.03884			
	RH 95%	0.04238			
	RH 99%	0.05215			
Sea-salt solution in water (Shettle and Fenn 1979)	RH 70%	0.2041	0.40	0.251188	
	RH 80%	0.3180			
	RH 85%	0.3777			
	RH 90%	0.3803			
	RH 95%	0.4606			
	RH 99%	0.7505			
Urban (Shettle and Fenn 1979)	RH 70%	0.02911	0.35	2.238724	
	RH 80%	0.03514			
	RH 85%	0.03961			
	RH 90%	0.04187			
	RH 99%	0.05996			
Desert Dust (Schütz 1980)		0.500	0.350	2.20	
Water soluble (WCRP 1986)		0.005	0.475	2.99	
Dust-like (WCRP 1986)		0.500	0.475	2.99	
Soot (WCRP 1986)		0.0118	0.300	2.00	
75% H ₂ SO ₄ (WCRP 1986)		$\frac{A}{324}$	$\frac{\alpha}{1}$	$\frac{\gamma}{1}$	$\frac{b}{18}$

three aerosols located in the boundary layer, the free troposphere and the stratosphere. Five 'standard assemblages' are defined, which only differ by the relative humidity of the maritime aerosol within the boundary layer (i.e. 70, 80, 85, 90 or 99%), the optical thickness of which can vary (contrary to the constant aerosol backgrounds within the free troposphere and the stratosphere, see table 4). The assemblage for $RH=85\%$ is only used to test the algorithm and is not accordingly a part of the look-up tables. This aerosol differs from the aerosols in the look-up tables, yet belongs to the same 'family'. To test the algorithm, marine reflectances were computed for various chlorophyll concentrations (equation (2)) and added to the simulated values of ρ_{path} in the visible to obtain the total reflectances at the TOA level. Note that the choice of a restricted set of four candidate aerosol models for maritime atmospheres is the basis of the algorithm implementation. These four models are systematically used in the first stage of the atmospheric correction; when more complex atmospheres are present (see later), they are identified by their divergence with respect to the basic models.

Table 4. Construction of the aerosol assemblages (the stratosphere always contains the same H_2SO_4 aerosol, with $\tau_a = 0.005$ at 550 nm, following WCRP (1986)).

Assemblage	Boundary layer (0–2 km)	Free troposphere (2–12 km)	<i>N</i>
Standard maritime	Maritime aerosol (S&F79 ^a) $RH = 70, 80, 85^b, 90, 99\%$	Continental aerosol (WCRP 1986) $\tau_{(550)} = 0.025$	5
Urban	Urban aerosol (small particles) (S&F79) with $RH = 70, 80, 85^b, 90, 99\%$	As above	5
Urban ^b	Urban aerosol (large particles) (S&F79) with $RH = 80\%$	As above	1
Mixing of dust plus maritime ^b	Maritime aerosol (S&F79) plus desert dust (Schütz 1980), 10 or 50% of the particle number	As above	1
Continental aerosol	Maritime aerosol (S&F79) with $RH = 70, 80, 85^b, 95, 99\%$	Continental aerosol (WCRP 1986) $mx^c = 25, 50$ or 75%	15
Desert dust	As above	Desert dust (Schütz 1980) $mx^c = 25, 50$ or 75%	15
Desert dust ^b	Maritime aerosol (S&F79) $RH = 80\%$	Desert dust (WCRP 1986) $mx^c = 50\%$	1
Desert dust ^b	As above	Desert dust (WCRP 1986) $mx^c = 50\%$ (layer thickness = 4 km)	1
Haze ^b	As above	Haze C, with $n = 1.33$ or 1.50	2
Mixing of dust plus maritime ^b	Maritime aerosol (S&F79) plus desert dust (Schütz 1980), 10 or 50% of the particle number. Scale height of 3 km		1
Urban ^b	Urban aerosol with small particles (S&F79), with $RH = 80, 99\%$ Scale height of 3 km		2

^a S&F79 stands for Shettle and Fenn 1979.

^b Aerosol assemblages used only for tests or sensitivity studies (i.e. not included in the look-up tables).

^c mx stands for mixing ratio, i.e. the contribution of the aerosol in the free troposphere to the optical thickness of the whole troposphere.

3.2.2. Testing the algorithm

Examples of errors in the retrieved marine reflectances at $\lambda=443$ nm and 560 nm (hereafter referred to as $\Delta\rho_{443}$ and $\Delta\rho_{560}$) are displayed in figure 6, for a test with the maritime aerosol model with $RH=85\%$ and $\tau_a(550)=0.1$ (i.e. a 'mean' for remote oceanic conditions). The geometries are extracted from MERIS scenes that would be acquired at the summer solstice (figures 6(a) and 6(b)) and vernal equinox (figures 6(c) and 6(d)). The results are presented either across track at latitude 45° north (figures 6(a) and 6(c)) or along track from the Equator to the latitude 70° north, and when viewing at the scan edge (figures 6(b) and 6(d)). The required accuracy is met by the algorithm for all geometries, with most of the errors well below 1×10^{-3} in reflectance, either at 443 or 560 nm, and nearly all errors within $\pm 2 \times 10^{-3}$. The errors at 560 nm are about $\frac{1}{2}$ to $\frac{1}{4}$ of the errors at 443 nm (even if sometimes $\Delta\rho_{443} < \Delta\rho_{560}$) as also found by Gordon (1997) for another algorithm. The performance of the algorithm remains roughly the same for a given θ_v whatever the sun altitude (and up to $\theta_s = 65^\circ$, figures 6(b) and 6(d)) and for a given value of θ_s whatever the viewing angle (figures 6(a) and 6(c)). Therefore, the accuracy of the present algorithm would be preserved regardless of latitude and time of the year. This point

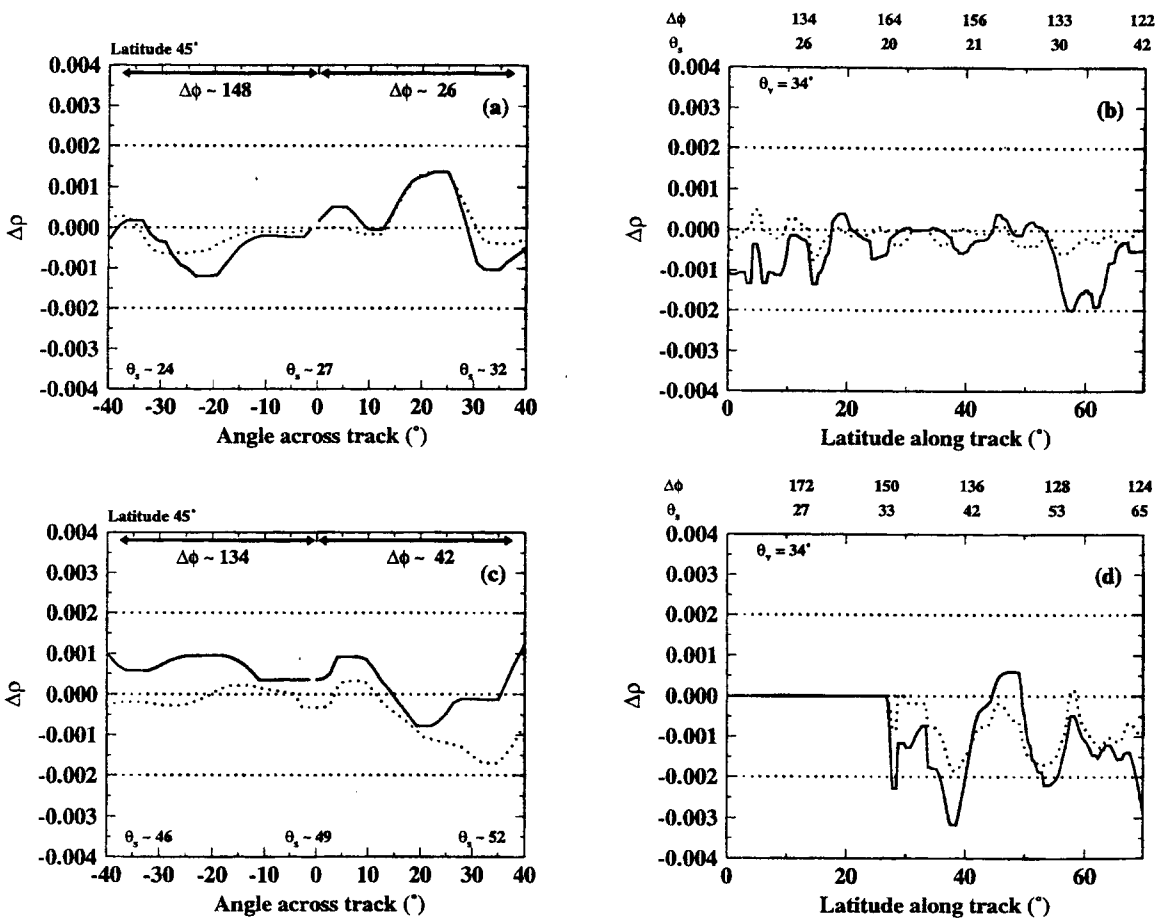


Figure 6. Error in the retrieved marine reflectance at 443 nm (solid curves) and 560 nm (dotted curves) for the maritime aerosol with $RH=85\%$ and $\tau_a(550)=0.1$. Panels (a) and (b): summer solstice (21 June). Panels (c) and (d): vernal equinox (21 March). The geometry corresponds either to a MERIS scan at 45° north (panels (a) and (c)), or to a MERIS track from the Equator to the latitude 70° north, the pixel observed being west of the sub-satellite point (panels (b) and (d)). In panel (d), results for latitudes $< 25^\circ$ were discarded as the geometry there corresponded to Sun glint area.

is critical for a meaningful assessment of the distribution and seasonal variations of the pigment concentration and aerosol optical thickness over the world ocean. The $\Delta\rho_{443}$ errors were pooled together for $\tau_a = 0.03, 0.1, 0.3$ and 0.5 at 550 nm, for the geometries corresponding to all pixels within each of the two scenes, and for the two dates. The distribution of these errors (not shown) showed no bias in the atmospheric correction, with 66% of the errors within $\pm 1 \times 10^{-3}$ and only 10% of the errors outside the range $\pm 2 \times 10^{-3}$. These percentages remained about the same when the pixels for $\tau_a = 0.5$ (a value unlikely above clear oceanic areas) were not included in the analysis, and this demonstrates that the algorithm accuracy does not depend too much on τ_a . The aerosol optical thickness at 865 nm was retrieved within $\pm 10\%$ in three-quarters of the cases examined and within $\pm 30\%$ for all of them. In summary, the algorithm is able to correctly retrieve the water-leaving reflectances for clear maritime atmospheres in most situations. In addition, it is likely that better results would have been obtained either by increasing the angular discretization in the look-up tables (i.e. decreasing the $\Delta\theta_s$, $\Delta\theta_v$, and $\Delta(\Delta\phi)$ given in table 2), or by increasing the number of candidate models (i.e. reducing the increment in RH).

Regarding atmospheric correction, 'apparent' marine reflectances are derived, i.e. reflectances affected by the error in atmospheric correction. The impact of these errors on the chlorophyll concentration retrieval was assessed by re-estimating the ratio (b_b/a) at 443 and 560 nm from these 'apparent' reflectances. This operation was performed through an iterative use of equation (2), which was initialized with mean values of the (f/Q) ratio (Morel and Gentili 1996). The ratio $A_{443,560}$ was then formed and a new pigment concentration derived.

Each of the three histograms in figure 7 merges the errors in the retrieved chlorophyll concentration for $\tau_a = 0.03, 0.1, 0.3$ and 0.5 at 550 nm, the geometries corresponding to all pixels within each of the two scenes, and for the two dates (summer solstice and vernal equinox). These errors are expressed in terms of a number of *Chl* classes: values between x and $x+1$ (x being an integer between 0 and 3) mean that the retrieved *Chl* concentration is overestimated by x (*Chl*) class. Along the same lines, values between $x-1$ and x mean that the retrieved *Chl* concentration

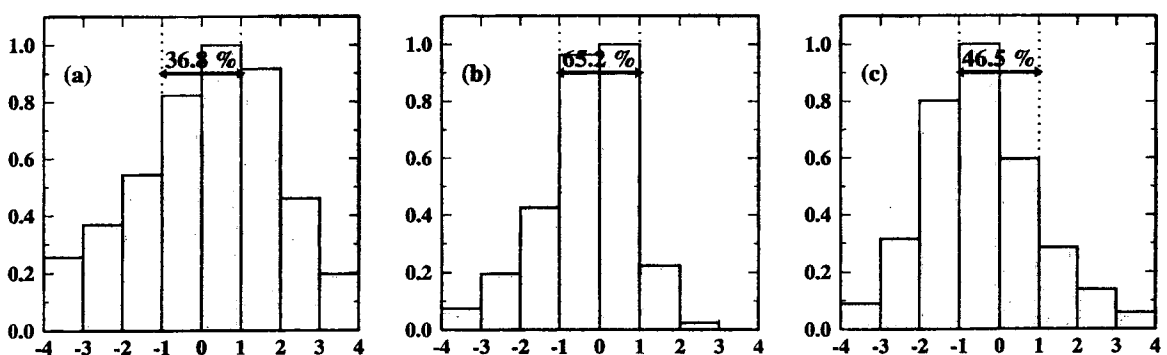


Figure 7. Histograms of the error in the retrieved chlorophyll concentration, *Chl*, due to the error $\Delta\rho$ in the atmospheric correction (see text for conditions). These errors are expressed as a number of *Chl* classes: values between x and $x+1$, with x being an integer between 0 and 3, mean that the retrieved *Chl* concentration is overestimated by x class. In the same way, values between $x-1$ and x mean that the retrieved *Chl* concentration is underestimated by x class. Therefore, all values between -1 and $+1$ correspond to an 'exact retrieval' in terms of *Chl* classes (as indicated by percentages). The initial chlorophyll concentration was $0.03\ mg\ m^{-3}$ for panel (a), $0.3\ mg\ m^{-3}$ for panel (b) and $3\ mg\ m^{-3}$ for panel (c).

is underestimated by x (Chl) class. Therefore, all values between -1 and $+1$ correspond to an 'exact' retrieval in terms of Chl classes. Less than 40% of the retrievals fulfil this condition when $Chl=0.03 \text{ mg m}^{-3}$ (figure 7(a)), and a slight positive bias affects the retrieved concentrations. The results for $Chl=0.3 \text{ mg m}^{-3}$ are in better shape, with no bias and 65% of exact retrievals (figure 7(b)). A bias of about minus one class (i.e. -20%) occurs for $Chl=3 \text{ mg m}^{-3}$, and 46% of the errors are within the limit of ± 1 class (figure 7(c)).

When $Chl=0.03 \text{ mg m}^{-3}$, the low percentage of exact retrievals is actually consistent with the severe accuracy requirement for the domain of low Chl (see figure 1(c); recall that a shift of only one class of concentration represents a -20% or $+25\%$ change in Chl). The discrimination of ten Chl classes between 0.03 and 0.3 mg m^{-3} , the initial aim, seems to be limited by the accuracy of the atmospheric correction. Lowering the number of Chl classes to be detected to five between 0.03 and 0.3 mg m^{-3} , for instance, would increase the acceptable errors in $\rho_w(443)$.

The bias observed when $Chl=3 \text{ mg m}^{-3}$ was not expected, to the extent that the errors in atmospheric correction are the same for the three panels of figure 7. Errors that do not bias the pigment retrieval for low and moderate chlorophyll concentrations (i.e. high $\rho_w(443)$) have an impact for higher concentrations because the actual blue-to-green ratio is close to one. This bias is a consequence of the nature of the algorithm, which performs extrapolation of the atmospheric contribution from the NIR toward the visible, with, in general, increasing errors with decreasing wavelength. As far as we know, this problem occurring for chlorophyll concentrations around 3 mg m^{-3} does not seem to have been acknowledged.

3.3. Atmospheres containing aerosols of continental origin, including absorbing ones

Compared to the mean composition previously used to model clear maritime atmospheres, significant changes in the concentration, type and vertical distribution of aerosols may occur within the troposphere. Air masses carrying particles of continental origin, either desert dusts or soot (strongly absorbing), or insoluble particles usually referred to as the 'rural aerosol' (moderately absorbing), are indeed often found above the ocean. The presence of such 'non-maritime' aerosols is neither totally anecdotal nor restricted to coastal areas. Saharan dust, for instance, is carried out westward over the North Atlantic, ultimately sinking within the ocean or on the coasts of eastern North America (e.g. Prospero and Carlson 1972, Savoie and Prospero 1977, Li *et al.* 1996). This dust is also blown northward over the western Mediterranean Sea (Moulin *et al.* 1997). Asian desert dusts are similarly observed over the Sea of Japan (Fukushima and Toratani 1997), and they probably also affect the whole north Pacific (Merrill *et al.* 1989). Moreover, the atmospheric transport of desert dusts could increase in coming years, due to changes in the use of land in desert regions (Andreae 1996). In coastal areas, aerosols of urban and industrial origin are also often observed, especially east of continents (Hoff *et al.* 1995). Aerosols produced by biomass burning have been also reported, particularly over the southern tropical Atlantic Ocean (Browell *et al.* 1995).

The spectral dependency of scattering as well as the single scattering albedo of these aerosols is markedly different from those of the 'standard' oceanic models (figure 5). As a consequence, the errors in the retrieved water-leaving reflectances might become prohibitively large to the extent that the atmospheric correction, based only on 'standard' maritime aerosols, cannot comply with the actual aerosol, exhibiting for instance a very different spectral dependence for scattering, or a strong

absorption. To account for the possible presence of such 'anomalous' aerosols, look-up tables can be built for an additional set of candidate aerosols, yet this necessary stage still remains insufficient. Indeed, when carrying out the correction, no *a priori* information can help in selecting either one look-up table or another, because the actual aerosol is unknown. In addition, it would be useless to consider all candidate models in the search, when only maritime aerosols are present most of the time. A method is proposed below to detect absorption, and the selection of adequate models for absorbing aerosols is detailed later on.

3.3.1. Detection of aerosol absorption

When only single scattering occurs, the spectral change of the aerosol reflectance (ρ_{as}) is governed by the spectral behaviour of the $\omega_a \tau_a p_a$ product (equation (8)). Assuming that ω_a is constant with wavelength (or, at least, without marked peaks), and with p_a approximately wavelength-independent, the spectral values of ρ_{as} do not allow absorbing and non-absorbing aerosols to be distinguished, because the product $\omega_a \tau_a$ may remain about the same for several combinations ($\omega_a < 1$ and high τ_a , or $\omega_a \sim 1$ and lower τ_a). The effect of absorption on the spectral change of reflectance becomes tangible only when multiple scattering occurs, and enhances absorption by increasing the photon path length (see the difference between the dotted and dashed curves in figure 2(b)). This phenomenon is significant in the visible domain. At these wavelengths, however, the marine signal is no longer negligible, and, in principle, prevents this part of the spectrum from being used to identify the actual aerosol. This dilemma can be resolved if assumptions are made about the marine signals at selected wavelengths, namely 705 and 510 nm in the present work (see also Carder *et al.* (1991) and Gordon *et al.* (1997a, b) who used other wavelengths).

The principle of detecting 'non-standard' aerosols (absorbing aerosols, or aerosols with a strong spectral dependence) is as follows: a first, tentative, correction is performed by using the standard set of four aerosol assemblages containing the maritime models. In this way, an estimate of the path reflectance at 510 nm is obtained. This estimated path reflectance is summed up to the supposed mean marine reflectance in order to derive a possible value for the total reflectance. If the assumption about the marine signal is correct, the difference between the actual and the guessed total reflectance provides the error in atmospheric correction.

For Case 1 waters the ocean is totally absorbing at 705 nm (i.e. no marine signal), so that the difference between the measured and estimated path reflectances directly provides the error in atmospheric correction

$$\Delta\rho(705) = \rho_{\text{path}}(705)_{\text{measured}} - \rho_{\text{path}}(705)_{\text{estimated}} \quad (19)$$

The 705 nm band, however, is still close to the bands at 775 and 865 nm, so that it would be useful only if absorption changed markedly from 775 to 705 nm, or, for less absorption or a flat absorption spectrum, if the spectral dependence of scattering of the actual aerosol significantly differed from that of the candidate models.

For oceanic Case 1 waters, experimental data suggest a rather stable reflectance at 510 nm, $R(0^-)(510)$, whatever *Chl* (the 'hinge point' (Duntley *et al.* 1974, Gordon and Clark 1981)). Bio-optical models (e.g. Gordon *et al.* 1988a, b, Morel 1988), mainly based on the interpretation of experimental data, accordingly predict a narrow range of values for $R(0^-)(510)$, over the whole domain of *Chl* (0.03 to 30 mg m⁻³). The curves displayed in figure 8 show limited variations of $R(0^-)(510)$. The data points in figure 8, extracted from measured reflectance spectra, also confirm

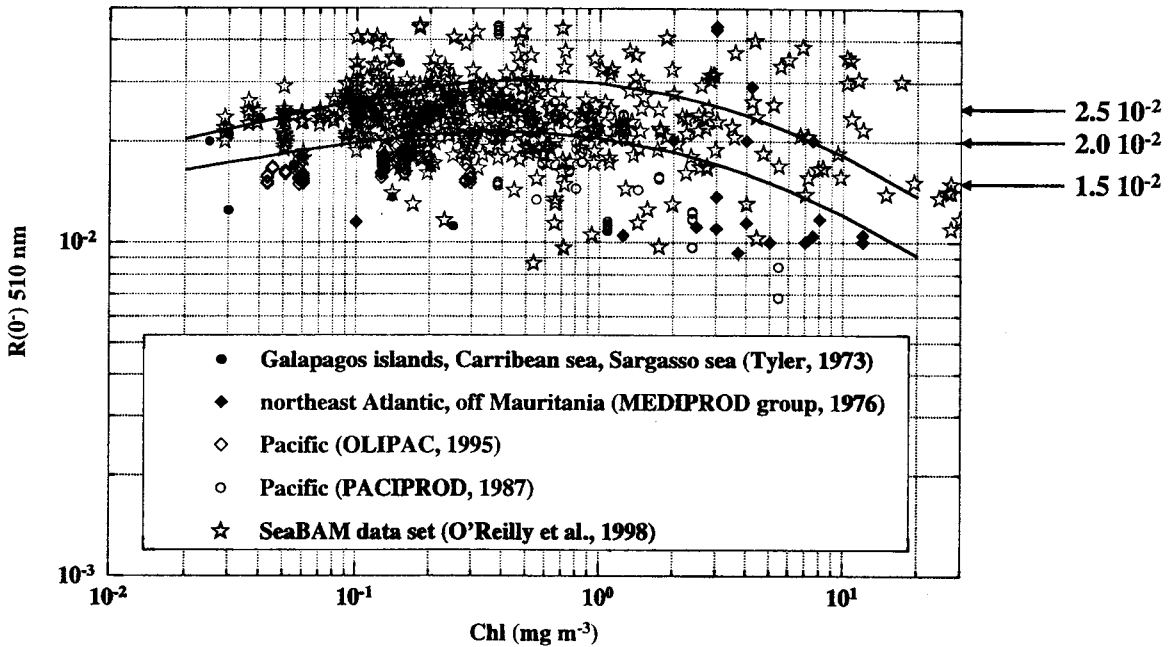


Figure 8. Diffuse reflectance of the ocean at 510 nm, $R(0^-)(510)$, for Case 1 waters with variable chlorophyll concentration. The two curves were obtained from the model of Morel (1988), either for the Sun at zenith (lower curve), or with a Sun zenith angle of 60° (upper curve) (see also Morel and Gentili 1991). Reflectance values extracted from spectra measured at sea are also shown, and the symbol corresponding to each cruise or dataset is shown in insert. The mean value of $R(0^-)(510)$, as well as this value plus or minus one standard deviation, is also indicated.

this constancy: however noisy these $R(0^-)(510)$ data may be, they at least do not show any significant trend. Therefore, it seems possible to assume a constant value of about 0.02 if the $R(0^-)(510)$ data shown in figure 8 are considered. The corresponding mean value for the normalized water-leaving reflectance, hereafter noted $[\rho_w(510)]_N$, would be then of about 1×10^{-2} (as $(\pi \mathcal{R}_0(f_0/Q_0)) \sim 0.47$), at least for the concentration range 0.03 to 3 mgChl m^{-3} (see figure 1(a)). This $[\rho_w(510)]_N$ value is slightly larger ($\sim +20\%$) than that (used in CZCS processing) derivable from a normalized water-leaving radiance of $5 \text{ mW m}^{-2} \text{ nm}^{-1} \text{ sr}^{-1}$ at 520 nm (Gordon and Clark 1981), when combined with an extraterrestrial irradiance of about $1900 \text{ mW m}^{-2} \text{ nm}^{-1}$ (Neckel and Labs 1984). The natural noise in the oceanic signal at 510 nm is accounted for by attaching to $[\rho_w(510)]_N$ an uncertainty of $\pm 5 \times 10^{-3}$ (at $\pm 1\sigma$).

To estimate the error in atmospheric correction at 510 nm , the $[\rho_w(510)]_N$ value has to be 'de-normalized', in view of being compared with the apparent water-leaving reflectance, which is the actual water-leaving reflectance plus the error in atmospheric correction. The transformation of $[\rho_w(510)]_N$ into $\rho_w(510)$ is performed through (see equations (2) and (3))

$$\rho_w(510) = [\rho_w(510)]_N (\varepsilon_c t_{\theta_s}) \frac{\mathcal{R}(\theta_s)}{\mathcal{R}_0} \frac{f(\theta_s)}{Q(\theta_s, \theta_v, \Delta\phi)} \left(\frac{f_0(\lambda)}{Q_0(\lambda)} \right)^{-1} \quad (20)$$

The use of the f/Q ratio in the above equation would necessitate that Chl is known, while it is not. The ratio of f/Q for the actual geometry to f_0/Q_0 is, however, nearly insensitive to Chl (changes are within $\pm 10\%$), at least in the concentration range 0.03 – 3.0 mg m^{-3} , and for geometries typical of ocean colour remote sensing.

Knowledge of the chlorophyll concentration is therefore not required for use of equation (20), and the error in atmospheric correction at 510 nm, $\Delta\rho(510)$, is obtained as

$$\Delta\rho(510) = [(\rho_t(510)_{\text{measured}} - \rho_{\text{path}}(510)_{\text{estimated}})/t_d(510)] - \rho_w(510) \quad (21)$$

The expression within the square brackets represents the 'apparent' water-leaving reflectance, and $\rho_w(510)$ is obtained through equation (20).

Thresholds of 2.5×10^{-3} for $|\Delta\rho(510)|$ and 1.5×10^{-3} for $|\Delta\rho(705)|$ were empirically adopted by examining the errors resulting from the use of the standard look-up tables, when the actual aerosol is absorbing. When errors are greater than these thresholds, they could result from an incorrect assumption of $[\rho_w(510)]_N$, rather than from an incorrect atmospheric correction. To lift the ambiguity, the test is carried out twice, first with the mean value of $[\rho_w(510)]_N$, and second with this value increased (decreased) by 5×10^{-3} when $\Delta\rho(510)$ is positive (negative). Absorbing aerosols are definitely identified if both tests indicate their presence. Practically speaking, the detection should occur when the difference between the actual and retrieved path reflectances at 510 nm is greater (in absolute value) than the sum of the threshold fixed above plus the uncertainty attached to the marine signal, i.e. $|\rho_{\text{path}}(510)_{\text{actual}} - \rho_{\text{path}}(510)_{\text{estimated}}| \gtrsim 6 \times 10^{-3}$ (i.e. about 10% of ρ_{path}). This $\rho_{\text{path}}(510)$ value approximately corresponds to $\tau_a = 0.2$ and represents the detection threshold of the method (it depends, however, on ω_a and on the spectral dependence of aerosol scattering). When absorption is detected, atmospheric correction in the visible channels is then carried out by using specific look-up tables, the content and use of which are now presented.

3.3.2. Selection of absorbing aerosol types

The stratospheric aerosol remains unchanged in any case, and three main categories of absorbing aerosols are considered as likely over the ocean, namely the continental aerosol, the desert dust aerosol (with 'long-range transport properties', i.e. absence of large particles (Schütz 1980)) and the urban aerosol (see table 3). The continental and desert dust aerosols are assumed to overlie the boundary layer maritime aerosol, within the free troposphere (2–12 km), as suggested by LIDAR experiments (e.g. Powell 1995). The urban aerosol replaces the maritime aerosol within the boundary layer (0–2 km).

For the urban aerosol, five assemblages are defined through the value of the relative humidity, with $RH = 70, 80, 85, 90$ and 99% . For the continental aerosol or the desert dust, the situation is more complicated, because two aerosols are simultaneously made varying, one within the free troposphere and the other within the boundary layer. The resulting aerosol assemblages are unambiguously defined by fixing the relative contributions of the two aerosols (boundary layer and free troposphere) to the total optical thickness of the whole troposphere at 550 nm. In view of encompassing several situations corresponding to increasing aerosol loads in the free troposphere, the contribution of this layer to the total optical thickness is set to 25, 50 or 75% (these percentages are not kept for other wavelengths because the spectral dependence of optical thickness differs between each aerosol within the assemblage). Assemblages were defined in this way for continental aerosols and for desert dust, with the above three values for the mixing ratio, combined with five values for the relative humidity of the maritime aerosol ($RH = 70, 80, 85, 95$ and 99%), leading to 15 assemblages for each of the two aerosol categories. Note that the assemblages

where $RH=85\%$ in the boundary layer are not part of the look-up tables—they are used for testing the algorithm. The look-up table for ‘anomalous’ candidate aerosols contains therefore 28 aerosol assemblages (four involving the urban aerosol, twelve involving the continental aerosol and twelve involving the desert dust; see table 4). It is believed that the spectral dependencies and single scattering albedos within this ensemble of models, including the standard assemblages, encompass most of the plausible situations for oceanic areas.

To avoid ambiguities when selecting aerosol models, all 28 models are not considered at once when the tests at 510 and 705 nm are positive. The sign of $\Delta\rho(510)$ indeed allows the number of candidate models to be restricted. In effect, the Ångström exponents for the continental aerosol (small particles) are larger than those of the maritime aerosol, and the errors $\Delta\rho(510)$ (equation (20)) are systematically positive (at least when these errors are significant). The converse situation ($\Delta\rho(510)$ negative) occurs in the presence of desert dust, which is characterized by strong absorption in the visible and larger particles. Groups of four aerosol models are then examined, each group corresponding to one value of the mixing ratio (i.e. 25, 50 or 75%) and to the four values of the relative humidity for the boundary layer maritime aerosol ($RH=70, 80, 95$ and 99%). Because the presence of the urban aerosol can lead to positive as well as negative errors, the group of four urban aerosols is actually always examined. A couple of aerosol models are selected within each group of candidate aerosols and the couple that leads to the minimum $|\Delta\rho(510)|$ is kept at the end.

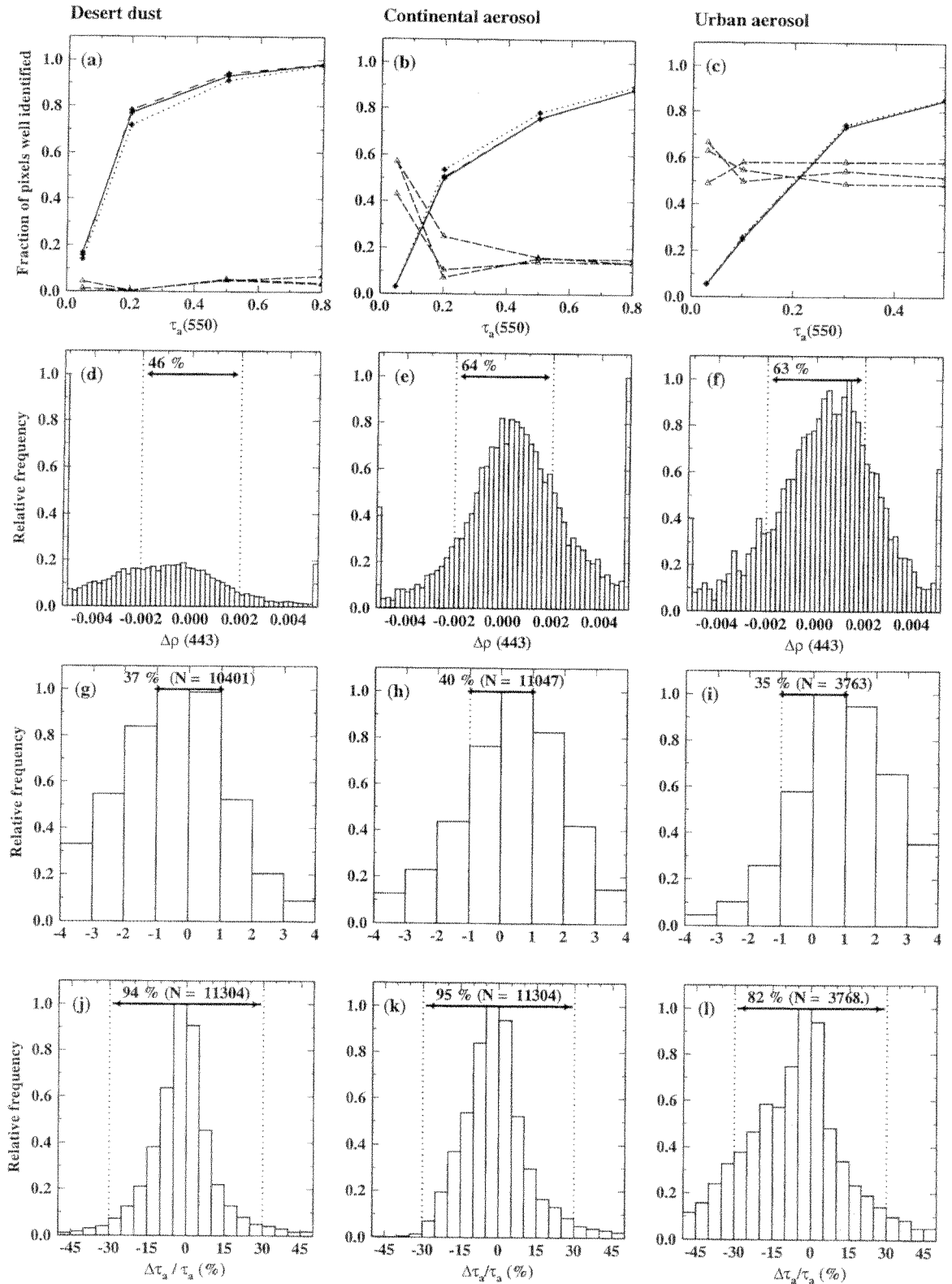
3.3.3. Testing the algorithm

The correction for ‘non-standard’ aerosols was tested for the assemblages containing desert dust and the maritime aerosol for $RH=85\%$ (mixing ratios of 25, 50 and 75% and $\tau_a=0.05, 0.2, 0.5$ and 0.8), for the assemblages containing the continental aerosol (same τ_a values as above) and the assemblage containing the urban aerosol for $RH=85\%$ (with $\tau_a=0.03, 0.1, 0.3$ and 0.5). All possible combinations of $(\theta_s, \theta_v, \Delta\phi)$, as regards the discrete values listed in table 2, are considered, except that θ_s is limited to 60 degrees and $\Delta\phi$ is sampled every 30 degrees (12 012 cases for desert dust and the continental aerosol; 4004 for the urban aerosol). There is no need for interpolation with respect to geometry within the look-up tables. The whole set of tests was carried out three times, by applying the algorithm to total reflectances computed for three chlorophyll concentrations ($0.03, 0.3$ and 3 mg m^{-3}). In this way, the validity of the tests (based on the assumption of a constant diffuse reflectance at

Figure 9. Synthesis of the results obtained when atmospheric correction is applied to atmospheres containing the three ‘non-standard’ aerosol assemblages, as indicated at the top of the figure (see text). In panel (d) to panel (l), vertical dotted lines delimit the domain of acceptable errors, also indicated by a percentage. The numbers in parentheses are the exact numbers of pixels considered in the histogram. Panels (a) to (c): fraction of pixels that were clearly identified by the tests at 510 and 705 nm (i.e. recognized as absorbing aerosols), as a function of τ_a . Solid curves are for actual *Chl* values of 0.03 mg m^{-3} , dotted curves for 0.3 mg m^{-3} , and dashed curves for 3 mg m^{-3} . The long dashed curves (open triangles) represent the fraction of pixels identified as containing absorbing aerosols, while the aerosol models were wrongly selected. Panels (d) to (f): histograms of the error in the retrieved marine reflectance at 443 nm. Panels (g) to (i): histograms of the error in *Chl* due to the error $\Delta\rho$ in the atmospheric correction, for nominal values of *Chl* of 0.3 mg m^{-3} (same situations as in panels (d) to (f)). Panels (j) to (l): histograms of the relative error in τ_a at 865 nm, for the same situations as in panels (d) to (f).

510 nm) can be assessed, provided that $[\rho_w]_N$ actually behaves with *Chl* as shown in figure 1(a). The results of these tests are displayed in figures 9(a) to 9(l).

As expected, the tests at 510 and 705 nm do not identify many of the absorbing aerosols when $\tau_a \lesssim 0.2$ at 550 nm (figures 9(a) to 9(c)). Most of the time, however, this failure has no significant impact on the accuracy of the marine reflectance retrieval, precisely because the addition of a moderate amount of absorbing aerosols



does not modify the TOA signals significantly. The function $f(\tau_a)$ (equation (13)) established for clear maritime atmospheres remains usable, even if the accuracy is a little less ($\Delta\rho(443)$ up to about ± 0.004). The detection skill of the model rapidly increases with optical thickness, so that absorbing aerosols are identified in 60 to 80% of the situations examined when $\tau_a \geq 0.2$. The uncertainty introduced in the detection of absorption by the assumption of a constant $[\rho_w]_N(510)$ is negligible, as shown in figures 9(a) to 9(c): the solid, dotted and dashed curves (black diamonds), which result from the use of $Chl=0.03$, 0.3 and 3 mg m^{-3} respectively, are nearly superimposed. The desert dusts were exclusively detected by the test at 705 nm in only 3% of the cases, whereas only the test at 510 nm was positive in about 24% of the remaining situations where dust was present. Both tests simultaneously identified absorption in 73% of the situations examined. The same three percentages are respectively 6, 24 and 70% for the continental aerosol, and 30, 21 and 49% for the urban aerosol. As expected, the efficiency of the test at 705 nm improves as aerosol absorption increases from 775 to 705 nm. The same conclusion is not so easily drawn for the test at 510 nm: a large Ångström exponent can be counterbalanced by a high absorption, leading sometimes to moderate errors at this wavelength. Finally, it is worth noting that the tests remain silent, as desirable, when there is no absorption by aerosols (i.e. for the standard atmospheres previously tested).

If attention had not been paid to whether absorbing or non-absorbing aerosols are present (i.e. no tests at 705 and 510 nm), the percentages of errors $\Delta\rho(443)$ within $\pm 2 \times 10^{-3}$ would have been only 8% for the desert dust, 32% for the continental aerosol and 48% for the urban aerosol. When the tests are performed and the additional look-up tables used, these percentages become 46, 64 and 63%, respectively, and their distribution is as shown in figures 9(d) to 9(f). About one third of the cases, however, lead to errors outside the $\pm 2 \times 10^{-3}$ limit. These larger errors correspond either to non-identification of the absorbing aerosol, or, when absorption has been identified, to inadequate selection of the couple of aerosol models. Such confusions are illustrated in figures 9(a) to 9(c) by the long-dashed curves (open triangles), which represent the fraction of pixels for which absorption was detected but an incorrect aerosol model was chosen. Ambiguities may indeed appear when the ratios ($\rho_{\text{path}}/\rho_r$) for several aerosol models are too close to one other.

When $Chl=0.3 \text{ mg m}^{-3}$, 37% of retrievals are exact for the situations with desert dust, 40% for the continental aerosol and 35% for the urban aerosol (figures 9(g) to 9(i)). These percentages become respectively 36, 23 and 15% when $Chl=0.03 \text{ mg m}^{-3}$, and 40, 48 and 45%, when $Chl=3 \text{ mg m}^{-3}$ (not shown). In addition, a bias of $\sim -20\%$ is observed for the higher chlorophyll concentration (as for the clear maritime atmospheres).

The aerosol optical thickness at 865 nm is retrieved without bias. Most of the relative errors in $\tau_a(865)$ are within $\pm 30\%$ and often considerably less (figures 9(j) to 9(l)). The results corresponding to the three aerosol assemblages, $\tau_a = 0.05, 0.2, 0.5$ and 0.8 (desert dust and the continental aerosol), or $\tau_a = 0.03, 0.1, 0.3$ and 0.5 (urban aerosol) are summarized in table 5.

The results obtained here for the 'non-standard' absorbing aerosols are not fully satisfactory, yet they are significantly better than those obtainable in the absence of detection of aerosol absorption. The situation with the urban aerosol and $Chl=3 \text{ mg m}^{-3}$ is the only case that does not show any improvement when the full algorithm is used. In a few intermediate situations, the percentage of exact Chl retrievals (in terms of Chl classes) is not much increased, whereas the median error

Table 5. Absolute and relative errors in the retrieved aerosol optical thickness at 865 nm, for the 'non-standard' aerosol assemblages, and the nominal values indicated for τ_a (550). The geometrical configurations pooled together for each case are as in figure 9.

		$\tau_a = 0.05$	0.20	0.50	0.80	Total
Desert dust	$\Delta\tau_a/\tau_a$ within $\pm 30\%$	82	98	99	99	94
	$\Delta\tau_a/\tau_a$ within $\pm 15\%$	48	88	94	92	82
	$\Delta\tau_a$ within ± 0.05	—	97	82	70	84
Continental	$\Delta\tau_a/\tau_a$ within $\pm 30\%$	92	96	99	99	96
	$\Delta\tau_a/\tau_a$ within $\pm 15\%$	60	70	71	73	79
	$\Delta\tau_a$ within ± 0.05	—	95	70	60	75
		$\tau_a = 0.03$	0.10	0.30	0.50	Total
Urban	$\Delta\tau_a/\tau_a$ within $\pm 30\%$	78	87	86	84	83
	$\Delta\tau_a/\tau_a$ within $\pm 15\%$	50	58	65	65	59
	$\Delta\tau_a$ within ± 0.05	—	—	65	52	58

is brought closer to zero. In fact, when the urban aerosol is excluded from the candidate models, the correct aerosol type is always selected for the desert dust and the continental aerosol. This observation indicates that the use of an aerosol climatology could probably increase the skill of the algorithm by allowing the elimination of *a priori* unlikely aerosols from the candidate models. An incorrect atmospheric correction is sometimes detectable through negative water-leaving reflectances at 443 nm. When these reflectances remain positive, the magnitude of the error at 510 nm may indicate which pixels should not be considered in a computation of chlorophyll concentration.

4. Sensitivity studies

4.1. Aerosol types and aerosol vertical distribution

The vertical structure adopted in the present work is derived from the observation that aerosols are not confined within the marine boundary layer. The persistence of a background of aerosols in the free troposphere and in the stratosphere is acknowledged, mainly thanks to LIDAR measurements (e.g. Merrill *et al.* 1989, Browell *et al.* 1995, Hoff *et al.* 1995). The rather simple sketch used for 'standard' maritime atmospheres was obviously not intended to encompass all possible situations. The maritime aerosol, for instance, is slightly different between the Pacific and Atlantic oceans (Villevalde *et al.* 1994). Saharan or Asian desert dusts have different optical properties, and their properties also evolve as a function of the time spent in the atmosphere and distance from the sources. Desert dust is not only present in the free troposphere, as it ultimately sinks into the ocean. Other peculiar situations could be described, differing more or less from the standard representation adopted here.

Examining the impact of the vertical distribution of aerosols is relevant to the case of absorbing aerosols, or, for non-absorbing aerosols, to the case where several types of particles are present within different atmospheric levels. For a unique non-absorbing aerosol, the path reflectance at the TOA level remains the same (at $\pm 0.5\%$) whatever the vertical distribution of the aerosol, at least for realistic distributions (e.g. see Antoine and Morel 1998). The peculiar case of stratospheric aerosols, either particles of volcanic origin or thin cirrus clouds, was not considered (but see Gordon

et al. 1997a, b), and the stratosphere remains unchanged in the situations which are defined below (see also table 4):

- (1) In the free troposphere, the desert dust model of Schütz (1980) is replaced by the more absorbing dust-like aerosol component described in WCRP (1986). This aerosol and the boundary layer aerosol (the maritime model with $RH=80\%$) are each responsible for half of the optical thickness, τ_a , which is set to 0.05 and 0.50 at 550 nm. This combination illustrates a situation where extinction by the aerosol in the look-up tables and extinction by the actual aerosol have a similar spectral behaviour in the NIR, but diverge for shorter wavelengths.
- (2) The continental aerosol within the free troposphere is replaced by an aerosol whose particle size distribution follows a Junge law, with $\nu=3$, with refractive indices of 1.33 (water) and 1.50 (continental particles), and with $\tau_a=0.1$ at 550 nm. The maritime model, with $RH=80\%$, is selected for the boundary layer, with an optical thickness of 0.03 or 0.3 at 550 nm. This situation corresponds to continental, non-absorbing, particles blowing over the ocean.
- (3) The urban model with small particles is replaced by a model with a larger mode (Shettle and Fenn 1979). The constant background in the free troposphere remains as in the standard cases (clear atmospheres). This situation is plausible over coastal waters, overlaid by air masses close to the source of soot particles.
- (4) A moderately absorbing mixture of oceanic particles and desert dust (either 10 or 50% of the total particle number) replaces the pure maritime model in the boundary layer. The constant background in the free troposphere remains as in the standard cases (clear atmospheres). This profile would correspond to the penultimate phase of desert dust, before sinking into the ocean.
- (5) A convective atmosphere is simulated by replacing the standard maritime and continental aerosols within the boundary layer and free troposphere by the same mixtures as in case (4), with a scale height of 3 km within the whole troposphere. The total aerosol optical thickness is set to 0.05 and 0.3 at 550 nm.
- (6) As in (5), but with the urban aerosol within the whole troposphere (with $RH=80$ or 99%).
- (7) The extension of the desert dust layer is reduced to 4 km (between altitudes 2 and 6 km), instead of 10 km (2 to 12 km) in the profiles previously used, and with an optical thickness of 0.1 at 550 nm. Dust layers indeed tend to narrow after a long transport over the ocean (Powell 1995). The boundary layer aerosol is the maritime model with $RH=80\%$ and $\tau_a=0.3$ at 550 nm.

These seven aerosol distributions have been used to simulate TOA total radiances for $\theta_s=20, 40$ and 60° . The results of atmospheric correction applied to these peculiar aerosols have been pooled together for all $(\theta_v, \Delta\phi)$ couples, as indicated in table 2; they are presented in terms of $\Delta\rho(443)$ in figure 10 and discussed below with reference to the numbering used above.

- (1) Absorption is systematically detected when $\tau_a=0.5$, and less frequently when $\tau_a=0.05$. The increasing departure of $[c(\lambda)/c(865)]$ ratios with decreasing wavelength between the two desert dust models (WCRP (1986) used for the test and Schütz (1980) in the look-up tables) leads to an over-correction at

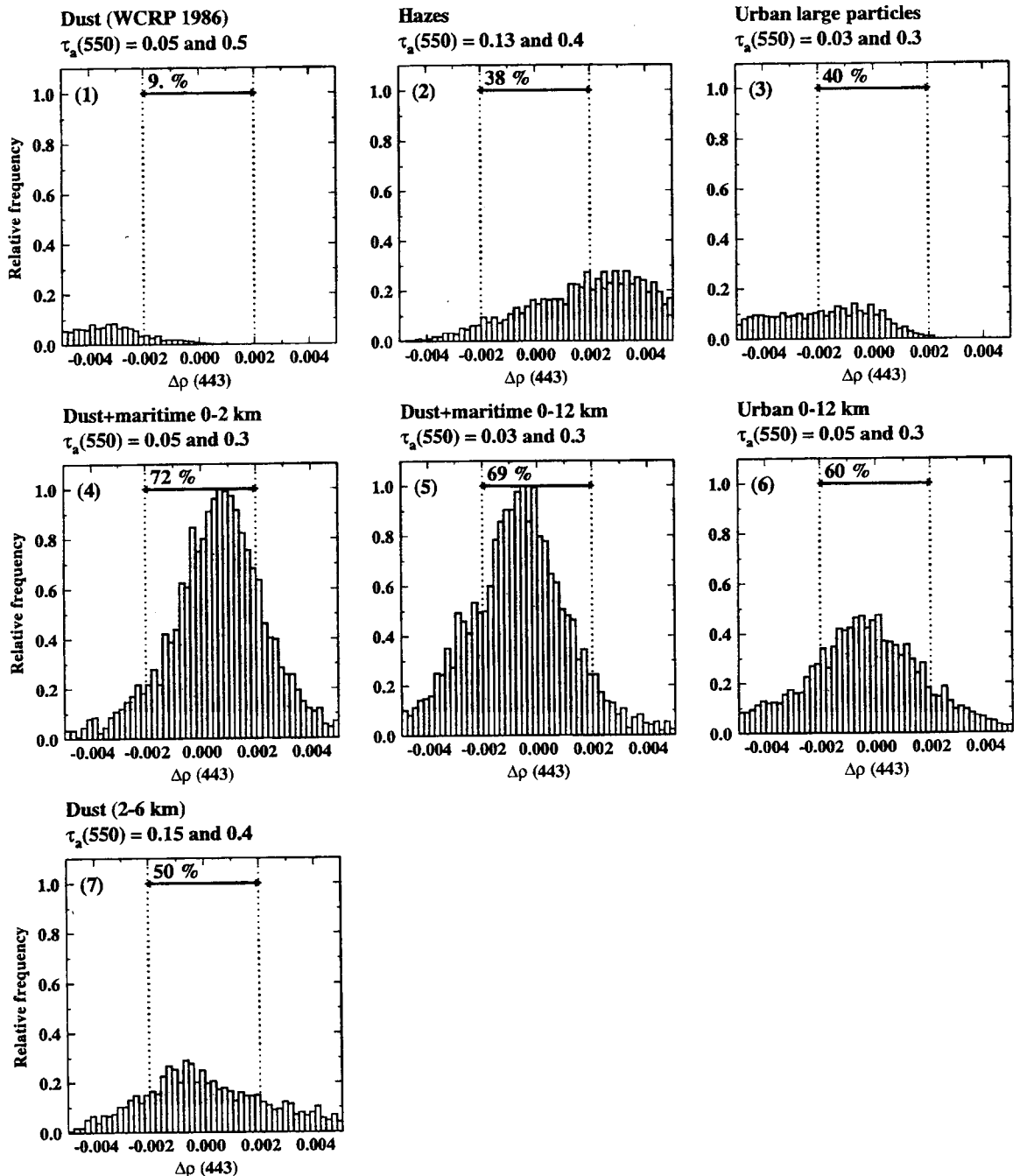


Figure 10. Histograms of errors in atmospheric corrections at 443 nm, for the sensitivity studies about aerosol types and aerosol vertical distributions as indicated (numbers in parentheses in the top left-hand corner of each panel refer to the numbering used in the text (§4.1)). Results for various geometries and aerosol optical thicknesses were pooled together in the construction of each histogram (see text).

443 nm, with mean errors in reflectances of about -0.004 . These results emphasize the need for a correct representation of the absorption properties of the aerosols in the visible domain.

- (2) The situation is roughly the converse of that in (1), i.e. an under-correction with, however, a greater percentage of errors within ± 0.002 . The largest spectral dependency among the aerosols within the look-up tables is still lower than that of the 'Junge aerosol' used here. Adding aerosols with a

- stronger scattering selectivity within the look-up tables (they are not represented here) would probably bring the bias observed here close to zero.
- (3) The reasonably good results for the correction of the large urban aerosols indicate that some uncertainty in the representation of the coarse mode of the aerosol size distribution is probably acceptable (large particles have a reduced impact on the reflectance in the visible to NIR region).
 - (4) With 72% of errors within ± 0.002 , the atmospheric correction is accurate when only a few absorbing particles are present in the boundary layer. The correction is actually performed with the standard aerosol assemblages (no detection of absorption).
 - (5) The high percentage of errors within ± 0.002 confirms that an exact representation of the vertical distribution of aerosols is not crucial as long as they are not very highly absorbing.
 - (6) and (7) The same comment as above could be made, except that now the aerosol is strongly absorbing. This result shows that some uncertainty in the vertical extension of the absorbing aerosol layer does not lead to large errors if the aerosol in the look-up tables is close enough to the actual one.

When the chlorophyll concentration is computed for the seven situations examined here, the percentages of exact retrievals vary from about 12 to 30% for $Chl = 0.03 \text{ mg m}^{-3}$, from about 25 to 60% for $Chl = 0.3 \text{ mg m}^{-3}$, and finally from about 9 to 36% for $Chl = 3 \text{ mg m}^{-3}$. The aerosol optical thickness is wrongly retrieved in situations (1) and (3) (large urban aerosols and desert dust model). For the five remaining cases, the retrieved aerosol optical thicknesses at 865 nm are within $\pm 15\%$ of the actual values in 50% to nearly 100% of the situations.

In summary, when used with the full set of aerosol models and when provided with the capacity of detecting absorption, the algorithm can provide water-leaving reflectances with an acceptable accuracy in many situations that are not represented in the look-up tables. This statement does not hold true when the actual aerosol absorption in the visible (case (1)) or its spectral selectivity (case (2)) differ significantly from those of the candidate models. In most cases an excellent accuracy is preserved for the retrieval of the aerosol optical thickness. The pigment concentration is less accurately retrieved than in the case of 'standard' absorbing aerosol assemblages (i.e. assemblages similar to those in the look-up tables). Nonetheless, the overall performance of the algorithm remains acceptable and clearly better than that obtainable with an algorithm not provided with the capability of detecting aerosol absorption.

4.2. Atmospheric pressure

Changes in atmospheric pressure, P , around the mean value of 1013.25 hPa adopted in the present work are typically of about 2%. Over the oceans, values above +2% of the mean are unrealistic, and values below -2% generally correspond to overcast conditions. Ignoring these variations leads to significant errors in atmospheric correction and in turn in pigment retrieval (Gordon *et al.* 1988a, b, André and Morel 1989). In an aerosol-free atmosphere, the relative change $\Delta\rho_r/\rho_r$ induced by a change ΔP in pressure is close to $\Delta P/P$, even if not strictly equal because of multiple scattering effects (Gordon *et al.* 1988a, b). Within a compound atmosphere containing molecules (optical thickness τ_r) and aerosols (τ_a), the change in ρ_{path} is not so simply connected to ΔP , and it can be interpreted via equation (11a). When

τ_r is increased, the Rayleigh reflectance, ρ_r^* , as well as the reflectance due to heterogeneous scattering, ρ_{ra}^* , tend to increase. In the meantime, however, the aerosol scattering reflectance, ρ_a^* , decreases. To a certain extent, the increase in molecule concentration 'masks' the aerosol signal, at least if τ_r is greater than τ_a . The effect of $\Delta P/P$ on $\Delta\rho_{\text{path}}/\rho_{\text{path}}$ thus progressively decreases when the contribution of τ_r to the total optical thickness decreases (i.e. when η_r , defined as $\tau_r/(\tau_a + \tau_r)$, decreases). When $\Delta P/P = +2\%$, for instance, $\Delta\rho_{\text{path}}/\rho_{\text{path}}$ at 443 nm is about $+1.5\%$ when τ_a is 0.05 ($\eta_r \sim 0.8$), less than $+1\%$ when τ_a is 0.3 ($\eta_r \sim 0.4$), and negligible at 865 nm when τ_a is 0.3 ($\eta_r \sim 0.05$). The following empirical correction is then proposed to account for the changes in atmospheric pressure

$$\rho'_{\text{path}} = \rho_{\text{path}} [1 + (\Delta P/P)\eta_r] \quad (22)$$

where ρ_{path} is the path reflectance for the standard pressure P , and ρ'_{path} is its value for a pressure $P' = P(1 + \Delta P/P)$. Using equation (22) allows the exact value of ρ_{path} to be retrieved within $\pm 0.5\%$ (figure 11). If atmospheric pressure differs significantly from the mean value ($\Delta P = \pm 5$ hPa, for instance), equation (22) is used to correct the measured value of ρ_{path} in the NIR, from P' to P , before introducing it into the algorithm. At this stage, τ_a is still unknown and is taken from the surrounding pixels (a $\pm 20\%$ error on τ_a does not appreciably degrade the accuracy of equation (22)). The whole scheme is then operated by using the look-up tables generated for the standard pressure, and the values of ρ_{path} obtained in the visible domain are again corrected, now from P to P' , by using equation (22) with the retrieved aerosol optical thickness. This technique has been applied to the situations shown in figure 6, with $P = 993$ and 1033 hPa (i.e. changing the standard pressure by plus or minus 2%), and no degradation of the atmospheric correction accuracy occurred (not shown).

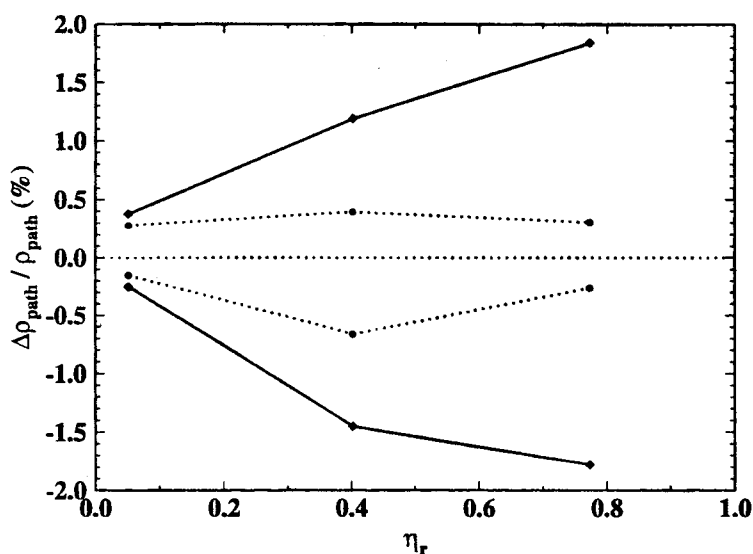


Figure 11. Relative change (per cent) of the TOA path reflectance in response to relative changes in atmospheric pressure, $\Delta P/P$, of $\pm 2\%$, and displayed as a function of η_r (solid curves). The conditions are: $\theta_s = 40^\circ$, maritime aerosol ($RH = 85\%$). The three points on each curve correspond to the mean change for several geometries (θ_v from 0 to 60° every 4° , and $\Delta\phi = 0, \pi/2$ and π), and to three increasing values of η_r , namely: (1) $\lambda = 865$ nm and $\tau_a(550) = 0.3$; (2) $\lambda = 443$ nm and $\tau_a(550) = 0.3$; (3) $\lambda = 443$ nm and $\tau_a(550) = 0.05$. The dotted curves show the relative errors in the path reflectances after equation (22) has been used to calculate their values for a standard pressure $P = 1013.25$ hPa from their values at $P' = P(1 + \Delta P/P)$.

4.3. Sea surface roughness

The relationship between $(\rho_{\text{path}}/\rho_r)$ and τ_a is likely modified when the sea surface is not flat, and the curves shown in figure 3 may not be valid in this case. When wind blows, whitecaps are one cause of changes in the TOA reflectances; correction for the effect of whitecaps has not been examined here (but see Gordon and Wang (1994 b) and Gordon (1997)). Sea surface roughness also changes the Sun glint pattern as well as the fate of any diffuse photon interacting with the surface. The latter effect has been examined (see also Gordon and Wang (1992a, b)), first by assuming that the Sun glint reflectance has been previously calculated and subtracted from the total reflectance. The effect of unidentified Sun glint contamination of the signal is examined next.

Monte Carlo simulations have been carried out for atmospheres bounded by a wind-roughened ocean, with facet slopes normally distributed, independently of the wind direction. The probability density of surface slopes for the direction $(\theta_s, \theta_v, \Delta\phi)$ is given by (Cox and Munk 1954)

$$p(\theta_s, \theta_v, \Delta\phi) = \frac{1}{\pi \sigma^2} \exp\left(\frac{-\tan^2 \beta}{\sigma^2}\right) \quad (23)$$

where β is the angle between the local normal and the normal to the facet and σ is the root mean square of slopes and is a function of wind speed, W , through (Cox and Munk 1954)

$$\sigma^2 = 0.003 + 5.12 \times 10^{-3} W \quad (24)$$

Shadowing effects are not accounted for in the Monte Carlo simulations. The glint reflectance ρ_G produced by such an interface can be expressed as

$$\rho_G(\theta_s, \theta_v, \Delta\phi) = \frac{\pi \rho_F(\omega)}{4 \mu_s \mu_v \cos^4 \beta} p(\theta_s, \theta_v, \Delta\phi) \quad (25)$$

Several $(\rho_{\text{path}}/\rho_r)$ versus τ_a curves, obtained at 443 and 865 nm with the maritime aerosol and $\sigma=0$ and 0.2, are displayed in figure 12, for $\theta_s = 36^\circ$, $\Delta\phi = \pi/2$ and $\theta_v = 12^\circ$ (figure 12(a)) or $\theta_v = 57^\circ$ (figure 12(b)). Here, ρ_G has been calculated exactly through equation (25), multiplied by $e^{-\tau(1/\mu_s + 1/\mu_v)}$, and subtracted from ρ_t to calculate ρ_{path} . The same subtraction is performed for the Rayleigh reflectance (also simulated for $\sigma=0.2$), so that $(\rho_{\text{path}}/\rho_r)$ only contains 'sky glitter'. The light field is more and more diffuse as the wavelength decreases, or, for a given wavelength, when θ_v increases. The impact of a rough surface on the reflectances is accordingly reduced in the visible, as compared to that in the NIR, and also when aiming at the ocean at large viewing angles in the NIR ($\lambda=865$ nm). The curves obtained at $\lambda=443$ nm are nearly superimposed when obtained either for $\sigma=0$ or for $\sigma=0.2$ because the spatial redistribution of reflected photons cannot further increase the diffuse character of the light field. On the contrary, the redistribution of radiances at 865 nm leads to some changes in the slope of the $(\rho_{\text{path}}/\rho_r)$ versus τ_a relationship when $\theta_v = 12^\circ$.

Two, perhaps three, sets of look-up tables should thus be generated (for the $f(\tau_a)$ function; equation (13)), in correspondence with $W=0$ and with moderate wind speeds, probably around 5 and 10 m s⁻¹. Higher wind speeds are not to be considered because the importance of the changes examined here would become much lower than those due to whitecap reflectance. Switching from one set of look-up tables to

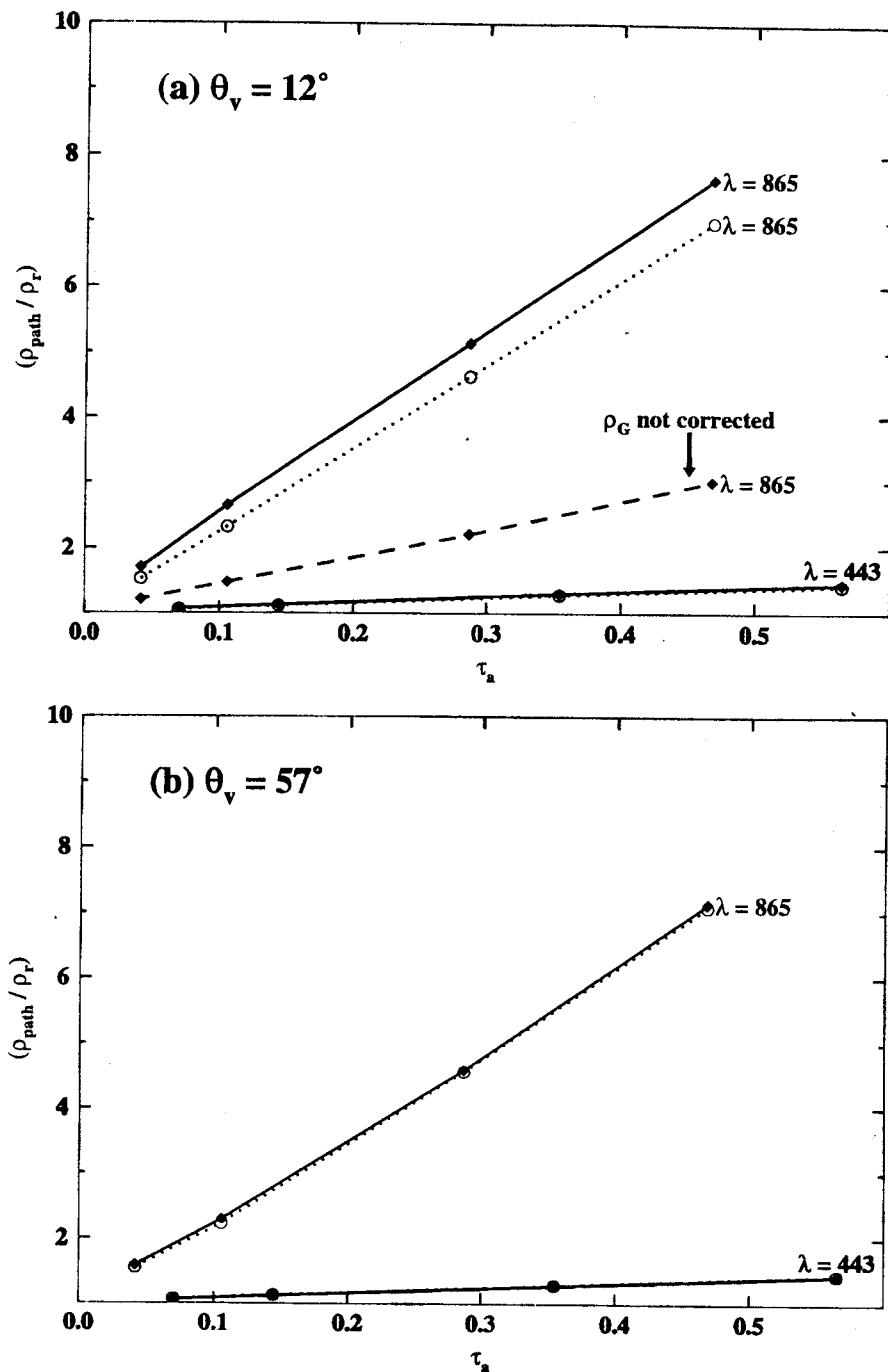


Figure 12. The $(\rho_{\text{path}}/\rho_r)$ ratio at 443 and 865 nm as a function of τ_a for $\theta_s = 36^\circ$, $\Delta\phi = \pi/2$ and $\theta_v = 12^\circ$ (a) or $\theta_v = 57^\circ$ (b). The aerosol is the maritime model for $RH = 80\%$. Dotted curves are for a perfectly flat sea surface, and solid curves are for a wind-roughened interface, characterized by $\sigma = 0.2$ (see text). The dashed curve in panel (a) is also for $\sigma = 0.2$, whereas the total reflectance ($\rho_{\text{path}} + \rho_G$) is erroneously used when forming the ratio to ρ_r , i.e. when the correction for Sun glint (ρ_G) is not made.

another, or interpolating between them, must rely on knowledge of wind speed, available either from other sensors, or from meteorological centres.

The above sensitivity study assumes that the Sun glint reflectance, ρ_G , has been correctly estimated and subtracted from the total reflectance before applying the atmospheric correction. This step is mandatory to the extent that the relationship $(\rho_{\text{path}}/\rho_r)$ versus τ_a is deeply modified if actually estimated with ρ_t (i.e. ρ_{path} plus a

non-identified contribution of ρ_G) instead of ρ_{path} (dashed curves in figure 12). Even with an exact knowledge of wind speed, existing models cannot actually provide an accurate value of ρ_G in the area of maximum Sun glint ($\Delta\phi \sim \pi$, $\theta_v \sim \theta_s$). The reflectance ρ_G there is much greater than the path reflectance, so that no attempt to perform the correction should be made within this area. For some other geometries around maximum Sun glint, the TOA total reflectance may still contain some photons directly transmitted through the atmosphere before and after reflection on a wave facet ('residual Sun glint'; ρ_G is then less than a half of ρ_{path}). If the value of ρ_G for these geometries is not calculable accurately, it should nevertheless be computed at least in view of identifying those pixels possibly affected by specular reflection. The identification could rely on a threshold, either on ρ_G (e.g. Gordon 1997), or on the ratio $\rho_G/\rho_{\text{path}}$ (for instance 0.5). For these pixels, atmospheric correction either would not be performed, or would be carried out and a flag raised. Note finally that ignoring the effect of shadowing on the Sun glint pattern, as done in the present work, can only lead to significant errors for grazing viewing direction and Sun illumination (i.e. for large θ_s and large θ_v values and $\Delta\phi$ around π). This geometrical configuration, where ρ_G anyway becomes small, actually does not occur along a MERIS track (maximum $\theta_v \sim 40^\circ$).

5. Discussion

An algorithm for atmospheric correction of ocean colour observations has been devised. Its principle rests on the observation that the relative increase in atmospheric path reflectance, due to the progressive introduction of a given aerosol within a molecular atmosphere, can be unambiguously related to the optical thickness of this aerosol (equation (13)). Such relationships, established for a set of aerosol models and used at two NIR bands, allow a couple of aerosol models to be identified as the closest to the actual aerosol assemblage. The atmospheric signal is thus estimated in the NIR and can be extrapolated toward the visible part of the spectrum. The approach to this problem of atmospheric correction is essentially the same as those adopted for several new multiple scattering algorithms, and was originally initiated by Gordon and Wang (1994a, b). The present algorithm, implemented as described in this paper, can cope with various situations as regards aerosol type and vertical structure. Tests and sensitivity analyses, making use of pseudo data obtained from radiative transfer simulations, are encouraging to the extent that the accuracy required to retrieve pigment concentration correctly is met in many situations.

In the atmospheric correction scheme proposed here, however, several steps rely on models, namely: (1) Monte Carlo simulations of the radiative transfer; (2) aerosol models used in these simulations; and (3) the bio-optical model used to select the $[\rho_w]_N(510)$ value. Therefore, the success of the scheme depends on the validity of the models used and especially on the data introduced into these models (e.g. the aerosol models).

Concerning radiative transfer in the atmosphere, the first condition is, in principle, fulfilled (see Mobley *et al.* 1993). The data used as input to simulations, however, are necessarily simplifications of nature (this is particularly true for aerosol types and vertical distributions) or are constant and discrete values (i.e. wind speed, atmospheric pressure). Sensitivity studies were therefore mandatory. They were carried out and their results found to be satisfactory. These studies, however, also make use of aerosol models—always questionable in terms of representivity. The size distributions and refractive indices of these models were derived from measurements

and laboratory studies and some of these models have been partly validated against measurements (Schwindling 1995). In some situations, however, they could turn out to be insufficiently representative of real aerosols. Does it therefore make sense to base an algorithm on look-up tables generated for about thirty aerosol assemblages, while much more are possibly encountered over the ocean, especially in coastal zones? The answer is positive when considering the results of the various tests performed here. In a way, the about thirty aerosol assemblages capture the essential features of possible spectral dependencies of aerosol extinction. As a consequence, when the actual aerosol type is not represented within the database, the correction remains possible and an acceptable accuracy is preserved. The same conclusion is reached about the representation of the vertical distribution of absorbing aerosols, which, besides the choice of relevant aerosol models, is also critical for the success of the algorithm.

Use of Mie theory also introduces some uncertainty as regards the estimated aerosol volume scattering functions. It is now confirmed that these functions are quite different for non-spherical particles and the equivalent spherical particles, especially at side-scattering and backscattering angles (Mishchenko *et al.* 1997). This problem exists for dust-like aerosols but is probably less critical for oceanic aerosols.

Improvements in the present algorithm implementation, as regards the representivity of aerosol models, would probably consist of using measured optical properties for aerosols rather than modelled ones and also trying to take advantage of LIDAR vertical profiling. Along the same line, the use of aerosol climatology could also prove useful in order to avoid totally irrelevant aerosol selections. Regional or global distributions of aerosol types and aerosol optical thickness have indeed been generated recently, either from Advanced Very High Resolution Radiometer (AVHRR) historical observations (e.g. Husar *et al.* 1997, Stowe *et al.* 1997, mapping of optical thickness), or from METEOSAT observations (Moulin *et al.* 1997, mapping of Saharan dust), or from Nimbus-7 TOMS observations (Herman *et al.* 1997, mapping of UV-absorbing aerosols). These possibilities mean that atmospheric correction would evolve towards the use of an *a priori* rough knowledge of the actual aerosol distribution and type.

The success of the tests performed at 510 and 705 nm depends on the validity of the bio-optical model used to define the thresholds of these tests. If the oceanic reflectance at 510 nm is actually more variable than has been assumed here, the test carried out at this wavelength, and hence the correction of the visible observations, will no longer be possible when absorbing aerosols are present. It is also conceivable that, in some instance (e.g. detached coccoliths), the marine signal at 705 nm is significant, so that erroneous answers will be given by the test at this wavelength. An increase of the thresholds used in the tests at 510 and 705 nm might be necessary to adjust the algorithm to applications in the real world.

Several aspects of radiative transfer in the ocean-atmosphere system have been neglected in the present work, for they do not bear upon the principle of the algorithm. The involved phenomena could have, however, an impact on the accuracy of the atmospheric correction. They include, not exhaustively, the presence of white-caps (but see Gordon and Wang 1994b, Gordon 1997), polarization of the TOA radiances (Gordon *et al.* 1988a, b, Gordon 1997), or the impact of the bidirectionality of oceanic reflectance on the diffuse transmittance (Yang and Gordon 1997).

In summary, the proposed algorithm seems able to perform an accurate atmospheric correction over most oceanic areas, as suggested by the results of the tests

and sensitivity studies carried out in the present work. These studies, however detailed they may be, cannot substitute for the use and test of the algorithm in actual conditions. This is one reason why calibration and validation of the sensor-plus-algorithm system are crucial for the development of MERIS and related algorithms (e.g. see Clark *et al.* 1997, Kishino *et al.* 1997).

All tests and sensitivity studies have indeed been carried out in the present paper as if there was no calibration error. This situation is obviously unrealistic—several arguments can, nevertheless, temper this observation. First, the pseudo data generated from Monte Carlo simulations of the radiative transfer, and to which the algorithm was applied, typically carry a noise of about $\pm 2\%$. Such a noise is actually comparable to the radiometric accuracy (relative to the Sun) expected for a sensor like MERIS (Rast and Bézy 1995), at least after vicarious calibration has been performed. Therefore, the tests performed in the present work illustrate, to a certain extent, the results expected from an instrument affected by a random radiometric noise of $\pm 2\%$. Second, the sensitivity studies to environmental parameters (vertical distribution of aerosols, state of the air–sea interface, etc.) can also be seen as just the application of a more or less randomly generated set of calibration errors in various bands, so that the problem of unpredicted changes in calibration is already dealt with. Things actually become more complicated because the sign of calibration errors may change with wavelength, even if it is reasonable to expect errors of the same sign at all wavelengths after vicarious calibration (Gordon 1997). In effect, it is reasonable to expect a 2% accuracy, under the proviso that careful in-orbit calibration of the sensor-plus-algorithm system is performed throughout the sensor's life (e.g. Clark *et al.* 1997).

Another side of the crucial problem of calibration, which was sorely experienced with the CZCS, is related to the possible long-term degradation of the calibration. In principle, MERIS, like most of the new-generation sensors, is equipped with appropriate devices that should allow any subtle change in the radiometric performances to be monitored. In the case of MERIS, flat, Sun-illuminated, white Spectralon[®] diffuser plates are to be used. One of these plates is to be used at each orbit, the other one being deployed on a few, well spaced in time, occasions, in order to prevent its degradation and thus to control the stability of the response of the first diffuser.

Acknowledgements

We would like to express our appreciation to two anonymous referees for their constructive suggestions, and also to Howard Gordon for many helpful discussions about the present problem, already addressed during the development of the Algorithm Theoretical Basis Document for MERIS. We are also grateful to Bernard Gentili for his unremitting help in the development of the Monte Carlo code and all related computing utilities. This work was essentially supported by the European Space Agency, through contract from the European Space Research and Technology Center 11878/96/NL/GS; this is duly acknowledged.

References

- ANDRÉ, J. M., and MOREL, A., 1989, Simulated effects of barometric pressure and ozone content upon the estimate of marine phytoplankton from space. *Journal of Geophysical Research*, **94**, 1029–1037.
- ANDRÉ, J. M., and MOREL, A., 1991, Atmospheric corrections and interpretation of marine radiances in CZCS imagery, revisited. *Oceanologica Acta*, **14**, 3–22.
- ANDREAE, M. O., 1996, Raising dust in the greenhouse. *Nature*, **380**, 389–390.

- ÅNGSTRÖM, A., 1964, The parameters of atmospheric turbidity. *Tellus*, **26**, 64–75.
- ANTOINE, D., and MOREL, A., 1998, Relative importance of multiple scattering by air molecules and aerosols in forming the atmospheric path radiance in the visible and NIR parts of the spectrum. *Applied Optics*, **37**, 2245–2259.
- BRICAUD, A., and MOREL, A., 1987, Atmospheric corrections and interpretation of marine radiances in CZCS imagery: use of a reflectance model. *Oceanologica Acta*, **SP**, 33–50.
- BROWELL, E. V., NOWICKI, G. D., FENN, M. A., and HOFF, R. M., 1995, LITE observations of biomass burning plumes over south America, Africa, and the southern Atlantic ocean. *EOS Transactions, AGU Fall Meeting Supplement*, **76**, S69.
- CARDER, K. L., GREGG, W. W., COSTELLO, D. K., HADDAD, K., and PROSPERO, J. M., 1991, Determination of Saharan dust radiance and chlorophyll from CZCS imagery. *Journal of Geophysical Research*, **96**, 5369–5378.
- CHARLSON, R. J., SCHWARTZ, S. E., HALES, J. M., CESS, R. D., COAKLEY, J. A., HANSEN, J. E., and HOFMANN, D. J., 1992, Climate forcing by Anthropogenic aerosols. *Science*, **255**, 423–430.
- CLARK, D. K., GORDON, H. R., VOSS, K. J., GE, Y., BROENKOW, W., and TREES, C., 1997, Validation of atmospheric correction over the oceans. *Journal of Geophysical Research*, **102**, 17 209–17 217.
- COX, C., and MUNK, W., 1954, Statistics of the sea surface derived from Sun glitter. *Journal of Marine Research*, **13**, 198–227.
- DESCHAMPS, P. Y., BRÉON, F. M., LEROY, M., PODAIRE, A., BRICAUD, A., BURIEZ, J. C., and SÈZE, G., 1994, The POLDER mission: instrument characteristics and scientific objectives. *IEEE Transactions in Geosciences and Remote Sensing*, **32**, 598–615.
- DESCHAMPS, P. Y., HERMAN, M., and TANRÉ, D., 1983, Modeling of the atmospheric effects and its application to the remote sensing of ocean color. *Applied Optics*, **22**, 3751–3758.
- DONAGHAY, P. L., LISS, P. S., DUCE, R. A., KESTER, D. R., HANSON, A. K., VILLAREAL, T., TINDALE, N. W., and GIFFORD, D. J., 1991, The role of episodic atmospheric nutrient inputs in the chemical and biological dynamics of oceanic ecosystems. *Oceanography*, **4**, 62–70.
- DUNTLEY, S. Q., WILSON, W. H., and EDGERTON, C. F., 1974, Detection of ocean chlorophyll from Earth orbit, In *Ocean Color Analysis*, S. Q. Duntley, R. W. Austin, W. W. Wilson, C. F. Edgerton and S. E. Moran (University California at San Diego: Scripps Institution of Oceanography), SIO Ref. 74-10.
- ELTERMAN, L., 1968, UV, visible, and IR attenuation for altitudes to 50 km. Environmental Research Paper, N° 285, AFCRL-68-0153, Air Force Cambridge Research Laboratories.
- FUKUSHIMA, H., and TORATANI, H., 1997, Asian dust aerosol: optical effect on satellite ocean color signal and a scheme of its correction. *Journal of Geophysical Research*, **102**, 17 119–17 130.
- GORDON, H. R., 1978, Removal of atmospheric effects from satellite imagery of the oceans. *Applied Optics*, **17**, 1631–1636.
- GORDON, H. R., 1990, Radiometric considerations for ocean color remote sensors. *Applied Optics*, **29**, 3228–3236.
- GORDON, H. R., 1997, Atmospheric correction of ocean color imagery in the Earth observing system era. *Journal of Geophysical Research*, **102**, 17 081–17 106.
- GORDON, H. R., BROWN, J. W., and EVANS, R. H., 1988a, Exact Rayleigh scattering calculations for use with the Nimbus-7 Coastal Zone Color Scanner. *Applied Optics*, **27**, 862–871.
- GORDON, H. R., BROWN, O. B., EVANS, R. H., BROWN, J. W., SMITH, R. C., BAKER, K. S., and CLARK, D. K., 1988b, A semianalytic radiance model of ocean color. *Journal of Geophysical Research*, **93**, 10 909–10 924.
- GORDON, H. R., and CASTAÑO, D. J., 1987, Coastal Zone Color Scanner atmospheric correction algorithm: multiple scattering effects. *Applied Optics*, **26**, 2111–2122.
- GORDON, H. R., and CLARK, D. K., 1980, Atmospheric effects in the remote sensing of phytoplankton pigments. *Boundary Layer Meteorology*, **18**, 299–313.
- GORDON, H. R., and CLARK, D. K., 1981, Clear water radiances for atmospheric correction of Coastal Zone Color Scanner imagery. *Applied Optics*, **20**, 4175–4180.
- GORDON, H. R., CLARK, D. K., BROWN, J. W., BROWN, O. B., EVANS, R. H., and BROENKOW, W. W., 1983, Phytoplankton pigment concentrations in the Middle Atlantic bight: comparison of ship determinations and CZCS estimates. *Applied Optics*, **22**, 20–36.

- GORDON, H. R., CLARK, D. K., MUELLER, J. L., and HOVIS, W. A., 1980, Phytoplankton pigments from the Nimbus-7 Coastal Zone Color Scanner: comparisons with surface measurements. *Science*, **210**, 63–66.
- GORDON, H. R., DU, T., and ZHANG, T., 1997a, Remote sensing of ocean color and aerosol properties: resolving the issue of aerosol absorption. *Applied Optics*, **36**, 8670–8684.
- GORDON, H. R., and MOREL, A., 1983, Remote assessment of ocean color for interpretation of satellite visible imagery. *Lecture Notes on Coastal and Estuarine Studies*, vol. 4, edited by R. T. Barber, C. N. K. Mooers, M. J. Bowman and B. Zeitzschel (Springer-Verlag: New York).
- GORDON, H. R., and WANG, M., 1992a, Surface-roughness considerations for atmospheric correction of ocean color sensors. I: The Rayleigh-scattering component. *Applied Optics*, **31**, 4247–4260.
- GORDON, H. R., and WANG, M., 1992b, Surface-roughness considerations for atmospheric correction of ocean color sensors. II: Error in the retrieved water-leaving radiance. *Applied Optics*, **31**, 4261–4267.
- GORDON, H. R., and WANG, M., 1994a, Retrieval of water-leaving reflectance and aerosol optical thickness over the oceans with SeaWiFS: a preliminary algorithm. *Applied Optics*, **33**, 443–452.
- GORDON, H. R., and WANG, M., 1994b, Influence of oceanic whitecaps on atmospheric correction of SeaWiFS. *Applied Optics*, **33**, 7754–7763.
- GORDON, H. R., ZHANG, T., HE, F., and DING, K., 1997b, Effects of stratospheric aerosols and thin cirrus clouds on the atmospheric correction of ocean color imagery: simulations. *Applied Optics*, **36**, 682–697.
- HERMAN, J. R., BHARTIA, P. K., TORRES, O., HSU, C., SETFOR, C., and CELARIER, E., 1997, Global distribution of UV-absorbing aerosols from Nimbus 7/TOMS data. *Journal of Geophysical Research*, **102**, 16911–16922.
- HOFF, R. M., WINKER, D. M., BROWELL, E. V., and MELFI, S. H., 1995, LITE observations of large scale anthropogenic hazes. *EOS Transactions, AGU Fall Meeting Supplement*, **76**, S67.
- HOOKE, S. B., ESAIAS, W. E., FELDMAN, G. C., GREGG, W. W., and MCCLAIN, C. R., 1992, SeaWiFS Technical Report Series, vol. 1, An overview of SeaWiFS and ocean color, NASA Tech. Memo. 104566, NASA, Greenbelt Space Flight Center, Greenbelt MD, USA.
- HOPPEL, W. A., FITZGERALD, J. W., FRICK, G. M., and LARSON, R. E., 1990, Aerosol size distributions and optical properties found in the marine boundary layer over the Atlantic ocean. *Journal of Geophysical Research*, **95**, 3659–3686.
- HOVIS, W. A., CLARK, D. K., ANDERSON, F., AUSTIN, R. W., WILSON, W. H., BAKER, E. T., BALL, D., GORDON, H. R., MUELLER, J. L., ELSAYED, S. Z., STURM, B., WRIGLEY, R. C., and YENTSCH, C. S., 1980, Nimbus-7 Coastal Zone Color Scanner: system description and initial imagery. *Science*, **210**, 60–63.
- HUSAR, R. B., PROSPERO, J. M., and STOWE, L. L., 1997, Characterization of tropospheric aerosols over the oceans with the NOAA advanced very high resolution radiometer optical thickness operational product. *Journal of Geophysical Research*, **102**, 16889–16909.
- KISHINO, M., ISHIZAKA, J., SAITOH, S., SENGA, Y., and UTASHIMA, M., 1997, Verification plan of ocean color and temperature scanner atmospheric correction and phytoplankton pigment by moored optical buoy system. *Journal of Geophysical Research*, **102**, 17197–17207.
- LEWIS, M. R., 1992, Satellite ocean color observations of global biogeochemical cycles. In *Primary Productivity and Biogeochemical Cycles in the Sea*, vol. 43, edited by P. G. Falkowski and A. D. Woodhead (New York: Plenum), 139–153.
- LI, X., MARING, H., SAVOIE, D., VOSS, K., and PROSPERO, J. M., 1996, Dominance of mineral dust in aerosol light-scattering in the north Atlantic trade winds, *Nature*, **380**, 416–419.
- MARTIN, D. L., and PERRY, M. J., 1994, Minimizing systematic errors from atmospheric multiple scattering and satellite viewing geometry in Coastal Zone Color Scanner level IIA imagery. *Journal of Geophysical Research*, **99**, 7309–7322.
- MEDIPROD GROUP, 1976, Résultats de la campagne CINECA 5–J. Charcot–Capricorne 7403 (1 Mars au 20 Avril 1974). Publications du CNEXO, N°10.

- MERRILL, J. T., UEMATSU, M., and BLECK, R., 1989, Meteorological analysis of long range transport of mineral aerosols over the north Pacific. *Journal of Geophysical Research*, **94**, 8584–8598.
- MISHCHENKO, M. I., TRAVIS, L. D., KAHN, R. A., and WEST, R. A., 1997, Modeling phase functions for dustlike tropospheric aerosols using a shape mixture of randomly oriented polydisperse spheroids. *Journal of Geophysical Research*, **102**, 16831–16847.
- MOBLEY, C. D., GENTILI, B., GORDON, H. R., JIN, Z., KATTAWAR, G. W., MOREL, A., REINERSMAN, P., STAMNES, K., and STAVN, R. H., 1993, Comparison of numerical models for computing underwater light fields. *Applied Optics*, **32**, 7484–7504.
- MOREL, A., 1988, Optical modeling of the upper ocean in relation to its biogenous matter content (Case 1 waters). *Journal of Geophysical Research*, **93**, 10749–10768.
- MOREL, A., and GENTILI, B., 1991, Diffuse reflectance of oceanic waters: its dependence on sun angle as influenced by the molecular scattering contribution. *Applied Optics*, **30**, 4427–4438.
- MOREL, A., and GENTILI, B., 1993, Diffuse reflectance of oceanic waters. II. Bidirectional aspects. *Applied Optics*, **32**, 6864–6879.
- MOREL, A., and GENTILI, B., 1996, Diffuse reflectance of oceanic waters. III. Implication of the bidirectionality for the remote sensing problem. *Applied Optics*, **35**, 4850–4862.
- MOREL, A., and PRIEUR, L., 1977, Analysis of variations in ocean color. *Limnology and Oceanography*, **22**, 709–722.
- MOULIN, C., GUILLARD, F., DULAC, F., and LAMBERT, C. E., 1997, Long-term daily monitoring of Saharan dust load over ocean using Meteosat ISCCP-B2 data. 1. Methodology and preliminary results for 1983–1994 in the Mediterranean. *Journal of Geophysical Research*, **102**, 16947–16958.
- NECKEL, H., and LABS, D., 1984, The solar radiation between 3300 and 12500 Å. *Solar Physics*, **90**, 205–258.
- OLIPAC (JGOFS) CRUISE, 1995, Unpublished data.
- O'REILLY, J. E., MARITORENA, S., MITCHELL, B. G., SIEGEL, D. A., CARDER, K. L., GARVER, S. A., KAHRU, M., and MCCLAIN, C., 1998, Ocean color chlorophyll algorithms for SeaWiFS. *Journal of Geophysical Research*, **103**(C11), 24937–24953, October 15, 1998.
- PACIPROD CRUISE, 1987, Unpublished data.
- POWELL, K. A., 1995, Observations of Saharan dust by LITE. *EOS Transactions, AGU Fall Meeting Supplement*, **76**, S73.
- PROSPERO, J. M., and CARLSON, T. N., 1972, Vertical and areal distribution of Saharan dust over the western equatorial north Atlantic ocean. *Journal of Geophysical Research*, **77**, 5255–5265.
- RAST, M., and BÉZY, J. L., 1995, The ESA medium resolution imaging spectrometer (MERIS): requirements to its mission and performance of its system. *RSS95, Remote Sensing in Action, Proceedings of the 21st Annual Conference of the Remote Sensing Society, University of Southampton, UK, 11–14 September 1995*, edited by P. J. Curran and Y. C. Robertson (London: Taylor and Francis), pp. 125–132.
- REDDY, P. J., KREINER, F. W., DELUISI, J. J., and KIM, Y., 1990, Aerosol optical depths over the Atlantic derived from shipboard sun photometer observations during the 1988 global change expedition. *Global Biogeochemical Cycles*, **4**, 225–240.
- SAITOH, S., 1995, OCTS on ADEOS. In *Oceanographic Application of Remote Sensing*, edited by M. Ikeda and F. W. Dobson (Boca Rota, FL: CRC), pp. 473–480.
- SALOMONSON, V. V., BARNES, W. L., MAYMON, P. W., MONTGOMERY, H. E., and OSTROW, X., 1989, MODIS: advanced facility instrument for studies of the earth as a system. *IEEE Transactions in Geosciences and Remote Sensing*, **27**, 145–152.
- SAVOIE, D. L., and PROSPERO, J. M., 1977, Aerosol concentration statistics for the northern tropical Atlantic. *Journal of Geophysical Research*, **82**, 5954–5964.
- SCHÜTZ, L., 1980, Long-range transport of desert dust with special emphasis on the Sahara. *Annals of the New York Academy of Sciences*, **338**, 515–532.
- SCHWINDLING, M., 1995, Modèles et mesures pour l'observation spatiale de la couleur de l'océan: diffusion atmosphérique par les aérosols et réflexion de surface par l'écume. Thèse de Doctorat de l'Université des Sciences et Techniques de Lille, France.
- SHETTLE, E. P., and FENN, R. W., 1979, Models for the aerosols of the lower atmosphere and

- the effects of humidity variations on their optical properties. Environmental Research Paper, N° 676, AFGL-TR-79-0214, Air Force Geophysics Laboratory.
- STOWE, L. L., IGNATOV, A. M., and SINGH, R. R., 1997, Development, validation, and potential enhancements to the second-generation operational aerosol product at the national environmental satellite, data, and information service of the national oceanic and atmospheric administration. *Journal of Geophysical Research*, **102**, 16923–16934.
- TYLER, J. E., 1973, Measurements of photosynthesis, available radiant flux, and supporting oceanographic data. Data Report, SOCR Discoverer Expedition, May 1970, S.I.O. Ref. 73-16, University California, USA.
- VILLEVALDE, Y. V., SMIRNOV, A. V., O'NEILL, N. T., SMYSHLYAEV, S. P., and YAKOVLEV, V. V., 1994, Measurement of aerosol optical depth in the Pacific ocean and the North Atlantic. *Journal of Geophysical Research*, **99**, 20983–20988.
- VIOLLIER, M., TANRÉ, D., and DESCHAMPS, P. Y., 1980, An algorithm for remote sensing of water color from space. *Boundary Layer Meteorology*, **18**, 247–267.
- WANG, M., and GORDON, H. R., 1994, A simple, moderately accurate, atmospheric correction algorithm for SeaWiFS. *Remote Sensing of Environment*, **50**, 231–239.
- WORLD CLIMATE RESEARCH PROGRAM (WCRP), 1986, A preliminary cloudless standard atmosphere for radiation computation. International Association for Meteorology and Atmospheric Physics, Radiation Commission, Boulder, CO., USA, 1984, WCP-112, WMO/TD-N° 24, March 1986.
- YANG, H., and GORDON, H. R., 1997, Remote sensing of ocean color: assessment of the water-leaving radiance bidirectional effects on the atmospheric diffuse transmittance. *Applied Optics*, **36**, 7887–7897.
- YODER, J. A., ESAIAS, W. E., FELDMAN, G. C., and MCCLAIN, C. R., 1988, Satellite ocean color—status report. *Oceanography*, **1**, 18–20.

Detection of blue-absorbing aerosols using near infrared and visible (ocean color) remote sensing observations

Delphine Nobileau, David Antoine*

Laboratoire d'Océanographie de Villefranche, 06230 Villefranche sur mer, France

Received 25 July 2004; received in revised form 22 December 2004; accepted 24 December 2004

Abstract

An algorithm is presented, which is designed to identify blue-absorbing aerosols from near infrared and visible remote-sensing observations, as they are in particular collected by satellite ocean color sensors. The technique basically consists in determining an error budget at one wavelength around 510 nm, based on a first-guess estimation of the atmospheric path reflectance as if the atmosphere was of a maritime type, and on a reasonable hypothesis about the marine signal at this wavelength. The budget also includes the typical calibration uncertainty and the natural variability in the ocean optical properties. Identification of blue-absorbing aerosols is then achieved when the error budget demonstrates a significant over-correction of the atmospheric signal when using non-absorbing maritime aerosols. Implementation of the algorithm is presented, and its application to real observations by the MERIS and SeaWiFS ocean color sensors is discussed. The results demonstrate the skill of the algorithm in various regions of the ocean where absorbing aerosols are present, and for two different sensors. A validation of the results is also performed against in situ data from the AERONET, and further illustrates the skill of the algorithm and its general applicability.

© 2005 Elsevier Inc. All rights reserved.

Keywords: Blue-absorbing aerosols; Near infrared; Visible remote sensing; Ocean color

1. Introduction

Recent studies based on the use of satellite remote sensing observations have estimated that 230 Mt of dust are transported annually from Africa to the inter Tropical Atlantic ocean (Kaufman et al., 2003) and that 252 Mt of dust are emitted, mostly between March and May, from Asian deserts to the north Pacific ocean (Gong et al., 2003). Other regions of dust emissions toward the ocean are Arabia and Australia (e.g., McGowan et al., 2000). This dominance in the total aerosol transport over the oceans (D'Almeida, 1986) is one of the reasons for the interest taken in the study of desert dusts, the second reason being their potential effect on the radiative budget and climate of the whole planet (e.g., Charlson et al., 1992; Li et al., 1996;

Sokolik & Toon, 1999; Tegen et al., 1996). Large-scale effects are indeed expected because these dusts, in particular when coming from the Sahara or from Asian deserts, concern extended regions far from their sources (e.g., Li et al., 1996; Prospero & Carlson, 1972; Savoie & Prospero, 1977).

The two opposite and direct effects of these aerosols are the scattering of solar radiation back to space, i.e., a cooling effect, and the absorption of solar and Earth radiation in the lower atmosphere, i.e., a heating effect (Brooks & Legrand, 2000; Levievel et al., 2002). Other radiative effects of dust aerosols are indirect, via their role as cloud condensation nuclei (Levin & Ganor, 1996) and via their effect on the photolysis rates of ozone (Bian & Zender, 2003). The balance of these effects is still controversial (IPCC, 2001), mostly because the absorption properties of these aerosols are insufficiently known, but also because their large scale distribution, their vertical repartition, and their seasonal variations are not enough characterized.

* Corresponding author.

E-mail address: antoine@obs-vlfr.fr (D. Antoine).

In a more controversial way, sand particles could either fertilize the upper oceanic layers by releasing nutrients adsorbed onto their surface (e.g., Donaghay et al., 1991; Duce & Tindale, 1991; Ridame & Guieu, 2002), or on the contrary deplete surface waters of phosphorus—one of the nutrients allowing phytoplankton growth—by carrying it away through adsorption and sinking (Krom et al., 1991). Dust also carries iron to the ocean, which might have a significant role in the areas where this micro-nutrient is missing, thus sustaining higher photosynthesis rates than possible without this aeolian input (e.g., Gao et al., 2001). This hypothesis was recently illustrated by the observation of parallel evolutions of aerosol optical thickness and chlorophyll concentrations at the daily scale in the south of Australia (Gabric et al., 2002). The characterization of the dust properties and of its distribution at global scale is therefore crucial to understand their role not only on the Earth radiative budget but also on the global biogeochemical cycles.

Identifying desert dust occurrences over the ocean and quantifying the associated burden are accordingly important missions that can be assigned to the new-generation ocean color sensors, which are recording the Earth reflectance in the visible and near infrared at the top of the atmosphere (TOA), in parallel to more aerosol-oriented missions such as the POLDER (Deschamps et al., 1994), the MODIS (Salomonson et al., 1992) or the PARASOL (<http://smc.cnes.fr/PARASOL/>).

A simple algorithm is proposed here in order to detect blue-absorbing (usually dust) aerosols from visible and near infrared remote sensing observations, such as those carried out by ocean color sensors. It is based on the use of one wavelength in the visible domain (around 510–520 nm) and of two wavelengths in the near infrared between 750 and 900 nm. The purpose of this technique is not to characterize in details the dust aerosols, which would probably necessitate the use of a larger number of spectral bands in several domains of the e.m. spectrum (King et al., 1999). The objective here is to detect the presence of absorption in the visible domain, in order to allow a mapping over the ocean of this important characteristic of the aerosols. Reaching this qualitative objective would be an important achievement as regards the general questions of today's aerosol science.

Basis for the proposed algorithm are to be found in Antoine and Morel (1998, 1999), where an atmospheric correction algorithm designed for the new-generation ocean color sensors was presented. At that time the effort was concentrated towards improving the atmospheric correction of the visible bands in nominal situations (maritime atmospheres), in particular by accounting for multiple scattering, and the detection of special types of aerosols was just sketched out. The focus is now on the dust detection, the atmospheric correction of all visible bands that are used for interpreting the ocean color signal being here a secondary objective. The aim is to end up

with an operational method that might be applicable to most of the ocean color sensors presently in orbit or planned in a near future, in order to advantageously complement other existing techniques that are applied to other types of remote sensing observations to detect absorbing aerosols, such as spectral observations in the UV domain (TOMS sensor, Herman et al., 1997), broadband observations in the visible (METEOSAT; Moulin et al., 1997), two-channel observations in the visible (AVHRR; Higurashi et al., 2000; Husard et al., 1997; Stowe et al., 1997), and observations within the sun glitter (Kaufman et al., 2002a).

After a brief reminder about the optical properties of desert aerosols and of oceanic Case 1 waters, the principles of the method developed to detect aerosol absorption is presented and its practical implementation is described. Then the algorithm is calibrated and tested by using simulated data, before tests are performed on real observations from two ocean color sensors, i.e., the SeaWiFS launched by NASA in September 1997 (Hooker et al., 1992) and the MERIS launched by ESA in March 2002 (Rast & Bézy, 1995; Rast et al., 1999). Finally, a validation is performed against in situ data taken from the “Aerosol Robotic Network” (AERONET; Holben et al., 1998, 2001).

2. Background

To detect absorbing dust aerosols over the ocean, one must know the optical properties of both the ocean and the aerosols, as well as the effect of these aerosols on the TOA signal recorded by a satellite borne sensor. An extensive literature exists about ocean Case 1 waters optical properties and their modeling (e.g., Garver & Siegel, 1997; Gordon et al., 1988; Morel & Maritorea, 2001; Morel & Prieur, 1977), about dust optical properties (e.g., D'Almeida et al., 1991; Haywood et al., 2001; Shettle & Fenn, 1979; Tanré et al., 2003) and about their effect on the TOA reflectance (e.g., Kaufman, 1993; Smirnov et al., 2002).

Therefore only specific aspects are briefly reminded below, in the somewhat bounded envision that is specifically needed to understand the rationale of the proposed algorithm. The quantity that will be used across this paper is the reflectance, defined as follows:

$$\rho(\lambda, \theta_s, \theta_v, \Delta\phi) = \pi L(\lambda, \theta_s, \theta_v, \Delta\phi) / E_S(\lambda) \mu_s \quad (1)$$

where L is radiance (either at the TOA or just above the sea surface; $W m^{-2} nm^{-1} sr^{-1}$), E_S is the extraterrestrial irradiance ($W m^{-2} nm^{-1}$), θ_s is the sun zenith angle (cosine is μ_s), θ_v is the satellite viewing angle, and $\Delta\phi$ is the azimuth difference between the half vertical plane containing the sun and the pixel and the half vertical plane containing the satellite and the pixel. Because π carries the unit of steradian, the reflectance ρ is dimensionless.

2.1. Dusts optical properties

Aerosol optical properties are determined by the size distribution and the chemical composition of the particles, hence by their refractive index. Typical values of these parameters are briefly recalled below in the case of mineral dust.

The particle size distribution of dust aerosols is best represented by the combination of two modal distributions, with a coarse mode around $2\ \mu\text{m}$ (Dubovik et al., 2002), the representation of which being heavily dependent upon wind speed and distance from the source (e.g. Alfaro & Gomes, 2001; Sokolik et al., 1998), and an accumulation mode around $0.2\ \mu\text{m}$. Three modes have been also used in other studies (Moulin et al., 2001). With a significant proportion of large particles (large with respect to the wavelengths in question here), the resulting scattering coefficient has a weak spectral dependency from the near infrared to the visible, with an Ångström exponent over this spectral domain usually below 0.5 and sometimes close to zero. Would the largest particles be removed from the aerosol, for instance after a long transport over the ocean, the spectral dependency would come closer to what is typical of non-absorbing aerosols mostly made of sub-micron particles, with Ångström exponents up to 1. This is shown on Fig. 1(a), where normalized scattering coefficients are displayed for maritime and dust aerosols.

Desert dusts have in common a dominant fraction of quartz and clay (in terms of mass), a non-hygroscopic character, and nearly no carbon (e.g., Longtin et al., 1988). The real part of the refractive index is accordingly little varying in the visible domain, where it is about 1.5–1.6 (Longtin et al., 1988; Sokolik & Toon, 1999), whereas a wide range of values are possible for the imaginary part of this index, hence for the single scattering albedo ω_0 (Fig. 1b). These changes in the imaginary part are produced in

particular by the varying contribution of quartz and hematite (iron oxide), the latter being usually embedded in quartz crystals (Sokolik et al., 1993), which are linked to the various origins of the particles (Sahara, Gobi, Arabia, etc.). Defining a typical model for desert dust is therefore always a compromise (e.g., see Moulin et al., 2001), and sensitivity studies are mandatory, for instance to assess the response of the remotely sensed dust optical thickness to changing properties of the actual dust.

From these particle size distributions and refractive indices, the absorption and scattering coefficients are usually computed following MIE theory, and this is what has been done here. It is noteworthy that doing so is questionable since desert dust particles are non spherical and of irregular shapes (Kalashnikova & Sokolik, 2000; Mishchenko & Travis, 1997). Approximating these particles by spheroids and using for instance T-Matrix calculations would allow more realistic volume scattering functions to be derived for the dust aerosols, which is of high relevance for the determination of the optical thickness, yet of poor relevance to the problem examined here, i.e., the detection of absorption in the visible. This detection is rather relying on the correctness of the spectral dependence of scattering.

What must be kept in mind from Fig. 1 is that the range of values for the spectral dependency of the scattering coefficient is small in the near infrared, and that maritime and dust aerosols behave quite similarly in this spectral domain. Therefore, observations in the near infrared are of little help in identifying absorbing aerosols. On the contrary, the single scattering albedo in the visible is markedly different for non-absorbing maritime aerosols and absorbing dusts. This difference has a strong impact on the remote sensing signal, so the visible domain is the one where absorbing aerosols are possibly identified.

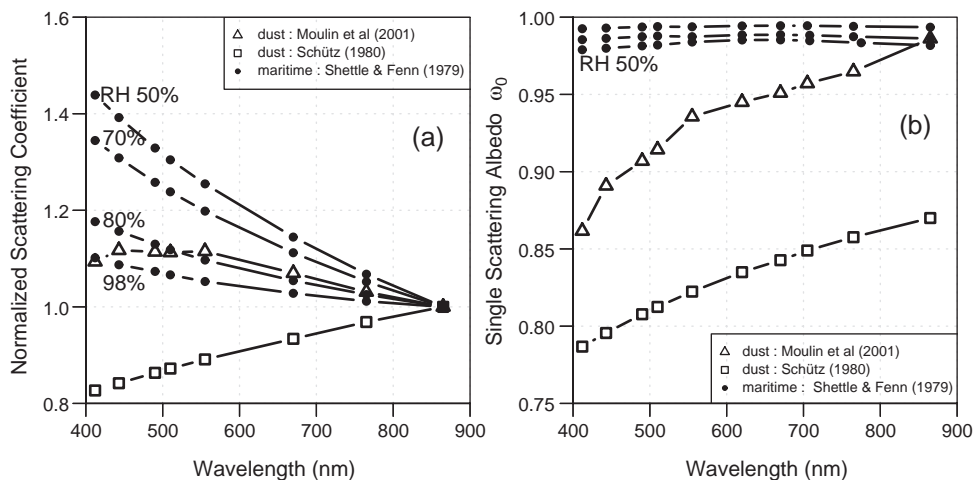


Fig. 1. (a) Aerosol scattering coefficient normalized at 865 nm for various aerosol models, as indicated. (b) Visible to near infrared aerosol single scattering albedo for the same models than in (a) (Schütz, 1980).

2.2. Effect on the top-of-the-atmosphere (TOA) signal

Illustration of the effect of absorbing dust on the TOA signal is provided in Fig. 2. The aerosol reflectance, actually approximated by the difference between the total minus the Rayleigh reflectance, is plotted in the principal and perpendicular planes as a function of the viewing angle, for a maritime aerosol with a relative humidity of 80% (Shettle & Fenn, 1979) and a dust aerosol (BDS1 model, Moulin et al., 2001), both for an optical thickness of 0.2 at 550 nm. Simulations were carried out for solar zenith angles of 20° and 60° and for the wavelengths 510 and 865 nm.

Because the optical thickness is the same the signals in the near infrared are close (bold continuous and dashed lines). Differences, however, are observed in the solar and anti solar planes, for viewing directions where the formation of the signal mostly involves the forward and backward parts of the aerosol volume scattering function, i.e., the ones that are the most dependent on the particle size distribution.

In contrast, the aerosol reflectances in the visible (510 nm) are very different for both aerosols (thin continuous and dashed lines); they are larger than in the near infrared for the

maritime aerosol whereas the converse holds for the dust aerosol (nearly flat spectral dependency). The reflectances evolve in opposite directions for the two types of aerosols, and the difference is larger for lower sun elevations (compare upper and lower panels of Fig. 2), which is due to the reinforcement of absorption effects by increased multiple scattering. The difference is also increasing as the optical thickness increases (not shown), with, however, a kind of saturation level for the reflectance of dust that is reached when optical thickness becomes large (e.g., Moulin et al., 2001).

As far as ocean color observations are concerned, the near infrared domain is where candidate aerosols are selected for the atmospheric correction of the visible bands, usually among predefined sets of representative non-absorbing maritime aerosol models. Selecting such models will end up in an over-correction of the signal in the blue bands when dusts are present, due to the rapid decrease of the reflectance with decreasing wavelength, as a result of the increase of absorption (Fig. 1b). This effect is reinforced by multiple scattering at short wavelengths. Detecting aerosol absorption therefore necessitates looking into the visible

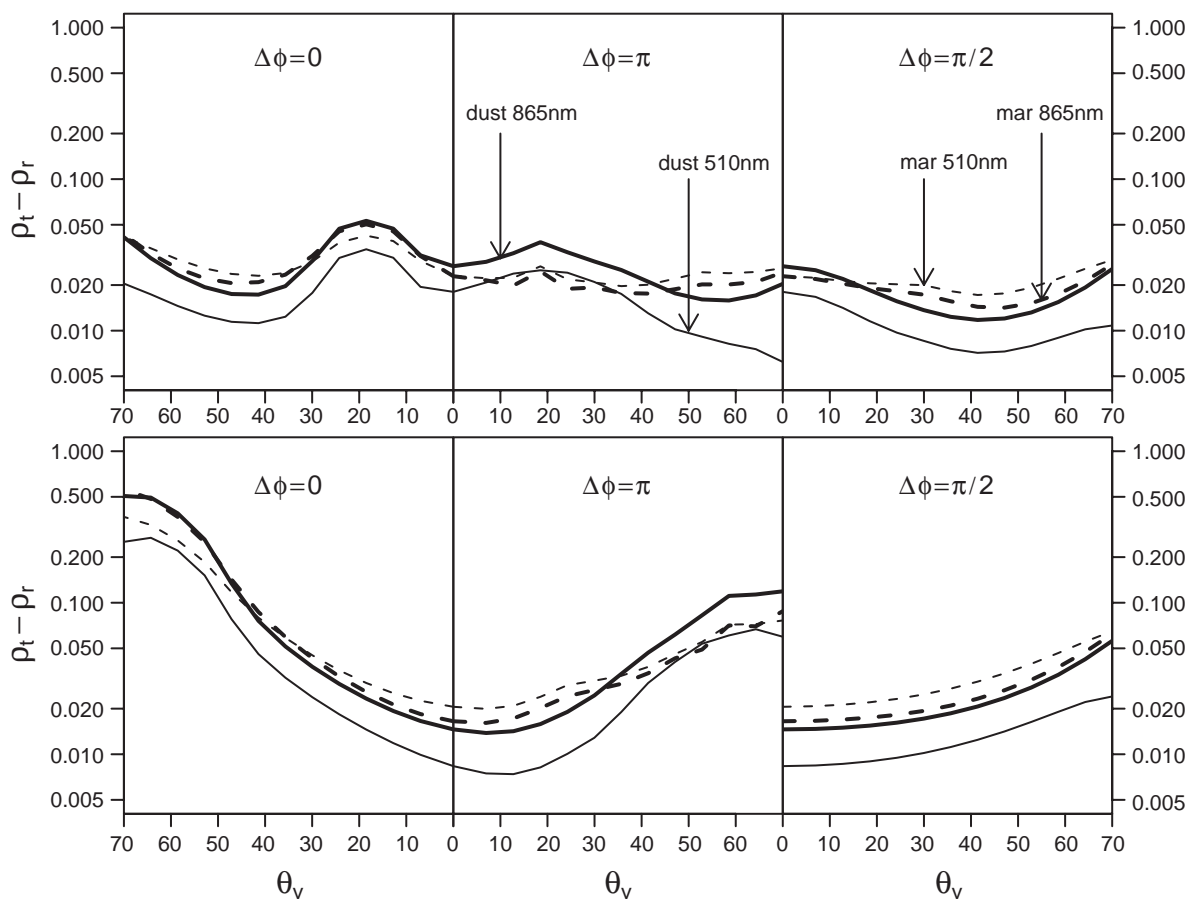


Fig. 2. Aerosol reflectance, approximated as the difference between the total and the Rayleigh reflectance, as a function of the satellite viewing angle, and in the solar ($\Delta\phi=0$), antisolar ($\Delta\phi=\pi$) and perpendicular ($\Delta\phi=\pi/2$) planes. The top and bottom panels are for a sun zenith angle of 20° and 60°, respectively. The bold lines are for $\lambda=865$ nm, with the continuous line for the dust (BDS1 model; Moulin et al., 2001) and the dashed line for the maritime aerosol (for RH=80%, Shettle & Fenn, 1979). The thin lines are for $\lambda=510$ nm, again with the continuous line for the dust and the dashed line for the maritime aerosol.

domain. The ocean reflectance in the visible, however, experiences large changes with the various water constituents, which are unknown when the atmospheric correction is attempted. It is now examined how to circumvent this difficulty.

2.3. The hinge point of ocean optical properties in Case 1 waters

Oceanic Case 1 waters are exclusively considered here; they have been defined (Morel & Prieur, 1977) as those waters where the inherent optical properties are fully determined, besides sea water itself, by phytoplankton and the ensemble of particles and dissolved substances that are associated to them. The key to the determination of the optical properties in these waters is their covariance with the chlorophyll concentration, Chl, which allowed general laws to be derived where Chl is used as the sole index of the optical properties. This is true in particular for the irradiance reflectance, $R(\lambda)$, the spectral changes of which being referred to as the ocean color, and which is the ratio of the upwelling to downwelling irradiances at null depth (i.e., just below the sea surface).

The specific feature of $R(\lambda)$ spectra that is used here is referred to as the “hinge point” (Clarke et al., 1970), which is located around 510–520 nm and where R is precisely little varying with Chl (insert in Fig. 3). The usefulness of this peculiarity clearly appears when considering what has been stated before about the optical properties of absorbing

aerosols, which necessitate looking at the visible part of the spectrum for their possible identification. In most part of this spectral domain, however, the large changes in $R(\lambda)$ caused by the changes in Chl, at least a factor of 10 at 440 nm, impair the detection of subtle changes in the atmospheric path reflectance due to absorption by aerosols. This is true in particular in the blue, where both aerosol and phytoplankton absorption would be maximum. Therefore a compromise is needed, which is precisely found in the 510–520 nm domain, where the effects of aerosol absorption are not maximum but where the changes in the water reflectance are minimum.

Knowing that R is, to the first order, proportional to backscattering and inversely proportional to absorption, the roughly parallel evolutions of these two inherent optical properties around 510 nm explains the relative steadiness of R at this wavelength. A bit farther into the green domain (about 550 nm), phytoplankton absorption is minimal and the changes in backscattering dominate, ending up with an increase of R with increasing Chl. A bit farther into the blue (around 490 nm for instance), i.e., coming closer to the main absorption peak of Chl at 440 nm, absorption dominates and R is rapidly decreasing with increasing Chl. These opposite evolutions are the basis of the quantification of Chl from the reflectance spectrum.

Therefore, the basic assumption onto which the proposed algorithm is based is that $R(510)$ can be considered as an a priori known constant, accompanied by a typical uncertainty. The mean value of $R(510)$ and its uncertainty (at 1σ)

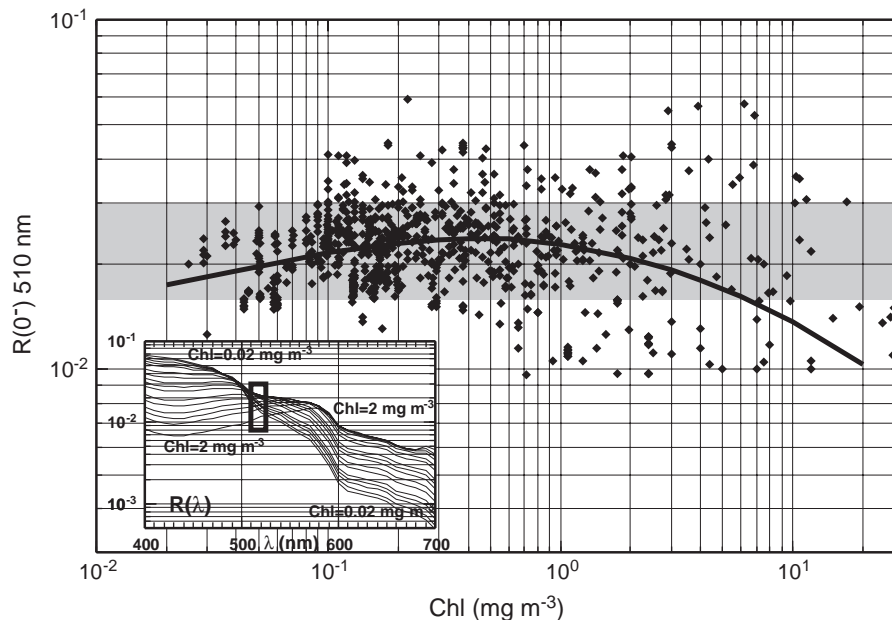


Fig. 3. Diffuse reflectance of the ocean at 510 nm, $R(510)$, as a function of the chlorophyll concentration, Chl. Reflectance values measured at sea in Case 1 waters are shown as symbols, pooling together data from cruises in various regions of the ocean: Galapagos, Caribbean and Sargasso Sea (Tyler, 1973), northeast Atlantic off Mauritania (MEDIPROD group, 1976), Pacific (OLIPAC in 1995; PACIPROD in 1987). The SEABAM data set (O'Reilly et al., 1998) is also included. The shaded area corresponds to the mean of these in situ data plus or minus one standard deviation (i.e., 0.025 and 0.007). The curve has been obtained from the model of Morel and Maritorena (2001), with a sun zenith angle of 30°. The same model has been used to draw the curves shown in insert, illustrating the large changes of the reflectance in the blue and green domains with the chlorophyll concentration, and the minimal change of this reflectance in the 510–520 wavelength range (the different curves are separated by a 0.3 increment in $\log(\text{Chl})$).

have been computed from the data displayed in Fig. 3; they are respectively equal to 2.3×10^{-2} and 7×10^{-3} . When expressed in terms of the directional reflectance above the sea surface, ρ_w , which is about half the below-water reflectance (R), these values translate into a mean $\rho_w(510)$ of about 1.2×10^{-2} and a $\sigma(\rho_w)$ of about 3×10^{-3} . These values are confirmed when examining global monthly composites of the ocean reflectance such as those produced from the SeaWiFS observations. The reflectance of the ocean being known, the error in the atmospheric correction can be determined (see later on for details).

It is however known that ocean optical properties are locally diverging from the mean values that would be predicted by general bio-optical models (e.g., Gordon et al., 1988; Morel & Maritorena, 2001). Using a single mean value for $\rho_w(510)$ is therefore probably unwise. It can be, however, easily foreseen to produce a global, seasonally varying climatology of this quantity, for instance from the global ocean color observations of modern sensors. Using this type of information would allow to reinforce the capability of the algorithm to detect aerosol absorption irrespective to the area of interest.

3. Algorithm description

3.1. Outline of the algorithm structure

The algorithm proposed here basically relies on the atmospheric correction scheme that was proposed for the MERIS ocean color observations (Antoine & Morel, 1998, 1999), and which is briefly recalled below.

Reflectances at the TOA level are hereafter considered in absence of wind-generated oceanic whitecaps or foam, and for viewing directions out of the sun glint (i.e., the direction

of specular reflection of sunrays by a more or less wavy interface). The total reflectance at the top of atmosphere level, ρ_t , is therefore

$$\rho_t = \rho_{\text{path}} + t_d \cdot \rho_w \tag{2}$$

where ρ_{path} is the atmospheric path reflectance and t_d is the diffuse transmittance along the pixel-to-sensor path. The reflectance ρ_{path} is formed by all photons reaching the TOA after several scattering events in the atmosphere, to the exception of those who entered the ocean. Atmospheric correction is the estimation of ρ_{path} , which requires that the contributions of scattering by aerosols, denoted ρ_a , and molecules, denoted ρ_r , be quantified.

It was shown that the $[\rho_{\text{path}}/\rho_r]$ ratios are monotonic functions of the aerosol optical thickness, τ_a , and are unique for a given aerosol and geometry (Antoine & Morel, 1998). They allow an aerosol type to be selected among several predefined models, by using Lookup tables (LUTs) generated from radiative transfer simulations (see later on for details about these computations), and which contain the coefficients of the quadratic relationship between the ratio $[\rho_{\text{path}}/\rho_r]$ and τ_a , for several aerosol models, geometries, and all relevant wavelengths. Although linearity between $[\rho_{\text{path}}/\rho_r]$ and τ_a is often observed for moderate values of τ_a (< 0.5), a quadratic expression is used to account for the decrease in the rate of change of $[\rho_{\text{path}}/\rho_r]$ as a function of τ_a (with a kind of saturating behavior for extreme values of τ_a).

Briefly, the scheme (see Fig. 4) starts with computing the ratio of the path reflectance, ρ_{path} , as measured by the sensor at two wavelengths in the near infrared (λ_{IR1} and λ_{IR2} , where there is no marine signal) to the reflectance of a pure Rayleigh atmosphere at the same wavelengths, ρ_r . The latter is simply obtained from pre-computed values. Because multiple scattering effects depend on the aerosol type,

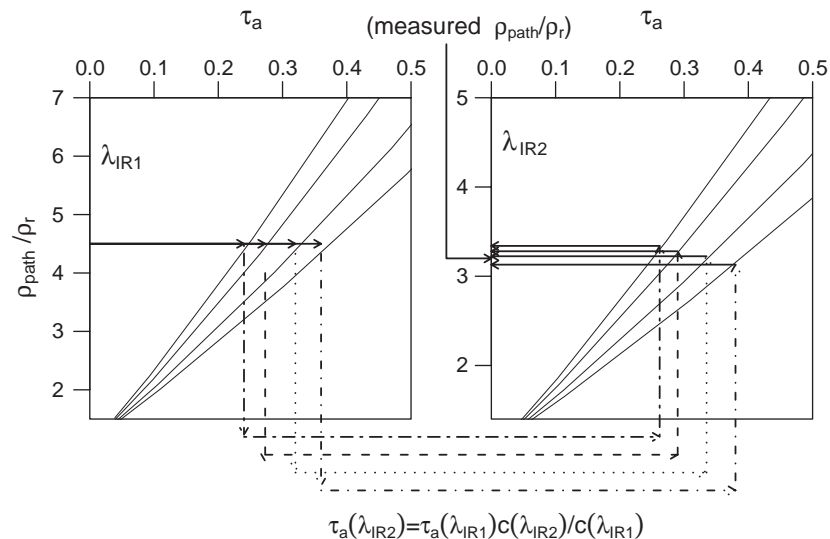


Fig. 4. Schematic diagram of the initial steps of the atmospheric correction, where a couple of candidate aerosol models is selected on the basis of the $[\rho_{\text{path}}/\rho_r]$ ratio (see text).

several values of $\tau_a(\lambda_{IR1})$ are compatible with the value of $[\rho_{path}/\rho_r]$ at λ_{IR1} , and each one corresponds to a given aerosol model. This set of $\tau_a(\lambda_{IR1})$ values is then converted into the equivalent set at λ_{IR2} , by making use of the spectral attenuation coefficients of each aerosol. To these $\tau_a(\lambda_{IR2})$ values correspond several values of the ratio $[\rho_{path}/\rho_r]$ at λ_{IR2} , which differ according to the aerosol type. Comparing this set of values to the actual ratio $[\rho_{path}/\rho_r]$ at λ_{IR2} allows the two aerosol models which most closely bracket the actual $[\rho_{path}/\rho_r]$ ratio to be selected. The remaining steps of the algorithm rest on the assumption that the mixing ratio that is derived by this way is invariable with wavelength (Gordon & Wang, 1994). It is then possible to estimate $[\rho_{path}/\rho_r]$ for the visible wavelengths from its values at λ_{IR2} and λ_{IR1} , provided that the relationships with τ_a have been previously established for the appropriate wavelengths. Atmospheric correction of the visible observations is achieved by re-multiplying the ratio $[\rho_{path}/\rho_r]$ by the value of ρ_r , leading to ρ_{path} , and therefore to the marine reflectance. The aerosol optical thickness is obtained at each wavelength as the weighted average of the two values corresponding to the selected couple of aerosol models, again using the mixing ratio obtained from the near infrared bands.

The accuracy of such a multiple scattering algorithm has been shown to be of about ± 0.002 in reflectance in the blue. The reader is referred to Antoine and Morel (1998, 1999) for further details about the algorithm.

3.2. Detection of aerosol absorption

After atmospheric correction, reflectance errors exceeding the ± 0.002 limit in the blue occur when absorbing aerosols are present within the atmosphere (Gordon, 1997), except if their presence and their optical properties would be both a priori known and a specific LUT generated for that

peculiar aerosol. Quantifying this error is the basis of the algorithm proposed here.

In order to separately identify absorbing dust aerosols and non-absorbing oceanic aerosols, atmospheric correction is performed at first with a limited set of aerosol models, supposedly representative of standard maritime atmospheres only. Making an assumption on the oceanic reflectance at 510 nm, the error in atmospheric correction is obtained at this wavelength as the total reflectance measured by the sensor minus the path reflectance estimated with the maritime models minus the adopted mean value for the ocean reflectance:

$$\Delta\rho(510) = \rho_t(510)_{\text{measured}} - \rho_{\text{path}}(510)_{\text{estimated}} - t_d\rho_w(510). \quad (3)$$

If this error is negative and below a predefined threshold (see later on for the determination of its value), it is an indication that ρ_{path} has been overestimated when using non-absorbing aerosols, and is a footprint of aerosol absorption.

The correction is then again performed by using specific LUTs, constructed using several dust models, until a model is selected as being the one leading to the minimum error at 510 nm. The overall logic is illustrated on Fig. 5. It is also noteworthy that the estimation of $\Delta\rho(510)$ includes several uncertainties, namely the possible calibration error on $\rho_t(510)_{\text{measured}}$, the inherent accuracy of the atmospheric correction for maritime aerosols that translates as an uncertainty on $\rho_{\text{path}}(510)_{\text{estimated}}$, and finally the possible error on $t_d\rho_w(510)$ that may arise because of the natural variability of the marine reflectance at this wavelength.

This method is therefore based on a preliminary detection of absorption before trying to infer a dust model and then to derive the optical thickness from the path reflectance. In that sense it is different from other methods previously published

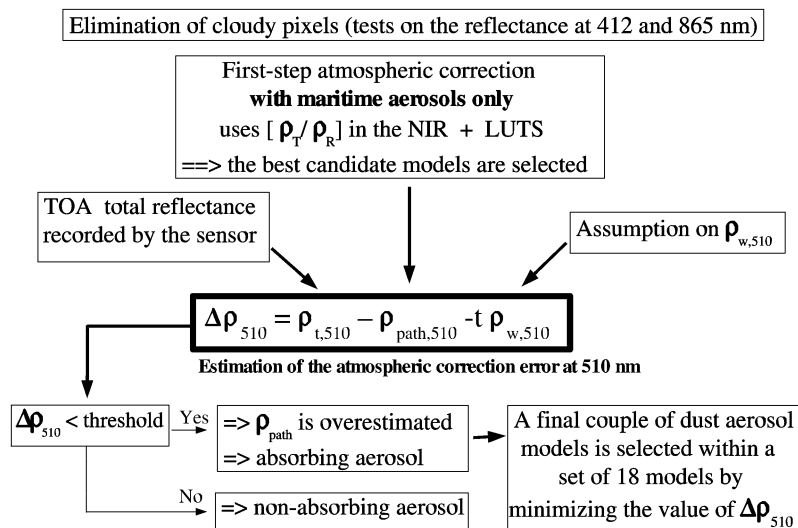


Fig. 5. Diagram of the overall logic of the algorithm.

(e.g., Dulac et al., 1996; Jankowiak & Tanré, 1992; Moulin et al., 1997), which implicitly assume the presence of absorbing dusts. The present algorithm can be applied in a routine and global processing of ocean color, without the a priori knowledge of the area that is actually observed, and it allows in principle to detect whether a plume of high aerosol optical thickness is made of absorbing or non-absorbing aerosols.

4. Practical implementation

4.1. Aerosol models and their vertical distribution

Before presenting the properties of the aerosol models that were used when implementing the algorithm, it must be reminded that the first step of this algorithm, i.e., the detection of absorption at 510 nm, is independent of the dust model that is possibly used in a second step where atmospheric correction of visible bands would be the objective. Besides the assumption on the marine signal, the detection capability depends only on the initial set of aerosol models onto which the initial correction of the 510 nm band is based. The optical properties of the maritime types of aerosol are, however, much less varying in the natural environment than it is observed for the dust-like aerosols (see, e.g., Holben et al., 2001), and some validation of their optical properties have been already reached (Schwindling et al., 1998; Smirnov et al., 2003).

Therefore, important parameters of the implementation are the background maritime aerosol models, the dust models and their vertical repartition in the atmosphere, and the practical way to perform the radiative transfer computations that are needed to generate the set of pre-computed results, i.e., the so-called “lookup tables” (LUTs).

A set of twelve aerosol models is used (from Shettle & Fenn, 1979). It includes four maritime aerosol models, four rural models that are made of smaller particles, and finally four coastal models that are a mixing between the maritime and the rural models. These twelve models have mean particle sizes, thus optical properties, that are varying as a function of the ambient relative humidity, set to 50%, 70%, 90% and 99% (hence the 3 times four models). This set is supposed to cover the range of spectral dependencies that may occur over most oceanic areas, from the clearest offshore regions to the more turbid coastal atmospheres. These twelve models are actually those used in the processing of the SeaWiFS observations (Gordon & Wang, 1994).

The six dust models as proposed by Moulin et al. (2001) have been used, which are defined by a combination of three log-normal particle size distributions and two sets of wavelength-dependent refractive indices. These models have been built in such a way that the best match was obtained between TOA total reflectances derived from the SeaWiFS observations off the west coast of Africa and

reflectances derived through radiative transfer calculations using these models.

The atmosphere is divided into three layers containing specific types of aerosols, as recommended by the WCRP (1986), namely the boundary layer (0–2 km) with maritime, coastal or rural aerosols, the free troposphere (2–12 km) with a permanent background of continental aerosol ($\tau_a=0.025$ at 550 nm) and the stratosphere (12–50 km) with a permanent background of H₂SO₄ aerosols ($\tau_a=0.005$ at 550 nm). When dust is superimposed onto this typical oceanic situation, the boundary layer still includes a background of maritime aerosols with an optical thickness of 0.1 at 550 nm, and the dust is uniformly distributed over the 0–2 or 0–7 or 0–12 km altitude ranges (Moulin et al., 2001). Several vertical distributions are needed because the TOA reflectance of an atmosphere containing absorbing aerosols is indeed depending on the altitude and thickness of the aerosol layer (e.g., Gordon, 1997), and because this distribution is unknown when applying the algorithm. The six models combined with these three vertical distributions end up with what is referred to as eighteen aerosol assemblages.

4.2. Radiative transfer computations

The MOMO code (Fell & Fischer, 2001), based on the Matrix Operator Method—a variant of the doubling-adding method—has been used to calculate the TOA total reflectances. The version of the code that we used did not include polarization. Simulations were performed for various atmospheres bounded by a black (i.e., totally absorbing), Fresnel-reflecting ocean. The water–air interface is possibly wind-roughened with a probability distribution function of wave facets modeled according to Cox and Munk (1954). The vertical profiles for molecules is taken from Elterman (1968), with a standard integrated content corresponding to an atmospheric pressure of 1013.25 hPa. The aerosol profiles are as described above. These parameters fully define the simulations needed to generate pseudo data and the accompanying lookup tables for gas-free atmospheres.

When more realistic atmospheres are simulated, ozone absorption is as well considered, with a vertical profile taken from Elterman (1968) and for a standard integrated content of 350 Dobson Units. Oxygen absorption is also accounted for in case one of the near infrared bands encompass the oxygen A-band, i.e., for the SeaWiFS sensor. This is performed through line-by-line computations based on the MODTRAN database.

5. Test and calibration with simulated data

5.1. Determining threshold values

As said before, the estimation of $\Delta\rho(510)$ (Eq. (3)) includes several uncertainties that remains to be quantified.

The first source of error comes from the satellite sensor calibration and is discussed below, the second one is linked to the inherent accuracy of the atmospheric correction for maritime atmospheres (error on $\rho_{\text{path}}(510)_{\text{estimated}}$) and will be determined through the use of simulated data, and the third one is the natural variability of the marine reflectance that will be assessed by examining in situ data.

Absolute calibration of ocean color sensors should be at least within an uncertainty of 2% (e.g., Gordon, 1990), which means that at 510 nm, where the TOA total reflectance remains below 0.1 for $\tau_a < 0.3$, the error due to calibration should not exceed 2×10^{-3} in terms of reflectance. It is likely that it is even lower for modern sensors, whose calibration budget is pushed towards uncertainties $< 1\%$.

As for determining the inherent accuracy of the method, histograms of the error $\Delta\rho(510)$, computed via Eq. (3) yet with $t\rho_w(510)=0$, are shown in Fig. 6, for various optical thicknesses and several geometries pooled together. These results were obtained with simulated data for an atmosphere above a black ocean; they are displayed on the one hand for maritime aerosols (Fig. 6a), and on the other hand, for absorbing dusts (Fig. 6b and c). In both cases, only maritime aerosols were considered to derive $\Delta\rho(510)$ through the atmospheric correction. Therefore, the first set of values obtained for a nominal situation with maritime aerosols simply provides the inherent accuracy of the method, while the use of the dust model provides a measure of how the $\Delta\rho(510)$ error increases when this type of aerosol is increasingly concentrated in the atmosphere.

These results clearly show that absolute errors $< \sim 1 \times 10^{-3}$ are typical of the atmospheric correction accuracy at 510 nm when maritime aerosols are present. Exceptions only exist when the optical thickness is very large, which is not realistic for maritime aerosols. It is also shown that the errors become nearly systematically negative and $< -1 \times 10^{-3}$ as soon as the optical thickness of the absorbing dust is larger than 0.2.

A simple threshold could therefore be set at -1×10^{-3} , and any error (Eq. (3)) below that value would indicate that absorbing dust is present. The results in Fig. 6 are however merging several geometries, without paying attention to a possible organization of the values according to the sun zenith angle or the satellite viewing angle. It is indeed well-known that the $\Delta\rho(510)$ error is increasing with increasing sun and viewing angles, so with the air mass, i.e., the sum of the inverses of the cosines of the sun zenith angle and of the viewing angle. This is primarily due to the increasing role of multiple scattering as the atmospheric paths are increased, and because these effects are heavily depending on the aerosol type. The accuracy of the extrapolation from the near infrared to the visible is lower in that case. Therefore, using the same threshold irrespective of the viewing or illumination geometry might be misleading. A larger value could be adopted for low sun elevations or grazing viewing angles. The $\Delta\rho(510)$ errors have been therefore plotted as a function of the scattering angle γ (Fig. 7), which better describes the geometry of the observation since it includes the $\Delta\phi$ angle, following:

$$\cos(\gamma) = -\cos(\theta_s)\cos(\theta_v) - \sin(\theta_s)\sin(\theta_v)\cos(\Delta\phi) \quad (4)$$

The decrease of the accuracy with increasing γ clearly appears, but actually only for values of this angle that are outside the remote sensing domain. Therefore one single threshold seems sufficient for remote sensing applications. It is set to 3×10^{-3} , i.e., the sum of the inherent uncertainty of the atmospheric correction for clear atmospheres and of the calibration uncertainty.

This value would be directly usable as the threshold for detection of an incorrect atmospheric correction in case the marine signal would be exactly known. The uncertainty that exists around the mean value of the ocean reflectance at 510 nm must be, however, accounted for. The test (Eq. (3)) being made with respect to a negative value, the uncertainty in $\rho_w(510)$ has actually to be added to the value just mentioned. Considering globally Fig. 3, the mean value for

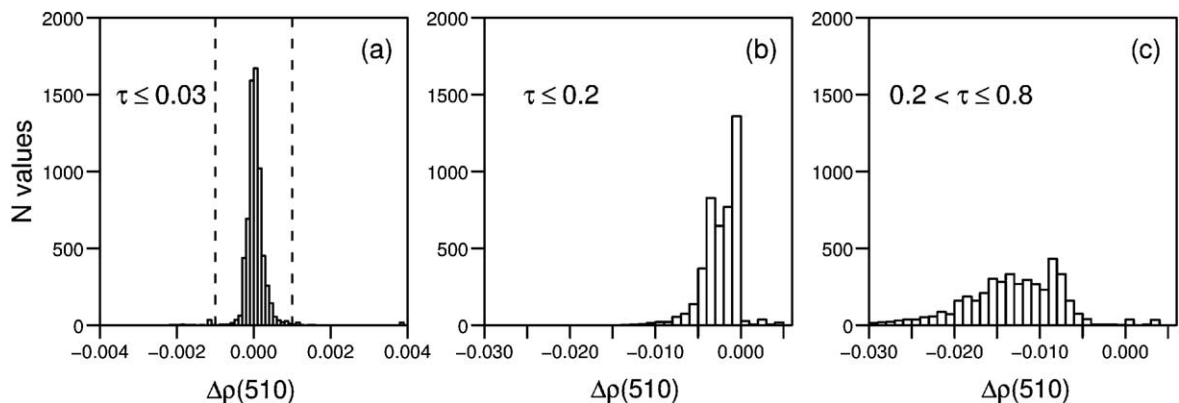


Fig. 6. Histograms of the atmospheric correction errors at 510 nm, for several ranges of the optical thickness, as indicated. The left panel is for a maritime aerosol (RH=80%), and the two other panels are for the BDS1 dust model (Moulin et al., 2001). The vertical dashed lines indicate the a priori typical accuracy of the algorithm when applied to maritime atmospheres. These histograms were obtained by pooling together results obtained for several geometries ($0^\circ < \theta_s < 70^\circ$, step 5° ; $0^\circ < \theta_v < 40^\circ$, step 5° ; $45^\circ < \Delta\phi < 135^\circ$, step 15°).

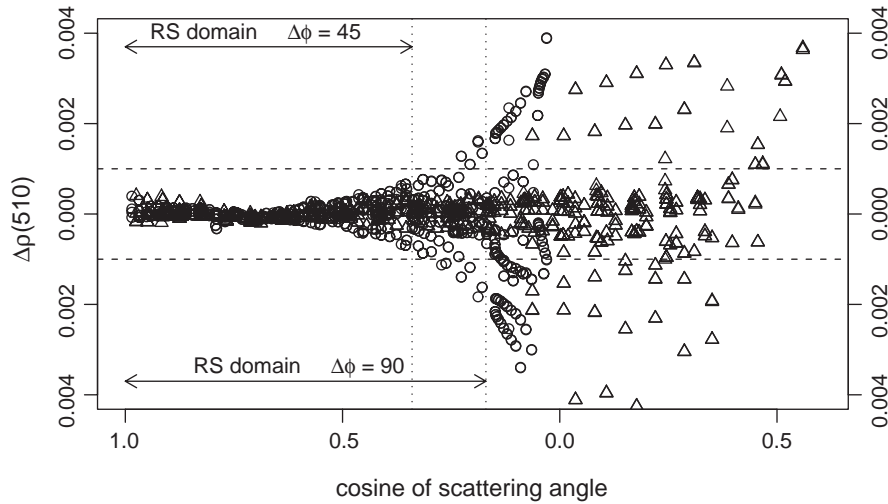


Fig. 7. Atmospheric correction error at 510 nm as a function of the cosine of the scattering angle. Results are for θ_s up to 80° and θ_v up to 70° , and are separately plotted for $\Delta\phi=90^\circ$ (circles) and $\Delta\phi=45^\circ$ (triangles). The usual remote sensing domain, i.e., $\theta_s < 70^\circ$ and $\theta_v < 50^\circ$, is indicated.

$\rho_w(510)$ and its associated uncertainty were set to 1.2×10^{-2} and 3×10^{-3} , which is the second component of the final threshold.

What is also shown in Fig. 6 is that the $\Delta\rho(510)$ error becomes much larger than $\sim 3 \times 10^{-3}$, i.e., the uncertainty on $\rho_w(510)$, as soon as the optical thickness of the absorbing dust is above ~ 0.5 . In that case, the uncertainty in the marine signal should no longer impair the capability of the algorithm to detect aerosol absorption.

It is likely that the uncertainties mentioned above can be decreased firstly by increasing as much as possible the radiometric accuracy of the satellite sensor, and second when the algorithm is applied over areas where the mean $\rho_w(510)$ and its associated uncertainty (natural variability) would be a priori known. This is actually at reach by generating global climatologies of these two quantities from the observations of ocean color sensors, on a monthly basis for instance.

5.2. Theoretical detection limit

At 510 nm, ρ_{path} is about 0.06–0.07 for $\tau_a \sim 0.1$ and for maritime aerosols (e.g., see Fig. 5 in Antoine & Morel, 1998), and the mean ρ_w is about 0.01 ± 0.003 . Therefore, when subtracting from the total reflectance (measured) the sum [estimated ρ_{path} + supposed mean value of ρ_w], the remaining quantity is the sum of the error in atmospheric correction (i.e., the error in ρ_{path}), plus the error in the mean value for ρ_w . The error in ρ_{path} is therefore obtained at ± 0.003 , i.e., something like 5% of ρ_{path} . If this uncertainty is above the error caused by wrongly using a maritime aerosol model while the actual aerosol is dust, the shortcoming is not detected. The errors in ρ_{path} due to the selection of an irrelevant aerosol model become, however, greatly larger than the ± 0.003 uncertainty as far as τ_a become greater than 0.1–0.2, which is usually the case when absorbing aerosols are blown above the ocean. In summary,

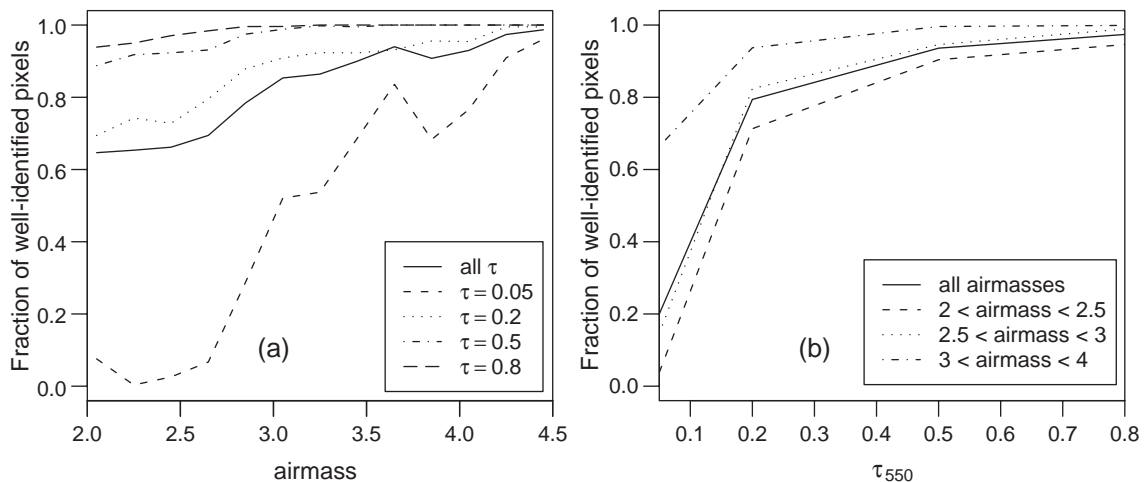


Fig. 8. (a) Fraction of well-identified pixels, i.e., dusty pixels recognized as such, displayed either as a function of the airmass, with different curves for different values of the optical thickness, as indicated, or as a function of the optical thickness (b), with different curves for different ranges of the airmass, as indicated.

the detection limit of the present method would be at $\tau_a \sim 0.15$ at 865 nm.

This is confirmed practically in Fig. 8, where the percentage of identification of dusty pixels, when the algorithm is applied to pseudo data, is displayed either as a function of the airmass, with different curves for different values of the optical thickness (Fig. 8a) or as a function of the optical thickness, with different curves for different ranges of the airmass (Fig. 8b). The percentage of well-identified pixels reaches on average more than 75% when optical thickness is greater than 0.2, and is still around 40% when optical thickness is 0.1. These percentages are higher for greater values of the airmass. These results indicate that the detection limit is actually quite low for large viewing angles and/or low sun elevations. It is also confirmed that the limit would be on average at an optical thickness of 0.2, which is here provided through the use of pseudo data; examination of real data actually confirms this limit (see later on).

5.3. Retrieval of the optical thickness

Although the primary objective of the technique proposed here is the identification, thus the mapping, of the blue-absorbing aerosols, it is nevertheless timely to check whether the aerosol optical thickness is correctly retrieved in the near infrared and the visible. This is first attempted on simulated data, and validation against real data will be presented later. The aerosol optical thickness is derived as

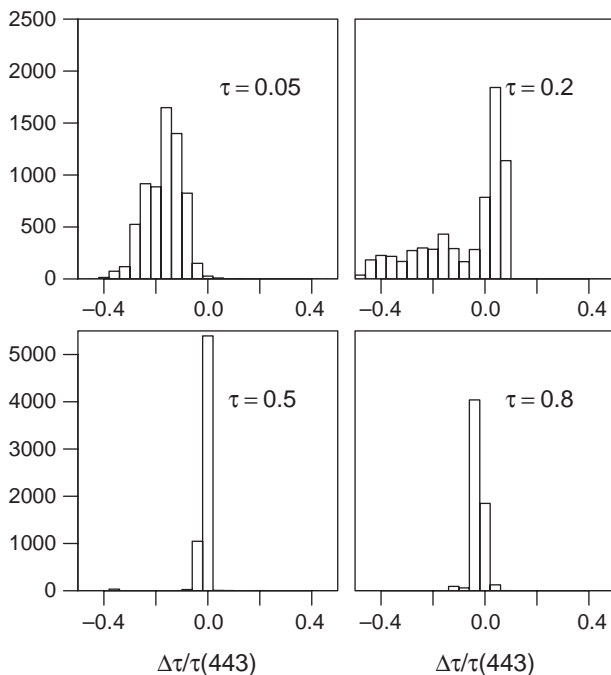


Fig. 9. Histograms of the relative error in the optical thickness retrieved at 865 nm, for four nominal values of this optical thickness at 550 nm. These histograms were obtained by pooling together results obtained for several geometries ($0^\circ < \theta_s < 70^\circ$, step 5° ; $0^\circ < \theta_v < 40^\circ$, step 5° ; $45^\circ < \Delta\phi < 135^\circ$, step 15°), and for the 18 models as defined by Moulin et al. (2001).

described in Antoine and Morel (1999), i.e., as the weighted average of the two values that correspond to the best couple of aerosol models selected on the basis of the near infrared [$\rho_{\text{path}}/\rho_r$] ratio (cf. Section 3.1).

Histograms of the relative error in τ_a are displayed in Fig. 9 for four different nominal τ_a values. These histograms were built by pooling together the results obtained for several geometries and the 18 dust models previously defined (i.e., 6 models times 3 vertical distributions). The relative error remains usually within $\pm 20\%$, i.e., within specification of the algorithm, except when the optical thickness is low (0.05) so that the dust is not detected and an inappropriate model is used to perform the atmospheric correction.

6. Application to ocean color remote sensing observations

6.1. Cloud screening

The algorithm proposed in this work applies to clear-sky observations, which are those that went through cloud screening procedures. As far as ocean color is concerned, these procedures are often simple tests based on a single and constant threshold applied to the reflectance in the near infrared. If the threshold is set to a sufficiently low value, this technique is efficient in removing any too bright targets, such as land masses, clouds of various brightness and cloud borders (this is used for the SeaWiFS, for instance). These tests, however, also eliminate all thick dust plumes, and which are moderately to highly bright in the near infrared (sometimes not discernible from land). The problem is critical as well because dust is often transported in perturbed areas where clouds are numerous so that distinguishing between both is essential.

Another technique than a simple threshold in the near infrared is needed. Among the possibilities is the use of a threshold on the local variance of the reflectance computed on several consecutive pixels, with the underlying assumption that dust plumes are more homogeneous than clouds are (Moulin et al., 1997a, 1997). This technique is used, for instance, in the processing of the POLDER (Bréon & Colzy, 1999) and MODIS (Martins et al., 2002) observations. Another solution is proposed here, which is based on the fact that dust aerosols absorb in the blue part of the e.m. domain, whereas clouds do not, which provides a discriminating tool in this spectral domain. A first rough elimination of the brightest clouds, and of land masses in particular, is still performed through a first test in the near infrared, using however a quite large threshold, i.e., 0.2. Land areas covered by vegetation might go through this test, which is not a serious difficulty since an a priori elimination of land masses can be performed based on geographical information. Then, a second threshold is used at the 412 nm band (one of the most common band amongst all ocean color sensors), which aims at refining the elimination of less

bright clouds, leaving dust plumes available for further processing.

This threshold is, by definition, applied to the TOA signal before any other treatment, and in particular before the reflectance due to Rayleigh scattering can be computed (not calculable since the cloud altitude is unknown). The large contribution of the latter in the blue, and the significant coupling between molecular and aerosol scattering in this domain, impede the use of a single threshold, which needs to be dependent on the geometry of the observation. Indeed, different answers in terms of the TOA signal might occur for a given aerosol load, as a function of the geometry; the same answer might fortuitously be provided by different loads and different geometries.

Therefore, a geometry-dependent threshold has been derived by simulating the TOA total reflectance for an atmosphere containing dust with a very high optical thickness, i.e., 2 at 550 nm, and using the BDW2 model

proposed by Moulin et al. (2001), distributed from the surface to an altitude of 7 km. This aerosol with such a vertical distribution was found by these authors to be among the most representative of real observations. The underlying idea is that any brighter target cannot be produced by a cloudless atmosphere. From the radiative transfer computations, a three-dimensional lookup table is generated, with the solar zenith angle, viewing angle and azimuth difference as entries. Any pixel with a TOA total reflectance above this threshold is eliminated from any further analysis.

The skill of the method is illustrated in Fig. 10. Panel a shows a true color image (SeaWiFS, October 28, 1999), where clouds, a plume of dust aerosols and clear sky are present. When examining the reflectance at 865 nm (Fig. 10b), both the clouds and the dust plume exhibit high reflectances, whereas the dust no longer appears when looking at 412 nm (Fig. 10c). In that case, land masses are neither clearly appearing (hence the necessity of an initial

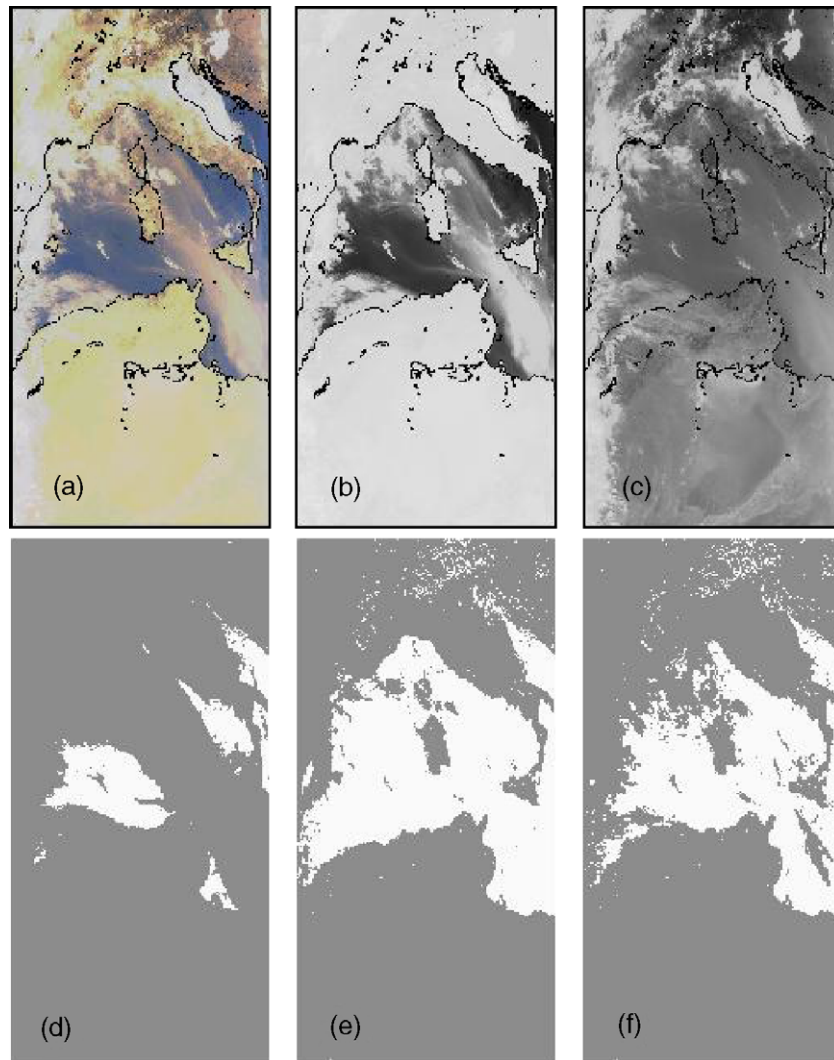


Fig. 10. True color SeaWiFS image of October 27, 2000 (combination of the bands at 412, 555 and 670 nm), (b) and (c): corresponding reflectance in the near infrared (865 nm) and visible (412 nm). (d) to (f): results obtained when different thresholds are used to discriminate between clouds and thick dust plumes (see text).

screening in the near infrared), whereas clouds of moderate to high brightness remain visible. The three lower panels of Fig. 10 respectively illustrate that too much pixels are eliminated by a low threshold in the near infrared (Fig. 10d, in particular the dust plume), that the same technique, when applied with a larger threshold, does not properly eliminates clouds (Fig. 10e), and finally that the combination of the near infrared technique plus the threshold at 412 nm provides the desired answer by eliminating clouds and leaving the dust plume available for further analysis (Fig. 10f). Further illustration of the skill of the technique is provided with the following analysis of aerosol identifications in various areas.

6.2. Examples using SeaWiFS and MERIS observations

Five examples (three in the Mediterranean, one off Senegal and one over the sea of Japan; see Fig. 11 for dates) are now discussed in order to illustrate the algorithm functioning through its application to TOA observations of the SeaWiFS and MERIS ocean color sensors.

The SeaWiFS is equipped with eight spectral bands, among which are the three bands specifically needed here, i.e., 865 nm (bandwidth 40 nm), 765 nm (20 nm) and 510 nm (20 nm). Three similar bands are found in the bandset of the MERIS sensor, at 865 nm (25 nm width), 779 nm (15 nm, essentially no oxygen absorption there) and 510 nm (10 nm). Specific lookup tables have been generated for these two sets of bands (cf. Section 4.2), so that the algorithm can be applied to the TOA level 1b calibrated total reflectances of these two sensors. In the case of the SeaWiFS band at 765 nm, no correction was performed on the measured radiances to account for the impact of minor changes in atmospheric pressure on the oxygen absorption (recall that oxygen absorption is accounted for in the lookup tables).

The SeaWiFS scene of October 27, 2000 (Fig. 11, top panels) shows a dust cloud extending from the South Ionian sea—its thicker part ($\sim 0.5 < \tau_a < \sim 1$)—to the northwestern Mediterranean sea where it is spread out on a larger area and where the optical thickness is lower ($\sim 0.2 < \tau_a < \sim 0.5$). This dust cloud is well-identified by the algorithm, and its boundary, as depicted by the algorithm, approximately matches with the area where the optical thickness is larger than about 0.15, which is slightly lower than anticipated by theoretical considerations. The Ångström exponent is about 0.30 inside the dust plume, which is characteristic of an aerosol made of large particles.

The skill of the algorithm is also clearly illustrated on the second example (February 12, 1999), with a less intense plume than on the first image (optical thickness lower than 0.5). The Ångström exponent is around 0.35. The detection again occurs at an optical thickness between about 0.1 and 0.2. It is also noteworthy that the discrimination between dust and moderately bright clouds is well performed (e.g., the region east and southeast of Crete).

The third example (MERIS, January 8, 2003) is located a bit further east in the Levantine basin, with a main dust cloud extending from the border between Libya and Egypt to the south Turkish coasts, and secondary transports from above the Nile river delta, and also toward the south of Turkey and around Cyprus. Only the main branch, with an optical thickness reaching 0.5, is identified by the algorithm. Areas of moderately high aerosol optical thickness (around 0.2) are not identified, which is probably an indication of the non-absorbing character of the aerosols in these plumes. This example emphasizes that a simple threshold on the optical thickness would not be sufficient to specifically target absorbing aerosols. On the contrary, some areas are erroneously identified as being contaminated by mineral dust, on the one hand in cloud shadows (e.g., northwest of Crete), and, on the other hand, above the sea of Marmara. As for cloud shadows, this is appearing since MERIS has an Equator crossing time of about 10:30 h (12 h for SeaWiFS) so that the sun zenith angle is large enough at the time of the satellite pass for shadows to be observed. Eliminating a fringe of pixels around identified clouds could be a simple empirical way to avoid this artifact. Concerning the Sea of Marmara, the algorithm flaw is due to the presence there of sediment-dominated Case 2 waters, for which the hypothesis of a known and nearly constant marine signal cannot hold. Therefore, the present algorithm should be only applied after an accurate screening on non-Case 1 waters.

The image off Senegal, shown as the fourth example, is fully covered by Saharan dust, with the densest parts on both sides of the satellite swath, yet with elevated optical thickness across the entire scene. In such a case, identification of the dust is achieved over the whole image, even when the optical thickness is ~ 0.1 , which is a likely indication of a strongly absorbing aerosol. In that case, a simple threshold on the optical thickness would not be relevant for identifying the absorbing aerosol.

The Asian aerosol is also well identified in the SeaWiFS image over the sea of Japan (fifth example, bottom of Fig. 11), again with a boundary that approximately matches the areas where the optical thickness is larger than 0.2.

The five examples provided in this section demonstrate the detection skill of the algorithm, with a clear delineation of the dust plumes. The boundary is, as expected, appearing when the optical thickness reaches values between about 0.1 and 0.2 at 865 nm, although sometimes lower values also lead to the identification of the pixel as dusty. Dust plumes of very high optical thickness remain difficult to analyze because they are sometimes eliminated after the test performed at 412 nm, which is unavoidable with such a simple threshold-based cloud screening. More sophisticated tests using spectral indices might be useful in such cases.

The three different regions and the two sensors considered here illustrate the general applicability of the technique. It is admittedly not possible to fully demonstrate its ubiquitous applicability before largest data sets are processed and the results analyzed (regional or global studies;

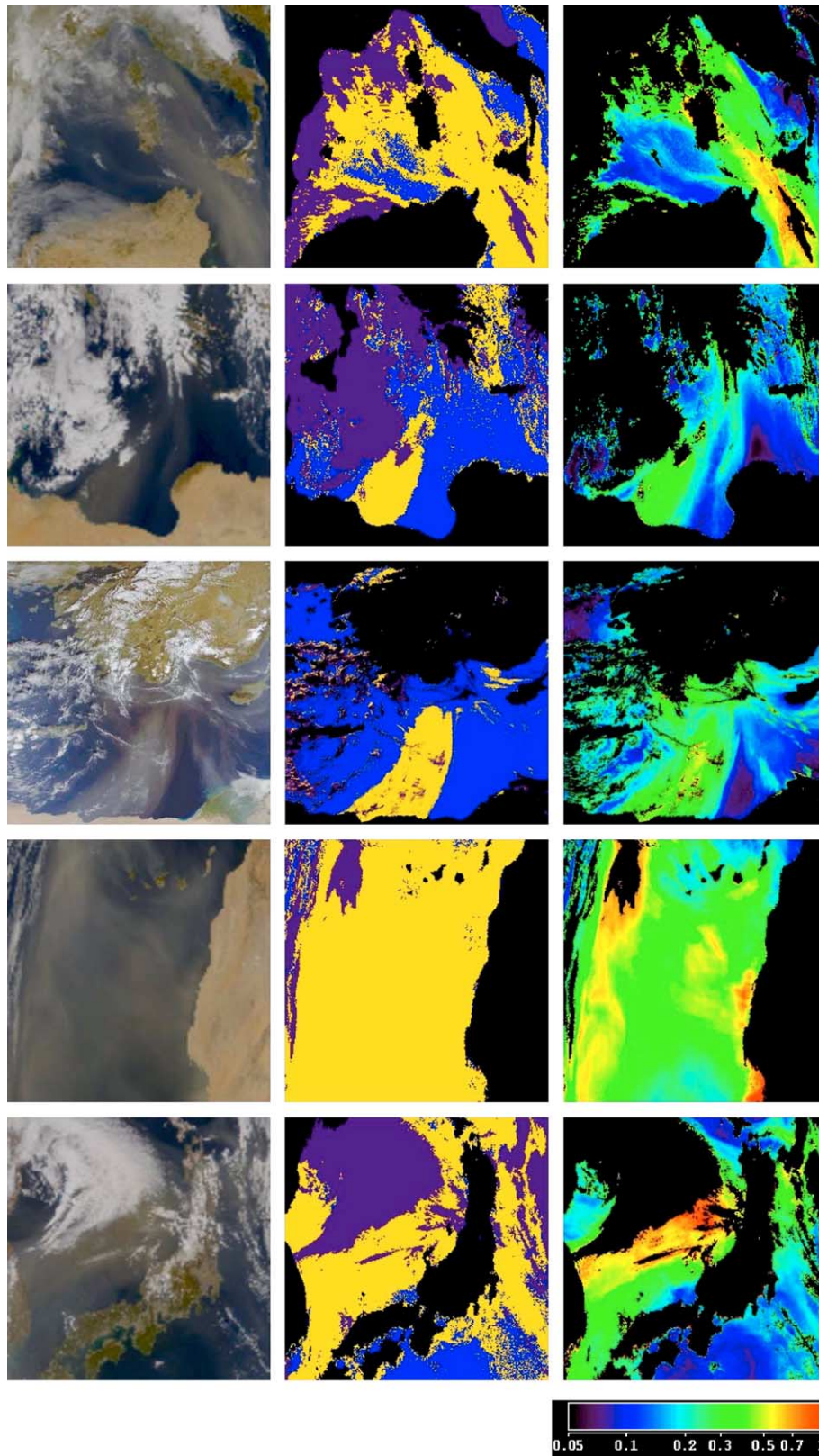


Fig. 11. Three upper panels: true color SeaWiFS image of October 27, 2000 over the Mediterranean sea (combination of the bands at 412, 555 and 670 nm, left panel), corresponding map of the aerosol types as detected by the present algorithm (mid panel: yellow: dust; blue: maritime; black: land; purple: clouds as detected at 412 nm), and aerosol optical thickness (right panel). Other groups of three panels are, from top to bottom, for the following locations, sensors and dates: Mediterranean sea, SeaWiFS, February 11, 1999; Mediterranean sea, MERIS, January 8, 2003; Atlantic off Senegal, SeaWiFS, February 1, 2000, and Sea of Japan, SeaWiFS, March 19, 2002.

out of scope here), including as well other areas where dust is transported such as the Arabian Sea and the oceans south and east of Australia.

6.3. Validation using data from the AERONET

The qualitative validation accessible when examining individual satellite scenes must be complemented by a quantitative validation, which can be made with respect to three quantities, namely the percent of well-identified dust pixels, and the aerosol optical thickness and its spectral dependence, all as derived either from the satellite observations (SeaWiFS in this particular instance) or from in situ measurements. The first parameter validates the method proposed here, while the two others are rather an independent verification of the relevance of the dust models proposed by Moulin et al. (2001).

The aerosol optical thicknesses and Ångström exponents have been obtained from data collected at two sites of the AERONET, namely the Lampedusa island in the Mediterranean sea (35°N, 12°E; about 9×3 km), and the Capo Verde islands off Senegal (Sal Island : 16°45N, 22°57W; about 12×30 km). These two spots have been selected for their position below well-known tracks of Saharan dust, and because they are small islands, which is minimizing the perturbations of the satellite observations by large continental bodies, either through the optical environment effect (sun photometers being necessarily installed on land, even if as close as possible to the shoreline) or by the addition of pollution aerosols.

Aerosol optical thickness is provided by the AERONET at 440, 670 and 870 nm, which is a bandset close to the one

of the SeaWiFS (443, 670 and 865 nm), and these small differences in wavelengths have been ignored. The Level-2 AERONET data have been used, for which the typical accuracy of optical thickness is better than 0.02 (Dubovik et al., 2000). The Ångström exponent is computed between the wavelengths 443 and 865 nm following:

$$\alpha(443, 865) = -\frac{\log[\tau_a(443)/\tau_a(865)]}{\log[443/865]} \quad (5)$$

The classification of observations as typical of either maritime or dusty atmospheres is based on the one hand on the value of the AERONET Ångström exponent, and, on the other hand, on the visual inspection of the corresponding SeaWiFS scenes. Thresholds are applied to the Ångström exponents, which have been determined empirically by confronting the exponent values and the visual, a priori detection of dust from the true color SeaWiFS images. For the Lampedusa site, the threshold is put to 0.5, i.e., any observation with an exponent lower than 0.5 is classified as dusty, and to 0.3 for the Capo Verde site. This difference might be due to a higher proportion of large particles and a higher absorption in the aerosol off Africa. A data set of concurrent AERONET and SeaWiFS observations is then built, and used to assess the detection skill of the algorithm. In order to match the SeaWiFS and AERONET measurements in space and time, the comparison is performed when two AERONET measurements are found within 15 min of the SeaWiFS overpass, and when at least one half of the SeaWiFS retrievals within a 5×5 pixels square box containing the AERONET site are valid. For the small Lampedusa island, the square box is centered onto the photometer location, whereas it is shifted to the west of the

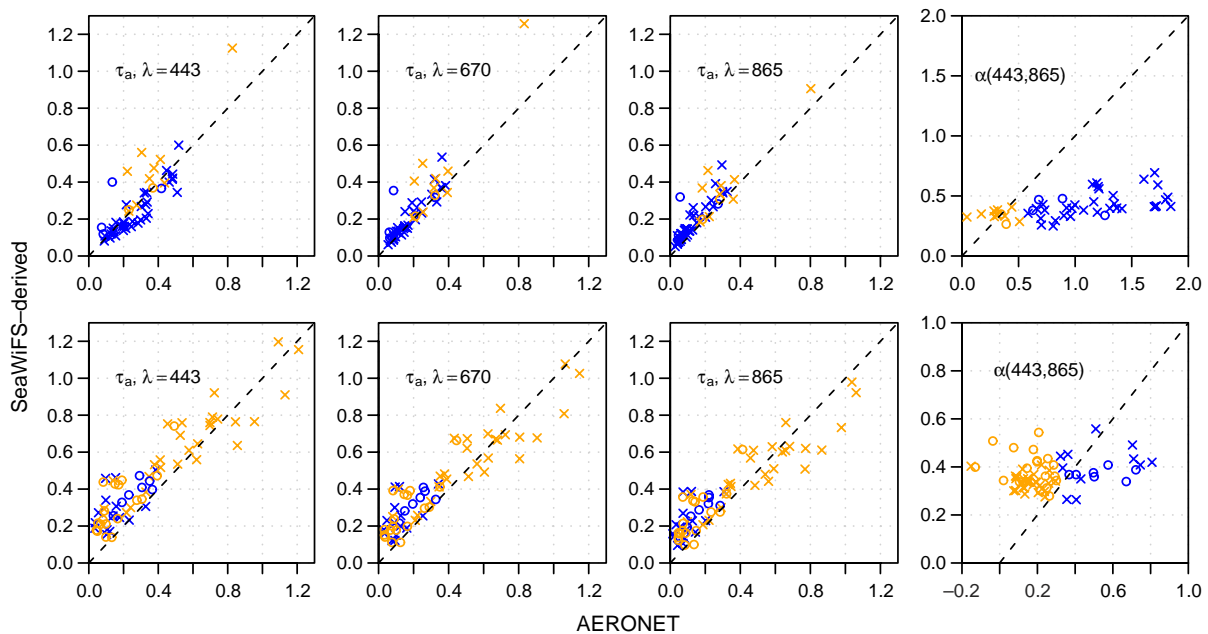


Fig. 12. Scatter plots of the optical thickness at 443, 670 and 865 nm, and of the aerosol Ångström exponent. The values derived from the algorithm are plotted as a function of the values extracted from the AERONET database. The four upper panels are for the Lampedusa site and the four lower panels for the Capo Verde site. Crosses (circles) indicate pixels that were well (wrongly) identified. Blue (yellow) symbols are for maritime (dusty) atmospheres.

Table 1
Detection statistics at the two AERONET sites

Site	Atmosphere type	Percent of well-identified pixels
Lampedusa (N=47)	Dusty	82
	Maritime	79
Capo Verde (N=68)	Dusty	61
	Maritime	68

larger Sal island (i.e., photometer location is on the eastern margin of the pixel box) in order not to include too much land pixels. At the end, 47 validation points are selected at the Lampedusa site (AERONET data only for the year 2000) and 68 at the Capo Verde (2000 and 2001).

Scatter plots of the aerosol optical thickness and Ångström exponents, as derived through the present algorithm and through the AERONET measurements, are displayed in Fig. 12, detection statistics are given in Table 1, and regression statistics in Table 2.

The percentages in Table 1 show that the algorithm correctly classifies the atmosphere types either as dusty or maritime, with a success rate between 61% and 82%, in agreement with the theoretical values displayed in Fig. 8. Identification is better performed around the Lampedusa site, as compared to the Sal Island region. In this case, this is mostly due to several situations that have been a priori classified as dusty while the optical thickness was below 0.2 or even 0.1 at 865 nm (recall that this classification is only based on the value of the Ångström exponent). A possibility to improve the detection statistics, in particular to decrease erroneous classification of maritime atmosphere as dusty, would have been not to apply the algorithm for $\tau_a < 0.1$, which would be actually consistent with what has been said about the theoretical detection limit of the algorithm.

For the Lampedusa site, the slope of the regression lines of the retrieved versus AERONET optical thickness are close to 1, except at 670 nm, and the intercept of the regression is significant only at 865 nm. The consequence is an underestimation of the retrieved Ångström exponents, because the algorithm slightly underestimates $\tau_a(443)$ and slightly overestimates $\tau_a(865)$. In addition, the range of values is narrower and centered on ~ 0.4 . Note that the underestimation of the Ångström exponents mostly occurs for maritime atmospheres.

At the Capo Verde site, there is a bias in the retrieval of the optical thickness, which are overestimated for $\tau_a < \sim 0.5$ and underestimated above (regression slopes around 0.7 and intercepts > 0.15). The Ångström exponents are not system-

atically underestimated, and the range of derived values (0.2 to 0.6) is closer to what is found in the AERONET retrievals (-0.2 to 0.8). The dispersion of the points is, however, still very large. Part of this scatter might as well be due to the non sphericity of the dust particles (e.g., Mishchenko et al., 1997), which is not accounted for when computing the aerosol optical properties since spherical particles are assumed and the MIE theory is used.

The results obtained at the two AERONET sites confirm the capability of the algorithm as well as the detection threshold of the method (i.e., at $\tau \approx 0.1$ – 0.2).

6.4. Ability of the method to detect other, non-dust, blue-absorbing aerosols

Although the title of this paper non-discriminatorily refers to blue-absorbing aerosols, the tests and validation that have been presented above were only considering mineral dusts, which represent the vast majority of the blue-absorbing aerosols. Carbonaceous aerosols are however another important family of absorbing aerosols, as produced either by biomass burning, pollution or volcanic activity (e.g., Kaufman et al., 2000b). Three SeaWiFS images have been selected to briefly examine the behavior of the algorithm in presence of such aerosols. The first image (top of Fig. 13; true-color images on the left panel) shows a large dust plume extending from Tunisia to Sardinia and to Spain, one smoke plume east of Corsica, and several smoke plumes along the Algerian coasts; the westernmost of these plumes is as well mixed with some dust. All these aerosols are detected by the algorithm, except the smoke plume east of Corsica, which is eliminated from the analysis by the 412-nm-threshold cloud screening. Volcanic ash is as well detected by the algorithm, as shown by the second image (eruption of the Etna volcano in July of 2001; middle of Fig. 13). Finally, a thicker and larger smoke plume (fires in California in October of 2003; bottom of Fig. 13) is partly detected and partly eliminated as a cloud.

These additional tests show that the method is performing as well with biomass burning aerosols or even with volcanic aerosols. As soon as a significant absorption exists in the blue-green region, it can be detected by the algorithm. The derivation of the optical thickness, however, cannot be valid as long as specific lookup tables are not generated, which, although possible as far as realistic optical properties are known for this type of aerosols, was out of the scope of the present work.

Table 2

Regression parameters of the linear fit between SeaWiFS-derived and measured optical thickness at the two AERONET sites, and for the three wavelengths indicated

	$\lambda=865$ nm			$\lambda=670$ nm			$\lambda=443$ nm		
	Slope	Intercept	R^2	Slope	Intercept	R^2	Slope	Intercept	R^2
Lampedusa	1.04	0.05	0.84	1.27	-0.01	0.84	1.05	-0.01	0.72
Capo Verde	0.68	0.15	0.83	0.72	0.16	0.84	0.77	0.19	0.84

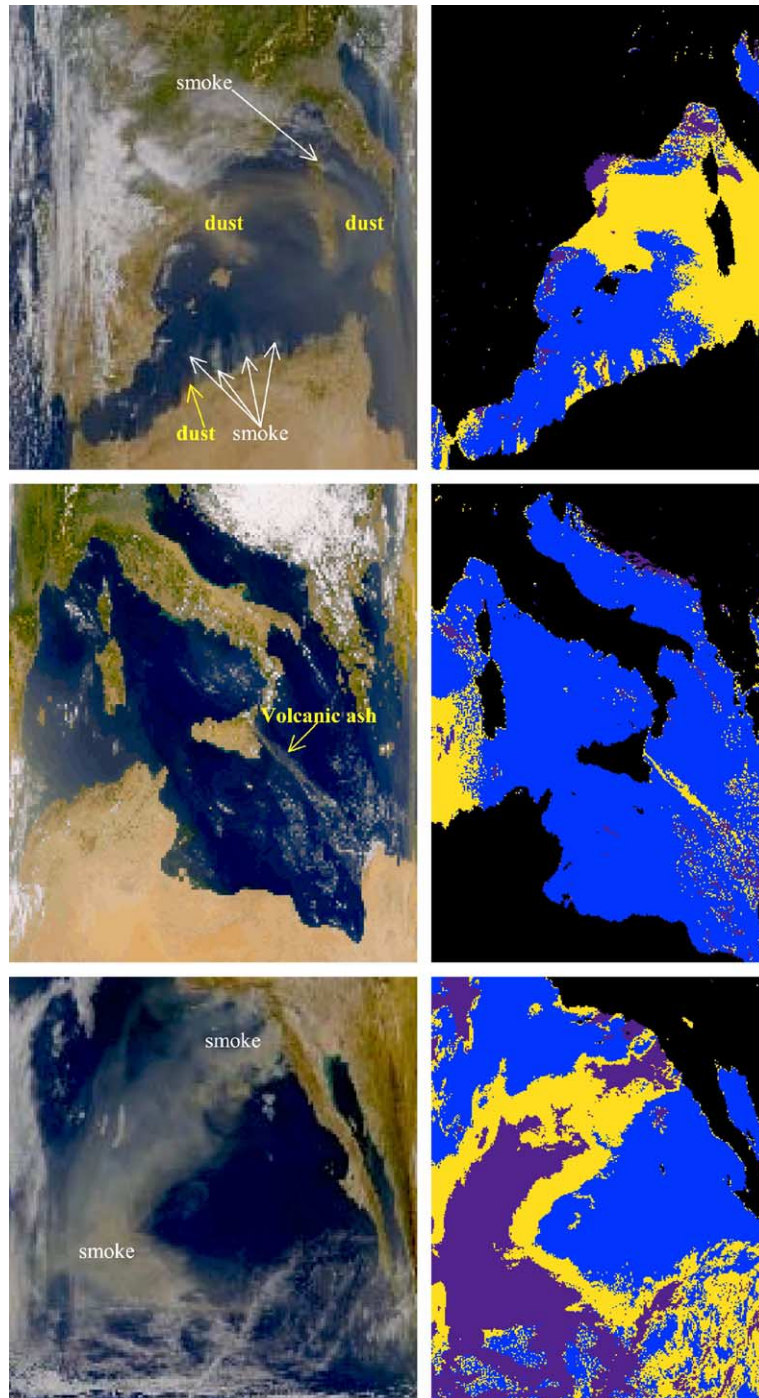


Fig. 13. Upper left panel: true color SeaWiFS image of August 26, 2000 over the Mediterranean sea (combination of the bands at 412, 555 and 670 nm). Upper right panel: corresponding map of the aerosol types as detected by the present algorithm (same color codes than for Fig. 11). Mid and lower panels: as for the upper panels, but for July 22, 2001 in the Mediterranean Sea and October 27, 2003 off California, respectively.

A limitation is however due to the cloud test performed at 412 nm, which is somewhat specific to mineral dusts. Scattering by small smoke particles has often a steeper spectral dependency than that of mineral dusts, so the test performed at 412 nm eliminates them as if they were clouds (smokes appear whiter than dusts on the true-color images).

In summary, the proposed algorithm is responding as soon as a significant absorption exists at 510 nm (mineral

dusts, volcanic aerosols, smokes), but the 412-nm cloud test is more specific to the case of dust.

7. Conclusions

A simple algorithm has been proposed that is capable of identifying blue-absorbing aerosols over the ocean from

near infrared and visible ocean color satellite observations. The detection is efficient as soon as the dust optical thickness is larger than about 0.1–0.2 at 865 nm, and it depends (i) on the sensor calibration, (ii) on the degree of absorption of the aerosol, and (iii) on the deviations of the actual ocean optical properties from the basic assumption used in the algorithm, i.e., the ocean reflectance at 510 nm in Case 1 waters is constant or at least can be a priori known.

The technique has been applied with equal success to satellite images from various regions of the ocean and for two sensors, as shown on the one hand by a qualitative validation, i.e., dust distributions provided by the algorithm compared to the a priori description of these distributions, and, on the other hand, by a quantitative validation against AERONET data.

This algorithm has been implemented into the operational processing chain of the MERIS sensor, so that it is applied systematically to all observations by this ocean color sensor. This is adding a new capability to this ocean-color-oriented mission, i.e., the possibility to monitor blue-absorbing aerosols (usually mineral dust) over the oceans at global scale, and possibly to quantify their absorption capabilities and thence their impact on the Earth radiation budget. This capability can complement the aerosols data sets that are produced by other, more aerosol-oriented, satellite missions such as the POLDER, the MODIS and the PARASOL.

Other techniques have been previously proposed in order to detect absorbing aerosol from ocean color remote sensing, which use the full spectral information provided by these sensors (e.g., Chomko et al., 2003; Gordon et al., 1997). To specifically consider the case of absorbing aerosols, these iterative methods require a modeling of the ocean optical properties as a function of the chlorophyll concentration in order to retrieve simultaneously both ocean and atmosphere parameters at several wavelengths. It is believed that the simple method proposed here, because it includes a single and minimum assumption about the ocean optical properties (i.e., $\rho_w(510)$ is sufficiently little varying so that a climatology can be used), is more generally applicable. In particular no assumption is needed about the ocean reflectance in the blue part of the spectrum, where it is the most variable and where the uncertainty about the optical properties is the largest.

However, because of this simple assumption, the method proposed here cannot apply to optically-complex Case 2 waters. In such waters, the marine signal is no longer negligible, is much more varying than in Case 1 waters, and is hardly predictable in the near infrared, so the first-step atmospheric correction cannot work properly. An accurate screening of Case 2 waters is therefore mandatory either before applying the algorithm or after it has been applied, as an a posteriori verification.

The present method does not provide information about the vertical repartition of aerosols, which is on the contrary

one of the parameters that enters into the construction of the lookup tables. Nothing prevents, however, the construction of specific lookup tables that might be relevant for certain regions where the vertical repartition of aerosols would be specifically known.

Finally, it must be stressed that a significant part of the mineral dust is transported within clouds, and thus escapes the present method and any other clear-sky method. Algorithms specifically designed to detect dusty clouds should be developed in order to eventually get a more comprehensive picture of the dust transport over the oceans.

Acknowledgements

This work has been supported through a Phd fellowship to Delphine Nobileau (University Pierre et Marie Curie), and through ESA/ESTEC contract No. 14393/00/NL/DC and the NAOC (“Neural network Algorithms for Ocean Color”) project that was funded by the European commission, for the development of the MERIS atmospheric correction algorithms. The AERONET is thanked for providing the data at the Lampedusa site, which is managed by Sergio Pugnaghi and Renato Santangelo, and at the Capo Verde site, which is managed by Didier Tanré. The SeaWiFS Level 1a data have been obtained through the Goddard Distributed Active Archive Center at the NASA GSFC, which is also duly acknowledged. The MERIS data have been obtained through ESA, and with the help of the ACRI-st and Brockmann-Consult companies. Pr. Jürgen Fischer is thanked for providing the MOMO radiative transfer code. François Marie Bréon and Cyril Moulin are thanked for useful discussions along the course of this work.

References

- Alfaro, S. C., & Gomes, L. (2001). Modeling mineral aerosol production by wind erosion: Emission intensities and aerosol size distributions in source areas. *Journal of Geophysical Research*, 106, 18075–18084.
- Antoine, D., & Morel, A. (1998). Relative importance of multiple scattering by air molecules and aerosols in forming the atmospheric path radiance in the visible and near-infrared parts of the spectrum. *Applied Optics*, 37, 2245–2259.
- Antoine, D., & Morel, A. (1999). A multiple scattering algorithm for atmospheric correction of remotely sensed ocean colour (MERIS instrument): Principle and implementation for atmospheres carrying various aerosols including absorbing ones. *International Journal of Remote Sensing*, 20, 1875–1916.
- Bian, H., & Zender, C. S. (2003). Mineral dust and global tropospheric chemistry: Relative roles of photolysis and heterogeneous uptake. *Journal of Geophysical Research*, 108, 4672.
- Bréon, F. M., & Colzy, S. (1999). Cloud detection from the spaceborne POLDER instrument and validation against surface synoptic observations. *Journal of Applied Meteorology*, 38, 777–785.
- Brooks, N., & Legrand, M. (2000). Dust variability over northern Africa and rainfall in the Sahel. In S. McLaren, & D. Kniveton (Eds.), *Linking Climate Change to Land Surface Change* (pp. 1–25). Dordrecht: Kluwer Academic Publishers.

- Charlson, R. J., Schwartz, S. E., Hales, J. M., Cess, R. D., Coakley, J. A., Hansen, J. E., et al. (1992). Climate forcing by anthropogenic aerosols. *Science*, 255, 423–430.
- Chomko, R. M., Gordon, H. R., Maritorena, S., & Siegel, D. A. (2003). Simultaneous retrieval of oceanic and atmospheric parameters for ocean color imagery by spectral optimization: A validation. *Remote Sensing of Environment*, 84, 208–220.
- Clarke, G. L., Ewing, G. C., & Lorenzen, C. J. (1970). Spectra of backscattered light from the sea obtained from aircraft as a measure of chlorophyll concentration. *Science*, 1119–1121.
- Cox, C., & Munk, W. (1954). Statistics of the sea surface derived from Sun glitter. *Journal of Marine Research*, 13, 198–227.
- D'Almeida, D. A. (1986). A model for Saharan dust transport. *Journal of Climate and Applied Meteorology*, 24, 903–916.
- D'Almeida, D. A., Koepke, P., & Shettle, E. P. (1991). *Atmospheric Aerosols. Global Climatology and Radiative Characteristics*. Hampton, Virginia, USA: A. DEEPAK Publishing.
- Deschamps, P. -Y., Bréon, F. M., Leroy, M., Podaire, A., Bricaud, A., Buriez, J. C., et al. (1994). The POLDER mission: Instrument characteristics and scientific objectives. *IEEE Transactions on Geoscience and Remote Sensing*, 32, 598–615.
- Donaghy, P. L., Liss, P. S., Duce, R. A., Kester, D. R., Hanson, A. K., Villareal, T., et al. (1991). The role of episodic atmospheric nutrient inputs in the chemical and biological ecosystems. *Oceanography*, 4, 62–70.
- Dubovik, O., Holben, B. N., Eck, T. F., Smirnov, A. V., Kaufman, Y. J., King, M. D., et al. (2002). Variability of absorption and optical properties of key aerosol types observed in worldwide locations. *Journal of the Atmospheric Sciences*, 59, 590–608.
- Dubovik, O., Smirnov, A., Holben, B. N., King, M. D., Kaufman, Y. J., Eck, T. F., et al. (2000). Accuracy assessments of aerosol optical properties retrieved from AERONET sun and sky-radiance measurements. *Journal of Geophysical Research*, 105, 9791–9806.
- Duce, R. A., & Tindale, N. W. (1991). Atmospheric transport of iron and its deposition in the ocean. *Limnology and Oceanography*, 36, 1715–1726.
- Dulac, F., Moulin, C., Lambert, C. E., Guillard, F., Poitou, J., Guelle, W., et al. (1996). Quantitative remote sensing of African dust transport to the Mediterranean. In S. Guerzoni, & R. Chester (Eds.), *The Impact of Desert Dust Across the Mediterranean* (pp. 25–49). Kluwer Academy.
- Elterman, L. (1968). UV, visible, and IR attenuation for altitudes to 50 km. AFCRL-68-0153. Air force cambridge research laboratories.
- Fell, F., & Fischer, J. (2001). Numerical simulation of the light field in the atmosphere–ocean system using the matrix-operator method. *Journal of Quantitative Spectroscopy & Radiative Transfer*, 69, 351–388.
- Gabric, A. J., Cropp, R., Ayers, G. P., McTainsh, G., & Braddock, R. (2002). Coupling between cycles of phytoplankton biomass and aerosol optical depth as derived from SeaWiFS time series in the Subantarctic Southern Ocean. *Geophysical Research Letters*, 29, 1112.
- Gao, Y., Kaufman, Y. J., Tanré, D., Kolber, D., & Falkowski, P. G. (2001). Seasonal distributions of aeolian iron fluxes to the global ocean. *Geophysical Research Letters*, 28, 29–32.
- Garver, S. A., & Siegel, D. A. (1997). Inherent optical property inversion of ocean color spectra and its biogeochemical interpretation: I. Time series from the Sargasso Sea. *Journal of Geophysical Research*, 102, 18607–18625.
- Gong, S. L., Zhang, X. Y., Zhao, T. L., McKendry, I., Jaffe, D., & Lu, N. M. (2003). Characterization of soil dust distributions in China and its transport during ACE-ASIA 2. Model simulation and validation. *Journal of Geophysical Research*, 108.
- Gordon, H. R. (1990). Radiometric considerations for ocean color remote sensors. *Applied Optics*, 29, 3228–3236.
- Gordon, H. R. (1997). Atmospheric correction of ocean color imagery in the earth observing system era. *Journal of Geophysical Research*, 102, 17081–17106.
- Gordon, H. R., Brown, O. B., Evans, R. H., Brown, J. W., Smith, R. C., Baker, K. C., et al. (1988). A semi-analytical radiance model of ocean color. *Journal of Geophysical Research*, 93, 10909–10924.
- Gordon, H. R., Du, T., & Zhang, T. (1997). Remote sensing of ocean color and aerosol properties: Resolving the issue of aerosol absorption. *Applied Optics*, 36, 8670–8684.
- Gordon, H. R., & Wang, M. (1994). Retrieval of water-leaving reflectance and aerosol optical thickness over the oceans with SeaWiFS: A preliminary algorithm. *Applied Optics*, 33, 443–452.
- Haywood, J. M., Francis, P. N., Glew, M. D., & Taylor, J. P. (2001). Optical properties and direct radiative effect of Saharan dust: A case study of two Saharan outbreaks using data from the U.K. Met. Office. *Journal of Geophysical Research*, 106, 18417–18430.
- Herman, J. R., Bhartia, P. K., Torres, C. J., Hsu, C., Sefter, C., & Celarier, E. (1997). Global distribution of UV-absorbing aerosols from Nimbus 7/TOMS data. *Journal of Geophysical Research*, 102, 16911–16922.
- Higurashi, A., Nakajima, T., Holben, B. N., Smirnov, A. V., Frouin, R., & Chatenet, B. (2000). A study of global aerosol optical climatology with two-channel AVHRR remote sensing. *Journal of Climate*, 13, 2011–2027.
- Holben, B. N., Eck, T. F., Slutsker, I., Tanré, D., Buis, J. P., Setzer, A., et al. (1998). AERONET-A federated instrument network and data archive for aerosol characterization. *Remote Sensing of Environment*, 66, 1–16.
- Holben, B. N., Tanré, D., Smirnov, A. V., Eck, T. F., Slutsker, I., Abuhassan, N., et al. (2001). An emerging ground-based aerosol climatology: Aerosol optical depth from AERONET. *Journal of Geophysical Research*, 106, 12067–12097.
- Hooker, S. B., Esaias, W. E., Feldman, G. C., Gregg, W. W., & Mc Clain, C. R. (1992). An overview of SeaWiFS and ocean colour. In S. B. Hooker, & E. R. Firestone (Eds.), *SeaWiFS technical report series. NASA Technical Memorandum, vol. 104566, 1* (p. 24). Greenbelt, Maryland: NASA Goddard Space Flight Centre.
- Husard, R. B., Prospero, J. M., & Stowe, L. L. (1997). Characterization of tropospheric aerosols over the ocean with the NOAA advanced very high resolution radiometer optical thickness operational product. *Journal of Geophysical Research*, 102, 16889–16909.
- IPCC. (2001). *Climate Change 2001: The Scientific Basis*. Cambridge University Press.
- Jankowiak, I., & Tanré, D. (1992). Satellite climatology of Saharan dust outbreaks: Methods and preliminary results. *Journal of Climate*, 5, 646–656.
- Kalashnikova, O., & Sokolik, I. N. (2000). Modeling optical properties of irregular mineral dust aggregates. *Proceeding de 5th Conference on Electromagnetic and Light Scattering by Non Spherical Particles, Halifax, Novo Scotia, Canada*.
- Kaufman, Y. J. (1993). Aerosol optical thickness and atmospheric path radiance. *Journal of Geophysical Research*, 98, 2677–2692.
- Kaufman, Y. J., Koren, I., Remer, L., Tanré, D., Ginoux, P., & Fan, S. (2003). Dust transport and deposition observed from the Terra-MODIS spacecraft over the Atlantic Ocean. *Proceeding of the 2nd Workshop on Mineral Dust, 10–12 September 2003, Paris*.
- Kaufman, Y. J., Martins, J. V., Remer, L. A., Schoeberl, M. R., & Tamasoe, M. A. (2002a). Satellite retrieval of aerosol absorption over the oceans using sunglint. *Geophysical Research Letters*, 29.
- Kaufman, Y. J., Tanré, D., & Boucher, O. (2002b). A satellite view of aerosols in the climate system. *Nature*, 419, 215–223.
- King, M. D., Kaufman, Y. J., Tanré, D., & Nakajima, T. (1999). Remote sensing of tropospheric aerosols from space: Past, present, future. *Bulletin of the American Meteorological Society*, 80, 2229–2259.
- Krom, M. D., Brenner, S., Kress, N., & Gordon, I. I. (1991). Phosphorus limitation of primary productivity in the E. Mediterranean sea. *Limnology and Oceanography*, 36, 424–432.
- Levieveld, J., Berresheim, H., Borrmann, S., Crutzen, P. J., Dentener, F. J., Fischer, H., et al. (2002). Global air pollution crossroads over the Mediterranean. *Science*, 298, 794–799.
- Levin, Z., & Ganor, E. (1996). The effects of desert particules on cloud and rain formation in the Eastern Mediterranean. In S. Guerzoni, & R.

- Lacis (Eds.), *The Impact of Desert Dust Across the Mediterranean* (pp. 77–86). Boston, MA: Kluwer Academic Publishing.
- Li, X., Maring, H., Savoie, D. L., Voss, K., & Prospero, J. M. (1996). Dominance of mineral dust in aerosol light-scattering in the North Atlantic trade winds. *Nature*, *380*, 416–419.
- Longtin, D. R., Shettle, E. P., Hummel, J. R., & Pryce, J. D. (1988). A wind-dependent desert aerosol model: Radiative properties. Air Force Geophysical Laboratory, Report AFGL-TR-88-0112, Scientific report N°6, Hanscom, Massachusetts 01731-5000, USA.
- Martins, J. V., Tanré, D., Remer, L., Kaufman, Y. J., Mattoo, S., & Levy, R. (2002). MODIS Cloud screening for remote sensing of aerosols over the oceans using spatial variability. *Geophysical Research Letters*, *29*.
- MEDIPROD group (1976). Résultats de la campagne CINECA 5 - J. Charcot-Capricorne 7403 (1er Mars au 20 Avril 1974), *Publications du CNEXO*, N°10.
- McGowan, H. A., McTainsh, G., Zawar-Reza, P., & Sturman, A. P. (2000). Identifying regional dust transport pathways: Application of kinematic trajectory modelling to a trans-Tasman case. *Earth Surface Processes and Landforms*, *25*, 633–647.
- Mishchenko, M. I., & Travis, L. D. (1997). Satellite retrieval of aerosol properties over the ocean using polarization as well as intensity of reflected sunlight. *Journal of Geophysical Research*, *102*, 16989–17013.
- Mishchenko, M. I., Travis, L. D., Kahn, R. A., & West, R. A. (1997). Modeling phase functions for dustlike tropospheric aerosols using a shape mixture of randomly oriented polydisperse spheroids. *Journal of Geophysical Research*, *102*, 16831–16847.
- Morel, A., & Maritorena, S. (2001). Bio-optical properties of oceanic waters: A reappraisal. *Journal of Geophysical Research*, *106*, 7163–7180.
- Morel, A., & Prieur, L. (1977). Analysis of variations in ocean color. *Limnology and Oceanography*, *22*, 709–722.
- Moulin, C., Gordon, H. R., Banzon, V. F., & Evans, R. H. (2001). Assessment of Saharan dust absorption in the visible from SeaWiFS imagerie. *Journal of Geophysical Research*, *106*, 18239–18249.
- Moulin, C., Guillard, F., Dulac, F., & Lambert, C. E. (1997). Long-term daily monitoring of Saharan dust load over ocean using Meteosat ISCCP-B2 data 1. Methodology and preliminary results for 1983–1994 in the Mediterranean. *Journal of Geophysical Research*, *102*, 16947–16958.
- OLIPAC (JGOFS) cruise (1995). Data unpublished.
- O'Reilly, J. E., Maritorena, S., Mitchell, B. G., Siegel, D. A., Carder, K. L., Garver, S. A., et al. (1998). Ocean color chlorophyll algorithms for SeaWiFS. *Journal of Geophysical Research*, *103*, 24937–24953.
- PACIPROD cruise (1987). Data unpublished.
- Prospero, J. M., & Carlson, T. N. (1972). Vertical and areal distribution of Saharan dust over the Western Equatorial North Atlantic Ocean. *Journal of Geophysical Research*, *77*, 5255–5265.
- Rast, M., & Bézy, J. -L. (1995). The ESA medium resolution imaging spectrometer (MERIS): Requirements to its mission and performance of its system. In P. J. Curran, & Y. C. Robertson (Eds.), Proc. 21st Annual Conf. Remote Sensing Soc., 11–14 September, 1995, University of Southampton. *RSS95, Remote Sensing in Action* (pp. 125–132). Taylor and Francis Pub.
- Rast, M., Bézy, J. L., & Bruzzi, S. (1999). The ESA Medium Resolution Imaging Spectrometer MERIS—a review of the instrument and its mission. *International Journal of Remote Sensing*, *20*, 1681–1702.
- Ridame, C., & Guieu, C. (2002). Saharan input of phosphate to the oligotrophic water of western Mediterranean Sea. *Limnology and Oceanography*, *47*, 856–869.
- Salomonson, V. V., Toll, D. L., & Lawrence, W. T. (1992). Moderate resolution imaging spectroradiometer (MODIS) and observations of the land surface. *Proceeding of "1992 International geoscience and remote sensing symposium" (IGARSS'92), Houston, Texas.*
- Savoie, D. L., & Prospero, J. M. (1977). Aerosol concentration statistics for the Northern Tropical Atlantic. *Journal of Geophysical Research*, *82*, 5954–5964.
- Schwindling, M., Deschamps, P. -Y., & Frouin, R. (1998). Verification of aerosol models for satellite ocean color remote sensing. *Journal of Geophysical Research*, *103*, 24919–24935.
- Schütz, L. (1980). Long-range transport of desert dust with special emphasis on the Sahara. *Annals of the New York Academy of Sciences*, *338*, 515–532.
- Shettle, E. P., & Fenn, R. W. 1979. Models for the aerosols of the lower atmosphere and the effects of humidity variations on their optical properties, Environmental Research Papers, N° 676, AFGL-TR-79-0214, Air Force Geophysics Laboratory, 20 September 1979.
- Smirnov, A. V., Holben, B. N., Dubovik, O., Frouin, R., Eck, T. F., & Slutsker, I. (2003). Maritime component in aerosol optical models derived from aerosol robotic network data. *Journal of Geophysical Research*, *108*(D1), 4033.
- Smirnov, A. V., Holben, B. N., Kaufman, Y. J., Dubovik, O., Eck, T. F., Slutsker, I., et al. (2002). Optical properties of atmospheric aerosol in maritime environments. *Journal of the Atmospheric Sciences*, *59*, 501–523.
- Sokolik, I. N., Andronova, A. V., & Jonhson, T. C. (1993). Complex refractive index of atmospheric dust aerosols. *Atmospheric Environment*, *27*, 2495–2502.
- Sokolik, I. N., & Toon, O. B. (1999). Incorporation of mineralogical composition into models of the radiative properties of mineral aerosol from UV to IR wavelengths. *Journal of Geophysical Research*, *99*, 9423–9444.
- Sokolik, I. N., Toon, O. B., & Bergstrom, R. W. (1998). Modeling the radiative characteristics of airborne mineral aerosols at infrared wavelengths. *Journal of Geophysical Research*, *103*, 8813–8826.
- Stowe, L. L., Ignatov, A. M., & Singh, R. R. (1997). Development, validation, and potential enhancements to the second-generation operational aerosol product at the National Environmental Satellite, Data, and Information service of the National Oceanic and Atmospheric Administration. *Journal of Geophysical Research*, *102*, 16923–16934.
- Tanré, D., Haywood, J. M., Pelon, J., Léon, J. F., Chatenet, B., Formenti, P., et al. (2003). Measurement and modeling of the Saharan dust radiative impact: Overview of the Saharan Dust Experiment (SHADE). *Journal of Geophysical Research*, *108*, 8574.
- Tegen, I., Lacis, A. A., & Fung, I. (1996). The influence of mineral aerosols from disturbed soils on the global radiation budget. *Nature*, *380*, 419–422.
- Tyler, J. E. (1973). Measurements of photosynthesis, available radiant flux, and supporting oceanographic data, Data report, SOCR Discoverer expedition, May 1970, S.I.O. Ref. 73-16, Univ. California.
- World Climate Research Program (WCRP) (1986). A preliminary cloudless standard atmosphere for radiation computation. *International Association for Meteorology and Atmospheric Physics*. Radiation Commission, Boulder, CO., USA, 1984, WCP-112, WMO/TD-N° 24, March 1986. 60 pp.



Recent increase of Saharan dust transport over the Mediterranean Sea, as revealed from ocean color satellite (SeaWiFS) observations

D. Antoine¹ and D. Nobileau¹

Received 21 October 2005; revised 17 February 2006; accepted 9 March 2006; published 29 June 2006.

[1] An algorithm was previously developed and validated, which is capable of detecting blue-absorbing aerosols from near infrared and visible remote-sensing observations, as they are in particular collected by satellite ocean color sensors. This algorithm has been applied to 7 years (1998–2004) of Sea-Viewing Wide Field-of-View Sensor (SeaWiFS) observations over the Mediterranean Sea, on the one hand to further illustrate the appropriateness of ocean color observations to provide relevant information about aerosol types and in particular absorbing aerosols, and, on the other hand, to describe the seasonal and interannual variability of Saharan dust over the Mediterranean Sea during the SeaWiFS era. This extensive application allowed the validation of the retrieved aerosol optical thickness to be more thoroughly performed, thanks to data from the Aerosol Robotic Network (AERONET). The results of this validation and the mapping of dust aerosols and of the associated optical thickness demonstrate the skill of the algorithm. These results are in agreement with, and provide a complement to, the results of previous studies based on other remote sensing techniques, which were applied to data from the 1980s and early 1990s. They also show an increase of the dust transport over the Mediterranean over the 1998-to-2004 time period.

Citation: Antoine, D., and D. Nobileau (2006), Recent increase of Saharan dust transport over the Mediterranean Sea, as revealed from ocean color satellite (SeaWiFS) observations, *J. Geophys. Res.*, *111*, D12214, doi:10.1029/2005JD006795.

1. Introduction

[2] The interest taken in the study of desert dust originates in its potential effect on the radiative budget and climate of the whole planet [e.g., Charlson *et al.*, 1992; Li *et al.*, 1996]. Large-scale effects are expected because Saharan or Asian dust affect extended regions far from their sources [e.g., Prospero and Carlson, 1972; Savoie and Prospero, 1977; Li *et al.*, 1996; Kaufman *et al.*, 2005] and because their amount in the atmosphere may have increased largely because of human activity [Andreae, 1996]. A large uncertainty remains, however, about the sign and magnitude of the radiative forcing of aerosols, and in particular of dust aerosols [Intergovernmental Panel on Climate Control (IPCC), 2001]. This uncertainty is primarily caused by an insufficient knowledge of the absorption properties of these aerosols [e.g., Bellouin *et al.*, 2003; Tanré *et al.*, 2003].

[3] Another effect of dust aerosols could be to either fertilize the upper oceanic layers by releasing nutrients or iron adsorbed onto their surface [e.g., Donaghay *et al.*, 1991; Duce *et al.*, 1991] or to deplete surface waters of phosphorus, a possible “feeding” source of phytoplankton,

by carrying it away through adsorption and sinking [Krom *et al.*, 1991]. Therefore there is undoubtedly a connection between dust and phytoplankton [e.g., Stegman, 2000], although the reasons for this link remain largely unexplained.

[4] Dust aerosols also modify cloud microphysical properties [e.g., Levin and Ganor, 1996], can influence rain acidity [Lojze-Pilot *et al.*, 1986] and can affect atmospheric convection [e.g., Brooks and Legrand, 2000]. The identification of desert dust occurrences over the ocean, and the quantification of the associated burden, are therefore important missions. The residence time of aerosols in the atmosphere, and in particular of mineral dusts, is however of only a few days, so their distribution is highly variable in space and time. This is the reason why remote sensing of desert aerosols has increasingly developed, as the best technique to catch individual events (aerosol “plumes”) and to integrate them into regional or global pictures of the aerosol transport.

[5] Remote sensing of aerosols has a long history, and a wide range of techniques have been developed in the past 20 years, using various sensors and various parts of the electromagnetic spectrum (see reviews of, e.g., Kaufman *et al.* [1997], King *et al.* [1999], and Kaufman *et al.* [2002]). It is more recently that ocean color has been incorporated into the panoply of methods considered as capable of providing reliable information about the amounts and types of aerosols (but see, e.g., Moulin *et al.* [2001a] and Wang *et al.* [2000]). This late consideration is simply due to the fact that the main concern of the ocean color science is actually to get

¹Laboratoire d’Océanographie de Villefranche, Observatoire Océanologique de Villefranche, CNRS/Université Pierre et Marie Curie-Paris 6, Villefranche sur mer, France.

rid of the aerosol effect on the recorded signal, i.e., the atmospheric correction, rather than studying aerosols themselves.

[6] The term ocean color actually means the observation of the spectral reflectance of the sea in the visible to near infrared domains, which is precisely where aerosols play a role and can be detected. In addition, ocean color is extremely demanding in terms of accuracy of the retrieved water-leaving reflectances, and in particular in the blue part of the spectrum [Gordon, 1990, 1997]. For the modern sensors, it has been necessary to drastically improve the atmospheric correction schemes as compared to what was done in the 1980s [Gordon, 1997] with the Coastal Zone Color Scanner (CZCS) [e.g., Gordon, 1978]. This was achieved by improving the direct and vicarious radiometric calibration of the sensors [e.g., Barnes *et al.*, 2001], by using a larger number of channels (in the near infrared in particular), and by using aerosol models to describe the spectral dependence of the atmospheric signal and in particular the multiple scattering effects. It is through this process that the by-products of the atmospheric correction of ocean color observations were improved and became relevant to aerosol science. Regional to large-scale quantitative assessment of aerosols over the ocean, and in particular of desert dust, is now within reach either using historical data sets (e.g., the CZCS [Stegman and Tindale, 1999]) or using the new generation of ocean color remote sensors such as Sea-Viewing Wide Field-of-View Sensor (SeaWiFS) [Jamet *et al.*, 2004; Stegman, 2004a, 2004b; Wang *et al.*, 2005], Moderate Resolution Imaging Spectroradiometer (MODIS) [Barnaba and Gobbi, 2004; Kaufman *et al.*, 2005; Remer *et al.*, 2005], Medium Resolution Imaging Spectrometer (MERIS) [Nobileau and Antoine, 2005], or Polarization and Directionality of the Earth's Reflectances (POLDER)-I and -II [e.g., Boucher and Tanré, 2000; Chiapello *et al.*, 2000; Deuzé *et al.*, 1999, 2000].

[7] In this context, and in particular within the frame of the development of the atmospheric correction algorithms for the European MERIS ocean color sensor [Rast *et al.*, 1999], a method was developed that is capable of detecting over oceanic waters the presence of blue-absorbing aerosols, in particular desert dusts, and then of determining their optical thickness and Ångström exponent. This algorithm has been described, tested on selected SeaWiFS and MERIS scenes [Nobileau and Antoine, 2005], and validated against in situ data from the AERONET [Holben *et al.*, 1998]. This algorithm is similar in spirit, yet simpler in its implementation, to other algorithms previously proposed to cope with the case of absorbing aerosols [e.g., Gordon *et al.*, 1997]. In the present work, the Nobileau and Antoine [2005] algorithm has been systematically applied to all SeaWiFS observations collected over the Mediterranean Sea from 1998 to 2004.

[8] The first aim is to conclusively demonstrate the applicability of the method when it is applied to large data sets, which include by definition all possible situations in terms of (1) the geometry of observation, (2) the amount and type of aerosols, and (3) the optical properties of the underlying ocean. This demonstration is important in particular because the ultra violet domain and the infrared for wavelengths above $\sim 1 \mu\text{m}$, where specific features of

absorbing aerosols are easier to identify than in the visible (e.g., Herman *et al.* [1997] for the UV), are usually unavailable in the bandset of ocean color sensors. The 400–900 nm range is therefore not optimal in this respect. The existing knowledge about the transport of the dust aerosols over the Mediterranean also provides a good context for the validation of the retrieved aerosol optical thickness and type.

[9] The second aim is the study of the seasonal and interannual variability of Saharan dust over the Mediterranean Sea during the SeaWiFS era, as a complement to previous studies that used single broadband visible information over previous time periods, in particular Moulin *et al.* [1998] who used Meteosat observations from 1983 to 1994 and algorithms developed by Moulin *et al.* [1997a, 1997b].

[10] Some recent studies have suggested that climate variability controls the Saharan dust export [Moulin *et al.*, 1997c; Brooks and Legrand, 2000; Chiapello and Moulin, 2002; Moulin and Chiapello, 2004]. A thorough understanding of the distribution and transport of atmospheric dust aerosol particles is therefore necessary to understand this interaction. Long-term time series are also desirable if the interactions and feedbacks between climate and aerosols are to be understood. The SeaWiFS record is, from this point of view, an invaluable data source.

2. Data (SeaWiFS) and Method

[11] Data from the SeaWiFS sensor [Hooker *et al.*, 1992] have been continuously collected by NASA since its launch by Orbital Science Corporation (OSC) in September of 1997. The so-called Level-1a data have been converted into Level-1b, i.e., top-of-atmosphere (TOA) calibrated total radiances in eight spectral bands from 412 to 865 nm, using SeaWiFS Data Analysis System (SeaDAS) [Fu *et al.*, 1998] version 4.4 and the calibration file delivered in 2003. The full set of 4-km Global Area Coverage (GAC) data available from 1998 to 2004 for the Mediterranean Sea, i.e., about 6700 images, have been processed with the algorithm summarized below. Only specific features relevant to the present regional application are briefly recalled, and the reader is referred to the references therein for more detailed information.

[12] The reflectance is first defined because it is the quantity in use for the rest of the paper

$$\rho(\lambda, \theta_s, \theta_v, \Delta\varphi) = \pi L(\lambda, \theta_s, \theta_v, \Delta\varphi) / F_0(\lambda) \mu_s \quad (1)$$

where L is radiance ($\text{W m}^{-2} \text{nm}^{-1} \text{sr}^{-1}$), F_0 is the extraterrestrial irradiance ($\text{W m}^{-2} \text{nm}^{-1}$), θ_s is the Sun zenith angle (cosine is μ_s), θ_v is the satellite viewing angle, and $\Delta\varphi$ is the azimuth difference between the half vertical plane containing the Sun and the pixel and the half vertical plane containing the satellite and the pixel. Because π carries the unit of steradian, the reflectance ρ is dimensionless.

[13] The central difficulty of the atmospheric correction of ocean color observations lies in the identification of the aerosol in presence and the quantification of the multiple scattering effects. All methods in use for the present generation of sensors somehow rely on precomputed signals, coupled to a method allowing navigation in these

signals in order to identify from the near infrared bands the most suitable aerosol to perform the correction of the visible bands [see, e.g., *Gordon, 1997*]. The MERIS algorithm [*Antoine and Morel, 1999*] belongs to this general category of methods. It is a full multiple scattering inversion method, based on aerosol models and precomputed lookup tables (LUTs).

[14] Because only the path reflectances in the near infrared are used by this method (the contribution of the ocean being null in this wavelength domain), it cannot alone discriminate between absorbing and nonabsorbing aerosols, which have similar signatures in this spectral domain. The effect of absorption is only detectable in the visible, where the marine contribution becomes however significant and varying with the chlorophyll content of oceanic waters, which is unknown when starting the atmospheric correction. It is precisely to overcome this difficulty that a specific technique was proposed by *Nobileau and Antoine [2005]*. It basically consists in determining an error budget at one wavelength around 510 nm, based on a first-guess estimation of the atmospheric path reflectance as if the atmosphere was of a maritime type, and on a reasonable hypothesis about the marine signal at this wavelength. The latter is possible because a hinge point exists in the spectrum of the marine reflectance around 510–520 nm [*Clarke et al., 1970*], so ρ_w is little varying there with the chlorophyll concentration. A mean reflectance and its associated uncertainty can be derived at this wavelength, $\bar{\rho}_w(510)$ and $\sigma(\rho_w)$, respectively, which were assigned fix values, i.e., 1.2×10^{-2} and 3×10^{-3} (but see later). This budget is therefore computed as the total reflectance minus the path reflectance estimated for maritime aerosols minus $\bar{\rho}_w(510)$ minus $\sigma(\rho_w)$. Identification of blue-absorbing aerosols is then achieved when this budget demonstrates a significant overcorrection of the atmospheric signal when using non-absorbing maritime aerosols, as a footprint of absorption. In the work of *Nobileau and Antoine [2005]*, the threshold for identification of absorption at 510 nm was set to -3×10^{-3} in terms of reflectance, which includes the typical accuracy of the correction for maritime aerosols and the typical calibration uncertainty of the sensor. The theoretical detection limit in terms of optical thickness at 865 nm was determined at about 0.15.

[15] It is worth noting that this method cannot discriminate among the most common types of absorbing aerosols (mineral dust, soot, or biomass burning aerosols). Some external information is required in order to assign the detected absorption to a given family of aerosols. In the frame of the present application to the Mediterranean, however, Saharan dust is likely to represent the vast majority of absorbing aerosols.

[16] After absorption has been detected, the atmospheric correction is restarted using specific sets of absorbing aerosol models (i.e., specific LUTs) until the couple of models that minimizes the error budget at 510 nm is found. The aerosol optical thickness at all wavelengths and the Ångström exponent are then derived.

[17] In the first step, a set of 12 aerosol models is used (from *Shettle and Fenn [1979]* and *Gordon and Wang [1994a]*). This set includes four maritime aerosols, four rural aerosols that are made of smaller particles, and four

coastal aerosols that are a mixing between the maritime and the rural aerosols. The mean particle sizes of these aerosols, thus their optical properties, are varying as a function of the relative humidity, which is set to 50, 70, 90, and 99% (hence the 3 times four models). This set covers the range of spectral dependencies that may occur over most oceanic areas, from the clearest offshore regions to the more turbid coastal atmospheres. This set of aerosol models is actually the one used in the standard NASA processing of the SeaWiFS observations [*Gordon and Wang, 1994a*]. It has been already validated against in situ observations [*Schwindling et al., 1998*]. In addition to these boundary-layer aerosols, constant backgrounds are introduced in the free troposphere (2–12 km), with continental aerosol with $\tau = 0.025$ at 550 nm [*World Climate Research Program (WCRP), 1986*] and the stratosphere (12–30 km), with H_2SO_4 aerosol with $\tau = 0.005$ at 550 nm [*WCRP, 1986*].

[18] The lookup tables specific to absorbing aerosols have been generated with the six dust models and the three vertical distributions proposed by *Moulin et al. [2001a]*, which have been derived as the most appropriate to reproduce the TOA total radiances recorded by SeaWiFS above thick dust plumes off western Africa. The mean Ångström exponent of these models is about 0.4 when computed between 443 and 865 nm. When these aerosols are present, a background of maritime aerosol is maintained, using the *Shettle and Fenn [1979]* maritime model for a relative humidity of 90% and an optical thickness of 0.05 at 550 nm [*Kaufman et al., 2001*]. The backgrounds in the free troposphere and the stratosphere are maintained.

[19] A specific test using the band at 412 nm was developed in order to eliminate clouds without eliminating thick dust plumes (see in the work of *Nobileau and Antoine [2005]*), which are quite bright in the near infrared and therefore are eliminated when using a low threshold in this wavelength domain (as done for instance in the standard processing of the SeaWiFS observations). This test is an alternative to other techniques based on the spatial heterogeneity of the scene [e.g., *Martins et al., 2002*].

[20] A correction for the whitecaps reflectance is performed following *Gordon and Wang [1994b]*, using the National Centers for Environmental Prediction (NCEP) wind speed that is provided as auxiliary data to the SeaWiFS products. The implementation of this technique follows the SeaDAS 4.7 software [*Fu et al., 1998*].

[21] Finally, because the algorithm has been designed for oceanic Case 1 waters where the contribution of the ocean in the near infrared bands is zero, turbid Case 2 waters, for which the near infrared signal is significant, are screened out by using a threshold on the reflectance at 555 nm, following *Bricaud and Morel [1987]*.

[22] In the work of *Nobileau and Antoine [2005]*, the adoption of unique values for $\bar{\rho}_w(510)$ and $\sigma(\rho_w)$ was possible in the frame of a demonstration study based on a few selected scenes. For the present regional application, including thousands of scenes and all seasons, the use of single mean values for $\bar{\rho}_w(510)$ and $\sigma(\rho_w)$ has been abandoned. Indeed, the changes of the marine reflectance at 510 nm are minimal yet significant enough so that ignoring them, in particular their seasonal changes, could lead to bias the dust detection.

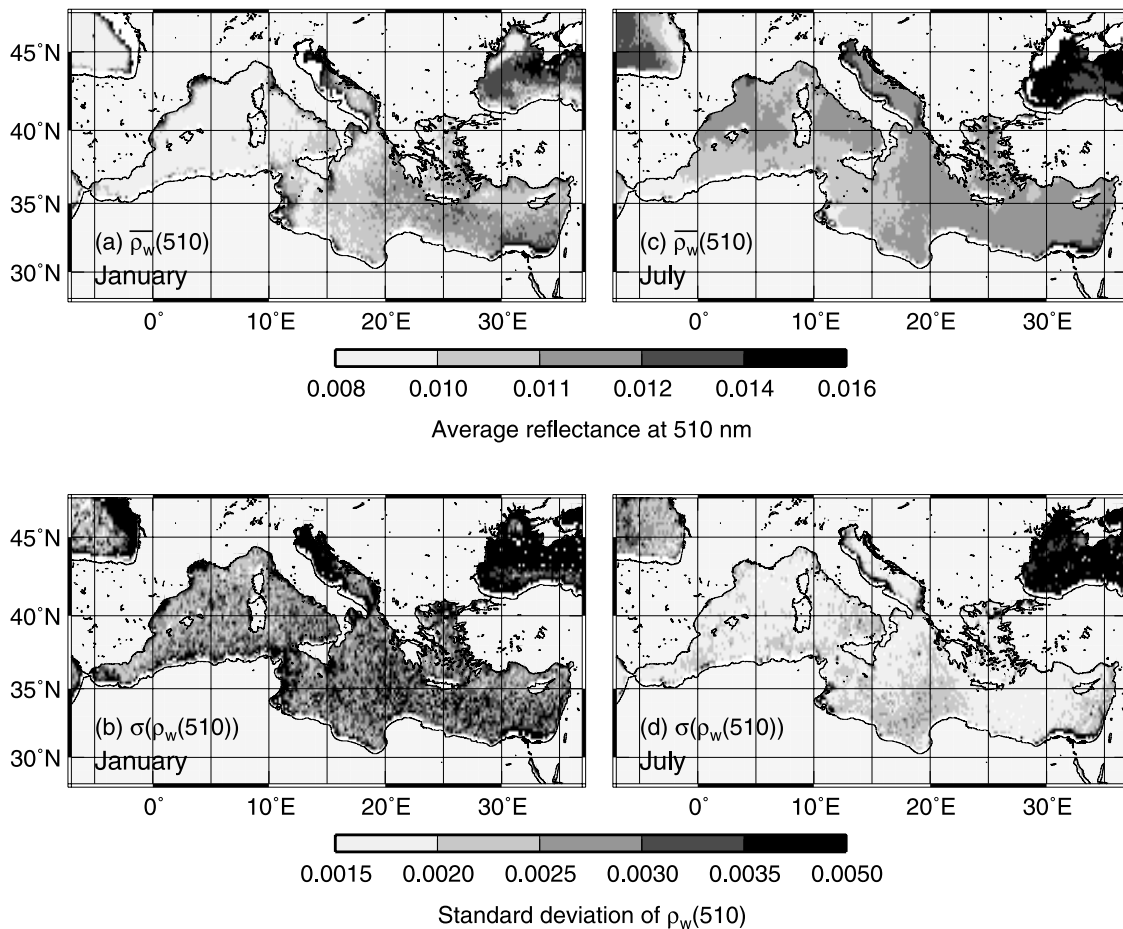


Figure 1. The 7-year (1998–2004) monthly climatology of the average marine reflectance at 510 nm, $\bar{\rho}_w(510)$, and of its standard deviation, $\sigma(\rho_w)$, for the months of (a, b) January and (c, d) July, and as derived from 7 years of standard SeaWiFS level-3 composite data.

[23] A climatology of the monthly average of these two quantities has been therefore derived from 7 years of the standard SeaWiFS level-3 data (1998 to 2004; data from the NASA reprocessing 4), at a spatial resolution of $1/6^\circ$, i.e., about half the resolution of the SeaWiFS level-3 “Standard Mapped Images” data. For a given month, the climatological monthly averages have been computed from the seven individual monthly composites, by (1) summing up the seven sums of individual daily values that are provided in the monthly composites (Level-3 “binned” data), (2) summing up the seven corresponding total number of pixels, and (3) dividing both totals to get the average (which is not therefore the mean of the monthly means but the true mean of all individual daily values). The standard deviation was similarly derived from seven monthly values of the sum of squares of the data and over the 7 years so that it includes both a spatial dimension (changes within the $1/6^\circ$ bin) and a temporal dimension (variability within a month and among the 7 years).

[24] Because the standard NASA atmospheric correction scheme for the SeaWiFS sensor cannot cope with absorbing aerosols, however, an overcorrection of the visible observations occurs when they are present in the atmosphere,

leading to underestimated marine reflectances at 510 nm [e.g., Schollaert *et al.*, 2003]. The lowest $\rho_w(510)$ values were therefore reset to a minimum value of 0.008, as empirically determined from in situ observations [see, e.g., Nobileau and Antoine, 2005, Figure 3]. Similarly, large values have been put to an upper limit of 0.016, assuming that larger values cannot be found in Case 1 waters. A similar bounding has been applied to $\sigma(\rho_w)$, with extrema of 1.5×10^{-3} and 5×10^{-3} .

[25] Examples of the climatology for the months of January and July are shown in Figure 1. As expected, the changes between these two seasons are low, yet significant enough as regards the error budget at 510 nm to justify the need for using this climatology instead of a unique value. It has been verified for instance that using this climatology avoids erroneous dust identifications in winter and beginning of spring in the northwestern Mediterranean, where the phytoplankton is blooming and the marine reflectance is significantly lower than 1.2×10^{-2} (i.e., the constant value used by Nobileau and Antoine [2005]).

[26] When processing a pixel in a 4-km resolution level-1b scene, $\bar{\rho}_w(510)$ and $\sigma(\rho_w)$ are spatially interpolated from the surrounding grid points of the monthly climatology.

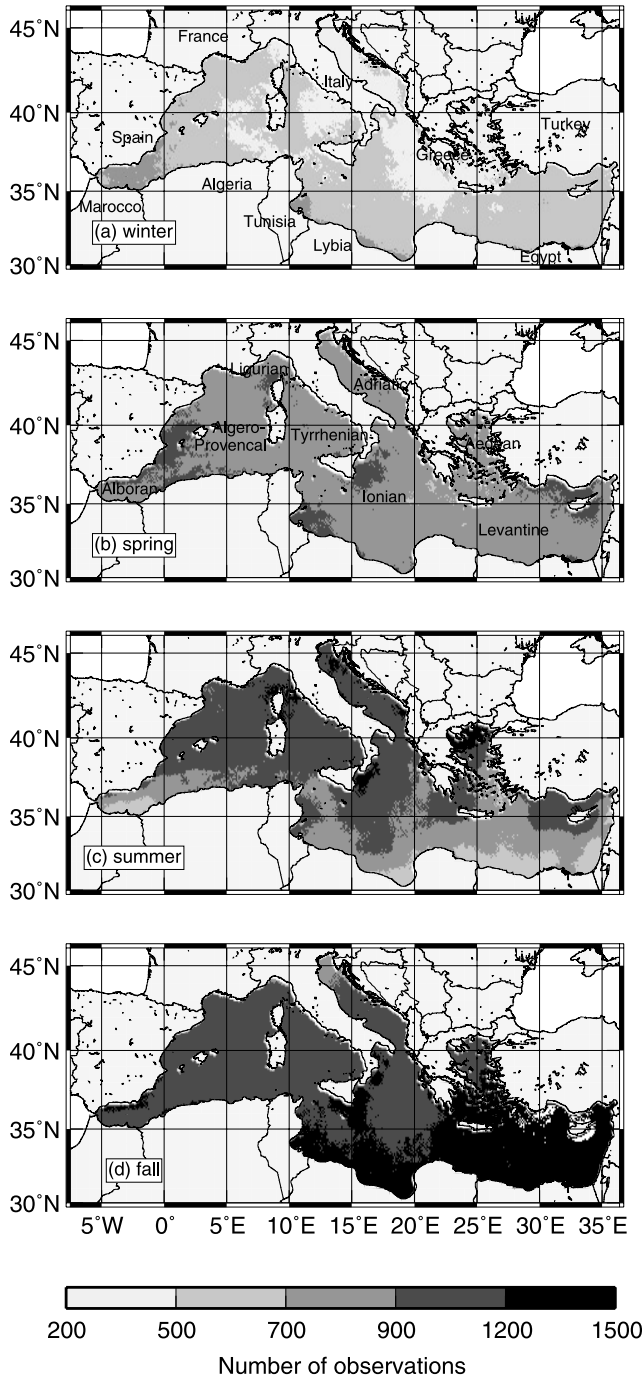


Figure 2. Total number of clear-sky, nonglint, SeaWiFS Global Area Coverage (GAC) observations collected over the Mediterranean Sea from 1998 to 2004 and for the four seasons. The names of the main basins are indicated on Figure 2b.

There is no time interpolation, i.e., the monthly averaged value for a given month is used for all days in this month.

[27] The algorithm has been applied on a pixel-by-pixel basis to the ~ 6700 SeaWiFS scenes, and the following outputs have been used: (1) The aerosol optical thickness at 865 nm, $\tau_{\text{tot}}(865)$, derived from the atmospheric signal at 865 nm through the multiple scattering inversion scheme

that was outlined above, (2) a flag set when absorption has been detected at 510 nm, and (3) the Ångström exponent computed between 443 and 865 nm, $\alpha(443,865)$, which has been preferred to the commonly used near infrared exponent because it is sensitive to absorption:

$$\alpha(443, 865) = -\frac{\log[\tau_{\text{tot}}(443)/\tau_{\text{tot}}(865)]}{\log[443/865]} \quad (2)$$

[28] These three quantities have been binned into a rectangular grid of 0.1° latitude and longitude resolution, to create monthly, seasonal, and annual composites, either for each individual year or for a “climatological” period where all 7 years are pooled together. Observations contaminated by sun glint or turbid Case 2 waters are removed from the binning process. Pixels identified as dusty are reset to maritime aerosols when their number is lower than half the number of valid pixels in a moving 3-by-3 pixel box. This filtering aims at removing isolated bright pixels that are essentially due to unidentified clouds or cloud borders.

[29] Concerning the optical thickness and Ångström exponent, the average quantity in each bin is derived as a simple arithmetic mean. Two average values are derived for the optical thickness. The first one, $\tau_{\text{tot}}(865)$, is computed whatever the selected aerosol type, whereas the second one is computed only for the pixels where dust has been detected, and after removal of the constant backgrounds of maritime, continental and H_2SO_4 aerosols (corresponding to an optical thickness of 0.06 at 865 nm); it will be referred to as τ_{dust} . For a given area, the mean optical thickness of dust plumes is obtained by averaging τ_{dust} over the total number of dust pixels (in that case, by definition $\tau_{\text{dust}} \geq \tau_{\text{tot}}$). On the contrary, the overall contribution of dust over the same area is obtained by averaging τ_{dust} over all pixels, whatever their classification (dusty or clear).

[30] For a given period of time, the frequency of dust detection, which will be referred to as f_{dust} (expressed as a percentage), is computed from the ratio of the number of clear-sky pixels for which the dust flag was raised to the total number of clear-sky pixels over the same period. The dust occurrence has been also examined in terms of the absolute number of detection events, which will be referred to as N_{dust} . The use of f_{dust} is adapted to the case of climatological composites for which the number of observations is large and similar among the different situations under examination, whereas the use of N_{dust} is necessary when examining month-to-month evolutions with a greatly fluctuating number of observations due to changes of the cloud coverage.

[31] The number of nonglint, clear-sky observations summed up for each season and over the 1998-to-2004 time period is provided in Figure 2. As expected, winter is the season with the smallest density of observations because cloudiness is high. Surprisingly, more valid observations are obtained in fall as compared to summer (especially in the Levantine basin), which is somewhat the opposite of usual expectations. This is not due to cloudiness, which is lower in summer than in fall over the whole Mediterranean Sea, but is actually due to the higher occurrence and extent of sun glint in summer. At this season, Sun glint leads to the elimination of ten times more pixels than in fall, which is

Table 1. Characteristics of the AERONET-SeaWiFS Matchup Data Set

Site Name	Location	Years ^a	N AERONET ^b	N SeaWiFS ^c	N Matchups ^d
Villefranche sur mer	43.684°N, 7.329°E French Riviera	2004	235	105	76
IMC Oristano	39.91°N, 8.5°E West coast of Sardinia	2000–2003	934	316	84
Venise	45.3142°N, 12.508°E Off the Venice lagoon	1999–2004	1261	274	159
Lampedusa	35.517°N, 12.632°E South of Sicily	2000, 2003, 2004	383	70	42
Forth Crete	35.333°N, 25.282°E North coast of Crete	2003, 2004	532	192	134
Erdemli	36.565°N, 34.255°E South coast of Turkey	2000, 2001 2003, 2004	909	172	64
All sites			4254	1129	559

^aThe years for which Level-2 AERONET data are available.

^bTotal number of days with Level-2 AERONET data.

^cThe total number of AERONET-SeaWiFS matchups, after Sun glint and Case 2 waters have been excluded.

^dThe total number of valid AERONET-SeaWiFS matchups, after rejection criteria have been applied (see text).

overcompensating for the potentially higher number of observations due to a low cloudiness.

3. Results

3.1. Comparison With AERONET

[32] Before discussing the distributions and temporal changes of the aerosol optical thickness and aerosol types, a validation is presented for $\tau_{\text{tot}}(865)$ and $\alpha(443,865)$ based

on Level-2, cloud-screened and quality-controlled data from six coastal sites of the AERONET [Holben *et al.*, 1998; Dubovik *et al.*, 2000], providing a sampling in the western, central, and eastern Mediterranean (see Table 1 and Figure 3).

[33] The procedure to generate matchup points is as follows: a 3 by 3 pixel box is extracted from the daily maps of optical thickness, centered on the marine area closest of the exact site location. The shift is of one or two

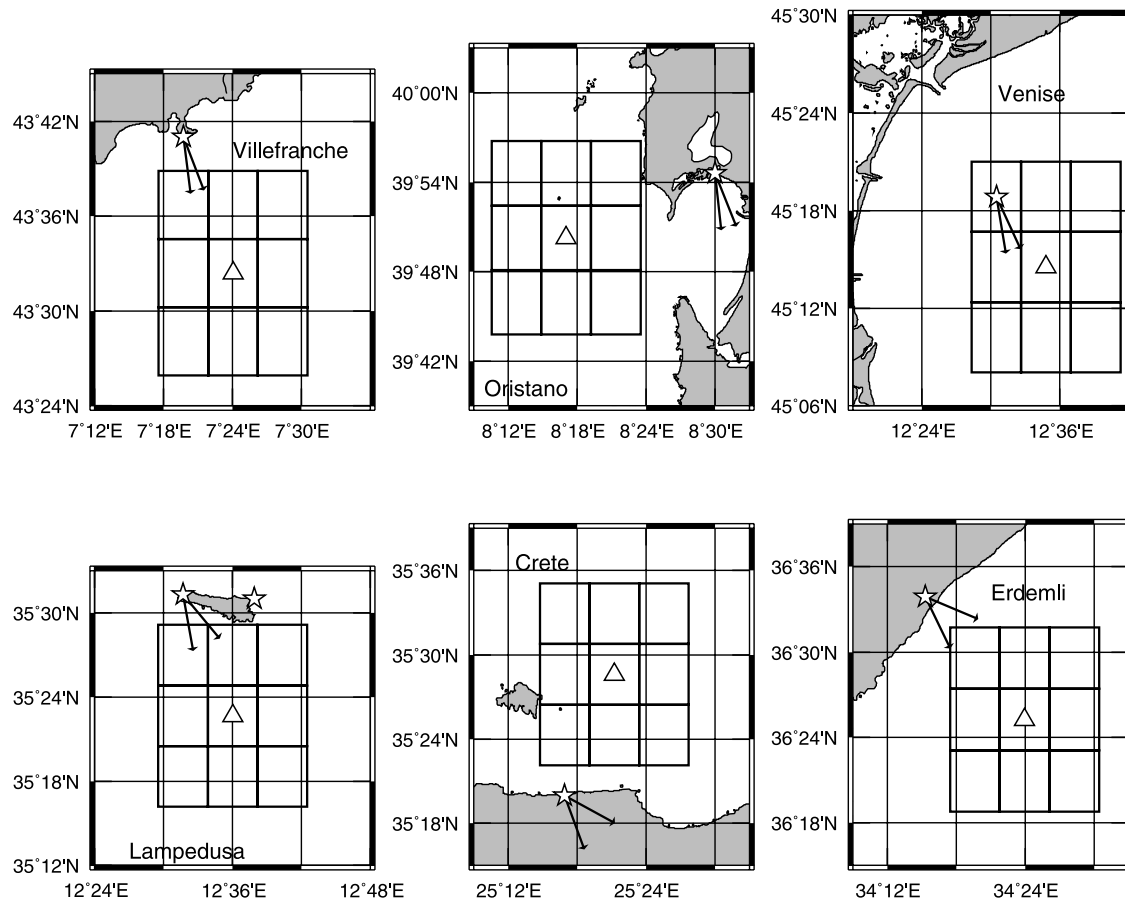


Figure 3. Location of the six AERONET sites (stars) selected for the validation of $\tau_{\text{tot}}(865)$ and $\alpha(443,865)$ (see also the red stars in Figure 5a and Table 1). The position of the 3 by 3 SeaWiFS pixel box used for the matchup with the AERONET data is indicated (triangle at the center), as well as the azimuth of the sun at the time of the satellite pass (two arrows; one is for 21 June and the other one for 21 December).

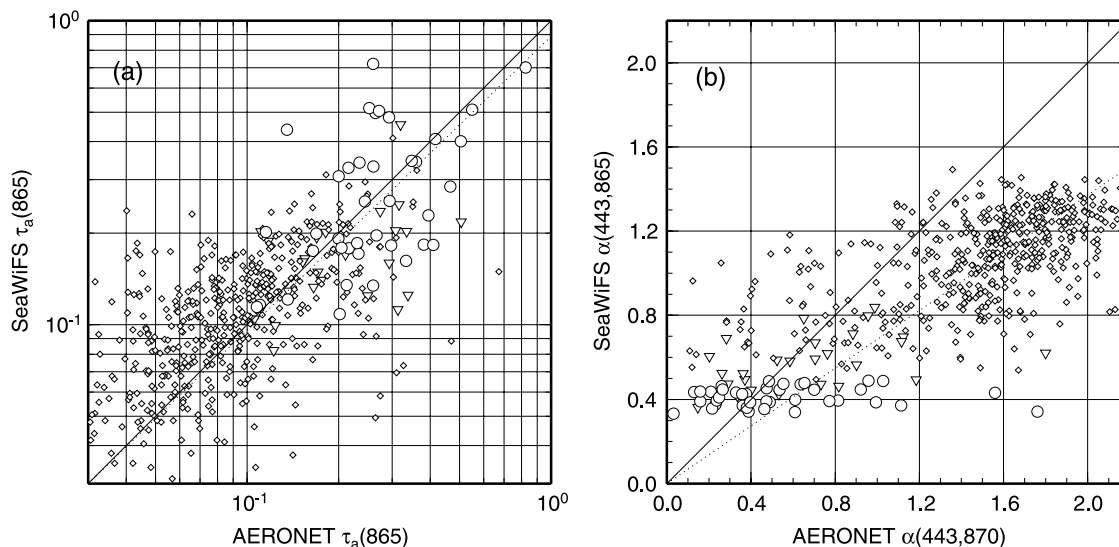


Figure 4. Comparison of (a) $\tau_{\text{tot}}(865)$ and (b) $\alpha(443,865)$, derived either from the AERONET or from the application of the algorithm to SeaWiFS. The rationale for producing this set of matchup points is explained in section 3.1 (see also Table 1). Diamonds are for nonabsorbing aerosols (i.e., the 3×3 pixels of the SeaWiFS images were all identified by the algorithm as nonabsorbing aerosols), circles are for dust atmospheres (all pixels identified as absorbing aerosols), and inverted triangles are for a mix of both types of aerosols. The solid line is the 1:1 line, and the dotted line is a simple linear fit with the intercept forced to zero.

(three in one case) SeaWiFS GAC pixels (Figure 3), in order to be sufficiently far away from the coast so that contamination either by the environment effect on the satellite radiance (bright land) or from Case 2 turbid waters is avoided. When the photometer is installed on a coastline oriented toward south, the 3-by-3 pixel area was also selected so as to be optimally placed with respect to the orientation of the Sun photometers when they took measurements at the time of the SeaWiFS pass (as indicated by the arrows in Figure 3).

[34] The group of nine pixels is rejected from the analysis as soon as one pixel is classified as cloud or glint or turbid Case 2 water, when the solar zenith angle is larger than 70 degrees, as well as when the standard deviation within the box is larger than 0.065 for $\tau_{\text{tot}}(865)$ or $\tau_{\text{tot}}(443)$ or larger than 0.2 for $\alpha(443,865)$. These thresholds were empirically determined in order to eliminate approximately 10% of the data with the highest standard deviations. Finally, situations where pixels are identified as absorbing aerosols, whereas the AERONET $\tau_{\text{tot}}(865)$ is lower than 0.1, which is the limit of detection of the algorithm [see Nobileau and Antoine, 2005], are considered as erroneous detections of absorbing aerosols and are removed from the validation exercise.

[35] The AERONET data are similarly screened in order to eliminate dubious data or unstable conditions, which are both undesirable when performing a validation exercise. Therefore data are not further considered when either $\alpha(443,865)$ is negative or the absolute value of the difference between $\alpha(443,865)$ and $\alpha(675,865)$ is larger than 0.4 or finally when the standard deviation of $\tau_{\text{tot}}(865)$ is larger than 0.065 within a time window of ± 1 hour around the SeaWiFS overpass.

[36] When all criteria are satisfied, average quantities are computed on the one hand over the nine SeaWiFS pixels

and, on the other hand, over all AERONET observations found within ± 15 min of the SeaWiFS overpass. A total of 559 matchup points have passed all criteria (see Table 1), 37 being in winter (DJF), 104 in spring, 291 in summer, and 127 in fall.

[37] The results of the comparison are satisfactory for $\tau_{\text{tot}}(865)$ (Figure 4a), with a regression slope close to 1 ($= 0.89$, with a correlation coefficient, r^2 , of 0.78). These numbers would not significantly improve by removing matchup points for which $\tau_{\text{tot}}(865) < 0.05$, as was done by Jamet *et al.* [2004] in order to remove obvious outliers. When only the dust pixels are considered (65 points), the slope is 0.88 and the correlation coefficient is 0.80. The dispersion of the points is important, albeit not larger than usually observed in such validation exercises [Santolero *et al.*, 2002; Jamet *et al.*, 2004; Wang *et al.*, 2005]. This validation, which includes high optical thicknesses, qualifies the inversion scheme and allows $\tau_{\text{tot}}(865)$ to be quantitatively discussed.

[38] The results are not so good for $\alpha(443,865)$ (Figure 4b), with a regression slope of only 0.69 (yet $r^2 = 0.94$). The overall underestimation of the SeaWiFS-derived Ångström exponents, as compared to AERONET values, has already been identified by other, similar, validation exercises performed over the Mediterranean Sea [e.g., Santolero *et al.*, 2002; Jamet *et al.*, 2004]. It is essentially explained by the characteristics of the 12 aerosol models considered in the first pass of atmospheric correction (cf. section 2), with ceiling values of the Ångström exponents at ~ 1.5 , whereas the AERONET provides values up to ~ 2.2 . These large exponents cannot be reproduced without a modification of the set of aerosol models, for instance by using Jünge models as in the work of Jamet *et al.* [2004]. This underestimation of $\alpha(443,865)$ implies that this exponent has to be discussed

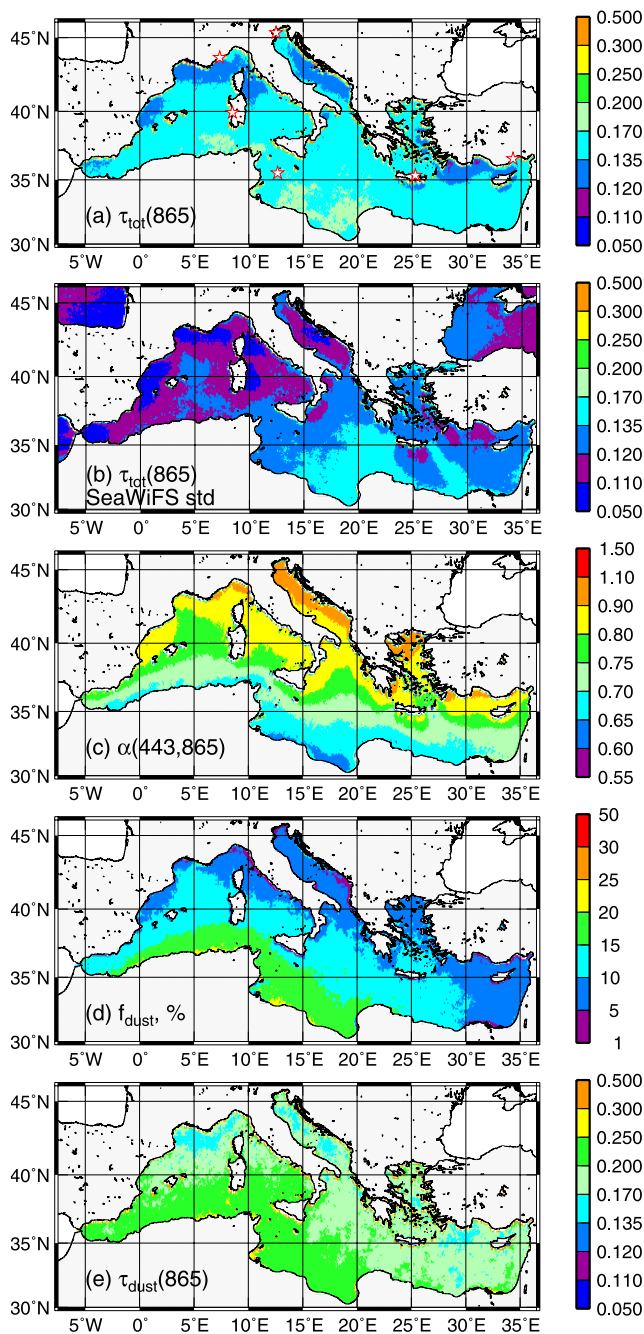


Figure 5. The 7-year (1998–2004) climatological averages of (a) $\tau_{\text{tot}}(865)$, (b) the same quantity as obtained from the NASA standard SeaWiFS products, (c) $\alpha(443,865)$, (d) f_{dust} , and (e) $\tau_{\text{dust}}(865)$. The red stars in Figure 5a are the six AERONET sites selected for validation (Figures 3 and 4).

only in a relative sense, i.e., only in terms of spatial distributions and temporal evolutions.

3.2. Climatological (1998–2004) Picture

[39] The 7-year average of the total aerosol optical thickness at 865 nm is of about 0.17 (Figure 5a), which is larger than the dust-free, open ocean values typically reported, for instance above the Pacific and Atlantic

[Villevaude *et al.*, 1994] or in Hawaii [Dubovik *et al.*, 2002]. This larger aerosol load, which is due to the surrounding of the basin by land masses, is consistent with previous determinations, as derived for instance from the Meteosat [Moulin *et al.*, 1998] or the SeaWiFS [Jamet *et al.*, 2004] observations. The well-known north-south gradient clearly appears, with, on the average, the clearest areas ($\tau_{\text{tot}}(865) \sim 0.125$) in the northernmost part of the western Mediterranean, the central Adriatic Sea, and the southern coasts of Turkey, whereas the south Ionian Sea, off Libya, shows the highest optical thickness (~ 0.2). The same overall organization appears in the NASA standard SeaWiFS products (Figure 5b), with lower values, however. This difference is likely due to the severe elimination of bright pixels in the NASA algorithms, which use a threshold of 0.027 on the total reflectance at 865 nm, eliminating therefore all moderately to highly thick dust plumes from further processing. When the algorithm proposed here is run with this low near infrared threshold for cloud elimination and without any use of the dust models (i.e., using only the 12 Shettle and Fenn models), the same average value is obtained for the optical thickness. The standard SeaWiFS product is therefore closer to a clear-sky maritime aerosol optical thickness, while the optical thickness produced here includes more turbid atmospheres as well.

[40] The distribution of $\alpha(443,865)$ (Figure 5c) nearly mirrors the distribution of $\tau_{\text{tot}}(865)$, with high exponents along the coasts of Europe and low exponents along the coasts of Africa. The association of high optical thicknesses with low exponents is the footprint of Saharan dust, which is characterized by low Ångström exponents due to a high proportion of large particles and to absorption in the blue. Large exponents are conversely typical of small particles, usually nonabsorbing small continental aerosols or pollution aerosols. These two types of aerosols are mostly originating from the European continent and its urbanized areas, which explain the observed distribution. It is worth noting, however, that the progressive settling of the largest dust particles along the Africa-to-Europe transport also leads to a progressive increase of the Ångström exponents. In spite of the well-known Saharan dust contamination of the Mediterranean atmosphere, very low $\alpha(443,865)$ values are not observed, which indicates the presence of permanent backgrounds of smallest particles of continental origin.

[41] The role of Saharan dust in shaping the distribution of $\tau_{\text{tot}}(865)$ and $\alpha(443,865)$ is confirmed by the f_{dust} distribution (Figure 5d), which again follows the same organization, except in the south Levantine basin where it remains on average $<10\%$ (but recall that this is the climatological average over 7 years). The mean optical thickness of dust plumes, τ_{dust} (Figure 5e), which is never lower than 0.2, again respects the same north-south organization, although large values (>0.25 – 0.3) are more homogeneously distributed than for the other parameters. This result only means that the average optical thickness of the dust plumes is, on this climatological representation, similar whatever the area.

3.3. Mean (1998–2004) Seasonal Variability

[42] The climatological (1998–2004) seasonal maps of τ_{tot} , $\alpha(443,865)$, f_{dust} , and τ_{dust} are displayed in Figure 6. The total optical thickness (panels on the left) shows a

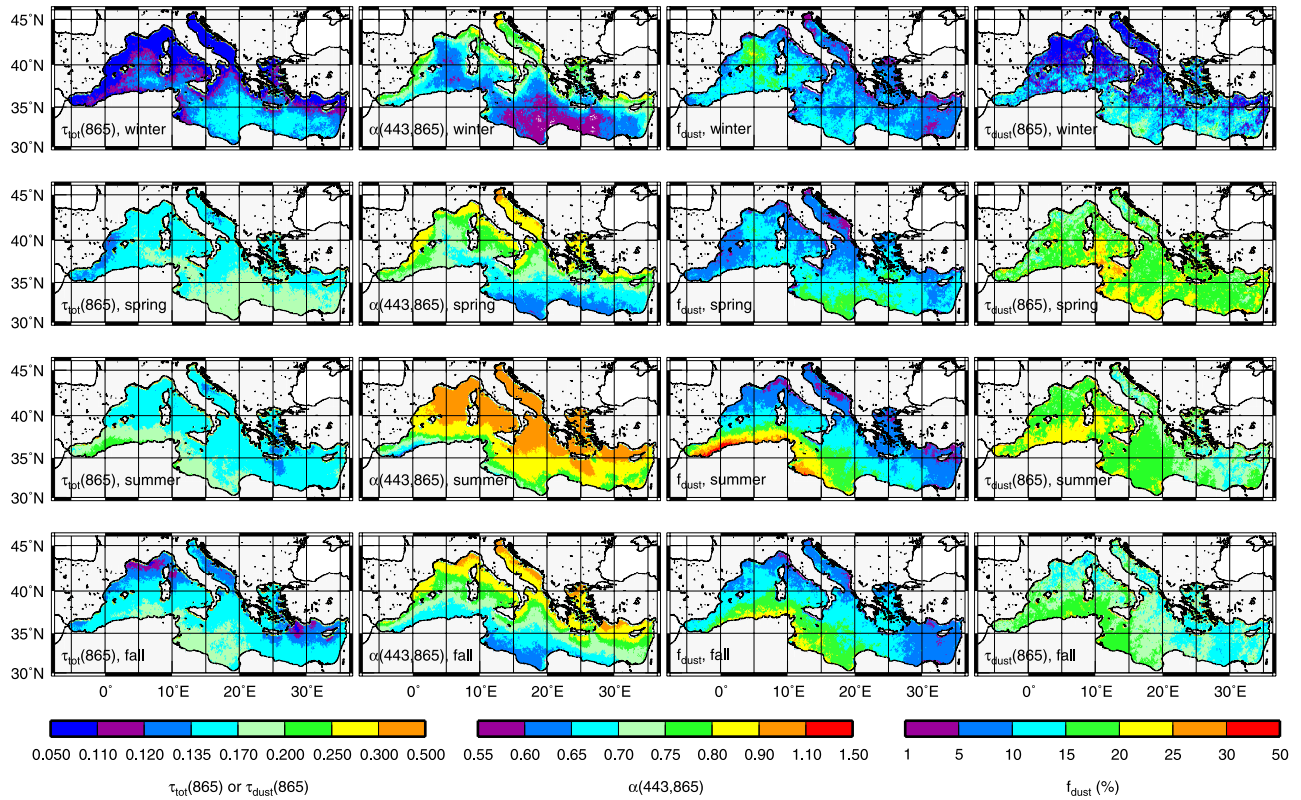


Figure 6. The 7-year (1998–2004) climatological seasonal averages of $\tau_{\text{tot}}(865)$ (left column), $\alpha(443,865)$ (second column from the left), (c) f_{dust} (second column from the right), and (d) $\tau_{\text{dust}}(865)$ (right column).

marked seasonality, with minimum values in winter, <0.125 in the western basin and <0.15 in the eastern part. During spring, the optical thickness first increases in the south eastern Mediterranean ($<35^\circ\text{N}$) and to a lower extent in the western part. The converse situation prevails in summer, with maximum $\tau_{\text{tot}}(865)$ in the southwest and south Ionian (about 0.25), whereas the south Levantine goes back to much clearer atmospheres ($\tau_{\text{tot}}(865) < 0.15$), especially south of Crete.

[43] Again, the distribution of $\alpha(443,865)$ (Figure 6, second column from the left) closely matches that of $\tau_{\text{tot}}(865)$, with the coupling already observed between high optical thicknesses and low exponents. The highest exponents are found in summer in the northern half of the Mediterranean.

[44] The seasonal cycle of f_{dust} (Figure 6, second column from the right) exhibits a distinct maximum in summer, with values $>20\%$ along the coasts of Africa. The same patterns appear in fall, with, however, f_{dust} on average 10% lower than in summer. The minimum of dust occurrence is clearly in winter, except in the northwestern basin, where a distinct spot of relatively high f_{dust} is observed between the Balearic Islands and Corsica. This spot still exists in spring, with lower values, however. During spring, the maximum of f_{dust} is located in the Ionian and Levantine basins, with moderate values ($<20\%$).

[45] If the maximum occurrence of dust is definitely found in summer, it does not seem to be associated to

denser aerosol plumes. Indeed, the mean optical thickness of these plumes, τ_{dust} (Figure 6, column on the right), is about the same in spring and summer (i.e., ~ 0.3), and is even larger in spring in the eastern part. At the end, the mean optical thickness is similar in spring and summer, whereas the dust transport is probably much larger in summer (because f_{dust} is higher), in terms of mass of particles.

[46] The present SeaWiFS-based climatological description of the seasonality of aerosol loads over the Mediterranean is consistent with the analysis of the 11 years (1983–1994) of daily Meteosat images by *Moulin et al.* [1998], except for the significant dust transport that is revealed here in fall and which was not previously detected. Whether this difference is of methodological order or reveals a change in dust transport between the two study periods cannot be resolved here.

[47] The data that were pooled together to produce the maps in Figure 6 have been also used to generate climatological seasonal cycles over the three main regions of the Mediterranean Sea (Figure 7). These three regions are used on the one hand because they correspond to the three main pathways of the dust transport from Africa to Europe [e.g., *Alpert et al.*, 1990], and, on the other hand, in order to allow comparison with previous studies that already used this subdivision [*Moulin et al.*, 1998]. They are of similar extent, with areas of 1.07 , 0.76 and $0.86 \times 10^6 \text{ km}^2$ for the western, central, and eastern basins, respectively.

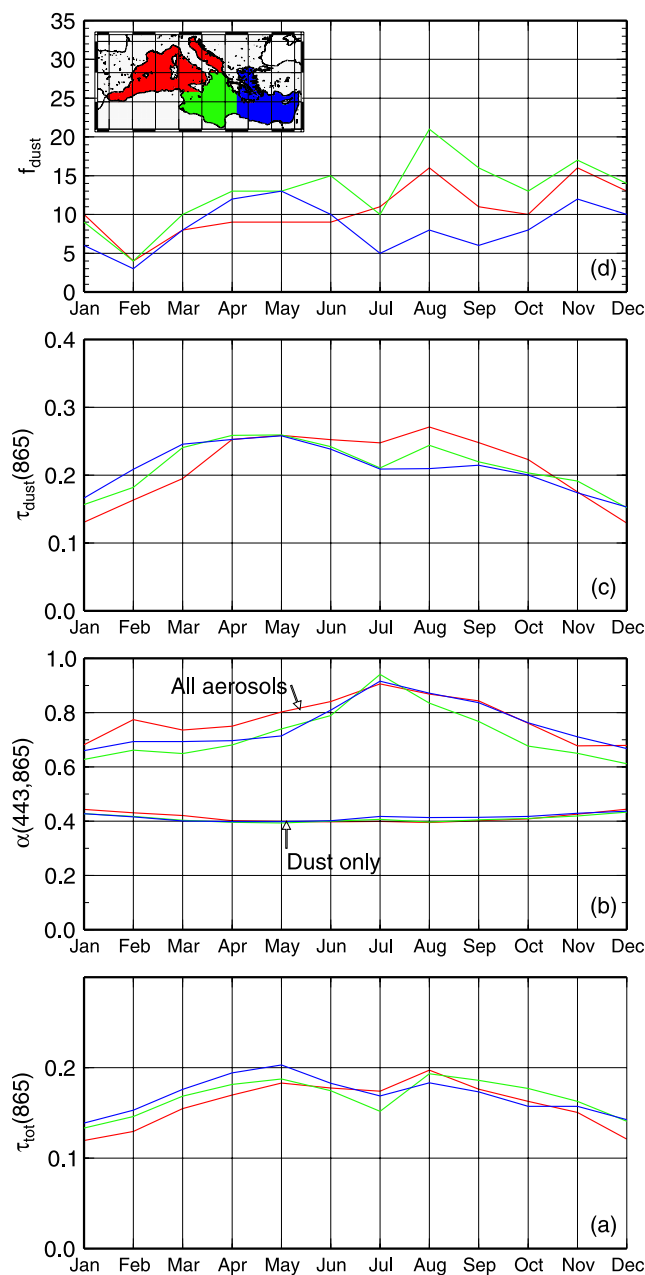


Figure 7. The 7-year (1998–2004) climatological seasonal cycles of (a) $\tau_{\text{tot}}(865)$, (b) $\alpha(443,865)$ for all aerosols or when only dust is considered, (c) $\tau_{\text{dust}}(865)$, and (d) f_{dust} . The red, green, and blue curves are for the western, central, and eastern Mediterranean basins, respectively. The delineation of the three basins is shown in insert.

[48] Very similar cycles are shown for $\tau_{\text{tot}}(865)$ in the three basins (Figure 7a), with minimum values in winter, two relative maxima in May and August, and a relative minimum in July (the latter being not obvious for the western basin). The eastern basin has the highest $\tau_{\text{tot}}(865)$ from December to June, and the minimum is usually in the western basin. Surprisingly, the same cycle does not show up for $\alpha(443,865)$ (Figure 7b), which has maxima in July–September for all three basins. This average cycle is actually strongly shaped by the large $\alpha(443,865)$ values in summer

along the northern coasts of the basins. Conversely, when the same exponent is computed for only those pixels that were identified as dusty, a nearly constant value of 0.4 is found. This value is simply characteristic of the *Moulin et al.* [2001a] dust models.

[49] The average cycle of the mean optical thickness of dust plumes, τ_{dust} (Figure 7c), is similar to that of the total optical thickness, except for the first relative maximum, which occurs in April instead of May. The largest differences among the three basins are observed in the f_{dust} cycles, with the central Mediterranean clearly showing the highest dust occurrences in summer and fall.

[50] The information displayed in Figures 6 and 7 are summarized in Table 2, as the seasonal averages of τ_{tot} , τ_{dust} , f_{dust} , and N_{dust} over the three subbasins. The maximum of f_{dust} is clearly in spring and fall in the eastern part and in summer and fall in the central and western parts. A relative maximum (10%) occurs in winter in the western basin. When looking at the absolute number of pixels identified as dusty (N_{dust}), the maximum is in fall in each basin. Looking successively at each season, the maximum of τ_{dust} clearly moves from the eastern to the central and the western basins, from winter to spring and to summer and fall, respectively. The overall maximum is in spring for the central and eastern seas. The three lower values are for the winter. A similar change occurs for the total optical thickness, except in fall when the maximum is in the central Mediterranean.

[51] Considering the method used by *Moulin et al.* [1998] to derive from METEOSAT what they called “average optical depth due to dust,” the values in Table 2 to be compared to the values in their Table 1 are the τ_{tot} to which the constant backgrounds of tropospheric and stratospheric aerosols are removed, and then transferred to 550 nm using a mean exponent of 0.6. After this transformation, the values derived here from SeaWiFS are usually larger than those derived by *Moulin et al.* [1998] from METEOSAT, by as much as 80% (eastern basin in winter and fall; western basin in fall) and often by more than 25%. The SeaWiFS values are lower than the METEOSAT values only in the central basin in summer (–18%), and nearly equal (3%) in the same area in spring. Although part of these increases might be attributable to methodological differences between these two studies, they are large enough to indicate that the transport of dust aerosols over the Mediterranean is more intense during the time period investigated here as compared to the early 1990s examined in the study by *Moulin et al.* [1998].

3.4. Aerosol Models

[52] The dust optical thickness is dependent on the aerosol model that is eventually selected during the atmospheric correction. Relatively few models have been proposed, and the 18 models recently published by *Moulin et al.* [2001a] have been adopted here. It is therefore timely to examine how frequently each of the 18 models has been used. The model names are starting with either “BDS,” corresponding to the refractive index of *Patterson* [1981] or with “BDW” for another refractive index leading to a lower absorption in the blue. The first number (1, 2, or 3) following the three-letter denomination refers to the size distribution, with a higher proportion of large particles for

Table 2. Climatological (1998–2004) Seasonal Averages of $\tau_{\text{tot}}(865)$, $\tau_{\text{dust}}(865)$, f_{dust} , and N_{dust} for the Western, Central, and Eastern Mediterranean

	$\tau(865)$			$\tau_{\text{dust}}(865)$			$f_{\text{dust}}, \%$			$N_{\text{dust}} (10^6 \text{ pixels})$		
	Western	Central	Eastern	Western	Central	Eastern	Western	Central	Eastern	Western	Central	Eastern
Winter (DJF)	0.120	0.136	0.143	0.129	0.150	0.162	10	9	7	0.622	0.395	0.332
Spring (MAM)	0.170	0.179	0.192	0.237	0.254	0.253	8	12	11	0.794	0.744	0.729
Summer (JJA)	0.184	0.175	0.179	0.260	0.236	0.221	12	16	8	1.369	1.064	0.563
Fall (SON)	0.160	0.173	0.161	0.208	0.202	0.189	12	16	9	0.424	1.376	0.960

“3” than for “2” than for “1.” The second number (2, 5, or 7) refers to the vertical repartition of the aerosol, which is homogeneously distributed from the surface to either 2, 5, or 7 km.

[53] Statistics of the aerosol model selections are provided in Table 3. They show that the BDW family of aerosols is selected in $\sim 80\%$ of the cases (up to 90% in summer and 60% in winter), and that among this family, the BDW1 model is dominant (BDW2 and BDW3 suit only in 4% and 3% of the cases, respectively). This model is moderately absorbing and has a small proportion of large particles, hence a relatively steep spectral dependency for its scattering coefficient. When it is selected, the BDW1 model is combined with the two vertical distributions that are the most frequently used, i.e., the aerosol distributed from 0 to 7 km ($\sim 60\%$) or from 0 to 2 km ($\sim 30\%$). Overall, the second most frequently used aerosol model is the BDS1 ($\sim 15\%$), which is made of the same particle size distribution than the BDW1 but is more absorbing in the blue. In third position is the BDS3 model ($\sim 6\%$ of all model selections). The BDS2 is the least used of all models.

[54] The most appropriate vertical distribution is when aerosols are from 0 to 7 km, and the second one is when aerosols are confined in the marine boundary layer (0–2 km). The intermediate case (0–5 km) is rarely selected. It is however difficult to assess whether this is representative of the true vertical distribution or sometimes results from compensating effects due to possible unrealistic vertical distributions combined with inappropriate optical properties.

[55] Overall, within the models proposed by *Moulin et al.* [2001a], the less absorbing models with the steeper spectral

dependence of scattering are the most appropriate to describe the dust aerosol over the Mediterranean Sea. The reader is referred to Table 3 for a closer examination of the occurrence of each model as a function of the season and of its vertical distribution.

3.5. Interannual Variability of the Seasonal Patterns of the Dust Distribution

[56] The five parameters (τ_{tot} , $\alpha(443,865)$, f_{dust} , N_{dust} , and τ_{dust}), in spite of their specific features that were previously described, have similar average distributions and seasonal cycles. For this reason, and also because f_{dust} has shown the greatest seasonal and regional variability among the four parameters, this parameter only is considered for the analysis of the interannual variability. To support this analysis, seasonal maps of f_{dust} are separately displayed for each of the 7 years in Figure 8.

[57] Although winter is generally characterized by the lowest values of f_{dust} across the entire Mediterranean, the region between the Balearic Islands and Sardinia shows significant frequencies of dust aerosols in most years, especially from 2000 to 2004. Regional scale transport also occurs across the entire western Mediterranean in winter of 2001, and even over the whole Mediterranean in winters of 2003 and 2004. These two “anomalous” years are also characterized by large areas with mean Ångström exponents below 0.5.

[58] Summer is confirmed as the season of maximum dust transport whatever the year, which is clearly revealed in Figure 8, with a band of large f_{dust} values along the African coast, from the Alboran Sea to the Ionian Sea.

Table 3. Statistics of the Dust Model Selections (See Text for the Meaning of the Model Names) in Terms of the Percentage of the Total Number of Pixels for Which Absorption Has Been Detected^a

Winter	Spring	Summer	Fall	All Seasons					
BDW17	45.2	BDW17	37.8	BDW12	44.6	BDW17	48.6	BDW17	41.6
BDS17	19.8	BDW12	31.3	BDW17	34.1	BDW12	20.3	BDW12	26.1
BDS37	8.0	BDW15	5.8	BDW15	5.2	BDS17	8.8	BDS17	9.2
BDW12	6.4	BDS17	5.7	BDS17	3.8	BDS37	3.9	BDS37	4.2
BDS27	4.5	BDW27	4.3	BDW27	3.0	BDW15	3.7	BDW15	4.1
		BDS12	3.1			BDW27	3.1	BDW27	3.0
BDS	40.6		14.9		10.3		19.8		20.7
BDW	59.4		85.1		89.7		80.2		79.3
0–2 km	12.9		38.5		47.5		25.6		31.5
0–5 km	6.1		7.7		6.0		6.4		6.5
0–7 km	81.0		53.7		46.5		68.0		62.0

^aThe models that were selected in less than 3% of the situations are not shown. The “BDS” and “BDW” lines summarize the contribution of both families of dust aerosols, whatever the size distribution and the vertical repartition, and the last three lines summarize the contribution of the three different vertical distributions, whatever the aerosol model.

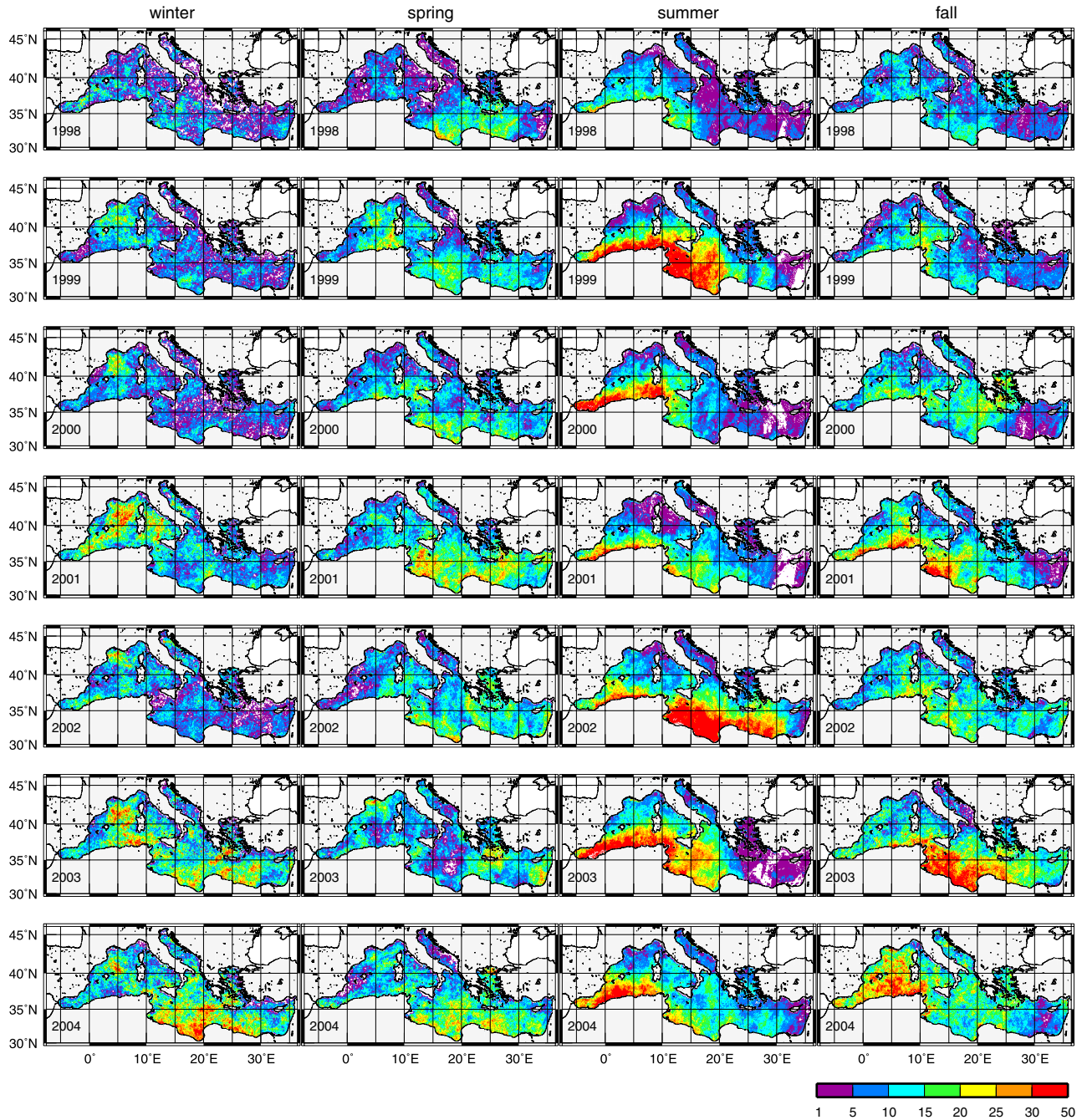


Figure 8. Seasonal occurrence of dust aerosols, f_{dust} (%), from 1998 (top) to 2004 (bottom).

[59] Spring and fall are showing the largest interannual changes. The area of maximum f_{dust} is nearly absent in fall of 1998, located between Sardinia, Sicily, and Tunisia in 1999, spread over a large band from the north of Algeria to Crete in 2000, concentrated along the Algerian, Tunisian, and Libyan coasts in 2001 (showing a “summer-like pattern”), spread over a large part of the basin in 2002, concerning mostly the south Ionian Sea and south Levantine basin in 2003, and finally nearly restricted to the western basin in 2004. Very high f_{dust} ($> 30\%$) are observed in falls of 2001, 2003, and 2004, whereas it generally does not exceed 25% at this season.

[60] Concerning spring, the maximum extent of dust was in 2001. For the other years, there is no clear organization, with areas of moderately high f_{dust} (about 20%) spread out over the different subbasins of the Mediterranean.

[61] These observations show that the interannual variability of the dust transport over the Mediterranean Sea does not show up as a slight modulation around a climatological and repeatable annual cycle. It is rather characterized by dramatic changes in the main pathways of atmospheric transport, resulting in highly contrasted situations. The only repeatable feature is the East-to-West shift of the transport from spring to summer and to fall, which has been previously described [Moulin *et al.*, 1998], and which can be

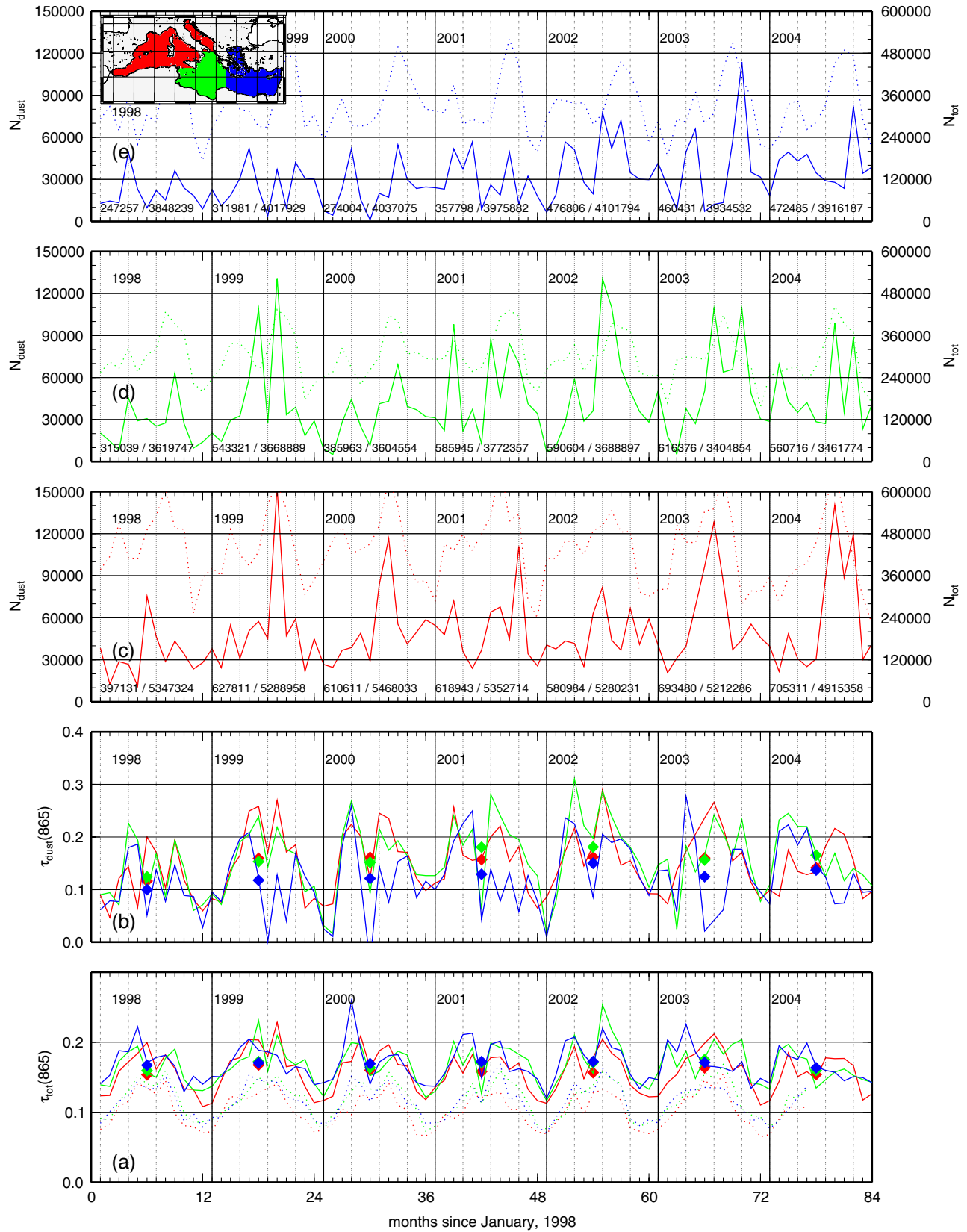


Figure 9

Table 4. Annual Averages of $\tau_{\text{tot}}(865)$ and $\tau_{\text{dust}}(865)$ for the Three Subbasins

	$\tau_{\text{tot}}(865)$			$\tau_{\text{dust}}(865)$		
	Western	Central	Eastern	Western	Central	Eastern
1998	0.153	0.159	0.167	0.116	0.124	0.100
1999	0.167	0.172	0.171	0.159	0.153	0.118
2000	0.160	0.163	0.169	0.161	0.152	0.121
2001	0.158	0.171	0.172	0.157	0.180	0.129
2002	0.157	0.171	0.172	0.162	0.181	0.150
2003	0.163	0.175	0.171	0.160	0.156	0.124
2004	0.154	0.160	0.163	0.141	0.165	0.137

mostly explained by the climatology of cyclonic circulations over the Mediterranean sea [Alpert *et al.*, 1990].

[62] The information provided in Figure 8 are summarized in Figure 9, as the 7-year, month-to-month, evolution of basin-average τ_{tot} (Figure 9a), τ_{dust} (Figure 9b), and N_{dust} in the western (Figure 9c), central (Figure 9d), and eastern (Figure 9e) Mediterranean.

[63] Concerning the total optical thickness (Figure 9a), the comments about the climatological cycle (Figure 7) remain grossly valid with a minimum in winter and relative maxima usually in spring or summer. The results obtained from the standard SeaWiFS products have been superimposed for comparison. The seasonal cycles are nearly identical when computed from the results of the standard SeaWiFS processing or from the present one, but the average values provided in the standard SeaWiFS products are lower by 38% on average. This difference disappears (not shown) when using the same technique for cloud elimination than in the standard SeaWiFS processing (as already mentioned for Figure 5). A recurrent feature is the seasonal westward shift of the dust transport, with the increase of optical thickness occurring one or two months later in the western Mediterranean than in the central and eastern basins. The central and eastern basins are actually where dust starts to become significant, sometimes as early as winter (for instance in 2003 and 2004).

[64] Concerning the dust optical thickness (Figure 9b), the seasonal evolution is similar to that of the total optical thickness, with however a larger range of values, from nearly zero in winter of 2001–2002 to a maximum of about 0.3 in spring of 2002. The annual averages (diamonds on Figure 9b; values reported in Table 4) regularly increase from 1998 to 2002 and then remain nearly stable.

[65] Concerning N_{dust} (Figures 9c, 9d, and 9e), none of the three basins show a clear picture, with usually one or two, sometimes three, relative maxima occurring at various moments in the year. These seasonal evolutions show a considerable interannual variability, which is certainly driven

by the complex patterns of atmospheric circulation and rainfall over the Mediterranean and over the source regions. The seasonal cycles often markedly differ from the climatological picture previously described [e.g., Moulin *et al.*, 1998]. Although some recent changes may have occurred in the seasonal patterns of dust transport over the Mediterranean Sea, it is believed that these differences are partly due to the capability of the present algorithm to discriminate between absorbing and nonabsorbing aerosols, so that a dust-specific optical thickness can be derived, as compared to the algorithms using broadband visible METEOSAT observations that essentially assign the Rayleigh-corrected signal to dust aerosols for any pixel, after constant backgrounds of sulfate and H_2SO_4 aerosols have been removed. The other obvious feature appearing in Figures 9c, 9d, and 9e is an increase of N_{dust} over the study period. This evolution of the dust transport is now described.

3.6. General Evolution Over the 7-Year Study Period (1998 to 2004)

[66] The seasonal patterns and the year-to-year changes have been also quantified by computing in each basin the area that is frequently affected by dust plumes. For a given monthly composite and a given subbasin, this is obtained by summing up the area of all $0.1^\circ \times 0.1^\circ$ grid cells where $f_{\text{dust}} > 25\%$ (results on Figure 10). The value of 25% was arbitrarily chosen as representative of high dust loads. It has been checked that the seasonal patterns and the year-to-year changes are not appreciably modified for percentages between 15% and 30%. The impact of lowering (increasing) the threshold is essentially to shift the curves shown in Figure 10 toward larger (lower) values.

[67] The largest dust-contaminated areas are usually in the central Mediterranean (the smallest of the three subdivisions), where they can reach up to 65% of the basin area, whereas they concern a maximum of 25% and 45% of the basins for the eastern and western parts, respectively. Exceptions are for 2000 and 2004, where the largest areas are in the western Mediterranean. In 2000, this is due to a strong decrease in the dust transport toward the central basin (it is therefore a relative maximum), while in 2004 it is clearly due to the anomalously high dust content over the western basin in fall. The curves displayed in Figure 10 again illustrate the huge interannual variability in the dust occurrences, with annual cycles that would hardly be superimposed one on top of each other.

[68] The running averages in Figure 10 show a general increase of the dust occurrences from 1998 to 2004, in particular in the eastern Mediterranean. In this subbasin the average area where significant dust is detected is multiplied by nearly a factor of 5, which represents a change from $\sim 3\%$ to $\sim 15\%$ of the basin area. If the year 1998 is not

Figure 9. Seasonal cycles of (a) $\tau_{\text{tot}}(865)$ (the red, green, and blue solid curves are for the western, central, and eastern Mediterranean basins, respectively; the dotted curves are from the standard SeaWiFS products), (b) $\tau_{\text{dust}}(865)$, and (c, d, e) the absolute occurrence of dust aerosols, N_{dust} , for the western, central, and eastern Mediterranean, from 1998 to 2004. In Figures 9a and 9b, the diamonds are the annual averages (values reported in Table 4). In Figures 9c, 9d, and 9e the dotted curves are the total number of clear-sky pixels (scale on the right axis), and the two numbers given at the bottom of each panel and for each year are the total number of dusty pixels and the total number of pixels. The delineation of the three basins is shown in insert. The vertical bold lines indicate the month of January for each year, and the vertical dotted lines are for the months of April, July, and October.

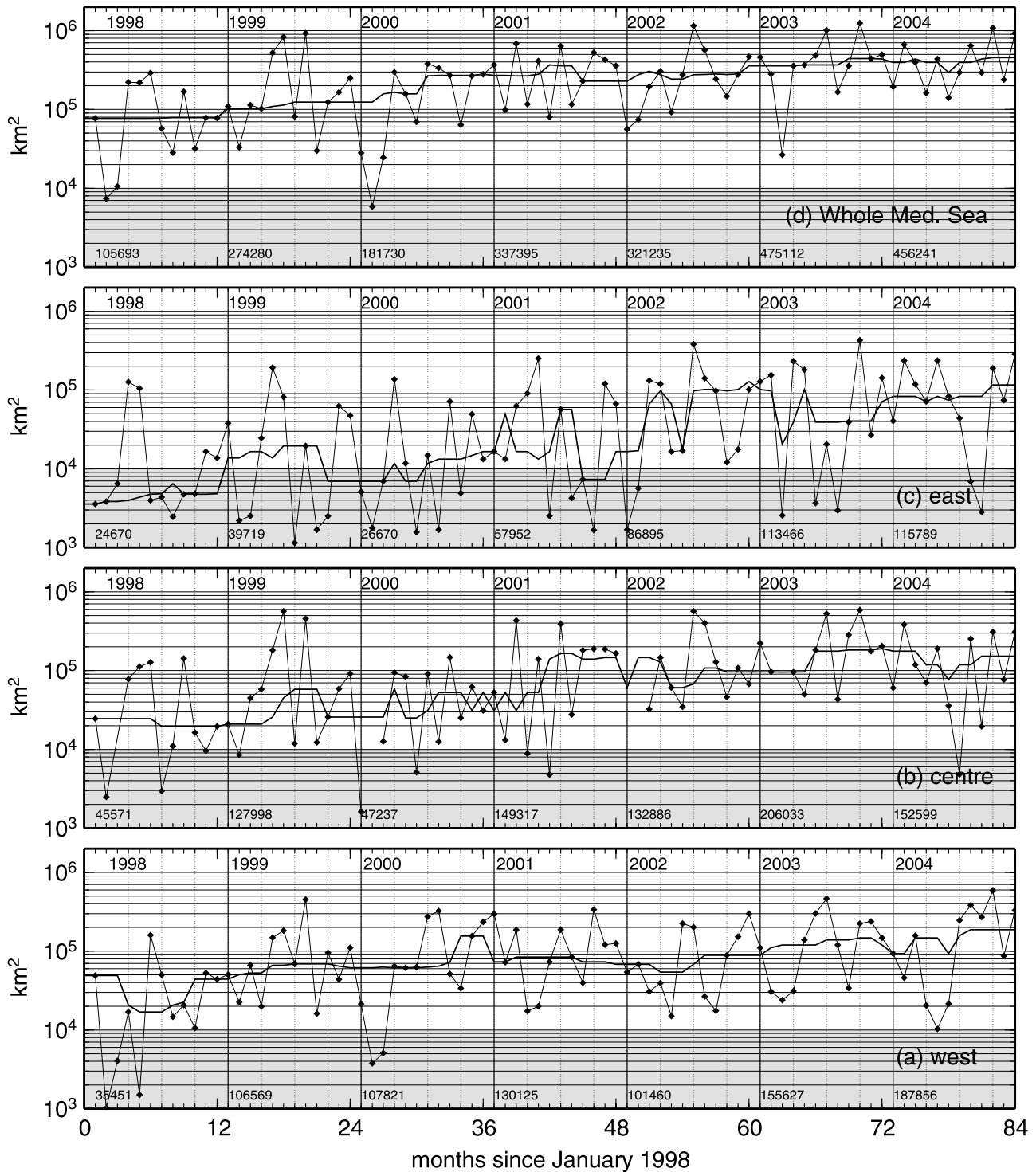


Figure 10. Month-to-month evolution, from 1998 to 2004, of the total area where $f_{\text{dust}} > 25\%$, for the (a) western, (b) central, (c) eastern, and (d) whole Mediterranean. The bold curve is a running average based on the monthly values (thin curve) and using a ± 5 months window. The numbers given at the bottom of each panel and for each year are the mean of the monthly values (km^2). The vertical bold lines indicate the month of January for each year, and the vertical dotted lines are for the months of April, July, and October.

considered because it looks quite atypical with very low dust occurrences, the increase is still by a factor of ~ 3 . Similar numbers are obtained for the western basin (factors of ~ 5 and ~ 2 , from $\sim 3\%$ to $\sim 15\%$ of the basin area),

whereas lower increases are observed in the central basin (~ 3 and ~ 1.5 , i.e., from $\sim 7\%$ to $\sim 20\%$). In the western and central basins, most of the increase occurs from 1998 to 2001, with a relative steadiness in the following years.

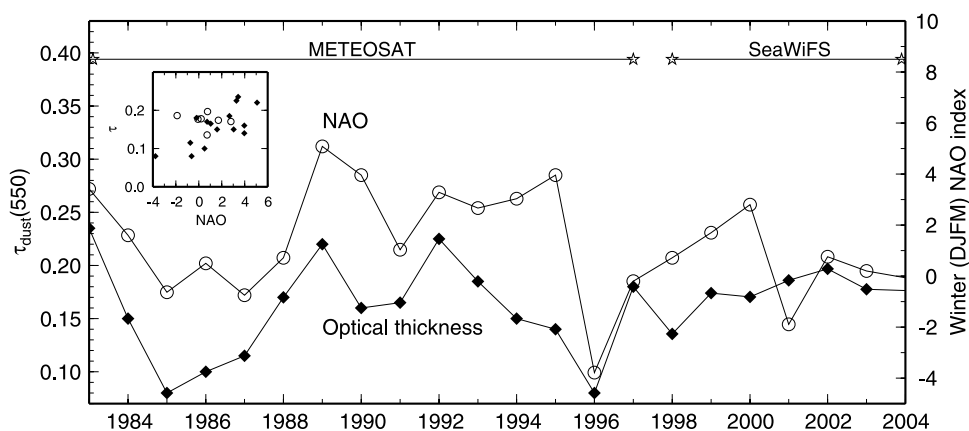


Figure 11. Time series of the North Atlantic Oscillation (NAO) winter index (scale on the right axis; open circles; data from <http://www.cgd.ucar.edu/cas/jhurrell/Data/naodjfmindex.1864-2005.xls>) and of the dust optical thickness (scale on the left axis; black diamonds). The values derived at 865 nm from the SeaWiFS data have been converted into values at 550 nm in order to be consistent with the results published by *Moulin et al.* [1997c] and *Moulin and Chiapello* [2004] (data courtesy C. Moulin). The transformation was performed with an Angstrom exponent of 0.4 (cf. Figure 7b). The inserted scatterplot of τ_{dust} versus the NAO includes the 15 points from the METEOSAT time series (black diamonds) and the seven points from the SeaWiFS time series (open circles).

[69] These evolutions are coherent with the average τ_{dust} values provided in Table 4, which are larger in 2004 than in 1998, by about 20%, 33%, and 37% in the western, central and eastern basins, respectively. The increase even reaches 50% between 1998 and 2002 (the year with maximum τ_{dust} everywhere) in the eastern basin. Because the dust transport looks really low in 1998, it is timely to also compute the percentages of change from 1999 to 2004. In that case, they become about -10% , 8% , and 16% . Therefore except for the western basin, the overall tendency is confirmed whatever the starting point used for the computation. It is worth noting that the changes displayed in Figure 10 somewhat overemphasize the increase over the study period, as compared to what can be seen when looking only at the average dust optical thickness (Figure 9b). The moderate increase observed in τ_{dust} actually occurs for levels close to the detection limit of the algorithm (optical thickness of about 0.15 at 865 nm), which explains the large increase of dust detection, with the optical thickness being more and more often above the detection threshold from the beginning to the end of the 7-year time series. This observation illustrates the sensitivity of the detection method.

[70] A number of processes may possibly be responsible for the observed increase in the dust optical thickness over the study period. They may include local changes in atmospheric circulation, local changes in rain rates and distribution, as well as modification of the dust mobilization from the source regions. A thorough examination of these local causes, which would require the corroborative study of several types of data over the same time period, is out of scope here. Another candidate has been examined, however, which is driven by atmospheric processes at larger scales, i.e., the change in the North Atlantic Oscillation (NAO) [e.g., *Hurrell*, 1995; *Hurrell et al.*, 2003]. This oscillation has already been identified as a driver of the decadal evolutions of the dust transport over the Mediterranean Sea and the North Atlantic [*Moulin et al.*, 1997c; *Moulin*

and *Chiapello*, 2004]. The 7-year τ_{dust} time series derived here from the SeaWiFS has been therefore appended to the 14-year time series previously derived from the METEOSAT observations. The complete series has been plotted in parallel to the “winter NAO index,” i.e., the average NAO index for the 4 months between December and March (Figure 11). The overall correlation between τ_{dust} and the winter index, which was first described by *Moulin et al.* [1997c], is confirmed for the SeaWiFS era, although the change in the NAO during this period is much less than during the METEOSAT era (from -2 to $+3$, as compared to -4 to $+6$). It is therefore legitimate to ascribe to the NAO the first-order changes observed here for τ_{dust} over the SeaWiFS era, whereas local and seasonal changes of τ_{dust} would stem from the processes briefly mentioned above (and possibly from other processes not identified here).

[71] To corroborate the trends observed here in f_{dust} , information about absorbing aerosols that might be provided by other remote sensing techniques have been sought for (other than simply the optical thickness). The most relevant parameter that was found is the Earth Probe-TOMS absorbing aerosol index [*Herman et al.*, 1997; *Torres et al.*, 1998], which is derived from measurements in the ultraviolet domain. Unfortunately, an unexplained wavelength-dependent calibration drift started after year 2000, which made these data unusable for a trend analysis (O. Torres, personal communication, 2005). The Ozone Monitoring Instrument (OMI) sensor on the AURA satellite [*Levelt et al.*, 2000] now provides the same index, yet only since October of 2004, which was useless to compare with the 7-year time series derived from SeaWiFS.

[72] Possible drawbacks in this temporal analysis might be produced on the one hand by a drift in the sensor calibration, which could bias the aerosol identification in the near infrared or the error budget at 510 nm, and, on the other hand, by a change in the average ocean reflectance at 510 nm. The first cause is unlikely however, since the

vicarious calibration of SeaWiFS has benefited from an outstanding effort that allowed maintaining the stability of the instrument. Concerning the ocean reflectance at 510 nm, there is not any indication of such a change.

[73] A modification in the balance between dry aerosol transport (the one accessible to the technique proposed here) and wet transport within clouds, which is by definition not seen by an inherently clear-sky method, might also lead to such an apparent increase of f_{dust} .

4. Conclusion

[74] A method was recently developed for the detection of blue-absorbing aerosols from ocean color satellite observations and was validated against in situ data [Nobileau and Antoine, 2005]. This method has been applied here to 7 years of observations from the SeaWiFS sensor, to describe the distribution of Saharan dust over the Mediterranean Sea, and to quantify the associated atmospheric burden. One objective was to conclusively demonstrate the applicability of the method when systematically used with large data sets and to validate more extensively its outputs by comparison with AERONET products.

[75] The general pictures that emerged from this work are consistent with the results from previous works, where the dust quantification over the Mediterranean Sea was performed either from broadband visible observations (i.e., METEOSAT) [Moulin *et al.*, 1998] or from other multi-channel visible ocean color observations either from MODIS [Barnaba and Gobbi, 2004] or from SeaWiFS [Jamet *et al.*, 2004]. The seasonal cycle of the optical thickness is well captured in the three subbasins, with the lowest values in winter and the highest values in spring and summer. In addition, a strong interannual variability is observed, as well as an increasing trend in the dust transport during the study period. The main difference with previous works is the importance of the dust transport in fall, and higher dust optical thicknesses on the average.

[76] The method is therefore suitable to routinely map blue-absorbing aerosols over the ocean from the various ocean color sensor observations. It is for instance implemented into the operational processing chain for MERIS. It can advantageously complement the other techniques, in order to provide the most comprehensive as possible picture of aerosols over the ocean from various satellite platforms. These results also confirm that the sampling provided by SeaWiFS (i.e., a full coverage of the Mediterranean Sea within 2 days) is adapted to the study of aerosols.

[77] Improvements of the method are still desirable, however, in particular before it can be generalized to the global ocean. A first possibility is to progressively improve the knowledge of the global seasonal distribution of the marine reflectance at 510 nm, which would lead to an improvement of the detection capability (in other words, improving the uncertainty budget at 510 nm). This is reachable by permanently revising the global climatology for $\bar{\rho}_w(510)$ and $\sigma(\rho_w)$, by using the fleet of ocean color sensors presently in orbit, and also through blending of these data along with in situ determinations of the marine reflectance at 510 nm.

[78] The second improvement would be to introduce additional sets of dust aerosols specific to the other regions

of the planet where they are transported, i.e., mostly the Arabian Sea, the north Pacific and the seas around Australia. There is indeed a significant variability in the dust optical properties, in particular their single scattering albedo, among the different source regions [Dubovik *et al.*, 2002]. Introducing these differences would improve the retrieval of the aerosol optical thickness, in particular in the visible.

[79] Another step would be the introduction of additional external information or the use of additional spectral bands, in order to specifically determine whether the absorption detected at 510 nm is due to dust or to other absorbing aerosols such as soot or biomass burning aerosols. In the present work, however, this cannot have a strong impact on the results because the vast majority of absorbing aerosols over the Mediterranean Sea are of desert origin.

[80] These improvements would in turn improve the ocean color products themselves, such as the normalized water-leaving radiance, by improving the atmospheric correction process [e.g., Moulin *et al.*, 2001b].

[81] **Acknowledgments.** This work has been supported through a Ph.D. fellowship to Delphine Nobileau (University Pierre et Marie Curie) and through ESA/ESTEC contract 14393/00/NL/DC and the NAOC (“Neural network Algorithms for Ocean Color”) project that was funded by the European commission, for the development of the MERIS atmospheric correction algorithms. The SeaWiFS Level 1a data have been obtained through the Goddard Distributed Active Archive Center (GES-DAAC) at the NASA Goddard Space Flight Center, which is duly acknowledged. The “Villefranche” AERONET site is managed by David Antoine, Guislain Bécu, and Alec Scott. The Principal Investigators and local managers of the five other AERONET sites are duly acknowledged: Didier Tanré, Filippo Angotzi and Béatrice Chatenet for the Oristano site, Giuseppe Zibordi for the Venice site, Brent Holben and Nilgun Kubilay for the Erdemli site, Sergio Pugnaghi, Renato Santangelo and Stefano Corradini for the Lampedusa site, and Manolis Drakakis for the Crete site. The AERONET is also thanked for the easy and fast data delivery on the Internet. This paper has benefited from discussions with Cyril Moulin, François Dulac, Robert Frouin, and Jean-Luc Deuzé, to whom we express our gratitude.

References

- Alpert, P., B. Neeman, and Y. Shay-El (1990), Intermonthly variability of cyclone tracks in the mediterranean, *J. Clim.*, 3, 1474–1478.
- Andreae, M. O. (1996), Raising dust in the greenhouse, *Nature*, 380, 389–390.
- Antoine, D., and A. Morel (1999), A multiple scattering algorithm for atmospheric correction of remotely sensed ocean colour (MERIS instrument): principle and implementation for atmospheres carrying various aerosols including absorbing ones, *Int. J. Remote Sens.*, 20, 1875–1916.
- Barnaba, F., and G. P. Gobbi (2004), Aerosol seasonal variability over the Mediterranean region and relative impact of maritime, continental and Saharan dust particles over the basin from MODIS data in the year 2001, *Atmos. Chem. Phys. Discuss.*, 4, 4285–4337.
- Barnes, R. A., R. E. Eplee Jr., G. M. Schmidt, F. S. Patt, and C. R. McClain (2001), Calibration of SeaWiFS. I. Direct techniques, *Appl. Opt.*, 40, 6700–6882.
- Bellouin, N., O. Boucher, D. Tanré, and O. Dubovik (2003), Aerosol absorption over the clear-sky oceans deduced from POLDER-1 and AERONET observations, *Geophys. Res. Lett.*, 30(14), 1748, doi:10.1029/2003GL017121.
- Boucher, O., and D. Tanré (2000), Estimation of the aerosol perturbation to the Earth’s radiative budget over oceans using POLDER satellite aerosol retrievals, *Geophys. Res. Lett.*, 27, 1103–1106.
- Bricaud, A., and A. Morel (1987), Atmospheric corrections and interpretation of marine radiances in CZCS imagery: use of a reflectance model, *Oceanol. Acta*, SP-7, 33–50.
- Brooks, N., and M. Legrand (2000), Dust variability over northern Africa and rainfall in the sahel, in *Linking Climate Change to Land Surface Change*, edited by S. J. McLaren and D. Kniveton, pp. 1–25. Springer, New York.

- Charlson, R. J., S. E. Schwartz, J. M. Hales, R. D. Cess, J. A. Coakley, J. E. Hansen, and D. J. Hoffman (1992), Climate forcing by anthropogenic aerosols, *Science*, *255*, 423–430.
- Chiapello, I., and C. Moulin (2002), TOMS and METEOSAT satellite records of the variability of Saharan dust transport over the Atlantic during the last two decades (1979–1997), *Geophys. Res. Lett.*, *29*(8), 1176, doi:10.1029/2001GL013767.
- Chiapello, I., P. Goloub, D. Tanré, J. Herman, O. Torres, and A. Marchand (2000), Aerosol detection by TOMS and POLDER over oceanic regions, *J. Geophys. Res.*, *105*, 7133–714.
- Clarke, G. L., G. C. Ewing, and C. J. Lorenzen (1970), Spectra of backscattered light from the sea obtained from aircraft as a measure of chlorophyll concentration, *Science*, *167*, 1119–1121.
- Deuzé, J.-L., M. Herman, P. Goloub, D. Tanré, and A. Marchand (1999), Characterization of aerosols over ocean from POLDER/ADEOS-1, *Geophys. Res. Lett.*, *26*, 1421–1424.
- Deuzé, J.-L., P. Goloub, M. Herman, A. Marchand, G. Perry, D. Tanré, and S. Susana (2000), Estimate of the aerosols properties over the ocean with POLDER, *J. Geophys. Res.*, *105*, 15,329–15,346.
- Donaghay, P. L., P. S. Liss, R. A. Duce, D. R. Kester, A. K. Hanson, T. Villareal, N. W. Tindale, and D. J. Gifford (1991), The role of episodic atmospheric nutrient inputs in the chemical and biological ecosystems, *Oceanography*, *4*, 62–70.
- Dubovik, O., A. Smirnov, B. N. Holben, M. D. King, Y. J. Kaufman, T. F. Eck, and I. Slutsker (2000), Accuracy assessments of aerosol optical properties retrieved from Aerosol Robotic Network (AERONET) sun and sky radiance measurements, *J. Geophys. Res.*, *105*, 9791–9806.
- Dubovik, O., B. N. Holben, T. F. Eck, A. V. Smirnov, Y. J. Kaufman, M. D. King, D. Tanré, and I. Slutsker (2002), Variability of absorption and optical properties of key aerosol types observed in worldwide location, *J. Atmos. Sci.*, *59*, 590–608.
- Duce, R. A., et al. (1991), The atmospheric input of trace species to the World ocean, *Global Biogeochem. Cycles*, *5*, 193–259.
- Fu, G., K. S. Baith, and C. R. McClain (1998), SeaWiFS Data Analysis System, paper presented at 4th Pacific Ocean Remote Sensing Conference, Qingdao, China.
- Gordon, H. R. (1978), Removal of atmospheric effects from satellite imagery of the oceans, *Appl. Opt.*, *17*, 1631–1636.
- Gordon, H. R. (1990), Radiometric considerations for ocean color remote sensors, *Appl. Opt.*, *29*, 3228–3236.
- Gordon, H. R. (1997), Atmospheric correction of ocean color imagery in the Earth Observing System era, *J. Geophys. Res.*, *102*, 17,081–17,106.
- Gordon, H. R., and M. Wang (1994a), Retrieval of water-leaving reflectance and aerosol optical thickness over the oceans with SeaWiFS: A preliminary algorithm, *Appl. Opt.*, *33*, 443–452.
- Gordon, H. R., and M. Wang (1994b), Influence of oceanic whitecaps on atmospheric correction of ocean-color sensors, *Appl. Opt.*, *33*, 7754–7763.
- Gordon, H. R., T. Du, and T. Zhang (1997), Remote sensing of ocean color and aerosol properties: resolving the issue of aerosol absorption, *Appl. Opt.*, *36*, 8670–8684.
- Herman, J. R., P. K. Bhartia, O. Torres, C. Hsu, C. Seftor, and E. Celarier (1997), Global distribution of UV-absorbing aerosols from Nimbus-7/TOMS data, *J. Geophys. Res.*, *102*, 16,911–16,922.
- Holben, B. N., et al. (1998), AERONET - A federated instrument network and data archive for aerosol characterization, *Remote Sens. Environ.*, *66*, 1–16.
- Hooker, S. B., W. E. Esaias, G. C. Feldman, W. W. Gregg, and C. R. McClain (1992), An overview of SeaWiFS and ocean colour, in *NASA Technical Memorandum 104566*, *SeaWiFS Tech. Rep. Ser.*, vol. 1, edited by S. B. Hooker and E. R. Firestone, pp. 24, NASA Goddard Space Flight Cent., Greenbelt, Md.
- Hurrell, J. W. (1995), Decadal trend in the North Atlantic Oscillation: Regional temperatures and precipitations, *Science*, *269*, 676–679.
- Hurrell, J. W., Y. Kushnir, M. Visbeck, and G. Ottersen (2003), An overview of the North Atlantic Oscillation, in *The North Atlantic Oscillation: Climate Significance and Environmental Impact*, *Geophys. Monogr. Ser.*, vol. 134, edited by J. W. Hurrell et al., pp. 1–35, AGU, Washington, D. C.
- Intergovernmental Panel on Climate Change (IPCC) (2001), *Climate Change 2001: The Scientific Basis*, Cambridge Univ. Press, New York.
- Jamet, C., C. Moulin, and S. Thiria (2004), Monitoring aerosol optical properties over the Mediterranean from SeaWiFS images using a neural network inversion, *Geophys. Res. Lett.*, *31*, L13107, doi:10.1029/2004GL019951.
- Kaufman, Y. J., D. Tanré, H. R. Gordon, T. Nakalima, J. Lenoble, R. Frouin, H. Grassl, B. M. Herman, M. D. King, and P. M. Teillet (1997), Passive remote sensing of tropospheric aerosol and atmospheric correction of the aerosol effect, *J. Geophys. Res.*, *102*, 16,815–16,830.
- Kaufman, Y. J., A. Smirnov, B. N. Holben, and O. Dubovik (2001), Baseline maritime aerosol: methodology to derive the optical thickness and scattering properties, *Geophys. Res. Lett.*, *28*, 3251–3254.
- Kaufman, Y. J., D. Tanré, and O. Boucher (2002), A satellite view of aerosols in the climate system, *Nature*, *419*, 215–223.
- Kaufman, Y. J., I. Koren, L. Remer, D. Tanré, P. Ginoux, and S. Fan (2005), Dust transport and deposition observed from the Terra-Moderate Resolution Imaging Spectroradiometer (MODIS) spacecraft over the Atlantic Ocean, *J. Geophys. Res.*, *110*, D10S12, doi:10.1029/2003JD004436.
- King, M. D., Y. J. Kaufman, D. Tanré, and T. Nakajima (1999), Remote sensing of tropospheric aerosols from space: past, present, future, *Bull. Am. Meteorol. Soc.*, *80*, 2229–2259.
- Krom, M. D., S. Brenner, N. Kress, and I. I. Gordon (1991), Phosphorus limitation of Primary Productivity in the E. Mediterranean sea, *Limnol. Oceanogr.*, *36*, 424–432.
- Levelt, P. F., et al. (2000), Science objectives of EOSAURA's Ozone Monitoring Instrument (OMI), paper presented at the Quadrennial Ozone Symposium, Int. Ozone Comm., Int. Assoc. for Meteorol. and Atmos. Sci., Sapporo, Japan.
- Levin, Z., and E. Ganor (1996), The effects of desert particules on cloud and rain formation in the Eastern Mediterranean, in *The Impact of Desert Dust Across the Mediterranean*, edited by S. Guerzoni and R. Chester, pp. 77–86, Springer, New York.
- Li, X., H. Maring, D. L. Savoie, K. Voss, and J. M. Prospero (1996), Dominance of mineral dust in aerosol light-scattering in the North Atlantic trade winds, *Nature*, *380*, 416–419.
- Loje-Pilot, M. D., J. M. Martin, and J. Morelli (1986), Influence of Saharan dust on the rain acidity and atmospheric input to the Mediterranean, *Nature*, *321*, 427–428.
- Martins, J. V., D. Tanré, L. Remer, Y. J. Kaufman, S. Mattoo, and R. Levy (2002), MODIS Cloud screening for remote sensing of aerosols over the oceans using spatial variability, *Geophys. Res. Lett.*, *29*(12), 8009, doi:10.1029/2001GL013252.
- Moulin, C., and I. Chiapello (2004), Evidence of the control of summer atmospheric transport of African dust over the Atlantic by Sahel sources from TOMS satellites (1979–2000), *Geophys. Res. Lett.*, *31*, L02107, doi:10.1029/2003GL018931.
- Moulin, C., F. Dulac, C. E. Lambert, P. Chazette, I. Jankowiak, B. Chatenet, and F. Lavenu (1997a), Long-term daily monitoring of Saharan dust load over ocean using Meteosat ISCCP-B2 data 2: Accuracy of the method and validation using Sun photometer measurements, *J. Geophys. Res.*, *102*, 16,959–16,969.
- Moulin, C., F. Guillard, F. Dulac, and C. E. Lambert (1997b), Long-term daily monitoring of Saharan dust load over ocean using Meteosat ISCCP-B2 data 1. Methodology and preliminary results for 1983–1994 in the Mediterranean, *J. Geophys. Res.*, *102*, 16,947–16,958.
- Moulin, C., C. E. Lambert, F. Dulac, and U. Dayan (1997c), Control of atmospheric export of dust from North Africa by the North Atlantic oscillation, *Nature*, *387*, 691–694.
- Moulin, C., et al. (1998), Satellite climatology of African dust transport in the Mediterranean atmosphere, *J. Geophys. Res.*, *103*, 13,137–13,144.
- Moulin, C., H. R. Gordon, V. F. Banzon, and R. H. Evans (2001a), Assessment of Saharan dust absorption in the visible from SeaWiFS imagery, *J. Geophys. Res.*, *106*, 18,239–18,249.
- Moulin, C., H. R. Gordon, R. M. Chomko, V. F. Banzon, and R. H. Evans (2001b), Atmospheric correction of ocean color imagery through thick layers of Saharan dust, *Geophys. Res. Lett.*, *28*, 5–8.
- Nobileau, D., and D. Antoine (2005), Detection of blue-absorbing aerosols using near infrared and visible (ocean color) remote sensing observations, *Remote Sens. Environ.*, *95*, 368–387.
- Patterson, E. M. (1981), Optical properties of the crustal aerosol: Relation to chemical and physical characteristics, *J. Geophys. Res.*, *86*, 3236–3246.
- Prospero, J. M., and T. N. Carlson (1972), Vertical and areal distribution of Saharan dust over the Western Equatorial North Atlantic Ocean, *J. Geophys. Res.*, *77*, 5255–5265.
- Rast, M., J. L. Bézy, and S. Bruzzi (1999), The ESA Medium Resolution Imaging Spectrometer MERIS—a review of the instrument and its mission, *Int. J. Remote Sens.*, *20*, 1681–1702.
- Remer, L. A., et al. (2005), The MODIS Aerosol Algorithm, Products and Validation, *J. Atmos. Sci.*, *62*, 947–973.
- Santoleri, R., G. L. Liberti, G. P. Gobbi, F. Barnaba, M. Ribera d'Alcala, F. D'Ortenzio, M. Ragni, G. L. Volpe, E. Bohm, and S. Marullo (2002), Validation of SeaWiFS ocean and atmospheric products in the Mediterranean sea: NASA SIMBIOS project 2001 annual report, *NASA Tech. Memo. 2002–210005*, edited by G. S. Fargion and C. R. McClain, pp. 176–184, NASA Goddard Space Flight Cent., Md.
- Savoie, D. L., and J. M. Prospero (1977), Aerosol concentration statistics for the Northern Tropical Atlantic, *J. Geophys. Res.*, *82*, 5954–5964.

- Schollaert, S. E., J. A. Yoder, D. L. Westphal, and J. E. O'Reilly (2003), Influence of dust and sulfate aerosols on ocean color spectra and chlorophyll-a concentrations derived from SeaWiFS off the East Coast U.S., *J. Geophys. Res.*, 108(C6), 3191, doi:10.1029/2000JC000555.
- Schwindling, M., P.-Y. Deschamps, and R. Frouin (1998), Verification of aerosol models for satellite ocean color remote sensing, *J. Geophys. Res.*, 103, 24,919–24,935.
- Shettle, E. P., and R. W. Fenn (1979), Models for the aerosols of the lower atmosphere and the effects of humidity variations on their optical properties, *Environ. Res. Pap.* 676, AFGL-TR-79-0214, Air Force Geophys. Lab., Hanscom Air Force Base, Mass.
- Stegman, P. M. (2000), Ocean-color satellites and the phytoplankton-dust connection, in *Satellites, Oceanography and Society*, edited by D. Halpern, pp. 207–223, Elsevier, New York.
- Stegman, P. M. (2004a), Remote sensing of aerosols with ocean colour sensors: then and now, *Int. J. Remote Sens.*, 25, 1409–1413.
- Stegman, P. M. (2004b), Characterization of aerosols over the North Atlantic ocean from SeaWiFS, *Deep Sea Res. II*, 51, 913–925.
- Stegman, P. M., and N. W. Tindale (1999), Global distribution of aerosols over the open ocean as derived from the coastal zone color scanner, *Global Biogeochem. Cycles*, 13, 383–397.
- Tanré, D., J. Haywood, J. Pelon, J. F. Léon, B. Chatenet, P. Formenti, P. Francis, P. Goloub, E. J. Highwood, and G. Myhre (2003), Measurement and modeling of the Saharan dust radiative impact: overview of the Saharan dust experiment (SHADE), *J. Geophys. Res.*, 108(D18), 8574, doi:10.1029/2002JD003273.
- Torres, O., P. K. Bhartia, J. R. Herman, Z. Ahmad, and J. Gleason (1998), Derivation of aerosol properties from satellite measurements of backscattered ultraviolet radiation: Theoretical basis, *J. Geophys. Res.*, 103, 17,099–17,110.
- Villevalde, Y. V., A. V. Smirnov, N. T. O'Neill, S. P. Smyshlyaev, and V. V. Yakovlev (1994), Measurement of aerosol optical depth in the Pacific ocean and the North Atlantic, *J. Geophys. Res.*, 99, 20,983–20,988.
- Wang, M., S. Bailey, and C. R. McClain (2000), SeaWiFS provides unique global aerosol optical property data, *Eos Trans. AGU*, 81, 197–202.
- Wang, M., K. D. Knobelspiesse, and C. R. McClain (2005), Study of the Sea-Viewing Wide Field-of-View Sensor (SeaWiFS) aerosol optical property data over ocean in combination with the ocean color products, *J. Geophys. Res.*, 110, D10S06, doi:10.1029/2004JD004950.
- World Climate Research Program (WCRP) (1986), A preliminary cloudless standard atmosphere for radiation computation, *WCP-112, WMO/TD-24*, 60 pp., Int. Assoc. for Meteorol. and Atmos. Phys., Boulder, Colo.

D. Antoine and D. Nobileau, Laboratoire d'Océanographie de Villefranche (LOV, UMR 7093), Observatoire Océanologique de Villefranche, CNRS/Université Pierre et Marie Curie-Paris 6, F-06230 Villefranche sur mer, France. (antoine@obs-vlfr.fr)



Assessment of uncertainty in the ocean reflectance determined by three satellite ocean color sensors (MERIS, SeaWiFS and MODIS-A) at an offshore site in the Mediterranean Sea (BOUSSOLE project)

David Antoine,^{1,2} Fabrizio d'Ortenzio,^{1,2} Stanford B. Hooker,³ Guislain Bécu,^{1,4,6} Bernard Gentili,^{1,2} Dominique Tailliez,^{1,2,7} and Alec J. Scott^{1,5}

Received 31 July 2007; revised 19 December 2007; accepted 6 March 2008; published 11 July 2008.

[1] The match-up of satellite-derived reflectances with in situ observations is crucial to evaluate their quality and temporal stability. To contribute to this effort, a project has been set up to collect a data set of in situ radiometric and bio-optical quantities, in support to satellite ocean color calibration and validation. The project has been named “BOUSSOLE”, and one of its key elements is a deep-sea optics mooring collecting data on a near-continuous basis since September 2003. This buoy is deployed in the deep clear waters of the northwestern Mediterranean Sea, and is visited on a monthly basis for servicing and acquisition of complementary data. The characteristics of the work area establish the site as a satisfactory location for validating satellite ocean color observations. A description of the data processing protocols is provided, followed by an analysis of the uncertainty of the buoy radiometry measurements. The results of a match-up analysis of the marine reflectances, diffuse attenuation coefficients, and chlorophyll concentrations for three major missions, i.e., MERIS, SeaWiFS, and MODIS-A, are then analyzed. They show poor performances for the bluest band (412 nm) of the three sensors, and performances within requirements at 443 and 490 nm for SeaWiFS and MODIS-A. These results suggest that a vicarious calibration should be introduced for the MERIS sensor. This analysis also demonstrates that a major effort is still required to improve atmospheric correction procedures whatever the mission.

Citation: Antoine, D., F. d'Ortenzio, S. B. Hooker, G. Bécu, B. Gentili, D. Tailliez, and A. J. Scott (2008), Assessment of uncertainty in the ocean reflectance determined by three satellite ocean color sensors (MERIS, SeaWiFS and MODIS-A) at an offshore site in the Mediterranean Sea (BOUSSOLE project), *J. Geophys. Res.*, *113*, C07013, doi:10.1029/2007JC004472.

1. Introduction

[2] Presently, three satellite ocean color missions provide a global monitoring of the marine biosphere, i.e., the United States National Aeronautics and Space Administration (NASA) Sea Viewing Wide Field of View Sensor (SeaWiFS) aboard the Orbital Science Corporation (OSC) Orbview-II satellite [Hooker *et al.*, 1992; Hooker and Esaias, 1993], the NASA Moderate Resolution Imaging Spectrometer (MODIS-A) aboard the NASA Aqua satellite [Salomonson *et al.*, 1992; Esaias *et al.*, 1998], and the European Space Agency (ESA) Medium Resolution Imaging Spectrometer (MERIS) aboard the ENVISAT satellite [Rast *et al.*, 1999].

Other missions exist, with more limited coverage however, such as the Indian OCM [Chauhan *et al.*, 2002] or the Korean OSMI [Yong *et al.*, 1999]. This series of sensors should be continued after 2012 with the launch of the ESA sentinels [Drinkwater *et al.*, 2005] and the U.S. *National Polar Orbiting Environmental Satellite Suite* mission (NPOESS) embarking the *Visible and Infrared Imaging Radiometer Suite* (VIIRS) instrument [Murphy *et al.*, 2006].

[3] Two of the three global missions mentioned above, i.e., SeaWiFS and MODIS-A, include a vicarious calibration program, which means that a long-term postlaunch effort has been maintained with the role of permanently collecting and analyzing field data (ocean plus atmosphere) and instrumental parameters in order to maintain the level of uncertainty of the derived products within predefined requirements [Bailey and Werdell, 2006; McClain *et al.*, 1992, 2006]. Without ground-truth data (more properly sea-truth data), it is impossible to maintain the uncertainty of the satellite-derived geophysical products at the desired level over the full course of the mission, which is generally designed to be on the order of about 5 years (although many satellites operate for longer periods of time as evidenced by SeaWiFS, which was launched in 1997). This need for vicarious calibration is not due to any weakness in

¹CNRS, Laboratoire d'Océanographie de Villefranche, Villefranche sur mer, France.

²UPMC Université de Paris, Observatoire Océanologique de Villefranche, Villefranche sur mer, France.

³NASA/GSFC, Greenbelt, Maryland, USA.

⁴Also at ACRI-st SAS, Sophia Antipolis, France.

⁵Now at Fugro GEOS Ltd., Wallingford, Oxfordshire, UK.

⁶Now at GEMS Survey Ltd., Devizes, Wiltshire, UK.

⁷Deceased 26 March 2008.

the sensor nor in the onboard calibration devices; it results from unavoidable physical considerations: *the goal of modern ocean color sensors is to provide the water-leaving radiance in the blue part of the e.m. spectrum with a 5% accuracy over oligotrophic, chlorophyll-depleted, waters* [Gordon, 1997], which can also be expressed as an uncertainty of 0.002 in terms of reflectance [Antoine and Morel, 1999]. Because this marine signal only represents about 10% (at most) of the radiance directly measured by the spaceborne sensor at the top of the atmosphere (TOA), achieving this goal requires that the instruments involved are calibrated to better than 0.5%, or approximately 1%. This is extremely challenging considering the present technology, and probably will remain an elusive goal. It is also worth noting that what is referred to as a “vicarious calibration” in the field of ocean color remote sensing is not an absolute calibration of the sensor only, but an adjustment of the overall response of the sensor plus the atmospheric correction algorithm [Gordon, 1997, 1998; Franz et al., 2007]. The goal is to absorb unavoidable residual uncertainties in order to get the correct answer in terms of the normalized water-leaving radiance, in particular for the blue bands.

[4] Typically, validation of geophysical products derived from satellite ocean color observations consists of collecting field data that are directly compared to the satellite products. The list generally includes spectral normalized water-leaving radiances (nL_w ; see later in section 3.2 for definitions) or reflectances (ρ_w), diffuse attenuation coefficient for downward irradiance at 490 nm ($K_d(490)$), phytoplankton total chlorophyll-a (TChl a), and spectral aerosol optical thickness (AOT), from which the aerosol Angstrom exponent can be computed. Assessing the uncertainty to which these parameters can be retrieved allows the different steps of the overall process to be verified, i.e., the atmospheric correction (using nL_w 's and AOT) and the bio-optical algorithms (using for instance TChl a).

[5] The strategy adopted for SeaWiFS and MODIS-A relies on a permanent marine optical buoy, MOBY [Clark et al., 1997, 2003], coupled with an extensive field data collection program [Werdell and Bailey, 2005]. The former provides data needed to derive vicarious calibration gains and the latter allows global verification of this calibration. Other long-term activities have progressively developed along these lines and support the same missions, such as the Coastal Atmosphere and Sea Time Series (CoASTS) project maintained near Venice (Italy) since 1995 [Berthon et al., 2002; Zibordi et al., 2002].

[6] The logic is somewhat different for the MERIS mission: it is assumed that the improvement of the onboard calibration devices compared to other sensors, coupled with a rigorous prelaunch characterization, are sufficient to provide the required level of uncertainty. Scattered field efforts nevertheless exist, essentially devoted to validation of the geophysical products, but none have been used to vicariously calibrate the MERIS instrument. To complement these activities, a project was started in 2000 with the objective of establishing a time series of optical properties in oceanic waters (Mediterranean Sea) to support the calibration and validation of MERIS. This activity has been named the “*Bouée pour l'acquisition de Séries Optiques à Long Terme*” (BOUSSOLE) project, which is literally

translated from French as the “buoy for the acquisition of a long-term optical time series” (“boussole” is the French word for “compass”). It is composed of three basic and complementary elements: (1) a monthly cruise program, (2) a permanent optical mooring, and (3) a coastal Aerosol Robotic Network (AERONET) station [Holben et al., 1998]. The details of this program are presented by Antoine et al. [2006]. Each of these three segments is designed to provide specific measurements of various parameters at different and complementary spatial and temporal scales. When combined together, they provide a comprehensive time series of near-surface (0–200 m) ocean and atmosphere inherent and apparent optical properties. The combined activity is designed to provide a long-term vicarious radiometric calibration of satellite ocean color sensors and the validation of the ocean color geophysical products, including the normalized water-leaving radiances, the pigment concentrations and the aerosol optical thickness and types. In parallel to these operational objectives, a bio-optics research activity was also developed. Although BOUSSOLE was initially established to support the MERIS mission, it rapidly became a multimission program, supporting the international data collection effort for several ocean color satellites.

[7] The present paper specifically deals with the validation segment of BOUSSOLE. The objectives are to (1) introduce the strategy that has been developed, (2) describe the measurement site and its specific characteristics that make it well suited to the task of ocean color satellite validation, and (3) assess the uncertainty of some of the geophysical products provided by MERIS, SeaWiFS and MODIS-A. The latter comparisons are particularly important, because of the different approaches used to calibrate MERIS on one hand, and SeaWiFS and MODIS-A on the other hand. Some protocol issues are also addressed; in order not to detract reading from the main topic, they are described in several appendices.

2. General Characteristics of the Measurement Site

2.1. Geography of the Area and Main Physical Constraints

[8] The characteristics of the work area are presented along with the relevant details establishing the site as a satisfactory location for validating satellite ocean color observations. The deep-water mooring is deployed in the Ligurian Sea, one of the subbasins of the Western Mediterranean Sea (Figure 1). The monthly cruises are carried out at the same location. The water depth varies between 2350–2500 m, and it is 2440 m at the mooring site (7°54'E, 43°22'N). Clear sky is often observed in the Mediterranean Sea, with minimum (maximum) cloud coverage in the boreal summer (winter). On the basis of the *International Satellite Cloud Climatology Project* (ISCCP) data [Rossow and Schiffer, 1989], the annual average is as low as 50%, which ensures a high density of cloud-free satellite observations over the work area.

[9] The prevailing ocean currents are usually weak ($<20 \text{ cm s}^{-1}$), because the selected position is in the central area of the cyclonic circulation that characterizes the Ligurian Sea [Millot, 1999]. The northern branch of this

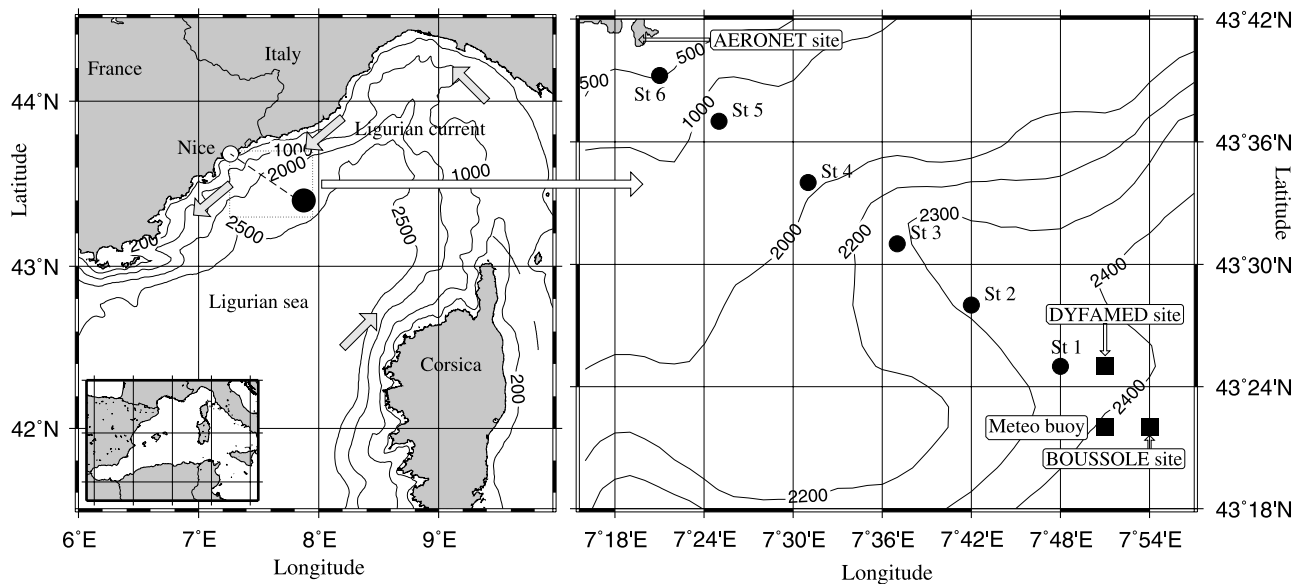


Figure 1. Area of the northwestern Mediterranean Sea showing (left map) the southern coast of France and the island of Corsica plus the generalized work area in the Ligurian Sea (black circle) for the BOUSSOLE activity, and a magnification (right map) showing the position of the BOUSSOLE mooring plus the “*Dynamique des Flux Atmosphériques en Méditerranée*” (DYFAMED [Marty, 2002]) site and the Meteorological buoy maintained by the French weather forecast Agency (METEO France). The positions of the six stations that are sampled once a month during transits from Nice to the BOUSSOLE site are also displayed (black circles).

circulation is the Ligurian Current, which manifests as a jet flowing close to the shore in a southwesterly direction which, in turn, establishes a front whose position varies seasonally, i.e., closer to shore in the winter than in the summer [Millot, 1999 and references therein]. The southern branch of the circulation is a northeasterly current flowing north of the island of Corsica; the eastern part of the circulation is essentially imposed by the geometry of the basin (see grey arrows in Figure 1).

[10] The dominant winds are from the west to southwest and from the northeast sectors, and are channeled into these two main directions by the general atmospheric circulation of the region and by the topography formed by the French Alps and the island of Corsica. A composite record of the physical conditions is displayed in Figure 2, using data collected near the BOUSSOLE site by a meteorological buoy deployed since 1999 by the French weather forecast Agency (Meteo-France). Wind speed maxima (Figure 2a) are observed in fall and winter, while the average summer values are around $3\text{--}5\text{ m s}^{-1}$. The resulting wave pattern is also shown in Figure 2a, as the average and maximum of the significant wave height.

[11] The surface wind stress, combined with an average surface heat budget that switches polarity around March (oceanic heat loss to heat gain) and September (oceanic heat gain to heat loss), leads to the seasonal cycles of the mixed-layer depth (MLD) and temperature as shown in Figure 2b. The minimum sea surface temperature (SST) is about 12.7°C (associated with a salinity of 38.4), which is a constant value reached in winter when the water mass is fully mixed, with MLD greater than 300 m. During some exceptionally windy and cold winters, this deep mixing

contributes to the formation of the dense waters of the western Mediterranean Sea [Gasparini *et al.*, 1999]. The summer stratification leads to SST values as high as 28°C in August, associated to MLD of about 10–20 m.

2.2. Biogeochemical and Bio-Optical Characteristics

[12] The marked seasonality of the physical forcing drives the seasonal changes of the nutrients and phytoplankton, as illustrated here by the surface nitrate and TChla concentrations (Figure 2c). Oligotrophic conditions prevail during the summer with undetectable nitrate levels and [TChla] lower than 0.1 mg m^{-3} (with minima around 0.05 mg m^{-3}). The higher concentrations are up to about 5 mg m^{-3} , during the early spring bloom (February to March or April) when surface waters are nitrate replete. Moderate [TChla], between $0.1\text{--}0.2\text{ mg m}^{-3}$, characterize most of the other periods of the year.

[13] This combination of a large range of trophic states and a 3-month period of stable oligotrophic waters in the summer provides a good set of conditions for collecting data for validation purposes. A more in-depth examination of this aspect will be provided later on, in section 4.2.

[14] An important consequence of the above characteristics, in particular water depth, circulation, and distance from shore, is that waters at the BOUSSOLE site are permanently of the Case-1 category, following the definition of Morel and Prieur [1977]. This assertion is quantitatively evaluated by plotting the irradiance reflectance at 560 nm determined from the buoy measurements as a function of the chlorophyll concentration ($R(560)$, Figure 3), and superimposing on top of the data a theoretical upper limit of this reflectance for Case 1 waters [Morel and Bélanger, 2006].

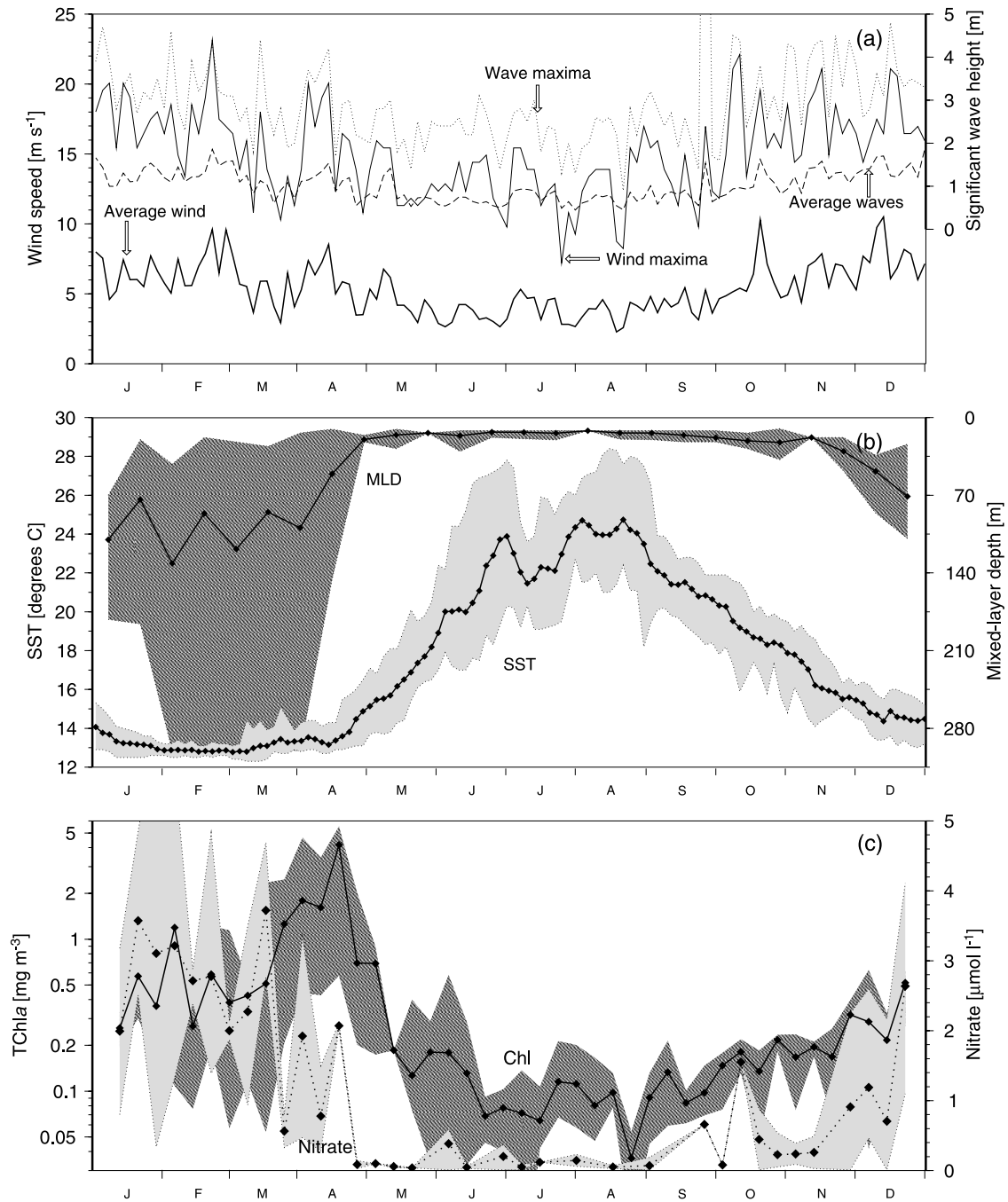


Figure 2. Composite time series at the BOUSSOLE site of (a) wind speed and significant wave height (built using 7 years (1999 to 2005) of data collected by the meteorological buoy; see Figure 1), (b) sea-surface temperature (SST; same data source than Figure 2a) and mixed-layer depth (MLD; built using 11 years (1994 to 2004) of data collected at DYFAMED; Marty *et al.* [2002]), and (c) surface (<10 m) nitrate and chlorophyll concentration (same data source than for the MLD, plus the BOUSSOLE data for TChla). For each parameter, one curve is showing the average value computed over a variable time step, which was chosen as a function of the time resolution of the initial data (e.g., 14 d for MLD and 3 d for the SST), and the minima and maxima encountered in the full time series are represented either with a shaded area or only by one curve for the maxima when the minima are by definition equal to zero (wind and waves, Figure 2a).

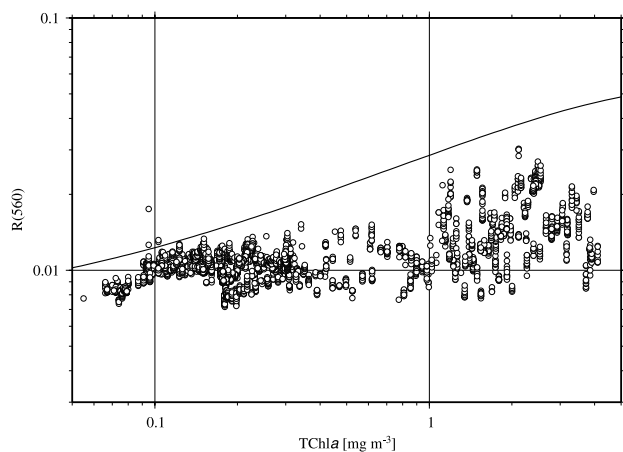


Figure 3. Irradiance reflectance at 560 nm, $R(560)$, as a function of $[TChla]$. The points are from 3 years of clear-sky quality-checked buoy measurements taken within one hour of solar noon. The curve is the upper limit for Case-1 waters [Morel and Bélanger, 2006].

With the exception of a few outliers, all the data points are below the curve, demonstrating that waters permanently belong to the Case-1 type at the BOUSSOLE site.

[15] Another important aspect to consider when comparing in situ measurements (horizontal sampling scale on the order of tens of meters) with satellite-derived quantities (sampling scale of about 1 km) is the spatial heterogeneity of the measurement site. Spatial surveys have, therefore, been conducted during several of the monthly cruises, by following a grid pattern of one square nautical mile centered on the buoy site, during which along-track fluorescence measurements were performed. Water sampling was carried out at the beginning, sometimes at midway, and at the end of this route for subsequent *High Precision Liquid Chromatography* (HPLC) analysis.

[16] The seasonal changes of this small-scale spatial variability of the chlorophyll concentration are illustrated in Figure 4. They show that the variability is, as expected, lower during the oligotrophic summer (around $\pm 10\%$). The horizontal gradients can reach large values during the spring bloom and during fall, with values from -70% to $+35\%$. The winter represents an intermediate situation (variability is within about 30%).

2.3. Other Activities Near the BOUSSOLE Site

[17] The BOUSSOLE site is located in an area that has been dedicated to scientific work since 1990. Another monthly cruise program takes place as part of the *Dynamique des Flux Atmosphériques en Méditerranée* (DYFAMED) program, which started in 1991 [Marty, 2002]. This service collects core data that are made publicly available to the scientific community, including CTD casts, phytoplankton pigments (HPLC), nutrients, oxygen, dissolved organic carbon (DOC), and primary production from short-time ^{14}C incubations. Other activities are carried out occasionally around this site [see, e.g., the Deep-Sea Research special issue 49(11), 2002, Studies at the DYFAMED French Joint

Global Ocean Flux Study (JGOFS) time series station, N.W. Mediterranean Sea].

3. Data and Methods

3.1. BOUSSOLE Buoy, and the Buoy Measurement Suite

[18] The BOUSSOLE buoy was specifically designed to perform radiometric measurements at sea. The objectives when developing this new platform were (1) to measure the upward and downward plane irradiances (E_u and E_d , respectively), and the upwelling radiance at nadir (L_u) at two depths in the water column, plus the above-surface downward irradiance (E_s), (2) to minimize the shading of the radiometers while maximizing their stability (i.e., keeping them as horizontally level as possible), and finally (3) to allow deployment at a deep-water site with swells up to 8m (but low currents). A full description of the theoretical work, practical design and construction, laboratory and in situ testing of the buoy, along with a description of the instrument suite and of some aspects of the data processing are presented by Antoine *et al.* [2008]. Only the main features of the design are recalled here (Figure 5). The basic principle is that of a reversed pendulum, with Archimedes thrust replacing gravity. A large sphere is stabilized at a depth out of the influence of most surface waves (17 m in this case), and connected at the end of a neutrally buoyant Kevlar™ cable anchored on the seafloor. This sphere is the main buoyancy of the system, above which a tubular structure is fixed, hosting the instrumentation on horizontal arms (at 4 and 9 m depths). The resulting approximately three tons of thrust ensures the stability of this so-called “transparent-to-swell” superstructure, which is subjected to very limited forces from waves and currents. The wave-interaction characteristics ensure the planar stability of the instruments, even for rather large swells.

[19] With this design, there is no large body at the surface, so the platform is a minimal source of shading and perturbations to the in-water light field. The center of the buoyancy sphere (diameter of approximately 1.8 m) is 8 m below the deepest radiometer (itself positioned at 9 m), so it only occupies about 0.05 sr within the upward hemisphere, i.e., less than 1%. The impact on the measurement of the upward irradiance is, therefore, negligible. The buoyancy sphere is essentially out of the field of view of the radiance sensors, so the measurement of the upwelling radiance is not affected either.

[20] One-minute acquisition sequences are performed every 15 min, with all instruments working simultaneously. The buoy radiometer suite is made of Satlantic 200-series radiometers measuring E_d , E_u , and L_u (nadir) at two depths (nominally 4 and 9 m) and at the following seven discrete wavelengths: 412 (alternatively 555), 443, 490, 510, 560, 670, and 681 nm. A Satlantic Multichannel Visible Detector System (MVDS) 200-series radiometer measures E_s at 4.5 m above the water surface and at the same seven wavelengths. Other instrumentation providing parameters entering into the processing of radiometry measurements are an Advanced Orientation Systems, Inc. (AOSI, Linden, New Jersey, USA) two-axis tilt and compass sensor at 9 m (EZ-Compass-dive), and a Sea-Bird Electronics (Bellevue, Washington) 37-SI CTD measuring conductivity, temperature, and

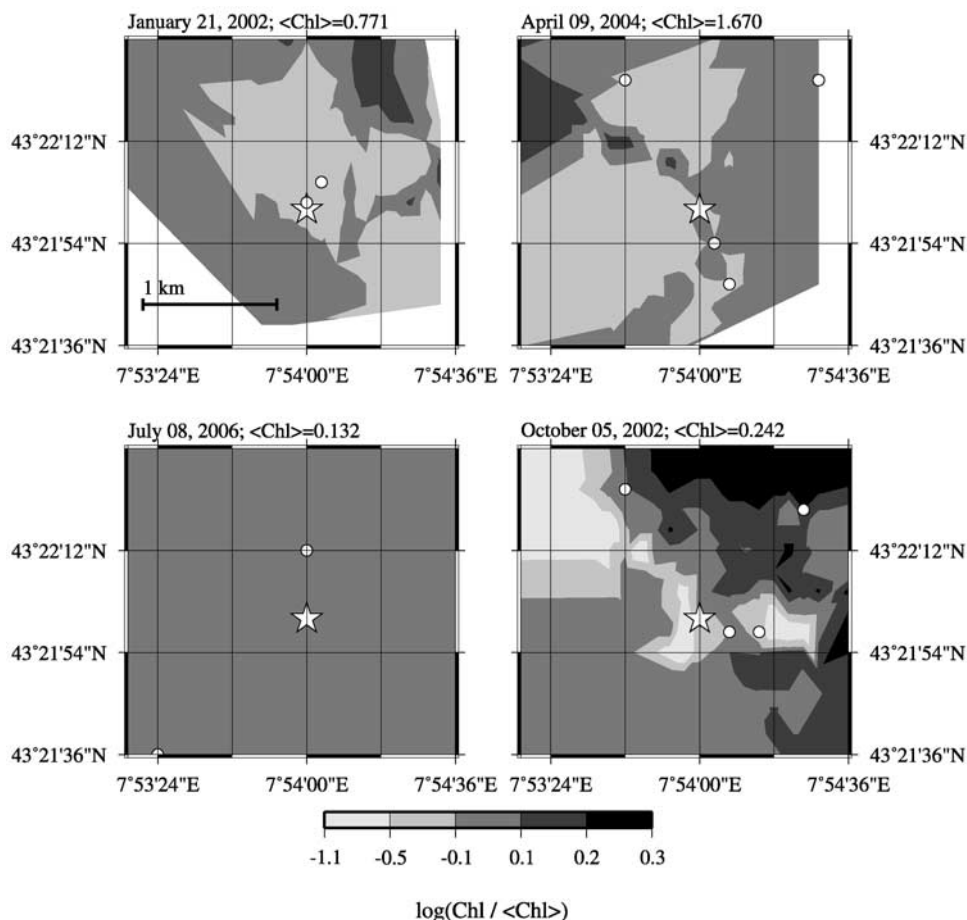


Figure 4. Contour plots of the variability of the surface chlorophyll concentration in the vicinity of the mooring point (white star) for the four dates indicated. The contoured quantity is the logarithm of the ratio of the concentration at any point divided by the average concentration over the displayed area (indicated on top of each panel). The chlorophyll concentration was derived from along-track measurements of the surface fluorescence, converted in units of concentration thanks to HPLC-determinations performed on surface samples taken along the route (open circles). The spatial scale is given in the top left panel.

pressure at 9m. Other instrumentation is described by *Antoine et al.* [2006]. It includes two Western Environment Laboratories (WETlabs) C-star transmissometers measuring the beam attenuation coefficient at 660 nm (25 cm path) at 4 and 9 m, two WETlabs ECOFLNTU chlorophyll fluorometers at 4 and 9 m, and a Hydro-Optics, Biology, and Instrumentation Laboratories Inc. (HOBILabs) Hydroscat-II backscattering meter at 9 m measuring a proxy to the backscattering coefficient at two wavelengths (442 and 560 nm).

3.2. Buoy Radiometric Data Processing

[21] The initial step of the data processing is a data reduction that derives one representative value of E_s , E_d , E_u or L_u for each of the 1-min acquisition periods, during which about 360 measurements are taken (the acquisition frequency of the radiometers is 6 Hz). The procedure consists in taking the median of the 360 measurements (details in *Antoine et al.*, 2008), and allows getting rid of the perturbations caused by the wind-roughened air-sea interface. Therefore it provides a value that would ostensibly be measured if the sea surface was flat. In addition, it is

verified that the coefficient of variation within the 360 E_s measurements is below 5%, which ensures that the above-surface irradiance was stable during the 1-min acquisition sequence.

[22] From the two values of $L_u(z, \lambda)$, the upwelling nadir radiance at null depth $z = 0^-$ (immediately below the sea surface) is then obtained as (omitting the wavelength dependence for brevity):

$$L_u(0^-) = L_u(z = 4)e^{K_L z} f_n(z, \theta_s, \text{Chl}), \quad (1)$$

where z is the measurement depth (not exactly 4m when the buoy is lowered or when swell goes through the superstructure), and K_L is the diffuse attenuation coefficient for the upwelling nadir radiance. The latter is computed from the measurements of L_u collected at the two depths:

$$K_L = -\frac{\log[L_u(z = 9)/L_u(z = 4)]}{\Delta z}, \quad (2)$$

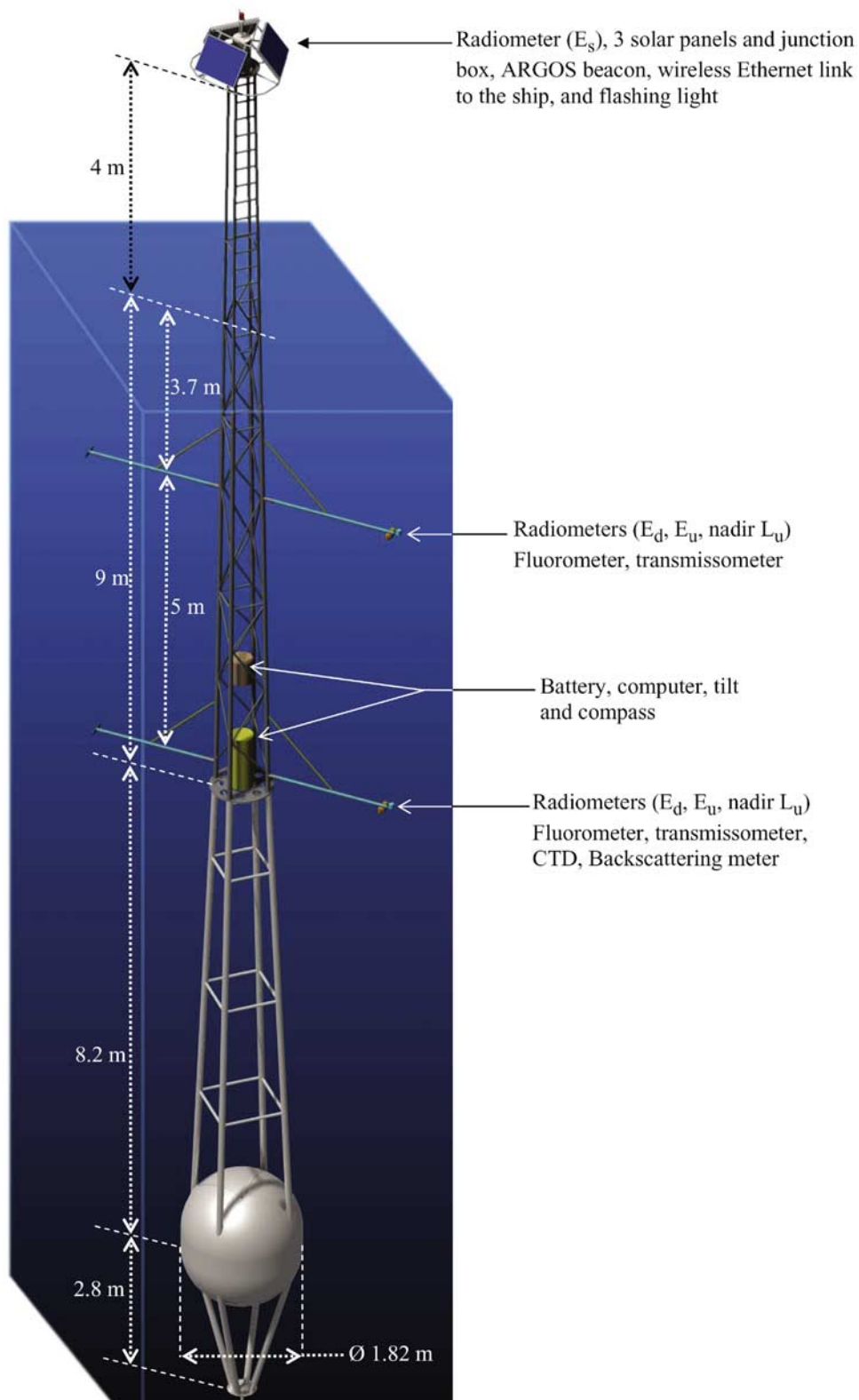


Figure 5. “Artist view” of the buoy with indication of the main dimensions and of the location of instruments. The buoy is actually entirely covered by a mat black antifouling paint.

where Δz is exactly 5 m. The rationale for, and the implementation of, the function appearing in the right hand side of equation (1) are provided in Appendix A. Equations (1) and (2) can be written for the upward irradiance, $E_u(z, \lambda)$, using the diffuse attenuation coefficient for the upward irradiance, K_u .

[23] The value of $L_u(0^-)$ is then corrected for instrument self shading as per *Gordon and Ding* [1992]. The parameters entering into this correction are the instrument radius, which is 4.5 cm (common to all Satlantic 200-series radiometers), the total absorption coefficient, which is computed following *Morel and Maritorena* [2001] using the chlorophyll concentration (see Appendix B), and the ratio between the direct-sun and diffuse-sky irradiances. This ratio is computed following *Gregg and Carder* [1990], using the atmospheric pressure and relative humidity measured in the vicinity (2 nm) of BOUSSOLE by a meteorological buoy, the ozone content provided by the US National Center for Environmental Prediction (NCEP) SeaWiFS near real-time ancillary data, and a horizontal visibility corresponding to a *Shettle and Fenn* [1979] maritime aerosol with an optical thickness of 0.2 at 550 nm.

[24] From the corrected value of $L_u(0^-)$, the water-leaving radiance at nadir, L_w , is obtained as

$$L_w = L_u(0^-) \frac{1 - \rho(\theta)}{n^2}, \quad (3)$$

where $\rho(\theta)$ is the Fresnel reflection coefficient for the water-air interface, and n is the refractive index of seawater. The fully normalized-water leaving radiance [*Morel and Gentili*, 1996] is then derived as

$$nL_w = \frac{L_w}{t_d(\theta_s) \cos(\theta_s)} \frac{\mathfrak{R}_0}{\mathfrak{R}(\theta')} \left\{ \frac{f_0(\text{Chl})}{Q_0(\text{Chl})} \left[\frac{f(\theta_s, \text{Chl})}{Q(\theta_s, \theta', \Delta\phi, \text{Chl})} \right]^{-1} \right\}, \quad (4)$$

where \mathfrak{R} is a factor including all refraction and reflection effects at the air-sea interface [*Morel and Gentili*, 1996]. The term within brackets expresses the functional dependence on the bidirectional nature of the light field. In this term, Q is the ratio of upward irradiance to upwelling radiance (the 0 subscript denotes a zenith sun or a nadir view), f is a factor that relates the irradiance reflectance R to the inherent optical properties, and other symbols describe the geometry of the problem (see list of symbols).

[25] The remote sensing reflectance is then obtained as

$$R_{rs} = \frac{L_w}{E_s}. \quad (5)$$

[26] Before forming the ratio in equation (5), E_s is corrected for the buoy tilt. The correction is a function of the orientation of the two axes of the tilt measurement with respect to the sun azimuth, and computes the ratio of the diffuse (unaffected by the tilt) to direct (affected simply through the cosine of the sun zenith angle) light for clear-sky conditions [*Gregg and Carder*, 1990] (see above for the parameters of the computation). The remote sensing reflectance is further multiplied by π in order to get a reflectance, which is consistent with the definition of the product

delivered by the MERIS mission:

$$\rho_w = \pi R_{rs}. \quad (6)$$

[27] A diffuse attenuation coefficient for the downward irradiance in the upper layers is also computed as

$$K_d = - \frac{\log[E_d(z)/E_d(0^-)]}{z}, \quad (7)$$

where z is the deepest of the two depths (nominally 9 m), and $E_d(0^-)$ is simply E_s reduced by transmission across the air-water interface, i.e., E_s times 0.97 [*Austin*, 1974].

[28] The final processing step for the buoy data consists in either eliminating or correcting data corrupted by bio-fouling. The growth of various types of marine organisms, such as algae and bacteria, is unavoidable with moored instruments, albeit it is much less severe in the clear offshore waters at BOUSSOLE than it can be, for instance, in turbid coastal environments. The cleaning of the instruments every two weeks (divers), in addition to the use of copper shutters, rings and tape (on the instrument bodies), contribute to maintaining biofouling at a low level. Possible bio-fouling is identified by comparison of the data collected before and after the cleaning operations, which allows either elimination or correction of the corrupted data. The way the correction is performed is not further discussed here because the corresponding data are not used in the match-up process.

3.3. Other Measurements

[29] A comprehensive set of measurements are carried out during the monthly cruises, including inherent and apparent optical properties, phytoplankton pigments, particle absorption and total suspended matter. The protocols, as well as sample results, are presented by *Antoine et al.* [2006]; they follow the ‘‘ocean optics protocols for satellite ocean color sensor validation’’ [*Mueller et al.*, 2003a, 2003b, 2003c; *Pegau et al.*, 2003]. In the present work, only two quantities are used, i.e., the reflectances (equation (6)) determined from the measurements of an in-water profiling radiometer (a Satlantic SeaWiFS Profiling Multichannel Radiometer; SPMR), and [TChl a]. The former are used to qualify the buoy-derived reflectances, and the latter is used for validation of the chlorophyll- a concentration derived through various algorithms by the three satellite missions. The TChl a referred to in this paper is the optically weighted surface concentration obtained from samples taken at 5 and 10 m. It includes the following pigments: chlorophyll a , divinyl chlorophyll a , chlorophyllid a , and chlorophyll a allomers and epimers. The concentration is determined using the HPLC technique.

3.4. Satellite Data and Match-Up Procedures

[30] The remote sensing data used in the analysis are a function of the satellite mission. They are all level-2 data, i.e., individual products providing the in-water geophysical quantities (radiances, chlorophyll concentration and the diffuse attenuation coefficient) corresponding to one given satellite pass.

[31] For MERIS, 1-km reduced resolution data processed by the MERIS processing prototype version 7.4.1 (MEGS7.4.1) are used. They provide ρ_w (equation (6)), and the chlorophyll

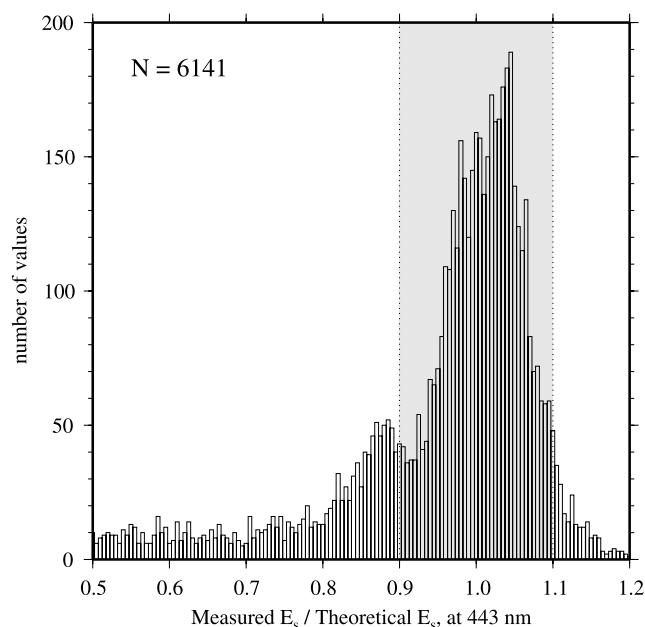


Figure 6. Histogram of the ratio of E_s measured at 443 nm to its theoretical clear-sky value computed from the *Gregg and Carder* [1990] model (see section 3.2 for the parameters introduced in this model). The value of this ratio must be between 0.9 and 1.1 (shaded area) for the corresponding data to be included in the validation process.

concentration derived through the *Morel and Antoine* [1999] algorithm. The diffuse attenuation coefficient at 490 nm, $K_d(490)$, is not part of the standard products for the MERIS mission. It has been directly derived here from the chlorophyll concentration using the algorithm recently proposed by *Morel et al.* [2007].

[32] For SeaWiFS, Merged Local Area Coverage (MLAC; until December 2004) or Global Area Coverage (GAC; 2005–2006) data from reprocessing #5 (completed 18 March 2005) are used. They provide the fully normalized water-leaving radiance (equation (4)). The chlorophyll concentration is derived through the OC4V4 algorithm [*O’Reilly et al.*, 1998, 2000] and $K_d(490)$ through the *Werdell* [2005] algorithm.

[33] For MODIS-A, GAC data from reprocessing #1 (completed in February 2005) are used. They provide the same product as the SeaWiFS mission, i.e., the fully normalized water-leaving radiance. The chlorophyll concentration is derived through the OC3MO algorithm [*O’Reilly et al.*, 2000], and $K_d(490)$ through the *Werdell* [2005] algorithm.

[34] Match-up analyses have been performed for ρ_w , [TChla], and the diffuse attenuation coefficients using the MERIS, SeaWiFS, and MODIS-A data products previously described (for SeaWiFS and MODIS-A, the nL_w ’s are transformed into ρ_w ’s as per equations (4)–(6)). The same procedure is used for the three sensors, wherein a 5×5 pixel box is extracted from the level-2 product, and the average quantity in this box is compared to the same quantity as derived from the quality-controlled data collected in situ from the buoy. The quality control criteria are as described by *Bailey and Werdell*

[2006]. Additional criteria specific to the use of the buoy data are the buoy tilt is less than 10° and the buoy depth is less than 11 m, with the “buoy depth” being the pressure recorded by a sensor mounted on a specific location on the buoy, and indicating 9m when the buoy is at equilibrium. Finally the E_s measured at 443 nm has to be within 10% of its theoretical clear-sky value (see section 3.2 for the calculation of the theoretical E_s), which is meant to select clear skies only. The 10% threshold was selected on the basis of the uncertainty in the atmospheric model and on the basis of the distribution of the measured-to-computed E_s ratio (Figure 6).

[35] The quality flags for the MERIS data are not the same than for SeaWiFS and MODIS-A. In order to be consistent, the glint flags (called “HIGH_GLINT” and “MEDIUM_GLINT”) and the cloud flags (“CLOUD” and “ICE HAZE”); the latter indicates the presence of haze or thick aerosols) were considered for MERIS. The normalization of the reflectances is performed following *Morel and Gentili* [1996], using the chlorophyll concentration computed as described in Appendix B.

[36] Last, a correction is applied to the satellite ρ_w to account for the difference between the wavelengths of the various sensors and those of the buoy’ radiometers. The difference is at most of 10 nm (551 nm for MODIS-A whereas the buoy has a 560 nm) and is only 2 nm for the band at 490 nm (488 nm for MODIS-A). There is no difference for the two bluest bands (412 and 443 nm). The correction is based on the *Morel and Maritorena* [2001] model, and uses the chlorophyll concentration computed as described in Appendix B.

[37] The combination of in situ and satellite data availability, orbit characteristics, and the quality criteria yield 64 reflectance match-ups for MERIS (data from September 2003 to October 2006), 168 for SeaWiFS (data from September 2003 to October 2006) and 152 for MODIS-A (data from September 2003 to December 2006). The numbers for the same three sensors are 80, 206 and 159 for K_d match-ups. The chlorophyll concentration is determined only during the monthly cruises, so the numbers of match-ups are smaller, i.e., 15, 44, and 31 for MERIS, SeaWiFS and MODIS-A, respectively.

[38] All subsequent analyses are performed in terms of ρ_w (equation (6)). Before commenting on the results in the following sections, it is worth noting that the MERIS observations have still not been vicariously calibrated, contrary to the SeaWiFS and MODIS-A observations.

3.5. Statistical Indicators

[39] The analysis of the match-up results uses several statistical indicators. Their definitions are given below, wherein x_i is the i^{th} satellite-derived value, y_i is the i^{th} buoy-derived value, and N is the number of points:

$$\bar{r} = \frac{1}{N} \sum_{i=1}^{i=N} \left(\frac{x_i}{y_i} \right) \quad (8)$$

is the average ratio of satellite-to-in situ data,

$$\text{RPD} = 100 \frac{1}{N} \sum_{i=1}^{i=N} \left(\frac{x_i - y_i}{y_i} \right) \quad (9)$$

is the average relative (signed) percent difference (%), used to assess biases,

$$|\text{RPD}| = 100 \frac{1}{N} \sum_{i=1}^{i=N} \left(\frac{|x_i - y_i|}{y_i} \right) \quad (10)$$

is the average absolute (unsigned) percent difference (%), used to assess uncertainties,

$$\text{UPD} = 100 \frac{1}{N} \sum_{i=1}^{i=N} \left(\frac{x_i - y_i}{(x_i + y_i)/2} \right) \quad (11)$$

is the unbiased percent difference, which is another measure of uncertainty, and

$$\text{RMSE} = \sqrt{\frac{1}{N} \sum_{i=1}^{i=N} (x_i - y_i)^2} \quad (12)$$

is the root mean square error (or root means square of differences).

[40] A least squares fit is also adjusted within the match-up points, with the associated coefficient of determination, r^2 , slope m , and intercept y .

[41] Chlorophyll concentration ranges over three to four orders of magnitude and is approximately lognormally distributed in the ocean [Campbell, 1995]. Thus in the above statistics, the chlorophyll concentration is log-transformed.

4. Results

4.1. Uncertainty in the Buoy-Derived Reflectances

[42] Radiometric sea-truth data used for match-up analyses with ocean color satellite measurements or for the development of bio-optical algorithms are essentially collected using in-water profiling radiometers [e.g., *Werdell and Bailey*, 2005]. Alternative techniques include in-water measurements at discrete depths [Morel and Maritorea, 2001], above-water measurements [e.g., *Hooker et al.*, 2004; *Hooker and Zibordi*, 2005] or fixed-depth mooring-based measurements [Clark et al., 1997, 2003]. The various measurement protocols attached to each of these techniques introduce specific uncertainties that have to be assessed in order to qualify the measurements in question as being usable for validation purposes. This section addresses this problem specifically for the radiometric data collected from the BOUSSOLE buoy.

[43] The first uncertainty in the measurement of the nadir upwelling radiance, L_u , comes from the absolute calibration of the radiometers. It is assumed to be around 3% [e.g., *Hooker et al.*, 2002].

[44] The next uncertainty comes from the determination of the diffuse attenuation coefficient for the radiance along the nadir direction, K_L , from the measurements performed at two depths on the buoy (equation (2)), $K_L^{4,9}$. Three sources of uncertainty arise in this computation: (1) the intercalibration of the instruments at the two depths, which is assumed to be properly established, (2) the correct estimation of the depth of the measurements (the distance between the two measurement depth is exactly known), and (3) the relevance of $K_L^{4,9}$ to perform the extrapolation of L_u

from 4 m to just below the sea surface. This last point is examined in Appendix A.

[45] For clear waters (i.e., K_L about 0.02 m^{-1} in the blue part of the e.m. spectrum), a large uncertainty of 1m in the measurement depth would lead to an error equal to e^{K_L} , i.e., a 2% uncertainty on the estimation of $L_u(0^-)$. Conversely, if it is assumed that Z is correctly estimated, an uncertainty of 10% for K_L would lead to an uncertainty equal to $e^{-0.1 K_L Z}$, i.e., an uncertainty less than 1% for $L_u(0^-)$ if Z is taken equal to 4m (or <2% if Z is 10 m). These numbers become about 2.5% and 5%, respectively, for $K_L = 0.05$, i.e., for mesotrophic waters (also encountered at the BOUSSOLE site when [TChla] is about 0.3 mg m^{-3}). In summary, assuming an average error of 3% on the estimation of $L_u(0^-)$, because of uncertainties in the extrapolation to the 0^- level, seems realistic.

[46] Before being compared to a satellite measurement, the in-water value of the upwelling nadir radiance has to be transformed into the upwelling radiance for the direction of the satellite view after refraction at the air-sea interface. The transformation is simply performed by ratioing the Q-factor at nadir to the Q-factor for the relevant direction. The uncertainty here is only in the relative values of Q for these two directions. In the blue, where the geometry of the light field does not depend much on the particle phase function, the Q factors are predicted within a few percent from the chlorophyll concentration [Voss et al., 2007]. The ratio of these Q factors at two bands is, therefore, expected to be correct to within a very few percent; thus a 2% uncertainty can be assumed here.

[47] The self-shading correction for $L_u(0^-)$, performed following *Gordon and Ding* [1992] is assumed to introduce a 3% uncertainty [“typically lower than 5%”; *Zibordi and Ferrari*, 1995].

[48] The last step to get the water-leaving radiance is to determine L_w from $L_u(0^-)$ (equation (3)). This step does not introduce any uncertainty as long as $\theta < 20^\circ$ and the sea surface is approximately flat (wind speed less than 15 knots).

[49] In summary, a quadratic error budget including the uncertainties due to radiometric calibration of field radiometers (3%), calibration decay over time (2%), toward-surface extrapolation (3%), self-shading (3%), and bidirectional effects (2%), would indicate an overall 6% uncertainty on the determination of ρ_w from the BOUSSOLE buoy measurements. The various uncertainties provided here are summarized in Table 1.

[50] This tentative uncertainty budget is supported by a comparison between the buoy-derived reflectances and the reflectances derived from the in-water profiling radiometer deployed during each of the monthly servicing cruises (SPMR, section 3.3). Each SPMR measurement was compared to the buoy measurement the closest in time. Because the buoy collects data every 15 min, the time difference was always less than 8 min. Other selection criteria were the buoy tilt was less than 10° , the buoy depth was less than 11 m, and the change in the ratio of the observed $E_s(490)$ to the theoretical clear-sky $E_s(490)$ was less than 0.1 between the buoy and profiler measurements. A total of 43 comparison points were obtained (Figure 7). The slope of the linear regression is 0.98, the coefficient of determination is 0.97, and there is a bias of about $9 \cdot 10^{-4}$ in terms of reflectance. It is worth noting that the correction described in Appendix A

Table 1. Summary of the Uncertainty Assessment for the Various Data Acquisition and Processing Steps^a

Data Acquisition or Processing Step	Percent Uncertainty	Reference/Comment
Absolute radiometric calibration of radiometers	3	<i>Hooker et al.</i> [2002]
Decay over time	2	Linear interpolation between absolute calibrations (performed roughly every 6 months).
Computation of K_L	3	see text (section 4.1)
Bidirectionality corrections	2	<i>Morel et al.</i> [2002]
Air-sea interface	0	<i>Austin</i> [1974]
Illumination changes during the measurement sequences	0	The coefficient of variation within the 360 measurements must be <5% (see text).
IOP changes during the measurement sequences	0	The coefficient of variation of $c_p(660)$ is less than 3% in 95% of the cases (see text).
Spectral corrections	N/A	<i>Morel and Maritorena</i> [2001] reflectance model
Bio-fouling	N/A	Instrument cleaning every 2 weeks. Use of copper shutters, rings and tape. Data suspected of bio-fouling are not included in the validation process.
Self-shading	3	<i>Gordon and Ding</i> [1992]; <i>Zibordi and Ferrari</i> [1995]
Buoy shading	N/A	Minimized by virtue of the buoy design [<i>Antoine et al.</i> , 2008].
Quadratic error	6	

^aN/A's indicate that no uncertainty estimate was possibly derived.

improves this comparison, in particular (and as expected) for the red bands. The average unbiased percent differences (UPD) are from -4.5% to $+7.5\%$ from 412 nm to 510 nm, 20% at 560 nm and 3.5% at 670 nm. The average UPD for all bands is 8%. These numbers are coherent with the above tentative uncertainty budget, assuming that the uncertainty in the profiler data is similar to those of the buoy data.

4.2. Representativeness of the Measurement Site

[51] An ideal site for the validation of satellite-derived parameters would provide ground truth data within a range and statistical distribution closely matching those of the satellite data. This ideal situation is never fully met, because the satellite data by definition encompass the full natural variability, while a measurement site is, by definition, a unique point. Consequently, in order to specifically determine the representativeness of the BOUSSOLE site within the objectives of validating ocean color products, the distributions of several parameters, either derived from satellite observations (SeaWiFS in this particular case) or derived from in situ measurements, have been compared. The objective is not a point-by-point comparison (see later) but an overall assessment of the data distributions.

[52] The results are displayed for normalized reflectances (Figures 8a–8d), chlorophyll concentration (Figure 8e), and aerosol optical thickness (AOT; Figure 8f). The latter is included in the analysis, because it has an impact on the quality of the atmospheric correction, although a detailed validation of AOT is not included here. In these figures, the distribution of in situ data has been derived from the 3-year time series of buoy measurements for the nLw's, from a 15-year (1991–2005) time series of near-surface (<20 m) HPLC determinations for the chlorophyll concentration (BOUSSOLE data plus DYFAMED data; *Marty et al.* [2002]), and from a 3-year time series of AERONET measurements at the coastal site (see Figure 1) for the aerosol optical thickness. The NOMAD data set [*Werdell and Bailey*, 2005], which is widely used for bio-optical algorithm development and testing, was also used as an additional source of in situ data. The distributions of SeaWiFS data have been derived from four climatological

months (level-3 binned data for February, June, September, and December) either globally or for the Mediterranean Sea only (see legend of Figure 8).

[53] The histograms in Figure 8a show that the normalized reflectances measured at the BOUSSOLE site in the blue part of the spectrum ($\lambda < 500$ nm) cover the lower half of the global distribution and about two thirds of the values possibly encountered in the Mediterranean Sea. The full range is sampled in the green part of the spectrum ($\lambda > 500$ nm). This is in agreement with the recurrent observation that the Mediterranean Sea is less blue than global bio-optical models would predict considering the measured (low) concentration of chlorophyll [*Claustre et al.*, 2002; *Bricaud et al.*, 2002]. The double-peak histogram for nLw at 412 nm is simply due to the undersampling at this wavelength, because only one of the two sets of radiometers is equipped with such a band. The continuation of the time series will progressively fill in the data distribution, ultimately producing a single-peak histogram, with a mode value around 1. The fact here is that the BOUSSOLE site, although it cannot be described as a globally representative site for all oceanic waters, nevertheless provides a sampling over a very significant part of the global natural variability of the normalized reflectance.

[54] The situation is even better for the chlorophyll concentration, with all histograms in Figure 8e being superimposed one on top of the other, which indicates that most of the range of concentration possibly encountered in the open ocean is sampled. The exception is for $[TChla] > 5$ mg m^{-3} , which represent a very small fraction of the global ocean [see, e.g., *Antoine et al.*, 1996].

[55] In terms of atmospheric properties (Figure 8f), the in situ sampling at the Cape Ferrat AERONET site is skewed toward low values of the aerosol optical thickness, whereas the satellite data are closer to being normally distributed, with a mode around 0.12 (and extremely similar histograms for the global ocean or only the Mediterranean). It is unclear whether the difference is really due to sampling over different domains or to the satellite values being improperly retrieved from the TOA observations. It has been recurrently observed that the AOT values derived from SeaWiFS are overestimated when compared to in situ data [see, e.g., *Jamet*

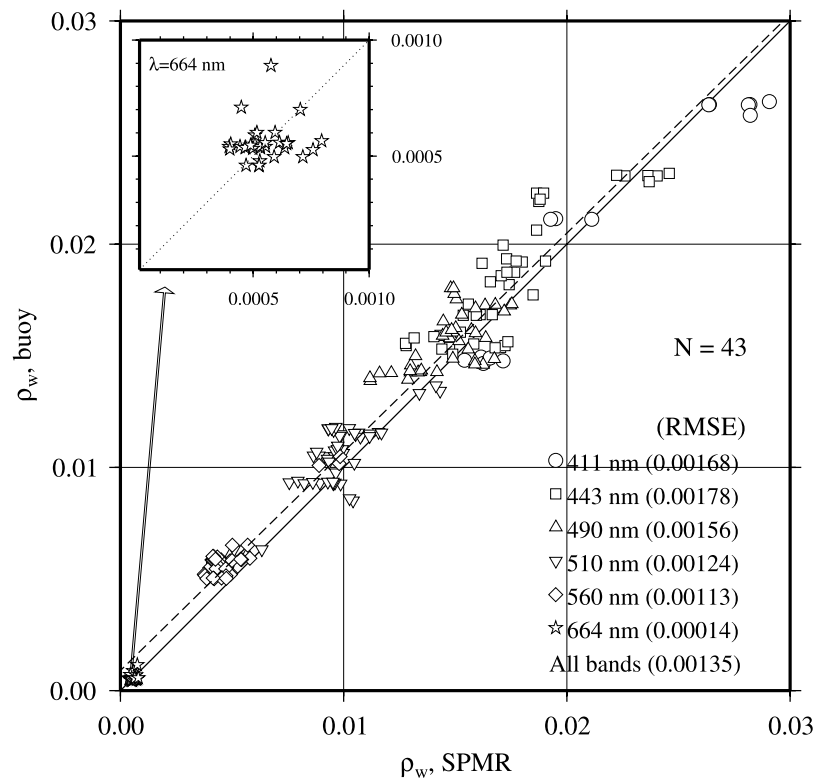


Figure 7. Buoy- versus SPMR-derived normalized reflectances, for the wavelengths indicated (see section 3.5 for the definition of the RMSE). A zoom on the results for $\lambda = 664$ nm is provided in insert. The conditions for the comparison are provided in the text, along with the parameters of the least squares fit to all points (dashed line).

et al., 2004]. In this case, analyzing the results in Figure 8f goes beyond the scope of the discussion about the representativeness of the measurement site, and enters into the level-2 product validation problem.

4.3. Results of the Match-Up Analysis

[56] A 3-year time series of reflectances at several wavelengths is plotted in Figure 9, including the values derived from quality-checked buoy measurements taken between 1000 and 1400 (GMT), and the values derived from MERIS, SeaWiFS, and MODIS-A (red, blue, and green symbols, respectively). The match-up quality criteria (section 3.4) are applied for the selection of the satellite data, which are also plotted when no field measurements are available, in order to show the full seasonal cycle as observed by the three satellite sensors.

[57] The dispersion of the satellite values increases for decreasing wavelengths, and is particularly large at 412 nm (Figure 9a). Although this is consistent with the known behavior of the atmospheric correction uncertainties, which increase from the red to the blue wavelengths [e.g., Gordon, 1997], this large dispersion at 412 nm looks incompatible with a meaningful interpretation of the data from this band. The seasonal cycle is hardly discernible.

[58] The seasonal changes are well captured by the three sensors. The maxima of $\rho_w(443)$ are usually observed in July (around 0.025; Figure 9b), except in 2006 when a second relative maximum occurs in March, corresponding to an intense mixing event. During this exceptionally deep

mixing, particles and dissolved substances present in the upper layers were distributed within the entire water column, leading to clear waters with $[TChl a]$ about $0.05 \text{ mg(Chl) m}^{-3}$. The minima of $\rho_w(443)$ are observed at the maximum of the spring phytoplankton bloom (values around 0.005), usually in April. Other relative minima occur at the end of summer, in particular in August of 2006. There is no correlative increase in chlorophyll at this time of the year, which means that another optically significant component intervenes.

[59] The best superposition of the buoy and satellite products is observed at 490 nm (Figure 9c) and to a lesser extent at 560 nm (Figures 9d).

[60] Whatever the wavelength, a significant number of red dots appear above the ensemble of data formed by the three sensors' data, meaning that the MERIS products are generally larger than those from SeaWiFS and MODIS-A.

[61] Atmospheric correction errors are usually of the same sign for the green and blue bands when aerosols are not absorbing, so they tend to cancel out when forming "blue-to-green ratios". Therefore reflectance ratios for all three sensors are much closer one of the other than the reflectances are (Figure 9e), which is important for obtaining coherent values of the chlorophyll concentration from the different sensors.

[62] It is noticeable that besides the overall coherence between the blue-to-green ratio and the chlorophyll concentration (dotted line in Figure 9e), i.e., a decreasing ratio for an increasing chlorophyll concentration and vice versa,

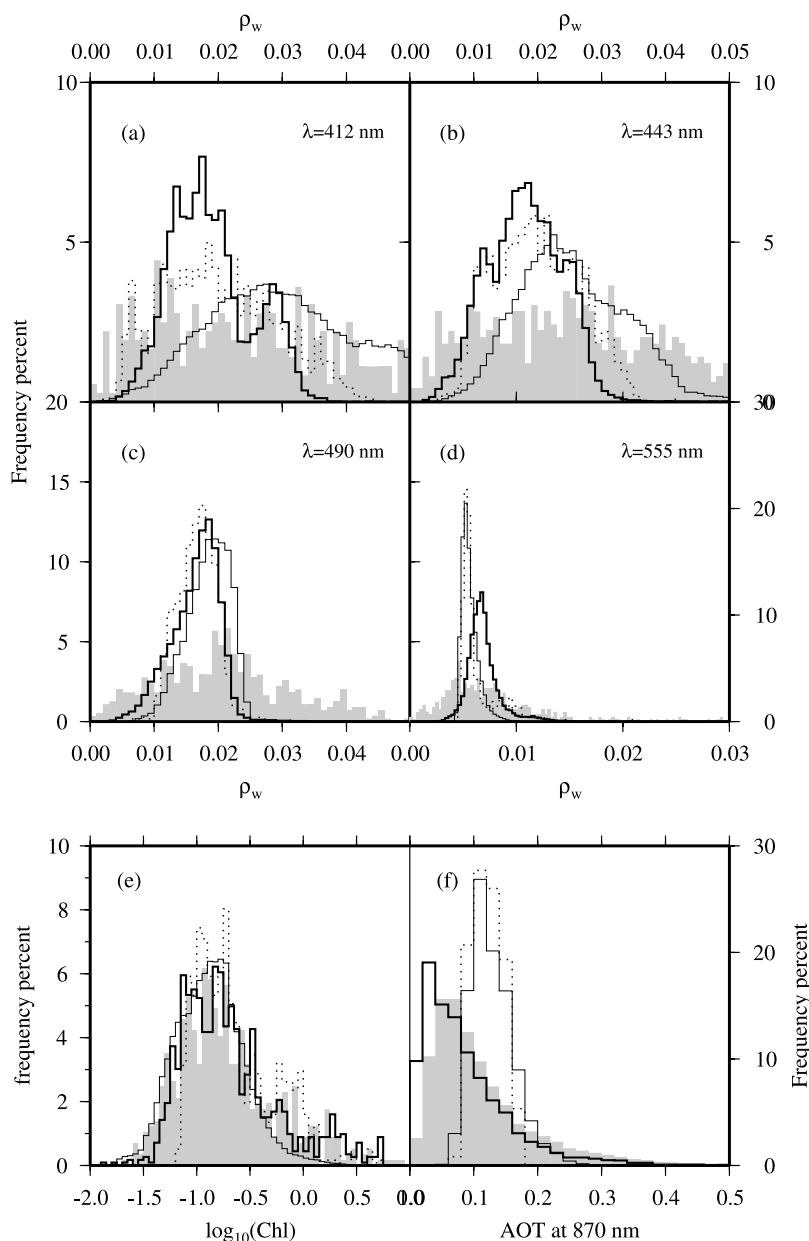


Figure 8. Histograms of normalized reflectances at the (a–d) four wavelengths indicated, (e) chlorophyll concentration, and (f) aerosol optical thickness at 870 nm. In each panel, the thick line corresponds to in situ data collected at the BOUSSOLE site (at the coastal AERONET station for AOT), the thin dotted line corresponds to SeaWiFS climatological monthly averages over the Mediterranean Sea for the two solstices and the two equinoxes (see text), the continuous thin line corresponds to the same SeaWiFS data for the World ocean (only depths > 500 m and latitudes within the 50°N–50°S band), and finally the shaded area to a subset of the NOMAD database [Werdell and Bailey, 2005], for depths >500 m and latitudes within the 50°N–50°S band.

several departures from this relationship are observed. The most striking is the sharp decrease of this ratio from a value of 4 to a value of 2 between mid July and the end of August 2006, when the chlorophyll concentration is nearly constant. Although it is beyond the scope of this study to analyze this type of event, they are all coherent with the known “summer anomaly” of the optical properties in the Mediterranean [Bricaud et al., 2002; Claustre et al., 2002; D’Ortenzio et al., 2002].

[63] To further quantify the uncertainty of the reflectances obtained from the three satellites, scatterplots of the satellite-derived versus in situ ρ_w (all wavelengths pooled together) and blue-to-green ratios are shown in Figure 10 (a, d and g for MERIS, b, e and h for SeaWiFS and c, f and i for MODIS-A). The match-up criteria are the same than for Figure 9.

[64] The data clouds in Figure 10 confirm the observations based on the time series plot (Figure 9), i.e., the overall

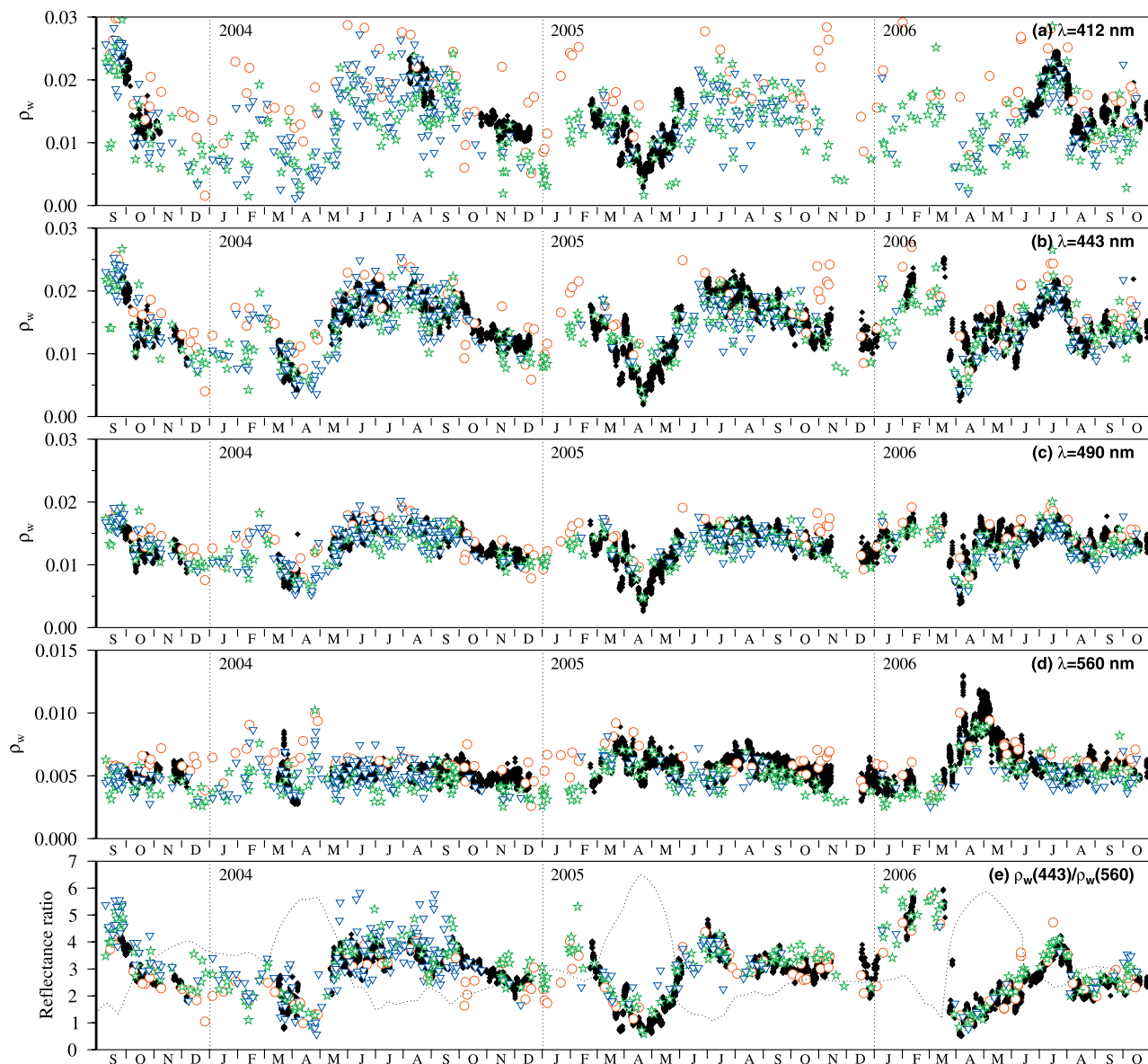


Figure 9. Three-year time series of the buoy reflectances (black symbols) at several wavelengths, as indicated (a to d), onto which the satellite-derived reflectances are superimposed. The red circles are for MERIS, the blue triangles for SeaWiFS and the green stars for MODIS-A. Figure 9e shows the reflectance ratio $\rho_w(443)/\rho_w(560)$, onto which the chlorophyll concentration is superimposed (dotted line).

variation of ρ_w is captured by the three sensors, and the dispersion increases toward higher reflectance values (toward the blue). This second observation is actually not totally verified for SeaWiFS (Figures 10b and 10e), with a maximal dispersion for values around 0.015, which is about the central value found in the in situ data for the three blue bands (412, 443, and 490 nm), and a lesser dispersion for values larger than about 0.023, which correspond to the largest reflectances at 412 nm. On the basis of the slope of the linear fit between the satellite and in situ values, the reflectance ratios (Figures 10g, 10h, and 10i) are best retrieved by the MODIS-A products, then by the SeaWiFS products, and finally by the MERIS products.

[65] In spite of the application of rather stringent match-up criteria, a number of outliers appear for all three sensors' products. Examining the corresponding images (which is anyway done for all match-ups) revealed "obvious" sub-optimal conditions for a match-up analysis (e.g., large clouds in the vicinity of the match-up point). These cases have been kept in the analysis, however, because no objective way to remove them presently exists. Therefore larger-scale match-up criteria, not restricted to the few pixels around the match-up location, might be introduced to objectively discard such situations. Such a wider screening of the satellite image would prevent from artificially degrading the match-up statistics.

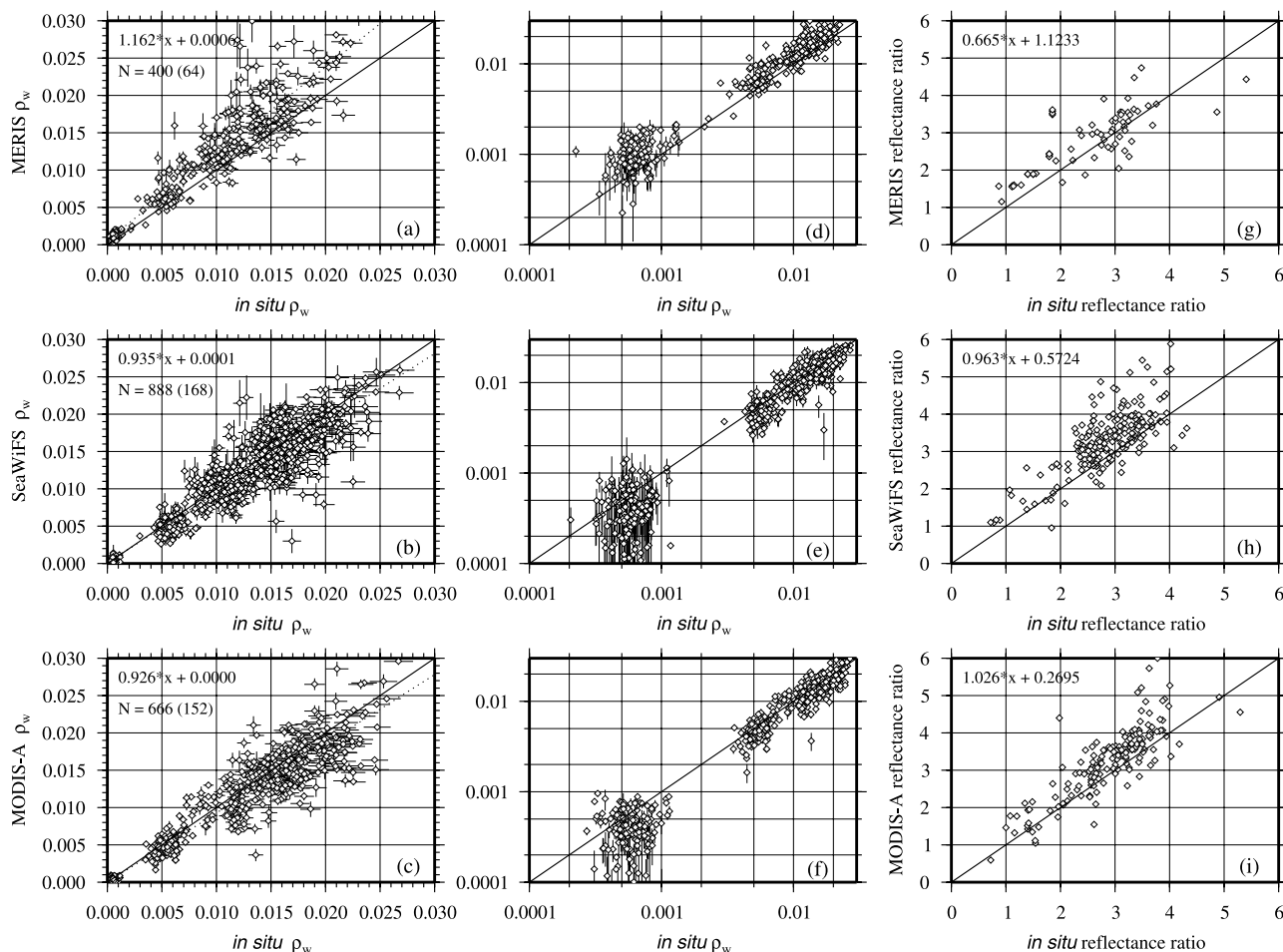


Figure 10. Scatter plots of satellite versus in situ reflectances (all bands pooled together), for (a) MERIS (wavelengths are 412, 443, 490, 510, 560, 670, and 683 nm); (b) SeaWiFS (412, 443, 490, 510, 555, and 670 nm); and (c) MODIS-A (412, 443, 488, 551, and 670 nm). The solid line is the 1:1 line. The number between parentheses is the number of match-up points (i.e., the number of spectra). For each match-up point, a thin vertical bar indicates the standard deviation with the 5×5 pixel box used for this match-up, and a thin horizontal bar represents a 5% uncertainty on the in situ values. Logarithmic scales for Figures 10a–10c are shown in Figures 10d–10f, respectively, in order to magnify the low values in the red domain (horizontal uncertainty bars don't appear because they are lower than the symbols). Panels g–i show the results for the “blue-to-green” reflectance ratios (i.e., reflectance at 443 nm divided by reflectance at 555 nm).

[66] The statistics (see section 3.5) associated to the data shown in Figure 10 are provided in Tables 2–4, for MERIS, SeaWiFS, and MODIS-A, respectively. The overall uncertainty in the comparison between the satellite-derived and the in situ reflectances is similar for the three sensors, when expressed in terms of RMSE, with values to within $1\text{--}2 \cdot 10^{-3}$ for all three sensors, except at 412 nm where they are about twice as large for MERIS than for SeaWiFS and MODIS-A. The minimum |RPD| is always found at 490 nm, and the maximum in the red bands (>600 nm). The |RPD| at 412 nm for MERIS is however close to that in the red bands. The SeaWiFS and MODIS-A products exhibit the lowest RPD for the three blue bands (412, 443, and 490 nm). The SeaWiFS and MODIS-A products meet the requirements at 443 and 490 nm, with RPDs $< 5\%$. The MERIS products are overestimated in all bands.

[67] The RPDs are in agreement with those of Zibordi *et al.* [2006], who performed a similar analysis at a coastal site

in the Adriatic Sea (their Table 1). The |RPDs| are also similar to those obtained with a global data set by Bailey and Werdell [2006] (their Table 2), except that our values are somewhat larger at 412 nm. It is worth noting that the statistics are not better when the analysis is restricted to $\text{Chl} < 0.2 \text{ mg m}^{-3}$, which would conform to the “5% accuracy in the blue for an oligotrophic ocean” requirement. The above comments can be summarized as follows.

[68] 1. The products for all three sensors have poor statistics for the bluest band (412 nm).

[69] 2. The 5% accuracy requirement in the blue is met by the SeaWiFS and MODIS-A products at 443 and 490 nm (RPD values less than 3%).

[70] 3. The MERIS data products are generally overestimated (the |RPD| and RPD values are nearly identical) and never meet the 5% requirement; their RMSE values are, however, similar to those of SeaWiFS and MODIS-A (to within $2 \cdot 10^{-3}$), except at 412 nm.

Table 2. Match-up Statistics for MERIS Products (see Section 3.5 for Definitions)^a

	λ	N	\bar{r}	RPD	RPD	r^2	m	y	RMSE
ρ_w	412	20	1.60	60.2	62.7	0.43	0.93	0.00880	0.00940
	443	61	1.32	31.6	35.8	0.38	0.70	0.00820	0.00539
	490	64	1.16	15.8	18.6	0.44	0.69	0.00610	0.00285
	510	64	1.22	21.5	23.5	0.24	0.52	0.00660	0.00260
	560	63	1.21	21.3	25.3	0.34	0.64	0.00300	0.00155
	665	64	1.59	59.0	69.1	0.16	0.89	0.00040	0.00052
	681	64	1.68	68.1	70.3	0.45	0.64	0.00070	0.00057
all	400	1.37	37.5	41.6	0.88	1.16	0.00060	0.00342	
TChla	31	1.17	17.0	46.0	0.78	0.56	-0.60804	0.60432	
	15	1.09	9.3	41.7	0.87	0.58	-0.48613	0.61219	
K_d	207	1.01	0.7	28.1	0.51	0.42	0.02636	0.02112	
	80	0.94	-5.6	23.4	0.61	0.45	0.02480	0.01830	

^aFor TChla and K_d , the first line reports statistics for all possible correspondences between field data and satellite observations, and the second line reports statistics for the subset of points that successfully passed the match-up criteria.

[71] 4. The MODIS-A products exhibit the smallest dispersion (RMSE values) and the best correlations (r^2) in all bands.

[72] A 3-year time series of the $K_d(490)$ is displayed in Figure 11, including the values derived from quality-checked buoy measurements taken between 1000 and 1400 (GMT), and the values derived from the three sensors (satellite data are plotted whatever in situ data are present or not, as in Figure 9). The seasonal changes of $K_d(490)$ are well captured by the three sensors (Figure 11), with about a 10-fold change, from values up to about 0.2 m^{-1} during spring phytoplankton blooms, and down to about 0.02 m^{-1} during the summer oligotrophic season (K_w being 0.0166 m^{-1} at 490 nm). The same range would be predicted by the *Morel and Maritorena* [2001] bio-optical model for chlorophyll concentration from 0.03 to 3 mg m^{-3} . The minima correspond to the reflectance maxima already shown for July (Figure 9). Both the field and the satellite data exhibit a large variability during the oligotrophic periods, with a coefficient of variation between 0.3 and 0.4.

[73] A significant number of $K_d(490)$ comparison points are obtained after the match-up criteria are applied (Figure 12). The uncertainty is large for the three sensors products, although it is somewhat better for the MERIS products (|RPD| about 20% instead of about 35% for SeaWiFS and MODIS-A). Most of the statistical indicators are actually better for MERIS than for SeaWiFS and MODIS-A, which would advocate for determining

$K_d(490)$ indirectly from [TChla] rather than directly from the reflectances.

[74] The 3-year time series of [TChla] is displayed in Figure 13, including field determinations and the values derived from the three sensors (satellite data are plotted whatever field data are present or not, as in Figure 9). The seasonal changes of the chlorophyll concentration are well reproduced by the three sensors, with more homogeneous results among them than for the reflectances. This is consistent with the results shown in Figure 9g for the blue-to-green reflectance ratio. The well-known overestimation of the low [TChla] in summer clearly appears in 2004 and 2005, less clearly in 2006. On the contrary, the low concentration in March 2006 is well reproduced, indicating that optically significant quantities other than phytoplankton chlorophyll are different between these two oligotrophic periods.

[75] The scatterplots built from the data shown in Figure 13 are displayed in Figure 14. They confirm the general tendency to overestimate the concentration in the low range, i.e., for [TChla] $< 0.2 \text{ mg m}^{-3}$, which is consistent with the well-known “summer anomaly” of optical properties in the Mediterranean (already mentioned when describing the reflectance match-ups). When the full concentration range is considered, the best results are obtained with the MERIS products (see Tables 2–4), which is unexpected considering the large uncertainties that the present match-up exercise has revealed on the reflectance product for this sensor. Again, the consistency of the reflectance ratio (Figure 9g) explains why the statistics of the chlorophyll match-ups are not so different between the three sensors. The average |RPD|’s are about 40–50% for MERIS and MODIS-A, and about 80% for SeaWiFS, which are all above the 35% uncertainty that is usually assumed for the satellite-derived chlorophyll concentration.

5. Conclusion

[76] Several facts emerge from the present match-up analysis of MERIS, SeaWiFS, and MODIS-A ocean color products at the BOUSSOLE site. The requirements in terms of accuracy of the atmospheric correction are only met at 443 and 490 nm by the SeaWiFS and MODIS-A products. The MERIS products do not presently meet the requirements. The reflectances provided by the three sensors at 412 nm are severely affected by atmospheric correction errors. The uncertainty is significantly reduced for the “blue-to-green” reflectance ratio. These results and the match-up statistics (Tables 2–4) are in agreement with the results

Table 3. As in Table 2, but for SeaWiFS Products

	λ	N	\bar{r}	RPD	RPD	r^2	m	y	RMSE
ρ_w	412	63	0.92	-7.6	20.6	0.44	0.74	0.00300	0.00455
	443	166	1.00	-0.3	14.8	0.42	0.68	0.00510	0.00303
	490	168	0.97	-3.2	11.7	0.32	0.57	0.00570	0.00218
	510	168	0.95	-4.8	13.0	0.09	0.32	0.00670	0.00180
	555	107	0.90	-9.9	16.9	0.09	0.43	0.00260	0.00121
	670	155	0.75	-24.9	47.4	0.02	0.23	0.00030	0.00034
	all	888	0.91	-9.0	20.7	0.89	0.94	0.00010	0.00226
TChla	55	1.39	38.9	61.1	0.68	0.61	-0.41214	0.60522	
	44	1.69	68.5	84.9	0.51	0.45	-0.66199	0.68610	
K_d	291	1.04	3.6	34.5	0.34	0.44	0.02681	0.02586	
	206	1.07	7.5	35.1	0.22	0.26	0.03339	0.02342	

Table 4. As in Table 2, but for MODIS-A Products

	λ	N	\bar{r}	RPD	RPD	r^2	m	y	RMSE
ρ_w	412	66	0.90	-10.1	21.4	0.59	0.84	0.00100	0.00418
	443	147	0.99	-1.5	15.7	0.55	0.75	0.00360	0.00298
	488	152	0.95	-4.7	11.8	0.48	0.64	0.00440	0.00218
	551	150	0.88	-12.4	17.0	0.39	0.71	0.00090	0.00116
	667	151	0.75	-24.5	42.5	0.01	0.10	0.00040	0.00031
	all	666	0.89	-10.7	21.7	0.91	0.93	0.00000	0.00226
	TChla	58	1.20	19.6	50.2	0.72	0.62	-0.49363	0.61499
31		1.21	20.7	40.9	0.82	0.77	-0.24622	0.42352	
K_d	286	1.11	11.4	33.8	0.47	0.53	0.02611	0.02232	
	159	1.10	9.6	37.2	0.24	0.31	0.03281	0.02316	

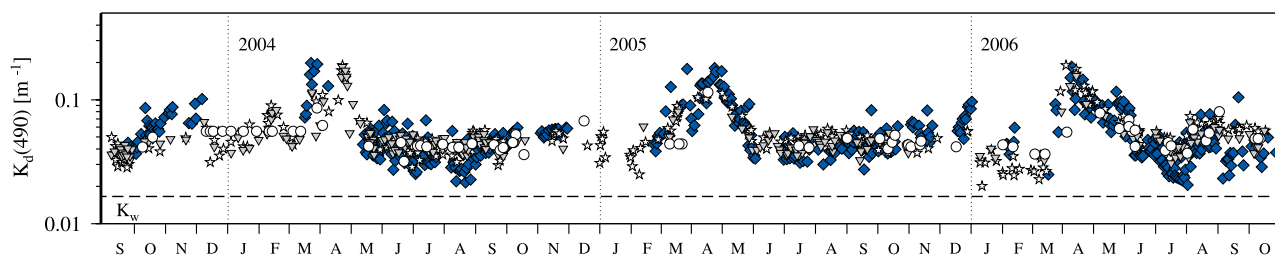


Figure 11. Three-year time series of $K_d(490)$ at the BOUSSOLE site, with buoy measurements taken from 1000 to 1400 (GMT) (blue diamonds), and MERIS, SeaWiFS, and MODIS-A-derived values (open circles, triangles, and stars, respectively). The pure water value is indicated by the dashed line.

obtained by two other similar efforts carried out at a coastal site [Zibordi *et al.*, 2006] and globally [Bailey and Werdell, 2006].

[77] The large noise in $\rho_w(412)$ indicates that atmospheric correction procedures must still be improved before a meaningful quantitative use of this band (and of bands at shorter wavelengths, e.g., 380 nm, which may equip future sensors) becomes possible. The improvement of the match-up statistics when examining reflectance ratios supports the use of band-ratio techniques to derive geophysical products, such as the chlorophyll concentration, in parallel to more sophisticated methods using all bands and the absolute values of reflectances [e.g., Chomko *et al.*, 2003; Schiller and Doerffer, 1999].

[78] The present results advocate for a major effort toward improving the atmospheric correction of ocean color observations, in particular to significantly decrease errors in the bluest bands, regardless of the mission. Research on atmospheric correction is currently focused primarily on solving difficulties in the coastal environment [e.g., Wang and Shi, 2005]. The results presented here and elsewhere [Zibordi *et al.*, 2006; Bailey and Werdell, 2006] show that issues still exist in open-ocean waters, even when aerosols are not absorbing.

[79] The comparison between the performances of the three sensors also advocates for a vicarious calibration of the MERIS observations. Vicarious calibration is a priori a mandatory process to meet the required accuracy of ocean color products. A variety of techniques exist [e.g., Barnes *et al.*, 2001; Eplee *et al.*, 2001; Martiny *et al.*, 2004], which are used, for example, with the SeaWiFS and MODIS-A missions, and which could advantageously be adapted and applied to MERIS. Efforts are presently devoted to improving as much as possible the atmospheric correction procedures for MERIS, which might eventually allow the required accuracy to be met without a vicarious calibration. In the converse situation, the unavoidable residual errors would be absorbed by a vicarious calibration, allowing the level of uncertainty to decrease to that of the other sensors. Such a situation would improve the ability to merge data from these three major missions. A better understanding of the respective roles of atmospheric correction and calibration uncertainties in forming the final uncertainty in the ocean color products would, however, require that space agencies keep nonvicariously calibrated TOA total reflectances available in parallel to the vicariously calibrated ones, at least over selected sites (e.g., the SIMBIOS Diagnostic Data Sites, [Bailey, 2003]).

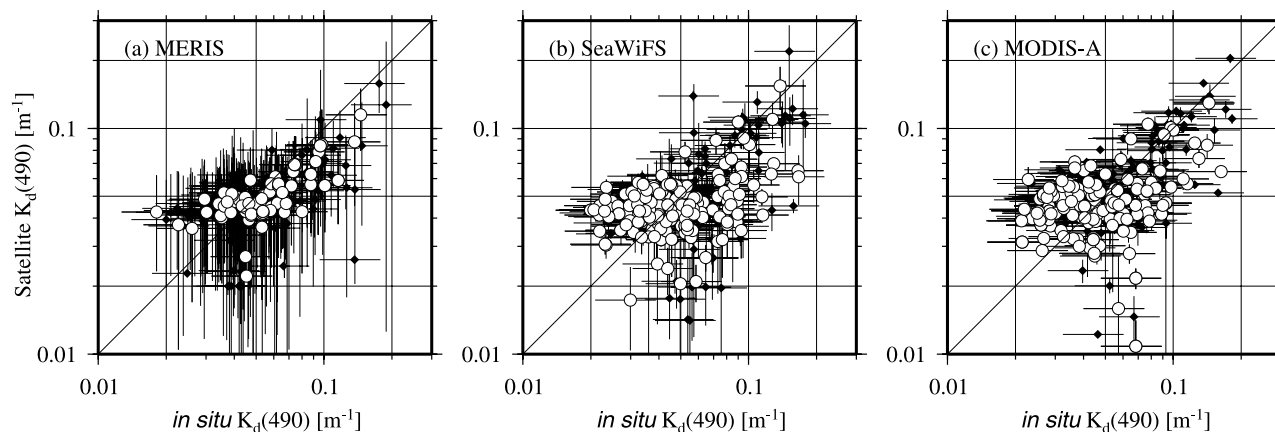


Figure 12. Scatter plots of satellite versus in situ $K_d(490)$ for (a) MERIS, (b) SeaWiFS, and (c) MODIS-A. The open circles are a subset built from the full set of possible match-ups (black diamonds) to which the match-up criteria were applied (see section 3.4). The uncertainty bar for a satellite value corresponds to one standard deviation within the 5×5 pixel box used to compute the average. The uncertainty bar for the in situ values is arbitrarily set to 30% of the average.

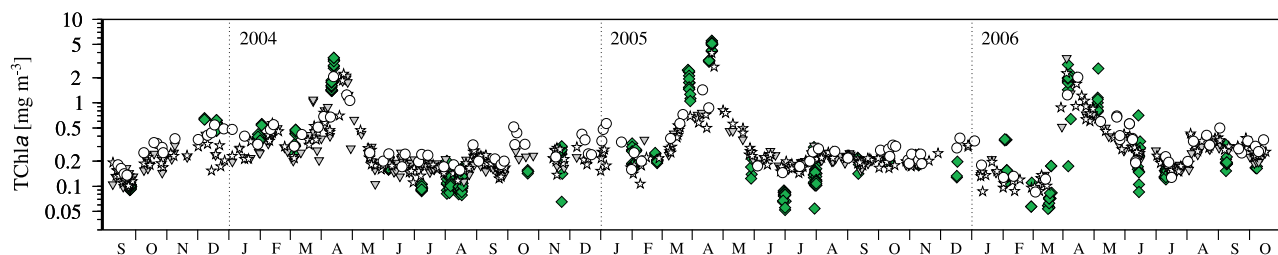


Figure 13. Three-year time series of TChla at the BOUSSOLE site, with field measurements (green diamonds), and MERIS, SeaWiFS, and MODIS-A-derived values (open circles, triangles, and stars, respectively).

[80] The results presented here also demonstrate that commercial off-the-shelf instrumentation can be used to provide high-quality radiometric data for validation purposes, as far as the measurement protocols and the deployment platform are adapted. This is tempering the usual feeling that moorings are prohibitively costly with providing a low-cost solution to the difficult problem of collecting large amounts of data in offshore environments. A permanent mooring like BOUSSOLE is also well adapted to maintain a consistent time series of in situ measurements over a long period of time. Ensuring the same level of consistency between equipment and protocols from different cruises inevitably adds some extra uncertainties in the data collection and processing. A permanent station is also well suited for developing and testing new instrumentation as well as new algorithms, and, therefore, to permanently improve the quality and the variety of products that can be derived from the ocean color observations. It is also a unique opportunity to establish the cross calibration between different sensors by anchoring them to the same in situ time series [IOCCG, 1999].

[81] Finally, it is worth noting that the data set assembled in the BOUSSOLE activity is not restricted to the radiometric measurements used in this study [see Antoine *et al.*,

2006]. It also facilitates validation of advanced ocean color products, such as inherent optical properties [IOCCG, 2006] or phytoplankton functional types [e.g., Alvain *et al.*, 2005]. This comprehensive data set is also useful for understanding the limitations or the causes of failure of the present atmospheric correction algorithms, and for a better understanding of bio-optics in Case-1 waters.

Appendix A: Near-Surface Extrapolation of L_u

[82] When extrapolating from an average depth of 4 m to the 0^- level using K_L as per equation (2), it is impossible to fully reproduce the curvature of the L_u profile just beneath the surface. Consequently, the value of $L_u(0^-)$ might be improperly determined, in particular for wavelengths greater than about 600 nm.

[83] The function on the right-hand side of equation (1) was introduced specifically to correct for this problem. It is based on the results of radiative transfer simulations using the Hydrolight code [Mobley, 1994], which is run using the parameterization of inherent optical properties as a function of the chlorophyll concentration described in Morel and Gentili [2004], also including the Raman effect. In the simulations, the water column is subdivided into 1-m

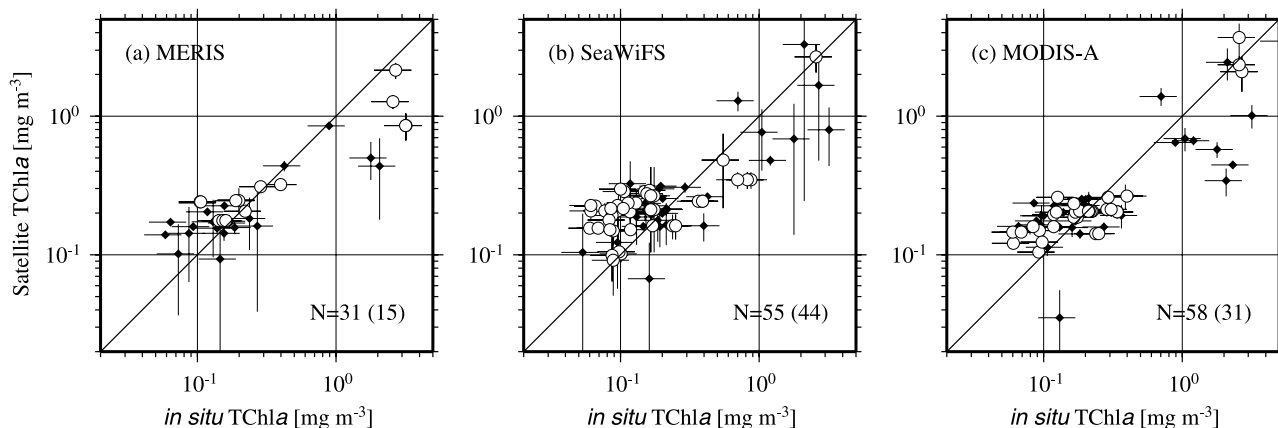


Figure 14. Scatter plots of satellite versus in situ chlorophyll concentration for (a) MERIS, (b) SeaWiFS, and (c) MODIS-A. The open circles are the subset from the full set of possible match-ups (black diamonds) to which the match-up criteria were applied (see section 3.4). The uncertainty bar for a satellite value corresponds to one standard deviation within the 5×5 pixel box used to compute the average. The uncertainty bar for the in situ value is arbitrarily set to 30% of the average.

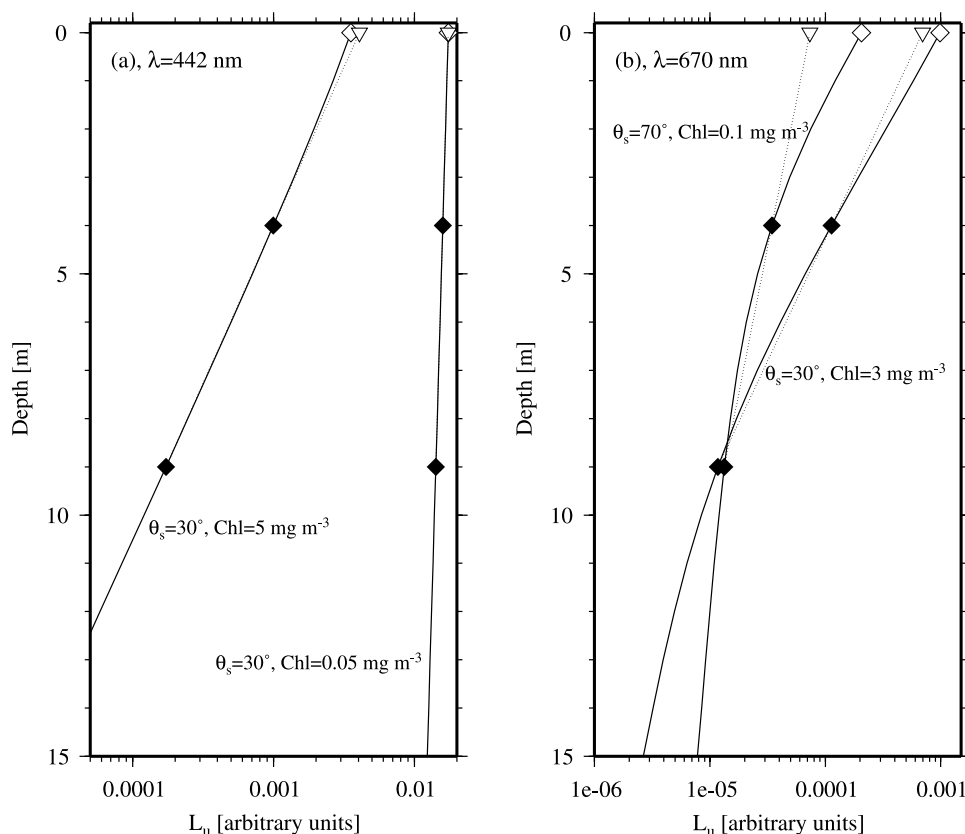


Figure A1. Typical vertical profiles of the upwelling radiance at nadir, L_u , for an arbitrary above-surface downward irradiance equal to 1, and for the sun zenith angle and chlorophyll concentration indicated on each panel. The solid curves are the results from the radiative transfer simulations (see Appendix A), and the dotted curves are the profiles reconstructed by extrapolating the value at 4 m using the K_L determined from the values at 4 and 9 m (black diamonds). The open diamonds are the $L_u(0^-)$ from the radiative transfer calculations and the open triangles are the extrapolated values of $L_u(0^-)$.

vertical bins from the surface down to 20 m, and then deeper layers have their lower boundaries at one fourth, one half and one time the depth of the 1% light level (when these levels are deeper than 20 m). The vertical profile of any radiometric quantity is, therefore, produced with a 1-m depth resolution near the surface (continuous curves in Figure A1), and can be compared to the profile that can be reconstructed from measurements at only two depths (dotted curves in Figure A1). The assumption here is that uncertainties in the radiative transfer computations might affect the absolute values and spectral shape of the computed radiometric quantities, but not or insignificantly the shape of the vertical L_u profiles. The other assumption is that the chlorophyll concentration is homogeneously distributed within the top 20 m, which is supported by the field observations. As expected, the curves in Figure A1 show that the extrapolation is close to perfect in the blue (Figure A1a), whereas it provides erroneous values in the red (Figure A1b).

[84] The correction applied in equation (1) is simply the ratio of $L_u(0^-)$ taken from the simulations (the “true” value) to $L_u(0^-)$ determined from the same simulations but using equations (1)–(2). Computations were tabulated for the seven wavelengths sampled by the buoy radiometers, for sun zenith angles in the range 20–80° in 20° increments, and for chlorophyll concentration equal to 0.05, 0.1, 0.3,

0.5, 1, 3, and 5 mg m^{-3} . Examples of the variability of the ratio of the extrapolated $L_u(0^-)$ to the “true” $L_u(0^-)$ are shown in Figure A2 for two wavelengths. For a given buoy measurement, the correction is interpolated from the tabulated values using the actual measurement depth, sun zenith angle, and chlorophyll concentration (for the latter see Appendix B).

[85] This correction is always less than 2% for the blue and green bands when $[\text{TChla}]$ is less than 0.5 mg m^{-3} , reaches about 5% for $[\text{TChla}]$ in the range 1–3 mg m^{-3} , and may be up to 15% for $[\text{TChla}]$ greater than 3 mg m^{-3} (Figure A2). There is almost no dependency on the sun zenith angle when its value is less than 60°. Considering the distribution of the chlorophyll concentration at the BOUSSE site (Figure 8), these numbers mean that the correction is within the radiometric noise except during phytoplankton blooms.

[86] For the red bands, however, the correction is at least 15%, and increases when the chlorophyll concentration decreases or the sun zenith angle increases, reaching values as high as 50%. It is worth noting that the same computations using an extrapolation depth of 2 m instead of 4, which is the situation when using a profiling radiometer, indicate a correction from 5 to 30%. This indicates that such a correction should be also applied when deriving radio-

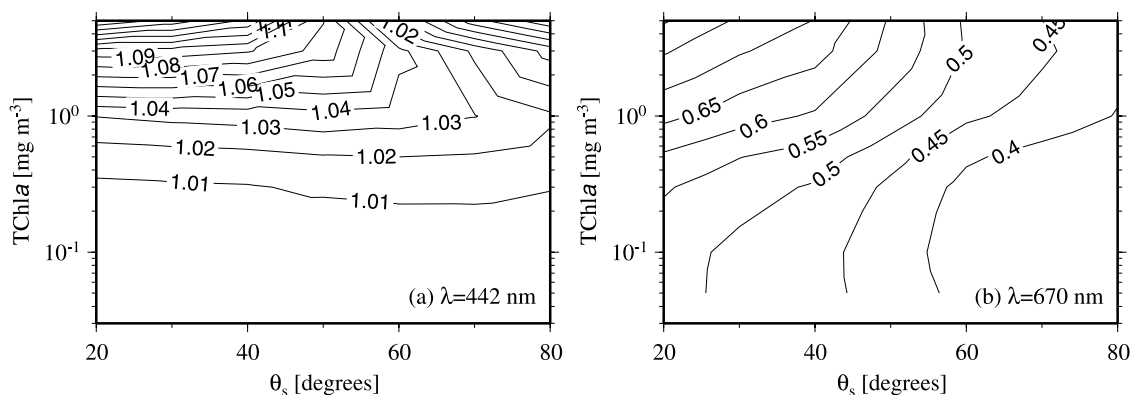


Figure A2. Contour plots of the ratio of $L_u(0^-)$ taken from the radiative transfer simulations described in Appendix A (the “true” value) to $L_u(0^-)$ determined from the results of the same simulations but using equations (1)–(2), in the chlorophyll–sun zenith angle space, and for the two wavelengths indicated.

metric quantities for wavelengths greater than about 600 nm at the “0” level from measurements collected at depths greater than 2 m by profiling instruments.

[87] The contours in Figure A2 also show a low sensitivity of the correction to the value of the chlorophyll concentration. In the blue domain, for instance, a 100% error in $[TChla]$ leads to an error less than 3% in the correction (less than 5% in the red).

Appendix B: Building a Continuous Record of Daily Chlorophyll Estimates

[88] The correction function in equation (1), which is described in Appendix A, must be applied to all buoy

measurements. One of its inputs is, however, only determined during the monthly cruises ($[TChla]$, section 3.3). A continuous record of average daily chlorophyll concentration at the mooring site was, therefore, generated, which combines the chlorophyll concentration determined from field samples (HPLC technique) and the chlorophyll product of ocean color satellite sensors. The idea is simply to use the HPLC-derived concentration to constrain (calibrate) a mean time series obtained from the satellite data.

[89] The method starts by pooling together the chlorophyll concentration taken from all valid observations by SeaWiFS, MODIS-A or MERIS to generate a composite time series. In this series, the average concentration from a given sensor and a given day is computed using all cloud-

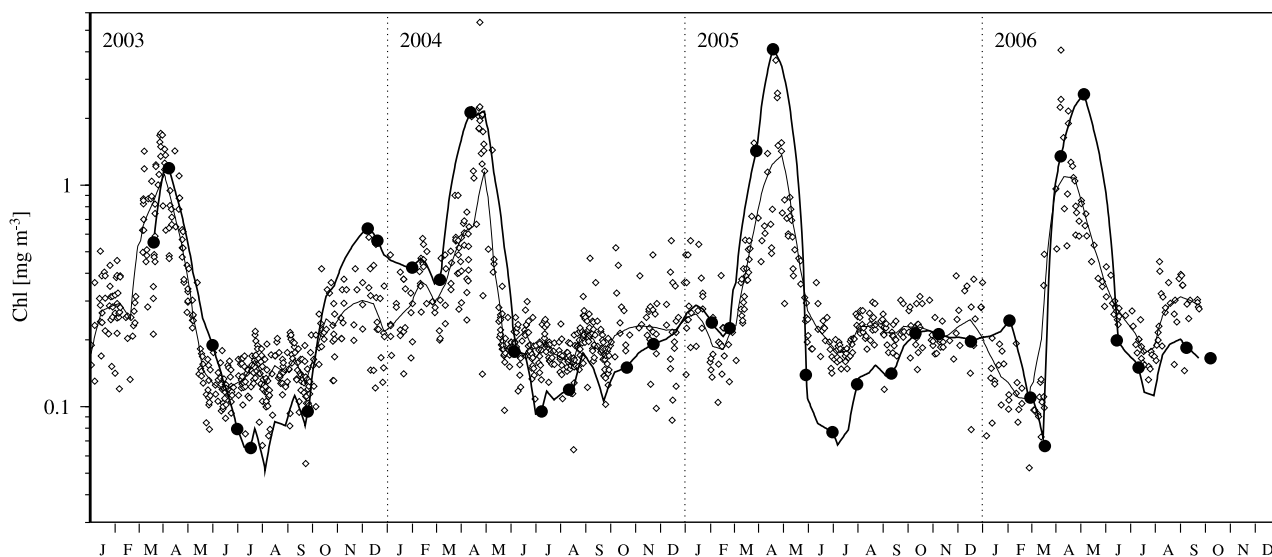


Figure B1. Seasonal cycles of the surface chlorophyll concentration at the BOUSSOLE site. The black circles are the average surface (<10 m) values determined from all field samples collected during each of the monthly servicing cruise. The open diamonds are all valid satellite chlorophyll determinations (from MERIS, SeaWiFS, and MODIS-A; see Appendix B). The thin curve is a fit to these satellite data, and the thick curve is obtained by constraining the interpolation between the monthly field values with the time changes derived from the fit to the satellite values (i.e., adjusting the thin curve to the field values).

free and glint-free pixels within a 3×3 box centered on the mooring position (open diamonds in Figure B1). A function is then fitted to the satellite time series, which describes the temporal change of the surface chlorophyll concentration (thin line in Figure B1). The final time series at a daily scale (thick line in Figure B1) is constructed by constraining the function using the field measurements, which are kept unchanged for the cruises days.

[90] This method was preferred over a simple linear interpolation between the monthly field measurements. It is not claimed to provide highly accurate values, but simply a reasonable estimate that can be used in equation (1).

[91] **Acknowledgments.** The BOUSSOLE project was set up thanks to the support and funding of several agencies and academic or governmental institutions, i.e., the *Centre National de la Recherche Scientifique* (CNRS) for permanent staff, the *Institut National des Sciences de l'Univers* (INSU) for ship time for the monthly cruises, and the *Observatoire Océanologique de Villefranche* (OOV) for logistic support. Financial support of the project comes from the French space agency “*Centre National d'Etudes Spatiales*” (CNES), from the European Space Agency (ESA) through the *European Space Research and Technology Center* (ESTEC) contract 14393/00/NL/DC and the ESRIN contract 17286/03/I-OL, and from the *US National Aeronautics and Space Administration* (NASA) through a Letter of Agreement with the *Université Pierre et Marie Curie* (UPMC), which allowed direct funding of the project as well as procurement of instrumentation. The captains and crews of the *Castor-02* vessel (*Foselev Marine* company; mooring operations), of the INSU R/V *Tethys-II* (monthly cruises), and of the *GG-IX* (*Samar* company; on-demand day operations on site), are also warmly thanked for their help at sea. We also thank one anonymous reviewer and Giuseppe Zibordi for their detailed and constructive comments that greatly helped improve the manuscript.

[93] This paper is dedicated to the memory of one of our coauthors, Dominique Tailliez, who died on 26 March 2008. He was a colleague and friend for over 20 years. He has unremittingly participated to all BOUSSOLE cruises, during which he was in charge of the hydrology casts (CTD and inherent optical properties), rosette sampling and water filtrations. He brought an invaluable contribution to the project.

References

- Alvain, S., C. Moulin, Y. Dandonneau, and F.-M. Bréon (2005), Remote sensing of phytoplankton groups in case 1 waters from global SeaWiFS imagery, *Deep Sea Res. I*, 52, 1989–2004.
- Antoine, D., and A. Morel (1999), A multiple scattering algorithm for atmospheric correction of remotely-sensed ocean colour (MERIS instrument): Principle and implementation for atmospheres carrying various aerosols including absorbing ones, *Int. J. Remote Sens.*, 20, 1875–1916.
- Antoine, D., J. M. André, and A. Morel (1996), Oceanic primary production. II: Estimation at global scale from satellite (Coastal Zone Color Scanner) chlorophyll, *Global Biogeochem. Cycles*, 10, 57–69.
- Antoine, D., et al. (2006), BOUSSOLE: A joint CNRS-INSU, ESA, CNES and NASA ocean color calibration and validation activity, *NASA Tech. Memo. 2006 – 214147*, 59 pp., NASA GSFC, Greenbelt, Md.
- Antoine, D., P. Guevel, J.-F. Desté, G. Bécu, F. Louis, A. J. Scott, and P. Bardey (2008), The «BOUSSOLE» buoy A new transparent-to-swell taut mooring dedicated to marine optics: Design, tests and performance at sea, *J. Atmos. Ocean. Technol.*, 25(6), 968–989.
- Austin, R. W. (1974), The remote sensing of spectral radiance from below the ocean surface, in *Optical Aspects of Oceanography*, edited by N. G. Jerlov and E. Steemann-Nielsen, pp. 317–344, Elsevier, New York.
- Bailey, S. W. (2003), Diagnostic Data Set, in *MODIS Validation, Data Merger and Other Activities Accomplished by the SIMBIOS Project: 2002–2003*, chap. 4, NASA Tech. Memo., August, 76 pp., NASA GSFC, Greenbelt, Md.
- Bailey, S. W., and P. J. Werdell (2006), A multi-sensor approach for the on-orbit validation of ocean color satellite data products, *Remote Sens. Environ.*, 102, 12–23.
- Barnes, R. A., R. E. Eplee Jr., G. M. Schmidt, F. S. Patt, and C. R. McClain (2001), Calibration of SeaWiFS. I. Direct techniques, *Appl. Opt.*, 40, 6682–6700.
- Berthon, J.-F., G. Zibordi, J. P. Doyle, S. Grossi, D. van der Linde, and C. Targa (2002), Coastal atmosphere and sea time series (CoASTS), Part 2: Data Analysis, *NASA Tech. Memo. 2002–206892*, vol. 20, edited by S. B. Hooker and E. R. Firestone, 25 pp., NASA Goddard Space Flight Center, Greenbelt, Md.
- Bricaud, A., E. Bosc, and D. Antoine (2002), Algal biomass and sea surface temperature in the Mediterranean basin: Intercomparison of data from various satellite sensors, and implications for primary production estimates, *Remote Sens. Environ.*, 81, 163–178.
- Campbell, J. W. (1995), The lognormal distribution as a model for biological variability in the sea, *J. Geophys. Res.*, 100, 13,237–13,254.
- Chauhan, P., M. Mohan, R. K. Sarangi, B. Kumari, S. Nayak, and S. G. P. Matondkar (2002), Surface chlorophyll a estimation in the Arabian Sea using IRS-P4 Ocean Colour Monitor (OCM) satellite data, *Intl. J. Remote Sens.*, 23, 1663–1676.
- Chomko, R. M., H. R. Gordon, S. Maritorena, and D. A. Siegel (2003), Simultaneous retrieval of oceanic and atmospheric parameters for ocean color imagery by spectral optimization: A validation, *Remote Sens. Environ.*, 84, 208–220.
- Clark, D. K., H. R. Gordon, K. J. Voss, Y. Ge, W. Broenkow, and C. Trees (1997), Validation of atmospheric correction over the oceans, *J. Geophys. Res.*, 102D, 17,209–17,217.
- Clark, D. K., M. A. Yarbrough, M. Feinholz, S. Flora, W. Broenkow, Y. S. Kim, B. C. Johnson, S. W. Brown, M. Yuen, and J. L. Mueller (2003), MOBY, a radiometric buoy for performance monitoring and vicarious calibration of satellite ocean color sensors: measurement and data analysis protocols, in *Ocean Optics Protocols for Satellite Ocean Color Sensor Validation, NASA Tech. Memo. 2003 – 211621/Rev4*, vol. VI, edited by J. L. Mueller, G. S. Fargion, and C. R. McClain, 139 pp., NASA GSFC, Greenbelt, Md.
- Claustre, H., A. Morel, S. B. Hooker, M. Babin, D. Antoine, K. Oubelkheir, A. Bricaud, K. Leblanc, B. Quéguiner, and S. Maritorena (2002), Is desert dust making oligotrophic waters greener?, *Geophys. Res. Lett.*, 29(10), 1469, doi:10.1029/2001GL014056.
- D'Ortenzio, F., S. Marullo, M. Ragni, M. R. d'Alcalá, and R. Santoleri (2002), Validation of empirical SeaWiFS chlorophyll-a algorithms retrieval in the Mediterranean Sea: A case study for oligotrophic seas, *Remote Sens. Environ.*, 82, 79–94.
- Drinkwater, M. R., et al. (2005), The roadmap for a GMES operational oceanography mission, *ESA Bull.*, 124, 43–48.
- Eplee, R. E., J. W. D. Robinson, S. W. Bailey, D. K. Clark, P. J. Werdell, M. Wang, R. A. Barnes, and C. R. McClain (2001), Calibration of SeaWiFS. II: Vicarious techniques, *Appl. Opt.*, 40, 6701–6718.
- Esaias, W. E., et al. (1998), An overview of MODIS capabilities for ocean science observations, *IEEE Trans. Geosci. Remote Sens.*, 36, 1250–1265.
- Franz, B. A., S. W. Bailey, P. J. Werdell, and C. R. McClain (2007), Sensor-independent approach to the vicarious calibration of satellite ocean color radiometry, *Appl. Opt.*, 46, 5068–5082.
- Gasparini, G. P., G. Zodiatis, M. Astraldi, C. Galli, and S. Sparnocchia (1999), Winter intermediate water lenses in the Ligurian Sea, *J. Mar. Syst.*, 20, 319–332.
- Gordon, H. R. (1997), Atmospheric correction of ocean color imagery in the Earth observing system era, *J. Geophys. Res.*, 102, 17,081–17,106.
- Gordon, H. R. (1998), In-orbit calibration strategy for ocean color sensors, *Remote Sens. Environ.*, 63, 265–278.
- Gordon, H., and R. Ding (1992), Self-shading of in-water optical instruments, *Limnol. Oceanogr.*, 37, 491–500.
- Gregg, W. W., and K. L. Carder (1990), A simple spectral solar irradiance model for cloudless maritime atmospheres, *Limnol. Oceanogr.*, 35, 1657–1675.
- Holben, B. N., et al. (1998), AERONET - A federated instrument network and data archive for aerosol characterization, *Remote Sens. Environ.*, 66, 1–16.
- Hooker, S. B., and W. E. Esaias (1993), An overview of the SeaWiFS Project, *Eos Trans. AGU*, 74, 241–246.
- Hooker, S. B., and G. Zibordi (2005), Platform perturbations in above-water radiometry, *Appl. Opt.*, 44, 553–567.
- Hooker, S. B., W. E. Esaias, G. C. Feldman, W. W. Gregg, and Mc C. R. Clain (1992), An overview of SeaWiFS and ocean colour, in *SeaWiFS Technical Report Series*, edited by S. B. Hooker and E. R. Firestone, *NASA Tech. Memo. 104566*, NASA Goddard Space Flight Centre, Greenbelt, Md.
- Hooker, S. B., S. McLean, J. Sherman, M. Small, G. Lazin, G. Zibordi, and J. W. Brown (2002), *The Seventh SeaWiFS Intercalibration Round-Robin Experiment (SIRREX-7)*, March 1999. *NASA Tech. Memo. 2002-206892*, vol. 17, edited by S. B. Hooker and E. R. Firestone, 69 pp., NASA Goddard Space Flight Center, Greenbelt, Md.
- Hooker, S. B., G. Zibordi, J.-F. Berthon, and J. W. Brown (2004), Above-water radiometry in shallow, coastal waters, *Appl. Opt.*, 43, 4,254–4,268.
- IOCCG (1999), *Status and Plans for Satellite Ocean-Colour Missions: Considerations for Complementary Missions*, edited by J. A. Yoder, Reports of the International Ocean-Colour Coordinating Group, No. 2, IOCCG, Dartmouth, Canada.

- IOCCG (2006), *Remote Sensing of Inherent Optical Properties: Fundamentals, Tests of Algorithms, and Applications*, edited by Z. Lee, Reports of the International Ocean-Colour Coordinating Group, No. 5, IOCCG, Dartmouth, Canada.
- Jamet, C., C. Moulin, and S. Thiria (2004), Monitoring aerosol optical properties over the Mediterranean from SeaWiFS images using a neural network inversion, *Geophys. Res. Lett.*, *31*, L13107, doi:10.1029/2004GL019951.
- Marty, J. C. (2002), Preface to volume 49 number 11: DYFAMED time-series program (France JGOFS), *Deep Sea Res. II*, *49/11*, 1963–1964.
- Marty, J. C., J. Chiavérini, M. D. Pizay, and B. Avril (2002), Seasonal and interannual dynamics of phytoplankton pigments in the Western Mediterranean sea at the DYFAMED time-series station (1991–1999), *Deep Sea Res. II*, *49*, 1965–1985.
- Martiny, N., R. Santer, and R. Frouin (2004), In-orbits calibration of SeaWiFS in the near infrared, *SPIE Proc.*, *5234*, 445–455.
- McClain, C. R., W. E. Esaias, W. Barnes, B. Guenther, D. Endres, S. Hooker, G. Mitchell, and R. Barnes (1992), Calibration and Validation Plan for SeaWiFS, in *NASA Tech. Memo. 104566*, vol. 3, edited by S. B. Hooker and E. R. Firestone, 41 pp., NASA Goddard Space Flight Center, Greenbelt, Md.
- McClain, C. R., S. B. Hooker, G. C. Feldman, and P. Bontempi (2006), Satellite data for ocean biology, biogeochemistry and climate research, *Eos Trans. AGU*, *87*, 337–343.
- Millot, C. (1999), Circulation in the western Mediterranean Sea, *J. Mar. Syst.*, *20*, 423–442.
- Mobley, C. (1994), *Light and Water: Radiative Transfer in Natural Waters*, 579 pp., Elsevier, San Diego, Calif.
- Morel, A., and D. Antoine (1999), European space agency ENVISAT-MERIS algorithm theoretical basis document 2.9, Pigment index retrieval in Case 1 waters, PO-TN-MEL-GS-0005, 25 pp., European Space Agency, ESRIN, Frascati, Italy.
- Morel, A., D. Antoine, and B. Gentili (2002), Bidirectional reflectance of oceanic waters: Accounting for Raman emission and varying particle phase function, *Appl. Opt.*, *41*, 6289–6306.
- Morel, A., and S. Bélanger (2006), Improved detection of turbid waters from ocean color information, *Remote Sens. Environ.*, *102*, 237–249.
- Morel, A., and B. Gentili (1996), Diffuse reflectance of oceanic waters. III: Implication of bidirectionality for the remote-sensing problem, *Appl. Opt.*, *35*, 4850–4862.
- Morel, A., and B. Gentili (2004), Radiation transport within oceanic (case 1) waters, *J. Geophys. Res.*, *109*, C06008, doi:10.1029/2003JC002259.
- Morel, A., and S. Maritorena (2001), Bio-optical properties of oceanic waters: A reappraisal, *J. Geophys. Res.*, *106*, 7163–7180.
- Morel, A., and L. Prieur (1977), Analysis of variations in ocean color, *Limnol. Oceanogr.*, *22*, 709–722.
- Morel, A., Y. Huot, B. Gentili, P. J. Werdell, S. B. Hooker, and B. A. Franz (2007), Examining the consistency of products derived from various ocean color sensors in open ocean (Case 1) waters in the perspective of a multi-sensor approach, *Remote Sens. Environ.*, *111*, 69–88.
- Mueller, J. L., R. W. Austin, A. Morel, G. S. Fargion, and C. R. McClain (2003a), Ocean optics protocols for satellite ocean color sensor validation, Revision 4, Volume 1: Introduction, background, and conventions, in *NASA Tech. Memo. 2003 – 211621/Rev4*, vol. I, edited by J. L. Mueller, G. S. Fargion, and C. R. McClain, 50 pp., NASA GSFC, Greenbelt, Md.
- Mueller, J. L., C. Pietras, S. B. Hooker, R. W. Austin, M. Miller, K. D. Knobelspiesse, R. Frouin, B. Holben, and K. Voss (2003b), Ocean optics protocols for satellite ocean color sensor validation, Revision 4, Volume 2: Instrument specifications, characterization, and calibration, in *NASA Tech. Memo. 2003 – 211621/Rev4*, vol. II, edited by J. L. Mueller, G. S. Fargion, and C. R. McClain, 56 pp., NASA GSFC, Greenbelt, Md.
- Mueller, J. L., R. R. Bidigare, C. Trees, W. M. Balch, J. Dore, D. T. Drapeau, D. Karl, L. Van Heukelem, and J. Perl (2003c), Ocean optics protocols for satellite ocean color sensor validation, Revision 5, Volume 5: Biogeochemical and bio-optical measurements and data analysis protocols, in *NASA Tech. Memo. 2003 – 211621/Rev5*, vol. V, edited by J. L. Mueller, G. S. Fargion, and C. R. McClain, 36 pp., NASA GSFC, Greenbelt, Md.
- Murphy, R. E., P. Ardanuy, F. J. DeLuccia, J. E. Clement, and C. F. Schueller (2006), The Visible Infrared Imaging Radiometer (VIIRS), in *Earth Science Satellite Remote Sensing*, edited by J. J. Qu et al., pp. 199–223, Springer and Tsinghua Univ. Press.
- O'Reilly, J. E., S. Maritorena, G. Mitchell, D. A. Siegel, K. L. Carder, D. L. Garver, M. Kahru, and C. R. McClain (1998), Ocean color chlorophyll algorithms for SeaWiFS, *J. Geophys. Res.*, *103*, 24,937–24,950.
- O'Reilly, J. E., et al. (2000), SeaWiFS postlaunch calibration and validation analyses, Part 3, in *NASA Tech. Memo. 2000-206892*, vol. 11, edited by S. B. Hooker and E. R. Firestone, 49 pp., NASA Goddard Space Flight Center, Greenbelt, Md.
- Pegau, S., J. R. V. Zaneveld, B. G. Mitchell, J. L. Mueller, M. Kahru, J. Wieland, and M. Stramska (2003), Ocean optics protocols for satellite ocean color sensor validation, Revision 4, Volume IV: Inherent optical properties: instruments, characterizations, field measurements and data analysis protocols, *NASA Tech. Memo. 2003 – 211621/Rev4*, vol. IV, edited by J. L. Mueller, G. S. Fargion, and C. R. McClain, 76 pp., NASA GSFC, Greenbelt, Md.
- Rast, M., J. L. Bézy, and S. Bruzzi (1999), The ESA Medium Resolution Imaging Spectrometer MERIS – A review of the instrument and its mission, *Int. J. Remote Sens.*, *20*, 1681–1702.
- Rossov, W. B., and R. A. Schiffer (1989), Advances in understanding clouds from ISCCP, *Bull. Am. Meteorol. Soc.*, *80*, 2261–2288.
- Salomonson, V. V., D. L. Toll, and W. T. Lawrence (1992), Moderate resolution imaging spectroradiometer (MODIS) and observations of the land surface, in *Proc. Int. Geoscience and Remote Sensing Symp. (IGARSS'92)*, pp. 549–551, Houston, Texas.
- Schiller, H., and R. Doerffer (1999), Neural network for emulation of an inverse model — Operational derivation of Case II water properties from MERIS data, *Int. J. Remote Sens.*, *20*, 1735–1746.
- Shettle, E. P., and R. W. Fenn (1979), Models for the aerosols of the lower atmosphere and the effects of humidity variations on their optical properties, *Environmental Research Papers*, No. 676, AFGL-TR-79-0214, 31 pp., Air Force Geophys. Lab., Hanscom AFB, Mass.
- Voss, K., A. Morel, and D. Antoine (2007), Detailed validation of the bidirectional effect in various Case 1 waters for application to Ocean Color imagery, *Biogeosciences*, *4*, 781–789.
- Wang, M., and W. Shi (2005), Estimation of ocean contribution at the MODIS near-infrared wavelengths along the east coast of the US.: Two case studies, *Geophys. Res. Lett.*, *32*, L13606, doi:10.1029/2005GL022917.
- Werdell, P. J. (2005), OceanColor K490 algorithm evaluation, http://oceancolor.gsfc.nasa.gov/REPROCESSING/SeaWiFS/R5.1/k490_update.html.
- Werdell, P. J., and S. W. Bailey (2005), An improved in-situ bio-optical data set for ocean color algorithm development and satellite data product validation, *Remote Sens. Environ.*, *98*, 122–140.
- Yong, S.-S., H.-S. Shim, H.-P. Heo, Y.-M. Cho, K.-H. Oh, S.-H. Woo, and H.-Y. Paik (1999), The ground checkout test of OSMI on KOMPSAT-1, *J. Korean Soc. Remote Sens.*, *15*, 297–305.
- Zibordi, G., and G. M. Ferrari (1995), Instrument self-shading in underwater optical measurements: Experimental data, *Appl. Opt.*, *34*, 2750–2754.
- Zibordi, G., J.-F. Berthon, J. P. Doyle, S. Grossi, D. van der Linde, C. Targa, and L. Alberotanza (2002), Coastal Atmosphere and Sea Time Series (CoASTS), Part 1: A Tower-Based Long-Term Measurement Program, in *NASA Tech. Memo. 2002–206892*, vol. 19, edited by S. B. Hooker and E. R. Firestone, 29 pp., NASA Goddard Space Flight Center, Greenbelt, Md.
- Zibordi, G., F. Mélin, and J.-F. Berthon (2006), Comparison of SeaWiFS, MODIS and MERIS radiometric products at a coastal site, *Geophys. Res. Lett.*, *33*, L06617, doi:10.1029/2006GL025778.

D. Antoine, F. d'Ortenzio, and B. Gentili, CNRS, UMR 7093, Laboratoire d'Océanographie de Villefranche, Caserne Nicolas, Quai de la Darse, BP 8, 06238 Villefranche sur mer, France. (antoine@obs-villefr.fr)
 G. Bécu, GEMS Survey Ltd., Devizes, Wiltshire, UK.
 S. B. Hooker, NASA/GSFC/Code 614.8, Greenbelt, MD 20771, USA.
 A. J. Scott, Fugro GEOS Ltd., Wallingford, Oxfordshire, UK.